UNIVERSIDAD DE CHILE
FACULTAD DE CIENCIAS FÍSICAS Y MATEMÁTICAS
ESCUELA DE POSTGRADO Y EDUCACIÓN CONTINUA

EXPERIMENTAL AND NUMERICAL STUDY OF UNDULAR BORE GENERATION, PROPAGATION, AND INTERACTION WITH A SEMI-SUBMERGED VERTICAL SQUARE CYLINDER

TESIS PARA OPTAR AL GRADO DE DOCTOR EN CIENCIAS DE LA INGENIERÍA, MENCIÓN FLUIDODINÁMICA

CHARLIE BARRAUD

PROFESOR GUÍA:
Rodrigo Hernández Pellicer

MIEMBROS DE LA COMISIÓN:
Claudio Falcón Beas
Gonzalo Tampier Brockhaus
Benjamin Herrmann Priesnitz
Wernher Brevis Vergara

SANTIAGO DE CHILE
2022

RESUMEN DE LA MEMORIA PARA OPTAR
AL TÍTULO DE DOCTOR EN CIENCIAS
DE LA INGENIERÍA, MENCIÓN FLUIDODINÁMICA
POR: **CHARLIE BARRAUD**
FECHA: 2022
PROF. GUÍA: Rodrigo Hernández P.

ESTUDIO EXPERIMENTAL DE LA GENERACIÓN, PROPAGACIÓN Y INTERACCIÓN DE UN MACAREO ONDULAR CON UN CILINDRO CUADRADO VERTICAL Y SEMISUMERGIDO

Los macareos pueden describirse como una transición rápida entre dos profundidades de flujo y suelen estar causados por las fuerzas de las mareas, pero también pueden ser consecuencia de terremotos, deslizamientos de tierra o roturas de represas y diques. Un tipo especial de macareo es el macareo ondular, que muestra una ola inicial seguida de un tren de ondas infinito de amplitudes más pequeñas que convergen a un nivel de agua constante y que se consideran una buena descripción de las olas de los tsunamis.

En este trabajo, se estudia la respuesta dinámica de un generador tipo pistón en un tanque de olas numérico. Las ecuaciones bidimensionales de Navier-Stokes se resuelven en una configuración de flujo bifásico. La respuesta a un escalón de velocidad son ondas similares a las de un macareo ondular que se propagan a lo largo del tanque. Se implementa una estrategia de absorción activa basada en un controlador retroalimentado que acciona un pistón secundario y se logra con éxito la absorción de ondas tanto en ondas regulares como irregulares.

Luego, se llevan a cabo cinco pruebas experimentales y una simulación numérica completa en 3D para estudiar el desprendimiento de vórtices inducido por las olas alrededor de un cilindro cuadrado vertical para el caso particular del macareo ondular. El macareo ondular interactúa con el cilindro cuadrado, se forman estructuras coherentes en sus cuatro bordes que son gatilladas por el movimiento de las olas. En cuanto a los vórtices que se sitúan en la cara posterior del cilindro, son principalmente verticales, atraviesan toda la columna de agua desde la superficie libre hasta el fondo marino, y se observa el emparejamiento de los dos vórtices. Finalmente, se observa la inestabilidad de esos vórtices y se interpreta como la inestabilidad de Crow.

Palabras clave: formación de olas, absorción de olas, macareo ondular, interacción ola-estructura, desprendimiento de vórtices, emparejamiento de vórtices.

EXPERIMENTAL AND NUMERICAL STUDY OF UNDULAR BORE GENERATION, PROPAGATION, AND INTERACTION WITH A SEMI-SUBMERGED VERTICAL SQUARE CYLINDER

Bores can be described as a quick transition between two flow depths and are usually caused by tidal forces but can also be the consequence of earthquakes, landslides, or dam and dike breaks. A special type of bore is the undular bore, which shows an initial wave followed by an infinite wave train of smaller waves converging to a constant water level and are now considered to be a good description of tsunami waves.

In this work, undular bore generation is carried out through the kinematic and dynamic characterization of an impulsive piston wavemaker. Then, the undular bore propagation along a wave tank and interaction with a vertical square cylinder is studied to identify, describe, and quantify the vortex generation and further self organization of vorticity at its edges.

We first study the dynamical response of a piston-type wavemaker in a numerical wave tank. Two-dimensional unsteady Navier-Stokes equations are solved on a two phase flow configuration using the volume of fluid method to capture the free surface dynamics. The wavemaker is a moving wall driven by an arbitrary signal waveform. The step response of the wavemaker generates pulse-like waves similar to an undular bore propagating along the tank. An active absorption strategy based upon a feedback controller driving a secondary piston is implemented and wave absorption is successfully achieved on regular as well as irregular waves.

Then, five experimental test cases and a full 3D numerical simulation are carried out to study the wave-induced vortex shedding around a vertical square cylinder for the particular case of the undular bore. As the undular bore interacts with the square cylinder, coherent structures form at its four edges and are triggered by the wave motion. As for the vortices which are situated at the rear face of the cylinder, they are mainly vertical, cross the entire water column from the free-surface to the seabed, and the pairing of the two vortices is observed. We are also able to show that the rear vortices become unstable in a similar way as the instability of Crow, leading to strong deformations. The circulation of the vortex pair is computed through the use of two methods, and it is shown that using a Lamb-Oseen vortex pair velocity fit gives a precise estimation. The dimensionless circulation is expressed as a function of the Froude number and the numerical simulation is validated. Finally, the seabed shear forces are measured which allows to describe the eventual scouring happening in the wake of the pile.

Keywords: wavemaking, wave absorption, undular bore, wave-structure interaction, vortex shedding, vortex pairing

To Priscila,
and to my family.

Acknowledgements

I would like to dedicate my first acknowledgement to my tutor, Rodrigo Hernández, whose guidance and encouragement have been most valuable throughout my PhD studies. This adventure actually started in 2013 with a short internship but I knew I could return to Chile for more. Rodrigo trusted me with the freedom which allowed me to to develop the themes I found most interesting and, at the same time, dedicated time to discuss and overview every stage of this thesis. I am grateful for his patience, despite my stubbornness, about my work, the numerous helpful advice and the great moments shared in the laboratory. I am also extremely grateful to my beloved Priscila who showed important support, specially in moments of doubts, tolerated my thesis obsession, made me grow as a human being and allowed me to enjoy my Chilean new life. I would also like to thank my family, parents, brother and sister for all the moral and financial assistance during my decade long studies at University. I would also like to thanks my good Chilean and French friends Étienne, Hortense, Pierre, Alix, Lucero, Jennifer, Fernando, Cesar,... who always helped to make my stay feel like home. My thoughts also go to my comrades at Universidad de Chile, Belén, Cristobal, Maximo, Christian, etc. for the important learning sessions either in a laboratory or solving the boundary layer equations, and all the others: Sebastian, Maheer, Felipe, Alejandra, Jonathan, Eric, etc. all good friends of the cuarto piso. A special thanks for Joseph who was always of good company during lunch. You showed me kindness and were always ready to help in any manner. I would also like to mention Matias who was my first fun office mate and Natalia who was of great assistance for the final part of the thesis, in particular the scouring analysis. I am also grateful to the Mechanical Engineering Department at Universidad de Chile for the financial support and to all staff members who helped me with administrative problems. In particular, I would like to thank Monica for her great reactivity, pro-activity and anticipation. I would also like to thank the LEAF-NL laboratory for the use of the computing cluster and experimental facilities. This work was funded by the National Agency for Research and Development (ANID)/Scholarship Program/Doctorado Nacional/2016–21160553 and (ANID)FONDEQUIP EQM 190029. This research was partially supported by the supercomputing infrastructure of the NLHPC (ECM-02). I am very thankful to the IT specialists who were always available to help and with a high reactivity. I am also grateful to the Marine Energy Research & Innovation Center (MERIC) and the Universidad Austral in Valdivia for organizing, hosting and sharing marine engineering related activities.

Table of Content

Index of Figures

Index of Tables

Part I

Introduction, objectives and problem statement

Chapter 1

Introduction

1.1. Motivations

In the world, one billion inhabitants live in low-lying coastal regions. Developing more resilient coastal communities is essential and implies to generate the knowledge about wave interaction with structures. These interactions, which can result from tides, storms or tsunami events, will induce forces that might be disastrous for the communities, with possibly the destruction or displacement of buildings, vessels in ports, scouring, etc. Many offshore and near-shore infrastructures are made of slender bodies, cylinders, such as offshore wind turbines, or bridge piles. These structures and substructures are often mono-piles or designs combining various cylinders (i.e. jackets). However, if circular piles are the most common design, others such as square based design also exist, as shown in figure 1.1, and it is important to also consider them, as the physics might be quite different from the common circular cylindrical column.

While numerous studies can be found for current structure interaction with vertical circular cylinders (Nishioka & Sato, 1978; Sarpkaya, 1986; Provansal et al., 1987; Longoria et al., 1991; Cheng et al., 2007), for impulsively started cylinder (Koumoutsakos & Leonard, 1995), for wave structure interaction with circular cylinder (Reid, 1957; Ishida & Iwagaki, 1978; Bihs et al., 2017) or the wave generation from impulsively moved horizontal cylinders (Tyvand & Miloh, 1995), it is not the case for wave structure interaction with square cylinder. At the authors' knowledge, only few studies were published about this topic and could be found: Arabi et al. (2019) experimentally and numerically studied the interaction between solitary waves and a square based impervious structure, showing the generation of vertical vortices at the four edges of the cylinder which extended from the free-surface to the seabed, Bremm et al. (2015) experimentally studied the interaction between depression led long waves and a square cylinder on a sloping beach, basing their geometrical configuration on a real tsunami event and measuring both the flow field and the forces on the square cylinder and Shafiei et

al. (2016) experimentally studied the interaction between a square prism and a bore under different incident angles, for bores propagating on a dry bed, and in a tank equipped with an automatic gate for the bore generation. Finally, P. Lin & Li (2003) simulated the interaction between a vertical cylinder and a combination of wave and current. They showed that the strength of the vortices is significantly reduced by the presence of the waves and the shedding frequency is correlated to the free-surface elevation.

(a)

(b)

Figure 1.1: Examples of vertical square cylinder. (a) View from the shore of the western end of the main span of the Courtney Campbell Causeway, Florida. (b) Na Kika offshore platform in the Gulf of Mexico.

Numerous studies also focused on the interaction with harmonic or solitary waves, but few tried to make the wave more realistic to real hazardous natural events (tsunamis) and thus bores and N-waves are still to be extensively studied. Bores can be described as a quick transition between two flow depths and are usually caused by tidal forces (Hatland & Kalisch, 2019). Bores can also be the consequence of earthquakes, landslides, dam and dike breaks. They can either be undular or non-undular: the first one can be described as an initial wave followed by a wave train of smaller waves, and the second one consists in a first breaking front followed by a flat interface. Undular bores are not only found in gravity waves, but can also be observed in other scientific fields such as plasma physics (Moiseev & Sagdeev, 1963) and fibre optics (Nuño et al., 2019). The understanding of the wave-structure interaction is necessary to assure more resilient design of marine, coastal and fluvial infrastructures. In particular, the study of the fluid-structure interaction with undular bore has gained interest in the scientific community since some clues indicate that tsunami waves are most likely un-

dular bores rather than solitary waves (P. A. Madsen et al., 2008), which leads to numerous changes in the wave description, as for example a much steeper wave front in the case of the undular bore. Undular bores were first experimentally studied by Favre (1935), who concluded that if a long wave travels in shallow still water, it will become more steep and form a bore, and if the surface elevation change is less than 0.28 of the water depth, it will become an undular bore. If the depth ratio, also called bore strength (Bjørnestad et al., 2021) and defined as a/h where a is the bore height and h the still water depth, is greater than 0.28 and less than 0.75 there is still undulation but the front wave is breaking and if this ratio is more than 0.75 then we observe a so-called turbulent bore. Numerous studies on turbulent and undular bores can be found, in particular the transition initial formation (Lemoine, 1948; Frazao & Zech, 2002; El et al., 2005), theory (Peregrine, 1966), experimental characterizations (Binnie et al., 1955; Yeh et al., 1989; Treske, 1994; Chanson, 2010; C. Lin et al., 2019; Shi et al., 2020), wave breaking (Gavrilyuk et al., 2016; Hatland & Kalisch, 2019), energy analysis (Sturtevant, 1965; Ali & Kalisch, 2010), turbulence (P. A. Madsen & Svendsen, 1983) or on-field measurements (Martins et al., 2017) were investigated. Examples of natural undular bore events can be found in figure 1.2, where both a river bore generated by the tide and the 2004 tsunami in the Indian ocean generated by an earthquake can be observed.

(a)

(b)

Figure 1.2: Examples of natural undular bore events. (a) The Sumatra 2004 tsunami reaching the island Koh Jum off the coast of Thailand (Grawin, 2006). (b) Undular bore, generated by tide, in the Turnagain Arm, Alaska (Dickerson, n.d.).

1.2. Objectives

Main objective

This work aims at studying the undular bore generation, propagation and interaction with a semi-submerged square cylindrical column, by means of numerical simulations and experimental trials in the *LEAF-NL* wave tank.

Specific objectives

This thesis seeks the following specific objectives:

$O1$: Define a suitable strategy for the undular bore generation by means of a piston wavemaker at laboratory scale.

$O2$: Characterize the incident undular bore waves during propagation along the wave tank.

$O3$: Study the formation and evolution of vortical structures past the square cylinder.

1.3. Thesis outline

This thesis is a numerical and experimental investigation of the generation, the propagation and the interaction of undular bores over a vertical column-like square cylinder. A description of the problem can be found in figure 1.3. A wave tank and its corresponding piston wavemaker have been designed and implemented to allow the generation of undular bores. In this work, the wavemaker itself, as the centerpiece of wave generation process, is a complete part of the study. The wavemaker response to velocity step input is numerically investigated and results in the generation of undular bores. A wave absorption strategy is deduced from the step response and is tested for a set of regular and irregular waves. The necessary experimental tools (piston wavemaker control, wave gauge, particle image velocimetry post-processing) have been designed and built. A square cylinder is then installed inside the wave tank and interacts with the undular bore. A full 3D mirror Computational Fluid Dynamics (CFD) model, solving the incompressible two phase Navier-Stokes equations, has been set up and allows to model the physical experiment. The numerical wave tank alongside with a set of experiments are used afterward to study the fluid structure interaction between the square cylinder and undular bore wave.

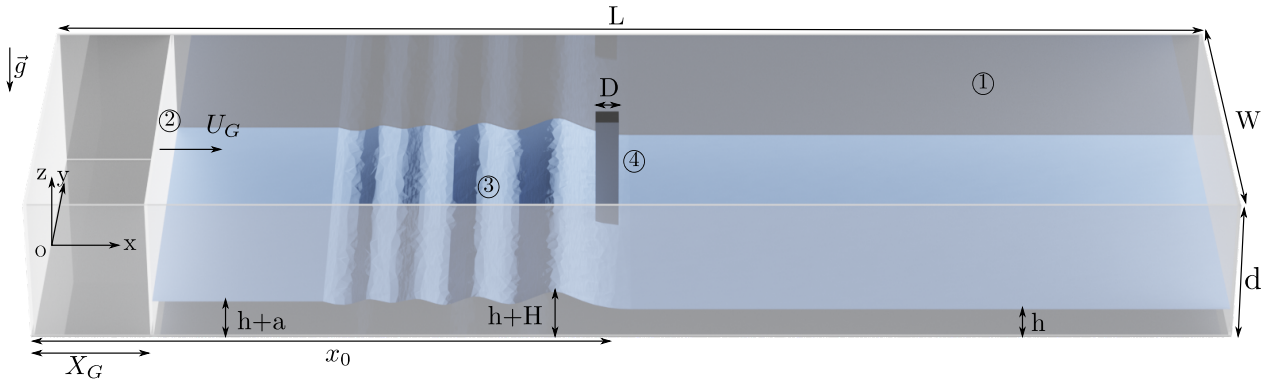

Figure 1.3: Undular bore interaction with a vertical square cylinder. The piston wavemaker ②, through the motion at velocity U_G, generates an undular bore ③ in the wave tank ① of length L, height d and width W. The undular bore, after propagating along the tank, interacts with a vertical square cylinder ④ situated at a position x_0. The mean water level is h, while the bore height is given by a and the first wave height by H.

This thesis, in order to complete the previous objectives, presents a methodology based on experimental and numerical trials as shown in figure 1.4. This thesis first reviews in chapter 2 the state-of-the-art concerning undular bores, wavemaking, numerical techniques and the wave-structure interaction problem. Chapter 3 then focuses on the CFD model: the geometry, the governing equations, the boundary conditions, the numerical methods, and post-processing are alternately set-up and reviewed. Space and time discretization is also studied in order to achieve independence. The experimental set-up consisting of a wave tank, a piston wavemaker, a wave gauge as well as a Particle Image Velocimetry (PIV) and image post-processing tool are designed and built, and the details are available in chapter 4. The experiments, apart from giving quantitative and qualitative data useful for the problem study, serve to validate the numerical simulation and assure credibility to the numerical results. Finally, results are presented in chapter 5 and 6 where detailed experimental data and numerical ones are compared and interpreted. In particular, the piston wavemaker is characterized by studying its kinematic and dynamic response to step input functions, a suitable strategy is validated for the generation of undular bores based on the numerical and experimental piston wavemaking techniques, the incident undular bore waves are characterized during their propagation along the wave tank, and the formation and evolution of coherent structures past the square cylinder is studied.

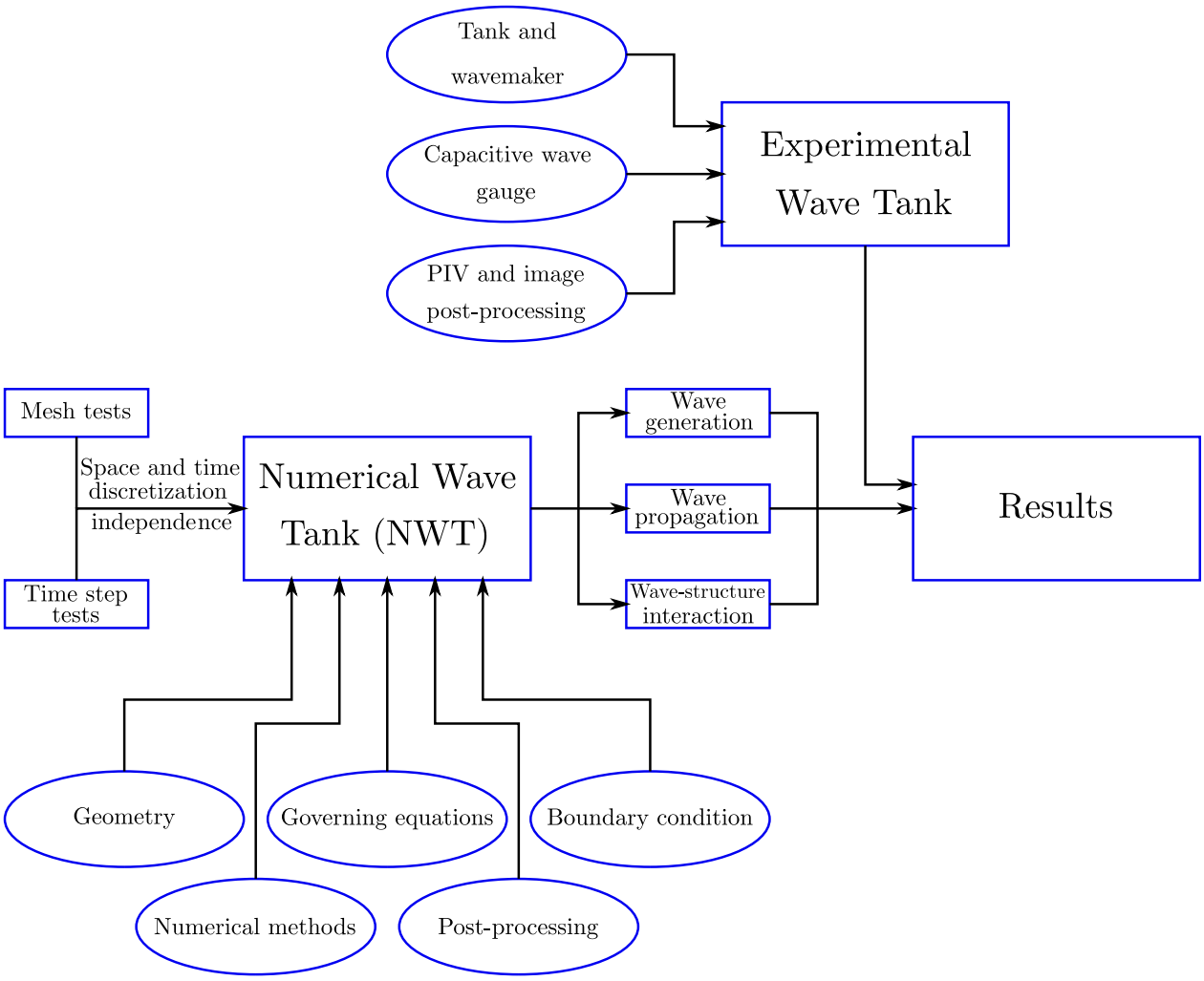

Figure 1.4: Methodology used in this thesis.

Chapter 2

Background and state-of-the-art

In this chapter, it is chosen to focus the review on the case of undular bores in section 2.1, even if a complete description of gravity waves can be found in appendix A. Wavemaking is then reviewed, and the case of the piston wavemaker is largely revised in section 2.2. Numerical techniques are then developed in section 2.3 and finally, wave structure interaction is reviewed in section 2.4 with a focus on the particular case of the square cylinder.

2.1. Bores

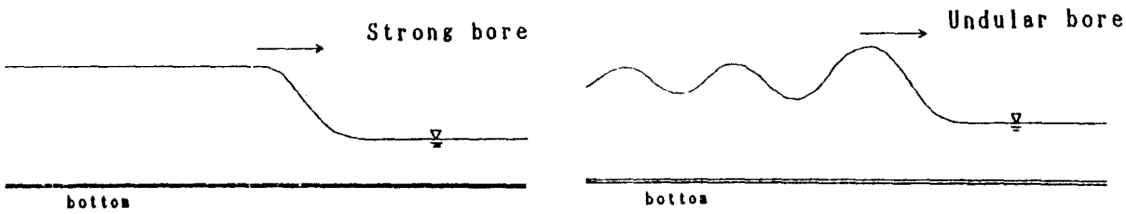

(a) (b)

Figure 2.1: Bore types from Tsuji et al. (1991). (a) Strong bore. (b) Undular bore.

According to the Cambridge dictionary a bore is "a very large wave that runs from the sea up a narrow river at particular times of year[1]". It is well known by scientists for the phenomena of tidal bore, that is to say that the transformation of the tidal surge into a wave, but it can also be found in tsunami related literature. Bores (wave propagating over a wet bed) and surges (wave propagating over a dry bed) can be generated by multiple reasons, like tidal forces (Bonneton et al., 2011), earthquakes, landslide (Ren et al., 2019), dam and dikes break. The consequential wave characteristics are difficult to understand due

[1] https://dictionary.cambridge.org/

to the great diversity of the causes. Tsuji et al. (1991) reported the observation of both undular and non-undular (flat) bores in Japanese rivers after the 1983 tsunami. The first one can be described as an initial wave followed by a wave train of smaller waves and the second one consists in a first breaking front followed by a flat interface as shown in figure 2.1. Undular bores were experimentally and theoretically studied by Favre (1935) and Peregrine (1966), respectively. Undular bores are of particular importance as they appear to more likely represent real tsunami wave instead of solitary wave (P. A. Madsen et al., 2008), such as the 2004 tsunami in the Indian Ocean shown in figure 1.2a which clearly showed an initial wave followed by a train of smaller waves. A complete study on the undular bore tsunami propagation in the Strait of Malacca after the 2004 event was carried out by Grue et al. (2008). If a long wave travels in shallow water, it will become more steep and form a bore (a shock Boussinesq wave), after some time (process is not instantaneous), and if the surface elevation change is less than 0.28 of the water depth, it will become an undular bore according to the observations of Favre (1935). If the depth ratio is greater than 0.28 and less than 0.75 there is still undulation but the front wave is breaking (Binnie et al., 1955). If the depth ratio is greater than this limit, no undulation is found. Favre (1935), in its series of experiments, also found well matching results with the shallow water De St Venant equations (De St Venant, 1871). To form a weak bore, one can send a stream of water into an area of still water, where the moving water is deeper than the still water (Peregrine, 1966). In the same study, finite-difference approximation is used to solve the equations of motion (KdV (Korteweg & de Vries, 1895)) for the generation of undular bore problem. By comparing the theoretical wave propagation velocity c_p with the experimental data of Favre (1935), G. H. Keulegan (1940) suggests that the undular bore undulations are similar to cnoidal waves and that the bore velocity of propagation can be corrected to take into account these oscillations above the mean water level:

$$c_p = \sqrt{gh}\left(1 + \frac{3}{4}\frac{h'}{h}\right)\left(1 - \frac{h'}{h+h'}\right) \tag{2.1}$$

where g is the gravity constant, h the mean water level of undisturbed water and h' is the mean level of the undular bore above h. Chester (1966) mathematically studied the two depth flow problem based on a viscosity dominated solution for the main bore, for which a limit of $Fr < 1.58$ was found in order to allow for the transition from the mean water level to the bore height with the hypothesis of a Poiseuille flow, and superimposing an inviscid perturbation on it, he found that an exponential decay in front of the bore and oscillations behind it can describe the free surface. Kamchatnov et al. (2012) made a full analytical description of the step problem for the Gardner equation (Gardner et al., 1974), finding different solutions with one of them being an undular bore. Most of the analytical studies were however carried out using the KdV equation, such as in Bjørkavåg & Kalisch (2011) and Brun & Kalisch (2018), where the Boussinesq scaling is used and considers that both parameters $\alpha = a/h$ (the bore

strength) and $\beta = h^2/\lambda^2$ are small. a is the bore height, h the mean water level and λ the typical wave length. The KdV equation is:

$$\eta_t + \eta_x + \tfrac{3}{2}\eta\eta_x + \tfrac{1}{6}\eta_{xxx} = 0. \tag{2.2}$$

The differences between bores and hydraulic jumps have been studied by P. A. Madsen & Svendsen (1983), using k-ϵ turbulence closure model. Treske (1994) carried out experiments in a similar configuration, and undular bores were obtained by removing a reservoir gate upstream. The gate generation technique seems the most used as it appears in many studies (Yeh et al., 1989; Chanson, 2010; Shi et al., 2020; C. Lin et al., 2020). It is however possible to generate an undular bore with an impulsive piston wavemaker (Stoker, 1957). More recently, Martins et al. (2017) made on-field measurements using LIDAR sensor and C. Lin et al. (2019) and C. Lin et al. (2020) experimentally studied the propagation of bores over horizontal and sloping bottom with the use of the Particle Image Velocimetry (PIV) technique.

2.2. Wavemaking

To generate waves, one should perturb the water. A way of doing so is to displace a certain amount of water by means of a wavemaker. Wavemakers are of different types: piston, hinged paddle, double articulated paddle, plunger, duck, etc., which are animated with a prescribed motion. The most natural one is a flexible panel, whose top edge would move at higher amplitudes than the lower parts, as the wave water particle velocity is greater at the free surface and smaller at seabed. An illustration of basic wavemakers is shown in figure 2.2. The design of wavemakers should take into account the following features (Biesel & Suquet, 1951):

- Inertia: It is of importance to reduce the inertia of the wavemaker to the minimum while keeping the stiffness and solidity of the elements. Indeed, forces imposed to the mechanism might be huge which implies to have stiff and heavy elements but the design should able the user to displace the elements easily to respect the wave generation functions and at an appropriate power consumption.

- Reflections: Wave reflections on the model or any element placed in the flume will come back against the wavemaker. The generation process should then take into account this additional wave by an active mechanism (filter).

- Wet back vs dry back: Two alternatives are available for the design of the wavemaker. A system with no water behind the wavemaker (waterproof) allows for more displaced water so higher waves but waterproof systems induce power losses due to friction and

a higher complexity.

– Cost: It is one of the driving feature which often leads to the simplification of the wavemaker. Most of the one used nowadays are piston or hinged paddle.

– Maintenance: The design should prevent any mechanical wear by notably minimizing contact with water.

The arrangement of wavemakers is listed in Guillouzouic (2014). It can either be (i) frontal: it is the most common configuration. The wavemakers, composed of several elements, are arranged on one side of the tank. The other side can be walls, artificial beaches or active absorption systems. (ii) corner and square: this configuration implies to have wavemakers on at least two consecutive sides of the tank. It allows the generation of oblique waves exempting the user any rearrangement of the model set up (re-orientation, mooring shifting). (iii) curved and circular: the wavemakers are arranged on a curved edge or complete circle allowing to generate waves from a a range of directions, as for the corner arrangement. The wave direction is controlled by applying the Huygens principle (Huygens, 1690): every point on a wave front can be considered as new source of spherical wavelets. The sum of these wavelets determines the form of the wave at any later time. Mixed seas in 3D wave tanks are obtained by the superposition of wave fronts.

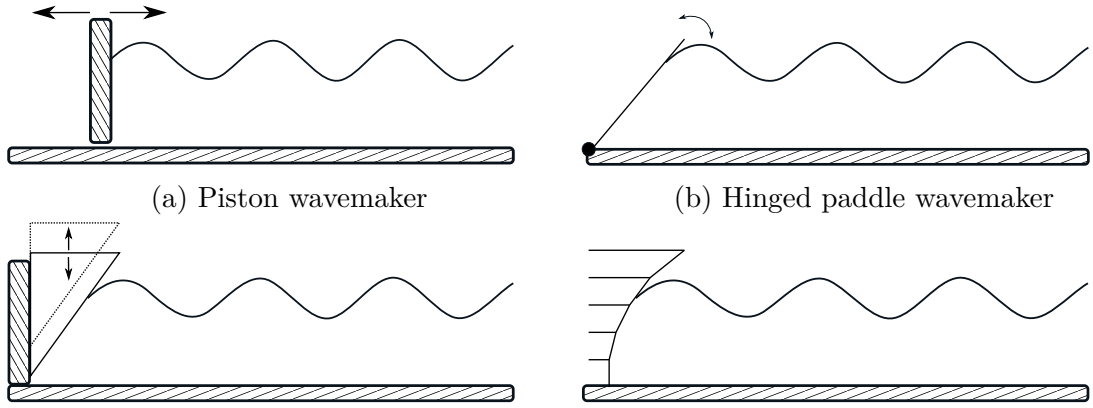

(a) Piston wavemaker (b) Hinged paddle wavemaker

(c) Plunger wavemaker (d) Flexible panel wavemaker

Figure 2.2: The different categories of basic wavemakers.

Theory of wavemakers

First order wavemakers theory has first been studied by Havelock (1929). Wave generation alternatives have been theoretically studied in the 50s (Biesel & Suquet, 1951) including piston, hinged paddle, or double articulated paddle. In this section, a special focus on piston generation wavemaker theory is done, as it will be used later on.

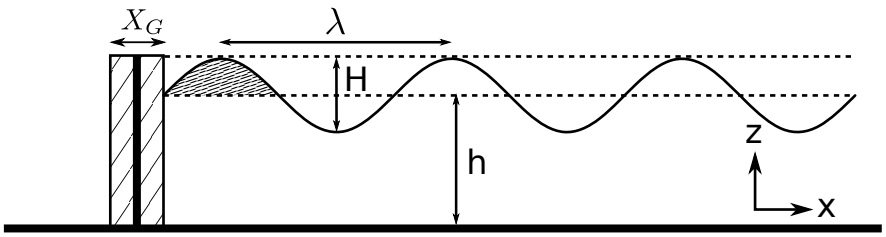

Figure 2.3: Piston wavemaker problem definition.

Harmonic waves The problem is quite simple and is represented in figure 2.3. If the piston stroke is X_G, then the area of displaced water $X_G h$ might equal the area of the semi wave length wave leading to:

$$X_G h = \int_0^{\lambda/2} H \sin(kx) dx = \frac{H}{k} \tag{2.1}$$

with k the wave number defined as $k = 2\pi/\lambda$. Biesel & Suquet (1951), by using potential theory and taking the particular boundary condition of the particle velocity at the wavemaker equals the one of the wavemaker, also gives a better estimation of the wavemaker transfer function which is the relation between wave height H and the piston stroke X_G for $x > 3h$ that is to say fully developed waves in the far field:

$$\frac{H}{X_G} = \frac{2\left(\cosh(2kh) - 1\right)}{\sinh(2kh) + 2kh} \tag{2.2}$$

O. S. Madsen (1971) developed a theory of wavemaker generation for pistons and gave the expression of wave elevation at any position in a wave flume, including the near field solution. For the case of the piston which runs from 0 to t', its motion is defined as:

$$U_G = \begin{cases} 0 \quad \text{if} \quad t < 0 \\ \frac{X_G}{2}\omega \sin(\omega t + \delta) \quad \text{if} \quad 0 < t < t' \\ 0 \quad \text{if} \quad t > t' \end{cases} \tag{2.3}$$

Using a similar strategy as Biesel & Suquet (1951) but widening the solution to infinite wave numbers, O. S. Madsen (1971) showed that the wave elevation is given by the following integral:

$$\begin{aligned} \eta(x,t) = & \frac{2}{\pi}\frac{U}{\omega}\int_0^\infty \frac{\tanh(kh)}{k}\frac{\omega^2}{\omega^2 - \sigma^2}\cos(kx) \\ & \left[\left[\cos(\sigma t) - \cos(\omega t)\right]\cos(\delta) + \left[\sin(\omega t) - \frac{\sigma}{\omega}\sin(\sigma t)\right]\sin(\delta)\right] \, dk \end{aligned} \tag{2.4}$$

where σ is defined by

$$\sigma^2 = gk \tanh(kh) \tag{2.5}$$

Ursell et al. (1960) experimentally verified the wavemaker theory for piston type wavemakers.

Solitary waves: Goring (1979) studied solitary wave generation with a piston type wavemaker, basing its solution on Boussinesq (1872) theory. He found that one can generate solitary waves by applying a velocity pseudo-step to the piston thanks to the hyperbolic tangent function. This procedure is also described in Anbarsooz et al. (2013) and Katell (2002) and the piston position X_G results in:

$$X_G(t) = S \tanh\left[7.6\left(\frac{t}{\tau} - \frac{1}{2}\right)\right] \tag{2.6}$$

where S the piston stroke, τ the duration of the motion and k the wave number are defined according to:

$$S = \frac{2H}{kh} = \sqrt{\frac{16H}{3h}}h, \tau = \frac{2}{kc}\left(3.80 + \frac{H}{h}\right), k = \sqrt{\frac{3}{4}\frac{H}{h^3}} \tag{2.7}$$

From which the piston velocity can be derived:

$$U_G(t) = \frac{7.6\,S}{\tau} sech^2\left[7.6\left(\frac{t}{\tau} - \frac{1}{2}\right)\right] \tag{2.8}$$

This procedure allows the generation of a soliton whose shape is based on the hyperbolic secant function:

$$\eta(x,t) = H sech^2\left(\sqrt{\frac{3}{4}\frac{H}{h^3}}(x - ct)\right) \tag{2.9}$$

In a more general case, if we consider the horizontal particle orbital velocities for waves of permanent form, the use of the continuity equation leads to the average of the horizontal velocity over depth (Svendsen, 1974):

$$\int_{-h}^{\eta} u(x,z,t)dz = c \cdot \eta + Q_s + U_c \cdot h \tag{2.10}$$

where u is the water particle velocity just in front of the wavemaker, Q_s is the non-linear mass flux averaged over a period and U_c is the averaged velocity of current below the wave trough. For an infinitely long wave the right-hand side reduces to $c \cdot \eta$ and as the particle velocity at the piston wavemaker is constant over the depth we get:

$$\bar{u} = \frac{1}{h+\eta}\int_{-h}^{\eta} u(x,z,t)dz = \frac{c\eta(x,t)}{h + \eta(x,t)} \tag{2.11}$$

Goring (1979), by equalizing the horizontal particle velocity averaged over the depth $\bar{u}(X_G, t)$ to the piston velocity defined a generation method:

$$U_G(X_G, t) = \bar{u}(X_G, t)$$
$$U_G(X_G, t) = \frac{c\eta(X_G, t)}{h + \eta(X_G, t)} \tag{2.12}$$

This strategy however supposes to know the celerity of the wave as well as its shape in order to be able to compute the piston velocity.

Active wave generation: During the generation process, one should take into account any reflection that might occur at the boundaries and disturbs the domain. For example, if the fluid structure interaction of an object placed in the flume with waves is carried out, the generation process shall take into account the wave reflected onto the object that comes back in direction of the wavemaker to suppress it (see figure 2.4). The control algorithm then can be similar to the so called active wave absorption presented in section 2.2. Such a method of filtering is presented in Frigaard & Andersen (2010).

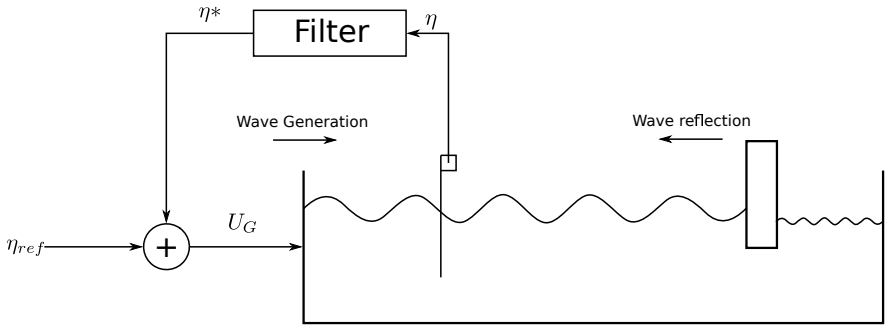

Figure 2.4: The active wave generation problem: here, the feedback system is composed of wave gauges in front the wavemaker.

Issues with wave generation

Evanescent Waves Evanescent waves are created when the vertical velocity of the wavemakers does not match the vertical velocity profile of the wave (Keaney et al., 2014). It is a mode whose amplitude decreases exponentially with the distance from the source. As a result, wave energy is concentrated close to the source. A bad handling of evanescent waves implies the need of bigger wave tank (to let time to these modes to vanish) and a lost in the wave generation power. The study of wave generation should take them into account.

Free Waves Free waves also result from a mismatch of the wavemaker geometry and the velocity profile. As the wavemaker does not succeed in describing the harmonic content in

the generation process, it leads to the creation of spurious waves or unwanted free waves. These one can be subharmonics or superharmonics (waves of lower or higher frequencies). If not controlled, they contaminate the testing area. Recent research showed that they can be avoided using a generation algorithm based on the force onto the wavemaker and not its position (force controlled vs position controlled, Aknin & Spinneken (2017)).

Trailing wave in solitary wave generation When generating solitary waves, it is perfectly known that without precaution the process generates a trailing wave (or secondary wave) which can be of real importance, more than 10% of the main pulse. In his work, Goring (1979) found that by taking duration larger than the theoretical one in the generation process can decrease the trailing wave amplitude, but with larger amplitude damping (more than the theoretical one). Using a procedure based on Rayleigh's solution allows to generate solitary waves more quickly and with trailing waves as small as with Goring's procedure according to Guizien & Barthélemy (2002).

Wave absorption

The wave, arriving at the end of the flume or tank, will eventually be reflected and thus contaminate the waves in the zone of study. Preventing this reflection allows for fully controlled environment, repeatability and longer test duration.

Passive Absorption: The historical way of absorbing waves at the end of a flume/tank is to used passive systems. For example, an artificial beach makes the wave break, while a porous media (or absorption mesh) artificially creates dissipation by turbulence. A few examples are shown in figure 2.5.

(a) (b)

Figure 2.5: A few example of passive absorbers. (a) Artificial beach (parabolic design) at École Centrale de Nantes. (b) Artificial beach (porous slope) at Tel Aviv University.

Active wave absorption: Active wave absorption is not of recent interest since H. Baumann seems to be the first one to have studied such mechanical systems, in 1954, proposing a hinged wavemaker linked to springs and a magnetic damper (Baumann, 1954). Active wave absorption systems, opposed to passive wave absorption systems (artificial beach, porous medium, etc), are capable of adapting and moving boundaries to avoid any reflection from it. The available control systems are numerous, according to the theories and feedback systems. Schäffer gives some clues to understand wave absorption principle (Schäffer & Klopman, 2000):

- Considering time as reversible, one can see that a wave can be absorbed with the wavemaker, playing the movie band backwards. However, by reversing time you also change the causal relation. In wave absorption, the motion of the paddle is not the cause of the waves.

- The superposition principle for linear systems allows to add a wave of same amplitude but in opposite phase with the incoming wave, resulting in the vanishing of the incoming wave.

- Consider the absorption wavemaker as a transparent boundary between the wave flume and the "outside sea". The generation mechanism generates waves to both sides of the wavemaker while the absorption mechanism lets pass the waves through the outside. The difference between the generation is illustrated in figure 2.6. The generated waves are in opposite phase while for the absorption system they have a continuity through the paddle.

Feedback systems are based on two different categories: (i) kinematic absorption, which relies on the wave elevation as an entry for the feedback control system. The sensor(s) can be implemented before the paddle (which gives time to the wavemaker to react but needs to calculate the wave propagation velocity to know when the wave will hit the paddle and thus commit some error) or at the paddle (which implies to have quick reactions)(Milgram, 1965; Schäffer & Klopman, 2000). (ii) Dynamic absorption, which bases its control algorithm on the measurement of the force on the paddle (Salter, 1981; Spinneken & Swan, 2009).

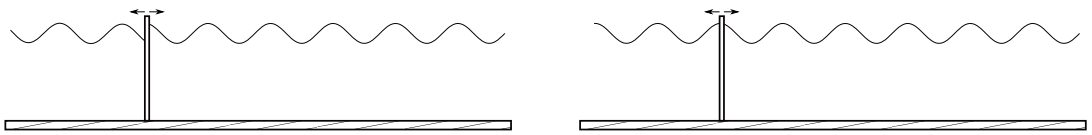

(a) Wave generation mechanism (b) Wave absorption mechanism

Figure 2.6: Illustration of the third clue given by Schäffer & Klopman (2000).

A focus is made on kinematic wave absorption systems as it is the one chosen later on to be implemented in the numerical wave tank. As seen in the previous section, the kinematic active algorithm is based on the measurement of the wave height in the flume, or at paddle. Schäffer & Klopman (2000) developed a rather simple technique: the water level at paddle is measured, and the transfer function linking water height and velocity is:

$$H = \frac{U_A}{\eta_{abs}} = -\sqrt{\frac{g}{h}} \tag{2.13}$$

This transfer function is called an *Infinite Impulse Response* filter (or IIR filter). For a quite complete review of active absorption, the reader can have a look at Andersen et al. (2016).

Wave tanks with active absorption system were constructed during the last decades. The most remarkable are the circular 28 m diameter wide *FloWave* in Edinburgh based on a hinged paddle force feedback algorithm (Gyongy et al., 2014)(see figure 2.7a), the circular 16 m diameter wide *Deep-Sea basin* at the National Maritime Research Institute in Tokyo which uses wave elevation at paddle for the absorption algorithm (Maeda et al., 2004) and the 14 m wide squared *Hydrodynamic Calibrator* at the University of São Paulo which is also based on wave elevation at paddle (de Mello et al., 2010)(see figure 2.7b).

(a) (b)

Figure 2.7: Wave tanks of interest. (a) *FloWave* (Edinburgh). (b) *Hydrodynamic Calibrator* (São Paulo).

2.3. Numerical Wave Tank (NWT)

In this section, we detail numerical methods employed for the application of wave generation and wave-structure interaction problems. A review of quality assurance criteria is carried out in appendix C, with a particular focus on the Convergence Grid Index (GCI) (I. B. Celik et al., 2008) which is employed further on in chapter 3.

Numerical Models

Wave modeling can be quite straightforward or really complicated and computationally costly according to the chosen model. We can make a distinction between two main categories: the depth-integrated models and depth-resolved models. In function of the phenomena of interest, one can elect the most suitable model, as for example in the case of breaking waves, really dependent on the water depth variations, a depth-resolved has to be taken. We can refer to Xie (2010) for more details about the different numerical models.

Depth integrated models are used to simplify the problem to a 1D or 2D wave propagation one. Few examples of such models are the KdV equation (Korteweg & de Vries, 1895), the regularized long wave (RLW) equation (Benjamin et al., 1972) for 1D cases, or the Kadomtsev-Petviashvili (KP) equation (Kadomtsev & Petviashvili, 1970) and the non-linear Shrödinger equation (Dingemans & Otta, 2001) for 2D. Also enter in this category the mild slope equation (Berkhoff, 1972) for refraction-diffraction problems, the shallow water equations (De St Venant, 1871; Titov & Synolakis, 1995) when vertical dimension is way smaller than wavelength, Boussinesq equations (Boussinesq, 1872) and all its inherited similar models (P. A. Madsen & Schäffer, 1999). These equations are relatively simple, can be solved through numerical finite difference schemes at low cost and are mainly used to study wave propagation, diffraction and refraction but fails to realistically model other phenomenon such as wave breaking and viscous effects.

Depth-resolved models can be sorted into two main categories: potential flow models, solving the Laplace's equation, and the Navier-Stokes models. The first one makes the assumption of inviscid and irrotational flow, while the other one solves the full Navier-Stokes equations, and thus is much more complicated. Potential flows are useful to simulate non-viscous phenomenon and are even able to reproduce breaking wave, but not after the wave touches down (Longuet-Higgins & Cokelet, 1976; Grilli et al., 2001). The modeling of vorticity and turbulence might also be complicated with potential flows. Their main advantages however is still the low computational cost compared to full Navier-Stokes resolution. This last one is used in Computational Fluid Dynamics (CFD) and use an interface tracking strategy to solve the full Navier-Stokes equations. A full review of CFD numerical wave tank is done in the following section. It can also be noticed some simplified models as the quasi-3D model which replaces the pressure by its hydrostatic value and allows to decouple it from the velocity computation (Casulli & Cheng, 1992).

Numerical Wave Tank

While experimental wave tanks are physical mean of implementing such systems, it often reveals to be expensive or not suitable for scale motivations, whereas numerical studies,

once performed exclusively with potential codes (irrotational, incompressible and non viscous flows) are now more and more carried out through viscous studies (Computational Fluid Dynamics), which nevertheless require more computational resources. As it evolves, it becomes more and more accessible and suitable to use CFD, which solves Navier-Stokes equations, especially in cases when the offshore platform scale is smaller than for the typical oil and gas cases and the potential codes are not able to reproduce the reality (for example extreme loads on wave energy converters devices) (Wolgamot & Fitzgerald, 2015). CFD numerical wave tank are divided into two main categories for wave generation and absorption: moving boundaries (which involve a dynamic mesh) and mathematical implementation (in the domain or the boundaries). It is chosen in this work to use the first alternative as it will represent what really happens in a laboratory and thus be a numerical mirror of the physical experiment. A numerical mirror is useful when it comes to validate a model and generate a database which involves to overpass experimental restriction (for example probing at any location without disturbing the flow (Higuera et al., 2015). Numerous numerical wave tank models were created, but the method most widely used is the VOF (Volume of Fluid) (Hirt & Nichols, 1981) as in Clauss et al. (2005) which used three commercial codes for extreme wave generation. New methods such as SPH (Smoothed-Particle Hydrodynamics) has been developed (Altomare et al., 2017). CFD simulations of wave tanks equipped with active absorption system were carried out: A. Maguire & Ingram (2009) developed a CFX model to test novel shaped wavemakers and concluded that the results did not match the expected theoretical value. In a later publication A. Maguire & Ingram (2010) concluded on the suitability of the code for wave generation problems while observing wave height attenuation during propagation along the canal. This was also observed by Bhinder et al. (2009), who also developed models on *STAR-CCM+*[2] and *FLOW3D*[3]. Higuera et al. (2015), after several development (Higuera et al., 2013), successfully created a 3D wave tank with active wave absorption in *OpenFOAM* using the theory developed by Schäffer & Klopman (2000), obtaining reflection coefficients smaller than 10%. When designing a NWT, one should consider the following features: (i) computing time, computational costs, (ii) implementation complexity (notably with mesh motions), (iii) preprocessing and postprocessing requirements, (iv) accuracy of the computations, calibration to experimental data and (v) range of waves (from harmonic to solitary waves).

[2] https://mdx.plm.automation.siemens.com/star-ccm-plus
[3] https://www.flow3d.com/

Numerical wave generation

All wave generation processes are described in Schmitt & Elsaesser (2015). An illustration of these methods is shown in figure 2.8 and are sorted according the following categories:

- Boundary method: the wave is created by applying boundary conditions to the domain boundaries. A simple of doing so is to describe water height and velocity profile at the boundary. The computational cost is the best of the present reviewed method but stability issues seems to appear.

- Moving Boundary: the closest alternative to real wavemaker. The moving boundary will reproduce the wavemaker motion of an experimental tank. A control strategy should then be applied to boundary motion. Computational cost is high due to remeshing and the implementation can be rather complicated.

- Relaxation method: waves theory is used to relax the results of the simulation inside the computational domain. At every time step, the variable values given by the theory are implemented in an upstream zone of the testing area. As the upstream values are updated at every time step no special attention has to be taken when reflected waves enter the relaxation zone. However, this method has a high computational cost. The pressure does not need to be set as it is generally computed from the velocity field (saving computational time).

- Mass source function: the wave is created by adding a source term to the continuity equation (see J. Larsen & Dancy (1983)). For example, an inlet velocity boundary condition can be applied on a cell face. The source mass function generates waves in all directions which implies to implement numerical in all directions to avoid contamination by reflected waves. The wavemaker does not interact with waves crossing it. The numerical cost is really low as it is implemented at one cell. However the simulations fails if the water surface reach the mass source. Creating high amplitude waves seems to be complicated if ever possible. An example can be found in P. Lin & Liu (1999).

- Impulse source function: The wave is created by adding an impulse term to the conservation of momentum equations. It is very similar to the mass source function method but the issue with high amplitude waves does not seem to be an issue. It allows also to define a direction of propagation to the generated waves. The computational cost is higher than for the mass source function as the impulse function is defined over a huge amount of cells (see figure 2.8).

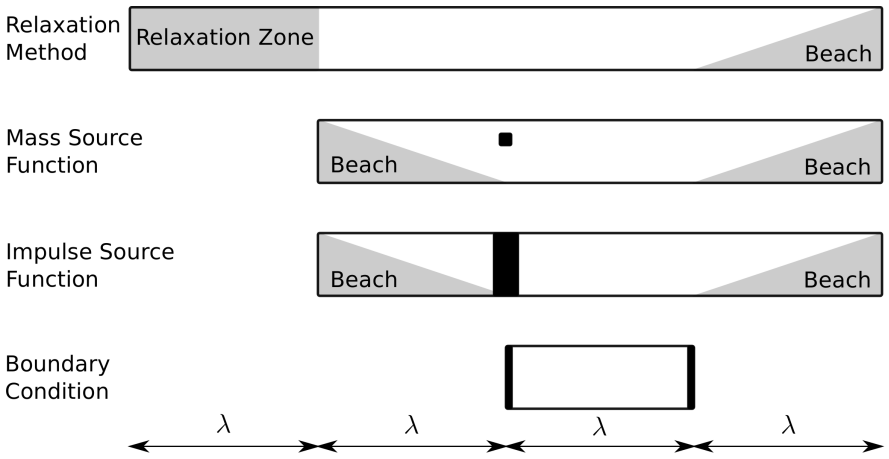

Figure 2.8: The different methods for the generation of waves in a numerical wave tank, inspired by Schmitt & Elsaesser (2015).

Numerical wave absorption

The different methods which are used for wave absorption in numerical wave tanks are presented in the following list:

- Moving Boundary: it is a numerical mirror of what would happen in an experimental wave tank. A control algorithm reacts in front of the incoming wave to move the boundary. As for the generation, this is quite costly to implement. Higuera et al. (2015) implemented a full 3D wave tank using this principle. Using such moving boundaries allows to reproduce the exact conditions of the experiment and legitimates the comparison with the experimental data.

- Boundary Velocity component: Higuera et al. (2013) used a simple velocity boundary condition to reproduce the velocity that would have an experimental moving boundary. This might be the simpler way and less costly way of implementing wave absorption while presenting in the general case reflection coefficient lower than 10%.

- Dissipative term - Sponge Layer: it was first proposed by Israeli & Orszag (1981). A sponge layer zone, generally of the size of 2 or 3 wavelengths, is created and variables are progressively set to reference values. A short description can be found in Mayer et al. (1998). For example, a velocity component u will be set at every time step to $u = (1-\gamma)u+\gamma u_{ref}$. γ is the relaxation parameter and depends on the x coordinate. It progressively increases from 0 to 1 as going deeper in the relaxation zone. This method prevents reflection when the waves enters the zones.

2.4. Wave-Structure interaction with semi-submerged bodies

Coastal communities as well as marine industries need the development of the understanding of fluid-structure interaction in order to design more resilient infrastructures as well as to protect them. Indeed, flow past semi-submerged bodies can generate turbulence, inducing higher loads, but also the generation of vortices. These interaction can be of different types, such as current-structure, wave structure or both wave and current. Degrees of complexity can be added, by considering highly turbulent flows, or breaking waves. The most common body which has been studied is the circular based cylinder and the famous Von Kármán street (Von Kármán, 1911). Other shapes are gaining interest as more representative of the variety of bodies which are or can be in interaction with such flows, such as square piles, or breakwaters. The reader is advised to refer to Sumer et al. (2006) for more details about flows around cylinders. In this part, we first review the vortex theory in section 2.4.1, then current-structure interaction and wave-structure interaction are revised in section 2.4.2 and 2.4.3 respectively, and finally the particular case of the wave-structure interaction with a vertical square cylinder is considered in section 2.4.3.

2.4.1. Vortex theory

Vortices and more generally vortical flows are present almost everywhere and many examples of such fluid motion can be cited: the whirlpool in a sink, smoke rings, or even the trailing vortices of air plane wings. A vortex is a region in a flow which revolves around a center line, the filament, and results in circular or nearly circular streamlines (Kundu et al., 2012). Vortex are important in fluid dynamics since they play a key role in turbulence but also for body force or energy considerations (Lu Ting, 1991). After defining vorticity and some vortex theoretical models, we shall take a look at the interaction between two parallel vortices which is called vortex pairing as a second step.

Vortex modelling

Vorticity represents the local rotation and is defined as the curl of the velocity field as:

$$\boldsymbol{\omega} = \boldsymbol{\nabla} \times \mathbf{u} \tag{2.1}$$

where $\mathbf{u}$ is the velocity field. According to Kundu et al. (2012), a vortex is a concentration of codirectional or nearly codirectional vorticity. It is possible to retrieve the velocity field from the vorticity field by applying the Biot and Savart relation, or by its regularized version, called

the local induction approximation (Da Rios, 1906; Hasimoto, 1972; Ricca, 1994; Saffman, 1993) according to:

$$\mathbf{u}(\mathbf{r}) = \frac{1}{4\pi}\int_{V'} \frac{\boldsymbol{\omega}(\mathbf{r}) \times (\mathbf{r} - \mathbf{r}')}{|\mathbf{r} - \mathbf{r}'|^3} \mathbf{d^3 r}' \tag{2.2}$$

where $\mathbf{r}$ is the position vector where the velocity is to be deduced, $\mathbf{r}'$ is the location of the vortex, and the volume V' contains a segment of the vortex. For more details about the application of the Biot and Savart relation, the reader can refer to Kundu et al. (2012). The most simple models of vortex are (i) the solid body motion, defined in cylindrical coordinate system (r, θ, z) as:

$$u_\theta = \frac{\omega r}{2} \tag{2.3}$$

which leads to a uniform distribution of vorticity in the normal plane direction ($\boldsymbol{\omega} = \omega \vec{e_z}$) while (ii) the perfect distribution of vorticity at $r = 0$ such as:

$$u_\theta = \frac{\Gamma}{2\pi r} \tag{2.4}$$

with Γ the circulation. These two models are steady and show circular closed streamlines but the second is an irrotational flow ($\boldsymbol{\nabla} \times \mathbf{u} = \mathbf{0}$), that is to say that a vortex does not necessarily involves fluid particle in rotation. Another useful model is (iii) the Lamb-Oseen vortex, which describes a Gaussian distribution of the vorticity according to:

$$\boldsymbol{\omega}(r) = \frac{\Gamma}{\pi r_c^2} e^{-(r/r_c)^2} \vec{e_z} \tag{2.5}$$

where r_c is the vortex core radius which depends on time according to $r_c(t) = \sqrt{4\nu t + r_c(0)^2}$. In this last experession, ν is the kinematic viscosity, which shows that the Lamb-Oseen vortex decays in time due to viscosity. This leads to the following angular velocity:

$$u_\theta = \frac{\Gamma}{2\pi r}\left(1 - e^{-(r/r_c)^2}\right) \tag{2.6}$$

The circulation, which is defined as the integral of the velocity over a closed line, is linked to the vorticity by the Stokes theorem:

$$\Gamma = \oint_C \mathbf{u} \cdot \mathbf{dl} = \iint_S \boldsymbol{\omega} \cdot \mathbf{dS} \tag{2.7}$$

where C is the perimeter of the surface S, so that the circulation, as an integral scalar quantity, is a macroscopic measurement of the rotation in a fluid. A simple comparison between these three vortex models (solid body motion, irrotational and Lamb-Oseen) is carried out in figure 2.9, for $\Gamma = 10$, $r_c = 0.25$ and $\omega = \Gamma/(\pi r_c^2)$. The solid body motion is

a linear function of r while the irrotational one exhibits a singularity in $r = 0$. The Lamb-Oseen vortex, which presents local maximum/minimum at $r = \pm r_c$, is a trade between both last models: it shows a decrease in the velocity inversely proportional to r at the vortex edges while it has a linear behaviour at the vortex center. Note that the Rankine vortex is a simpler model than the Lamb-Oseen one which behaves exactly as a solid body motion for $r \leq r_c$ and as an irrotational vortex outside ($r > r_c$):

$$u_\theta(r) = \begin{cases} \frac{\Gamma r}{2\pi r_c^2}, & r \leq r_c, \\ \frac{\Gamma}{2\pi r}, & r > r_c \end{cases} \tag{2.8}$$

Vortex filaments have a self-induced motion which may change in function of the filament shape, as in the example of the effect of torsion on the motion of helical filaments (Ricca, 1994).

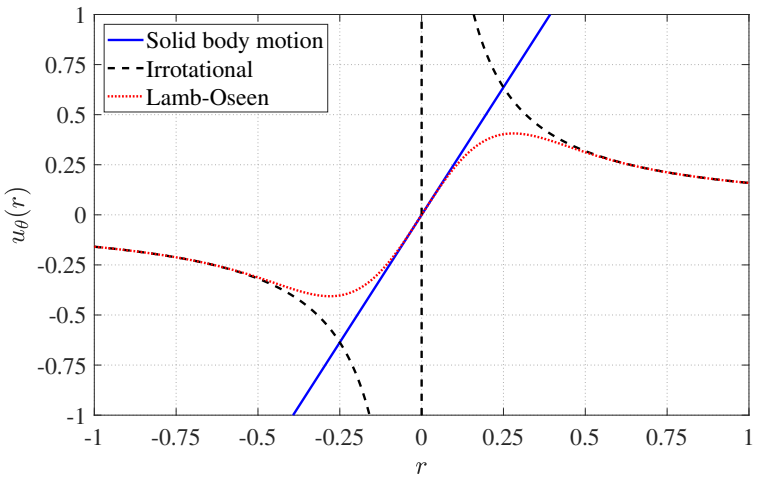

Figure 2.9: Comparison between three vortex models.

Some useful theorems are now listed. The first one, Kelvin's circulation theorem, states that for a barotropic ideal fluid, the circulation around a closed curve moving with the fluid remains constant with time (Kundu et al., 2012) so that:

$$\frac{D\Gamma}{Dt} = 0 \tag{2.9}$$

A corollary to this theorem states that vortex tubes move with the fluid and is called the Helmholtz's theorem.

Vortex in free-surface flows

Many example of free-surface deformation can be found, the most common one being the plughole vortex in bathtub. Let's study the example of a solid body motion vortex, such

as equation 2.3, placed in a tank and presenting a free-surface. It can be shown that the Newtonian viscous tensor reduces to $\sigma_{ij} = -p\delta_{ij}$ (or $S_{ij} = 0$). Euler equations are then valid and are written as:

$$\rho\left(\frac{\partial \mathbf{u}}{\partial t} + (\mathbf{u}\cdot\boldsymbol{\nabla})\,\mathbf{u}\right) = -\boldsymbol{\nabla}p + \rho\mathbf{g} \tag{2.10}$$

$$\boldsymbol{\nabla}\cdot\mathbf{u} = 0 \tag{2.11}$$

For a steady flow and replacing $\mathbf{u} = u_\theta(r)\vec{e_\theta}$, then equation 2.10 becomes:

$$\rho\frac{u_\theta^2}{r} = \frac{\partial p}{\partial r} \tag{2.12}$$

$$\frac{\partial p}{\partial z} = -\rho g \tag{2.13}$$

These last equations consider the z-direction pointing upward and the origin of the coordinate system at the centre of the vortex and at the seabed as shown in figure 2.10. By integrating equations 2.12 and 2.13 we obtain, respectively:

$$p(r,z) = \frac{\rho\omega^2 r^2}{8} + f(z) \tag{2.14}$$

$$p(r,z) = -\rho g z + g(r) \tag{2.15}$$

Note that the functions f and g contain constants. In order to fulfill equations 2.14 and 2.15, $f(z) = g(r) = p_0$. So finally, we solve for z these equation and find:

$$z = \frac{\omega^2 r^2}{8g} - \frac{p(r,z) - p_0}{\rho g} \tag{2.16}$$

So that surfaces of constant pressure are paraboloids of revolution, as shown in figure 2.10. If we consider now an irrotational vortex such as in equation 2.4, a similar argumentation leads to hyperboloids of revolution which are also shown in figure 2.10 such as:

$$z = -\frac{\Gamma^2}{8\pi^2 r^2 g} - \frac{p(r,z) - p_0}{\rho g} \tag{2.17}$$

In case of considering a Lamb-Oseen vortex and keeping the perfect fluid hypothesis results in the following constant pressure curves:

$$z = -\frac{\Gamma^2}{4\pi^2 r_c^3 g}\frac{2r^{*2}\mathrm{Ei}\left(-2r^{*2}\right) - 2r^{*2}\mathrm{Ei}\left(-r^{*2}\right) + e^{-2r^{*2}}\left(e^{r^{*2}} - 1\right)^2}{2r^{*2}} - \frac{p(r,z) - p_0}{\rho g} \tag{2.18}$$

where $r^* = r/r_c$ and Ei is the exponential integral defined as $\mathrm{Ei}(x) = -\int_{-x}^{\infty} e^{-t}/t\, dt$. We can observe the free-surface deformation $p(r, z = h + \eta) = p_{atm}$ in figure 2.10.

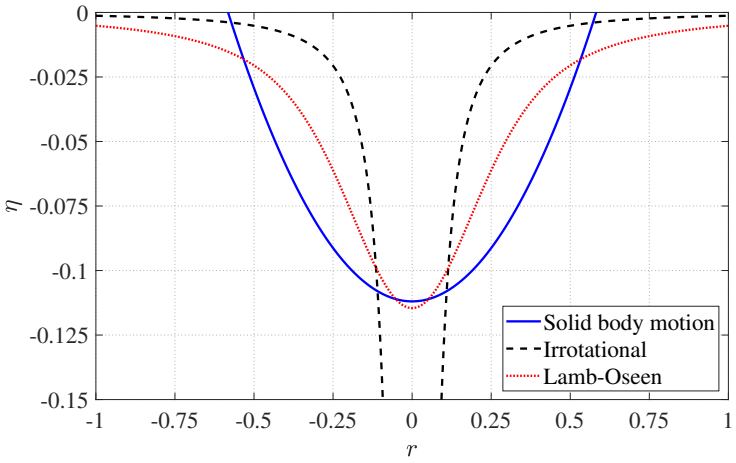

Figure 2.10: Comparison between three vortex model free-surface deformation. The parameters used are $\omega = 5.1$ s^{-1}, $r_c = 0.7$ m, $h = 0.05$ m for the solid body motion vortex, $\Gamma = 1$ m^{2}s^{-1} and $r_c = 0.25$ m for the irrotational and Lamb-Oseen vortices.

Vortex stretching

According to Helmholtz's theorem, vortex tubes move with the fluid. Since the fluid is incompressible, the tube volume is constant so that any stretching comes with a shrinking of its cross-section. However, according to Kelvin's theorem, its circulation or strength is constant with time so if the cross-section area decreases then the vorticity magnitude increases. According to Taylor (1938), stretching of vortex and the subsequent amplification of rotation is one of most important mechanism that acts in fluid dynamics. It can be shown by taking the curl of the Navier-Stokes equations that the vorticity equation is Tennekes et al. (1972):

$$\frac{D\boldsymbol{\omega}}{Dt} = (\boldsymbol{\omega} \cdot \boldsymbol{\nabla})\, \mathbf{u} + \nu \Delta \boldsymbol{\omega} \tag{2.19}$$

Let analyze the equation above. First, if we make the assumption of inviscid fluid, the last term of the above equation disappears. The $D\boldsymbol{\omega}/Dt$ is the material derivative of the vorticity $\boldsymbol{\omega}$, which depends on non steady vorticity term $\partial\boldsymbol{\omega}/\partial t$ and on the convective term $\mathbf{u} \cdot \boldsymbol{\nabla}\boldsymbol{\omega}$. The right hand term $(\boldsymbol{\omega} \cdot \boldsymbol{\nabla})\, \mathbf{u}$ is the so-called vorticity stretching term. Now if the velocity field is in the direction of the vorticity, $(\boldsymbol{\omega} \cdot \boldsymbol{\nabla})\, \mathbf{u}$ is positive and amplifies the vorticity. Generally speaking, stretching of a vortex leads to its amplification and confinement (Petitjeans, Philippe, 2003). Vortex stretching is the mechanism which transfers turbulent energy to smaller scales (Taylor, 1938), so Bradshaw & Woods (1971) defines turbulence according to: "Turbulence is a three-dimensional time-dependent motion in which vortex stretching

causes velocity fluctuations to spread to all wavelengths between a minimum determined by viscous forces and a maximum determined by the boundary conditions of the flow. It is the usual state of fluid motion except at low Reynolds numbers". In 2D flows, the stretching term is zero, so that the 2D models lack this mechanism. As on average vortices are more lengthened than compressed, vortex cores are reduced. The axial stretching rate γ can also be mathematically defined as the vertical variation of the axial velocity along the vortex core filament according to:

$$\gamma = \frac{\partial u_z}{\partial z} \tag{2.20}$$

in the case of a vertical vortex.

One of the well known model of stretched vortex are the equations of Burgers (1940), which is an exact solution of the Navier-Stokes equations. Burgers (1940)'s equations consider a constant stretching γ (in both space and time) and corresponds to the meridional direction (Abid et al., 2002; P. G. Drazin, 2006):

$$v_r = -\frac{1}{2}\gamma r, v_z = \gamma z \tag{2.21}$$

The resulting angular velocity v_θ is a trade between stretching and viscous diffusion and in the stationary regime leads to:

$$v_\theta = \frac{\Gamma}{2\pi r}\left(1 - \exp\left(-\frac{r^2}{R^2}\right)\right) \tag{2.22}$$

where $R = \sqrt{4\nu/\gamma}$ is the vortex core radius which depends on viscosity and stretching and $2\pi\Gamma$ is the velocity circulation.

Vortex pairing

In some cases, the generation and the pairing of counter-rotating parallel vortices can be observed. The pairing of vortices was first studied as it is an undesired effect in the wake of plane, notably at take off (Spreiter & Sacks, 1951). A visualization of a vortex pair can be found in figure 2.11a. In particular, the description of a sinusoidal instability which leads to the merging of the vortex pair into a series of vortex rings was carried out (Smith & Beesmer, 1959) and stability theories were elaborated (Crow, 1970). This mechanism can be seen in figure 2.12a. In particular, Leweke & Williamson (1998) generated a pair of counter-rotating vortices, which are well represented by two Lamb-Oseen vortices as shown in figure 2.11b. The vortex pair center lines are straight and uniform at the beginning of the pairing phenomena, before two instabilities start to deform the pair of vortices. The first one is characterized by its long wavelength, similar to the one observed by Crow (1970)(see figure 2.12a) while the

second one is a short wavelength instability which deforms the cross-section of the vortices and are shown in figure 2.12b. They demonstrated this is an elliptic instability and they also highlighted that the symmetry, with respect to the plane separating the two vortices, is lost.

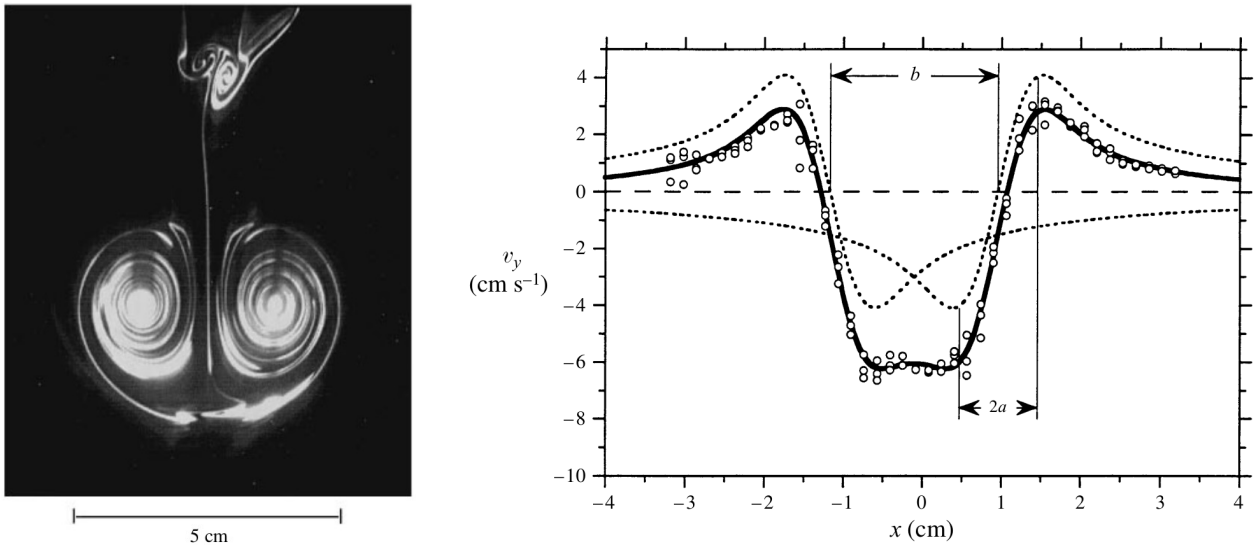

(a) (b)

Figure 2.11: (a) Fluorescent visualization of a counter-rotating vortex pair, from Leweke & Williamson (1998). (b) Velocity profile along a line passing by the vortex centers of figure (a) (Leweke & Williamson, 1998).

Ortega et al. (2003) experimentally studied by means of flow dye visualization and PIV the instability of wing trail vortices of unequal strength, where they describe the rapid transformation of the wake into a highly three-dimensional flow. The transient formation of a counter-rotating pair of vortices in a jet flow by the folding of a vortex ring was studied in Cortelezzi & Karagozian (2001). Vortex pairing was also observed in the shear-layer in the mixing layer of two streams of water brought together (Winant & Browand, 1974), and where neighboring pairs of vortices can be seen to roll around each other before collapsing into a unique and larger vortex, the free-shear layers (Moon & Weidman, 1988) and a double helical pairing can also be found in the work of Estevadeordal & Kleis (1999).

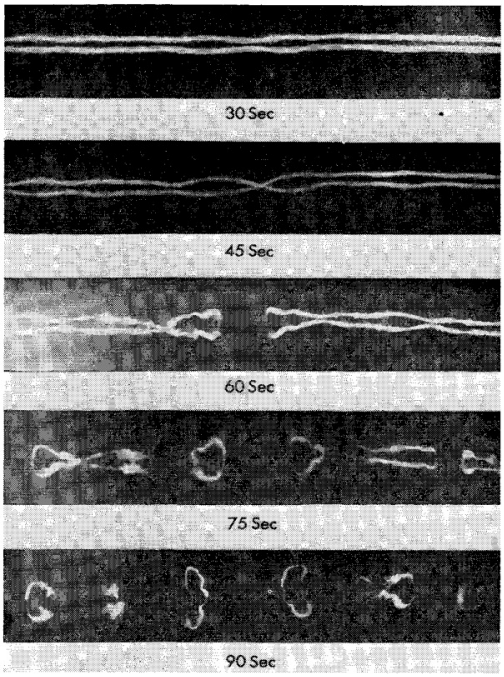

(a)

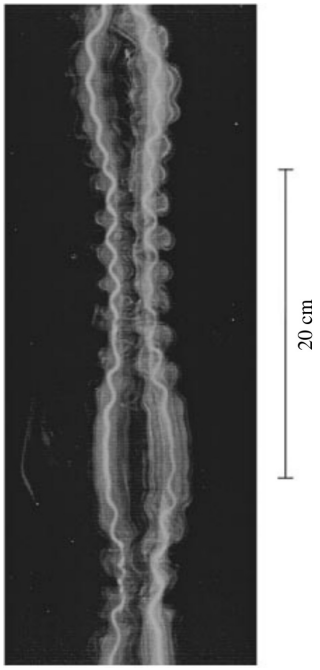

(b)

Figure 2.12: Vortex pair instabilities. (a) Vortex trail from a B-47, photographed from upward. Image from the work of Crow (1970). Growth of the Crow's long-wavelength instability and formation of the vortex rings. (b) Short-wavelength instability from Leweke & Williamson (1998).

Marshall (1992) studied the vortex pair stability under axial stretching, finding that the stretching mechanism exerts a stabilizing influence on the vortex pair. He also found that the stability of the pair depends on four dimension parameters from which two characterize the stretching. Marcus & Berger (1989) numerically studied the interaction between a pair of horizontal counter-rotating vortices with a free-surface, in particular they solved the free-surface deformation and wave generation. Similar studies (Willmarth et al., 1989; Hirsa & Willmarth, 1994) experimentally generated the counter-rotating vortex pair by using flaps below the free-surface, and described the motion of the vortices when they reach the free-surface, notably how they move apart from each other.

2.4.2. Current structure interaction

The Von Kármán street might be the most famous phenomena studied until now in the domains of hydro and aerodynamics. If Von Kármán (1911) gave the name to the instability, Mallock (1907) and Bénard (1908) had observed and studied it earlier on. Numerous experimental (Provansal et al., 1987) and numerical (Koumoutsakos & Leonard, 1995) studies

can be found in the literature. Other interesting studies includes: the interaction of current with conical island in shallow water (Lloyd & Stansby, 1997), tidal flow past various types of barrier islands Nicolau del Roure et al. (2009) or tsunami induced currents with breakwater Borrero et al. (2015).

Vortex shedding

Vortex generation is the consequence of the boundary layer detachment (or flow separation) at the sides of the body. The resulting downstream flow depends then on the regime in which is forced the cylinder, characterized by the Reynolds number (Lienhard, 1966) which is defined as $Re = \rho DU/\mu$ with ρ the fluid density (in kg/m^3), D a characteristic length (here the diameter, in m), U the flow speed (in m s^{-1}) and μ the dynamic viscosity (in kg m^{-1} s^{-1}). In figure 2.13, from the same author, the different regimes of the wake of the flow past a circular cylinder are presented. For really low Reynolds number ($Re < 5$) the flow does not separate and follows the body contour. For Reynolds number between $5 \leq Re \leq 45$ a symmetric pair of steady vortices appears behind the cylinder in the near wake and are called recirculation region. Their longitudinal size linearly increases with Reynolds number according to Nishioka & Sato (1978). For Reynolds number between $40 \leq Re \leq 150$ the wake is no longer steady, and an instability appears: the Van Kármán street, with the periodic creation of vortices of opposite signs as illustrated in figure 2.14a. For Reynolds number $150 \leq Re \leq 300$, transition to turbulence takes place: the vortices become turbulent as they travel in the wake but boundary layer (till separation) at the cylinder keeps being laminar Roshko (1954). If Reynolds number is higher than 300, then the flow can be classified into three regimes: the subcritical regime ($300 \leq Re \leq 1.5 \times 10^5$), the transitional regime ($1.5 \times 10^5 \leq Re \leq 3.5 \times 10^6$) and the supercritical one ($Re > 3.5 \times 10^6$) (Blevins, 1977). The subcritical flow is characterized by a boundary layer separation around 80° (considering 0° at the stagnation point), and a strong and periodic shedding, while in the transitional regime the boundary layer at the cylinder becomes turbulent and separation happens further away at 140° while drag coefficient highly decreases to reach 0.3. Flow is non longer 2D and 3 dimensional effects are to be taken into consideration and the wake is disorganized. Finally, in the supercritical regime vortex shedding reappears. The Strouhal number is another important number as it is proportionality constant which links the shedding frequency to the ratio between the free flow velocity and the cylinder diameter as: $f_s = SU/D$ (f_s is the shedding frequency in Hz, and S is the Strouhal number). This number is a function of the Reynolds number for the cylinder case and subsonic flow as showed in figure 2.14b, and in the transitional regime depends on the roughness of the body. Regarding the forces in the subcritical regime, the lift force (perpendicular to flow direction) oscillates at the same frequency as the vortex shedding frequency while it happens at twice this frequency for the drag force. Roshko

(1961) experimentally showed that the Strouhal number is inversally proportional to the drag coefficient (or an increase in drag leads to a decrease of the shedding frequency). According to Newman (2017), the Strouhal number can be defined as $S \approx 0.23/C_D$ for Reynolds number between $10^2 \leq Re \leq 10^7$ and outside of the transition range ($Re \approx 10^6$). The oscillation of the lift and drag forces are at the origin of the hydro-elastic phenomena called Vortex Induced Vibration (VIV) which are either problematic (strumming of mooring lines, risers, etc) or can be harnessed to produce energy (Bernitsas et al., 2008). An elliptic shaped splitter plate enrolling along the slender body is often used to destroy the vortex shedding and thus the oscillating forces. Non-circular based cylinders, including square ones, also form vortex wakes with very similar characteristics as the circular cylinder case (Blevins, 1977). Luo et al. (2003) numerically studied the hysteresis phenomenon in the galloping (lateral oscillation) of a square cylinder.

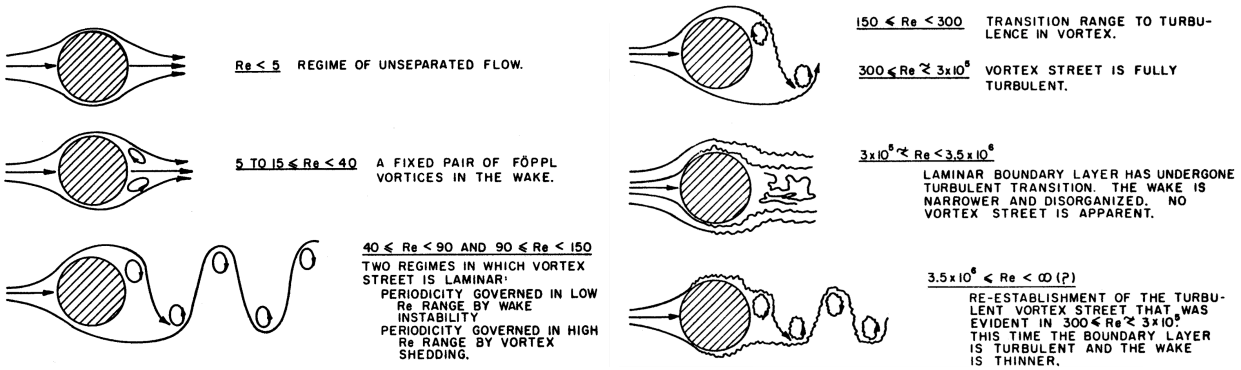

Figure 2.13: Vortex shedding regimes according to Lienhard (1966).

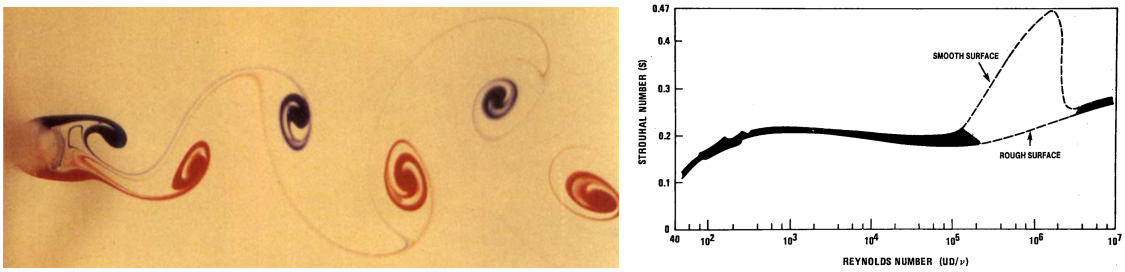

(a) (b)

Figure 2.14: (a) Von Kármán street according to experiment of Perry et al. (1982). The red ink marks negative vortices while the blue positive ones and Reynolds number is $Re = 80$. (b) Strouhal number ($S = Df_s/U$) in function of the Reynolds number ($Re = UD/\nu$) (Blevins, 1977).

Oscillating flows

Oscillating flows are unsteady flows whose direction periodically changes. It is often used to model wave loading as particle orbital velocity can be considered as an oscillatory flow, especially in shallow water. It is also very well documented as studied for a long time with experimental (Honji, 1981; Bearman et al., 1985; Williamson, 1985; Sarpkaya, 1986) or numerical (Lu et al., 1997; C.-C. Chen et al., 2009; Suthon & Dalton, 2012) procedures. An important non-dimensional number, apart from the Reynolds number, is the Keulegan-Carpenter number (G. H. Keulegan & Carpenter, 1958) (or period number) defined as $KC = U_m T/D$, where U_m is the maximum flow velocity, T the oscillation period and D a characteristic length equal to the diameter in the case of a cylinder. The Keulegan-Carpenter number determines the contribution of inertia and drag forces (KC = drag/inertia = $\rho D U_m^2/(\rho D^2 U_m/T)$). A third practical number is the ratio between these last two numbers: $\beta = Re/KC$. These forces were theoretically predicted by G. Stokes (1851) and later on by C.-Y. Wang (1968). Williamson (1985) carried out a series of experiment, first with an oscillating cylinder in a water tank and then with a pair of cylinders. He qualitatively describes the wake characteristics in function of the KC number. Results, from his photographs, can be found in figure 2.15. Finally, observations are made about the forces and he is able to identify for each flow regime the lift force frequency as a multiple of the shedding frequency. Honji (1981) demonstrates that the 2D coherent structure that are created at low KC number, become 3D structures as KC increases, due to an instability of the flow. The instability is a steady mushroom-like structure appearing at the side of the cylinder and perpendicular to the direction of the flow. Particles situated close to the boundary, detache and reach positions outside of the boundary layer: the motion of the particles describe a mushroom-like pattern which appears and disappears during a period of the forcing flow (Grue, 2011). Such pattern is shown in figure 2.16a. Stability and instability regime are drawn in figure 2.16b. For example, if $\beta = 1035$, 3D wakes (Honji's instability) appear at $KC = 1.1$, transition to turbulence at $KC = 1.5$ and separation at $KC = 1.9$ (Sarpkaya, 1986). Suthon & Dalton (2012) state that the instability originates from other reasons than the Taylor, Dean and Görtler instabilities. The horizontal forces, according to Morison et al. (1950) are defined as the sum of the quasi-static inertia and the drag forces, which depends on the Keulegan-Carpenter number KC, the Reynolds number Re, the roughness and interaction parameters:

$$F = F_d + F_m = \frac{1}{2}\rho D C_d U|U| + \frac{1}{4}\pi\rho D^2 C_m \frac{dU}{dt} \tag{2.23}$$

in which ρ is the fluid density, D the cylinder diameter, $U = U_m \cos(2\pi t/T)$ the free flow velocity, T the oscillation period, t the time, C_d and C_m are the drag coefficient and inertia coefficient respectively. According to Sarpkaya (1986), this equation is an estimation (not a

perfect solution of a complex problem), its origin is pragmatic and is experimentally validated. Morison's equation range validity (rule of thumb) is for $KC > 6$ (Chakrabarti, 2005). These coefficient can be approximated, in the case of large β by (Sarpkaya, 1986):

$$C_d = \frac{3\pi^3}{2KC}\left[(\pi\beta)^{-1/2} + (\pi\beta)^{-1} + \mathcal{O}\,(\pi\beta)^{-3/2}\right] \tag{2.24}$$

$$C_m = 2 + 4\,(\pi\beta)^{-1/2} + \mathcal{O}\,(\pi\beta)^{-3/2} \tag{2.25}$$

These solution can be expanded to order $\mathcal{O}\,(\pi\beta)^{-3/2}$ and in the case of $KC \ll 1$, $Re{\cdot}KC \ll 1$ and $\beta \gg 1$ give (C.-Y. Wang, 1968):

$$C_d = \frac{3\pi^3}{2KC}\left[(\pi\beta)^{-1/2} + (\pi\beta)^{-1} - \frac{1}{4}\,(\pi\beta)^{-3/2}\right] \tag{2.26}$$

$$C_m = 2 + 4\,(\pi\beta)^{-1/2} + (\pi\beta)^{-3/2} \tag{2.27}$$

Sarpkaya (1986) demonstrates that the Keulegan-Carpenter number KC at which the drag coefficient C_D deviates from the prediction of Stokes and Wang nearly corresponds to the critical KC at which the vortical instability occurs. In the case of a square cross-section, Okajima et al. (1998) made one of the first comparisons between circular and square cylinder by executing experiments in a U-tube and measuring in-line and perpendicular forces. KC number range was between 1 and 90, and they found good agreement with Morison's equation, and differences between the two shapes are observed: a phase shift appears in the in-line force while the flow pattern in the case of the square cylinder, in particular the dominant frequency, does not correlate well with the transverse force results contrary to the circular case. In a latter publication (Okajima et al., 2000), they studied the aspect ratio influence on shedding and forces. Nomura et al. (2003) carried out experiments in a wind tunnel with an oscillatory flow with non-zero mean (equivalent of the case current more wave) and conclude on the suitability of the Morison's formula to predict the forces.

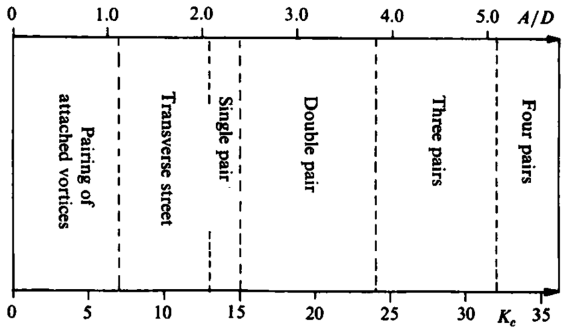

(a) Flow regimes

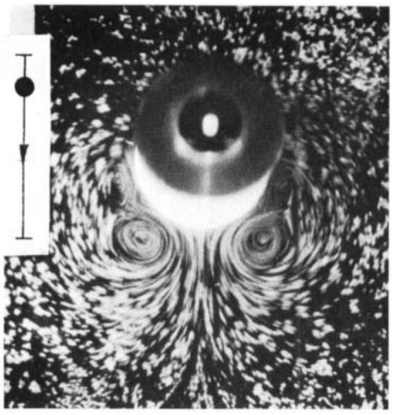

(b) Attached pair of vortices

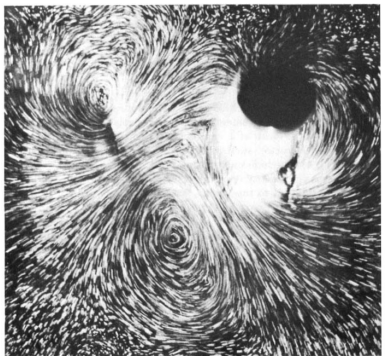

(c) Single pair

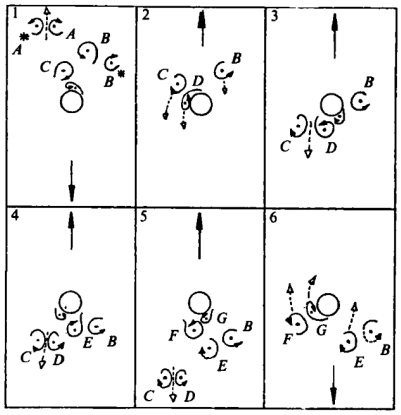

(d) Three pairs

(e) Transverse street

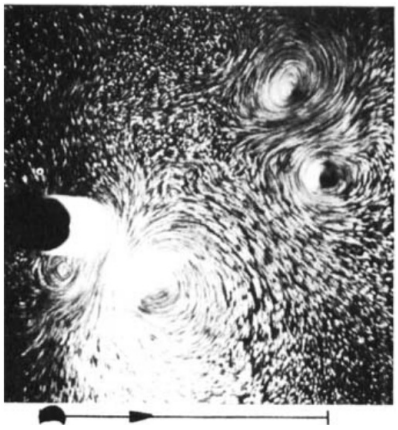

(f) Double pair

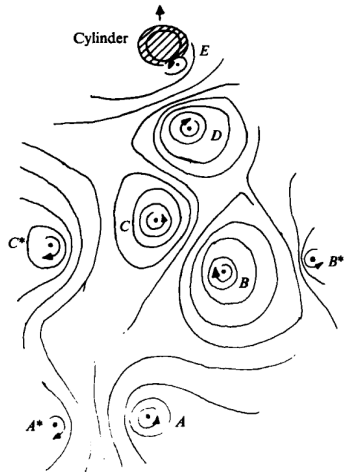

(g) Four pairs

Figure 2.15: Regimes flows according to Williamson (1985).

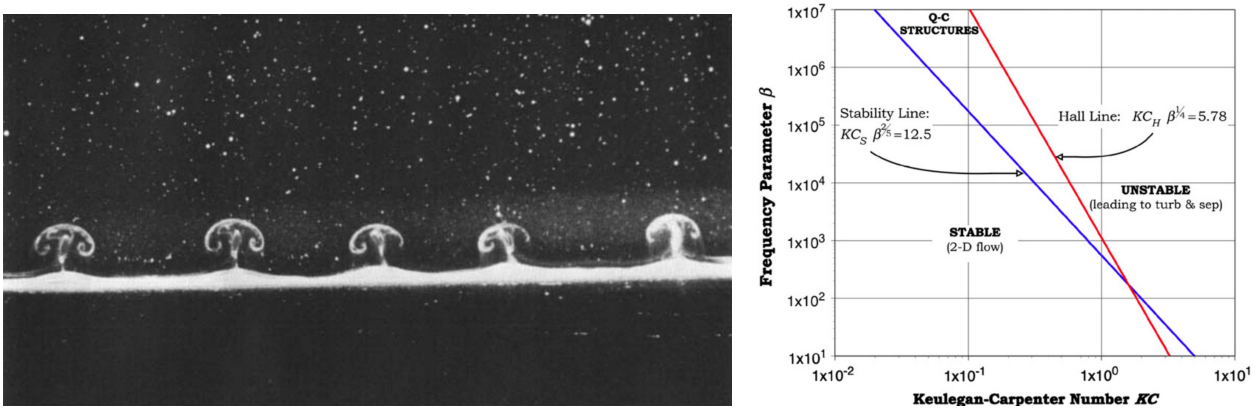

(a) (b)

Figure 2.16: (a) Experimental observation of the Honji instability (Honji, 1981). (b) Limits of stability and transition to turbulence and separation (from Suthon & Dalton (2012)). Red line was proposed by Sarpkaya (2002) and blue line is a linearized form from Hall (1984).

Influence of the seabed

We have seen that if the interaction of current and/or waves with vertical cylinders generates vortices at the cylinder sides, the influence of a wall at one extremity (the seabed) is important and has various consequences. For example, the separation of the boundary layer on the seabed due to the influence of the adverse pressure gradient produced by the pile forms an horizontal vortex which takes the appearance of a horseshoe. The first visualization of the phenomena was observed by Schwind (1962) thanks to smoke techniques in a wind tunnel while visualization using hydrogen bubbles was made in Dargahi (1989) (the full details of such mechanisms can be found in (Baker, 1979; Sumer et al., 1997)). These effects can cause strong shear over the seabed and thus displace sediments which can lead to scour and the failure of the piles. Baker (1979) visualized different horse-shoe vortex systems depending on the Reynold's number which are: (i) steady systems with 2,4 or 6 vortices (the number of vortices increasing with the Reynold's number), (ii) systems which exhibits oscillatory motion and (iii) systems which exhibit irregular unsteady motion. Baker (1979) defines the horseshoe position (in the case of the steady case) as the location of pressure minima on the seabed. It has also been shown that the bed shear stress can be amplified by a factor of 7-11 with respect to its undisturbed value, highlighting the importance of the phenomena. In the case of the wave-structure interaction, the formation of the horseshoe vortex is controlled by the Keulegan-Carpenter number, so that no horseshoe vortex exist if $KC < 6$ for a circular pile or $KC < 4$ for a square pile and it increases in both size and lifespan as KC increases (Sumer et al., 1997). In the same study, they found that superposing a current to the waves significantly increases both size and lifespan.

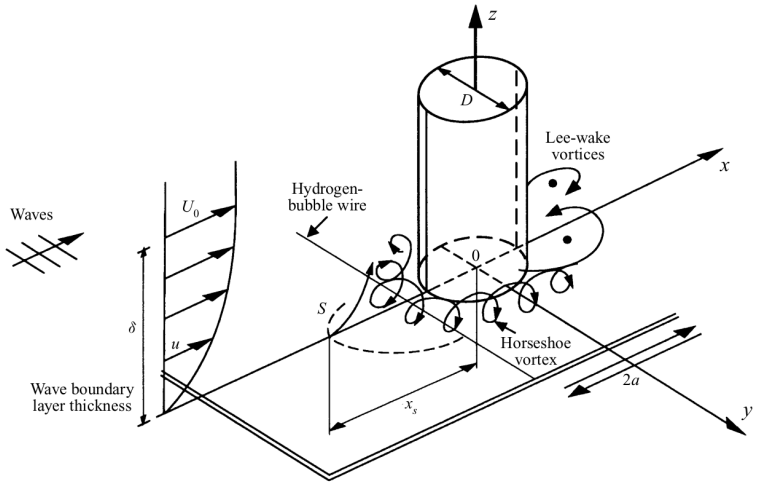

Figure 2.17: Horseshoe vortex schematics from Sumer et al. (1997).

2.4.3. Wave structure interaction

General case

Loads on an offshore structure can come from multiple sources and are often categorized as static and dynamic loads (Chakrabarti, 2005). Static loads are considered to be constant in time such as gravity, hydrostatics or constant current loads. Dynamic loads are the ones varying in times, for instance waves or non-constant wind loads. Steady currents, as seen before, can also generate non steady loads in the transverse direction of the structure. Waves also generate a steady load known as Stokes drift. When it comes to the computation of the loads on a body, the distinction between slender and large body is made as different methods apply. Morison's equation is used for the first ones while diffraction/radiation theories are used for the second one. The diffraction parameter, defined as $\pi D/\lambda$, is used to determine in which category is a structure. It is considered that diffraction/radiation theories are valid for $\pi D/\lambda \geq 0.5$, which corresponds to cases where the incident wave field is significantly modified by the presence of the body (Chakrabarti, 2005). Other important parameters are the Reynolds number, and Keulegan-Carpenter number as seen above. To get an idea why these parameter are important one can apply the Buckingham-π theorem (Buckingham, 1914) to determine the parameters the forces depend on. Let's express the force F in function of all parameters it can depend on, considering a non-flexible and perfectly smooth (no-roughness) body (see also Chakrabarti (2005) and Newman (2017) for similar analysis):

$$f\left(F, \rho, g, \nu, H, \lambda, h, D, t, T, U\right) = 0 \tag{2.28}$$

These are 11 variables and three independent units so according to the Buckingham-π theorem, the equation can be reduced to a non-dimensional form dependent on 8 variables:

$$f(F/\tfrac{1}{2}\rho DU^2,\ U/\sqrt{gh},\ H/\lambda,\ h/\lambda,\ UT/D,\ UD/\nu,\ \pi D/\lambda,\ \omega t) = 0 \tag{2.29}$$

Force coefficient
Froude Number
Steepness
Deep/Shallow water
Keulegan-Carpenter Number
Reynolds Number
Diffraction parameter
Non-dimensional time

The above analysis allows us to show the importance of non-dimensional number such as the Froude, Reynolds, steepness, deep/shallow water limit, Keulegan-Carpenter, and the diffraction parameter. The different theory range of applicability are shown in figure 2.18. In this section, we shall focus on the forces exerted by waves on slender and larger bodies. We will review how to apply the Morison's equation as well as the diffraction theory. As the body of reference is fixed in the wave tank, radiation does not play any role and won't be detailed.

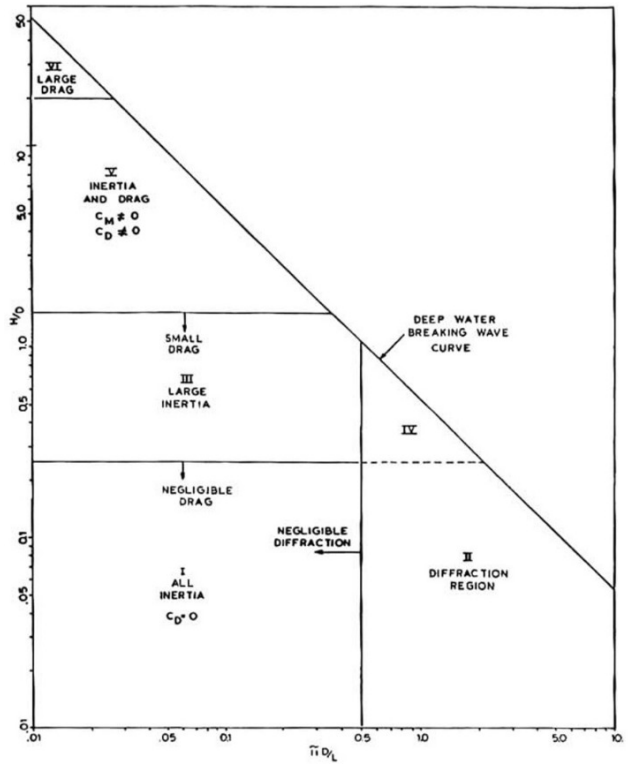

Figure 2.18: Limits of application for large/slender structure from Chakrabarti (2005). X-axis is the diffraction parameter $\pi D/\lambda$ while the y-axis corresponds to the Keulegan-Carpenter number in deep-water ($KC = U_m T/D = \pi H/D$).

Slender bodies The forces exerted by (non-breaking) waves on a pile are generally computed with the integration over the water height of semi-empirical Morison equation (Morison et al., 1950) described in equation 2.23:

$$F = F_D + F_M = \frac{1}{2}\int_{-h}^{\eta} \rho_w C_D D u|u|\, dz + \int_{-h}^{\eta} \rho_w C_M A \dot{u}\, dz \tag{2.30}$$

This equation corresponds to a case where the reference frame origin is situated at the mean water level. F_D is the drag force, F_M is the inertia force, C_D is the drag coefficient, C_M is the inertia coefficient, ρ_w is the water mass density, D is the cylinder diameter, A is the cross-section area, u is the water particle orbital velocity and $\dot{u} = \frac{\partial u}{\partial t}$ is the water particle acceleration. The inertia force can be divided into two terms: the first one is the Froude-Krylov force which is due to the unsteady pressure field ($\mathbf{F_{FK}} = -\int\int_S p\mathbf{dS} = \rho A\dot{\mathbf{u}}$, see also section 2.4.3) and the added mass term (or hydrodynamic mass force, $\mathbf{F_m} = \rho C_m A\dot{\mathbf{u}}$). The resulting coefficient C_M is then given by $C_M = 1 + C_m$. For a cylinder in an oscillatory flow and low KC numbers, C_M tends to 2 as the flow corresponds to the potential flow Sumer et al. (2006). The Morison equation however can only be applied if the pile diameter is way smaller than the wave length ($D/\lambda < 0.2$ according to Chella et al. (2012)). Another effect to take into account is the orbital motion of particles, especially in deep water condition, since orbitals tend to be horizontal in shallow water. Morison also alerts on the differences between non-breaking and breaking waves forces on piles, as the second ones are impulsive and reach a value much greater. The main challenge is to determine the value of the drag and mass coefficient. This can be done by experimentally testing a scaled model of the structure of interest. This last one is fixed at a reasonable distance from the wavemaker and periodic waves are generated. The water level close to the object is measured, as well as the water particles velocities. Acceleration is obtained from differentiation of the velocities. Once done, and knowing the inline loads, we are able to compute the coefficients from equation 2.30. It is necessary however to take into account the Keulegan-Carpenter and Reynolds numbers dependency of these coefficients as shown by experiments by Sarpkaya et al. (1976). The preceding procedure shows the importance of the execution of experimental investigation, notably to calibrate theoretical or numerical model. In the case of computing forces in irregular waves, it is necessary to compute the new velocities and acceleration due to sum of all wave component, as explained in Ishida & Iwagaki (1978). This can be done applying linear filters based on small amplitude wave theory (Reid, 1957). It seems however than particle velocities are underestimated with such method, especially when the wave steepness of the wave becomes high and the non linearities cannot be ignored. Another way of dealing with irregular way is to experimentally determine the inertia and drag coefficient under irregular oscillating forcing as in Longoria et al. (1991), where KC and Re numbers are defined based on statistical treatment of the irregular waves.

Froude-Krylov theory Froude Krylov forces are computed considering the following hypothesis: potential theory is used, fluid is inviscid (no drag forces are considered), incompressible, and the flow is irrotational. The potential flow can then be divided into three terms: the undisturbed incident flow, the diffracted flow and radiated flow such as $\Phi = \Phi_I + \Phi_D + \Phi_R$. For each potential flow, we can then compute the forces acting on the semi-submerged body by computing the pressure p. The undisturbed flow can then be separated into two components, the static and dynamic ones. Then the static Froude-Krylov force is obtained by integrating the static pressure $p_{stat} = -\rho g z$ over the wet area of the body and adding the gravity contribution $\mathbf{F}_{\tilde{\mathbf{g}}}$: $\mathbf{F}_{\mathbf{FK_{stat}}} = \mathbf{F}_{\tilde{\mathbf{g}}} - \int\int_S p_{stat}\,\mathbf{n}\,dS$. For the dynamic component of the force, the use of Bernouilli's relation for non-steady flow is used such as $p_{dyn} = -\rho\frac{\partial \Phi_I}{\partial t} - \rho\frac{|\nabla \Phi_I|^2}{2}$ and $\mathbf{F}_{\mathbf{FK_{dyn}}} = -\int\int_S p_{dyn}\,\mathbf{n}\,dS$. If we assume that the body is small enough so that it has no influence on the incident flow, then diffraction terms can be ignored. This is the Froude-Krylov hypothesis. For example, a small enough body in a wave field whose flow around it is kept attached is suitable for the use of this theory (Chakrabarti, 2005). Linearization of Bernouilli's equation lead to $p = -\rho\frac{\partial \Phi}{\partial t}$. In the case of a linear system (free-surface elevation and body motion are assumed to be low), it is convenient to define the static Froude-Krylov force as a mass spring system such as $\mathbf{F}_{\mathbf{FK_{stat}}} = K_H x$ for a one dimension system, where K_H is the hydrostatic stiffness matrix while the dynamic Froude Krylov force and the diffraction ones are computed with the following relation: $\mathbf{F}_{\mathbf{FK_{dyn}}} + \mathbf{F}_{\mathbf{Dif}} = -\int_{-\infty}^{+\infty} h(t-\tau)\eta(\tau)d\tau$. For a linear system, the output force ($\mathbf{F}_{\mathbf{FK_{dyn}}} + \mathbf{F}_{\mathbf{Dif}}$) is the convolution of the excitation impulse-response function h with the input excitation, the wave height η (Penalba et al., 2017).

Diffraction theory If the semi-submerged body is large enough, it will affect the surrounding wave field. In this case, the flow in most cases will remain attached to the body and the flow can be well described by potential theory (Chakrabarti, 2005). The wave diffraction component of the forcing on a structure is a function of the diffraction potential as seen above, which is solution of a boundary value problem (BVP). Let's consider a fixed structure which wet surface is called S_B. At this location, from free-slip condition, the wave diffraction problem is retrieved from $-\frac{\partial \Phi}{\partial \mathbf{n}} = -\frac{\partial \Phi_I + \Phi_D}{\partial \mathbf{n}} = \mathbf{V}(t)\cdot\mathbf{n}$, with $\mathbf{n}$ the normal to the outward unit normal vector to the surface and $\mathbf{V}(t)$ the velocity of the body. So that $\frac{\partial \Phi_D}{\partial \mathbf{n}} = -\frac{\partial \Phi_I}{\partial \mathbf{n}}$ on S_B for a fixed body. This problem can be solved thanks to the boundary element method (BEM) which divides the body into small panels, and is widely use in commercial (*WAMIT*, *AQWA*) or open-source solvers (*Nemoh*) (Babarit & Delhommeau, 2015)).

Note on radiation theory: As the body moves into water, it will generate a radiated wave field whose potential is Φ_R, and thus forces associated with this wave field. Forces in phase with the velocity of the body are called damping forces while forces in phase with the acceleration acts as inertia and is called added mass. A method to compute damping force

was given by Cummins (1962), known as the Cummins equation which links the damping forces to the convolution of the impulse response function and the velocity of the body.

Wave structure interaction with a square cylinder

A very few studies concentrated their effort on square or even rectangular cross-section cylinders. We can however underline the work of Arabi et al. (2019), who experimentally and numerically studied the generation and evolution of coherent structures induced by the interaction between a vertical square cylinder and solitary waves. The experimental data were used to understand the phenomenon and validate a CFD model based on VOF (Volume of fluid) for the interface determination and LES formulation for turbulence modeling. The conclusion of their work shows the formation of vortices behind the cylinder that can migrate far away from it during the motion of the solitary wave, with strong velocity gradient at the trailing edge of the square cylinder, sustaining the formation of the vortical structures. They show that such structures are formed, after flow separation, from the free-surface to the bottom of the tank. They observe also that the number of vortices correspond to the number of sharp corner (4), and vortex core of the primary vortices are highly deformed along the vertical direction. They also report the trajectory of the primary vortices along the tank and finally they got interested in the production of turbulent kinetic energy and the different scales associated with it. Another experimental similar study, by Bremm et al. (2015), focuses on the interaction between depression led long waves and a square cylinder on a sloping beach, basing their geometrical configuration on a real tsunami event and according to the author it is the first study of its kind. They record velocity profiles thanks to a PIV set-up, as well as both inertia and drag forces on the structure, the first one being an order of magnitude lower than the last one (and thus are neglected) and reach the following conclusions. As the Reynolds number is not steady when the waves passes by the square cylinder, the use of the time-history drag coefficient is of much importance for the analytical calculation of the force. They were able to accurately predict the drag forces, however without reaching to establish a link with vortex shedding. They observe bow wave separation upstream, the hydraulic jump condition, a turbulent wake and vortex shedding. Shafiei et al. (2016) experimentally studied the interaction between a square prism and a bore under different incident angles, in a tank equipped with a an automatic gate for the bore generation. The bore heights and velocities, as well as the forces and pressure on the structure were measured. They deduced a relation between the bore velocity and the bore heights at about $u_b = 1.7\sqrt{gh_b}$ with h_b the bore height, g the gravitational constant and the 1.7 value is an empirical coefficient based on the experimental data. They also give some procedure to easily evaluate the forces over the structure. A final article of interest is from Foster et al. (2017), who experimentally validated a set of equation capable of predicting the force of very

long tsunami like waves over rectangular structure, without the need of expensive calculus. They also observe that the pressure over the building is hydrostatic.

Part II

Methodology

Chapter 3

Numerical Wave Tank

As solution of the Navier-Stokes equation are unavailable most of the cases, we rely on numerical simulation to capture and approximate the physics of the phenomenon. This section describes how the CFD model will be implemented. As a first try, Fluent 6.3 was used to simulate the 2D wave tank. However, as the number of computational node is limited, the simulations will be run with OpenFOAM 5 (for the piston wavemaker study) and OpenFOAM-v19.06 for the remaining studies of this thesis.

3.1. Numerical Model Review

In this section, all the relevant numerical set-up and assumptions are presented. The geometry is shown and the problem is settled in section 3.1.1. Turbulence models are presented in section 3.1.2 and laminar or Reynolds Averaged Navier Stokes (RANS) equations might either be used and are detailed in section 3.1.2 and 3.1.2 respectively. The dynamic mesh handling is outlined in section 3.1.3, while the boundary conditions are described in section 3.1.4. The numerical methods used to the resolution of the governing equations are introduced in section 3.1.5 and in section 3.1.6 the computer infrastructure is described as well other technical details.

3.1.1. Problem definition

The problem is described in the schematics of figure 3.1. We consider a 2D wave tank of length L and height d, equipped with a moving piston wavemaker placed at the left wall and the opposite wall of the tank is situated on the right. The mean still water level is noted h and can be varied at will. The origin of the coordinate system is located at the left bottom of the wave tank and all different measurement stations along the wave tank are referred to this coordinate system. The pistons occupy the overall height of the canal so that they

do not allow for the fluid to access the part behind it, to the contrary of the experimental facility which is composed of a wet-back paddle. Wave gauges can be set up at paddles and along the canal. The set-up with the square cylinder is presented in figure 3.2. Refinement zone comprises the wavemaker zone (in yellow), the wave propagation zone (in red) and the near cylinder regions. For each zone, a specific grid size is chosen either from grid refinement studies (at the wavemaker and for the wave propagation) or theoretical assumptions (size of the boundary layer).

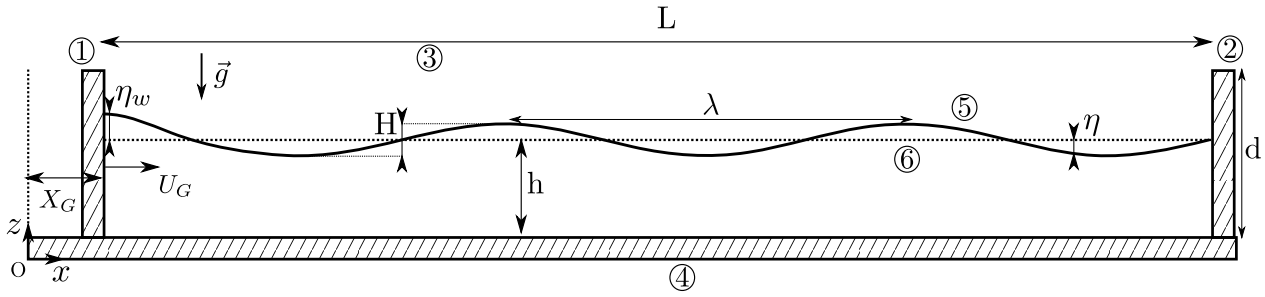

Figure 3.1: Schematics of the problem. Lateral view. The numerical domain is composed of (1) the piston wavemaker, (2) the tank end boundary, (3) the atmosphere and (4) the seabed. The generated waves (5) at the free-water surface are measured with respect to the mean still water level (6) h.

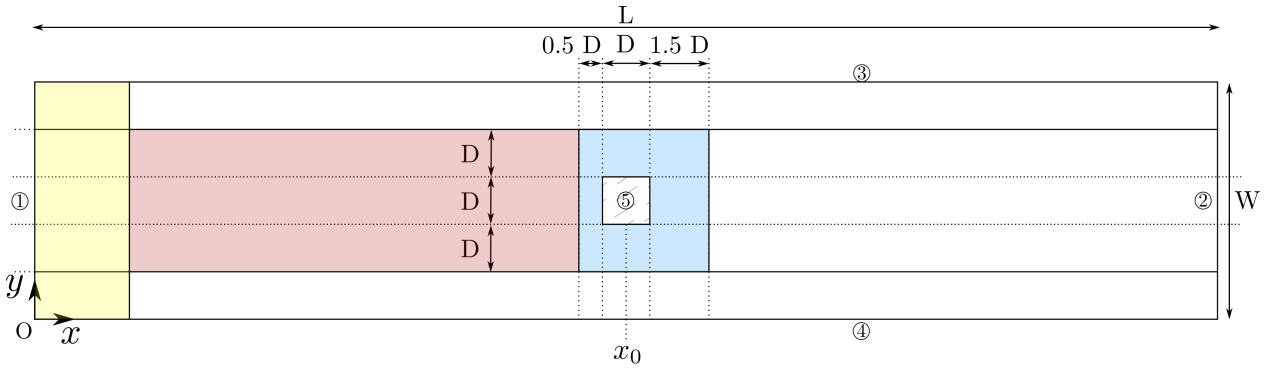

Figure 3.2: Schematics of the problem. Top view. The numerical domain is composed of (1) the piston wavemaker of width W, (2) the tank end boundary, (3) the left wall of length L, (4) the right wall and (5) the square cylinder placed at x_0 from the origin and of diameter D. The refined zone are: the wavemaker zone (in yellow), the wave propagation zone (in red) and the square cylinder zone (in blue).

3.1.2. Governing equations

The numerical simulation solves the 2D two-phase laminar Reynolds Averaged Navier-Stokes equations (RANS) with two incompressible fluids (water and air phases). DNS simulations were considered to be numerically too expensive to carry out. The momentum

equation (equation 3.11) and the continuity equation (equation 3.10) allows to describe fluid motion, linking pressure to fluid velocity components. The momentum equation for the "InterFoam" solver is presented in G.-H. Kim & Park (2017). The solver uses the continuum surface force (CSF) model (Brackbill et al., 1992) to model surface tension. The VOF model is traduced by the scalar α which represents the volume fraction of water (1 if the cell is full of water, 0 if full of air, and in-between values are for cells belonging to the interface). α follows classical advection equation (it is a Lagrangian invariant, see Hirt & Nichols (1981)). The mass conservation equation is also solved in primitive variables incorporating the VOF model to deal with each fluid phase (Hirt & Nichols, 1981).

Choice of turbulence models

Turbulence is "characterized by the superposition of a highly irregular and oscillatory velocity pattern upon an otherwise "smooth" flow" according to Newman (2017). If Navier-Stokes equations remain valid for turbulent flows, it is essential to include these variations to the main flow resolution, as they might have an great importance on the flow development and the efforts associated with it. The difficulty then relies in the choice of the turbulence model, and the different scales associated to them. Observations led also to classify flows in function of their turbulent properties, which can be laminar (no turbulence levels), transitional (apparition of fluctuations) or turbulent (high fluctuation levels), and these regimes are characterized by the Reynolds number (low Reynolds numbers characterize laminar flows while high Reynolds numbers characterize turbulent flow). The most known example, the flow in a pipe, is considered laminar for Reynolds number lower than 2300 and fully turbulent for one higher than 4000. Turbulence is an energy transfer mechanism where energy of large eddies (of scale L) is transferred to lower scale eddies until the smallest scale l. It then dissipated by the form of heat through viscosity (Kolmogorov, 1941). The smallest scale, called Kolmogorov scale and written η_k, as well as time and velocity, can be estimated by the following expressions:

$$\eta_k = \left(\frac{\nu^3}{\epsilon}\right)^{\frac{1}{4}}, \quad \tau_k = \left(\frac{\nu}{\epsilon}\right)^{\frac{1}{2}}, \quad u_k = (\nu\epsilon)^{\frac{1}{4}} \tag{3.1}$$

where ν is the kinematic viscosity in m^2/s and ϵ is the turbulent kinetic energy dissipation rate in m^2/s^3. The Reynolds number associated to this scale is equal to $\eta_k u_k/\nu = 1$ showing the prevalence of viscous forces over inertial forces. This scale is also accessible through the use of the Reynolds number as (Tennekes et al., 1972):

$$\eta_k = L \cdot Re^{-\frac{3}{4}} \tag{3.2}$$

Wavemaking problem We define the following Reynolds number for the wavemaking problem. The length of reference is the mean water level h (from 0.05 m to 0.15 m) and the velocity of reference is the one of the wavemaker U_G, which ranges from 0.05 $\mathrm{m\,s^{-1}}$ to 0.4 $\mathrm{m\,s^{-1}}$, for the step velocity which is going to be run further on. The associated Reynolds number is then comprised between 250 to 60000, that is to say that for the highest Reynolds number, it is necessary to use a turbulence model, as illustrated by figure 3.3, where tests have been run for a velocity step of 0.4 m/s and a still water level of 0.150 m, corresponding to a Reynolds number of 60000. It is possible to observe the differences between the laminar test case results with the ones including a turbulence model, whether it is a $k-\epsilon$ model or the buoyancy modified $k-\omega$ SST models. The main discrepancy is situated at the overshoot value which is around 5% lower with turbulence. No differences seems to appear for the steady state value however. This shows that for higher Reynolds number cases, a turbulence model should be included in the simulation set-up.

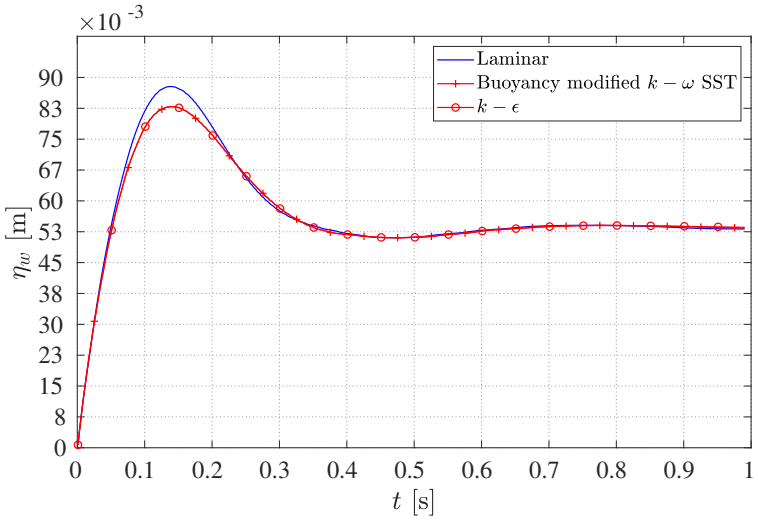

Figure 3.3: Comparison of wave height at wall for a step velocity of m/s between laminar and turbulent models.

Wave-structure problem The most faithful strategy, called Direct Numerical Simulation (DNS), consists in simulating all scales of the turbulence cascade, forcing the spacial discretization to reach the Kolmogorov scale. An estimation with the geometry we deal with can be carried out. If the mean water level h is 0.05 m, the cylinder width D is 4 cm and we consider a solitary wave of height $H = 0.02$ m, then the particle horizontal velocity is given by McCowan (1891) and is equal to:

$$u = \frac{c_p m H}{\tan\left(m(h+H)/2\right)} \frac{1+\cos(mz)\cosh(mx)}{\left(\cos(mz)+\cosh(mx)\right)^2} \tag{3.3}$$

where c_p is the phase celerity of the wave, m is McCowan (1891) constant coefficient, and x, z are the horizontal and vertical coordinates, respectively. The maximum is found for $x = 0$, $z = H$ and leads to a value of $u_{max} = 0.31\ \mathrm{m\,s^{-1}}$. The associated Reynolds is $Re = u_{max}D/\nu = 1253$ and the Kolmogorov scale is $\eta_k = 3 \times 10^{-5}$ m. This corresponds to a very small cell size and would certainly lead to grid size of various tens of millions. Large Eddy Simulation (LES) (Smagorinsky, 1963; Lilly, 1966; Deardorff, 1970) is another technique that explicitly solves large eddies and take into account the small ones with sub-grid models. In order to solve only large eddies, the Navier-Stokes equation are filtered (low-pass) both in space and time, which leads to cut-off frequencies. LES results to be very accurate in free-flow regions or highly separated flows but fails in near-wall regions(Pope, 2004). The LES is becoming more popular but is still very computationally expensive and thus time consuming.

Reynolds-Averaged Navier Stokes equations (RANS) are the most used and studied family of turbulence models as it is the oldest one. As the turbulence problem is an open one (more unknown variables than equations), a variety of models try to close it by using a turbulent viscosity term. RANS models might not be able to accurately simulate a flow when this last one shows strong anisotropy or when turbulent transport by large structures is predominant (Rodi, 2017). I. Celik (2003) reviewed a certain amount of studies comparing LES/RANS models and states that in general, LES is in better agreement with experimental data than RANS, but at the price of a sufficiently refined mesh. Regarding the determination of this grid refinement, it is however complicated to define it before any knowledge of the flow characteristics, even if an attempt is made in Pope (2004). In this work, RANS equations will be solved in the general case even for some sections laminar equations will be used, and will be explicitly specified. The choice of RANS models over LES or DNS is mainly due to its simplicity and is computationally the cheapest, while it seems that the gain of using LES in boundary layer is not clear, and worst could have an adverse effect if the grid scale is not correct (Pope, 2004). Moreover, experimental validation is carried out and we will be able to trust or not the model.

Laminar equations

These equations can be written in vector form:

$$\nabla \cdot \mathbf{U} = 0 \tag{3.4}$$

$$\frac{\partial(\rho \mathbf{U})}{\partial t} + \nabla \cdot (\rho \mathbf{U}\,\mathbf{U}) - \nabla \cdot (\mu \nabla\,\mathbf{U}) - \nabla\,\mathbf{U} \cdot \nabla \mu = -\nabla p^* - \mathbf{g} \cdot \mathbf{x} \nabla \rho + \sigma \kappa \nabla \alpha \tag{3.5}$$

$$\frac{\partial \alpha}{\partial t} + (\nabla \cdot \mathbf{U})\alpha = 0 \tag{3.6}$$

Where $\mathbf{U}$ is the velocity vector, p^* the pseudo-dynamic pressure ($p^* = p - \rho \mathbf{g} \cdot \mathbf{x}$), ρ the density, μ the dynamic viscosity, g the gravity acceleration, $\mathbf{x}$ the position vector, σ the fluid surface tension coefficient. The volume fraction α is introduced to deal with the two-phase formulation within the volume of fluid (VOF) framework. κ is defined as followed:

$$\kappa = -\nabla \cdot \frac{\nabla \alpha}{|\nabla \alpha|} \tag{3.7}$$

In the two-phase formulation, density and viscosity on each domain cell are computed as a weighted mean of the form (Berberović et al., 2009; Rusche, 2002):

$$\rho = \alpha \rho_{water} + (1 - \alpha)\rho_{air} \tag{3.8}$$

$$\mu = \alpha \mu_{water} + (1 - \alpha)\mu_{air} \tag{3.9}$$

with α the fraction function which is equal to 1 when the cell is fully filled with water and 0 when it is filled with air.

Reynolds Averaged Navier Stokes (RANS) equations

The RANS equations are solved and a turbulence closure model is chosen: the buoyancy modified $k - \omega$ SST (shear stress transport) model, developed by Devolder et al. (2018) for wave applications. The main advantage of this model is to avoid the over-estimation of turbulent kinetic energy that are often problematic in free-surface flow simulation, leading to over-damped waves during propagation along the wave tank or change in the beaking location in the example of breaking wave studies. The RANS equations for two immiscible fluids as solved by *OpenFOAM* can be written in vector form as:

$$\nabla \cdot \mathbf{U} = 0 \tag{3.10}$$

$$\frac{\partial(\rho \mathbf{U})}{\partial t} + \nabla \cdot (\rho \mathbf{U}\,\mathbf{U}) - \nabla \cdot (\mu_{eff} \nabla\, \mathbf{U}) - \nabla\, \mathbf{U} \cdot \nabla \mu_{eff} = -\nabla p^* - \mathbf{g} \cdot \mathbf{x} \nabla \rho + \sigma \kappa \nabla \alpha \tag{3.11}$$

$$\frac{\partial \alpha}{\partial t} + (\nabla \cdot \mathbf{U})\alpha = 0 \tag{3.12}$$

where $\mathbf{U}$ is the velocity vector, p^* the pseudo-dynamic pressure ($p^* = p - \rho \mathbf{g} \cdot \mathbf{x}$), ρ the density, μ the dynamic viscosity, g the gravity acceleration, $\mathbf{x}$ the position vector, σ the fluid

surface tension coefficient. The volume fraction α is introduced to deal with the two-phase formulation within the volume of fluid (VOF) framework. κ is defined as followed:

$$\kappa = -\nabla \cdot \frac{\nabla \alpha}{|\nabla \alpha|} \tag{3.13}$$

In the two-phase formulation, density and viscosity on each domain cell are computed as a weighted mean of the form (Berberović et al., 2009; Rusche, 2002):

$$\rho = \alpha \rho_{water} + (1 - \alpha)\rho_{air} \tag{3.14}$$

$$\mu_{eff} = \alpha \mu_{water} + (1 - \alpha)\mu_{air} + \rho \nu_t \tag{3.15}$$

Note the additional term ν_t which is the turbulent kinematic viscosity defined as:

$$\nu_t = a_1 \frac{k}{\max(a_1 \omega, SF_2)} \tag{3.16}$$

where k is the kinetic turbulent energy, ω is the turbulence specific dissipation rate, $a_1 = 0.31$ is a constant coefficient, S is the mean rate of strain of the flow and F_2 is the second blending function. The two transported variable k and ω determines the energy in the turbulence process and the scale of the turbulence respectively. The buoyancy-modified SST (shear-stress transport) $k - \omega$ model (Devolder et al., 2018) has various advantages, such as the possibility to use it through the whole boundary layer (through the viscous sub-layer until the wall), the switch to the $k - \epsilon$ model in the free-stream and this version also allows to avoid non-physical extra-turbulence at the interface, leading to damping of the wave (Devolder et al., 2018). The main differencences are the explicit inclusion of the density ρ in the equations and the addition of a buoyancy term G_b in the turbulent kinetic energy equations which is defined further on. The blending functions are defined as (see Menter, Kuntz, & Langtry (2003)):

$$F_1 = \tanh\left[\left\{\min\left[\max\left(\frac{\sqrt{k}}{\beta^* \omega y}, \frac{500\nu}{y^2 \omega}\right), \frac{4\rho\sigma_{\omega 2} k}{CD_{k\omega} y^2}\right]\right\}^4\right] \tag{3.17}$$

$$F_2 = \tanh\left[\left[\max\left(\frac{2\sqrt{k}}{\beta^* \omega y}, \frac{500\nu}{y^2 \omega}\right)\right]^2\right] \tag{3.18}$$

with $CD_{k\omega} = max\left(2\rho\sigma_{\omega 2}\frac{1}{\omega}\nabla k \cdot \nabla \omega, 10^{-10}\right)$ and y is the distance to the nearest wall. According to Menter, Kuntz, & Langtry (2003), F_1 is equal to 0 far from the wall (leading to the behaviour of a $k - \epsilon$ model) and progressively changes to 1 as the cells are situated inside the boundary layer thus behaving as a $k - \omega$ model. The closure equations for both k and ω are:

$$\frac{\partial(\rho k)}{\partial t} + \mathbf{U}\cdot\nabla(\rho k) - \nabla\cdot\left(\rho\left(\nu + \sigma_k\nu_t\right)\nabla k\right) = \rho P_k + G_b - \rho\beta^*\omega k \tag{3.19}$$

$$\frac{\partial(\rho\omega)}{\partial t} + \mathbf{U}\cdot\nabla(\rho\omega) - \nabla\cdot\left(\rho\left(\nu + \sigma_\omega\nu_t\right)\nabla\omega\right) = \frac{\gamma}{\nu_t}\rho G - \rho\beta\omega^2 + 2\left(1 - F_1\right)\rho\frac{\sigma_{\omega 2}}{\omega}\nabla k\cdot\nabla\omega \tag{3.20}$$

$$P_k = \min\left(G, 10\beta^* k\omega\right) \tag{3.21}$$

$$G = 2\nu_t S : S = \nu_t\frac{\partial u_i}{\partial x_j}\left(\frac{\partial u_i}{\partial x_j} + \frac{\partial u_j}{\partial x_i}\right) \tag{3.22}$$

where S is the strain tensor defined as $S = 1/2\left(\nabla\mathbf{U} + \nabla\mathbf{U}^\intercal\right)$. The added buoyancy term G_b, active only close to the interface, is defined as follows:

$$G_b = -\frac{\nu_t}{\sigma_t}\mathbf{g}\cdot\nabla\rho \tag{3.23}$$

and all parameter σ_k, σ_ω, β and γ follow the following equation:

$$\phi = F_1\phi_1 + (1 - F_1)\phi_2 \tag{3.24}$$

with $\phi_{1,2}$ defined as in table 3.1.

ϕ	σ_k	σ_ω	β	γ
ϕ_1	0.85034	0.5	0.075	0.5532
ϕ_2	1.0	0.85616	0.0828	0.4403

Table 3.1: Default value for ϕ_1 and ϕ_2 used in equation 3.24.

3.1.3. Mesh handling

Moving boundaries are not so popular yet because of the complexity of its numerical implementation and because the method runs usually slower than a simpler boundary condition implementation method, as it involves a dynamic mesh in the model. It may however reveal to be closer to the physical phenomena. In this work, a regular 2D grid is generated. Then, a mesh layer addition/removal strategy was adopted: when the boundary moves, cell size decreases on one side of the paddle while it increases on the other side. When the size is critical (the user can arbitrary chose what value should be implemented), the cells merge with the following layer on one side while a new layer of cells is created on the other side. This strategy is presented in figure 3.4. The cells on top of the piston and at the bottom follows

the piston motion so that the interface where the layer addition/removal is performed stays constant. An advantage of the cell layer addition/removal compared to unstructured grid remeshing or grid contraction/expansion techniques is that the mesh transformation only concerns a few cells (the first layer on both sides of the piston) which should decrease the time spent for dynamic mesh execution. However, the use of this technique revealed to be complicated because of the "aleatory"-like motion of the absorption paddle which caused the creation of negative volume cells; it also created problems for stability of explicit schemes as the creation of really small layer cells which made exponentially increased the Courant number. For all these reasons, a simpler but slower model using mesh contraction is used in this work. The mesh uniformly contracts and expands when the flume ends move, conserving the global mesh cell volumes as this motions are relatively smalls compared to the flume length. Such strategy is also shown in figure 3.4.

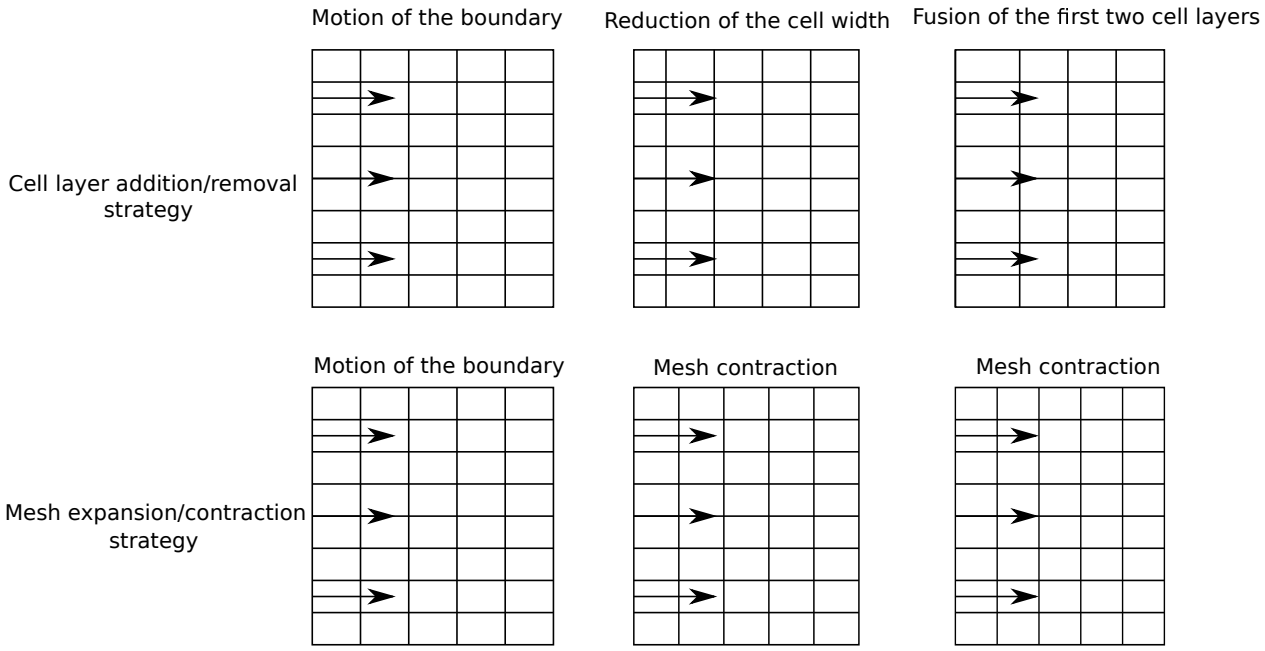

Figure 3.4: Cell layer addition/removal and mesh expansion/contraction strategies can be employed for dynamic mesh motions.

3.1.4. Boundary conditions

Boundary conditions employed in this work are summarized in equation 3.25. On the piston wavemaker wall we impose no-slip condition for all velocity components. The initial still water level h is always established before any wavemaker motion by initializing α. The volume fraction α is bounded and may adopt any value between $0 \leq \alpha \leq 1$ in any place of the physical domain and Neumann boundary conditions, set to 0, are applied at all boundaries for the α variable as well so that the volume of fluid is the same at the boundary as at the first cell.

In particular, at the wavemaker, such condition forces the contact angle of the interface to be perpendicular to the wavemaker wall which agrees with the experimental results of Uddin & Needham (2015) and S. Yang & Chwang (1992) for the case of a continuously accelerated wavemaker. In this work, the piston wavemaker moves according to an input velocity signal. At the piston wavemaker wall the velocity matches the velocity of the moving boundary in the x direction only. A no-slip condition is used at the seabed wall and the right end wall. The pressure is set to a pressure of reference (in this case 0) at the atmosphere boundary and 0-Neumann conditions are used at the other locations. A zero-gradient condition is applied at the atmosphere for outflow and a velocity u_ϕ is assigned for inflow based on the flux in the patch-normal direction. The boundary conditions for the velocity, pressure and α variables can be summarized as:

$$\text{Wave tank} \begin{cases} x = X_G(t) & \rightarrow & u_x = U_G(t), u_y = 0, u_z = 0, & \frac{\partial p^*}{\partial x} = 0, & \frac{\partial \alpha}{\partial x} = 0 \\ x = L & \rightarrow & u_x = 0, u_y = 0, u_z = 0, & \frac{\partial p^*}{\partial x} = 0, & \frac{\partial \alpha}{\partial x} = 0 \\ z = 0 & \rightarrow & u_x = 0, u_y = 0, u_z = 0, & \frac{\partial p^*}{\partial z} = 0, & \frac{\partial \alpha}{\partial z} = 0 \\ z = d & \rightarrow & \begin{matrix}\text{inflow: } u_x = 0,\ u_y = 0,\ u_z = u_\phi, \\ \text{outflow: } \frac{\partial u_x}{\partial z} = 0,\ \frac{\partial u_y}{\partial z} = 0,\ \frac{\partial u_z}{\partial z} = 0,\end{matrix} & p^* + \tfrac{1}{2}|\mathbf{u}|^2 = 0, & \frac{\partial \alpha}{\partial z} = 0 \end{cases} \tag{3.25}$$

$$\text{Cylinder} \left\{ \quad u_x = 0, \quad u_y = 0, \quad u_z = 0, \quad (\nabla p^*) \cdot \mathbf{n} = 0, \quad (\nabla \alpha) \cdot \mathbf{n} = 0 \right. \tag{3.26}$$

where $\mathbf{n}$ is the normal unitary vector of the boundary. As for the turbulent model variables k and ω, as the mesh is not refined enough to resolve the flow at the wavemaker and side walls of the tank, wall functions are used for both variables. At the atmosphere, inlet/outlet boundary condition is set up where the values for outlet flow (velocity field at atmosphere pointing outside of the domain) is a zero gradient condition (0-Neumann boundary condition) while for the inlet flow (velocity field at atmosphere pointing inside of the domain) we set $k = 10^{-4}$ $\mathrm{m^2\,s^{-2}}$ and $\omega = 2$ $\mathrm{s^{-1}}$. At the square cylinder, the boundary conditions that are applied depends on the grid resolution at the wall. Indeed, in the general case and for turbulence modeling, low Reynolds turbulence number model use the first point in the viscous sublayer ($y^+ \approx 1$) while high Reynolds number use the first grid point in the buffer layer ($5 \leq y^+ \leq 30$) (Moukalled et al., 2016). In our case, section 3.1.2 showed that the problem is characterized by a relatively low Reynolds number so that we chose to fully resolve the boundary layer (that is to say that we make sure that the first grid points corresponds to $y^+ < 1$). The turbulent kinetic energy boundary condition is a zero Neumann condition at all walls (*kqRWallFunction* in *OpenFOAM*) and its initial condition is set to 0 $\mathrm{m^2/s^2}$ (in practice it is set to a really low non zero value $k = 10^{-8}$ $\mathrm{m^2/s^2}$) and the turbulence specific

dissipation rate ω is set to (Menter, Ferreira, et al., 2003):

$$\omega_w = \frac{6\nu}{\beta_1 y^2} \tag{3.27}$$

where $\beta_1 = 0.075$ and y is the distance from wall to the first point. In practice, the *omegaWallFunction* boundary condition is used in *OpenFOAM* which sets the first grid point ω value in function of the y^+ value, that is to say depending on the position of the first grid point whether it is inside the viscous sublayer or it is inside the log-law sublayer.

3.1.5. Numerical Methods

The governing equations were solved with the open source software *OpenFOAM* version 5 or *OpenFOAM* version 19.06 (Weller et al., 1998). *OpenFOAM* is an object oriented C++ toolbox for solving continuum mechanics problems with the finite volume method. It can be used in applications such as turbulence modeling, fluid flows, chemical reactions, multiphase flows, electromagnetics, compressible flow among others. Pre-processing tools are included such as meshing tools (*blockMesh*, *SnappyHexMesh*), mesh conversion tools, field initialization, boundary definition, gauge definition... *OpenFOAM* presents many advantages: as released under the GNU General Public license it is free and open-source (no licensing fees, unlimited number of jobs, users and cores). It is also largely used in the scientific community and thus has been validated for many applications. Numerous ready to use cases are available which allow for quick set up and a large user community is ready to help making it more accessible. It is designed to support parallel computations and its text file structure allows for an easy automation in case of parametric studies. We use *interDyMFoam/interIsoFoam*, solvers of the Navier Stokes equations for two incompressible isothermal immiscible phases using the volume of fluid (VOF) method. It increases the capabilities of previous solvers allowing to handle dynamic mesh motion. *OpenFOAM* solves a single equation of momentum for the two-phase mixture by introducing a volume fraction advection equation of the VOF method used to capture the interface between the phases. Hirt & Nichols (1981) presented this method as an efficient and simple way of treating the free surface in numerical simulations, as it stores a minimum of information. This method should be carefully used when the surface tension becomes important.

interFoam/interDyMFoam Some numerical solvers like *interFoam/interDyMFoam*, which uses *MULES* algorithm, impose some restrictions in order to keep a sharp interface between both fluid phases. An additional term called artificial compression is introduced here (Rusche, 2002):

$$\frac{\partial \alpha}{\partial t} + \nabla \cdot (\alpha \mathbf{U}) + \nabla \cdot (\mathbf{U_c} \alpha (1 - \alpha)) = 0 \tag{3.28}$$

$$U_c = min(C_\alpha \left|\mathbf{U}\right|, max(\left|\mathbf{U}\right|)) \tag{3.29}$$

C_α is a user defined coefficient whose default value is 1. The additional term is only active close to the interface because of the product $\alpha(1-\alpha)$ and does not impact the solution outside the interface region. Its role is to compress the interface and maintain α between 0 and 1 if used with discretization techniques. In the post-processing stage, the value of $\alpha = 0.5$ is chosen to detect the free-surface, which is carried out thanks to linear interpolation.

interIsoFoam If *interDyMFoam* showed accurate results in the simplest configuration of the NWT, it showed to prove unstable in the case of unstructured meshes or hybrid meshes. Smearing of the free-surface was appearing for example. The overall idea of the isoAdvector algorithm (Roenby et al., 2016) is to improve the sharpness of the interface by more accurately computing the face fluxes. The general steps of the algorithm is: (i) reconstruction of the interface, (ii) advection of the interface. At every time step, the first stage allows to retrieve the interface position and orientation in every cells (the isoface, much more accurate than the 0.5-isosurface used in *interFoam*). It is followed by the motion of the interface in function of the velocity field during the time interval $[t, t + \Delta t]$. Roenby et al. (2016) implemented and tested the algorithm and found very satisfactory results, in terms of interface sharpness, shape preservation, volume conservation, boundedness and efficiency. They compared their results with other VOF-based algorithm, notably *MULES*. According to them, *MULES* behaves well for interface Courant number below 0.1 while this value can be increased to 0.5 for the *isoAdvector* algorithm. Since then, the method has been used with success to model coastal engineering flows (Vukcević et al., 2018; Elsafti et al., 2019; B. E. Larsen et al., 2019), sloshing (Li et al., 2019), annular flows (Fan et al., 2019), and even avalanches flows (Pétursson et al., 2019).

interDyMFoam and *interIsoFoam* solvers use the PIMPLE algorithm which combines both SIMPLE (Semi-Implicit Method for Pressure Linked Equations) (Patankar, 1980) and PISO (Pressure Implicit Split Operator) (Issa, 1986) algorithms and allows for bigger time steps. Simulations were performed on a CPU Xeon E5-2660 v2/Intel Xeon Gold 6152 cluster running on Simple Linux Utility for Resource Management (*Slurm*) and based on MPI libraries. The CPU run time for a one second transient simulation and a typical wave was about 2.4 hours for a 400000 element mesh and $\Delta t = 5 \cdot 10^{-4}$ s time step. The geometry of the wave tank required a fine spatial discretization, particularly in zones like the water-air interface and zones of high velocity gradients such as the wavemaker walls. Explicit schemes are used so that special care is taken when choosing the time step regarding the mesh size and CFL condition below 1. As a result of the rapid input velocity signals during the wave formation

and subsequent progression along the wave tank, the temporal discretization requires time steps smaller than 10^{-3} s.

3.1.6. Miscellaneous

Surface tension effects The importance of the surface tension compared to gravitational forces are characterized by the Bond number:

$$Bo = \frac{\Delta\rho g}{\sigma k^2} = \frac{\Delta\rho g}{\sigma} l^2 \tag{3.30}$$

with $\Delta\rho$ the difference of density between the two phases, g the gravitational acceleration, σ the surface tension, k the wave number and l is the characteristic length. If $Bo >> 1$ then the surface tension does not play any major role in the wave physics. This is the case in the simulation we carry out, as the wave length is quite long. For more information and detail on the influence of the surface tension on wave the reader can refer to Dias & Kharif (1999). We decide however to keep the surface tension as it might be important for lower scale phenomena (small vortices, blockage at cylinder, meniscus at walls), and the computational overcost is low. In *OpenFOAM*, miscalculations of the surface tension forces is source of spurious currents (high velocities) in the air interface and is a well-identified problem without solution for now for really low scale problems such as in drops or microfluidics studies.

Water/Air interface detection It is chosen, for its simplicity of implementation, to detect the interface water/air at a given x position by calculating the VOF variable $\alpha = 0.5$ through linear interpolation in the vertical direction.

Cluster use and scaling test The National Laboratory for High Performance Computing[1] (NLHPC) of the faculty of engineering at Universidad de Chile is doted with a cluster whose main characteristics are presented in table 3.2. The total capacity of *Leftraru* is 266 TFlops. The cluster is accessible for any research related tasks. It is hosted at CMM (Center of Mathematical Modeling). The workload is handled with the well known open-source *SLURM*[2]. Each researcher/student may use until 40 processors with a testing account.

[1] /www.nlhpc.cl
[2] https://slurm.schedmd.com/

Partition	Number of Nodes	Number of Processors per nodes	Total number of processors	Available RAM per node (GB)
general	48	2x22	2112	192
slims	128	2x10	2640	48
largemem	9	2x22	396	768

Table 3.2: Main characteristics of the cluster *Leftraru* at CMM.

The aim of this paragraph is to study the scaling of *OpenFOAM* when using an increasing number of processors. To do so, we chose a base case which is presented in table 3.3. It is executed with different number of processors. Results are shown in figure 3.5. The speed up is defined as:

$$\text{Speed Up} = \frac{\text{Reference Time}}{\text{Improvement Time}} \tag{3.31}$$

In the same figure is plotted the efficiency which allows to better read the speed-up results, as an efficiency close to 1 is very good and an efficiency close to 0 shows no improvement by scaling the computation. The efficiency is computed according to the following formula:

$$\text{efficiency} = \frac{\text{Speed Up} \times \text{Reference Processor Number}}{\text{Number Of Processors}} \tag{3.32}$$

A program which is scaling well has a linear speed-up. It means that the time to execute a program is half the necessary time when using twice the number of processors. It is accepted that an efficiency superior to 0.5 means that the time gain worths it. For *OpenFOAM* and a typical 3D case, which characteristics are shown in table 3.3, the results of the scaling tests are presented in figure 3.5. The program behaves very well with an nearly linear speed-up until 200 cores and efficiency superior to 0.5 for all tested cases.

Number of Cells	Time Step (s)	Simulation duration (s)	Mesh Motion	U_G $[\mathrm{m\,s^{-1}}]$	solver
4213293	0.00005	0.005	yes	0.1832	*interIsoFoam*

Table 3.3: Main characteristics of the *OpenFOAM* test case.

Number of Processors	20	40	80	100	200	300	400
Time Of execution (s)	928	482	230	175	95	72	62
SpeedUp	1.0	1.93	4.034	5.30	9.768	12.89	14.97
Efficiency	1.0	0.96	1.01	1.06	0.98	0.86	0.75

Table 3.4: Results of the speed up test.

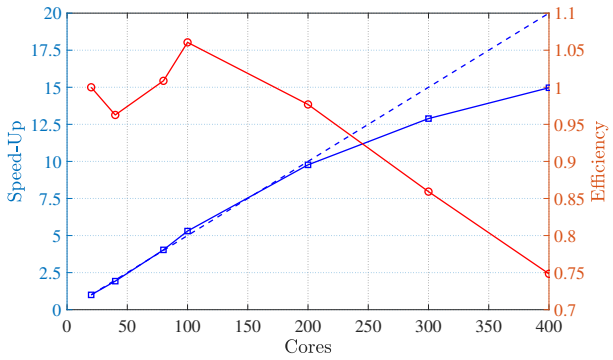

Figure 3.5: Speed up of the NWT CFD simulation with *OpenFOAM*. The dashed blue line corresponds to a linear speed-up.

3.2. Space and Time discretization

In this section, series of mesh tests are performed to look for mesh independent results. Two solvers are considered: the *interDyMFoam* solver which is used in the wave generation problem of section 5.1 and *interIsoFoam* solver in the wave structure interaction problem of section 5.2. The choice of using *interIsoFoam* solver in the latter problem is motivated by more precision in the free-surface detection and motion as well as more stability, avoiding smearing of the interface as well as damping.

3.2.1. *interDyMFoam* solver

We consider two test cases in order to achieve mesh convergence: (i) the study of the response to an input velocity step characterized by the overshoot and the steady-state water height, and the rising, peak and settling times, as found on the time response of linear dynamical systems, and (ii) the wave propagation of linear waves along the 2D wave tank (wave height, wave length). In the first case, a set of uniform rectangular cell mesh are generated to look for mesh independence. Most sophisticated meshes, with an uniform zone at water-air interface which includes the minimum and maximum water height during the whole simulation, are also set up. They include refinement at the wavemakers and are

denominated "non-uniform". They allow to decrease the computation time as the mesh size is kept in reasonable limits. The mesh, generated thanks to the *blockMesh* program, is built from three characteristic elements: the cell width at the piston wall Δx_w, the cell width in the wave propagation zone (far from the walls) Δx and the cell height in the wave propagation zone Δz. Δx_w will be determined from the uniform mesh study in (i). From the wavemaker, the longitudinal element size Δx_i is being computed with the following geometric law, $\Delta x_i = \Delta x_w r^{(i-1)} \ \forall \ i < n_j$, where r is the geometric growth rate. After n_j cells the elements reach a constant size Δx in the wave propagation zone. A similar calculation allows to define the vertical element size from outside the interface zone. Both Δx and Δz are set up considering the number of cells per wave length and cells per wave height respectively. These parameters will be set in (ii). Figure 3.6 shows the mesh in the x-z plane, while a one cell size is set up in the y-direction. Mesh type and properties are displayed in table 3.10. These preliminary tests with different meshes allow an appropriate choice of the mesh size without compromising accuracy and CPU time (see figure 3.6). The dynamic mesh is modeled using a mesh expansion/contraction strategy. The mesh uniformly contracts and expands, conserving the global mesh cell volumes as these motions are relatively small compared to the tank length.

		Δx_w [m]	Δx [m]	Δz [m]	a [m^2]	Number of cells	η_o [m]	η_{ss} [m]	t_r [s]	t_p [s]	t_s [s]
Uniform	M_U^1	0.0100	0.0100	0.0050	$5 \cdot 10^{-5}$	10000	0.0356	0.0257	0.0536	0.1253	0.2819
	M_U^2	0.0050	0.0050	0.0025	$1.25 \cdot 10^{-5}$	40000	0.0342	0.0257	0.0481	0.1116	0.2979
	M_U^3	0.0025	0.0025	0.0010	$2.5 \cdot 10^{-6}$	200000	0.0340	0.0259	0.0479	0.1298	0.2905
	M_U^4	0.0015	0.0015	0.00075	$1.125 \cdot 10^{-6}$	443889	0.0340	0.0258	0.0491	0.1237	0.2939
	M_U^5	0.0013	0.0013	0.0005	$6.5 \cdot 10^{-7}$	769000	0.0341	0.0259	0.0493	0.1246	0.2927
	M_U^6	0.0011	0.0011	0.00026	$2.9 \cdot 10^{-7}$	1748916	0.0341	0.0259	0.0494	0.1247	0.2909
Non-Uniform	M_{NU}^7	0.0010	0.0363	0.0010	-	17115	0.0340	0.0258	0.0491	0.1264	0.2976
	M_{NU}^8	0.0010	0.0181	0.0010	-	20055	0.0340	0.0258	0.0492	0.1262	0.2965
	M_{NU}^9	0.0010	0.0091	0.00057	-	47025	0.0341	0.0258	0.0488	0.1250	0.2954

Table 3.5: Mesh properties to study the wavemaker response to a velocity step. Δx_w is the cell size in the x-direction at the piston wavemaker, Δx is the cell size in the x-direction in the wave propagation zone, Δz is the cell size in the z-direction at the water-air interface, η_o is the overshoot water height at the piston wavemaker, η_{ss} is its steady state value and t_r, t_p, t_s are the rising time, the peak time and the settling time, respectively. The area a is used as an entry for the GCI study (I. B. Celik et al., 2008).

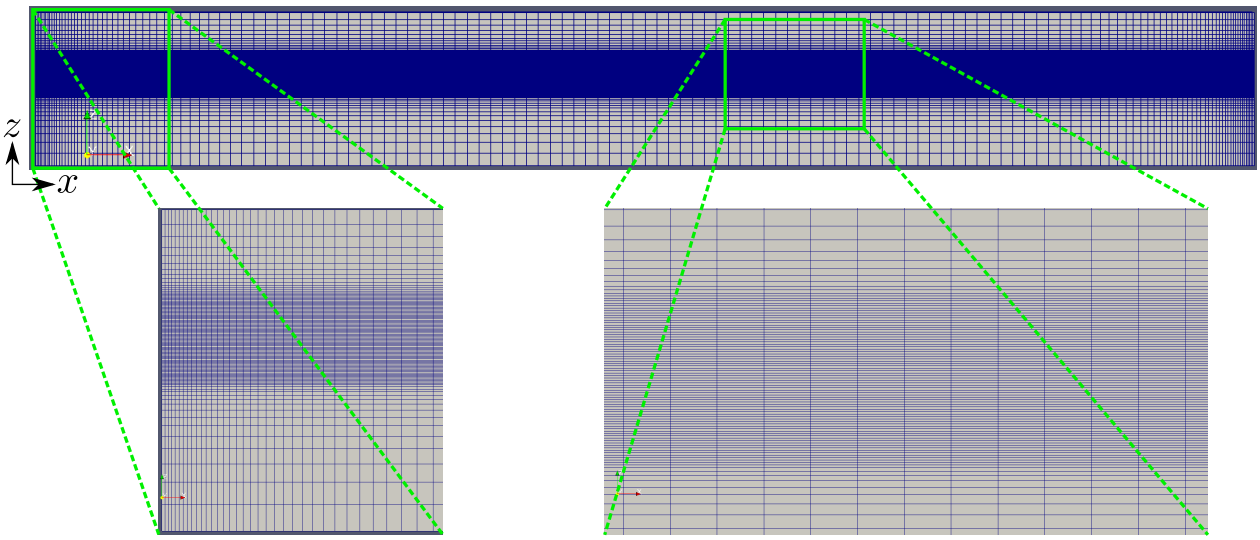

Figure 3.6: Non-uniform mesh overview and zoom at wavemaker and water-air interface. In this case, the wave tank dimensions are 2 x 0.25 m and water depth is 0.15 m.

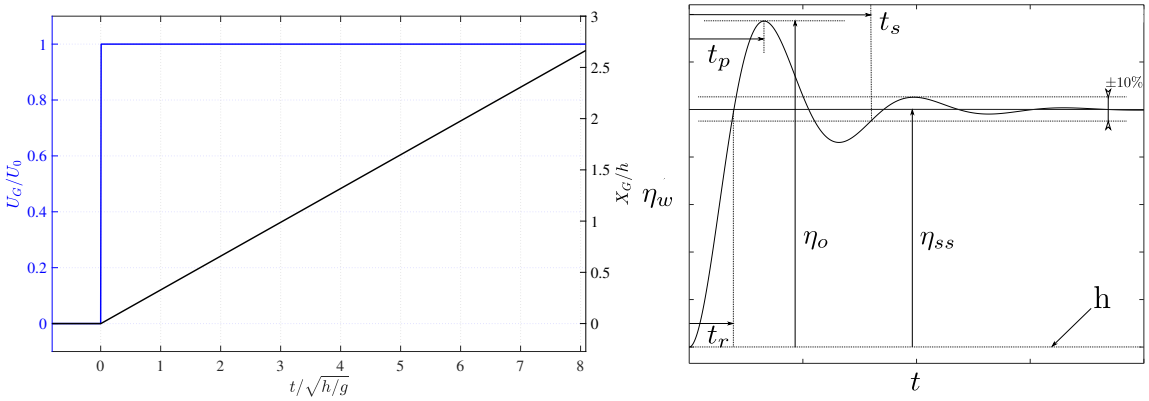

(a) (b)

Figure 3.7: (a) Normalized input signal for the step response test as a function of non-dimensional time. The piston velocity $U_G(t)$ is normalized by its maximum value U_0. We also display the piston position X_G normalized by the water depth of the wave tank. (b) Characteristic amplitude and time scales in the step response of a second order system. η_o, η_{ss} the overshoot and steady state values respectively and t_r, t_p, t_s , the rising, peak and settling times respectively. The steady state height is $\eta_{ss} > h$ as the piston wavemaker moves constantly at U_G.

Step response

In order to fully test the capacity of the code to represent sudden and rapid water surface elevation we choose to perform a step response of the numerical wave tank. The input signal is a velocity step as shown in figure 3.7a and given by $U_G(t) = U_0\Theta(t)$ where $\Theta(t)$ is the

Heaviside function. The step value is 0 for negative times and $U_G = U_0$ for positive times, resulting in a linear displacement $X_G(t)$ of the piston wavemaker. In this part of the study, we set the tank length to $L = 4$ m, the tank height to 0.25 m and the mean still water level to $h = 0.15$ m. Mesh M_U^1 is the coarsest and M_U^6 the finest. M_{NU}^7 to M_{NU}^9 are non-uniform mesh as previously described. They use cell size at wall defined later on in the conclusion of the uniform mesh study and geometric growth rate $r = 1.05$ in the x-direction and $r = 1.2$ in the z-direction. For the finest mesh in the z direction (mesh M_U^6), it is necessary to reduce the time step to keep the Courant number below 1. This is why the time step is set for all meshes to $\Delta t = 10^{-4}$ s. The measured quantity is the water elevation at wavemaker η_w. The variables of interest are described in figure 3.7b and are the following: η_o, η_{ss} the overshoot and steady state values respectively and t_r, t_p, t_s , the rising, peak and settling times respectively. Results are reported in table 3.10 and shown in figure 3.8. Figure 3.8a shows the time series of the water elevation at the piston wavemaker, $\eta_w(t)$, for each mesh. The results of the 4 finest meshes are similar. A Grid Convergence Index (GCI) study (I. B. Celik et al., 2008) is carried out with the meshes 4, 5 and 6. The local order of accuracy p ranges from 0.18 to 17.57 with a global average of 4.98. This apparent average order is used to assess the GCI error at every point as suggested in I. B. Celik et al. (2008). The error made in the last mesh is really low (the maximum GCI error is 0.3 %) which allows to say that the results do not depend on the mesh. Figure 3.8b shows the error for every point, and a zoom around the overshoot is displayed in the inset where errors increase. The mean error is an order of magnitude lower (0.03%). The errors on the overshoot and the steady state values are very low. Figures 3.8c and 3.8d show the convergence of the different parameters composing the typical response to the step (overshoot and steady states water elevation, rising, peak and settling times). They show that for these parameter, the limit of convergence is mesh M_U^3. It is chosen, for obvious practical reasons, to work with mesh M_U^3 at the wavemaker, which allows to decrease computational times while assuring convergence. A non-uniform mesh shows good agreement with the uniform ones for all variables. In the rest of the work, we make sure that the first cell at the piston wavemaker wall is kept below $\Delta x_w = 0.0025$ m in the x direction and $\Delta z = 0.001$ m in the z-direction in order to keep the results independent from the mesh. The number of cells per wave length and height in the wave propagation zone is analysed in the following paragraph.

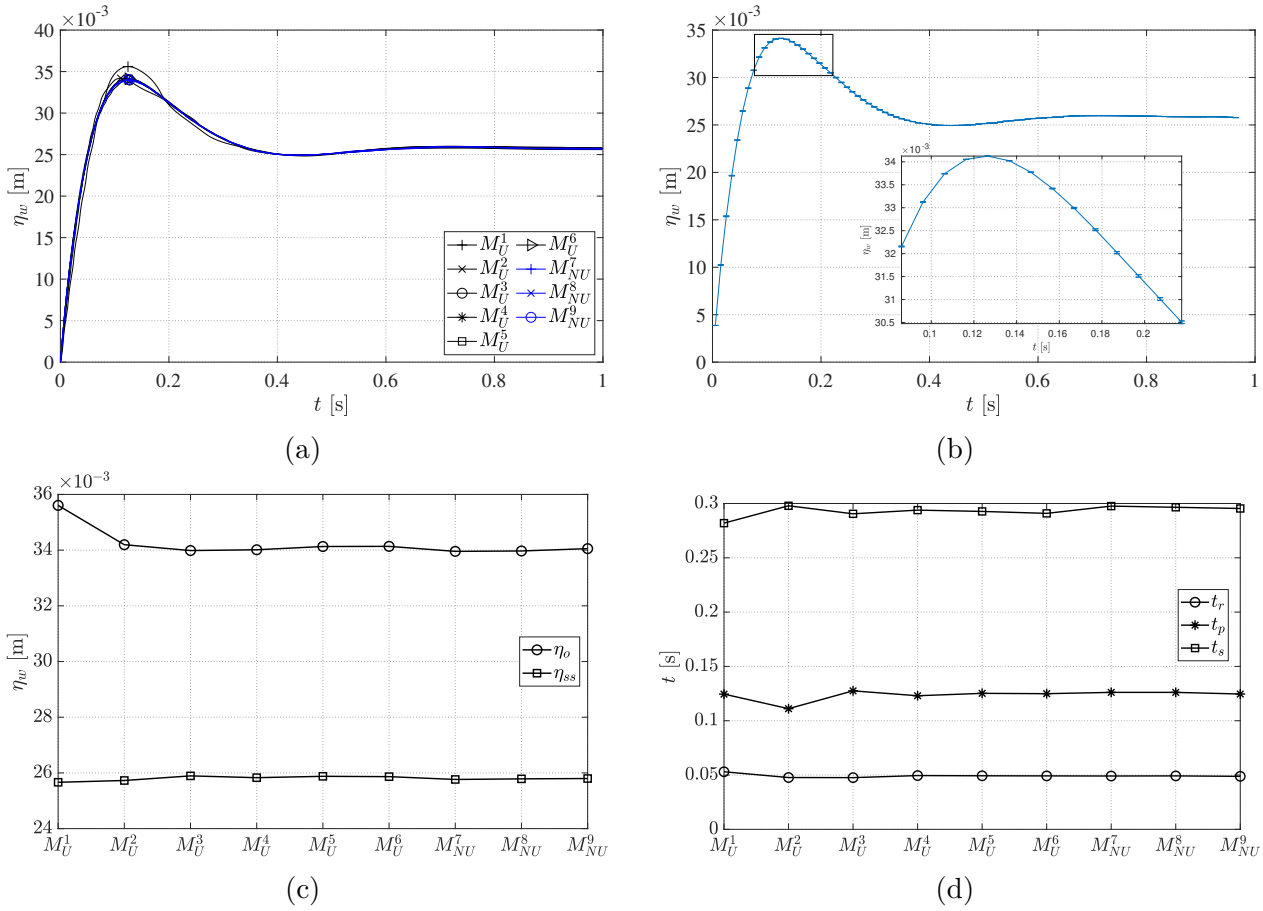

Figure 3.8: Step response. (a) Water height at the piston wavemaker for different meshes. Convergence is achieved from mesh M_U^3. (b) Error made due to mesh discretization calculated with the GCI method (I. B. Celik et al., 2008). A zoom in the overshoot region is also displayed. (c) Overshoot and steady state water height (η_o and η_{ss} respectively) in function of the mesh. These variables seem to have converged at mesh M_U^3. (d) Characteristic times (rising time t_r, peak time t_p and settling time t_s) as a function of the mesh type. Converged values are found from mesh M_U^3.

Wave propagation

In order to properly study wave propagation properties as a function of the mesh type and quality, we use an extended numerical wave tank with $L = 8$ m. The mesh is finer at the water air interface and is kept uniform in the zone where the wave propagates. At the wavemaker we set $\Delta x_w = 0.001$ m and a transition is made with a 1.05 cell to cell ratio. The piston stroke is set to $X_0 = 0.004$ m, the wavemaker frequency $f = 1.25$ Hz and the piston wavemaker velocity to $U_G(t) = X_0(\omega/2)\sin(\omega t + \delta)$ with $\delta = -\pi/2$. The corresponding wavelength can be estimated from the dispersion relation $\omega^2 = gk\tanh(kh)$ where k is wave number, and gives in this case $\lambda = 0.82$ m. A common discretization is given by 20-25 elements per wave height and 60-70 elements per wave length in recent works (Didier et al., 2016). We

conduct our test based on three meshes whose properties are shown in table 3.6 where M^7_{NU} is the coarsest mesh and M^9_{NU} the finest one. The number of cells per wave height ranges from 15 to 60 while the number of cells per wave length from 60 to 240. The time step is set to $\Delta t = 0.001$ s and the theoretical Courant–Friedrichs–Lewy number (CFL number) is reported. Even if it shows to have value below 1, the time step for the finest mesh M^9_{NU} had to be decreased to $\Delta t = 0.0005$ s to avoid divergence due to the use of explicit schemes. The simulation end time is 10 s and two probes are set at $x = 2$ m and $x = 4$ m from the origin of the coordinate system (see figure 3.1).

	M^7_{NU}	M^8_{NU}	M^9_{NU}
cells/H	15	30	60
cells/λ	60	120	240
Δx_w [m]	0.00100	0.00100	0.00100
Δx [m]	0.01360	0.00680	0.00340
Δz [m]	0.00030	0.00015	0.00007
Total number of cells	40734	107184	303232
CFL number	0.15	0.29	0.59

Table 3.6: Mesh characteristics and their theoretical CFL number for the wave propagation problem.

	$\Delta_{RMS}\,(x = 2m)$ [m]	$\Delta_{RMS}\,(x = 4m)$ [m]
M^7_{NU}	$7.2 \cdot 10^{-5}$	$1.10 \cdot 10^{-4}$
M^8_{NU}	$4.3 \cdot 10^{-5}$	$0.80 \cdot 10^{-4}$
M^9_{NU}	$4.4 \cdot 10^{-5}$	$0.83 \cdot 10^{-4}$

Table 3.7: RMS deviation relative to the theory of O. S. Madsen (1971) over the 10 s simulation for both wave gauges at $x = 2$ m and $x = 4$ m. The RMS deviation is calculated according to: $\Delta_{RMS} = \sqrt{\sum_{j=1}^{N} \left(\eta_j - \eta_j^{theo}\right)^2 / N}$.

Δx_w [m]	cells/λ	cells/H	r_x	r_z
0.001	120	30	1.05	1.20

Table 3.8: Characteristics of the final mesh.

Figure 3.9a shows the water level at wavemaker wall $\eta_w(t)$. No differences between the meshes are observed as expected, since the refinement in x direction and in the z direction

is finer than the necessary one studied in (i). Figure 3.9b shows the differences between the meshes that are used at $x = 4$ m. A zoom over the highest value and for three wave periods are shown in figure 3.9c. The coarse mesh M^7_{NU} effectively produces minor differences with the two others, specially at the maxima and minima. The results for probe at $x = 2$ m are compared with the theory of O. S. Madsen (1971) and shown in figure 3.9d. The error of wave crests and trough with the wavemaker theory are shown in table 3.7. The results are quite accurate for the three meshes (almost all cases with RMS deviation below 0.1 mm) although the coarse mesh lacks of accuracy at the maxima and minima. It is chosen to work with the medium mesh M^8_{NU} in the rest of this work as it allows accurate wave height data and reduces the computational time compared to the fine mesh.

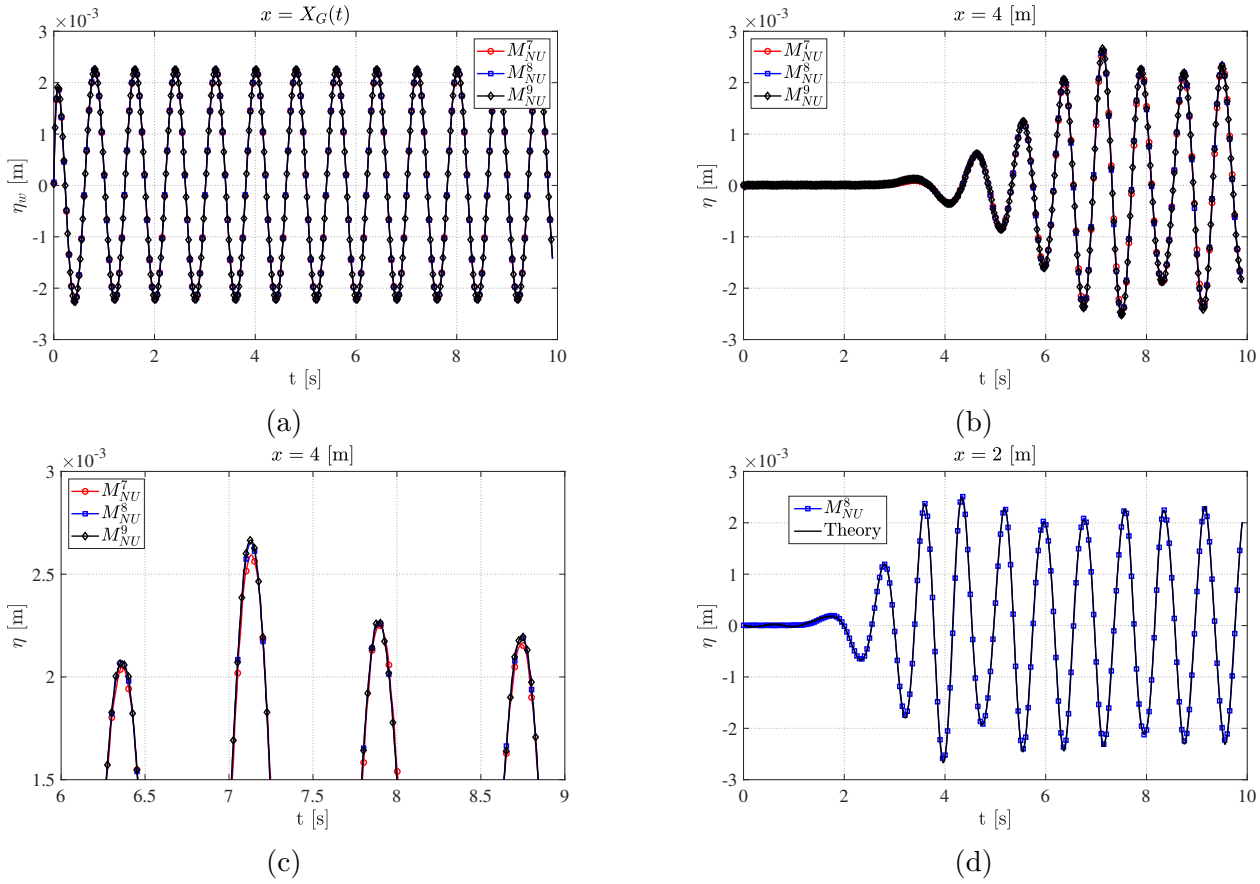

Figure 3.9: Continuous wave propagation. (a) Water height at the piston wavemaker η_w as a function of time. (b) Water height at $x = 4$ m as a function of time. (c) Water height at $x = 4$ m as a function of time, zoom over times between 6 and 9 s. (d) Comparison between the medium mesh and the wavemaker theory (O. S. Madsen, 1971) at $x = 2$ m. The medium mesh well represents the wavemaker theory. It allows us to validate the wave generation process with the medium mesh for small waves.

3.2.2. *interIsoFoam* solver

In this part, the NWT dimensions are $L = 2$ m, $d = 0.10$ m, and $h = 0.05$ m, which correspond to the dimensions of the experimental facility at the *Leaf-nl* laboratory. They are summarized in table 3.9. The test case consists of the generation of a short undular bore by applying a square velocity signal to the generating wavemaker such as:

$$U_G(t) = U_0 \left(\Theta(t) - \Theta(t - \Delta t_G)\right) \tag{3.1}$$

where U_0 is equal to 0.192 $\mathrm{m\,s^{-1}}$ and $\Delta t_G = 0.65$ s. This test case can be considered as extreme at the scale of the experiment and thus obtaining convergence for it will allow us to assume that all other cases will not depend on the grid. The space discretization will be reviewed as a first step and the time discretization will then be studied.

L [m]	d [m]	h [m]	U_G [m/s]	Δt_G [s]
2.000	0.100	0.050	0.192	0.650

Table 3.9: Wave tank main dimensions for the spacial and temporal grid study. L is the length of the wave tank, d is its height, h is the MSWL, U_G is the piston wavemaker step velocity and Δt_G is the step duration.

Space discretization

In order to execute simulation independant of the grid size, a study is carried out where four meshes (M_1 to M_4) are tested. The mesh at the wavemaker is kept equal to the characteristics of section 3.2.1, that is to say with a first cell of 0.001 m width at the wavemaker wall and a smooth transition cell-to-cell ratio of 1.05 in the x-direction, and the hypothesis of convergence is made for the step response at wavemaker for the *interIsoFoam* solver. The number of cells per wave length and wave height is varied in order to check mesh independence and these characteristics are reported in table 3.10. M_1 is the coarsest mesh with 83 cells per wave length and 25 cells per wave height and M_4 the finest one with 691 and 149 cells respectively. Note that the wave length and height reference are taken from the main wave. The results, consisting in the measurement of wave height at every location of the wave tank for the time $t = 2$ s, are presented thereafter for laminar, $k - \epsilon$ and buoyancy modified $k - \omega$ SST turbulence models, and the time discretization is adaptive where upper boundary such as the maximum Courant number in the mesh domain is either 0.1 or 0.45. They are analyzed both qualitatively and in terms of Grid Convergence Index (GCI) according to the work of I. B. Celik et al. (2008). The variable of interest are the maximum wave height H at $t = 2$ s and the x-position of this maximum x_{wave}.

	Δx_w [m]	Δx [m]	Δy [m]	a [m^2]	N/λ	N/H	Cells
M_1	0.001	0.00912	0.00100	$9.12 \cdot 10^{-6}$	83	25	16302
M_2	0.001	0.00457	0.00067	$3.04 \cdot 10^{-6}$	166	37	42676
M_3	0.001	0.00227	0.00033	$7.57 \cdot 10^{-7}$	335	74	152048
M_4	0.001	0.00110	0.00017	$1.83 \cdot 10^{-7}$	691	149	568944

Table 3.10: Grid properties to study the wavemaker response to a velocity step. The area a is used as an entry for the GCI study I. B. Celik et al. (2008).

Laminar case The simulation are run for laminar Navier-Stokes equations for the different meshes and results are presented in figure 3.10. If the maximum allowed Courant number is 0.45, it seems that the meshes have converged for meshes M_3 and M_4, while convergence is achieved for all meshes in the case of using a maximum Courant number of 0.1. These observations are also valid for the secondary waves or trailing waves. These results are confirmed by the GCI study reported in table 3.11, where the maximum error GCI is 6.5% for the maximum wave height H for mesh M_3 and using $Co = 0.45$. It implies that the results are independent of the grid for all meshes if the Courant number is kept low ($Co = 0.1$) or in case of using a larger one by at least applying M_3 characteristics. The use of low Courant number is time consuming but shall be privileged as it allows not to depend on the grid size and thus optimization of this last one can lead to serious time gain.

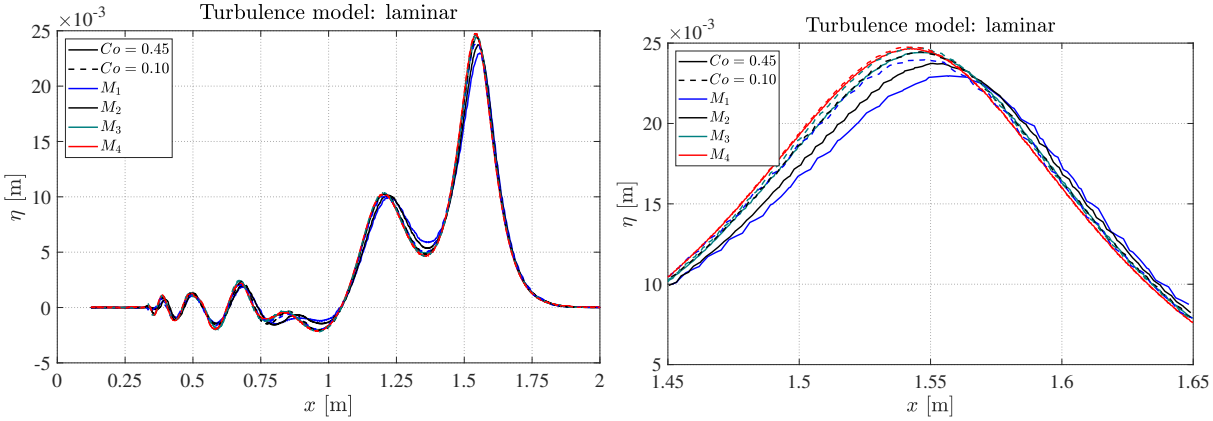

(a) (b)

Figure 3.10: Grid independence study for laminar flow simulation. (a) Global case. (b) Zoom over the main wave.

	$Co = 0.1$				$Co = 0.45$			
	H [m]	GCI [%]	x_{wave} [m]	GCI [%]	H [m]	GCI [%]	x_{wave} [m]	GCI [%]
M_1	0.02396	–	1.5479	–	0.02296	–	1.5571	–
M_2	0.02445	–	1.5459	–	0.02374	–	1.5508	–
M_3	0.02473	0.924	1.5448	0.051	0.02441	6.593	1.5461	0.472
M_4	0.02475	0.009	1.5408	0.125	0.02465	0.642	1.5427	0.757

Table 3.11: Results of the grid study for the laminar case.

Turbulent case The study is now carried out by solving the RANS equations with either a $k-\epsilon$ or a buoyancy modified $k-\omega$ SST model and results are presented in the same way than in the laminar case. The whole wave is shown in figure 3.11 for both turbulence models while a zoom on the main wave is presented in figure 3.12. We observe a similar behaviour as for the laminar case, that is to say that the convergence seems achieved for meshes M_3 and M_4 in the case of $Co = 0.45$ and for all meshes in the case of low Courant number $Co = 0.1$, and this for both turbulence models. It is confirmed by the GCI analysis, shown in tables 3.12 and 3.13, which gives the highest error to be 3.95% for H and the $k-\epsilon$ model, while it is 6.63% for the $k-\omega$ models. Such low values shows that convergence appear for both models and both Courant number from M_3 mesh. To conclude and as for the laminar case, the use of low Courant number or at least the M_3 mesh is sufficient to assure convergence.

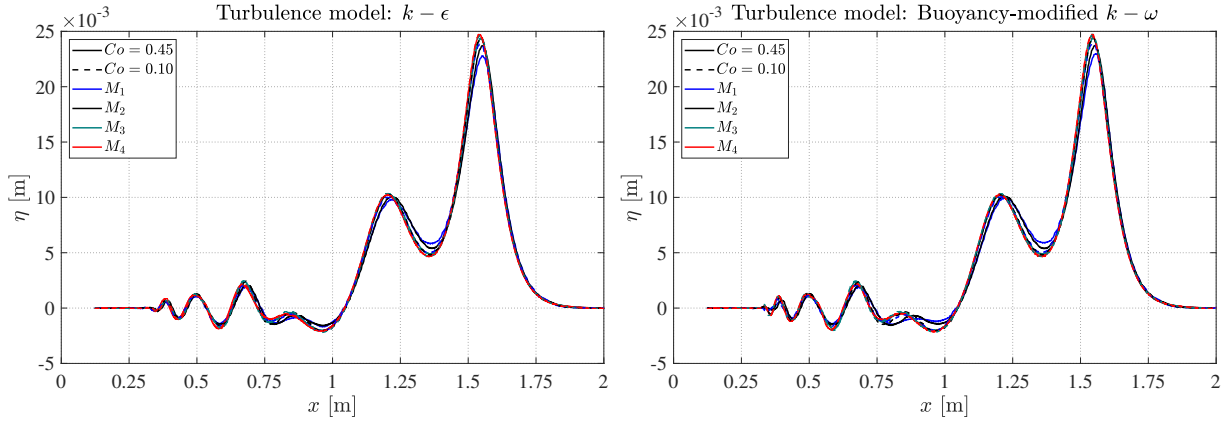

Figure 3.11: Grid independence study for two turbulence models. (a) $k-\epsilon$ model. (b) Buoyancy-modified $k-\omega$ SST model developed by Devolder et al. (2018).

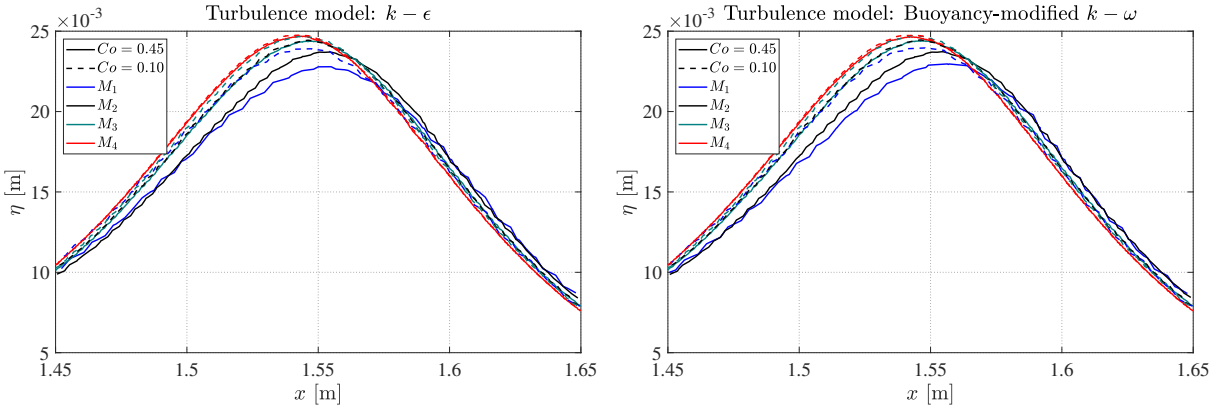

(a) (b)

Figure 3.12: Grid independence study for two turbulence models. Zoom at the overshoot wave (main wave) (a) $k-\epsilon$ model. (b) Buoyancy-modified $k-\omega$ SST model developed by Devolder et al. (2018).

	$k-\epsilon$							
	$Co = 0.1$				$Co = 0.45$			
	H [m]	GCI [%]	x_{wave} [m]	GCI [%]	H [m]	GCI [%]	x_{wave} [m]	GCI [%]
M_1	0.02391	–	1.5475	–	0.02279	–	1.5549	–
M_2	0.02444	–	1.5460	–	0.02370	–	1.5544	–
M_3	0.02468	0.561	1.5450	0.066	0.02437	3.953	1.5463	0.082
M_4	0.02476	0.211	1.5430	0.154	0.02468	1.290	1.5438	0.087

Table 3.12: Results of the grid study for the $k-\epsilon$ turbulence model.

	Buoyancy-modified $k-\omega$							
	$Co = 0.1$				$Co = 0.45$			
	H [m]	GCI [%]	x_{wave} [m]	GCI [%]	H [m]	GCI [%]	x_{wave} [m]	GCI [%]
M_1	0.02396	–	1.5479	–	0.02296	–	1.5564	–
M_2	0.02445	–	1.5459	–	0.02372	–	1.5543	–
M_3	0.02473	0.892	1.5448	0.050	0.02439	6.632	1.5463	0.394
M_4	0.02474	0.001	1.5430	0.217	0.02464	0.746	1.5426	0.230

Table 3.13: Results of the grid study for the buoyancy-modified $k-\omega$ turbulence model (Devolder et al., 2018).

Summary In order to summarized the previous results, the main wave height H and the position of the main wave is plotted in figure 3.13 in function of the mesh, as well as the maximum allowed Courant number. The dimensionless form is also shown and H_0, x_0 are the reference values taken as the M_4 results for the laminar case. Regarding the wave height of the main wave, it is clear that convergence is achieved for $Co = 0.1$ and from M_3, but if we rely on the GCI study it seems that we can consider converged for all meshes for low Courant number as even for the coarsest mesh the error will be lower than 4%, as seen in the non dimension form of the graph (see figure 3.13c). In the case of larger Courant number

much care has to be taken and at least M_3 shall be used. These results are true whatever the turbulence model is used. Regarding the wave position variable, the results from curves 3.13b does not strictly show convergence, this is mainly due to the low error that differentiates all tested meshes and we shall not take as relevant these results in order to decide the mesh size. This can be perfectly observed if the variables is plotted in dimensionless form as in figure 3.13d, where effectively the maximum error between all meshes is around 1% and thus we can consider that all results are converged.

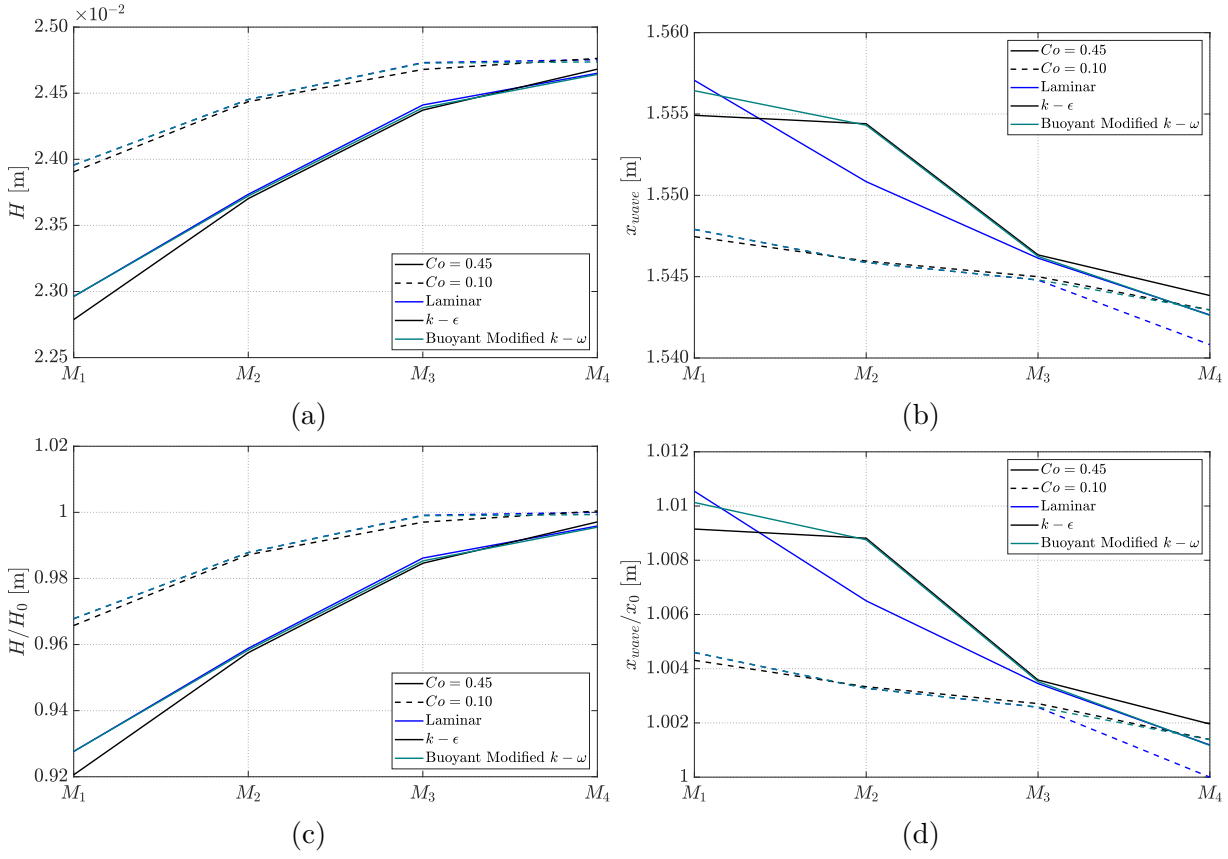

Figure 3.13: Summary of the mesh convergence studies. (a) Wave height as a function of the grid refinement. (b) X-position of the wave crest as a function of the grid refinement. (c) Dimensionless wave height as a function of the grid refinement. H_0 is the value of H for M_4 case and the laminar model. (d) Dimensionless wave position as a function of the grid refinement. x_0 is the value of x_{wave} for M_4 case and the laminar model.

To summarize, if the maximum Courant number is 0.1, then mesh size can be as low as M_1 that is to say 83 cells per wave length and 25 cells per wave height. In the case of considering a maximum Courant number of 0.45, then mesh M_3 shall be used with 335 cells per wave length and 74 cells per wave height. If we compare these results with the *interDyMFoam* results then we can see that lowering the time step allows to use coarser meshes while in the

contrary higher time step are used then the mesh will be much more significant.

Time discretization

M_3 is used to study the influence of the time step (through variations of the Courant number from 0.9 to 0.1). A laminar turbulence model is set up (we have seen that the global behaviour is similar between laminar, $k-\epsilon$ or $k-\omega$ models). Results are shown in figure 3.14. We can observe that for all maximum Courant numbers, the results are really close, confirming that the use of M_3 allows to avoid influence of the time step. However, M_3 has a mesh size of around 152000 cells, which is really large, since the future will be carried out in 3D. Thus, we should favour a low Courant number approach in order to decrease the computational coast.

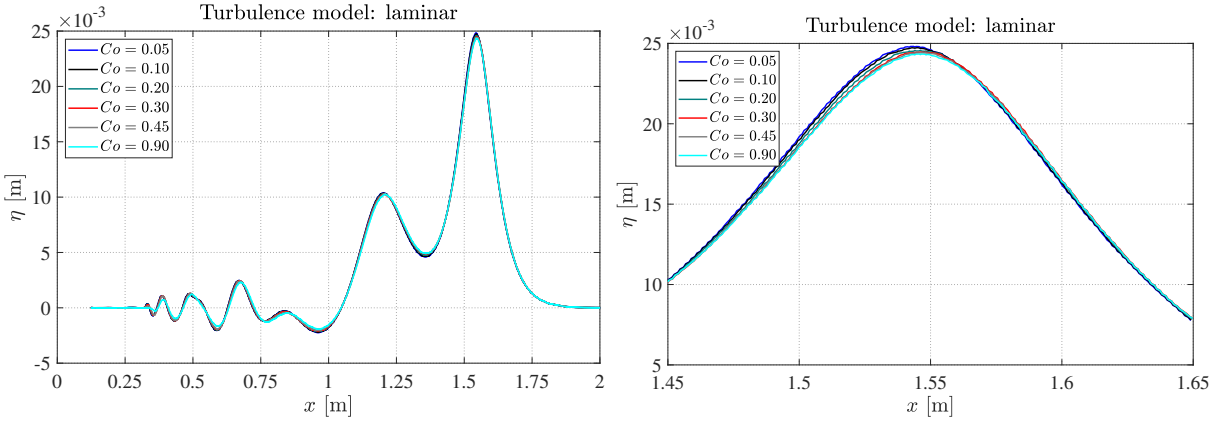

Figure 3.14: Grid independence study for laminar flow simulation. (a) Global case. (b) Zoom over the main wave.

3.2.3. 3D grid and square cylinder case

The creation of the coherent structures such as the vortices strongly depends on the resolution of the flow close to the boundaries, in the case of this study close to the square cylinder. The no slip boundary condition at the wall implies large velocity gradient as well as for the kinematic turbulent energy k. There are different strategies for the resolution of such flow, from wall treatment strategy to the full resolution of the boundary layer.

The Reynold's number is defined as follows, as seen in part 3.1.2:

$$Re = \frac{Du_{max}}{\nu} \tag{3.2}$$

where D is the cylinder diameter, ν is the kinematic viscosity and u_{max} is the maximum orbital velocity of the wave. The Reynolds number order of magnitude is 1000, yet the boundary layer will have different size in function of the flow regime. In especial the turbulent

boundary layer is greater than the laminar one (Newman, 2017). Thus if we are able to solve the boundary layer for the laminar case, it will also be the case for the turbulent one. The laminar boundary layer theory will allow us to estimate its size, and thus the size of the grid at the cylinder. Blasius (1907) solution for a steady laminar flow and $u(y = \delta)/U = 0.99$ is:

$$\delta = \frac{4.9x}{Re_x^{1/2}} = 4.9\sqrt{\frac{\nu x}{u_{max}}} \quad \text{if} \quad 10^3 \leq Re_x \leq 10^6 \tag{3.3}$$

where U is the particle velocity far away from the boundary, ν is the kinematic viscosity of the fluid, x is the distance from the leading edge. In the case of the unsteady motion of a flat plate, corresponding to a sinusoidal motion, the boundary layer thickness depends on time according to (Newman, 2017):

$$\delta = 3.64\sqrt{\nu t} \tag{3.4}$$

For small times, this estimation can then be really small. In the case of turbulent boundary condition, the flow profile can be subdivided into three regions which are the viscous sublayer ($0 < y^+ < 5$), the buffer sublayer ($5 < y^+ < 30$) and the inertial sublayer ($30 < y^+ < 200$) where y^+ is the normalized distance to the wall defined as:

$$y^+ = \frac{u_\tau y}{\nu} \quad \text{with} \quad u_\tau = \sqrt{\tau_0/\rho} \tag{3.5}$$

where τ_0 is the shear stress at wall. It is however essential to know the shear stress at wall. An estimation of the boundary layer thickness is given by Prandtl (1925) for turbulent flows:

$$\delta = \frac{0.16x}{Re_x^{1/7}} = 0.16x^{6/7}\left(\frac{\nu}{u_{max}}\right)^{1/7} \quad \text{if} \quad 10^6 \leq Re_x \tag{3.6}$$

The turbulent boundary layer thickness increases as $x^{6/7}$, more rapidly than for the laminar case which increases as $x^{1/2}$.

The skin friction coefficient definition, which gives the fraction of wall shear stress compared to the local dynamic pressure, is:

$$C_f = \frac{\tau_0}{\frac{1}{2}\rho u_{max}^2} \tag{3.7}$$

From the previous boundary layer theories, it is possible to estimate the wall shear stress with the use of the following empirical formulas from the flat plate theory (White, 2010):

$$C_f = \frac{0.664}{Re_D^{1/2}} \quad \text{for laminar flows and according to Blasius results,} \tag{3.8}$$

$$C_f = \frac{0.027}{Re_D^{1/7}} \quad \text{for turbulent flows according to Prandtl 1/7th law (Prandtl, 1925).} \tag{3.9}$$

For turbulent flows, the skin friction coefficient decreases at a lower rate ($Re_D^{-1/7}$) than for the laminar case ($Re_D^{-1/2}$).

We choose to estimate the boundary layer size according to Blasius theory and solve the boundary layer by having 10 grid points inside the boundary layer. We make also sure that the first cell y^+ value is around 1 from estimation with equation 3.5-3.7. In the case of a wave height was $H = 0.0102$ m, the water depth $h = 0.05$ m and the cylinder width $D = 0.04$ m and a velocity estimation made thanks to the Mc Cowan equation, the resulting Reynolds number is 5760, so that Blasius theory may be used, leading to a boundary layer $\delta = 2.5\times10^{-3}$ m. The cell size at the cylinder is taken as $y_{wall} = \delta/10$. A slightly more conservative value is taken with $y_{wall} = 2.5 \times 10^{-4}$ m. This is in agreement with the observation of Jagadeesh & Murali (2005) who found that 5 cells in the boundary layer with $y^+ < 2$ is sufficient to correctly solve the boundary layer for $Re \approx 10^6$ however. They also find that a 100 nodes along the body length are necessary to reach grid convergence.

The numerical domain, as described in figure 3.2, is composed of (1) the piston wavemaker of width W, (2) the tank end boundary, (3) the left wall of length L, (4) the right wall and (5) the square cylinder placed at x_0 from the origin and of diameter D. The numerical domain is composed of several refined zones which are: the wavemaker zone (in yellow) where the mesh is finer at the wavemaker and the water-air interface, the wave propagation zone (in red) where the refinement is carried out at the water-air interface and the square cylinder zone (in blue) where the mesh is refined at the cylinder and the interface. This last refinement zone is made of a cylinder diameter D wide space at each side of the cylinder, while a half-cylinder diameter wide zone is refined ahead of the cylinder and a diameter and a half is refined in the wake of the cylinder. The mesh specificities of every zones are listed in the following paragraph.

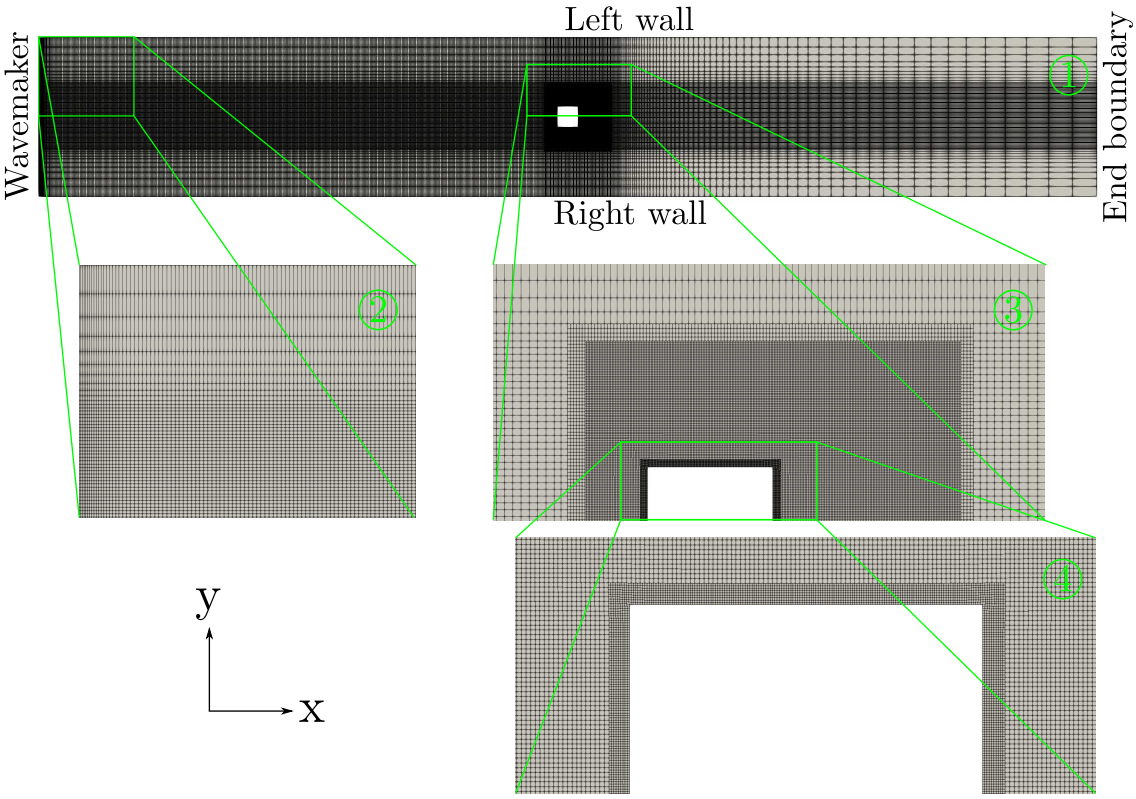

(a)

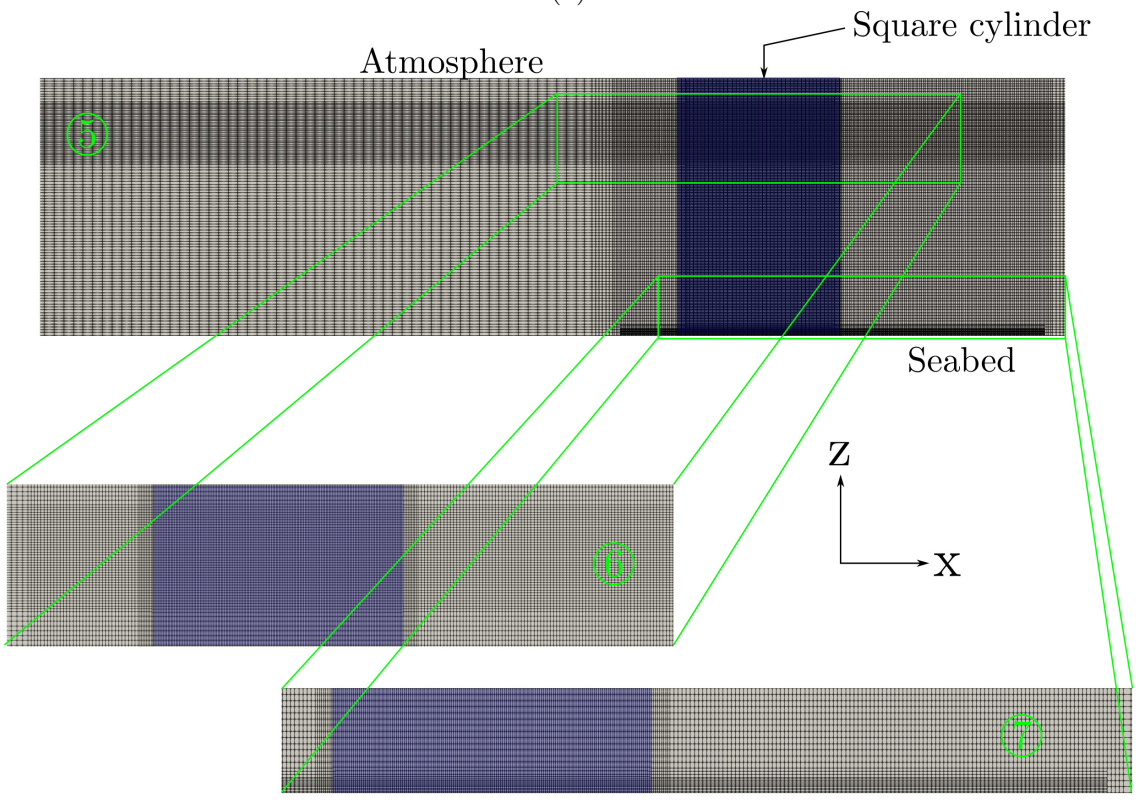

(b)

Figure 3.15: (a) Top view of the mesh. (b) Lateral view of the mesh.

The global mesh can be visualized in part (1) of figure 3.6. The mesh is mainly formed of hexahedral cells , with a uniform refined zone at the water-air interface which includes the minimum and maximum water height during the whole simulation and which is visible in zoomed part number (5) of figure 3.6. The other refinement zones at both the wavemaker and the square cylinder can also be observed in part (2) and (3), respectively. The first cell size at the wavemaker is based on the study of 3.2.1 and is 1 mm wide. A 1.05 cell-to-cell growth ratio is used in the x-direction leading to a smooth transition from the wavemaker to the cell propagation zone. The same ratio is used from the wave propagation zone to the cylinder zone and another refinement is carried out, in addition, with cells cut in 2 in the x and y direction. Outside the refined zone, a 1.2 cell-to-cell growth ratio is used in the y-directions. In the z-direction, the cell height is kept constant and an extra-refinement in the interface zone allows to reach the 25 cells per wave height, as shown in part (6) of figure 3.6. The wave propagation zone has an homogeneous cell size, which is based on numerical independence tests. These showed a great dependence over both the cell size and time step. However, the decrease of the time step makes disappear these discrepancies and an adjustable time step based on the maximum Courant number of 0.1 is chosen to keep both reasonable computation time and mesh size. The final mesh is composed of a minimum of 83 cells per wave length and 25 cells per wave height. The first cells close to the cylinder are built in order to achieve at least 10 cells in the boundary layer, considering the Blasius solution for the flat plane and a laminar flow of magnitude U given by McCowan (1891) theory of solitary wave which shows to be a good approximation of the orbital particle horizontal velocity of the undular bore main wave. Part (4) of figure 3.6 shows the first cell layers at the cylinder of width $2.4 \cdot 10^{-4}$ m. Outside these boundary layers cells, the mesh exhibits cells of aspect ratio equal to 1 and size twice the boundary layer cells. The domain past the cylinder (after $1.5D$) is not refined as it is not of interest for this study, but allows the wave to keep propagating along the tank. At the seabed, exposed on part (7), vertical extra refinement is set-up with 10 cells of height $1.9 \cdot 10^{-4}$ m which also allows to solve the boundary layer.

Even if the numerical implementation of dynamic mesh can be more complex than for static one, and it executes more slowly than a simpler boundary condition, dynamic mesh turns out to be closer to the physical phenomena, and thus is very useful to model the piston wavemaker motion. In this work, the mesh uniformly contracts when the flume end moves, conserving the global mesh cell volumes as this motion is relatively small compared to the flume length.

3.3. Post-processing of numerical simulation

Interface detection Interface detection is carried out by using an iso-surface such as $\alpha = 0.5$, where α is the Volume of Fluid variable. No reconstruction is done, as in the *interIsoFoam* solver. The error, due to error in orientation of the interface in the cells is however minimized by the use of a refined zone at the water-air interface.

Force computation The forces over the wavemaker or the cylinder, which can either be pressure (perpendicular to the wall) or viscous (tangential to the wall) forces, can be calculated from the pressure and velocity fields at the wavemaker using the stress tensor $\underline{\underline{\epsilon}}$, the elementary surface area dS (which is in the 2D case an elementary length) and $\mathbf{n}$ its normal:

$$\mathbf{F_w} = \int_z \underline{\underline{\epsilon}} \cdot \mathbf{n}\, dS \tag{3.1}$$

The stress tensor is defined as:

$$\underline{\underline{\epsilon}} = -p \begin{bmatrix} 1 & 0 \\ 0 & 1 \end{bmatrix} + 2\mu \begin{bmatrix} \frac{\partial u_x}{\partial x} & \frac{1}{2}\left(\frac{\partial u_z}{\partial x} + \frac{\partial u_x}{\partial z}\right) \\ \frac{1}{2}\left(\frac{\partial u_z}{\partial x} + \frac{\partial u_x}{\partial z}\right) & \frac{\partial u_z}{\partial z} \end{bmatrix} \tag{3.2}$$

Note that the previous results are true for the laminar equations. In the case of the study of a turbulent case, and the use of RANS equations, which can be written as (in Einstein notation):

$$\rho u_j \frac{\partial \overline{u_i}}{\partial x_j} = \rho \overline{f_i} + \frac{\partial}{\partial x_j}\left(-\overline{p}\delta_{ij} + 2\mu \overline{S_{ij}} - \rho \overline{u_i' u_j'}\right) \tag{3.3}$$

The total stress tensor therefore corresponds to the stress tensor for the laminar case plus the Reynolds stress, which can be expressed as:

$$\tau_{ij}' = -\rho \overline{u_i' u_j'} \tag{3.4}$$

Boussinesq (1877) formulated the possibility of expressing this tensor (symmetric as all stress tensors) as:

$$\tau_{ij}' = -\rho \overline{u_i' u_j'} = 2\mu_t \overline{S_{ij}} - \frac{2}{3}\rho k \delta_{ij} \tag{3.5}$$

where μ_t is the turbulent dynamic viscosity or eddy viscosity, $\overline{S_{ij}}$ is the mean rate of strain tensor, $k = \frac{1}{2}\overline{u_i' u_i'}$ is the turbulent kinetic energy and δ_{ij} is the Kronecker symbol.

Vortex representation Vorticity is a vector field which allows to measure the rotational characteristic of a flow (its tendency to rotate). The first works on vorticity can attributed to d'Alembert (1749) and Euler (1752), while Lagrange (1760) and Cauchy (1815) are the first ones to use single letter to refer to vorticity according to Truesdell (1954). Vorticity can

be defined as:

$$\omega = \nabla \times \mathbf{u} \tag{3.6}$$

If the vorticity concept is well known, and is of importance in the study of turbulence, the definition of vortex has been debated during the last decades, as expressed by Jeong & Hussain (1995). The most common way of representing vortices is to use iso-vorticity surface, such as in Hernández & Reyes (2017), where a percentage of the maximum vorticity magnitude was taken (30%), in a study of multiple symmetrical collision of vortex rings. But the presence of vorticity does not nessassarily means that a vortex is present (Chong et al., 1990). Jeong & Hussain (1995) discuss the validity of three common and intuitive indicators of vortices, that is to say pressure minimum, closed and spiraling streamlines and pathlines and finally iso-vorticity surface and show they are characteristics which are not adequate to describe vortices in general. With the purpose of properly defining a vortex, Chong et al. (1990) proposed the following criteria: a vortex core region has complex eigenvalues of $\nabla \mathbf{u}$, which is equivalent to:

$$\Delta = \left(\frac{1}{3}\mathbf{Q}\right)^3 + \left(\frac{1}{2}\mathbf{R}\right)^2 > 0 \tag{3.7}$$

with Q is defined in equation 3.8 and $\mathbf{R} = \mathrm{Det}\left(\nabla \mathbf{u}\right)$. Hunt et al. (1988) proposed to call eddies any region where the quantity Q, the second invariant of $\nabla \mathbf{u}$, is positive. $\mathbf{Q}$ is defined as the following quantity:

$$Q = \frac{1}{2}\left(||\mathbf{\Omega}||^2 - ||\mathbf{S}||^2\right) \tag{3.8}$$

where $||\mathbf{\Omega}|| = \left[\mathrm{Tr}\left(\mathbf{\Omega}\mathbf{\Omega}^\intercal\right)\right]^{\frac{1}{2}}$, $||\mathbf{S}|| = \left[\mathrm{Tr}\left(\mathbf{S}\mathbf{S}^\intercal\right)\right]^{\frac{1}{2}}$. $\mathbf{\Omega}$ and $\mathbf{S}$ are the skew-symmetric and symmetric component of $\nabla \mathbf{u}$ respectively, that is to say $\mathbf{\Omega} = \frac{1}{2}\left(\nabla \mathbf{u} - \nabla \mathbf{u}^\intercal\right)$ and $\mathbf{S} = \frac{1}{2}\left(\nabla \mathbf{u} + \nabla \mathbf{u}^\intercal\right)$. The quantity Q locally compares the shear strain rate and vorticity magnitude. At a wall, this quantity is 0, meaning that shear strain and vorticity have the same importance. Jeong & Hussain (1995) however shows that there is no connection between regions with $Q > 0$ and a region of pressure minimum, which is a characteristic of vortex. They instead put forward the following criteria: a vortex core region is characterized if $\mathbf{S}^2 + \mathbf{\Omega}^2$ has two negative eigenvalues, or considering λ_1, λ_2 and λ_3 the eigenvalues such as $\lambda_1 \geq \lambda_2 \geq \lambda_3$, if $\lambda_2 < 0$. Upon all techniques described, we will use the Q-criterion and/or the iso-vorticity visualization as they are more simple to implement.

Chapter 4

Experimental Wave Tank

The experiments, which were fully designed for the purposes of this thesis, are based on the generation of undular bores thanks to a piston wavemaker and its interaction with a vertical square cylinder. In this chapter, we present the different elements which allowed the data capture of the main characteristics of the undular bore and the kinematics around the square cylinder. It consists in the full description of wave tank facility in section 4.1.1, with emphasis to the piston wavemaker in section 4.1.2 and the vertical square cylinder in section 4.1.1. Then the capacitive wave gauge design and tests are developed in section 4.2, notably review of the capacitive sensing and working principles, the electronics, and the different test cases are presented in sections D.3.2, 4.2.2, and 4.2.3, respectively. Finally, a PIV system is described in section 4.3, where the concept is reviewed in section 4.3.1, the free-surface detection with Radon transform is detailed in section 4.3.3, the post-processing tool is implemented in section 4.3.1 and the extensive validation test cases are presented in section 4.3.2.

4.1. Wave Tank

4.1.1. Facility

The wave tank consists of a rectangular flume whose dimensions are 2 m length, 60 cm wide and 25 cm high as specified in table 4.1 and is situated at the LEAF-NL laboratory. It was, along with the wavemaker, created and built throughout this thesis work.

L	d	W	h	D
2 m	0.25 m	0.60 m	0.05 m	0.04 m

Table 4.1: Main dimensions of the LEAF-NL wave tank.

Schematics of the wave tank can be found in figure 4.1. At the left end, a wavemaker is placed and a piston frontal system is chosen as it is the wavemaker system which displaces the most important volume of water and thus is able to generate undular bores. The piston wavemaker is also able to generate harmonic waves or solitary wave as it is computer-controlled. The wave tank walls, seabed and piston wavemaker are made of plexiglass, an easy to work and fully transparent material, allowing to easily observe inside the tank from any location around. No beach is installed at the right wall since the undular bore experiment is stopped before any wave reflections reach back the square cylinder.

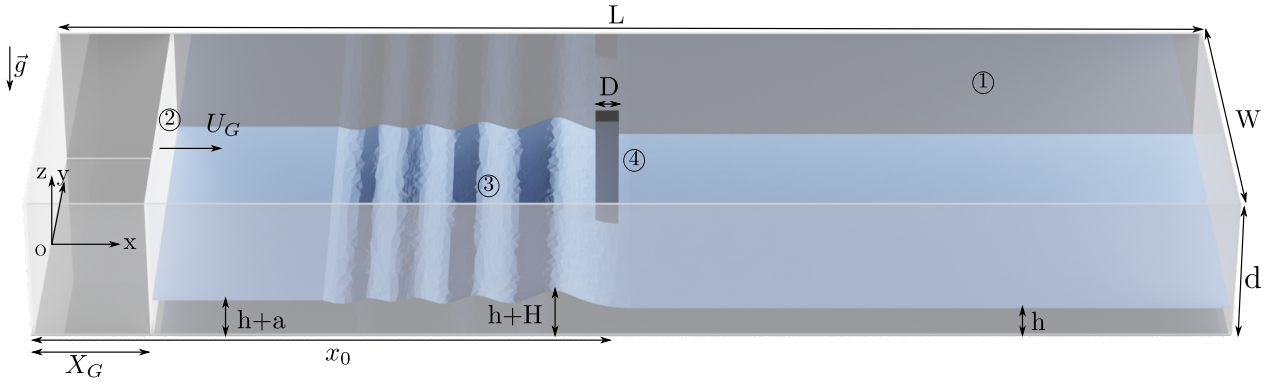

Figure 4.1: Scheme of the wave tank ① at LEAF-NL. The piston wavemaker ② creates an undular bore ③, which propagate along the tank which has a length L, a height d, a width W and the mean water level is set at h. The tank end wall is situated at the opposite side from the wavemaker. The vertical square cylinder ④, whose side measures D, is placed at a distance x_0 from the original position of the wavemaker (at the left wall).

The vertical cylinder is a 4 cm wide square based cylinder made of aluminum. It is placed at the center of the the wave that is to say at $x = 1$ meter from the wavemaker and at 30 cm from the lateral walls (which corresponds to $y = 0$ m). The cylinder is held by a vertical beam which anchors it from the top and so that any motion is prevented, specially when the wave impacts it. A picture of the experimental cylinder installed in the wave tank can be found in figure 4.2b.

A global view of the wave tank can be found in the pictures of figure 4.2a. The wave tank is equipped with an in-house capacitive wave gauge described in section 4.2 and a Particle Image Velocimetry (PIV) system described in section 4.3.

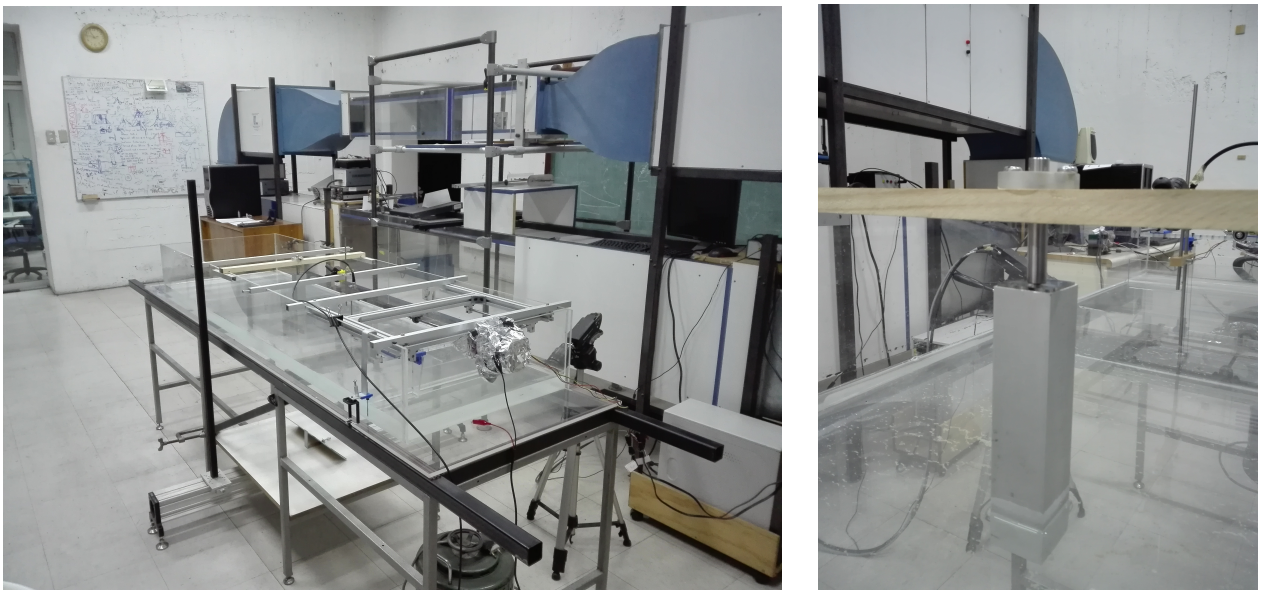

(a) (b)

Figure 4.2: Wave tank set-up. (a) Photograph of the wave tank at LEAF-NL. (b) Vertical square cylinder used in the experiments.

4.1.2. Piston wavemaker

General Configuration The wet-back piston wavemaker module is constructed with the help of an aluminum frame and can be observed in figure 4.3. Special care is taken to avoid too much losses due to the wet-back character of the wavemaker at the bottom and lateral open spaces. The piston moves thanks to an endless screw put in rotation by a stepper electric motor NEMA 34. To allow perfect straight motion and rigidity to the wavemaker, the piston is driven with the help of two guides and ball bearings connect the piston to the guides which are made of stainless steel tubes. The piston plate is stiffened by the addition of vertical stiffeners which allows to decrease the thickness of the plate, and thus its weight while keeping it stiff.

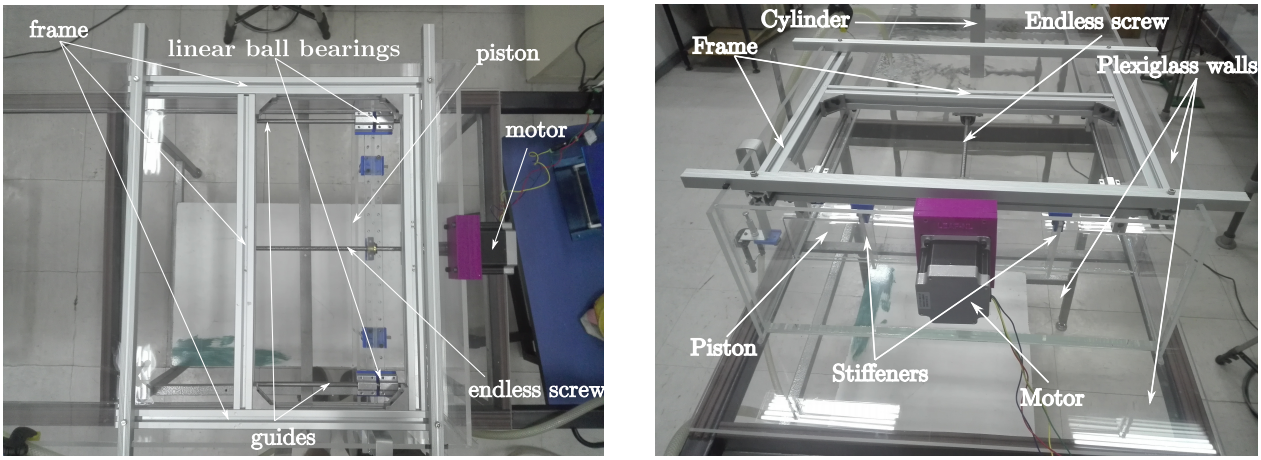

(a) (b)

Figure 4.3: Piston wavemaker set-up. (a) Top view. (b) Rear view.

Stepper motor A stepper motor is capable of turning its shaft by a number of discrete angular motion, that is to say an angle, corresponding to the 360 deg /Number of steps. The stepper motor is chosen because of its price accessibility and high controllability, notably with the common available microprocessors such as the arduino UNO. The stepper motor is controlled by a series of electrical impulses. The Nema 34 is a bipolar stepper motor that offers both precision (200 steps or 1.8 deg) and powerful holding torque (4.5 N.m). The dynamic torque however decreases notably at high pulse rate. The NEMA 34 motor main characteristics are summarized in table 4.2. Both direction and shaft revolution per minute (RPM) are controlled throughout a DM860 driver, which converts the input pulse into the necessary power that the motor windings need. This last one includes a H bridge to allow the motor to rotate in reverse direction and microsteps (from 400 to 40000 steps per revolution). It is powered by either a direct current (30 V) from EZ GP-4308D DC Power Supply or an alternative current (till 80 V) and is controlled by an arduino UNO. The overall wavemaking system is shown in figure 4.4. A drawback of using a stepper motor is the impossibility to start the shaft rotation at high speed. In the case of the step motion, a ramp is needed to get to the constant velocity. The slope of the ramp depends on the holding torque of the motor which itself depend on the feeding voltage. A high voltage allows more important acceleration of the motor.

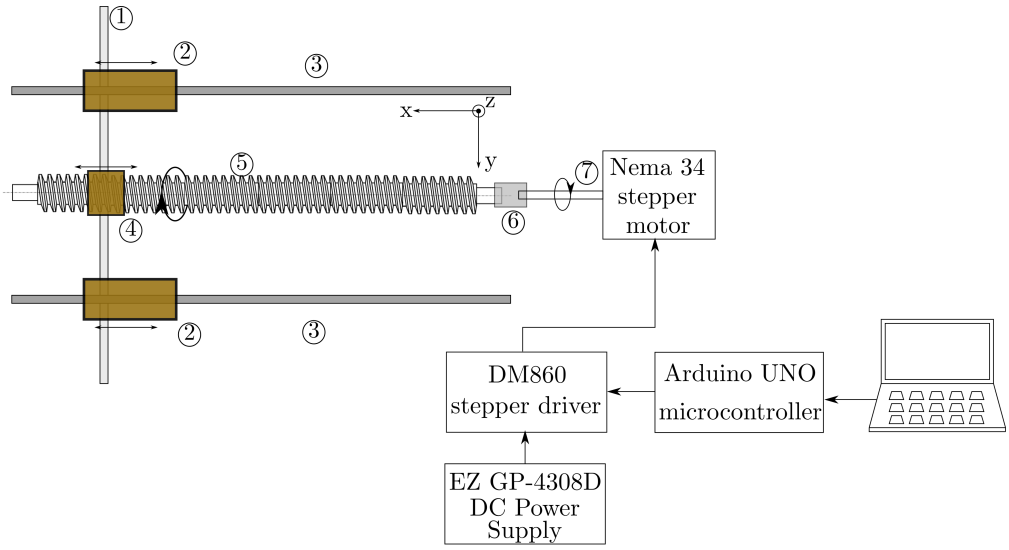

Figure 4.4: Control of the piston wavemaker. The piston wavemaker is put in motion through the use of a power screw system which is presented here. The piston wavemaker ① is guided by the translation ball bearings ② along the rails ③. The wavemaker is fixed to the nut ④ and put in translation through the rotating motion of the endless screw ⑤. A connection ⑥ allows the screw to rotate with the motor shaft ⑦. The NEMA 34 motor is controlled by an arduino UNO microcontroller and the help of a DM860 stepper driver and a DC power supply.

Rated Voltage	Rated Current	Steps	Angle	Holding Torque
2.2 V	5.5 A	200	1.8 °	4.5 N m

Table 4.2: Main characteristics of the NEMA 34 stepper motor.

Open-loop control of the piston wavemaker The paddle motion is set by a function of time, which can be sinusoidal, a step, or a custom function as represented in figure 5.18, where a step velocity is preceded by a ramp so that the motion of the piston is progressive, which allows the stepper motor to reach the constant step velocity without jamming. There is no feedback loop that would allow the correction of the motion. This is the most common way of producing waves. The module is controlled with an *Arduino Uno R3*[1]. *Arduino* is an open source electronic micro-controller whose prime objective is to make electronics available for beginners and yet powerful and flexible enough for more complicated applications. It is widely used to create low cost sensors, robots or any application needing system control. The control of stepper motors is made easy with the use of the so-called "stepper library", but in our case,

[1] https://www.arduino.cc

the "accelStepper" library[2] is employed which offers much more control on the stepper motor, such as acceleration, deceleration, multiple stepper motors, or even very slow speed. It allows us to receive and process analogical signal from sensors and control the stepper motor shaft rotational velocity. *Arduino* uses its own language which is hopefully close to C and the code used to generate the undular bore can be found in appendix D.2. The connections between the *Arduino* board, the driver and the motor are detailed in appendix D.1.

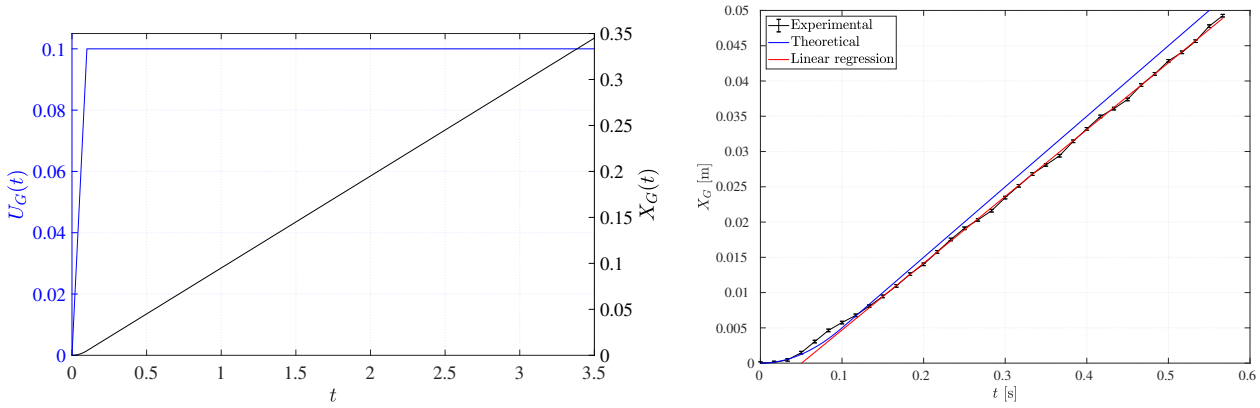

(a) (b)

Figure 4.5: (a) Piston wavemaker velocity and displacement. (b) Experimental piston wavemaker displacement.

A check of the experimental piston velocity is carried out in the tank filled with $h = 0.05\,\mathrm{m}$ water and by filming the displacement of the wavemaker from the side with a CCD camera. The frame rate is 60 Hz and to ease the detection process a black marker is stuck on the wavemaker side. The results of the procedure is shown in figure 4.5b where it is observed that the piston displacement is quite close to the theoretical one, with a mean error of 5% when the velocity is constant. We can also compute the mean velocity of the piston through a linear regression on times $t > 0.1$ s (when the piston velocity is set to be constant). We obtain a value of 0.0947 m/s, that is to say a 5.3% error from the theoretical velocity, which is acceptable. Note also that if we take times larger than 0.3 s, the error drops to 3.6%. We can conclude that the generation process is precise enough and the velocity step is correctly carried out.

4.2. Capacitive wave gauge

In this section, the capacitive wave height sensor is described and important features about its working capabilities are summarized. It is important to be able to determine with precision the free-surface dynamics in the experimental wave tank as it will be one of the

[2] http://www.airspayce.com/mikem/arduino/AccelStepper/

comparison point that will be carried out with the numerical simulations. The sensor consists of a U-shaped PTFE wire of small diameter which constitutes the first "plate" of the capacitor while the water is the other "plate". The dielectric of the capacitor is the plastic coating, acting as the insulation from the water. As the water oscillates up and down, the capacitance of the device varies, allowing to get a relation between the wet length (wave height) and the capacitance. By measuring the capacitance, we are able to deduce the water level at the sensor. Such measurement is done thanks to a charge amplifier circuit. Stray capacitances are taken into account and suppressed and thus the sensitivity of the device is improved. Finally, a full-wave rectifier with smoothing capacitance circuit allows to retrieve the output of the charge amplifier circuit by measuring a DC signal. As a consequence, the sampling frequency of the acquisition card does not need to be extremely high and the measurement is done easily. The device calibration, as well as important parameters influence are shown.

4.2.1. Review of measurement techniques and choice of the sensor

This section aims at specifying the specifications the design must respect according to the wave gauge and wavemaker system application. A review of water level sensing techniques can be found in appendix D.3.1.

Water level sensor specifications. For the application of the small wave tank at the LEAF-NL laboratory, the following requirements are expected from the wave gauge. The spacial resolution should be at least of 1 millimeter and the sampling frequency should be at least 100 Hz. Moreover, the sensor shall not modify the fluid motion. In the case of the sensor placed at the wavemaker, it might have a protection against possible effects of the wet back piston: while an elevation of water is observed at the generating side of the piston, a decrease of water height is generated at the wet back. It is important then that it does not interact with the water level detection. If any calibration is used it should be simple and an automated procedure is welcome. Cables for information transmission should be the shortest possible in order to avoid picking noise and decrease stray capacitance.

Choice of the sensor. Floats sensors, hydrostatic devices and load cells are excluded from the choice panel as they appear not to be accurate enough. Pressure sensors are limited to stationary problems and are not suitable in our case. Ultrasonic Level Transmitters and Laser/Radar Level Transmitters could be a solution but they are more complicated to build and more expensive than a capacitive or resistive wave gauge which are composed of simple geometric elements and basic electronics components. It is chosen to work with a capacitive

wave gauge, which is widely used for this purpose, as they present advantages over resistive gauges such as no salinity sensitivity (which however in our case is not important as we are working with tap water), no cross talk (or at really close proximity) (Chapman & Monaldo, 1995) and less sensitive to temperature change (allowing for example to calibrate them only one time per day). This choice implies however some drawback such as flowback error more important than for the resistive gauge (Boudan, 1953), but according to the same author it can be avoided by using wire of really small diameter (which order of magnitude is 0.01 mm).

4.2.2. Design of the capacitive sensor

In this section, the design of the sensor (shown in an artist view in figure 4.6) is detailed, that is to say that the physical device is described, how the electronics signal conditioning is designed to both maximize sensibility and get straightforward measurements and finally the results and validation of the device are shown.

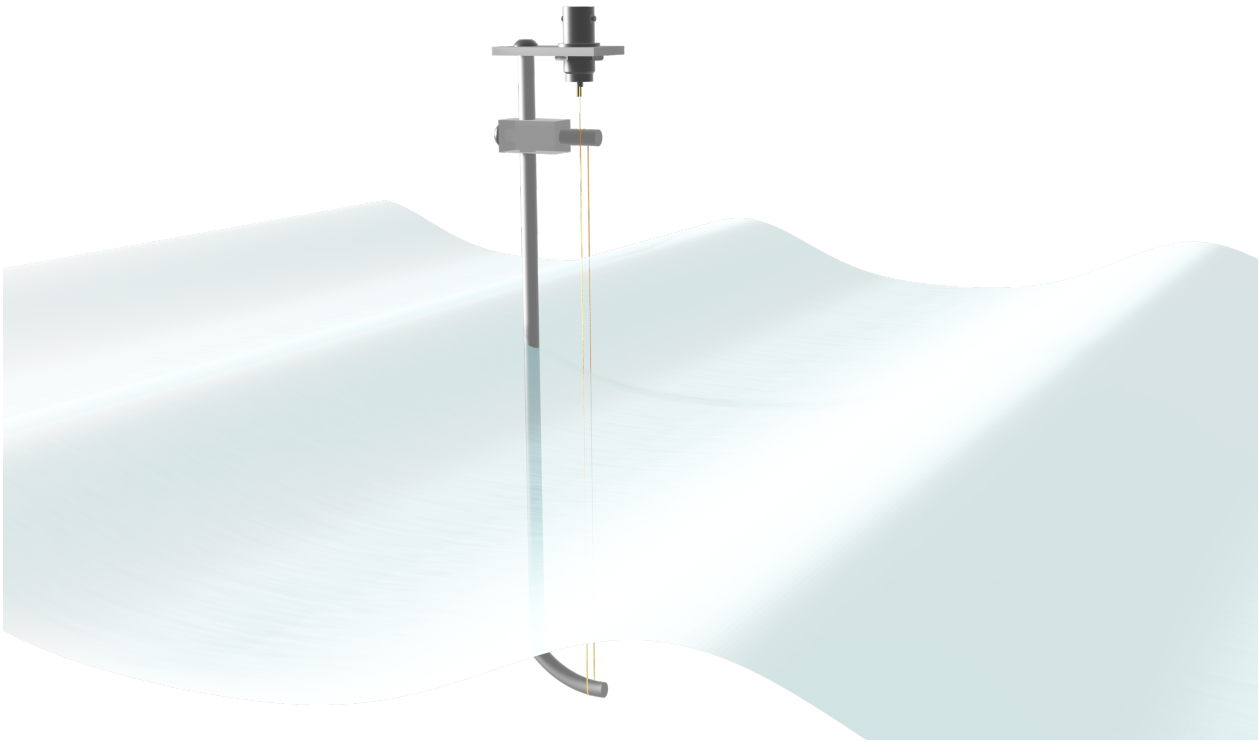

Figure 4.6: Artist view of the sensor use in the wave tank.

4.2.2.1. Capacitance and impedance of a wire immersed in a conducting fluid

The device wire immersed in water (which conducts electricity) can be seen as a transmission line, similar to a coaxial cable. Thus it is important to theoretically estimate the order of

magnitude of its capacitance and the effects of other phenomena associated to transmission line such as the inductance.

Capacitance derivation: The immersed wire, insulated from the conducting fluid (in this case water), constitutes a capacitor where one plate is the inner copper wire, the second plate is the water and the dielectric is the coating, in this case enamel (even if other material can be use, such as teflon (PTFE) as in S.-A. Yang & Chwang (1989), or polythene Tucker & Charnock (1954)). Let's first calculate the electric field induced by a charged vertical cylinder as exposed in figure 4.7. To apply Gauss' law, we consider a cylinder surface of radius r, length l and centered on the charged cylinder symmetry axis. The law states that the electric field flux through a closed surface S is equal to the total charge contained in the volume delimited by S and divided by ϵ:

$$\Phi = \oint_S \vec{E} \cdot d\vec{S} = \frac{Q}{\epsilon} \tag{4.1}$$

$$\int_{lateral} \vec{E} \cdot d\vec{S} + \int_{top} \vec{E} \cdot d\vec{S} + \int_{bottom} \vec{E} \cdot d\vec{S} = \frac{Q}{\epsilon} \tag{4.2}$$

As at the top and bottom of the surface the elementary surface and electric field are perpendicular we get $\vec{E} \cdot d\vec{S} = 0$. We also have, according to the symmetry of the problem, that the electric field only depends on the radial coordinate r, i.e. $\vec{E} = \vec{E}(r)$. The flux expression can then be simplified:

$$\begin{aligned} E \int_{lateral} dS &= \frac{Q}{\epsilon} \\ E 2\pi r l &= \frac{Q}{\epsilon} \\ E &= \frac{Q}{2\pi\epsilon r l} \end{aligned} \tag{4.3}$$

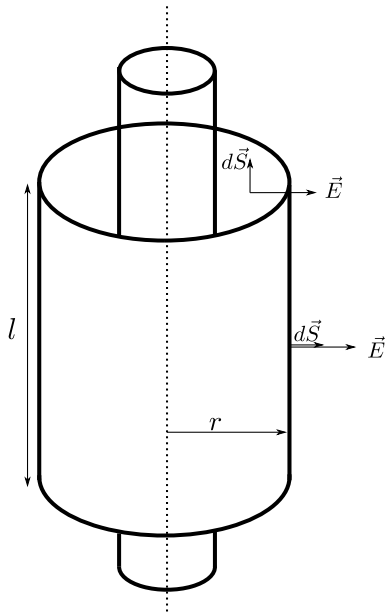

Figure 4.7: Case of study for the application of Gauss' law.

Let's now consider a vertical wire of radius r_1, length l and a second cylinder of radius r_2, coaxial to the first wire. The space between the first and second cylinder is filled with the coating, in this case enamel of permittivity ϵ. We have then $r_2 > r_1$. We can write:

$$\vec{E} = -\vec{\nabla}V \tag{4.4}$$

$$E = -\frac{dV}{dr} \quad \text{as V only depends on } r$$

$$dV = -E dr$$

$$\Delta V = -\int_{r_1}^{r_2} E\, dr$$

$$\Delta V = -\frac{Q}{2\pi\epsilon l}\int_{r_1}^{r_2}\frac{dr}{r}$$

$$\Delta V = -\frac{Q}{2\pi\epsilon l}\ln\left(\frac{r_2}{r_1}\right) \tag{4.5}$$

Leading to the capacitance:

$$C = \left|\frac{Q}{\Delta V}\right| = \frac{2\pi\epsilon}{\ln\left(\frac{r_2}{r_1}\right)}\cdot l \tag{4.6}$$

If we write $r_2 = r_1 + e$ with e the thickness of the coating, considering $e \ll r_1$ and the approximation $\ln(1+x) \approx x$ if $x \ll 1$, we get:

$$C = 2\pi\epsilon\frac{r_1}{e}l \tag{4.7}$$

It is important to notice that the wider is the central wire (r_1 increases) or the thinner is the coating (e decreases), the more sensitive becomes the sensor as the value of the capacitor

C increases. Let's consider a coating thickness of a tenth of the radius, and a coating of polyester ($\epsilon_r = 3$) then $C = 166 \cdot 10^{-12} F$ for a 10 cm submerged cable. We will see later on that this value is consistent with the experiment.

Impedance of a transmission line It can be shown (see appendix D.3.3) that the impedance of a transmission line can be written according to the following equation:

$$Z(l) \approx \frac{1}{j\omega C' l} \tag{4.8}$$

if $kl \ll 1$ and where k is the wave number of the light wave propagating in the medium and is defined as $k = \omega\mu\epsilon = \omega/c$ and l is the wire length. Equation D.13 shows that the impedance of a wire immersed in a conductive fluid is mainly capacitive if $\omega\sqrt{L'C'}l \ll 1$. According to Prunkl et al. (1958), the enamel coating are generally composed of plastics such as polyurethane, polyvinylformale, polyesther, copolymer of vinylchloride vinylacetate, carbamide resin or polyamide (perlon), which have relative dielectric constant[3] $\epsilon_r = \epsilon/\epsilon_0$ (with $\epsilon_0 = 8.854187 \cdot 10^{-12}$ F/m the dielectric permittivity of vaccum) between 2.8 and 4. We can also consider the relative magnetic permeability of such components to be of the order of magnitude of 1 (considering the magnetic permeability of vacuum to be $\mu_0 = 4\pi \cdot 10^{-7}$ H/m). If the excitation frequency of the transmission line is 10 kHz then $\omega\sqrt{L'C'}l = \omega\mu\epsilon l \approx 10^{-13} \ll 1$ for a 20 cm long sensor. We will consider hereafter that this condition is fulfilled and that the sensor device can be considered to be a pure capacitor C_S.

4.2.2.2. Physical set-up

A design is proposed in figure 4.8 and the dimensions are reported in table 4.3. The sensor consist of a support rod vertically tensing a wire. The support rod connects the electronic ground to the water thanks to the BNC connector and a joining plate. The wire loops around the rod base and is fixed to the other end by a knot. This end can be vertically adjusted to tense more or less the wire. The wire ends are connected to the BNC core by welding. As the diameters of the wire and support rod are small they should not be intrusive. The capacitor is then constituted between the water at ground and the inner part of the wire while the coating is the dielectric. The author wants to underline that this configuration, made for testing the general concept of the sensor, can be be adapted to the needs of the experiments, especially for measuring at walls by mean of copper bands for example.

[3] The dielectric constant depends on the excitation frequency and the temperature.

d_{wire}	d_{rod}	L	Metal	Coating
0.25 mm	5 mm	20cm	Copper	Enamel

Table 4.3: Dimensions of the capacitive sensor.

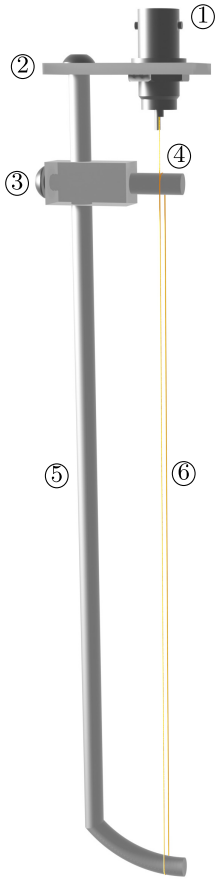

Figure 4.8: Sensor design. The BNC connector ① allows to connect the sensor to the electronics, the BNC support plate ②, besides its role of fixing the connector to the sensor, is used to connect the ground plate of the BNC cable to the support rod, the wire is attached to one end of its support thanks to a node ④, the acrylic support ③ is used to tense the copper wire thanks to a vertical adaptive position, the inox steel support rod ⑤ connects the water to the ground of the electronic circuit while serving as a rigid support for the sensor elements. Finally, the enameled copper wire ⑥ is connected to the virtual excitation potential of the electronic circuit and is the place where the measurement takes place.

4.2.2.3. Signal conditioning

To allow the measurement of the capacitance, a charge amplifier circuit is used in a configuration where two capacitors (of which one is the sensor) are mounted in a bridge. The circuit is fed with a sine wave V_{in}. The output is a harmonic signal whose amplitude provides the information of about the capacitance value. It is however relatively unpractical to measure it directly as the excitation frequency reaches several dozens of kilo hertz and thus a precision full-wave rectifier, with a smoothing capacitance is used to convert the AC signal to a DC one. Finally the signal is low-pass filtered to clean it. The practical circuit is shown in figure 4.9. For the whole circuit, *TL082CP* operational amplifiers are used as they allow to work at higher frequencies than cheaper op-amp such as the *LM741* and are more compact as they integrate two op-amps in a single chip. The over-cost is really small

(around 300 $CLP a piece). They are powered by a ±12 V signal from a dual battery set-up. The electronic component lists and a PCB design can be found in appendix D.3.4. The data acquisition with the sensor in this thesis was however carried out from the protoboard since all electronic workshops at Universidad de Chile stayed closed due to the coronavirus crisis. In the following paragraphs we review all circuit part and give the transfer function of each of them.

Capacitor bridge: The value of the immersed wire capacitor can be relatively low, and then can be totally covered by stray capacitances that appear in the practical circuit, such as the capacitance from the coaxial line connecting the sensor to the rest of the circuit (which can reach values of $C'_{stray} = 100$ pF/m), the capacitance of the wire placed in the air (part which is not immersed) and also capacitances from the PCB conductive tracks or the input of the operational-amplifiers in use. Therefore, a strategy consisting in artificially subtracting a capacitance from the measured one is adopted thanks to the use of a bridge. Other possibilities is the use of an inductor (Wilner, 1960) or the so-called resonant bridge carrier system (Cook, 1951). We call V_{out}^{bridge} the output of the first amplifier (left bottom corner) and we have:

$$\frac{V_{out}^{bridge}}{V_{in}} = \frac{R_2}{R_1} + 1 = 2 \quad \text{as } R_2 = R_1 \tag{4.9}$$

Now we can write the following equation according to Kirchhoff's nodal rule:

$$\begin{aligned} i &= i_s + i_0 \\ &= C_S \frac{d(0 - v_{in})}{dt} + C_0 \frac{d(2v_{in} - v_{in})}{dt} \end{aligned} \tag{4.10}$$

$$I = j\omega \left(C_0 - C_S\right) V_{in} \tag{4.11}$$

The resulting current i depends on both C_S and C_0. If now we consider that $C_S = C_m + \Delta C + C_{stray}$ and adjust $C_0 = C_{stray}$, we obtain that the measured capacitance does not take into account the stray capacitance and as we will see a better sensitivity of the sensor.

Charge amplifier: The output voltage of the charge amplifier circuit (second op-amp) is called V_{out}^{CA}. It can be shown, by equalizing the i current with the current in the feedbcak branch, that the transfer function of such circuit (capacitor bridge + charge amplifier) is:

$$TF = \frac{V_{out}^{CA}}{V_{in}} = 1 + \frac{j\omega R_3 \left(C_S - C_0\right)}{j\omega R_3 C_1 + 1} \tag{4.12}$$

and thus:

$$C_m + \Delta C = \frac{\left(\frac{V_{out}^{CA}}{V_{in}} - 1\right)\left(j\omega R_3 C_1 + 1\right)}{j\omega R_3} \tag{4.13}$$

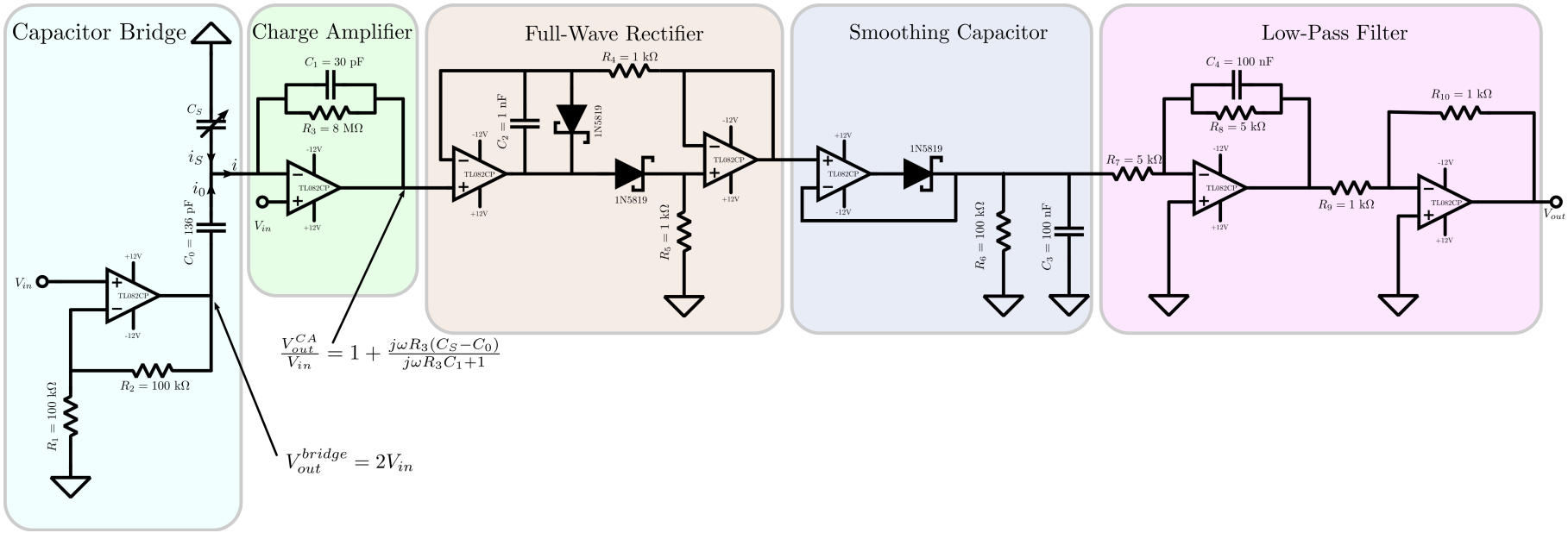

Figure 4.9: Scheme of the electronic circuit allowing for the capacitance measurement: the so-called charge amplifier.

If $\omega >> \frac{1}{R_3 C_1}$:

$$C_m + \Delta C = \left(\frac{V_{out}^{CA}}{V_{in}} - 1 \right) C_1 \tag{4.14}$$

By using the capacitor and the charge amplifier, we are able to measure the capacitance of the immersed wire, without the overweight of the stray capacitances and at the condition that $\omega_c >> \frac{1}{R_3 C_1}$. If $R_3 = 8$ MΩ and $C_1 = 30$ pF, we get $f_c = 663$ Hz, thus the excitation frequency shall be much higher than this particular frequency $f_{in} \gg f_c$ and we will consider working at frequency always higher than 6 kHz. In practice, we will only measure V_{out}^{CA} as it is directly proportional to the water level at the probe.

Precision Full-Wave Rectifier: The charge amplifier, if it allows to measure capacitances, has the drawback of necessitating high excitation frequency and implies difficulties to measure its amplitude unless to possess high frequency acquisition cards. To remedy to this problem, the signal is rectified thereafter with a precision full-wave rectifier which avoids voltage drops through the diodes (Ye, 2013) and then passes through smoothing capacitor circuit which allows to convert the AC signal to a DC signal whose level is the amplitude of the AC signal. We use Schottky diode for the whole circuit, which has a lower drop, even if in this part simple diode would also work as the circuit actively compensates this drop. This circuit is tested in the following section (see section 4.2.3.1).

Smoothing capacitor: The signal from the output of the precision full-wave rectifier is still alternative even if it passed through an absolute value converter. It needs a smoothing capacitor to be transformed to DC signal. To that end, we use a Schottky diode and a capacitor set up in parallel. The Schottky diode still has a voltage drop, which is compensated thanks to an active op-amp set-up. The author tried to avoid the use of this diode, whose drop is annoying but no satisfying solution was found.

Low-pass filter: Finally, an active low-pass filter is set-up to filter eventual high-frequency noise that may appear. The first filter is an inverting low pass filter but as the output is negative it is followed by an inverting amplifier. The total transfer function is the following:

$$TF = \frac{R_{10}}{R_9} \frac{R_8}{R_7} \frac{1}{1 + j\omega R_8 C_4} \tag{4.15}$$

and the cut-off frequency is $f_c = 1/(2\pi R_8 C_4)$ and the numerical application gives $f_c = 318$ Hz. The total gain of the filter is one as $R_{10} = R_9$ and $R_8 = R_7$.

4.2.3. Sensor characterization

All data is measured thanks to the DT9804 data acquisition card and *QuickDAQ* software from *Data translation* enterprise[4]. The sensor signals (V_{in} and V_{out}) are recorded at a sampling rate of 100 kHz when not specified otherwise. Post-processing consists in measuring the peak-to-peak value of the signals over a certain number of periods in the case of measuring the output tension from the charge amplifier, or the DC output voltage from the rectifier. The error associated with such processes is characterized with the standard deviation method. In the following sections, the precision rectifier and the charge amplifier will be tested and the calibration curves will be given.

4.2.3.1. Rectifier Characterization

Ripples The main source of error when it comes to rectify a signal is the creation of ripples as explained in figure D.7c. This error however seems not to impact the final measurement as it applies equally on all input voltage amplitude. This is true however only if the output voltage is important enough so that the ripple error can be neglecting compared to the overall amplitude.

Transfer function The rectifier characterization is carried out by applying directly at its entry an input signal from the function generator (circuit parts consisting oof the full-wave rectifier, the smoothing capacitor and the low-pass filter). The first test case consists in applying a $V_{pp} = 2$ V sine input signal and vary the frequency. The results are reported in figure 4.10a as the gain which is the quotient between the output DC signal and the amplitude of the input signal in function of the frequency. The amplitude measurement error is superimposed on the same figure. The second test case is now keeping the frequency constant at $f_{in} = 10$ kHz and varying its amplitude. The results are presented in figure 4.10b, and as for the first case the error is also displayed. The precision rectifier and smoothing capacitor behaves well, *i.e.* $G_{dB} \approx 0$, for a frequency range between 7 kHz and 20 kHz and for input peak-to-peak amplitude between 2 and 15 V, maintaining the error below 2% for this range. The sensor will need to work at these frequencies and amplitude to behave as needed. Lower frequencies and lower amplitudes gives more important errors and a gain further away from 1 or $G_{dB} = 0$. At higher frequency or higher input amplitude the error remains low but the gain is lower than 1.

[4] https://www.mccdaq.com/Data-Translation

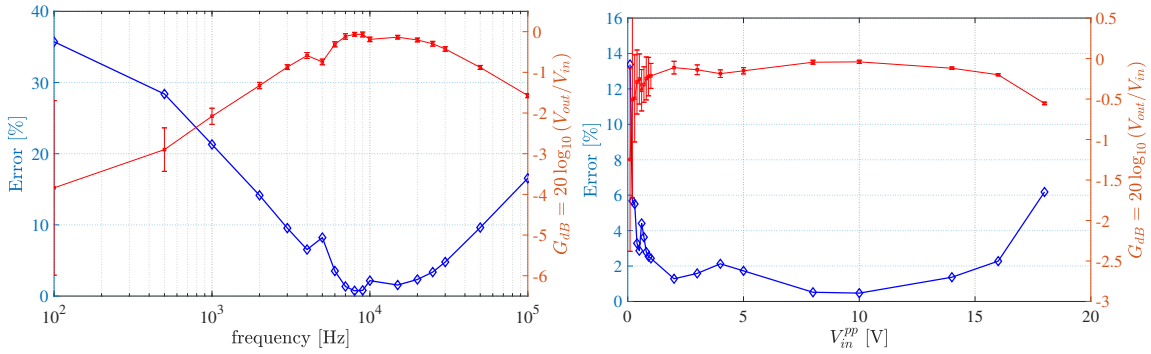

(a) (b)

Figure 4.10: Transfer function of the rectifier and smoothing capacitor circuit. The transfer function gain is expressed in decibel and the error is defined as $\epsilon = \left|\frac{V_{out}-V_{in}}{V_{in}}\right|$. (a) Gain vs input voltage frequency. Peak-to-peak amplitude of the input signal is 2 V. (b) Gain vs input voltage peak-to-peak amplitude. Input frequency is 10 kHz.

Dynamic test In order to study the dynamics of the rectifier, smoothing capacitor and low-pass filter circuit, a modulated signal is given at the input of this circuit. The carrier frequency, which corresponds to the working frequency of the sensor, is a 10 kHz wave (see figure 4.11b) and the modulation waveform is a variable frequency sine signal of amplitude of 2 or 8 V as shown in figures 4.11a and 4.11c. Frequency range is 10 to 200 Hz. The modulated signal is generated thanks to the waveform generator. It is interesting to remark that the cut-off frequency of the low-pass filter is $f_c = 318$ Hz and therefore the filter does not impact the measurements for the lower frequencies. We can however assume that it does have an influence on the higher ones as the maximum tested modulation frequency is 200 Hz. From these tests, we can compute the frequency dependent transfer function gain between the modulation waveform (containing the information of the wave height) and the recovered one from the electronics. Results are shown in figure 4.11d. We can observe first a gain close to 0 for low frequencies and the 2 V input signal. For frequencies till 50 Hz the gain stays close to 0, while decreasing for higher values. In the case of less favorable input signal, that is to say for the 8 V case, amplitude is lower than for the 2 V case, conducting to imprecision in the measurement. The loss, for low input signal is however low (2.5% error over the 8 V). At 200 Hz, the error is close to -1 dB and corresponds to a 20% error, which is quite important, but is due to the signal filtering. However, high variations at such short time is not likely to happen in the wave tank. We can conclude that the rectifier, smoothing capacitor and low-pass filter circuit behaves well and is able to follow huge voltage variations at relatively high frequencies (higher than the physical phenomena that is measured). In practice, the voltage variation is for a 1 cm wave height will only be of the order of magnitude of 1, thus we can consider that the error generated by the rectifier will be low ($< 2\%$).

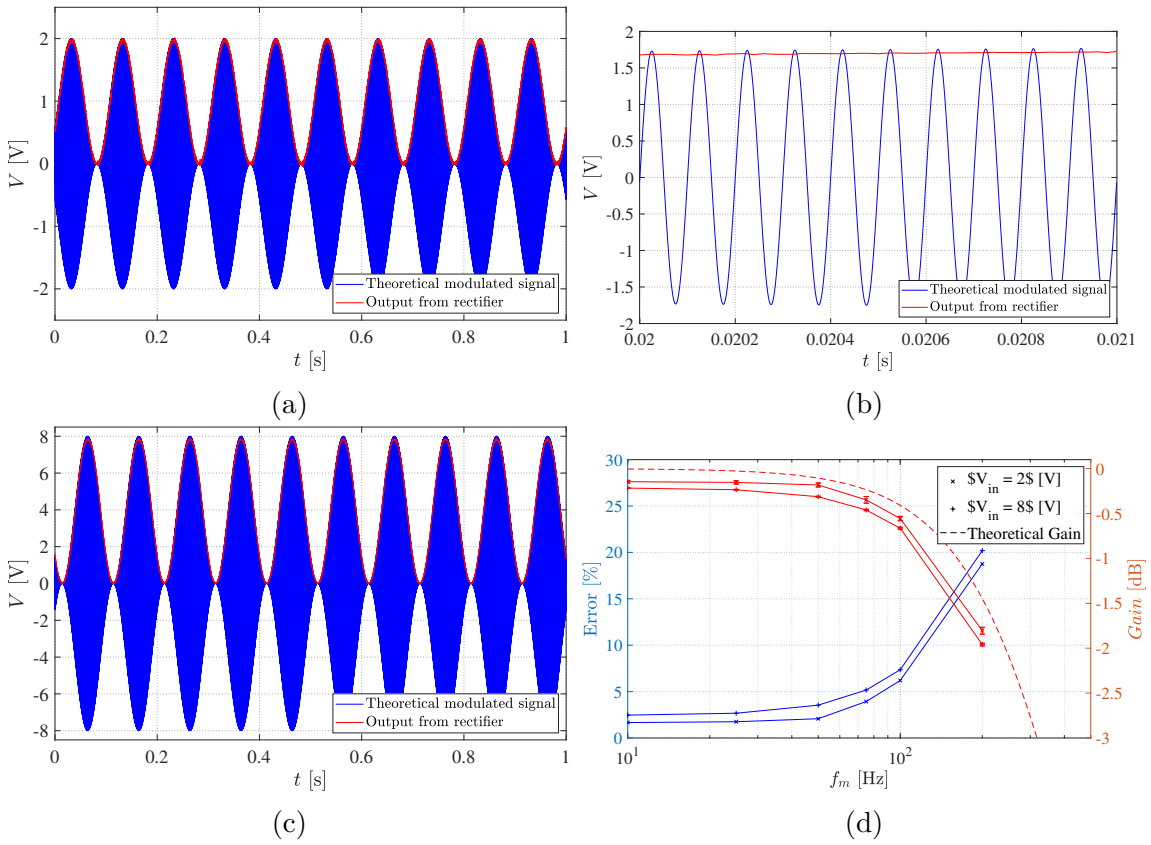

Figure 4.11: Dynamic tests of the rectifier. (a) Voltage in function of time for the theoretical input signal (in blue) and the measured output from the rectifier. The input modulated signal is a sine function of amplitude 2 V, and the carrier frequency is 10 kHz. (b) Zoom over a short time showing the carrier frequency. (c) Case of a 8 V modulation waveform amplitude. (d) Gain of the transfer function between the input signal (modulation waveform) and the recovered signal from rectifier.

4.2.3.2. Charge Amplifier Characterization

In this section, we aim at studying the influence of the excitation frequency on the measurement of the capacitance which is done by the first part of the electronics, that is to say the bridge capacitance and charge amplifier circuits. In order to disconnect these tests from the physical sensor, a 47 pF nominal capacitor replaces the sensor, even if it is still connected to the circuit with the coaxial circuit. The experimental (squared) gain of the charge amplifier circuit is shown in figure 4.12a. Input frequency varies between 100 Hz and 30 kHz. To be able to study the circuit, we need to precisely measure the different capacitors which compose the bridge and the charge amplifier. We also need to measure the stray capacitance from the coaxial cable. Results of the measurements (done with a *Mastec Ultra Precision MY-65* multimeter) are shown in table 4.4. The error, according to the constructor, is 0.3% +2×

least significant digits for the resistance measurement and 4% +10× least significant digits for the capacitance ones.

The results show convergence at high frequencies ($f_{in} > 3$ kHz) according to the theory (see section 4.2.2.3) even if for the highest frequencies ($f_{in} > 8$ kHz) the error associated with the gain measurement strongly increases due to the inability to precisely measure the AC amplitude from the acquisition card whose maximum sampling frequency is 100 kHz. Influence of the input signal amplitude is low, even if some discrepancies can be observed at low frequency. Finally the results appear coherent with the theoretical gain while the error associated with the multimeter capacitance measurements leads to high uncertainties (transparent grey). The general behavior is nevertheless really similar between the measured gain and the theoretical one. In the case of calculating the equivalent capacitance, a good estimate is obtained at high frequencies, but the error associated to the process is still huge (±10 pF). We could gain accuracy by lowering the uncertainty on every capacitance measurements. The estimate is however good, showing the capabilities of the charge amplifier to measure capacitance, concomitantly with the bridge capacitance circuit.

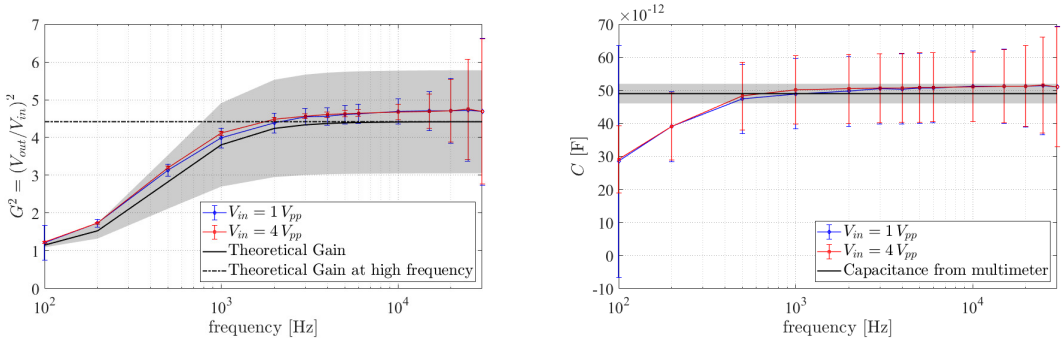

(a) (b)

Figure 4.12: (a) Transfer function of the charge amplifier circuit in function of the excitation frequency. The blue curve corresponds to an input peak-to-peak voltage of 1 V while the red one to a 4 V input. The continuous black line shows the transfer function theoretical results and the black dashed line corresponds to the predicted value from circuit theory at high frequency. Error for the theoretical value is represented in transparent grey color. (b) Equivalent capacitance in function of the input frequency. The measured value of the capacitance from the multimeter is shown in black and its associated error in transparent grey.

	C_0	C_1	R_3	C_{stray}	C_{47pF}
Value	147.2 pF	33.4 pF	10.210 MΩ	131.2 pF	49.3 pF
Error	6.9 pF	2.3 pF	32.630 kΩ	7.4 pF	3.0 pF

Table 4.4: Capacitor measurements from multimeter and their associated error.

4.2.3.3. Calibration

Calibration is carried out by placing the sensor vertical and linked to a graduated ruler with a precision of 1/10 mm. A series of measurements is done for different water levels. Results are shown in figure 4.13. The output of the circuit V_{out} is plotted in function of the water depth (the immersed distance) of the sensor. Two cases are investigated: first the sensor is sank in the water (blue curve), then once it has reached its deepest position it is risen (red curve). A linear fit is carried out (dashed dark straight line) based on the blue curve and three deepest points (40, 60 and 80 mm). Finally, we study the effect of letting the whole sensor out of water during a long time (typically a night, see figure 4.13a) and letting immersed overnight before calibrating it (see figure 4.13b). The first observation we can make is that the sensor output voltage is linear with the water depth even if some discrepancies appears when the sensor is fully outside of the water (only its base is touching the water (0 mm)). The influence of the wetting effects can be seen as the sinking and rising curves display differences, even if the global behavior and the line slope are very similar. From this translation we can define an error due to wetting whose amplitude is 1 mm approximately. Letting the sensor immersed during a long time seems to decrease this error. In comparison, the maximum error from calibration curves obtained by *Akamina* AWP24 20 cm high wave gauge is 0.28% of its total height that is to say 0.55 mm (Laurich, 2009).

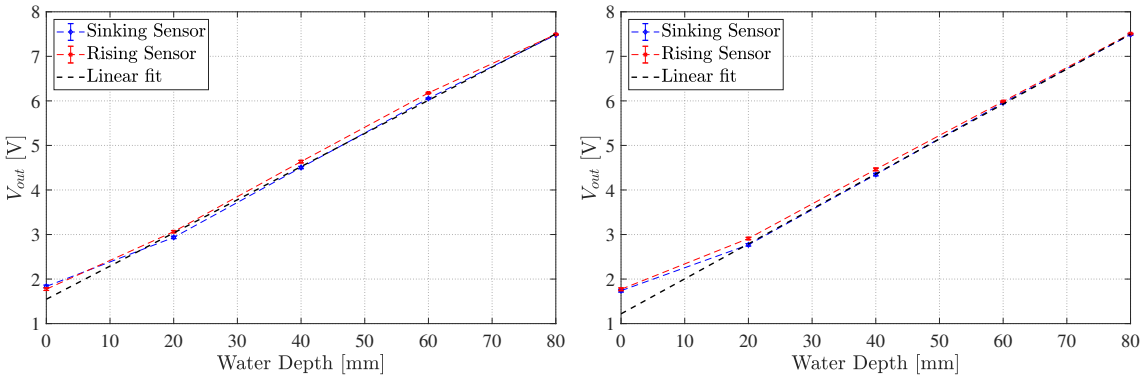

Figure 4.13: Calibration of the water level sensor. The red curve corresponds to the sinking method of the sensor calibration process while the the blue curve corresponds to rising one. (a) Dry sensor. (b) Sensor left during the night in water.

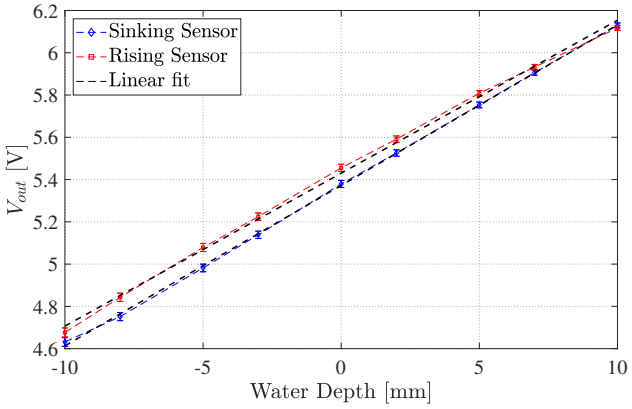

Figure 4.14: Calibration around working depth. $V_{rising} = 0.0724\eta + 5.4302$, $R^2_{rising} = 0.9975$, $V_{sinking} = 0.0759\eta + 5.3722$, $R^2_{sinking} = 0.9995$

4.2.3.4. Limitations due to the probe head

Non-uniformity of the insulation Non-uniformity of the dielectric coating may cause an error in the measurements. However, new wire production techniques nowadays offer more guaranty than 60 years ago when the first capacitive wave gauge appeared (Boudan, 1953; Millard, 1969). It is moreover complicated to evaluate the influence of such parameter in the present work.

Flowback Flowback, also called rundown, is the change of measured capacitance due to the presence of a film at the wire when water is flowing down or receding, as described in Wilner (1960), and illustrated in figure 4.15a. The effects are the flattening of the maximum wave height (maximum immersion) and the sharpening of the trough (minimum wave height) while

a phase shift and a lowering of the peak-to-peak amplitude are also observed. Wilner (1960) proposes however some design rule, which are the following: (i) use small cross section wire to limit effect of surface tension, (ii) keep conduction path short in order to be able to distinguish main level and flow back and finally (iii) choose a frequency just below the relaxation frequency ($f = 1/2\pi RC$) of the RC system composed of the sensor capacity and the resistance of the water conduction path. In order to avoid any influence of the film on the measurement, one way is to increase the water resistance (in series with the wire capacitance) such that it is tremendously higher than the capacitance impedance then it will not be measured. Tucker & Charnock (1954) shows that the ratio of the conduction path resistance to the capacitance impedance of the immersed wire system can be estimated as:

$$\frac{R}{Z_C} = 10^{-12}\rho\epsilon_r f \left[\log\left(\frac{2S}{D_2}\right)/1.8\log\left(\frac{D_2}{D_1}\right)\right] \tag{4.16}$$

with ρ the water resistivity (in $\Omega\,$cm), ϵ_r the relative dielectric constant, f the frequency, S the distance from the wire to the earth connection (in our case the vertical rod), D_2 and D_1 the outer and inner diameter of the wire. An estimation of f such as $R/Z_C = 0.1$ (upper limit according to Tucker & Charnock (1954)) gives 1 MHz (with $\rho = 1000\ \Omega\,$cm, $\epsilon_r = 4$, $S = 2$ cm, $D_2 = 0.25$ mm and $D_2 = 0.20$ mm), a value which is really higher than the 10 kHz in use. To get closer the excitation frequency to the upper limit given before, we can increase the ratio R/Z_C on the one hand, by using distilled water thus drastically increasing water resistivity ρ, connecting the earth further away (increasing S) but this strategy has some limitation (wave tank dimension for example) or using a wire which coating is really small thus giving $D_2 \approx D_1$. In the other hand, we could improve the electronics in order to be able to use a higher excitation frequency. In any case, the use of really thin wires appears to greatly help and even make this phenomena disappear as observed by Tucker & Charnock (1954).

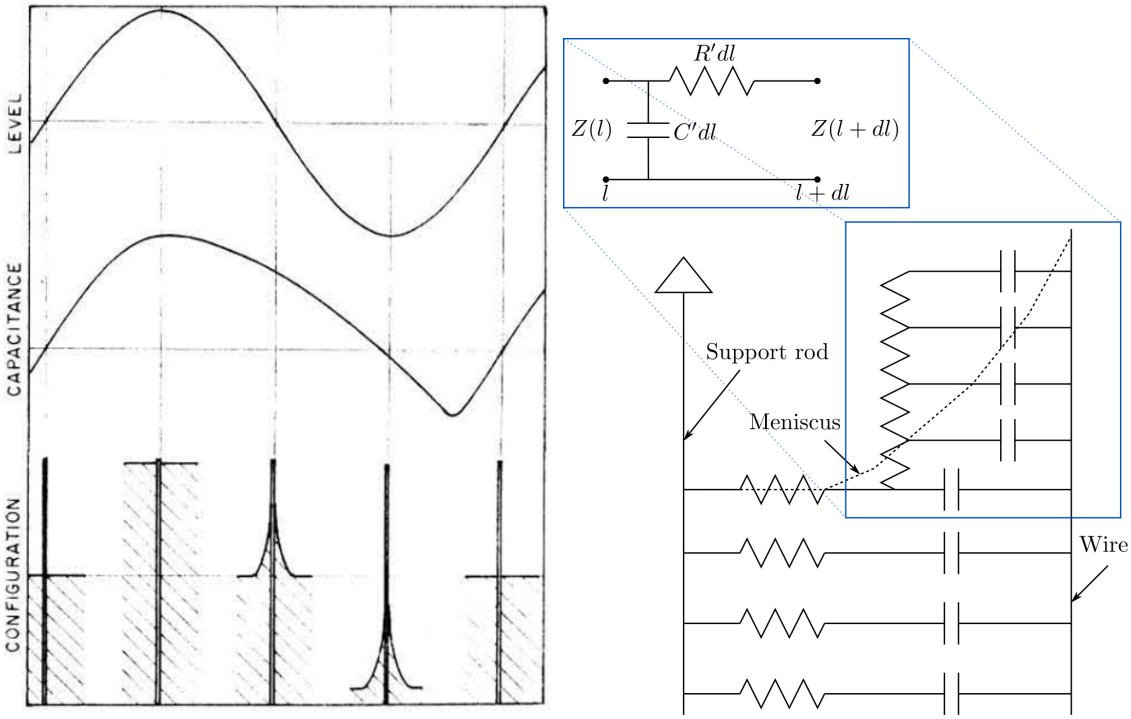

(a) (b)

Figure 4.15: (a) Flowback effect on the capacitive sensor (from Wilner (1960)). (b) Electric equivalent circuit of the wave height probe with the presence of the meniscus.

We now make an estimate of the flowback impedance for the meniscus part of the complete system represented in figure 4.15b. Let's simplify the problem by considering that the shape of the flowback meniscus is rectangular. We can then model this phenomena by an equivalent electric circuit, where R' and C' are constant[5]. This problem is from all point of view similar to the problem of the transmission line described in section D.3.3. It comes that:

$$Z(l+dl) = Z + dZ = R'dl + \frac{Z(l)}{j\omega C'dlZ(l)+1} \tag{4.17}$$

Leading to the non-linear first order equation:

$$\frac{dZ}{dl} + j\omega C'Z^2 = R' \tag{4.18}$$

whose solution has the form: $Z(l) = A\tan(Bl+C)$, with $Z(0) = \pm\infty$. It leads to the following system:

$$\begin{cases} A = \frac{-B}{j\omega C'} \\ AB = R' \end{cases} \tag{4.19}$$

[5] If the meniscus shape was not considered as rectangular (or of the same width), R' and C' would depend on the l coordinate and not be constant anymore: $R'(l)$ and $C'(l)$. This would considerably complicate the resolution of the differential equation that is derivated.

which gives:

$$\begin{cases} A = \sqrt{\frac{R'}{2\omega C'}}\,(1+j) \\ B = \sqrt{\frac{\omega R'C'}{2}}\,(1-j) \\ C = -\frac{\pi}{2} \end{cases} \tag{4.20}$$

and finally:

$$Z(l) = \sqrt{\frac{R'}{2\omega C'}}\,(1+j)\tan\left(\sqrt{\frac{\omega R'C'}{2}}\,(1-j)\,l - \frac{\pi}{2}\right) \tag{4.21}$$

By considering that if a complex number $z = x + jy$ and the following identity:

$$\tan(z) = \frac{\sin(2x) + j\sinh(2y)}{\cos(2x) + \cosh(2y)} \tag{4.22}$$

$$Z(l) = \sqrt{\frac{R'}{2\omega C'}}\,(1+j)\,\frac{-\sin\left(2l\sqrt{\frac{\omega R'C'}{2}}\right) + j\sinh\left(-2l\sqrt{\frac{\omega R'C'}{2}}\right)}{-\cos\left(2l\sqrt{\frac{\omega R'C'}{2}}\right) + \cosh\left(-2l\sqrt{\frac{\omega R'C'}{2}}\right)} \tag{4.23}$$

$$= \sqrt{\frac{R'}{2\omega C'}}\,(1+j)\,\frac{-\sin\left(\sqrt{2\omega R'C'l^2}\right) + j\sinh\left(-\sqrt{2\omega R'C'l^2}\right)}{-\cos\left(\sqrt{2\omega R'C'l^2}\right) + \cosh\left(-\sqrt{2\omega R'C'l^2}\right)} \tag{4.24}$$

Let's simplify the above equation in function of two cases: $R/Z_C \ll 1$ and $R/Z_C \approx 1$[6]. In the first case, we can develop $cos(x)$ as a Taylor series:

$$Z(l) = \sqrt{\frac{R'}{2\omega C'}}\,(1+j)\,\frac{-\sqrt{2\omega R'C'l^2} + j \times 0}{-\left(1 - \left(\sqrt{2\omega R'C'l^2}\right)^2/2\right) + \cosh(0)} \tag{4.25}$$

So if $R/Z_C \ll 1$ then $|Z(l)| = 2/\omega C'l$, that is to say that the meniscus impedance has a capacitive effect. This is not a surprise at all since if the resistance is low then remains only the effect of the capacitors. In order to get rid of this effect, a choice could be to increase the frequency which is impossible while maintaining the ratio $R/Z_C = \omega RC$ really small. Now if $R/Z_C \approx 1$ or $\omega R'C'l^2 \approx 1$ then:

$$Z(l) = \sqrt{\frac{R'}{2\omega C'}}\,(1+j)\,\frac{-\sin\left(\sqrt{2}\right) + j\sinh\left(-\sqrt{2}\right)}{-\cos\left(\sqrt{2}\right) + \cosh\left(-\sqrt{2}\right)} \tag{4.26}$$

and

$$|Z(l)| \approx \sqrt{\frac{R'}{\omega C'}} \approx \frac{1}{\omega C'l} \tag{4.27}$$

By increasing the input frequency we get $|Z(l)| \to 0$ which is achievable for the hypothesis

[6] $R/Z_C = \omega R'C'l^2$

$R \approx 1/\omega C$ for high frequencies. We demonstrated that by using large enough frequencies, we can get rid of the measurement of the meniscus capacitance. This is however a delicate operation as one could also make disappear the capacitive effect of the immersed part of the wire if the frequency is too high (Wilner, 1960).

Spacial/frequency limiting effects Long & Huang (1976), comparing data from capacitive probes and optical (laser) techniques, shows that any device recording real-time wave amplitude is wavelength or frequency limited and that this limit is estimated to correspond to wavelength approaching ten times the spot size (in case of the laser techniques) or wire diameter (in the case of the capacitance probe). A similar study was previously carried out by Sturm & Sorrell (1973), concluding that "the attached meniscus increases the effective diameter of the probe by a factor on the order of 20 in clean water".

Wetting Effects - drift The enamel coating of the sensor has a main drawback which is to slowly absorb water when plunged into the wave tank, changing the dielectric constant of the cable. This was highlighted by Tucker & Charnock (1954), who also used enamel wire to design a capacitive wave height sensor. They however suggest to maintain the sensor dry before any measurements (or at the contrary fully immersed) and to regularly execute calibration in order to overcome this problem, especially when working at small scale when greater precision is needed. They finally suggest to use polythene coated wire in order to avoid any absorption. This type of wire was not found in Chile. As explain above, they can be observed by measuring the the output voltage in function of time. Let's place the sensor at 30 mm depth and plunge it at 40 mm. The time response is shown in figure 4.16a while replacing it afterward at 30 mm leads to the results of figure 4.16b. A moving window average filter function is apply to the data in order to smooth the results. For the first one, the output voltage slowly derives from 4.355 V to a higher value stabilizing to a constant value of 4.487 V, that is to say a difference of $\Delta V = 0.132$ V. According to the calibration curve it corresponds to an error of 1.77 mm. As for the second case, the output voltage slowly derives from 3.860 V to a smaller value stabilizing to a constant value of 3.694 V, that is to say a difference of $\Delta V = 0.166$ V or 2.23 mm. To overcome the wetting effect, it is suggested to use PTFE (teflon) wire (Millard, 1969). This kind of wire is however complicated to obtain in Chile.

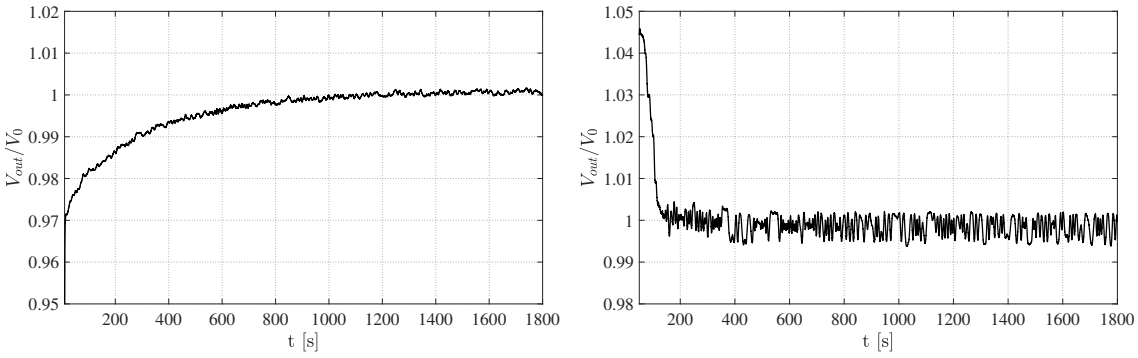

(a) (b)

Figure 4.16: Normalized output voltage of the sensor in function of time when plunging or rising it to a new level. (a) Plunging sensor. (b) Rising sensor.

4.2.3.5. Improvements by using PTFE wire

We were able to procure a 34 AWG teflon (PTFE) coated wire from a well-known international Chinese trade company. The external diameter is 0.16 mm. Results of calibration and drift are shown in figure 4.17. The calibration is done by lowering the sensor and rising it afterwards as explicated above. We observe a real effect of the use of PTFE on the calibration curve as no hysteresis is observed. The calibration curve from figure 4.17a shows high linearity with a correlation coefficient of $R^2 = 0.99985$ really close to 1. Regarding the drift effect, we observe also a real improvement as no drift is observed, for both lowering and rising positions, as demonstrated in figures 4.17b and 4.17c. As for the flowback effect, as the wire has a really small diameter, it is expected that it will not have any significant influence on the measurements. These results give us great confidence on the precision of the device.

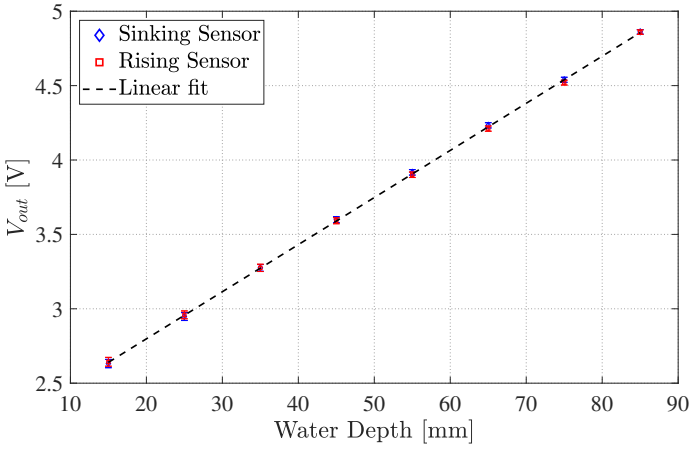

(a)

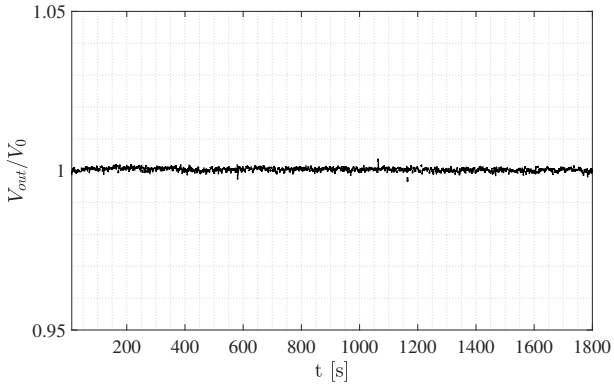

(b)

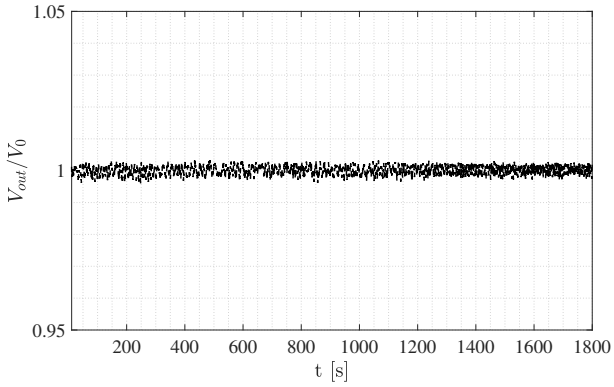

(c)

Figure 4.17: (a) Calibration curve results. Dashed line corresponds to a fit of a linear function: $V_{out} = 0.03166 \cdot \eta + 2.16490$ with η in millimeter. The corresponding correlation coefficient (for both rising and sinking data sets) is $R^2 = 0.99985$. (b) Normalized output voltage of the sensor in function of time when plunging or rising it to a new level for plunging sensor and (c) for rising sensor.

4.2.3.6. Sensor use alongside stepper motors

After the sensor was independently tested from the wave tank and the wavemaker, it was placed in the canal at 54.5 cm from the wavemaker in order to measure the generated wave profile. However, the recorded signal from the sensor has shown a huge amount of noise when the stepper motor is working, and at rest particularly, that is to say energized and providing full torque. These results in a noisy signal as displayed in figure 4.18 (in blue), which can be used as such, but needs post-processing by low-pass filtering. We choose to reduce this noise and to do so, an active shield is installed by wrapping an aluminum sheet around the stepper motor and setting it to the ground potential so that the electromagnetic field from the motor coils do not bypass this "barrier", similarly to the description of section D.3.2.3. The results are presented in figure 4.18 where we compare the signals with (in black) and without (in blue) active shielding. Results are interesting since there is a clear reduction of noise in the black signal even if we identify isolated higher peaks which are however easily removed by filtering. In the future experiments involving the wavemaker and the capacitive sensor, we will make sure to active the motor shielding.

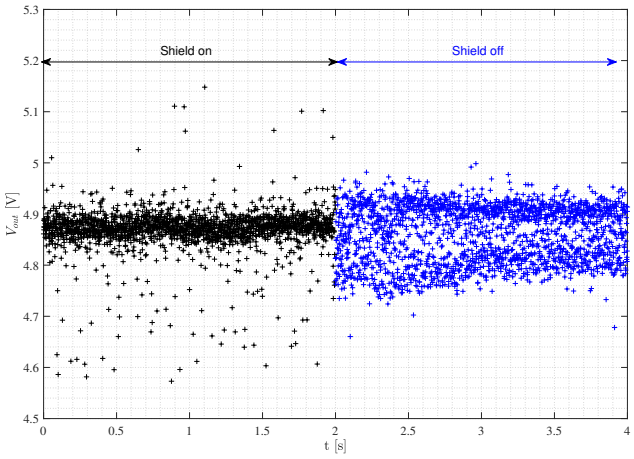

Figure 4.18: Sensor output voltage when the stepper motor shielding is active (in black) and when the shielding is inactive (in blue).

4.2.3.7. Validation

A validation is carried out with an image processing measurement as reference in order to check the suitability of the wave sensor to its application: the undular bore height quantification. An image post-processing experiment is set-up and is similar in all points as the one described further on in section 6.1.1: an undular bore is generated on one side of the wave tank through the action of the piston wavemaker. A laser vertical light plane is generated so that it parts the wavemaker in half and PIV particles are poured into the water. The water-air interface is then visible and can be followed thanks to the Radon transform technique explained in section 4.3.3 so that we are able to automatically follow the interface displacement by filming from the side. The test case corresponds to the E2 case that is to say a piston step velocity of 7 cm/s with a ramp of 0.1 s. The reader is invited to look for further details in the sections of interest of this work. The capacitive wave gauge is placed at the side of the laser plane and at the center of the camera field of view, and we make the hypothesis that the wave front is perfectly perpendicular to the tank walls. We compare both signals in order to quantify the error between both measurement techniques which is showed in figure 4.19. We can also express the error according to:

$$\epsilon = \left| \frac{\eta_{WG} - \eta_{image}}{\eta_{image}} \right| \tag{4.28}$$

where η_{WG} is the wave gauge signal and η_{image} is the one from the image post-processing. We can observe the undular bore composed of the main wave followed by wiggles which oscillate around the bore mean height. The wave gauge signal is much noisier than the one from the image post-processing and can be explained by various reasons as the electronics set-up on protoboard and not a PCB, the sensor head wire which might lengthen during the wave

passage or the stepper motor which has an impact on the signal quality. However, the two signals are really close from one another and great precision is obtained by both techniques, even if the image post-processing one is much neater. In particular, the sensor seems to have trouble in catching the wiggles variations which are small such as in the troughs. The maximum error peaks at the sudden rise and decrease of the bore but this is mainly due to an error in the signal synchronization and thus should not be considered in the analysis.

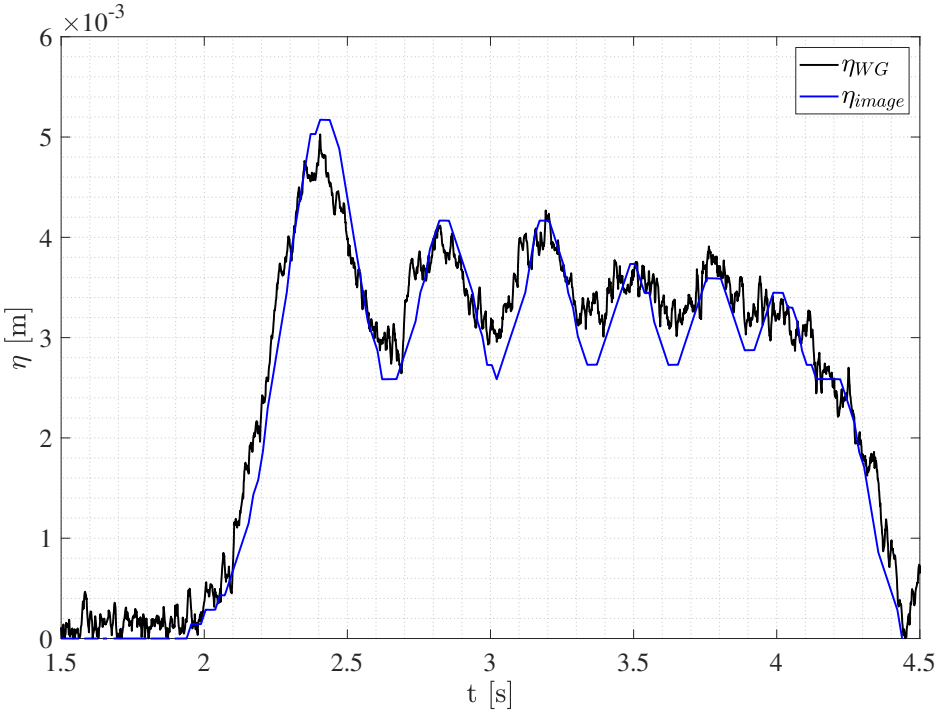

Figure 4.19: Comparison between signals obtained by the wave gauge η_{WG} in black and the image post-processing technique η_{image} in blue in function of time.

Regarding the root-mean-square error, it is defined as:

$$RMSE = \sqrt{\frac{\sum_{i=1}^{N} \left(\eta_{WG}^{i} - \eta_{image}^{i}\right)}{N}} \tag{4.29}$$

and normalized by:

$$NRMSE = RMSE/\bar{\eta}_{image} \tag{4.30}$$

with $\bar{\eta}_{image}$ the mean of the image post-processing signal. A summary of the different characteristics of the error that are measured is reported in table 4.5. The error was computed over two times series to take into account or not the great errors found at the rise and decrease of the bore. It corresponds to times between $2 \leq t \leq 4.4$ s and $2.4 \leq t \leq 4$ s for the whole bore and only the points between the first and last wave crest, respectively. The mean error is 12.9 % if considering the whole bore but drops to 8.5 % which is quite correct considering

the scale at which is conducted the experiment with a bore height inferior to 5 mm. The maximum errors are quite high for both time series and are mainly attributed to synchronization for the first one and to the low resolution of the wiggle trough for the second one. The root-mean square error however reveals to be quite low, with around 10 % error for both which is accpetable, considering it corresponds to a 0.33 mm error which is low and down to the primary objective of this design which was a resolution lower than 1 mm. Finally, and that might be the most important feature of these results due to its high impact on the interpretation of the future results, the main wave height measurement error showed only 2.8 % error or 0.15 mm which is really low. Note also that the sensor is capable of measuring quick changes in the water level since the main wave height increase happens in around 0.5 s and many points describe this quick change. We can conclude that the sensor design is validated and that it is suitable for the measurements of undular bores of small size.

Time interval [s]	Error type	[%]	[mm]
$2 \leq t \leq 4.4$	Mean error	12.9	0.27
$2 \leq t \leq 4.4$	Maximum error	99.7	0.8
$2 \leq t \leq 4.4$	Root-mean-square error	10.9	0.33
$2.4 \leq t \leq 4$	Mean error	8.5	0.27
$2.4 \leq t \leq 4$	Maximum error	26.7	0.8
$2.4 \leq t \leq 4$	Root-mean-square error	9.6	0.33
$2.4 \leq t \leq 4$	Main wave error	2.8	0.15

Table 4.5: Summary of the errors measured to in the test case E2 comparing the wave height measured with the capacitive wave gauge and the image post-processing technique.

4.2.4. Conclusion

The wave gauge design is simple and can be implemented in any laboratory. It is composed of standard, cheap and widely available parts. One of its great advantage is stability over time, even if the probe head construction requires precaution. The sensor is validated against experimental data measured with another method and showed a low mean-root-square error (for this test case) of 0.33 mm, or other said a third of millimeter. Finally, the capacitive sensor is suitable for the measurement of undular bore.

The electronic circuit, designed from a charge amplifier and capacitance bridge basis, allows to accurately measure any kind of capacitance and increase the sensitivity of the procedure by getting rid of stray capacitances. The input frequency excitation shall be

between 6 and 20 kHz (with nominal design frequency of 10 kHz) while the input peak-to-peak amplitude depends on the sensitivity of the circuit (notably the feedback capacitor of the charge amplifier and bridge capacitor). It is however advised to work at higher peak-to-peak tension. The dynamics of the circuit respond well at relatively high frequencies, the limitation source being the last low-pass filter, which can however be tuned. The ripple error, due to the precision rectifier circuit, is low, and applies equally to all amplitude, thus it is important to work at higher amplitude to be able to neglect it.

The design of the wave probe is critical, as it can be source of many errors. The first error can come from the non-uniformity of the coating. We will however trust the manufacturer capabilities to deliver a quite uniform coating. The second source of error is the flowback of water when the wave is receding. There are various ways of diminishing this phenomena, from increasing overall water resistance or increasing the excitation frequency. In our case, the small cross-section of the wire allows us to neglect the effect of flowback on the measurement. It has also for consequences to increase the spacial resolution measurement capabilities of the probe. Finally, the main source of error is the wetting effect of water on the probe, which conducts to a slow drift of the capacitance as the coating dries out or gets wet. This was observed for the enamel coated wire. This effect however can be minimized by letting the probe fully immersed when not in use, or by using a different coating material such as PTFE or polythene (but generally at the cost of having to use larger cross-section wire). This last solution is chosen in order to minimize the effect of drift. Another important trouble we bumped into was the way the sensor wire was tensed. This aspect should be improved in order to obtained both a constant high tension during time (to avoid motion due to the wave interaction), and avoid any decrease in the wire diameter due too much tension.

If the sensor has shown positive results, it would be interesting to test its limits, specifically by measuring its frequency response. A validation could also be carried out with commercially available sensors.

4.3. Particle Image Velocimetry (PIV)

In this PhD work, an essential tool is PIV (Particle Image Velocimetry), whose post-processing tool was not available at the lab while all experimental elements (laser, seeds and camera) were accessible. An approach for a PIV tool had been developed in 2013 for steady flows (Hernández et al., 2015). This approach however was based on fixed interrogation windows and no sub-pixel detection nor outlier detection were available. It is of real interest to determine flow fields in the canal and PIV is a relatively cheap (numerical post-processing and experimental setting) way to achieve it. PIV is an optical technique, thus non-intrusive, which allows both qualitative and quantitative measurements of a 2D velocity field. First

developed by means of complex opto-mechanical set-up, it has been made easier with the appearance of computer science and digital cross-correlation techniques. The first insight for digital PIV was given by Adrian (1991) and numerous works have been developed since then.

4.3.1. General overview

Working Principle

A typical set-up for PIV measurements involves a laser sheet, a flow seeded with reflecting particles and a camera as showed in figure 4.20. The particles, illuminated by a laser sheet, are recorded by a camera a two different times: t_0 and $t_0 + \Delta t$. Determining the displacement of the particles leads to the velocity field (two components) of the image. For some applications, the laser pulses and recording have to be synchronized in order to achieve small time steps and displacement between the images. Then, pre-processing and post-processing of the images are carried through a computer program. The pre-processing step consists of transforming the image with different filters (histogram equalization, high-pass, intensity capping...) in order to enhance post-processing. The post-processing is done according to the following steps: both images are cut into interrogation windows, then the cross-correlation of each interrogation window of image A and its corresponding in B is done. The maximum of the cross-correlation map gives the mean displacement of the particle in the window (Raffel et al., 2018). PIV technique is very interesting because it is not intrusive compared to other techniques using probes (pressure tubes, hot wires) (Raffel et al., 2018) and it is a whole field technique: a large portion of the flow field can be recorded at once. New techniques now allow for 3D PIV: the stereoscopic PIV, which uses two cameras. This last one is not part of this work scope.

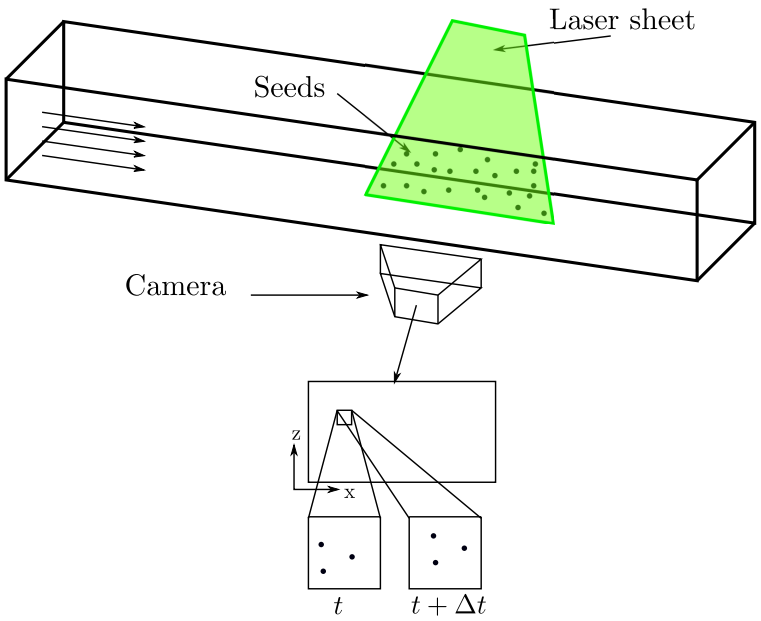

Figure 4.20: Experimental overview of PIV and general working principle.

Experimental set-up

Lasers are a good way of illuminating the domain of interest (Adrian, 1991), because of their ability to generate monochromatic light with high density energy (Raffel et al., 2018). It is quite easy to transform the light beam into a light sheet with the use of a cylinder. According to Raffel et al. (2018), the duration of the illumination light pulse must be short in order to "freeze the motion of the particles". Large pulse could lead to the blurring of the images. The quality of the cross-correlation peak and the loss of correlation can be directly linked to the laser sheet light profile (Raffel et al., 2018). In this work we illuminate the particles with a 58GCS Melles Griot Nd:YAG (doubled) laser (High Performance Diode Pumped Solid State Laser) whose wavelength is 532 nm. It can be operated in pulsed mode or in constant wave mode. This last one leads to an easier experimental set up (with no need of synchronization between the laser and the camera) but can also generate blurring. C. Willert (1996) found that spatial resolution can be increased if the experimental set-up contains various illumination pulses.

As we add particles to the fluid, it is important to be sure that these will accurately follow the flow. Indeed, with PIV, we are not measuring the fluid velocity but the particle velocity. In a continuously accelerating fluid, Stokes drag law (Raffel et al., 2018) allows to estimate the lag between flow velocity and the particle velocity:

$$\mathbf{U_s} = \mathbf{U_p} - \mathbf{U} = d_p^2 \left(\frac{\rho_p - \rho}{18\mu} \mathbf{a} \right) \tag{4.1}$$

with $\mathbf{U_s}$ the velocity lag, $\mathbf{U_p}$ the particle velocity, $\mathbf{U}$ the fluid velocity, d_p the particle diameter, ρ_p the particle density, ρ the fluid density, μ the dynamic viscosity of the fluid and $\mathbf{a}$ the acceleration. According to equation 4.1, small particles will more likely follow the flow as well as particles which have the same density than the flow. In liquid flow, larger particle can be accepted (Raffel et al., 2018). The step response leads of $\mathbf{U_p}$ follows an exponential law:

$$\mathbf{U_p} = \mathbf{U}\left[1 - \exp\left(-\frac{t}{\tau_s}\right)\right] \tag{4.2}$$

with

$$\tau_s = d_p^2\left(\frac{\rho_p - \rho}{18\mu}\right) \tag{4.3}$$

τ_s represent the necessary time for the particles to reach the velocity of the fluid. In this work, the fluid is seeded with glass micro-balls *Spherical®110P8* whose density is 1100 ± 50 kg/m^3 and the mean size is $9 - 13$ µm. This leads to:

$$\tau_s = 6.9 \cdot 10^{-7}\text{s} \tag{4.4}$$

In this case, τ_s is way smaller than the time between frames of the camera (until 60 frames/s or 0.0167 s between frames), which means that any variation of the velocity field will be well represented by the particle velocity.

The characteristic sedimentation time t can also be computed from the Stokes formula according to

$$t = \frac{h}{v_s} \tag{4.5}$$

where h is the water height and v_s the sedimentation velocity which is computed according to

$$v_s = \frac{2}{9}\left(\frac{\rho_p - \rho}{\mu}\right) g \left(\frac{d_p}{2}\right)^2 \tag{4.6}$$

It leads to a value of $t_s \approx 7600$ s so that we can assure that no particle settling is observed during frame recording. We observed however that some particles tended to cluster and create bigger particles which decreases this sedimentation times at various minutes, so that it was not an issue for the experiment operation.

A homogeneous distribution of the particle is desired in order to get the maximum precision during post-processing. The particle density is associated with different techniques as shown in figure 4.21 and according to Raffel et al. (2018). Particle Tracking Velocimetry (PTV) is used for low density, where all particles can be detected, Particle Image Velocimetry (PIV) where all particles still can be distinguished but can't be identified between the image pairs. Medium density is required to assure the statistical treatment of the PIV technique. The last case, with high particle density does not allow to determine individual images of the

particles, as they overlap. This technique is called Laser Speckle Velocimetry (for more information, especially about the speckle limit in terms of dimensionless source density definition, the reader can refer to Adrian (1984)).

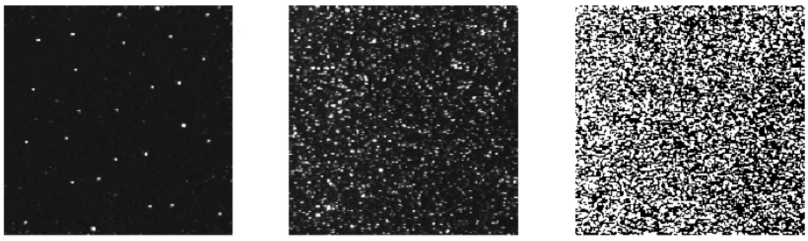

Figure 4.21: Three particles densities lead to different techniques: (a) low (PTV), (b) medium (PIV) and (c) high (LSV) (source: Raffel et al. (2018))

The time delay between the frame recording must be long enough to able to determine the displacement of the particles and short enough so that the particle won't leave the laser plane sheet due to motion in the third direction (Raffel et al., 2018). For relatively slow motions, a standard 25 Hz camera can resolve the flow (Raffel et al., 2018). Resolution is an important feature since it allows to obtain more or less vectors: for a 1024×1280 pixels image, considering interrogation windows of 32×32 leads to 32×40 vectors, while using a camera with more resolution can increase the number of vectors. C. Willert (1996) found, via Monte-Carlo statistical process, that the number of gray levels in the image only plays a minor role in the final measurement uncertainty. For this work, we use a camera COHU progressive scan 6600 Model 3000 and a NIKON AF micro nikkor 60 mm 1:2.8 D lens.

Algorithm overview

The algorithm, implemented in a *matlab*[7] script, is briefly presented in this section, and a complete review can be found in appendix D.4. The first step, before applying the cross-correlation subroutine, is an image enhancement step which can be judicious to allow better detection of the particles. During the development of PIV, many image preprocessing techniques were proposed, in particular, histogram equalization, Contrast Limited Adaptive Histogram Equalization (CLAHE) (Pizer et al., 1987), intensity capping (Shavit et al., 2007) and high-pass (Sciacchitano & Scarano, 2014) preprocessing techniques were implemented, and are further tested in section 4.3.2.3.

For the calculation of the mean particle displacement, two algorithms were implemented, the Integer Window Shifting (IWS) algorithm (Adrian, 1991) and the Window Deformation

[7] https://www.mathworks.com/products/matlab.html

(WD) one based on the work of H. T. Huang et al. (1993). The first one is less costly while the second one shows more accuracy and less outliers. For both algorithm, the cross-correlation can either be directly computed or using the Fourier transform based cross-correlation which is numerically more efficient. Both of them are then normalized (Gonzalez, 1987).

The IWS algorithm is a process where the images are sliced into interrogation windows and cross-correlation is applied on each of them and between the consecutive snapshots. In the next stage, windows are refined (their size is decreased to gain resolution) and they are shifted according to the first estimation of the particle displacement. Cross-correlation is newly applied. The process is repeated until reaching the minimum size that the user has defined. In between every cross-correlation, sub-pixel detection (Nobach & Honkanen, 2005), outlier filtering (Westerweel & Scarano, 2005), interpolation to replace the missing vectors and smoothing (B. J. Kim & Sung, 2006) are carried out in order to improve the displacement calculation.

The WD algorithm is an iterative process which implies the computation of predictor and corrector displacement fields. It starts with a first pass using the IWS algorithm. From the resulting displacement field, a predictor is built for every pixel by interpolation and the image couple are deformed according to this predictor. A cross-correlation is newly applied on the interrogation windows and sub-pixel detection is carried out. The predictor is updated from the computed displacement field which is called the corrector. Outlier vectors are detected, interpolation is done to replace missing vectors and the displacement field is smoothed. A new iteration is started to compute a new corrector and so on. The process stops when convergence is achieved (residuals in both x and y directions are relatively constant) or the maximum iteration defined by the user is reached.

4.3.2. Test cases and validation

Our tool needs to be tested and validated in order to know the uncertainty of the measurements. Uncertainties are affected by a bunch of parameters such as particle image size, intensity and density, turbulent fluctuations, velocity gradients, noise level and interrogation window size (Raffel et al., 2018). To evaluate their impacts, one can focus its effort on looking only at the correlation signal which is a concentrate of all these parameters or one can study the impact of every single one of these parameters (supposedly known) (Raffel et al., 2018).

We propose to follow the process described in (Raffel et al., 2018) to evaluate the measurement uncertainty of PIV, based on Monte Carlo simulation. First, realistic PIV images have to be generated. Then, statistical studies will allow us to measure the sensitivity of our tool to the parameters described before.

4.3.2.1. Synthetic particle generation

The generation of the synthetic images is done following instructions of Raffel et al. (2018) and Lecordier & Westerweel (2004). The particle images are generated from known characteristics: diameter, shape, spatial density, image depth... The particle images are described by a Gaussian intensity profile as long as the particles are in focus according to Raffel et al. (2018) :

$$I(x,y) = I_0 \exp\left[-\frac{(x-x_0)^2 + (y-y_0)^2}{(1/8)d_\tau^2}\right] \tag{4.7}$$

where the center of the particle is described by its coordinates (x_0, y_0), the particle diameter is d_τ and the peak intensity I_0 is defined as:

$$I_0(z) = q \exp\left[-\frac{1}{\sqrt{2\pi}}\left|\frac{2z^2}{\Delta z_0^2}\right|^s\right] \tag{4.8}$$

z is the coordinate in the direction perpendicular to the laser plane, q is the efficiency with which the particles reflect the incident light, Δz_0 is the thickness of the light sheet at which the intensity drops to 0.67 of the maximum intensity and s is the shape factor ($s = 2$: Gaussian, $s = 10^4$: top-hat). Then we proceed according to the following steps:

1. A random generator specifies the positions (x_1, y_1, and z_1 coordinates) of the number of particles N. This last one determines the concentration of seeds in the fluid.

2. The peak intensity $I_0(z_1)$ is calculated for every particles according to equation 4.8 and replaced in equation 4.7.

3. The particle image is calculated for every pixels integrating equation 4.7:

$$I(i,j) = I_0(z_1) \int_{i-0.5}^{i+0.5} \exp\left[-\left(\frac{x-x_1}{\frac{d_\tau}{2\sqrt{2}}}\right)^2\right] dx \times \int_{j-0.5}^{j+0.5} \exp\left[-\left(\frac{y-y_1}{\frac{d_\tau}{2\sqrt{2}}}\right)^2\right] dy \tag{4.9}$$

   which can also be easily written with the help of the error function:

$$I(i,j) = I_0(z_1)\frac{\pi}{32}d_\tau^2 \left[erf\left(\frac{i+0.5-x_1}{\frac{d_\tau}{2\sqrt{2}}}\right) - erf\left(\frac{i-0.5-x_1}{\frac{d_\tau}{2\sqrt{2}}}\right)\right] \times \left[erf\left(\frac{j+0.5-y_1}{\frac{d_\tau}{2\sqrt{2}}}\right) - erf\left(\frac{j-0.5-y_1}{\frac{d_\tau}{2\sqrt{2}}}\right)\right] \tag{4.10}$$

4. All the particles images are summed up to construct the image. Note that if two

particle images superimpose, their intensities are summed. This is true only if the scattered light is incoherent but most pulsed laser light is coherent. It is important then to respect the speckle limit (i.e. source density below 30%) to avoid interference effects (Lecordier & Westerweel, 2004). If the sum of the intensities reach the value of a particle image centered at a full pixel, all values are cropped to this limit.

5. New coordinates x_2, y_2 and z_2 for particle image centers of image 2 are calculated from a given displacement field. Particle images are generated according to the previous point and image 2 is created.

6. Background noise may eventually be added to both images.

7. Both images are quantized to the desired image depth (bits per pixels, generally 8 bits, from 0 to 255). The maximum value (255 for a 8 bits image) is chosen for a particle image centered at a full pixel location.

To test our PIV program, we generate for each case 512 x 512 pixels image pairs with an aleatory displacement between 0 and 1 pixel. We take the perfect case where particle reflect all light ($q = 100\%$), the thickness at which the light sheet intensity drops to 67% equals the sheet thickness ($\Delta z_0 = \Delta_z$) and a top hat profile ($s = 10^4$). If not specified otherwise, no noise is added. Statistics will be based on 100 pairs in order to have significant results.

4.3.2.2. Error sources and quantification

According to H. Huang et al. (1997), there are three sources of errors: the outliers, the mean-bias errors and the the root-mean-square (RMS) errors. The outliers are easily detected as they correspond to vectors which are very different from their neighbors. By nature they randomly appear both in direction and amplitude (H. Huang et al., 1997). They correspond to low correlation peaks (meaning correlation cannot be trusted). Outlier errors are large (> 1 pixel) and the main causes to outliers generation are low density of particle, strong gradient or three dimensional flows (H. Huang et al., 1997). In this work, outlier error reduction is performed by the multiplication of neighbor cross-correlation tables (see figure D.17) and outlier removal by the detection described in section D.4.6. The mean-bias errors is defined considering a uniform displacement d applied to all particles and N displacement d_i for $i = 1, 2, ...N$ have been calculated from the PIV algorithm, if

$$\bar{d} = \frac{1}{N} \sum_{i=1}^{N} d_i \tag{4.11}$$

is the mean displacement, then the mean-bias error is defined as:

$$\epsilon_{bias} = \bar{d} - d \tag{4.12}$$

and the RMS error is defined as:

$$\epsilon_{RMS} = \sqrt{\frac{1}{N}\sum_{i=1}^{N}\left(d_i - \bar{d}\right)^2} \tag{4.13}$$

The mean-bias error ϵ_{bias} appears because of peak-locking (J. Chen & Katz, 2005; H. Huang et al., 1997) due to the mismatch between the smooth fitted curve and the discrete cross-correlation value table. The RMS error ϵ_{RMS} is due to a large number of phenomena: particle density, strong velocity gradients, three-dimensional motion, camera's noise, non-linear and non-uniform response of the camera, bad illumination (non-uniformity, non-uniform reflection of the particles), cable noise and digitization (H. Huang et al., 1997). As illustrated in figure 4.22 from Raffel et al. (2018), a measurement can be precise (low random error) and inaccurate (large bias error) at the same time.

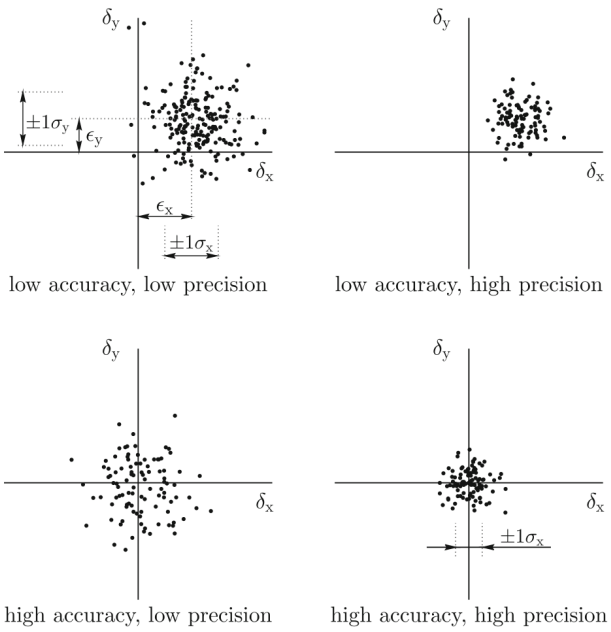

Figure 4.22: Illustration of the notions of accuracy and precision, from Raffel et al. (2018). δ_x and δ_y are the measurement error respectively in the x and y directions. The scatter of the measurement points is due to random errors while the bias error is responsible for the mean offset to the true value.

4.3.2.3. Test cases

In order to qualify and validate our PIV tool, it is important to test it against different conditions as homogeneous displacement, sheared flows, vertices and determine the influence of important parameters such as the particle image size, particle density or noise. From the following studies, we are able to determine the perfect image profile in order to obtain the best behaviour of our PIV tool.

Particle image size In this section, the influence of the particle image size is studied. A density of 1/64 (=0.0156) particle per pixel per pixel is taken to generate the synthetic images. Image examples can be found in figure 4.23. Results are shown in figure 4.24. The bias error is displayed in figure 4.24a. For the integer window shift technique, the bigger is the window the lower is the bias error. This is not the case for the window deformation technique where the bias error is of the same magnitude for the three studied window sizes for particle image diameters superior to 2 px. The window deformation bias error is at least 10 times smaller than for the integer window shifting one. For both techniques the error drastically increases for small particle image diameters except for the 64^2 wide window. This can be explained by the "peak locking" phenomena as explained in Raffel et al. (2018). In the case of the random error or RMS error, displayed in figure 4.24b, for both techniques the smaller is the interrogation window the more important is the error. It can be explained by the lower number of particles in the windows on which the statistics are based. The error also drastically increases for small particle images (below 3 pixels) and for all interrogation window sizes. The window deformation techniques allows to decrease the random error from one order of magnitude for the smallest window size and less for the other window sizes. The consequences of this study for the experimental case are as follows: the importance of the particle image when recording the images is relative for the window deformation technique if the particle image diameter is at least 3 pixels. In the case of the simpler integer window shifting technique a minimum error can be achieved when the particle image is 3 pixels wide. A compromise might be found between the bias and the random errors. These conclusions give a real advantage to the window deformation although it is computationally more costly. As stated in Raffel et al. (2018), it is important to be aware that the low uncertainty achieved with the synthetic images can never be reached in the real experiment.

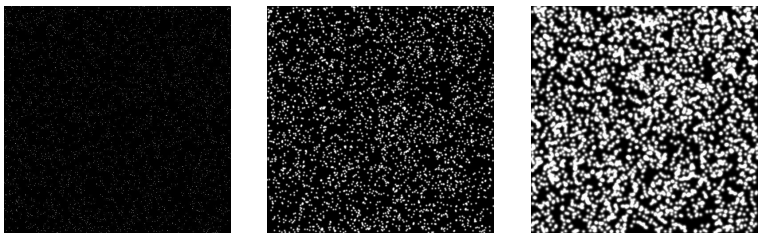

(a) (b) (c)

Figure 4.23: Synthetic images generated for a density of 1/64 ppp and different particle diameters: (a) 0.5 px. (b) 5 px. (c) 10 px.

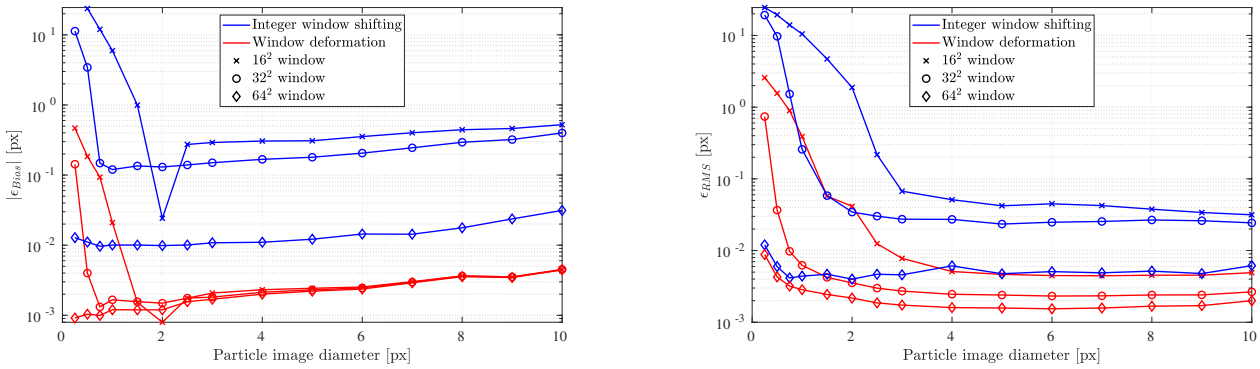

(a) (b)

Figure 4.24: Errors in function of the particle image diameter for the integer window shift and window deformation techniques. Three window sizes are studied (16^2, 32^2 and 64^2 px^2). (a) Bias error. (b) RMS error.

Particle density T study the particle density, the particle image diameter is set to 5 px in the synthetic images, which corresponds to a case where the particle image diameter uncertainty is low (see section 4.3.2.3). Examples of synthetic images for three different densities are displayed in figure 4.25. Results are shown in figure 4.26. This study does not take into account the in-plane loss of image pairs which strongly contributes to an increase of the uncertainty. It is for example the case for 3D flows or extremely turbulent flows. The bias error is displayed in figure 4.26a. In the case of the integer window shifting technique the error drops with the increase of the interrogation window size while the error is quite the same for the window deformation algorithm even if the bias error rapidly increases for low densities (for the 16^2 interrogation windows, the minimum is found for 0.01 particle per pixel per pixel while this minimum is lower for 32^2 around 0.004 particle per pixel per pixel). In the case of the RMS error, a minimum exists for the window deformation algorithm around 0.03 particles per pixel per pixel and this for the three window sizes. For both errors the window deformation technique gives better results than the integer window shifting one. For both techniques minimum bias and random errors exist which shows the importance of

reproducing images with an adequate particle density. A compromise should be taken, a good value being a density between 0.03 and 0.1 particle per pixel per pixel.

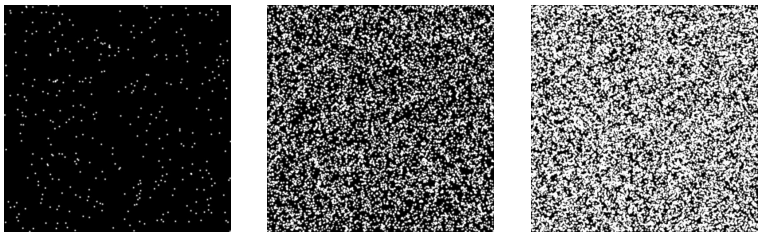

(a) (b) (c)

Figure 4.25: Synthetic images generated for a particle image diameter of 5 px and different particle densities (unit: particles per pixel per pixel or ppp). (a) 0.002 ppp. (b) 0.05 ppp. (c) 0.1 ppp.

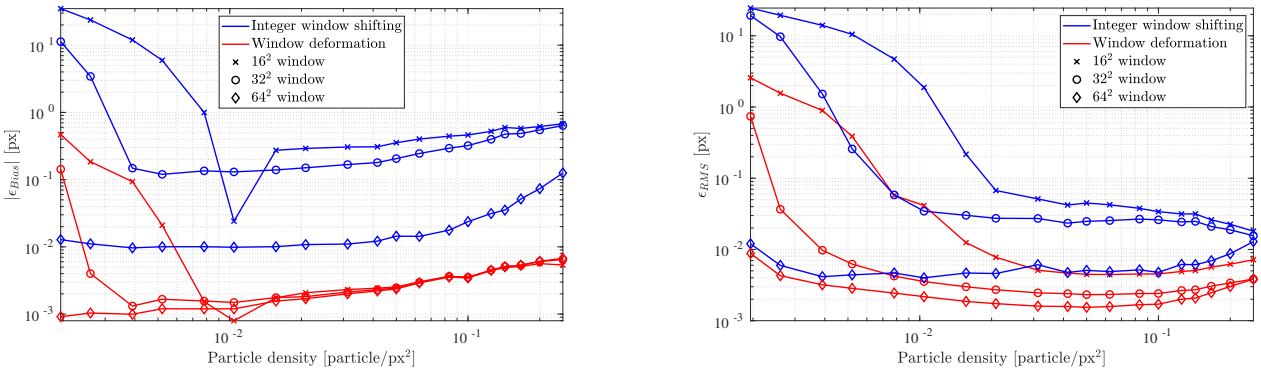

(a) (b)

Figure 4.26: Errors in function of the particle density for the interger window shift and window deformation techniques. Three window sizes are studied (16^2, 32^2 and 64^2 px^2). (a) Absolute value of the bias error. (b) RMS error.

Particle Displacement The influence of the particle displacement is studied here. Homogeneous displacement is applied to particle images in the range from 1 to 20 px. Synthetic images are generated with a particle density of 0.05 ppp and a particle diameter of 5 px which corresponds to ideal density and particle diameter to minimize uncertainties for the window deformation technique (see sections 4.3.2.3 and 4.3.2.3). Results are shown in figure 4.27. Huge differences appears between the two algorithms still giving a real advantage to the window deformation technique which always keeps the uncertainties below the one from the integer window shifting. For the bias error (see figure 4.27a) and for displacement lower than 10 pixels, the interrogation window size does not influence the order of magnitude of the bias error. For displacement larger than 10 pixels, the smallest interrogation window bias error increases to an order of magnitude higher than for the two others sizes. Local variations

can be explained by peak locking as explained further on. The random error (figure 4.27b) is kept relatively constant for the window deformation technique except for displacement higher than 10 pixels and the 16^2 px^2 interrogation window. If this last window size is used we should take care that the maximum displacement will not exceed 10 pixels as this implies a significant increase of the uncertainties. A zoom over displacements between 0 and 2 px can be found in figure 4.28. Some periodic patterns appear in the errors with minimums at round displacement. It is most probably due to the peak locking phenomena . A 100 factor however appears between the integer window shifting and the window deformation errors showing how much improvement there is with the window deformation technique. Moreover, for displacements between 0 and 1 px there is no difference between the interrogation window sizes for the window deformation algorithm. To the contrary the integer window shifting algorithm is very sensitive to the window sizes. The case of the RMS error, relatively small for the window deformation (inferior to $5 \cdot 10^{-3}$ px), shows unacceptable levels for the integer window shifting technique especially for displacements higher than 1 px. In deed, the RMS error jumps to an order of magnitude higher for the biggest interrogation window size.

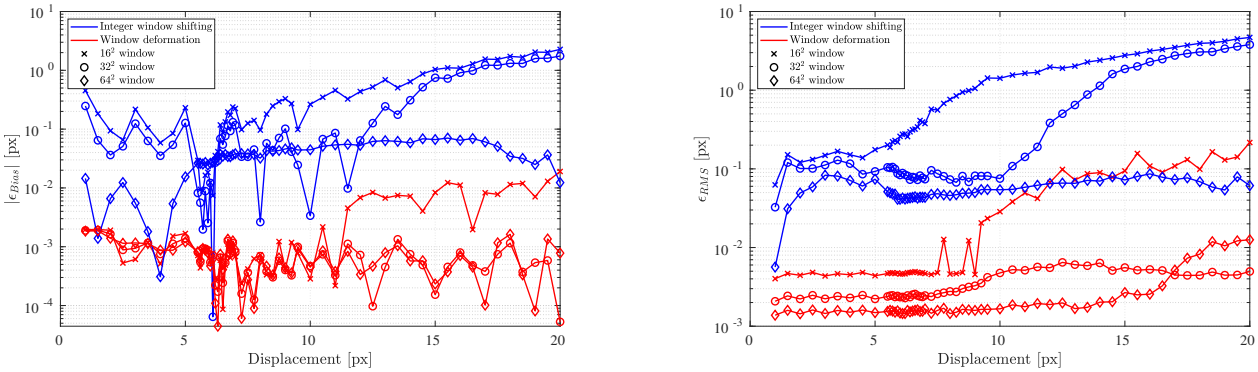

(a) (b)

Figure 4.27: Errors in function of the particle displacement (from 0 to 20 px) for the integer window shift and window deformation techniques. Three window sizes are studied (16^2, 32^2 and 64^2 px^2). (a) Bias error. (b) RMS error.

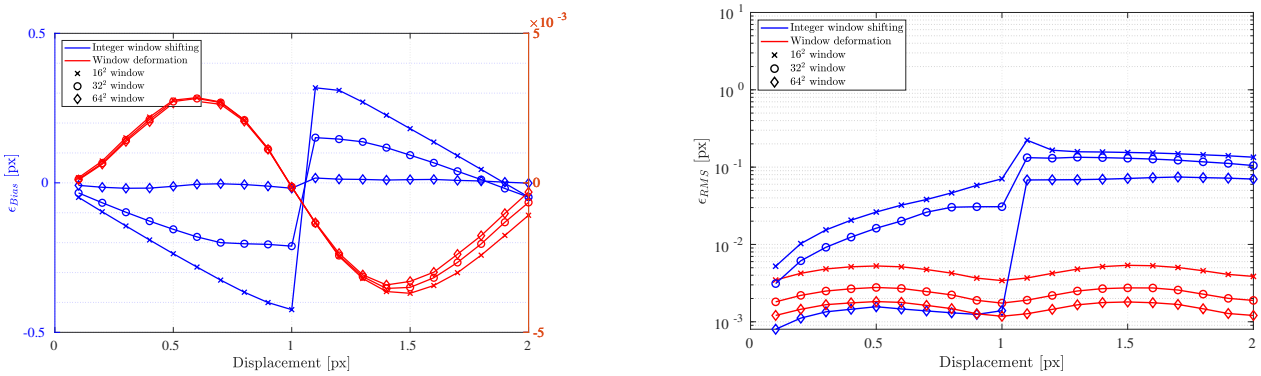

(a) (b)

Figure 4.28: Errors in function of the particle displacement (from 0 to 2 px) for the integer window shift and window deformation techniques. Density is 0.05 ppp and particle diameter is set to 5 px. Three window sizes are studied (16^2, 32^2 and 64^2 px^2). (a) Bias error. Note the difference of scale between the left and the right y axes. (b) RMS error.

Noise level We propose to study in this section the influence of the addition of white Gaussian noise to the synthetic images. The synthetic image generation process is described in Scharnowski & Kähler (2016a). The errors are plotted in function of the Signal-To-Noise Ratio (SNR) which is defined as follows:

$$SNR = \frac{I_0}{\sigma_n} \tag{4.14}$$

where I_0 is the maximum intensity of the image and σ_n is the standard deviation of the Gaussian white noise which is added to the image after adding all particle images. A mean value or background intensity of $5\sigma_n$ is used in the generation of the images as referenced in Scharnowski & Kähler (2016b). The study has only been conducted for the window deformation algorithm since we will use this one to carry out the PIV post-processing from now on, as it reveals to be much more accurate than the integer window shifting algorithm. Figure 4.30 shows the influence of noise in the PIV post-processing. We can observe that SNR levels as low as 30 already has an influence on the random error. For example, a SNR of 10 implies a RMS error ten times higher. This is not true for the bias error which is less sensitive to noise, except for really low SNR values below 10. Special care should be taken when designing the experiment and during the data acquisition to avoid such levels of noise.

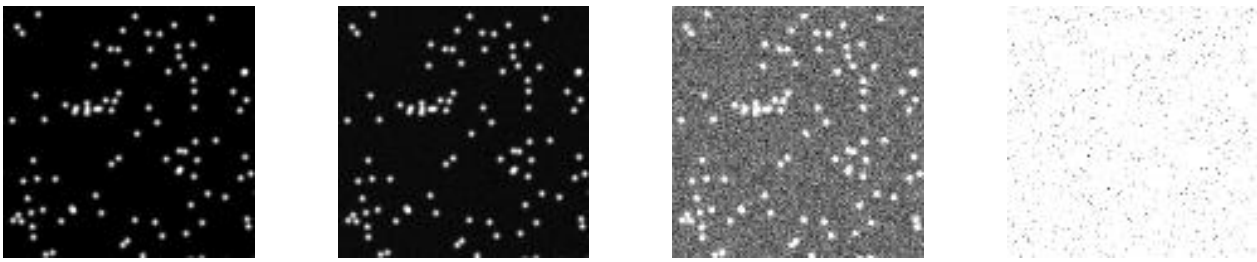

(a) (b) (c) (d)

Figure 4.29: Synthetic image parts (100 px × 100 px) generated for a particle image diameter of 5 px and a particle density of 0.05 ppp. (a) No added noise. (b) SNR = 100. (c) SNR = 10. (d) SNR = 3.3.

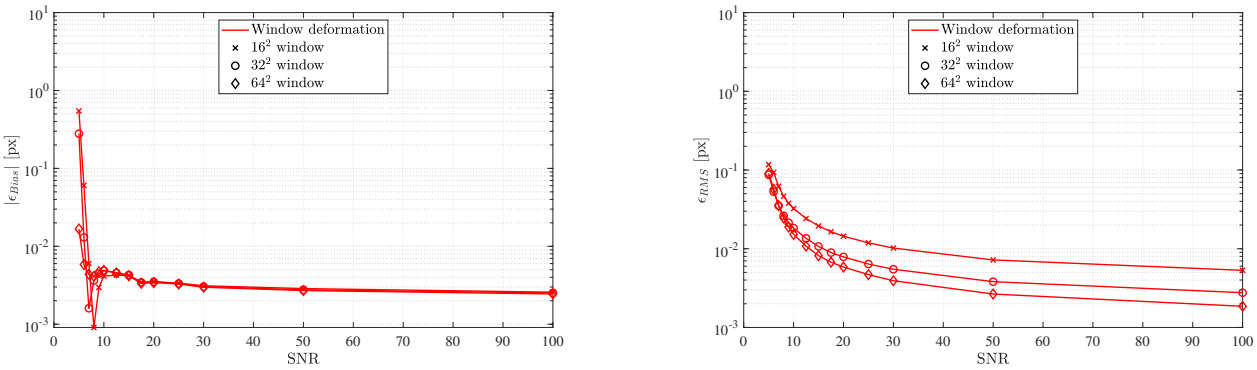

(a) (b)

Figure 4.30: Errors in function of the Signal to Noise Ratio (SNR) for the window deformation technique. Three window sizes are studied (16^2, 32^2 and 64^2 px^2). (a) Bias error. (b) RMS error.

Effect of 3D motions (out of plane motion) The effect of 3D motions can be studied by varying the particle pair losses. An example of 50% particle pair loss is shown in figure 4.31. In this case, half of the particles from an image to another disapear because they leave the laser plane. We consider that no particle enter the plane (which is unreallistic) but alows to study the particle loss phenomena importance in PIV measurements. Uncertainties related to the particle pair loss are displayed in figure 4.32. The bias error (figure 4.32a) is kept quite low for 64^2 and 32^2 px^2 interrogation windows increasing hugely for high pair loss ratio while for the 16^2 px^2 windows the increase starts at particle loss pair ratio as low as 10%. For the random error case (figure 4.32b), the increase is felt for any particle loss ratio, even if this increase is less important for value between 5% and 90% for 64^2 and 32^2 px^2 interrogation windows and 5% and 65% for the smallest window size.

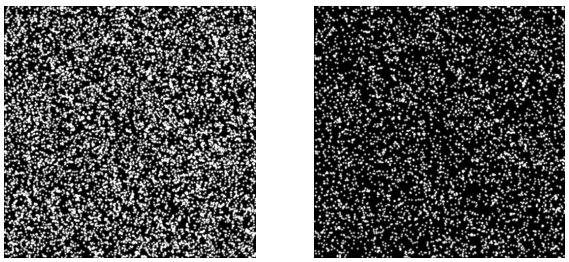

(a) (b)

Figure 4.31: Synthetic images with and without pair loss. (a) Original image. (b) 50% pair loss.

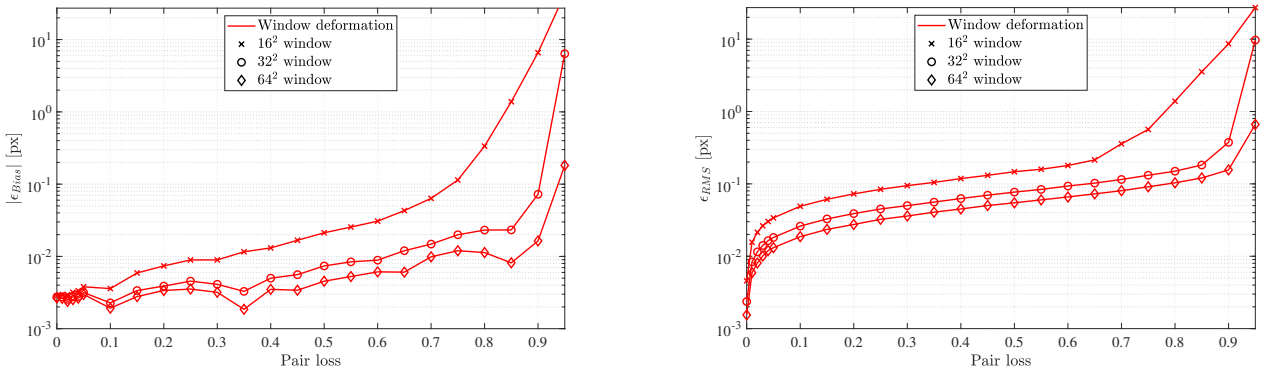

(a) (b)

Figure 4.32: Errors in function of the particle pair loss ratio for the window deformation technique. Three window sizes are studied (16^2, 32^2 and 64^2 px^2). (a) Bias error. (b) RMS error.

Vortex case Images pair, representing a Lamb-Oseen vortex (Lamb, 1993; Oseen, 1912), are produced according the following equation (Devenport et al., 1996):

$$V_\theta(r) = V_{\theta_{max}} \left(1 + \frac{1}{2\alpha}\right) \frac{r_{max}}{r} \left[1 - \exp\left(-\alpha \frac{r^2}{r_{max}^2}\right)\right] \tag{4.15}$$

where r is the radius, $r_c(t) = \sqrt{4\nu t + r_c(0)^2}$ is the core radius of the vortex, $r_{max} = \sqrt{\alpha} r_c(t)$ is the radius at which velocity reaches its maximum value, and $\alpha = 1.25643$. We set $r_c = 100$ pixels and $V_{\theta_{max}}$ ranges from $\pi/1000$ to $\pi/3$ pixel $\cdot$ rad. No particle motion is set in the z direction. The displacement profile along the line uniting both vortex centers is shown in figure 4.33.

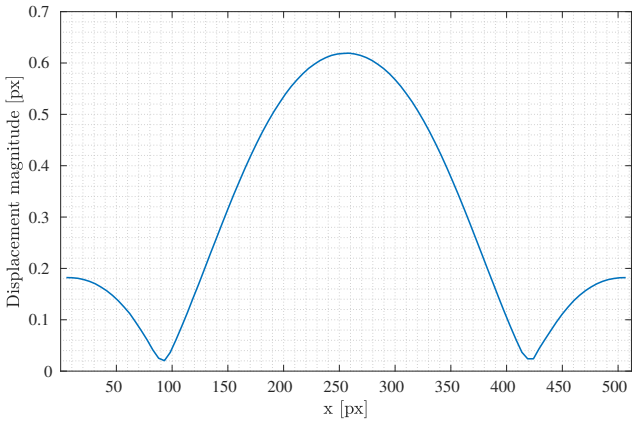

Figure 4.33: Displacement magnitude profile along the line uniting both vortex centers in the case $V_{\theta_{max}} = \pi/10$ px $\cdot$ rad.

The uncertainties are shown in figure 4.34 and an example of the vortex velocity field and its error is shown in figure 4.35. The bias error, shown in figure 4.34a, rapidly increases with the angular displacement and eventually reaches a plateau but at high values (between $6 \cdot 10^{-2}$ and $2 \cdot 10^{-1}$ pixel). It also increases when interrogation windows are smaller. The random error (see figure 4.34b) has a similar behaviour although the increase of uncertainty is higher with bigger interrogation windows. The influence of the window size is underscored in figure 4.35 where the case of $V_{\theta_{max}} = \pi/10$ px $\cdot$ rad is shown. The 64 px^2 interrogation windows PIV velocity field is shown in figure 4.35b and the associated bias error in figure 4.35c. The results are quite similar to the theoretical velocity field, the maximum error locally reaching around 10^{-1} px and corresponds to the maximum displacement magnitude which is underestimated. In the case of 16 px^2 interrogation windows (figures 4.35d and 4.35e) the maximum error reaches $3.5 \cdot 10^{-1}$ px which correspond to around 50% of the maximum displacement magnitude. The choice of the interrogation window size is once more really important in order to minimize the uncertainties. Moreover, to detect the correct velocity field, it is necessary to maintain the maximum displacement small.

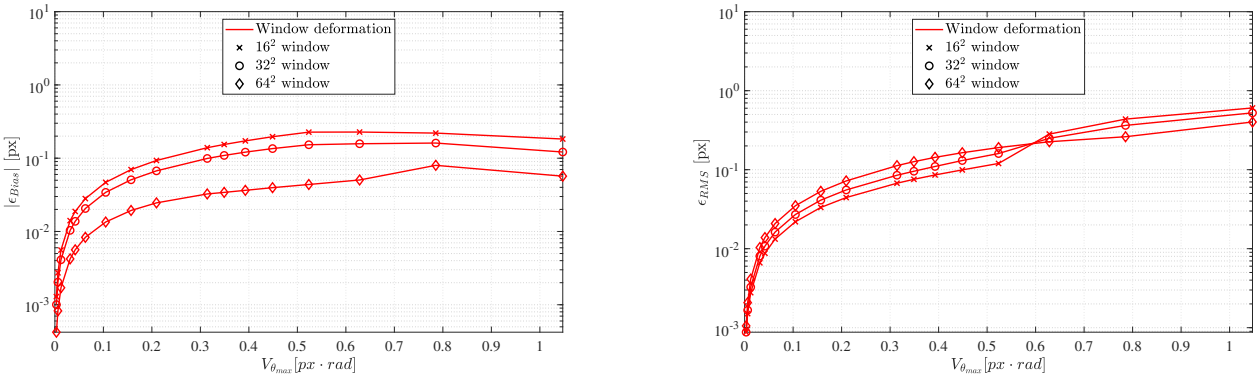

(a) (b)

Figure 4.34: Errors in function of the angular displacement $V_{\theta max}$ for the window deformation technique. Three window sizes are studied (16^2, 32^2 and 64^2 px^2). (a) Bias error. (b) RMS error.

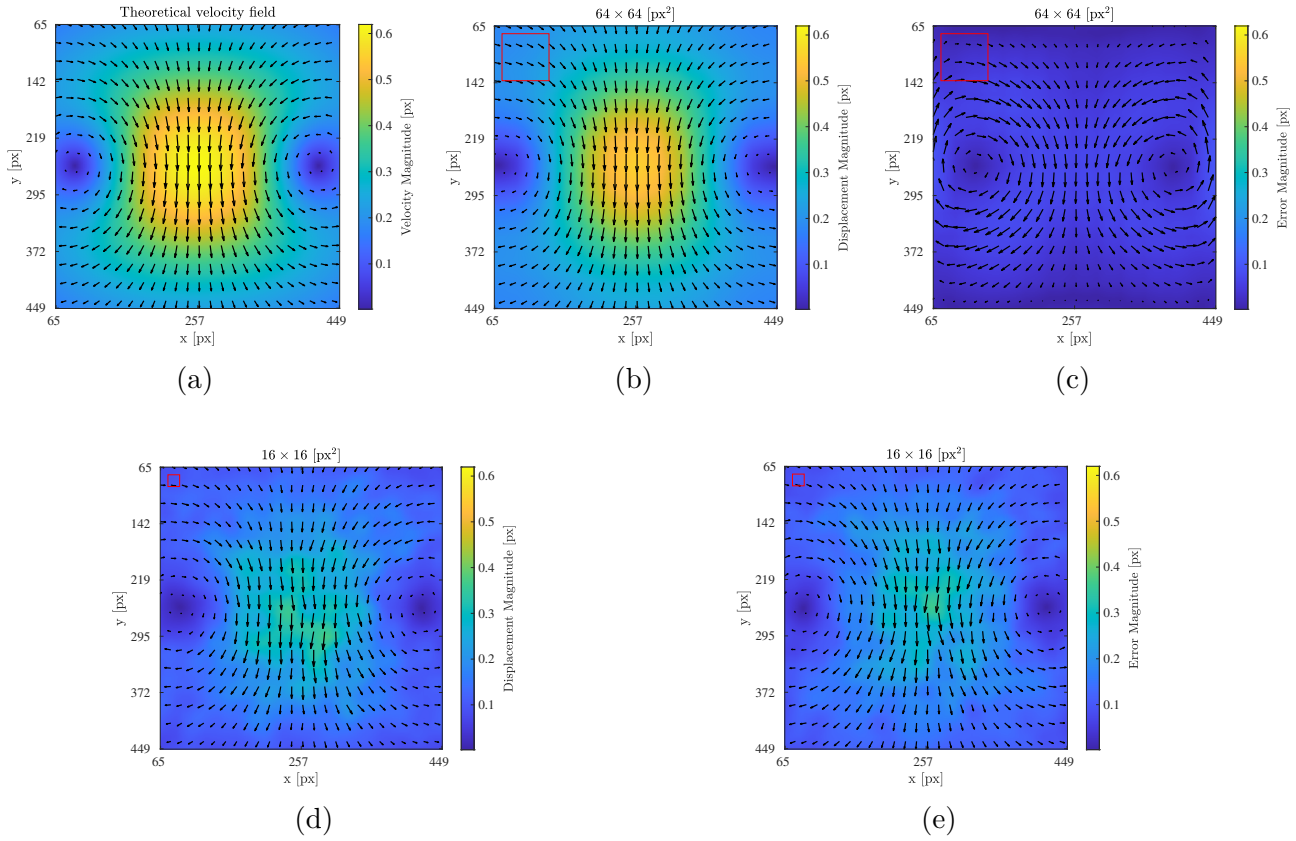

Figure 4.35: Application of the PIV window deformation algorithm over a pair of counter-rotating vortices. Arrows represent the displacement field while background color is the magnitude. The 64^2 px^2 and 16^2 px^2 windows are drawn in red. (a) Theoretical displacement field used to generate the image pair on which the PIV is applied. This case corresponds to $V_{\theta_{max}} = \pi/10$ px $\cdot$ rad. (b) PIV results with 64^2 px^2 interrogation windows. (c) Error with the theoretical data for 64^2 px^2 interrogation windows. (d) PIV results with 16^2 px^2 interrogation windows. (e) Error with the theoretical data for 16^2 px^2 interrogation windows.

Shear case A series of images representing sheared flows are generated. The flows correspond to a triangle function as shown in figure 4.36. Two variables can be changed: the number of shear layers in the vertical direction, ranging from 2 to 20 and the maximum amplitude of the U_x motion ranging from 1 to 10 px. In this example, 2 and 10 layers shear flows are represented for a maximum displacement of 5 px. The results of the application of the window deformation algorithm can be found in figures 4.38 and 4.39. The first one shows the case of the 2 layers field while the second one the 10 layers field. It is important to underline the importance of the interrogation window size: in the first case, small windows (16^2 px^2) leads to an underestimation of the maximum displacement and vector not fully colinear with the x-direction while the 64^2 px^2 windows give a good estimation of the

maximum displacement amplitude and direction. In the contrary, for the case with more layers, the small windows allows to detect such layers even if the maximum amplitude is not well detected while the bigger windows leads to completely incorrect vector field with both direction and amplitude far from the true field: as the flow structure are smaller than the interrogation windows, these last one cannot detect the variation inside. It will be really important to keep the window size smaller than the studied flow in the experiments in order to be able to detect small flow structures. A compromise might be done between increasing the window size which leads to both better amplitude and direction estimates and decreasing it to be able to detect small flow structures. The uncertainties linked to shear rates are shown in figure 4.37 and reflects what we already commented about the importance of the interrogation window size, notably reflected by the bias error inversion of the order of the curves (in the case of 10 layers the smallest error is given by 16^2 px^2 windows while for the 2 layers it is the 64^2 px^2 windows which give the best results).

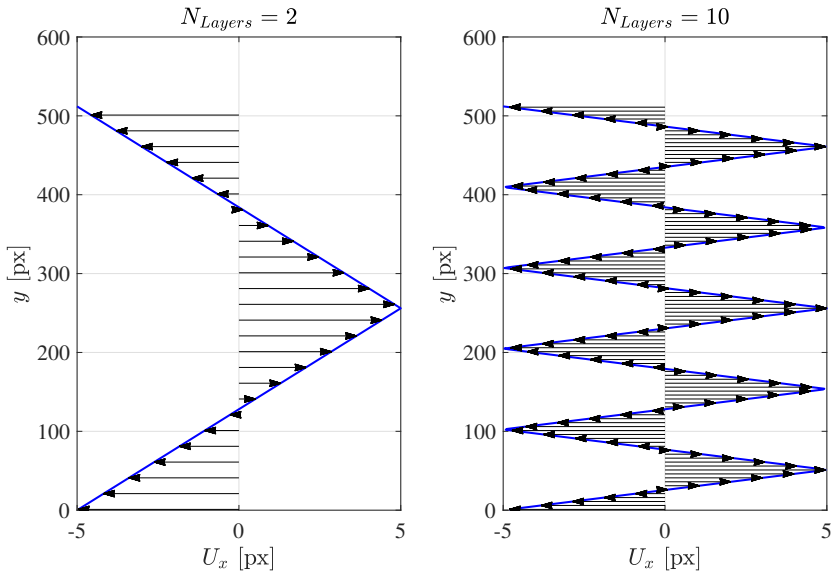

Figure 4.36: Examples of the shear flows: the number of layers is changed while the maximum horizontal displacement is kept constant.

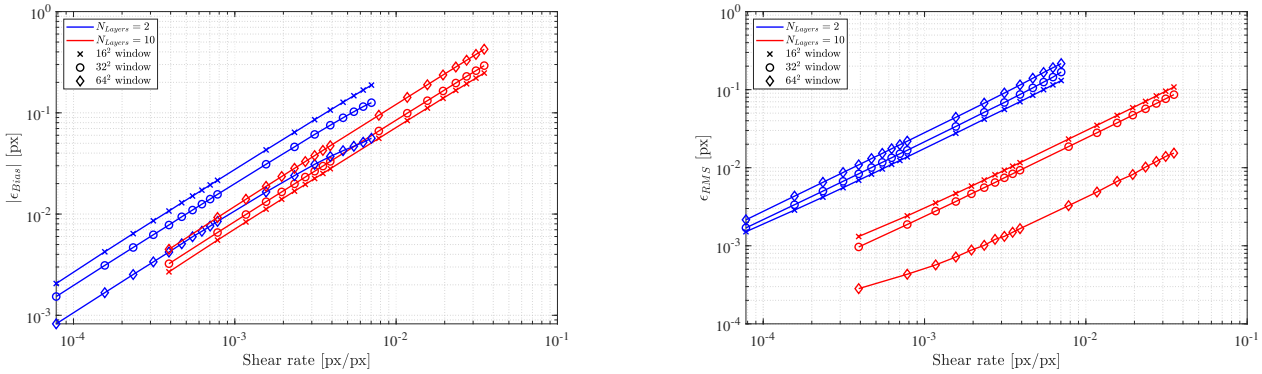

(a) (b)

Figure 4.37: Errors in function of the maximum horizontal velocity for cases with strong shear for the window deformation technique. Three window sizes are studied (16^2, 32^2 and 64^2 px^2). (a) Bias error. (b) RMS error.

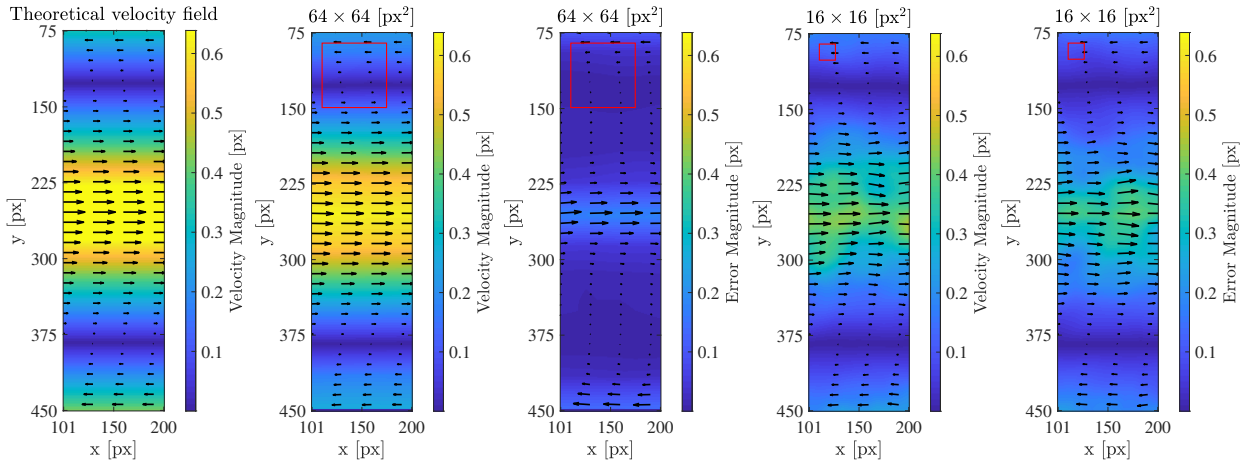

(a) (b) (c) (d) (e)

Figure 4.38: Application of the PIV window deformation algorithm over a sheared flow. The numbered of shear layers is 2 and the maximum horizontal displacement to 0.8 px. Arrows represents the velocity field while background color is the magnitude. The 64^2 px^2 and 16^2 px^2 windows are drawn in red. (a) Theoretical velocity field used to generate the image pair on which the PIV is applied. (b) PIV results with 64^2 px^2 interrogation windows. (c) Error with the theoretical data for 64^2 px^2 interrogation windows. (d) PIV results with 16^2 px^2 interrogation windows. (e) Error with the theoretical data for 16^2 px^2 interrogation windows.

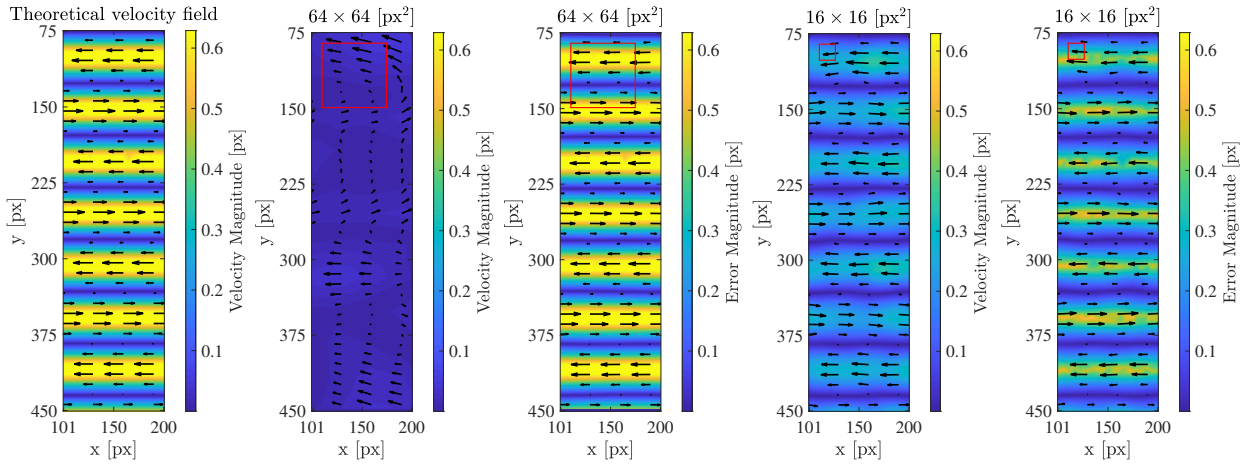

Figure 4.39: Sheared flow analysis. This case corresponds to $N_{Layers} = 10$ and $U_{x_{max}} = 0.8$ px. Arrows represents the velocity field while background color is the magnitude. The 64^2 px^2 and 16^2 px^2 windows are drawn in red. (a) Theoretical velocity field used to generate the image pair on which the PIV is applied. (b) PIV results with 64^2 px^2 interrogation windows. (c) Error with the theoretical data for 64^2 px^2 interrogation windows. (d) PIV results with 16^2 px^2 interrogation windows. (e) Error with the theoretical data for 16^2 px^2 interrogation windows.

Image preprocessing In this section, the effect of image preprocessing and enhancement is studied. To do so, four preprocessing techniques (intensity capping, CLAHE, histogram equalization and high-pass) are independently applied to the images before analyzing them with the PIV window deformation algorithm. An aleatory homogeneous particle displacement from 0 to 1 px is applied to the image particles. The intensity capping coefficient is set to 0.5 and the high-pass filter width to 10 px. Examples of the application of such techniques over the synthetic images can be found in figure 4.40. The comparison between the image enhancement techniques is shown in figure 4.45. The points to the left corresponds to the comparison basis, that is to say images which are not treated with any image enhancement techniques. From the different studied techniques, the histogram equalization ones (named here CLAHE and histogram equalization) seem to decrease substantially the bias error, especially for bigger interrogation size while the increase in the RMS error is contained. The intensity capping does not have the wanted effects on the analysis since both errors increase. This does not correspond to the observation made in section D.4.1. Finally, the high pass filter does not help since it tends to make disappear some of the particle pairs. These observations may however be taken with precaution since the test has only be partial. It seems however that CLAHE enhancement might help getting more precise results and might be consider as the best option to enhance experimental images.

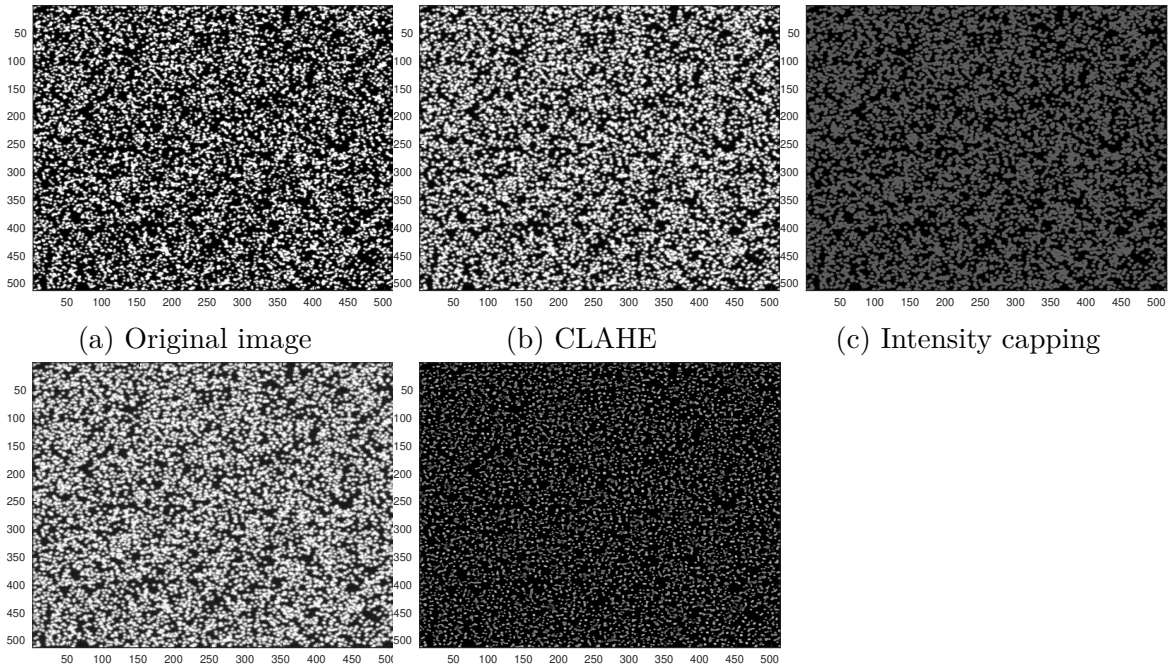

(a) Original image (b) CLAHE (c) Intensity capping

(d) Histogram equalization (e) High-pass

Figure 4.40: Pre-processing of the images.

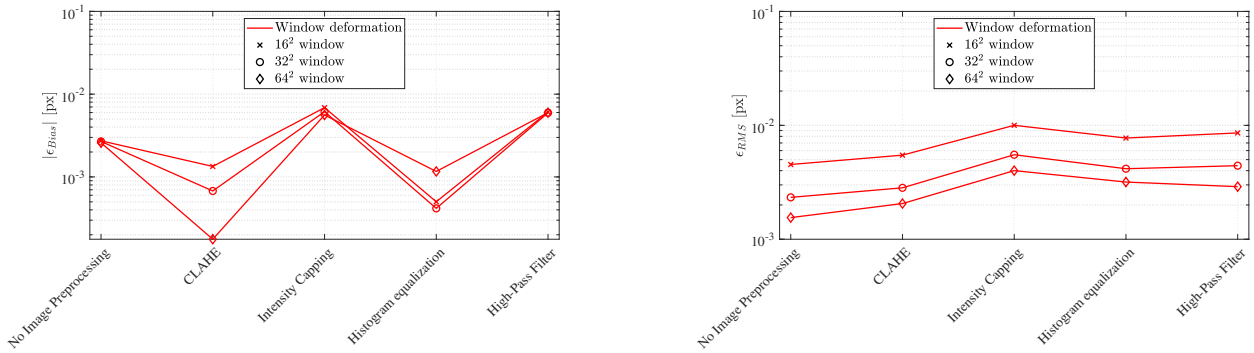

(a) (b)

Figure 4.41: Errors in function of the preprocessing image enhancement techniques. Three window sizes are studied (16^2, 32^2 and 64^2 px^2). (a) Bias error. (b) RMS error.

Program speed The processing speed of the algorithms is investigated in this section. We use *Matlab* and a 3.1 GHz quad core AMD A8-7600 Radeon and 15 GB RAM machine. Images to be analyzed are 512 x 512 pixels and a 50% overlap is set up. We first measure time of the first pass for different window sizes which is a common stage between the algorithms and then the total time of execution of the integer shift and the window deformation algorithms for 2 sets of multipass window sizes ([128^2 64^2 32^2] and [64^2 32^2 16^2] px^2). Results are shown in figure 4.42 and table 4.6. The processing time dramatically increases with the decrease of the window size from 32 px wide windows. A minimum is reached for 64^2 px^2 windows.

Local minimums can be found and correspond to power of 2 which makes the FFT faster. The difference of processing time between the algorithms is tremendous: it is needed around 17 times more time to execute the window deformation algorithm than the integer window shift one. This is mainly due to the numerous iterations and interpolations taking place in the window deformation algorithm. It is however not an issue in this work since it is possible to run the algorithm in *Leftraru*, the university cluster, and thus time resolved PIV can be treated in parallel.

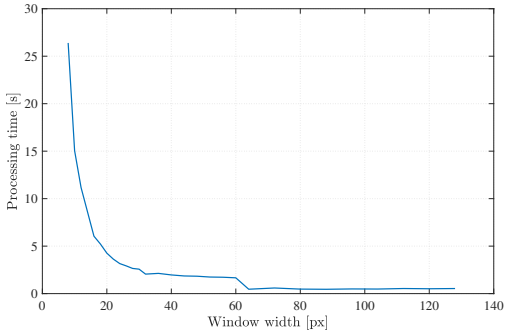

Figure 4.42: Processing time of the first pass stage in function of the interrogation window size.

Multi-pass Window Sizes [px^2]		128^2 - 64^2 - 32^2	64^2 - 32^2 - 16^2
Processing Time [s]	Integer Window Shifting	8.176	8.023
	Window Deformation	143.279	136.443

Table 4.6: Processing times for the integer window shifting and window deformation algorithms. Two multi-pass strategies are considered: [128^2 64^2 32^2] and [64^2 32^2 16^2] px^2.

4.3.2.4. Experimental images: stirring in a glass

Experimental Set-up. A first attempt in order to assess the global behavior of the PIV set up and post-processing consists of a simple experiment: the stirring in a glass. A close enough cylindrical glass is filled up with water and seeded with the *Spherical®110P8* particles. The laser plane is generated thanks to a cylindrical lens resulting in a horizontal plane at around 2 thirds of the water level. A mirror is placed at the other side of the glass in order to reorientate the light that crossed a first time the liquid and thus obtain more homogeneous lighting conditions. The camera is looking downward and takes 662 x 476 pixels picture of the full glass diameter at a rate of 60 fps. Two pictures are taken with the presence of a ruler at the plane water level and allow to convert pixels to distance in both x and y directions. The fluid is energetically stirred by a magnetic stirrer for a few seconds, the video starts

when the flow is stabilizing. This set up is shown in figure 4.43a. A mask, represented by the white lines in figure 4.44b is applied to all images in order to discard any calculation in zones where no particles are present. The window deformation PIV algorithm is applied to 16 x 16 pixel^2 interrogation windows and 50% overlapping and CLAHE image enhancement. In a first step the instantaneous velociy field is retrieved between image 1 and 2. A comparison of the velocity profile is then carried out with the mean of the velocity profile over 10 images according to the folllowing equation:

$$\overline{\vec{v}}^{x,y} = \frac{1}{10}\sum_{i=1}^{10} \overrightarrow{v_i}^{x,y} \tag{4.16}$$

with $\overrightarrow{v_i}^{x,y}$ is the velocity vector of image i at position (x, y).

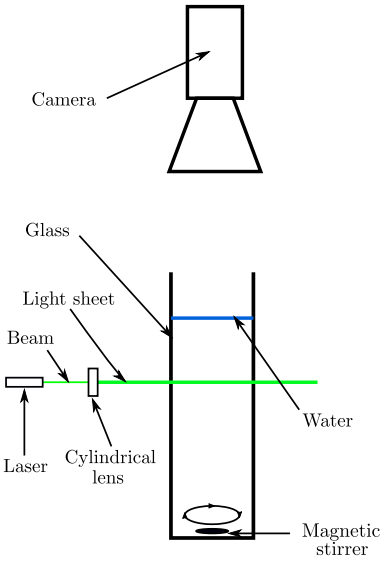

(a)

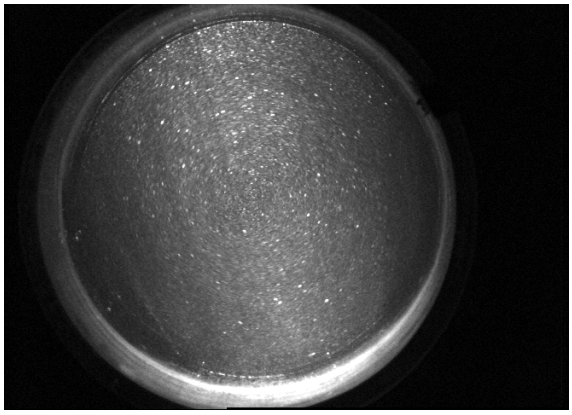

(b)

Figure 4.43: Stirring in a cup experiment. (a) Experimental set-up. (b) Image from camera

Results. An example of a picture can be found in figure 4.43b. From this last one, we can observe an inhomogeneous lighting with parts at the left and right of the glass plunged into the shadow. We can also observe the different sizes of the particles, with some conglomerates (biggest white dots), which shows the inhomogeneous seeding process which needs to be improved. The flow field is shown in figures 4.44a and 4.44b. in the first one the background indicates the magnitude of the field while the arrow length is kept constant. In the second one, the length of the arrows indicate the magnitude of the flow. It is interesting to note that the PIV algorithm is capable of detecting the vortex flow and that this one is relatively symmetrical around the center of the vortex. We are also able to keep a low size of the interrogation window since difference with bigger one does not significantly impact the results

(not shown in here). During this test, we were made conscious of the importance of the generation of a correct mask to avoid zones where no particles are present and impact greatly the results. The vertical velocity profile is shown in figure 4.45a. The instantaneous flow between images 1 and 2 is displayed in blue and a linear fit based on the three consecutive points at the center is plotted in red. We can verify the motion follows a solid body rotation at the center (linear behavior of the velocity). The velocity reaches a maximum before decreasing when getting closer to the boundary. The boundary layer is not fully resolved. Figure 4.45b compares the instantaneous profile with the mean over 10 images. The main effect of the mean is correcting the value of the maximum velocity, reestablishing the symmetry between the top and low parts of the profile. The difference at the center of the vortex is less important.

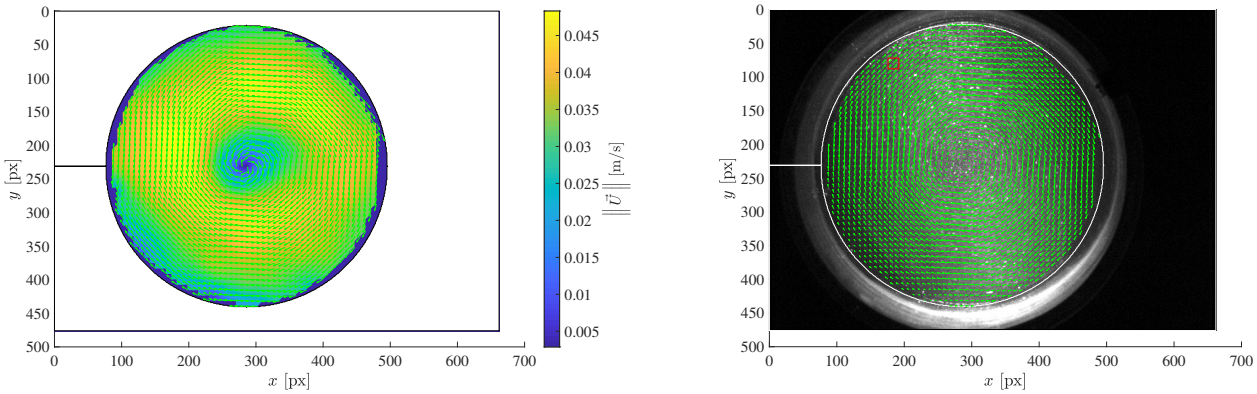

(a) (b)

Figure 4.44: Stirring in a cup experiment results: instantaneous velocity field between image 1 and 2. (a) Arrows shows direction and background amplitude. (b) Arrows indicate both direction and amplitude.

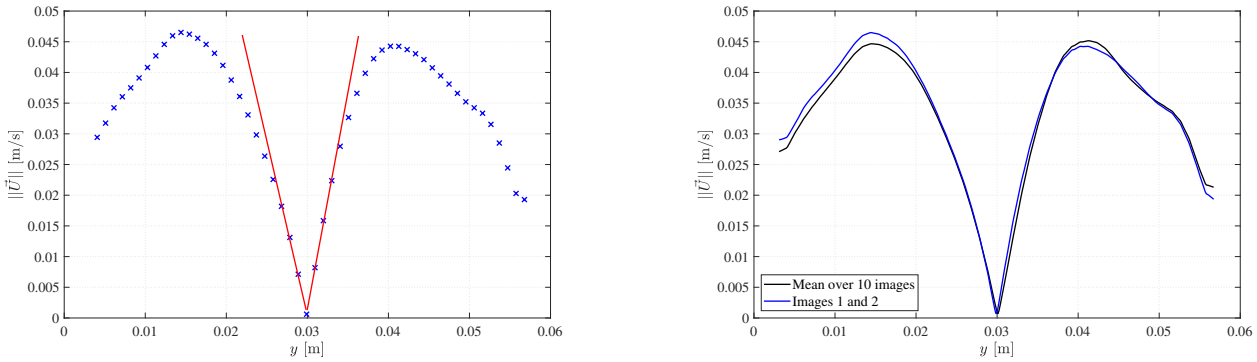

(a) (b)

Figure 4.45: Vertical velocity profile. (a) Instantaneous flow between images 1 and 2. (b) Mean flow over 10 images according to equation 4.16.

4.3.3. Free-surface detection and image masking

Free surface detection is an essential feature of the code, since to obtain the velocity vector field, one has to apply a mask on the air phase of the images taken with a vertical laser plane. A Radon transform-based technique, presented by Sanchis & Jensen (2011), allows the automatic detection of the air-water interface in a stream of particle images acquired from a single camera. Ideal images consist of bright spots over a dark background. It is most of the time not the case, especially for flow with free surface, to obtain such images. Before applying the post-processing tool, areas outside of the flow (the air or the semi-submerged objects in our case), which could reflect light and appear really bright, should be removed (Roth & Katz, 2001). If not, it could affect the results as they would be detected as a self-correlation (Thielicke, 2014). To do so, a binary filter can be used to get rid of the atmosphere and other objects that can appear on the images by padding with zeros these zones.

Air/water surface detection In this work, it is chosen to detect the air/water interface by using the Radon transform (Radon, 2005) as proposed in Sanchis & Jensen (2011). The radon transform has various advantages compared with other interface detection based algorithm (essentially based on vertical intensity gradient across the interface). It can detect various lines in an image and thus an election can be made based on a suitable criteria. But the most important feature of the radon transform is to offer, along with the interface coordinates, the orientation of the interface at such points (that is to say the slope). The Radon transform, first described by J. Radon in 1917, is defined as:

$$\mathscr{R}(\theta,\rho) = \int\int f(x,y)\delta(\rho - x\cos(\theta) - y\sin(\theta))\,dx\,dy \tag{4.17}$$

with $f(x,y)$ the image intensity function and δ the Dirac function (or impulse function). The second term passed as input of the Dirac function is the line defined by the following equation:

$$\rho - x\cos(\theta) - y\sin(\theta) = 0 \tag{4.18}$$

As shown in figure 4.46, ρ is the offset relative to projection of the origin on the line and θ is the orientation of the line. The radon transform therefore consists in the computation of the intensity function along lines. The detection of the maximum of the Radon transform in the ρ/θ plane allows to locate the interface and its orientation. Moreover it is well suited for the detection of lines in noisy images since the integration tends to cancel noise (Sanchis & Jensen, 2011). The radon transform is easy to use in *octave/matlab* since it is a built-in function (*radon.m*). It is however important to normalize the Radon transform to take into

account the aspect ratio of rectangle images (Sanchis & Jensen, 2011). It is done by dividing the input image radon transform by the radon transform of an image of same dimension as the input one filled with ones. We also propose to use the enhancement as exposed in Xing et al. (2012): the radon transform is not applied to $f(x, y)$ but to $f(x, y) - \bar{f}$ where $\bar{f}$ is the 2D mean of the image. An example of these different steps can be found in figure 4.47. The procedure described before is applied to the original image 4.47a, from one of our PIV experiments. We can observe the useful normalization which allows to limit artificial peaks to rectangular images (figure 4.47c). The use of the enhancement also allows to limit peaks which are not of interest (figure 4.47d). The general algorithm for the interface detection is as follow:

1. Image preprocessing and enhancement consisting in the elimination of reflections, intensity capping and filtering (blurring).

2. The image is parted into N vertical bands and the radon transform is applied on each of them. A first approximation of the water interface is found. In the case of breaking waves, various points can be detected along the vertical.

3. Outlier points are detected. This is carried out thanks to a standard deviation and moving window based filter.

4. A second pass is done with a square window centered on the first estimation. Outlier filter is then applied.

5. A cubic hermite spline is then used to determine interface position at every pixel.

The cubic hermite spline is defined as follows. If x is the x-coordinate of points between the k^{th} and $k + 1^{th}$ points detected at the interface, y the corresponding y-coordinate to be determined, x_r and y_r the points found with the radon transform then we can define:

$$h = x_r(k + 1) - x_r(k) \tag{4.19}$$

$$s = x - x_r(k) \tag{4.20}$$

$$t = s/h \tag{4.21}$$

Then,

$$\begin{aligned} y =& (2t^3 - 3t^2 + 1)y_r(k) + (t^3 - 2t^2 + t)y'_r(k)h \\ &+ (-2t^3 + 3t^2)y_r(k + 1) + (t^3 - t^2)y'_r(k + 1)h \end{aligned} \tag{4.22}$$

Results of the water/air interface detection are shown in figure 4.48. The first image is from our experiments and we can observe the effectiveness of the method.

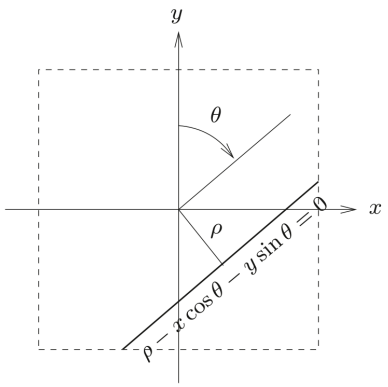

Figure 4.46: Radon transform definition.

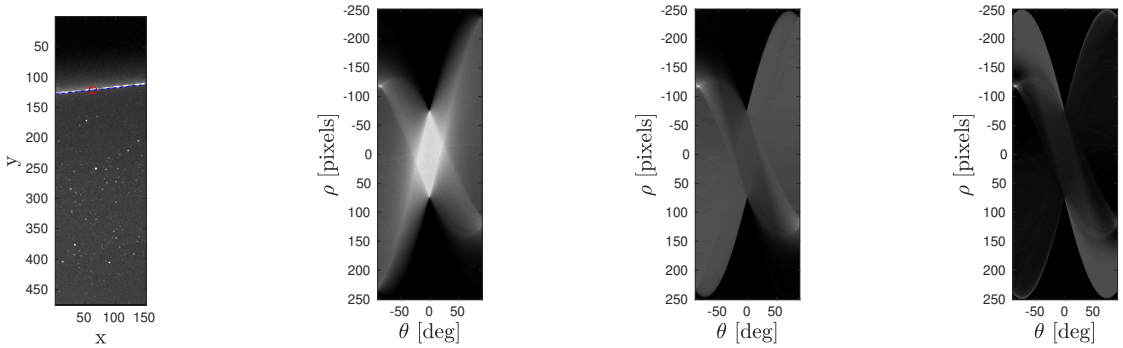

(a) (b) (c) (d)

Figure 4.47: Steps of the interface detection by Radon transform. (a) Original image to which the radon transform is applied. Results are presented through the red circle and the blue line is constructed with θ angle. (b) Results of the raw radon transform of image (without enhancement and normalization) of image (a) in the θ/ρ plane. (c) Radon transform of image (b) without enhancement but with normalization. (d) Radon transform of image (b) with enhancement and normalization. It is now way easier to detect the maximum corresponding to the interface. The maximum gives $\rho = 117$ pixels and $\theta = -84$ degrees.

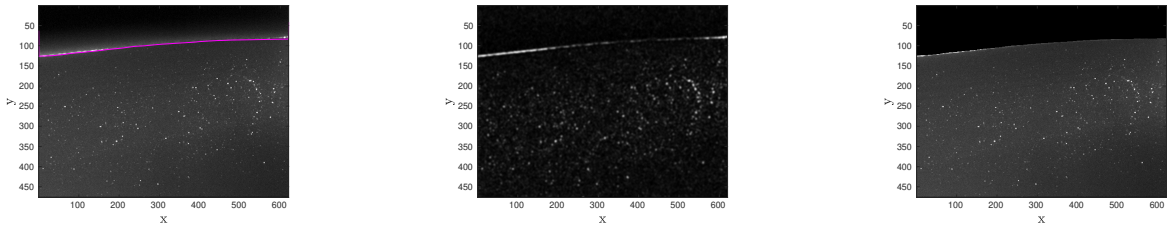

(a) (b) (c)

Figure 4.48: (a) Original PIV image. The magenta line represents the detected interface. (b) Image (a) after preprocessing and enhancement. (c) Masked image ready for PIV post-processing analysis.

4.3.4. Conclusion

A PIV experimental set-up and post-processing tool were elaborated in order to measure both qualitatively and quantitatively flow fields in the wave tank. If the experimental set-up is relatively simple once the experimentalist has access to the correct laser and camera configuration, the post-processing tool accuracy depends highly on the image quality. Several parameters associated to the image quality (particle image diameter, particle density, particle displacement, noise level, pair loss, pre-processing) were tested, and the errors associated with theses parameters were measured thanks to the generation of the synthetic particles. We were able to determine rules to respect in order to achieve accuracy in the flow field measurement as summarized in table 4.7 and they should be followed whenever possible in any future measurement with this tool. Post-processing of synthetic shear flows and counter-rotating vortices revealed that the tool is not able to retrieve the flow field magnitude when the shear rate or vortex angular displacement are too high, even if the qualitative analysis showed good results in all cases. A first example of the PIV was put in practice with an experiment of stirring in a glass, and the solid body motion at the center of the glass was retrieved. The limitations and possible improvements are presented in the following sections.

Parameter	Best practice
Particle image diameter	$d > 2$ pixels
Particle density	$0.03 < \rho < 0.1$ particles per pixel per pixel
Particle displacement	$\Delta X < 10$ pixels
Noise level	$SNR > 30$
Pair loss	$loss < 10\%$
Pre-processing	CLAHE or no pre-processing

Table 4.7: PIV image pair parameter best practice.

As the first pass on the window deformation algorithm is based on the window shifting algorithm, it is essential that this last one return a rather correct velocity field. Our experience using the algorithm has shown that bad quality images, including but not only poor lighting, blurring, resolution, out of plane motions, particle size and density, etc.. lead to erroneous first estimation and thus the window deformation algorithm does not help to improve the post-processing. In the case of poor images, pre-processing can be useful but should be used with care as it can have both improving and deteriorating effects. This is why the use of fast cameras (which can be synchronized with the laser) is recommended in order to avoid error in the post-processing.

Shear and vortex flow post-processing quality is highly dependent on the shear intensity

(shear rate and layers), vortex intensity and core size, as well as the size of the interrogation windows. Special care is to be taken when measuring quantitative data from PIV on these types of flows. The window deformation algorithm is quite time consuming so that the number of image pairs to be post-processed is also an important featuring, specially when cameras cannot be set-up to take images pair at a certain rate. In some cases, multiple peaks can appear in the correlation plane, with the highest representing an outlier. It is then important to be able to detect the other ones in order to calculate the true displacement. During the programming of the PIV post-processing tool, the sensitivity to the interpolation schemes (bilinear, bicubic or spline) have been observed, notably the management of the image sides vectors in particular revealed to be tricky when using other option than *MATLAB* "spline" option. The implementation of higher order schemes (Lagrange or sinc for example) could also be a way of improvement as shown in B. J. Kim & Sung (2006).

Part III

Results

Chapter 5

Numerical Results

In this chapter, the main numerical results and findings of this research work are presented. First, we characterize through numerical simulations the piston wavemaker system by applying velocity steps in section 5.1. From these results, we identify the generated waves as undular bores and we are able to compute the necessary power delivery. Then, an active absorption strategy is deduced from the recording of the water height at the piston wavemaker and the absorption is tested under a set of different wave types. In a second part, in section 5.2, we study the interaction between an undular bore and a square vertical cylinder which is mounted at the center of the wave tank. We present then the physics taking place in the wave tank and the vortices which are generated around the cylinder, and we identify a phenomena of vortex pairing taking place at the rear of the cylinder.

5.1. Characterization of the piston wavemaker

Note: most of the content exposed in this section was summarized in the article reproduced in appendix E from the journal *AIP Advances* and whose title is **Dynamic and kinematic characterization of the impulsive wavemaker system in a numerical wave tank**. However, we extend the study to negative velocity steps in this thesis. Step velocities are applied to the piston wavemaker in the NWT in order to carry out a dimensionless analysis of the very first instant of the wave generation as well as the undular bore creation, and compute the forces involved in the process. From these results, an active wave absorption strategy is defined and tested on a set of harmonic and irregular waves.

5.1.1. Kinematic and dynamic characterization of the piston wavemaker

One of the objectives in this work is to characterize the piston wavemaker system by applying a series of velocity steps. First, a qualitative approach is taken and observations are made about the wave generation at small times and the generated wave pulse is studied at longer times and far away from the wavemaker. Then, we compare the characteristic variables with the theory developed in Joo et al. (1990) and explore higher Froude number regimes. The forces exerted on the wavemaker and the power involved in the wave generation process is finally studied. The step velocity tests are carried out at four mean still water levels: $h = 0.050$ m, 0.075 m, 0.100 m, 0.150 m and for velocities ranging from $U_G = 0.005$ to $U_G = 0.4$ m/s. In this problem the fundamental velocity, length, and time scales are $\sqrt{gh}$, h and $\sqrt{h/g}$ respectively. The problem can be written as $f(\eta_w, \rho, g, h, t, U_G) = 0$, but according to the Buckingham π theorem (Buckingham, 1914), it can be reduced to $f(\eta_w^*, t^*, Fr) = 0$ where η_w^* and t^* are the dimensionless water height at piston wavemaker and time respectively. In the next sections, as a consequence of this analysis, we will express the results in a dimensionless way using the relevant variables η_w^*, t^* and Fr.

5.1.1.1. First instants - The overshoot-wave

After the wave leaves the wavemaker, the water height at the wavemaker remains constant. The wave pulse profile for times $t = 0.05, 0.13, 0.20, 0.31$ s, which correspond to the first instants of the pulse formation, are displayed in figure 5.1. On the same figures, the wave steepness, defined as $|d\eta/dx|$, is superimposed. We observe that the wave steepest shape occurs at the very first instants of its formation, i.e, at $t = 0.05$ s, where the maximum steepness is higher than 3. When the pulse starts leaving the piston wavemaker, its steepness decreases to values under 1. Such high steepness is associated to the non-linear properties of the overshoot-wave. Another important parameter useful to evaluate when it comes to apply linear theory is the wave height to mean still water level ratio η/h. It is relatively important (values around 0.5 in this example), therefore Airy theory of linear waves cannot be applied here. The profile of the generated pulse at longer times is shown in figure 5.2, as well as its steepness in function of the x coordinate. We can notice the generation of wiggles after the main pulse propagating downstream as already described. The wiggles are trailing waves whose height decrease in the vicinity of the piston wavemaker while the front wave height increases as it travels. These wave structures are described in the work of Joo et al. (1990), and are a consequence of wave dispersion. The piston motion creates a wave packet in which each wave travels at different velocities due to dispersion effects. We identify the

created wave to be an undular bore which is experimentally and theoretically studied by Favre (1935) and Peregrine (1966), respectively, while Stoker (1957) predicted that an impulsive wavemaker would generate an undular bore. Undular bore are of particular importance as they appear to more likely represent real tsunami wave instead of solitary wave (P. A. Madsen et al., 2008). Important values of the wave steepness are observed during the pulse formation, which decrease rapidly as the pulse propagates. In the time snapshots of figure 5.1 and 5.2 we observe the vector velocity field of the numerical solution of the Navier Stokes equations. The vector field becomes intense precisely near the steepness peaks as the overshoot-wave propagates along the tank. The higher the wave height the higher the intensity of the vector field which is associated to particle velocity.

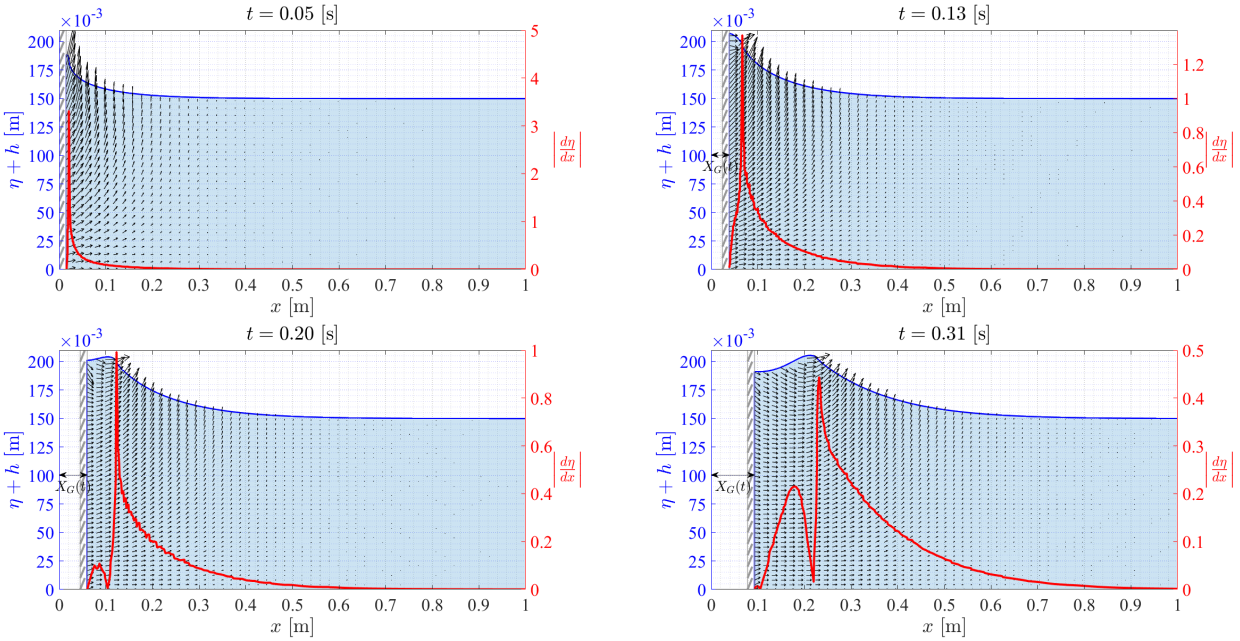

Figure 5.1: Time snapshots of the wave pulse generated (from left to right) by a velocity step applied to the wavemaker motion. The wave pulse is called here the overshoot-wave as it is created by the overshoot of the water elevation at the piston wall. Wave profile (wave height as a function of x) is plotted in blue and the wave steepness as a function of x in red. The velocity step is 0.3 m/s and the mean still water level h is 0.15 m. The shown times are $t = 0.05$ s $\approx t_r$, $t = 0.13$ s $\approx t_p$, $t = 0.20$ s, and $t = 0.31$ s $\approx t_s$.

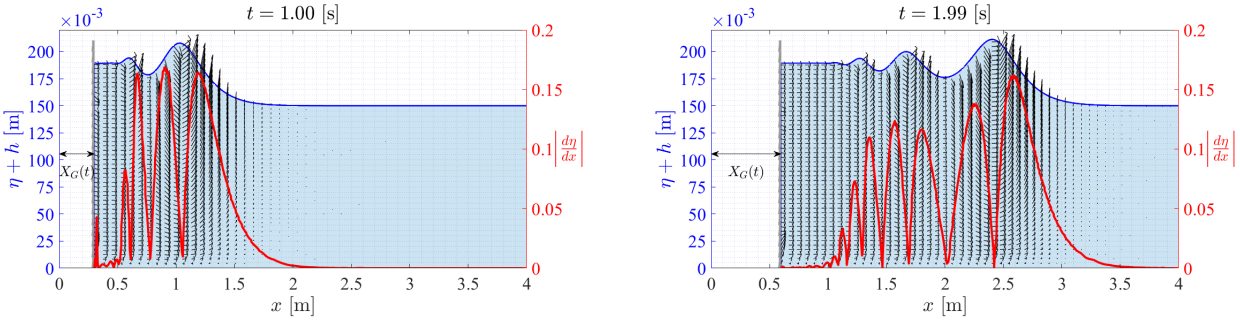

Figure 5.2: Snapshots at times $t = 1.00$ s and $t = 1.99$ s of the wave pulse generated (from left to right) by a velocity step applied to the wavemaker motion. Wave profile (wave height as a function of x) is plotted in blue and the wave steepness as a function of x in red. The velocity step is 0.3 m/s and the mean still water level h is 0.15 m. Note the change in scale in the x abscissa compared to figure 5.1.

The starting overshoot-wave displays a phase celerity C_p as a function of time t which may be compared with two characteristic properties, the shallow water wave speed $C_p = \sqrt{g(h+H)}$ and with the piston velocity U_G as shown in figure 5.3. The overshoot-wave celerity may be estimated from the mean celerity as $C_p = \delta x/\delta t$ between consecutive wave crests or looking for maximum steepness at different time steps during the propagation as shown in figure 5.1. As the phase celerity of the overshoot-wave is found to be higher than the piston velocity from the first instants of motion, the overshoot-wave travels fast enough to leave the piston wavemaker. As the wave propagates along the tank, its phase celerity increases with time, approaching the shallow water phase speed given by $C_p \to \sqrt{g(h+H)}$. This behaviour agrees with potential theory and therefore allows to validate the capabilities of the numerical wave tank for wave propagation.

In the case of a negative step, the wave which is generated does not take the form, as seen before, of an undular bore. A leading trough wave will be generated and propagate in the inverse direction of the the piston wavemaker motion. This trough will evolve rapidly and deform with the increase of the wave crest that immediately follows the trough. The wave generated by a negative step was not studied in further details in this work.

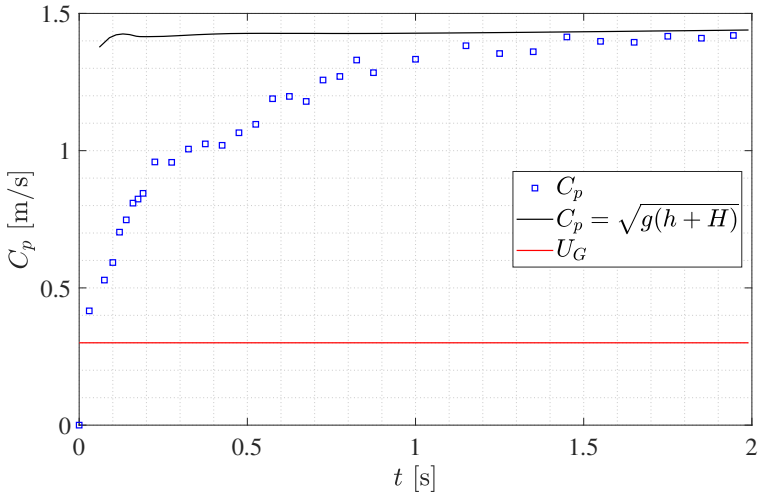

Figure 5.3: Instantaneous overshoot-wave phase celerity $C_p(t)$ (in blue) as a function of time for the case $h = 0.15$ m and $U_G = 0.3$ m/s. For times lower than 0.2 s, the maximum of the steepness is used to determine the location of the overshoot-wave. For later times, the maximum of the wave profile is taken as the location of the wave. The wave celerity can be compared to the piston step velocity U_G and to the phase velocity of shallow water waves.

5.1.1.2. Response to a velocity step

A positive velocity step ($U_G > 0$) creates a water pulse which leaves the wavemaker wall as it propagates along the tank. The step response is recorded as the water height or water elevation at the wavemaker wall $\eta_w(t)$ and is presented in figure 5.4a.

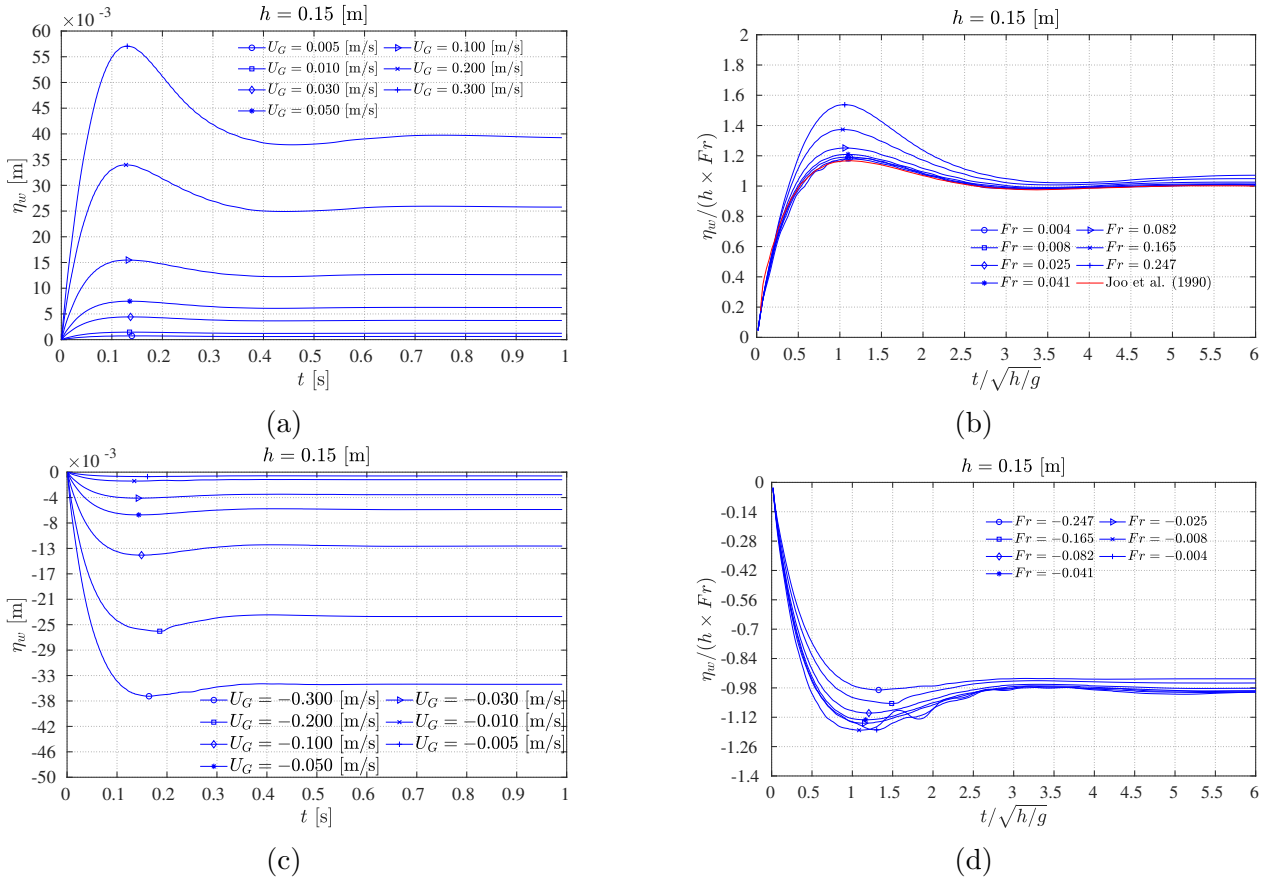

Figure 5.4: (a) Water height at wavemaker as a function of time for positive step velocities. (b) Non dimensional water height as a function of non dimensional time for positive step velocities. A comparison between the CFD simulation and the theoretical study carried out in Joo et al. (1990) is shown. (c) Water height at wavemaker as a function of time for negative step velocities. (d) Non dimensional water height as a function of non dimensional time for negative step velocities.

The water height first increases, reaching a maximum or overshoot η_o at peak time t_p, before approaching a lower steady state value η_{ss}. It is of particular interest to note the similarity of this dynamic response with step response of second order system (cf. figures 3.7 and 5.4). The time response of second order linear systems depends on the type of input signal. For a step input the system exhibits a charateristic response defined by the rising time t_r, the maximum overshoot η_o, and the steady state value η_{ss} obtained at a given settling time t_s (Nise, 2011). All these parameters are shown in figure 3.7b. In figure 5.4b we present the normalized time response using the Froude number as in the theory proposed by Joo et al. (1990). We can observe that after reaching its maximum value, the overshoot, the water height slightly oscillates and decreases to its steady state value $\eta_{ss} = h\,Fr$. The step response for small Froude numbers found in this work are in agreement with the theoretical work of Joo et al. (1990). Nevertheless, some differences with the theory are observed in the overshoot behaviour for higher Froude numbers. The overshoot starts to increase beyond the

theoretical prediction and the steady state value approaches a slightly higher value than the expected one from theory, $\eta_{ss} = h\,Fr$ as we will discuss in the next section.

U_G	$h = 0.05$ [m]		$h = 0.075$ [m]		$h = 0.10$ [m]		$h = 0.15$ [m]	
[m/s]	Δ_o [%]	Δ_{ss} [%]	Δ_o [%]	Δ_{ss} [%]	Δ_o [%]	Δ_{ss} [%]	Δ_o [%]	Δ_{ss} [%]
0.005	5.97	1.86	2.42	0.09	3.64	3.96	1.77	0.61
0.010	3.33	1.19	2.14	0.16	1.15	0.34	0.98	0.39
0.030	3.69	1.35	3.26	0.80	2.79	0.85	2.00	0.82
0.050	5.98	2.40	5.09	1.48	4.54	1.60	3.54	1.26
0.100	11.96	4.11	10.60	3.42	9.33	2.81	7.20	2.37
0.200	25.73	7.00	23.02	5.97	20.77	5.35	17.64	4.52
0.300	43.67	10.48	40.42	8.75	37.72	7.72	31.67	6.39

Fr ↓

← Fr

Table 5.1: Relative deviation from model of Joo et al. (1990) at different water depth and step velocity ($0.005 < U_G < 0.3$ m/s). The relative deviation is defined as: $\Delta_o = \left|\eta_o - \eta_o^{ref}\right| / \eta_o^{ref}$, $\Delta_{ss} = \left|\eta_{ss} - \eta_{ss}^{ref}\right| / \eta_{ss}^{ref}$. The subscript ref refers to the study of Joo et al. (1990). The arrows indicate how the Froude number varies with the step velocity and the mean still water level.

The relative deviation from theory (Joo et al., 1990) is presented in table 5.1 for the four mean still water levels and the velocity range from 0.005 m/s to 0.3 m/s. The relative deviations are defined as: $\Delta_o = \left|\eta_o - \eta_o^{ref}\right| / \eta_o^{ref}$ and $\Delta_{ss} = \left|\eta_{ss} - \eta_{ss}^{ref}\right| / \eta_{ss}^{ref}$, where the subscript ref refers to the study of Joo et al. (1990). The arrows indicates how the Froude number changes while varying the step velocity or the mean still water level. It is interesting to note that the relative deviation stays low for the steady state value (< 10.5 % for all velocities and mean still water levels). For both overshoot and steady state values the deviation decreases with the increase of the water level (which actually corresponds, for a given step velocity, to lower Froude numbers). Finally, the deviation for the overshoot value can reach high values (> 40 %) for the highest Froude numbers (high velocity, low mean still water level). In the case of a negative step velocities, shown in figures 5.4c and 5.4d for the dimensional and dimensionless cases respectively, the steady state values are also equal to $\eta_{ss} \to h \times Fr$, so that this behavior is similar to the one for positive step velocities. However we can observe that for the overshoot value, if the velocity step is faster then the overshoot is lower than for slower cases, as shows figure 5.4d. This is the opposite behavior compared to positive steps and this difference will be observed in figure 5.5b where the curve does not show symmetry with respect to the origin of the plot.

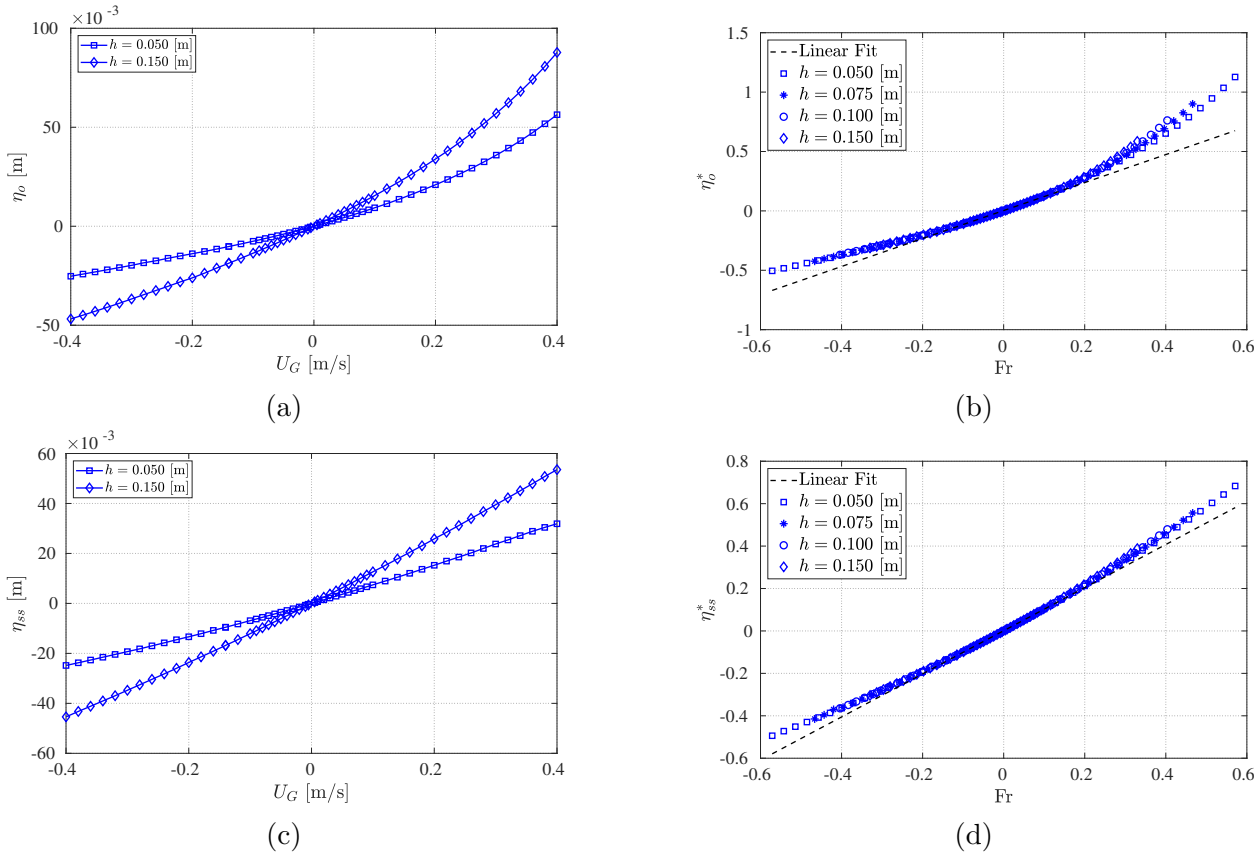

Figure 5.5: (a) Overshoot η_o of the water elevation at the piston wall as a function of the piston step velocity U_G. Two still water levels are considered: 0.05 m and 0.15 m. (b) Dimensionless overshoot at the piston wall $\eta_o^* = \eta_o/h$ versus Froude number. A linear fit for low Froude number $Fr < 0.1$ is drawn in dashed black line for comparison and is given by $\eta_o^* = 1.267 \cdot Fr - 0.0015$ and $R^2 = 0.9994$. (c) Steady state water elevation η_{ss} as a function of the piston step velocity U_G. Two still water levels are considered: 0.05 m and 0.15 m. (d) Dimensionless water height steady state at the piston wall $\eta_{ss}^* = \eta_{ss}/h$ vs Froude number. A linear fit for low Froude number $Fr < 0.1$ is drawn in dashed black line for comparison and is given by $\eta_{ss}^* = 1.046 \cdot Fr - 0.0005$ and $R^2 = 0.9997$. The different still water levels are represented with symbols.

The dominant controlling parameter in this work is the Froude number Fr defined as the ratio between inertia ($\rho h^2 U_G^2$) and gravitational ($\rho g h^3$) forces thus $Fr = U_G/\sqrt{gh}$. The similarity of the system response with the typical 2^{nd} order response under a step velocity can be analysed through the characteristic time scales and maximum overshoot of the response. Time scales as well as the amplitude of the water height response must be plotted as a function of the step velocity U_G. As in many feedback control systems, the time response of a 2nd order system will be completely determined when one knows the maximum overshoot η_o, the steady state amplitude η_{ss} and the rising, peak and settling times t_r, t_p, t_s respectively. If the time response is correctly described by the the 2nd order response, we should find a

scaling law for the characteristic time scales at different water depth h and step velocity U_G otherwise said the Froude number.

The overshoot η_o as a function of the step velocity U_G is plotted in figure 5.5a and the steady state η_{ss} is plotted in figure 5.5c, both for two mean still water levels $h = 0.05$ m and $h = 0.15$ m. The steady state values evolve linearly with the generation step piston velocity as they correspond to the water height of the displaced volume which increases linearly in time as the step velocity U_G is constant for $t > 0$. However, the overshoot dependence on U_G is not linear as the overshoot-wave originates during a rapid transient process. The curve collapse under the proposed scaling is relatively good in the range of mean still water levels shown $0.05 \leq h \leq 0.15$. The scaling for the overshoot fails when $Fr > 0.2$ as the overshoot-wave height increases over the linear limit and start to move faster with higher U_G.

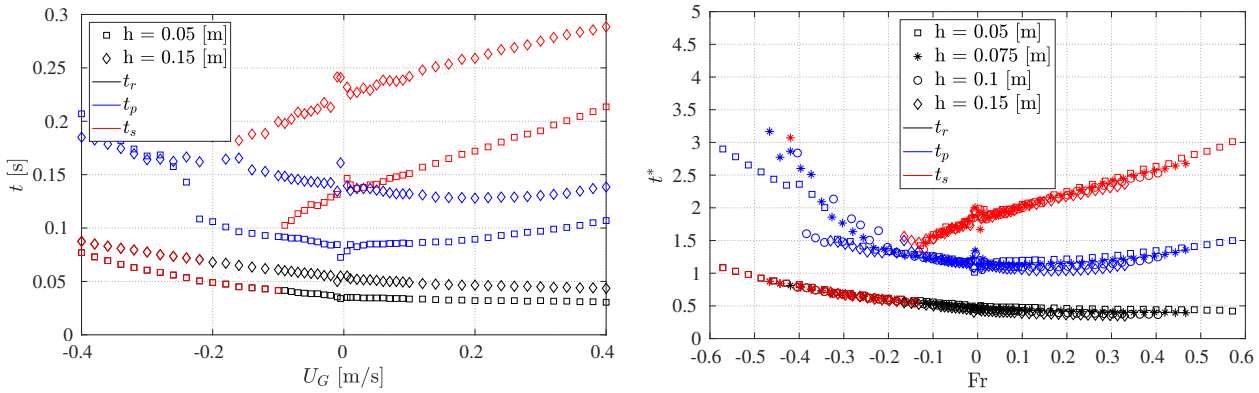

(a) (b)

Figure 5.6: (a) Characteristic time scales as a function of the wavemaker step velocity U_G. (b) Dimensionless characteristic time scales $t^* = t/\sqrt{h/g}$ as a function of the Froude number.

The evolution of the characteristic time scales of the response to a velocity step are shown in figure 5.6. As it was indicated in figure 3.7, these time scales are associated to a 2nd order dynamical response, where the water height at the piston wall η_w is measured and compared to the steady state height η_{ss}. The rise time t_r and the peak time t_p are associated to the very first instants of the wave motion, when the overshoot-wave is created. Both time constants appear to be independent of the step velocity and provide an interesting scaling independent of the Froude number where the dimensionless time scale is written as:

$$t^* = \frac{t}{\sqrt{h/g}} \tag{5.1}$$

As shown in figure 5.4, after the main wave leaves the piston zone, the water height on the piston wall scales perfectly with the Froude number as $\eta_w/(hFr) = 1$ because the displaced volume in the steady state regime is entirely determined by the steady state water elevation

η_{ss}. The associated settling time t_s is computed within a 10% band and slightly grows with Froude number for positive steps while a jump in the curve is observed for the lowest negative velocities and is explained by the failure of the detection method of such time. In figure 5.6b the time scaling indicated in equation 5.1 produces a very tight collapse of each characteristic time as a function of Froude number, except for the lowest negative steps which show differences for the peak time.

The scaling seems to confirm the similarity of the water elevation response with a 2nd order response. As the wave pulse is created by the excess or overshoot of the water elevation at the piston wall we called it the overshoot-wave. The piston motion produces the displacement of a water volume (per unit depth) given by the $V(t) = U_G t\, h$ which displays an initial transient peak, the overshoot, superimposed into a water slug rising over the mean still water level h. The overshoot-wave has its own dynamics, moving at shallow water speed, running over the water slug and therefore leaving the displaced volume faster than the linear waves. Let's calculate the change of volume of the water slug between two times t_1 and t_2. We consider that $C_p(t_1) = \sqrt{g(h+\eta_{ss})} = \sqrt{g(h+hFr)} = \sqrt{gh(1+Fr)} \approx \sqrt{gh}$.

$$\begin{aligned} V_{slug} &= l\eta_{ss} \\ &= C_p(t_2 - t_1)hFr \\ &= \sqrt{gh}(t_2 - t_1)hFr \\ &= \frac{U_G}{Fr}(t_2 - t_1)hFr \\ &= U_G(t_2 - t_1)h \\ V_{slug} &= V_{piston} \end{aligned} \tag{5.2}$$

This shows that the volume displaced by the piston wavemaker is found under the water slug at steady state times in the limit of low Froude number. These relations can be useful to estimate the loss of slug height in experimental wave tank where the piston wavemaker in most of the current facilities leaves a space between the seabed and itself. This loose can have a great impact on the slug height in particular in small tanks.

5.1.1.3. Forces involved in the step response

In this section, we present new findings such as the force decomposition and the maximum power in function of the Froude number. The objective of this section is to determine the forces originated on the piston wavemaker during the step response. As the problem is 2D there are only two components of the forces projected on the piston wall in the x and z-direction, which are inertial, pressure and viscous forces. These forces can be calculated from the pressure and velocity fields at the wavemaker using the stress tensor as presented

in section 3.3. In figure 5.7 we display the resulting normal and tangential force profiles (respectively $f_x(z)$ and $f_z(z)$) as a function of the vertical coordinate starting from the bottom of the tank and across both fluids phases. As the mean still water level is $h = 0.15$ m we note a marked change at the air-water interface $z = 0.15$ on both type of forces. However, as expected, there is approximately a five orders of magnitude difference between both components. The normal force profile $f_x(z)$ is mainly hydrostatic and insensitive to time and the viscous or tangential force profile $f_z(z)$ is dependent on time at low U_G values. Wall shear is created during the formation of the overshoot-wave which indicates the positive increase in the resulting vertical force $F_z(z)$ of figure 5.9b. When the overshoot-wave leaves the piston, and the progressing volume pushed by the piston reach a steady state motion, the shear forces become very small. When the step velocity is increased to $U_G = 0.3$ m/s the normal force profile $f_x(z)$ displays notorious changes in time but finally evolving into an almost hydrostatic vertical profile as shown in figure 5.8b.

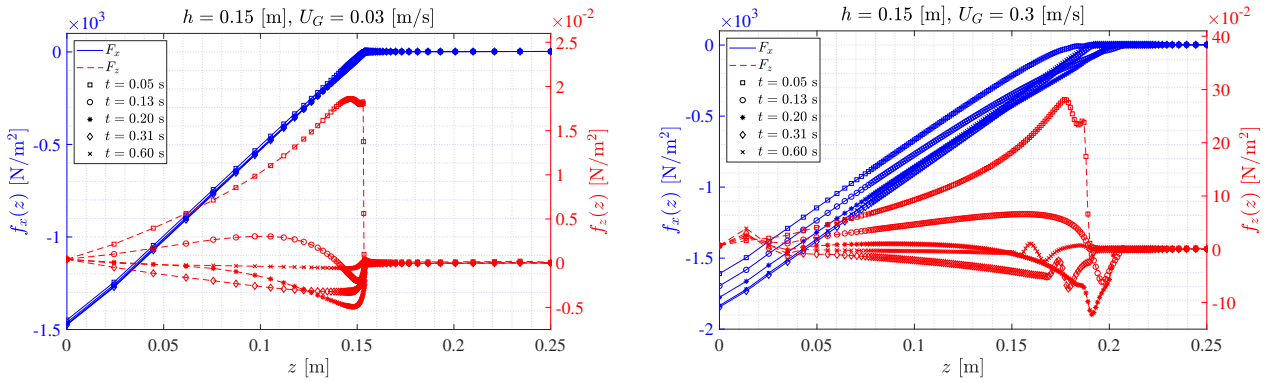

Figure 5.7: Normal and tangential force profiles (along z axis, respectively f_x and f_z) per unit area at the wavemaker for times 0.05, 0.13, 0.20, 0.31 and 0.60 s and $h = 0.15$ m. Notice the difference of power of ten between the two plot vertical axis. (a) $U_G = 0.03$ m/s. (b) $U_G = 0.30$ m/s.

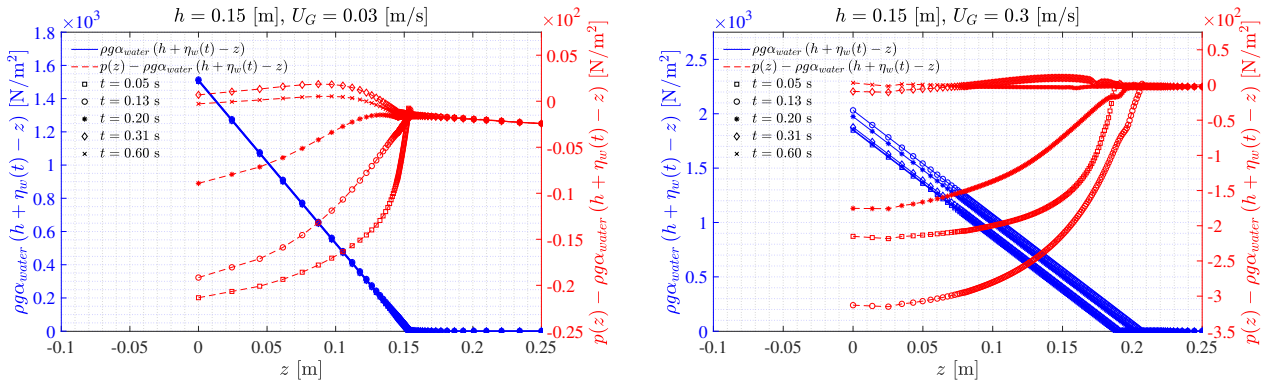

Figure 5.8: Pressure forces (hydrostatic $\rho g(h+\eta)$ and $p-\rho g(h+\eta)$) (along z axis) at the wavemaker for times 0.05, 0.13, 0.20, 0.31 and 0.60 s and $h = 0.15$ m. (a) $U_G = 0.03$ m/s. (b) $U_G = 0.30$ m/s.

In order to verify the effects of the initial fluid motion on the pressure field during the step response, we recorded the pressure profiles at both step velocities $U_G = 0.03$ m/s and $U_G = 0.3$ m/s. The sudden increase of water elevation at the piston wall is more important at higher U_G, which is explained by the higher volume displaced during the initial times. Shear forces change in sign during the formation of the overshoot-wave as shown in figure 5.7 at both step velocity values. The first water elevation motion produces a positive shear on the piston wall and therefore a positive shear force which start to decrease, becoming negative as the overshoot-wave leaves the piston wall and the force points downwards before vanishing in the steady state regime. The pressure profile is dominated by hydrostatics as shown in figure 5.7. However, when we subtract hydrostatic pressure due to the initial wave elevation along the z axis, i.e., we plot $p(z) - \rho g(h + \eta)$, we observe traces of the creation of the overshoot-wave on the remanent pressure. As time progresses and the overshoot-wave leaves the piston wavemaker, this remanent dynamic pressure contribution approach very low values with respect to hydrostatics.

In order to compute the power delivery involved in the process we must get a good estimate of the resulting forces on the piston. In figure 5.9 we present the normal and tangential forces on the piston wall as a function of time, uncovering the initial transient associated to the overshoot-wave formation and during the steady state regime. The normal and tangential force profiles are obtained integrating the force profiles of figure 5.7 along the piston wall during each time step, providing an accurate estimation of the net forces shown in figure 5.9. The resulting normal forces $F_x(t)$ are negative as they oppose to the piston motion. If we plot the absolute values we find a time evolution very similar to that of water elevation $\eta_w(t)$ in figure 5.4. The first rising part is associated to the force excess resulting from the creation of the overshoot-wave followed by a steady state force associated to the progressive motion of the mass of the water slug moving at constant velocity U_G. On the other side, the

tangential averaged forces $F_z(t)$ shown in figure 5.9 display a change of sense (sign) indicating how the fluid is moving on a boundary layer created on the piston wall. At first the fluid moves upward then stops and then moves downward reaching a local (downward) maximum precisely when the overshoot wave leaves the piston. The critical time when the resultant shear force is zero $t \sim 0.2$ s does not correspond to the peak time as water is still rising at the bottom of the wavemaker as shown in figure 5.1. X-Force characteristic times (rise and peak time) are much larger than for the kinematic observations. The minimum shear force time corresponds to the maximum force in the x direction, showing the correlation between both phenomenon. We can imagine that a feedback controlled piston wavemaker might also be designed by measuring the vertical force instead of the one in the direction of the piston motion. If the overshoot wave is going away leading to a fluid flow downward at the interface, the global motion is more complicated, with a flow still going upward at the base of the piston.

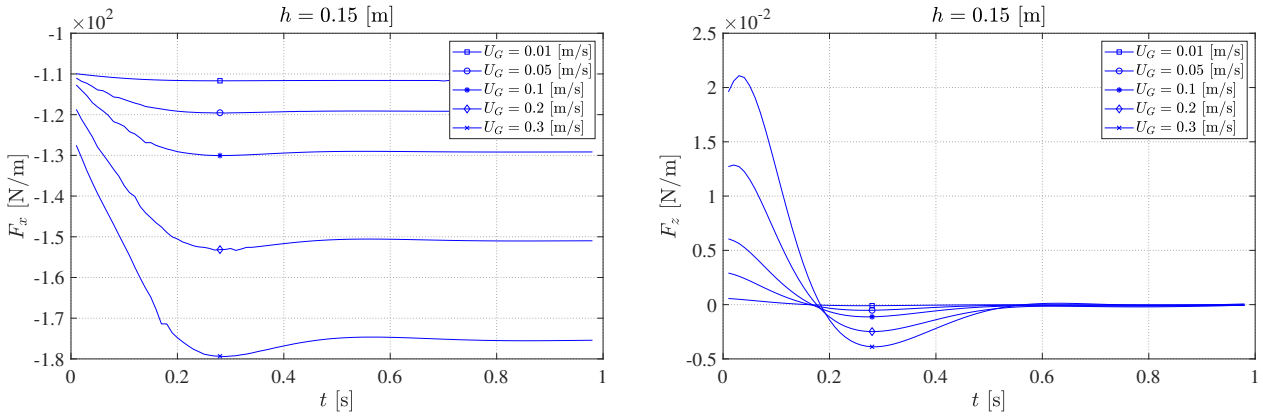

Figure 5.9: Resulting net forces per unit length as a function of time. (a) Normal net force $F_x(t)$ and (b) tangential net force $F_z(t)$. Mean still water level is $h = 0.15$ m and the step velocity ranges from $0.01 \leq U_G \leq 0.3$ m/s.

During the design of a piston wavemaker it is important to evaluate the power input during the step response associated to the wave generation process, as it can be particularly useful in determining the scaling. For example, the *Flowave* facility power demand can creep close to 300 kW when it creates a sea state moving the 168 paddles (Ingram et al., 2014). Dimensioning the necessary power supply is then of crucial importance. This section is devoted to the evaluation of the energy input required to create a wave pulse resulting from a piston velocity step. The power involved in the step motion of the piston wavemaker is calculated according to the following equation,

$$P(t) = \mathbf{F}_w \cdot \mathbf{U}_w \tag{5.3}$$

In this case, the piston wall velocity is $\mathbf{U}_w = U_G\hat{x}$ which is the Heaviside step function. Maximum power delivery as a function of the step velocity is shown in figure 5.10a. The maximum power corresponds to the maximum water elevation at the piston wall. An expected power increase is found when the step velocity increases, but more impressive is the radical change of the power delivery when the mean still water level is increased. If we look for a scaling of the power delivery, we may use a characteristic force per unit length and velocity to perform the normalization. The normalized maximum instantaneous power can be written as:

$$P^* = \frac{P}{\rho g h\, h\sqrt{gh}} = \frac{P}{\rho g^{3/2} h^{5/2}}$$

where P is the power per unit length. The involved force is the hydrostatic pressure force and the velocity is the corresponding shallow wave celerity $\sqrt{gh}$. In figure 5.10b, the normalized maximum power P^* versus Froude number collapse for different mean still water levels, confirms that the scaling has been properly defined and it follows accurately a quadratic fit (obtained by least square fitting). This law can be used as a entry design tool to define the maximum power that is necessary to generate waves.

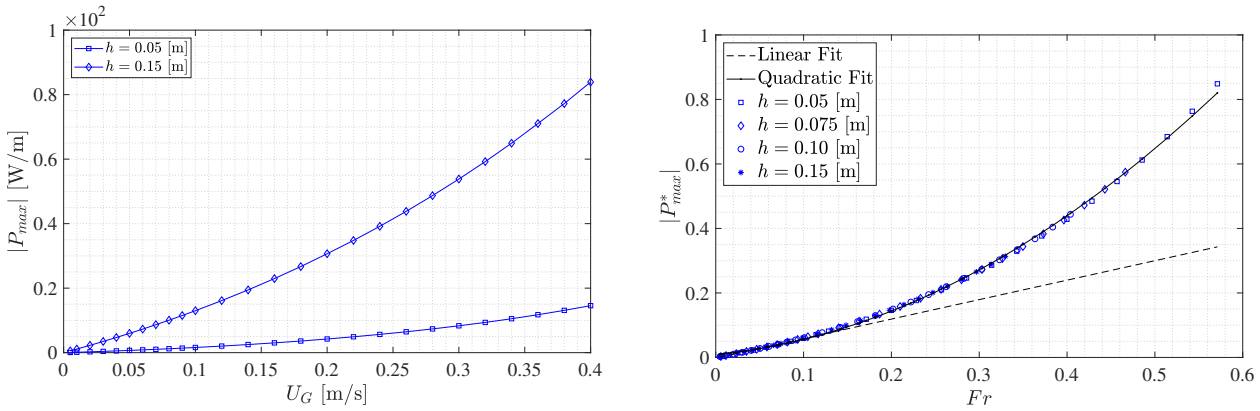

(a) (b)

Figure 5.10: Power delivery during wave generation. (a) Maximum power per unit length P_{max} versus step velocity U_G at $h = 0.05$ m and $h = 0.15$ m. (b) Dimensionless maximum power per unit length P^*_{max} as a function of Froude number Fr at different mean still water level. A quadratic fit is carried out and gives $P^* = 2.0079Fr^2 + 0.2740Fr + 0.0087$ (with correlation coefficient $R^2 = 0.99906$).

5.1.2. Definition of an active absorption strategy

In this section, an active proportional controller is defined based on the previous results on the step response of section 5.1.1. The controller is tested on different waves types and the reflection coefficient is computed from two strategies which are detailed.

5.1.2.1. Proportional controller

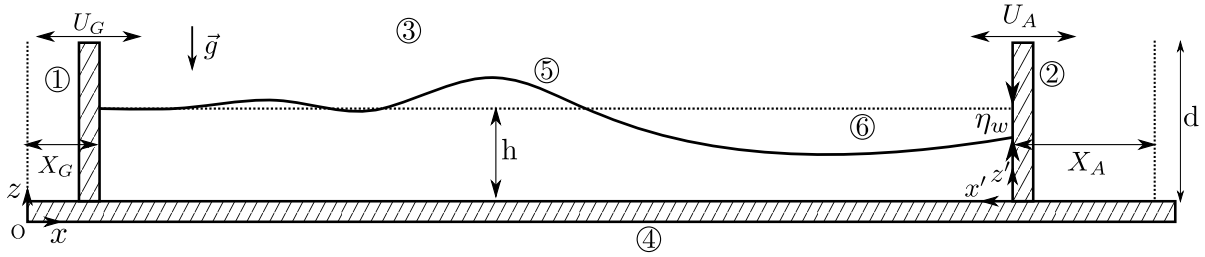

Figure 5.11: Schematics of the wave absorption problem. The numerical domain is composed of (1) the piston wavemaker, (2) the piston wave absorber on which the error ϵ is measured, (3) the atmosphere and (4) the seabed. The generated waves (5) at the free-water surface are measured with respect to the mean still water level (6) h. A second frame of reference, proper to the wave absorber, is denoted (x', z').

An active wall driven by a feedback controller may be useful not only to cancel wave reflections but also to attenuate wave impacts associated to extreme waves on a vertical wall and reduce their consequences (McHugh & Watt, 1998). We have here implemented an active wave absorption strategy using our results from the response of the wavemaker to velocity steps discussed in section 5.1.1. First, consider a wave created at the wavemaker, propagating from left to right, whose shape is a leading trough as shown in figure 5.11. To absorb this wave at the right active wall, a wave crest of nearly opposite phase has to be superimposed, which is generated by the motion of a wave-absorber, a wavemaker situated at the right side of the tank, according to the following strategy.

Consider a wave-absorber consisting of an active flat wall with a sensor which measures the water level at the wall η_w. On the frame of reference (x', z') associated to this wave-absorber the positive motion is from rigtht to left (note that x' direction is the opposite of x). The wall water level η_w can be compared to a reference value $\eta_{ref} = 0$ in order to attenuate reflections. The error $\epsilon = \eta_{ref} - \eta_w$ is permanently computed and fed into a proportional controller of gain K, which provides the absorption velocity $U_A = K\,\epsilon$. The corresponding block diagram of the feedback control strategy using a proportional controller, is shown in figure 5.12a. The efficiency of the control strategy relies on the choice of K where we propose to use the kinematic results of the step response rather than typical methods (Nise, 2011). In section 5.1.1.2 we have shown that the wall water level at the wavemaker reaches an overshoot value after a short time (as seen in figure 5.4) corresponding to the standard peak time of the system (see figure 5.6). The overshoot η_0, the maximum water level at the wavemaker during the step, was related to the piston velocity U_G by a linear relationship at lower part ($Fr < 0.2$) of figure 5.5b. If we want to absorb a wave of given amplitude at the wave-absorber wall, then we are more efficient if the change in amplitude,

$\eta_w \longrightarrow \eta_0(U_G)$, takes into account the corresponding step velocity U_G.

The slope of the linear scaling of figure 5.5b (the lower part of the plot) will determine the proportional controller gain K. The absorption velocity is then computed as $U_A = K\epsilon = -K\eta_w$ where $K = 1/1.267\sqrt{g/h}$, represents the inverse of the linear fit slope of figure 5.5b.

The dimensionless controller gain $K^* = K\sqrt{h/g}$ is reproduced on figure 5.12b at different water levels, for a better understanding of the gain selection.

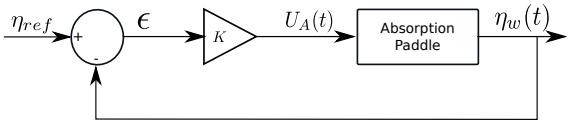

(a)

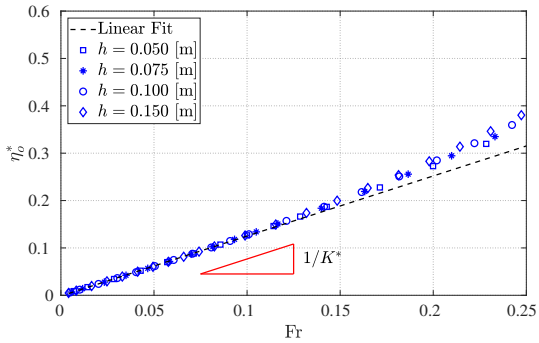

(b)

Figure 5.12: (a) Absorption block system. A proportional controller compares the value of the water level at the wave-absorber wavemaker η_w with a reference value η_{ref}. It multiplies then the error with a constant coefficient K which gives the absorption velocity U_A. Error ϵ and absorption velocity in function of time. (b) Dimensionless overshoot wave height at paddle in function of the Froude number, zoom on figure 5.5b. The dimensionless proportional coefficient K^* is represented on the curve as the inverse of the slope (in red). $K^* = 1/1.267$ so that $K = 1/1.267\sqrt{g/h}$.

5.1.2.2. Reflection coefficient evaluation

Method of Goda & Suzuki (1976) It is essential to accurately determine the reflection coefficient of irregular wave trains in order to characterize the efficiency of the absorption mechanism. In order to do so, the separation of the incident and reflected waves is necessary. The first work, based on two probes data, originates from Goda & Suzuki (1976) and allows the separation of both wave fields for regular and irregular waves. It consits of considering, in the case of reflection of a regular wave, that the wave heights records (noted η_1 and η_2) are constituted of the sum of the incident and the reflected components such as:

$$\begin{aligned}\eta_1(t) &= \eta_I(x = x_1, t) + \eta_R(x = x_1, t) \\ &= a_I \cos(kx_1 + \epsilon_I - \omega t) + a_R \cos(kx_1 + \epsilon_R + \omega t) \qquad (5.4)\\ \eta_2(t) &= \eta_I(x = x_2, t) + \eta_R(x = x_2, t) \\ &= a_I \cos(kx_2 + \epsilon_I - \omega t) + a_R \cos(kx_2 + \epsilon_R + \omega t) \qquad (5.5)\end{aligned}$$

Considering the trigonometric identities, we can develop the cos and write the following equations:

$$\begin{aligned}\eta_1(t) &= [a_I\cos(kx_1+\epsilon_I)+a_R\cos(kx_1+\epsilon_R)]\cos(\omega t)+[a_I\sin(kx_1+\epsilon_I)-a_R\sin(kx_1+\epsilon_R)]\sin(\omega t)\\ &= A_1\cos(\omega t)+B_1\sin(\omega t) \qquad (5.6)\\ \eta_2(t) &= [a_I\cos(kx_2+\epsilon_I)+a_R\cos(kx_2+\epsilon_R)]\cos(\omega t)+[a_I\sin(kx_2+\epsilon_I)-a_R\sin(kx_2+\epsilon_R)]\sin(\omega t)\\ &= A_2\cos(\omega t)+B_2\sin(\omega t) \qquad (5.7)\end{aligned}$$

$A_{1,2}$ and $B_{1,2}$ are the Fourier series coefficients for the wave number k. These coefficients can be obtained by applying the discrete Fourier Transform to $\eta_{1,2}$ signals and if $c_{1,2}$ is the FFT result then: $A_{1,2} = 2\,\mathrm{Re}(c_{1,2})$ and $B_{1,2} = -2\,\mathrm{Im}\{c_{1,2}\}$ These results lead to the determination of a_I and a_R:

$$a_I = \frac{1}{2|\sin(k\Delta x)|}\sqrt{(A_2 - A_1\cos(k\Delta x) - B_1\sin(k\Delta x))^2 + (B_2 + A_1\sin(k\Delta x) - B_1\cos(k\Delta x))^2} \qquad (5.8)$$

$$a_R = \frac{1}{2|\sin(k\Delta x)|}\sqrt{(A_2 - A_1\cos(k\Delta x) + B_1\sin(k\Delta x))^2 + (B_2 - A_1\sin(k\Delta x) - B_1\cos(k\Delta x))^2} \qquad (5.9)$$

where Δx is the distance between the two probes and where k is solution of the linear dispersion relation $\omega^2 = gk\tanh(kh)$. The reflection coefficient is calculated according to:

$$C_R = \frac{a_R}{a_I} \qquad (5.10)$$

In the case of incident irregular waves, by the mean of the hypothesis that they are constituted by the infinite sum of sine waves, we are able to calculate the previous coefficient for any wave number k and thus obtain $a_{I,R}$ in function of the frequency. The energy of the spectrum is then computed by;

$$E_{I,R} = \int_{f_{min}}^{f_{max}} |a_{I,R}|^2 \, df \qquad (5.11)$$

and finally,

$$C_R = \sqrt{E_R/E_I} \qquad (5.12)$$

f_{min} and f_{max} are the lower and upper limits chosen in order to avoid divergence at wave number $k\Delta x = n\pi$. Goda & Suzuki (1976) advise to take as lower and higher limits the frequencies corresponding to $\Delta x/\lambda_{max} = 0.05$ and $\Delta x/\lambda_{min} = 0.45$ respectively. This method is a good starting point in the evaluation of the reflection coefficients, but its application requires the waves to be linear. Newer methods have been designed to take care of it such as by C.-Y. Lin & Huang (2004) or Andersen et al. (2017).

Method by energy considerations It is known that the energy density per unit area of the mean free surface is equal to the sum of the kinetic energy and the potential energy such as Newman

(2017):

$$E = E_c + E_p = \rho \int_0^{h+\eta} \left[\frac{1}{2} \left(u_x^2 + u_z^2 \right) + gz \right] dz \tag{5.13}$$

where u_x and u_z are the horizontal and vertical fluid velocities respectively. For plane progressive and linear waves, this results yields to the following results:

$$E = \frac{\rho \omega^2 A^2}{4k} e^{2k\eta} + \frac{1}{2} \rho g \eta^2 \tag{5.14}$$

and if we consider small amplitude (such as $k\eta \ll 1$) then the total energy is proportional to the wave amplitude A. It allows to define a reflection coefficient based on the energy such as:

$$C_R^2 = \frac{E_R}{E_I} \tag{5.15}$$

where E_R is the total energy of the reflected waves and E_I is the total energy of the incident waves. In the case of the wave tank, we will compute its energy for the water phase according to:

$$E_c = \frac{1}{2} \rho \int_{X_G}^{X_A} \int_0^{h+\eta} \left(u_x^2 + u_z^2 \right) dxdz, \quad E_p = \rho g \int_{X_G}^{X_A} \int_0^{h+\eta} z dxdz \tag{5.16}$$

where u_x and u_z are the horizontal and vertical fluid velocities respectively. Note that during the computation of the potential energy, a terms appears corresponding to the energy of the water at rest such as:

$$E_0 = E_p(t=0) = \frac{1}{2} \rho L g h^2 \tag{5.17}$$

This term is of no interest and shall be omitted in the reported results. As the tank length is not constant in time since both generating and absorbing wavemakers moves at positions $X_G(t)$ and $X_A(t)$, a reference energy, which corresponds to the potential energy of the tank for a still water level retrieved by volume conservation considering these new positions, is defined as:

$$E_{ref}(t) = \frac{1}{2} \rho g \left(\frac{L^2 h^2}{X_A(t) - X_G(t)} \right) \tag{5.18}$$

Finally, the reflection coefficient is given according to:

$$C_R = \sqrt{\frac{|E_p(t_f) + E_c(t_f) - E_{ref}(t_f)|}{max(|E_p(t) + E_c(t) - E_{ref}(t)|)}} \tag{5.19}$$

where E_I and E_R are the incident and reflected wave energies, and t_f is the time when the error reaches and stays inside the 5% of the error band such as $|\epsilon(t \geq t_f)| \leq \max(|\epsilon(t)|) \times 5/100$ is verified. We make sure that at this time, no re-reflection on the absorbing wavemaker has occurred. Perfect wave absorption would lead to $E_{tot} = E_{ref}(t_f)$, but as some reflection happens this energy level is not reached. It is important to take into account the reference energy as the length of the wave tank is not constant thus impacting the general level of potential energy.

5.1.2.3. Preliminary results

In order to determine the efficiency and limits of the feedback strategy, an irregular wave train, an undular bore and regular waves cases were tested. The first example of the implementation of such absorption strategy for irregular waves is shown in figure 5.13. A wave train is generated by the wavemaker on the left with the help of a smooth velocity pulse function defined as:

$$U_G(t) = -\frac{S}{\tau}\,\mathrm{sech}^2\left(\frac{t-t_0}{\tau}\right) \tag{5.20}$$

with $S = 0.077$ m, $t_0 = 1.30$ s and $\tau = 0.342$ s. This function can be visualized in figure 3.7a. The wave train is moving in direction of the wave-absorber at the right end part of the wave tank, and is formed of a leading trough followed by wiggles (see time $t = 3.5$ s). The waves are then absorbed according to the feedback control strategy with an update of the absorption velocity at every time-step, and where the error at the wave-absorber wavemaker is plotted in figure 5.14a. The error alternates between positive and negative values causing the absorption velocity U_A, which is also shown in the same graph, to behave similarly. The error decreases to zero while the wave-absorber perform the cancelling action. The maximum error corresponds to 21% of the mean water level, that is to say at the limit of the non-linear portion of the plot of figure 5.5b. It results in an almost fully absorbed wave state at times $t = 7$ and 8 s, where the water surface is calm at every location of the wave tank. Note that a reflected wave will take a time greater than $t > 8$ s to arrive into the wave-absorber re-reflected at the left wavemaker. That means the error $\epsilon(t)$ falls to zero rapidly. In figure 5.13, in the last snapshot at $t = 8$ s, the black dashed curve was obtained with the controller off, thus the wave-absorber was at rest, allowing to qualitatively compare the efficiency of the absorption strategy.

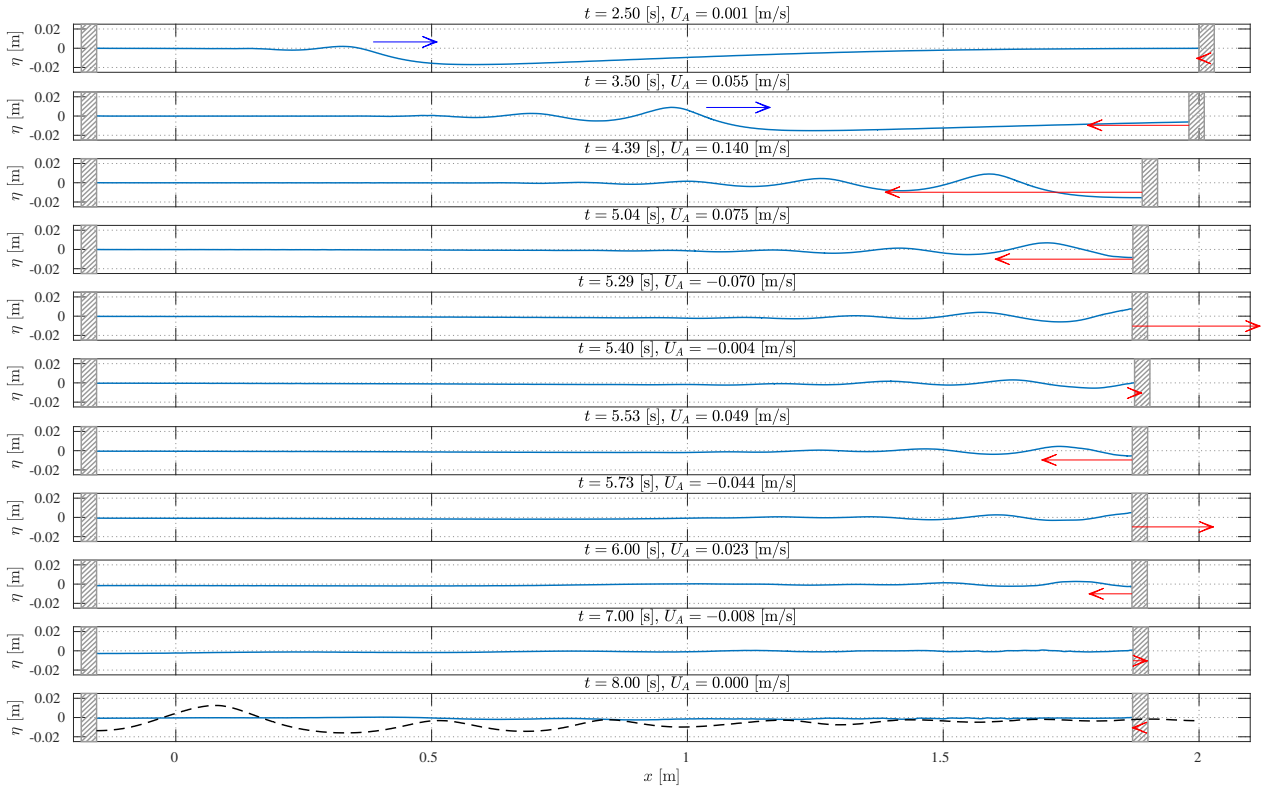

Figure 5.13: Wave profile η in function of the x-coordinate and for times from 2.50 to 8.00 s. For times $t = 2.20$ and 3.50 s, a blue arrow indicates the direction of the incident wave train. The active feedback absorber velocity and direction (in the frame of reference (x', z')) are shown with the red arrows. For the last time ($t = 8$ s), the wave state for the case without absorption is superimposed in the dashed black line.

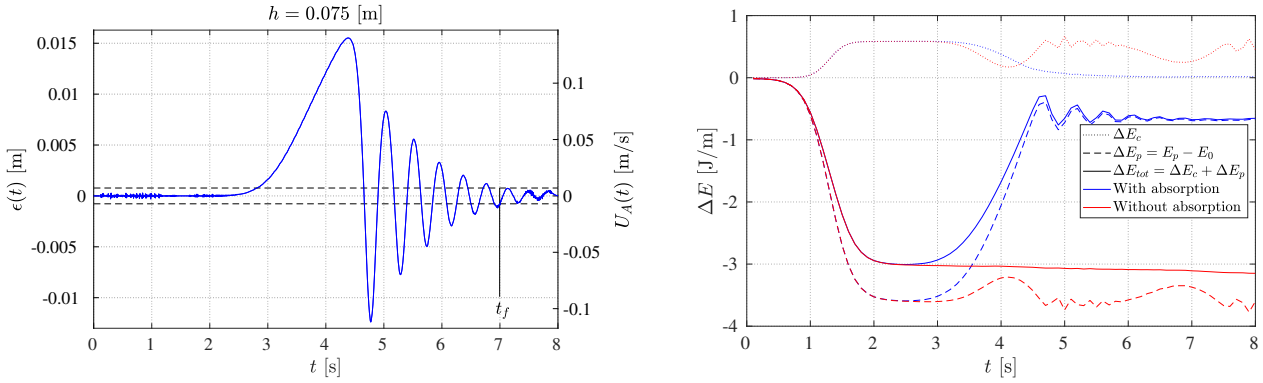

(a) (b)

Figure 5.14: Case of the absorption of an irregular wave train generated by equation 5.20 for a still water level $h = 0.075$ m. (a) Proportional controller error ϵ in function of time. The corresponding velocity of the wave-absorber (in the frame of reference (x', z')) is indicated in the second y axis on the right. The 5% error band are indicated in the black dashed curve and the corresponding final time $t_f = 7.00$ s is indicated. (b) Energy in function of time. Kinetic, potential and total energy are shown with reference to the initial energy in the tank E_0.

It is possible to compute the energy of the wave tank in order to evaluate (and propose) the absorption efficiency of our method. The computation of the reflection coefficient with the energy method leads to $C_R = 16\%$. Another analysis is carried out thanks to the separation of incident and reflected wave fields by means of the Fourier transform of two wave gauge data recordings at different tank locations (Goda & Suzuki, 1976). It leads to the value of $C_R = 15$ %, which is similar to the previous one and shows the attenuation in the wave absorption process. The waterfall plot of figure 5.15a helps to visualize the motion of the wavemakers as illustrated by the extension of the wave tank at the left during the wave generation, and the oscillations of the wave-absorber wavemaker as the incident waves make contact with the wall sensor. Finally, the efficiency of the process can be observed as the reflected waves are small compared to the initial waves. A comparison with the case without absorption is also plotted in figure 5.15b and shows that the wave height at the (still, controller off) wave-absorber wavemaker fully fluctuates between low $\eta_w < -0.025$ m, and high values $\eta_w > 0.03$ m. When the controller is turned on those fluctuations disappear and $\eta_w \to 0$ as a result of the absorption mechanism.

The second test case consists in an undular bore which is generated with a velocity square function defined as:

$$U_G(t) = U_0 \left(\Theta(t) - \Theta(t - t_0)\right) \tag{5.21}$$

with $U_0 = 0.2$ m/s, $t_0 = 2.5$ s and Θ is the Heaviside function, for a 4 m long wave tank and a still water level of $h = 0.075$ m. The undular bore, shown in figure 5.16, is generated on the left, propagates toward the wave-absorber wavemaker on the right and is absorbed according to the proportional strategy. In this case, the error is almost always negative at the wave-absorber wall, with variations due to the incoming bore wiggles, as shown in figure 5.17a. The starting error

is important due to the high amplitude incoming undular bore, but rapidly the controller action decrease it and make the stationary error converge to zero. In figure 5.17b the energy analysis is shown and a similar behaviour is observed as in the previous case, with an increase in the total energy during the wave generation and a constant level during the propagation stage ($0 \leq t \leq 2.5$ s for the first one and $2.5 \leq t \leq 4$ s for the second one).

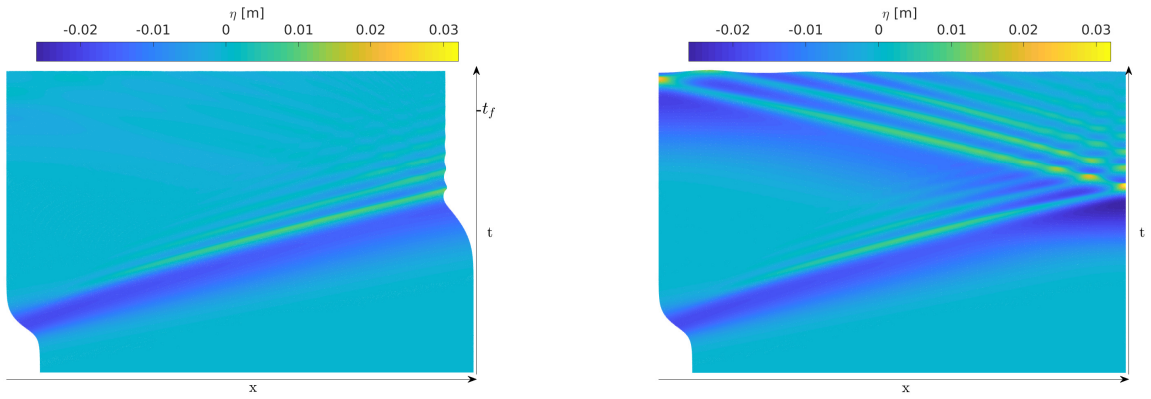

(a) (b)

Figure 5.15: Waterfall plot of the wave train propagating in the wave tank for a still water level of $h = 0.075$ m. The generating wavemaker follows the velocity defined by equation 5.20. (a) with active absorption, (b) without active absorption.

The total energy then decreases as long as the wave-absorber actuates and converges to the final energy which corresponds to the final still position of both wavemakers. An estimation of the reflection coefficient can be made with the energy analysis and conducts to $C_R = 10\%$. The analysis of the reflection coefficient by Goda & Suzuki (1976) leads to $C_R = 16\%$. The difference can be explained by the method of Goda & Suzuki (1976) which is not well suited for high amplitude non-linear waves as can be the undular bore. This analysis shows that the strategy is interesting and can effectively absorb non-regular waves even steep waves.

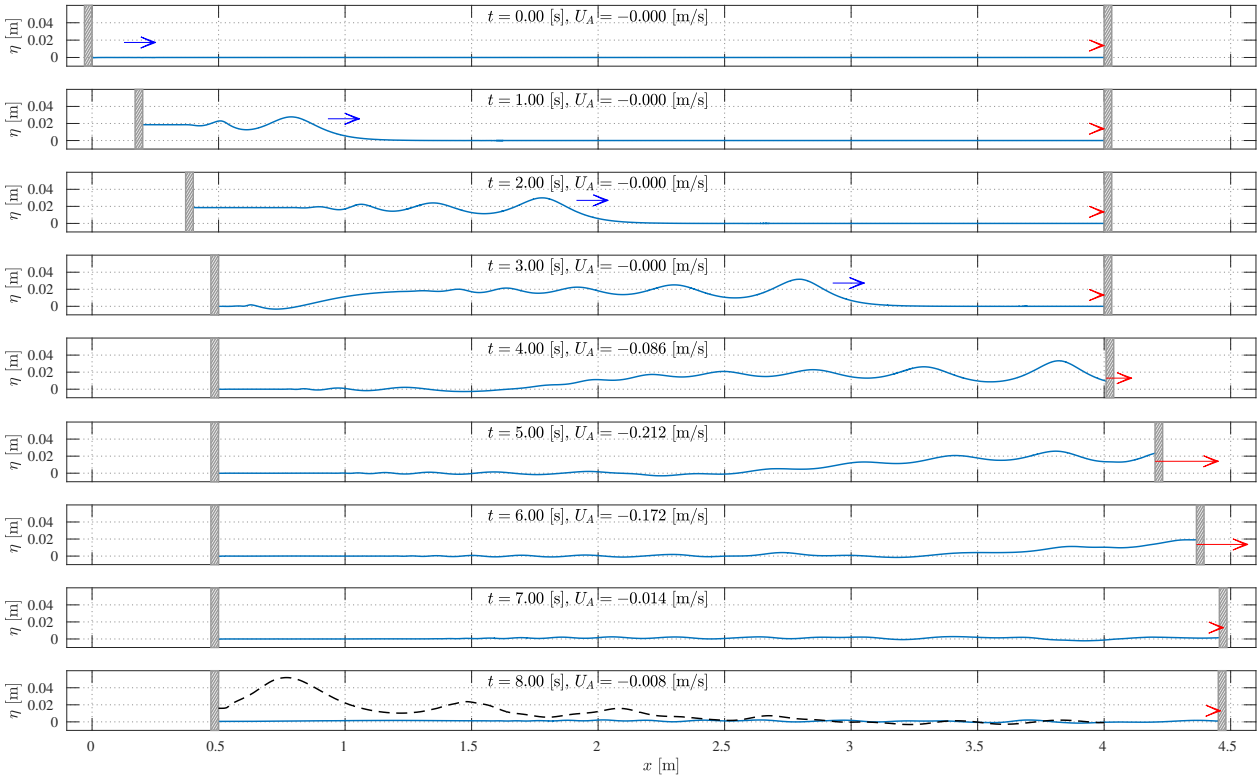

Figure 5.16: Wave profile η in function of the x-coordinate and for times from 0 to 8.00 s for the undular bore absorption. For times $t = 0$ and 3 s, a blue arrow indicates the direction of the incident wave train. The active feedback absorber velocity and direction (in the frame of reference (x', z')) are shown with the red arrows. For the last time ($t = 8$ s), the wave state for the case without absorption is superimposed in the dashed black line.

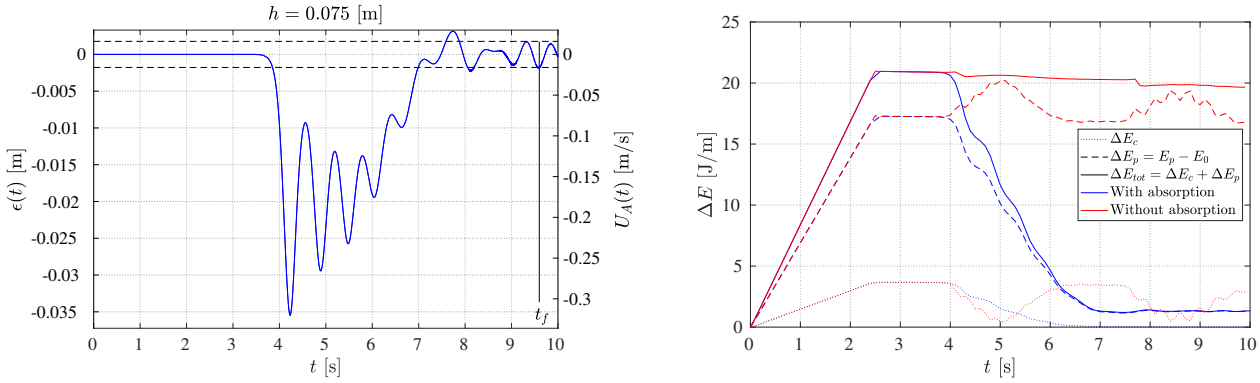

Figure 5.17: Case of the absorption of an undular bore generated by equation 5.21 for a still water level $h = 0.075$ m. (a) Proportional controller error ϵ in function of time. The corresponding velocity of the wave-absorber (in the frame of reference (x', z')) is indicated in the second y axis on the right. The 5% error band are indicated in the black dashed curve and the corresponding final time $t_f = 9.49$ s is indicated. (b) Energy in function of time. Kinetic, potential and total energy are shown with reference to the initial energy in the tank E_0.

Finally, tests are carried out on harmonic cases, consisting of the absorption of regular waves generated as for the wave propagation mesh study of section 3.2.1. The excitation functions and general set-ups are reported in table 5.2. The reflection coefficient is calculated according to Goda & Suzuki (1976) and leads to reflection coefficient lower than 10% for both cases, showing the efficiency of the proposed strategy in order to absorb waves. A summary of all test cases is reported in table 5.2 and the reflection coefficients are given.

When we considered the steady state value of the step response, η_{ss} it was shown that the water level at wavemaker reached a constant value after a short time, t_s, at which $\eta_w/h = Fr$, as shown in figure 5.4b. The absorption velocity and constant coefficient K may be alternatively defined according to: $U_A = K\epsilon(t)$ with $K = \sqrt{g/h}$. This coefficient was already given by Schäffer & Jakobsen (2003) and was deduced from a mathematical study of the problem which is laid out in appendix B. The choice of the first strategy based on the overshoot ($K = 1/1.267\sqrt{g/h}$) rather than this last one is justified by the peak time t_p associated to the overshoot which is shorter than the settling time t_s associated to the steady-state as shown in figure 5.6, or better said the wavemaker moving at constant speed generates a transient wave which is used to cancel the incident wave.

The active wall driven by a feedback controller has proven to be useful not only to cancel wave reflections but also seems to attenuate high amplitude irregular wave impacts as in the undular bore example. In a future work we will push further the absorption strategy to effectively reduce the consequences of extreme high amplitude waves using controllers for non-linear waves.

Wave type	Piston velocity function $U_G(t)$	Parameters	Reflection coefficient C_R	
			Goda & Suzuki (1976) method	Energy method
Irregular Wave Train	$-\frac{S}{\tau}\,\mathrm{sech}^2\left(\frac{t-t_0}{\tau}\right)$	$h = 0.075$ m, $S = 0.077$ m, $\tau = 0.342$ s, $t_0 = 1.30$ s, $L = 2$ m	15%	16%
Undular Bore	$U_0\left(\Theta(t) - \Theta(t-t_0)\right)$	$h = 0.075$ m, $U_0 = 0.2$ m/s, $t_0 = 2.5$ s, $L = 4$ m	16%	10%
Harmonic	$X_0\pi f \sin(2\pi f t + \delta)$	$h = 0.15$ m, $X_0 = 0.004$ m, $f = 1.25$ Hz, $\delta = -\pi/2$, $L = 8$ m	5%	-
Harmonic	$X_0\pi f \sin(2\pi f t + \delta)$	$h = 0.05$ m, $X_0 = 0.04$ m, $f = 0.5$ Hz, $\delta = -\pi/2$, $L = 8$ m	9%	-

Table 5.2: Test cases for the absorption controller and reflection coefficients.

5.1.3. Conclusion

In this work we performed numerical simulations of a two dimensional wave tank in order to study the piston-type wavemaker initial-value problem and wave generation using the free and open-source code *OpenFOAM*. The numerical model reproduced the motion of a solid body piston-type wavemaker by moving a solid boundary driven by an external arbitrary signal waveform. We considered a full viscous model solving the unsteady Navier-Stokes equations on the basis of a two phase flow strategy and the volume of fluid method to capture the free surface dynamics. Velocity steps signals (Heaviside functions) were applied to the piston-type wavemaker, generating a pulse-like wave which propagated along the tank followed by smaller waves or wiggles, which was identified as an undular bore. Recording of wave elevation time series at the moving wall and in different tank locations were compared with theoretical data, providing a very good agreement and proving the capabilities of *OpenFOAM* solver *interDyMFoam* to simulate two phase flows with wave propagation involving both free surfaces and moving boundaries. Wave elevation at the piston wall was found to be in close similarity with the time response of second order system found in feedback theory. In particular, the overshoot, rise time, peak, and settling time scales performed very closely with the theory. The scaling found for water elevation at the piston wall at different step velocities and mean still water levels was in close agreement with the theory for low Froude numbers (Joo et al., 1990). At higher Froude numbers the scaling differs considerably from the theory, being unable to take into account the main wave dynamics. The resulting main wave pulse is generated and detaches from the piston wall at the same time as the overshoot takes place in the wall elevation signal, thus we call this wave the overshoot-wave. Results along the tank downstream agree with potential theory. The overshoot-wave propagates faster than piston velocity increasing its velocity and reaching asymptotically the shallow water celerity downstream the tank. As we solved full viscous equations, we were able to quantitatively determine the power input during the

step response associated to the wave generation process using the entire stress tensor at the piston wall. Net piston forces were obtained integrating pressure and shear stresses on the piston wall. A power scaling was found for different mean still water levels and step velocities as a function of the Froude number.

Finally, in this work we proposed a feedback proportional controller driving a secondary piston for wave absorption, where the controller gain was determined from the wavemaker step response. The feedback controlled piston method proved to be very efficient on both regular and irregular wave absorption. This novel approach provided the basis from which more complex active wave generation/absorption strategies can be further implemented on numerical as well as experimental wave tanks to improve efficiency under the influence of different parameters such as the water depth, the wave steepness and negative velocity steps.

5.2. Undular bore structure interaction with a vertical square cylinder

The previous study allowed to characterize the wavemaker in a 2D numerical wave tank without any cylinder placed inside. In this section we study the wave-induced vortex generation and shedding from a vertical square cylinder interacting with an upcoming undular bore wave train. A numerical simulation, solving the full turbulent viscous 3D Navier-Stokes equations is carried out in order to study and characterize both the undular bore wave properties and the vortex dynamics during the interaction. No base flow is set-up and the undular bore is generated by the impulsive translational motion of a piston wavemaker performed on a laboratory scale numerical wave tank. The piston motion leads to the formation of a neat propagating wave train which was fully characterized. While the undular bore interacts with a downstream rigid square cylinder, coherent structures form at the four cylinder's edges which are triggered by the wave motion, leading to a vortex shedding frequency which matches the wave instantaneous frequency. Filamentary vertical vortices are observed extending along the entire water column from the free-surface to the seabed. At the rear downstream face of the cylinder, the pairing of two vortices is observed in close similarity with the Oseen vortex pair. These vortices are present during the whole simulation and are submitted to the mechanical forcing and downstream advection by the undular bore induced flow.

5.2.1. Undular bore generation

In order to generate undular bores, the most common technique is a water discharge from a reservoir by opening a gate (Yeh et al., 1989; Treske, 1994; Chanson, 2010; Shi et al., 2020). This method repeatability is however not fully satisfying. We propose to generate the undular bores thanks to a velocity step which is applied to the piston wavemaker, as studied previously in section 5.1. This strategy was first suggested by Stoker (1957). In practice, the step is not perfect since wavemakers in real facilities cannot instantaneously reach the step velocity, and that is why this one is ramped during the very first instants of the wavemaker motion. The ramp also avoids the eventual formation of breaking waves at the first instants of the piston motion. The velocity step is applied during the whole simulation leading to an undular bore without end, that is to say that the water level at the wavemaker is constant during the whole simulation, with the exception of the very first instants (see section 5.1). The piston velocity as a function of time is plotted in figure 5.18 as well as its position. Its mathematical definition is:

$$U_G(t) = \begin{cases} \frac{t}{\Delta t} U_0, & t \leq \Delta t \\ U_0, & t > \Delta t. \end{cases} \tag{5.1}$$

where Δt is the ramp duration equal to 0.1 s and U_0 is the final constant velocity $U_G(t > \Delta t) = 0.1$ m/s. The tank end wall is kept still, although the simulation stops before any reflection reaches

back the square cylinder.

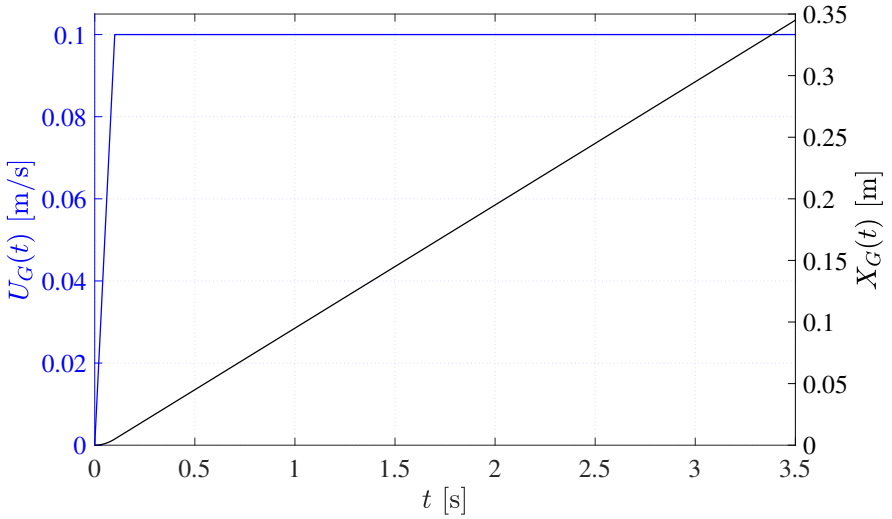

Figure 5.18: Piston wavemaker velocity $U_G(t)$ and displacement $X_G(t)$ as a function of time.

5.2.2. Incident wave characteristics

The numerical simulation, as shown in figure 5.19, can be described as follows: (i) the water level, set at $h = 0.05$ m, is at rest at $t = 0.00$ s, (ii) at $t > 0$ s, the piston wavemaker is put in motion according to equation 5.1 and a deformation of the free-surface takes place, (iii) the undular bore is formed and propagates along the wave tank for times $t < 1.00$ s, (iv) the undular bore interacts with the vertical square cylinder for later times, (v) the undular bore free surface is modified after being perturbed by the cylinder.

It is chosen, for its simplicity of implementation, to detect the water/air interface at a given x position by finding the VOF variable $\alpha = 0.5$ position through linear interpolation. It allows to retrieve the free-surface position, as shown in figure 5.20a. In this figure, besides the free-surface, the velocity field below the undular bore is represented, as well as the local wave steepness defined as $d\eta/dx$. The undular bore is composed of a main bore (or water slug) of height $a = 0.0074$ m on which are superimposed wiggles. This leads to a bore height to mean water level $a/h = 0.148$, value lower than the experimental result of $a/h = 0.28$ from Favre (1935) marking the limit between non-breaking and breaking undular bore. The main wave is $\eta = 0.0102$ m high with reference to the main water level, and so the wave height to mean water level ratio $H/h = 0.20$ and the steepness of the wave is relatively high, specially at the transition between the wave crest and troughs, reaching value as high as 0.06, so that linear wave theory cannot be used. The maximum velocity is $U_x = 0.151$ m/s and corresponds to the particles at the top of the main wave (1). A full summary of these parameters can be found in table 5.3. The wave field is horizontal close to the seabed and the Z-component of the velocity vector field gains amplitude as it is closer to the free-surface. This is typical of the shallow water condition. Finally, close to the wavemaker, the velocity

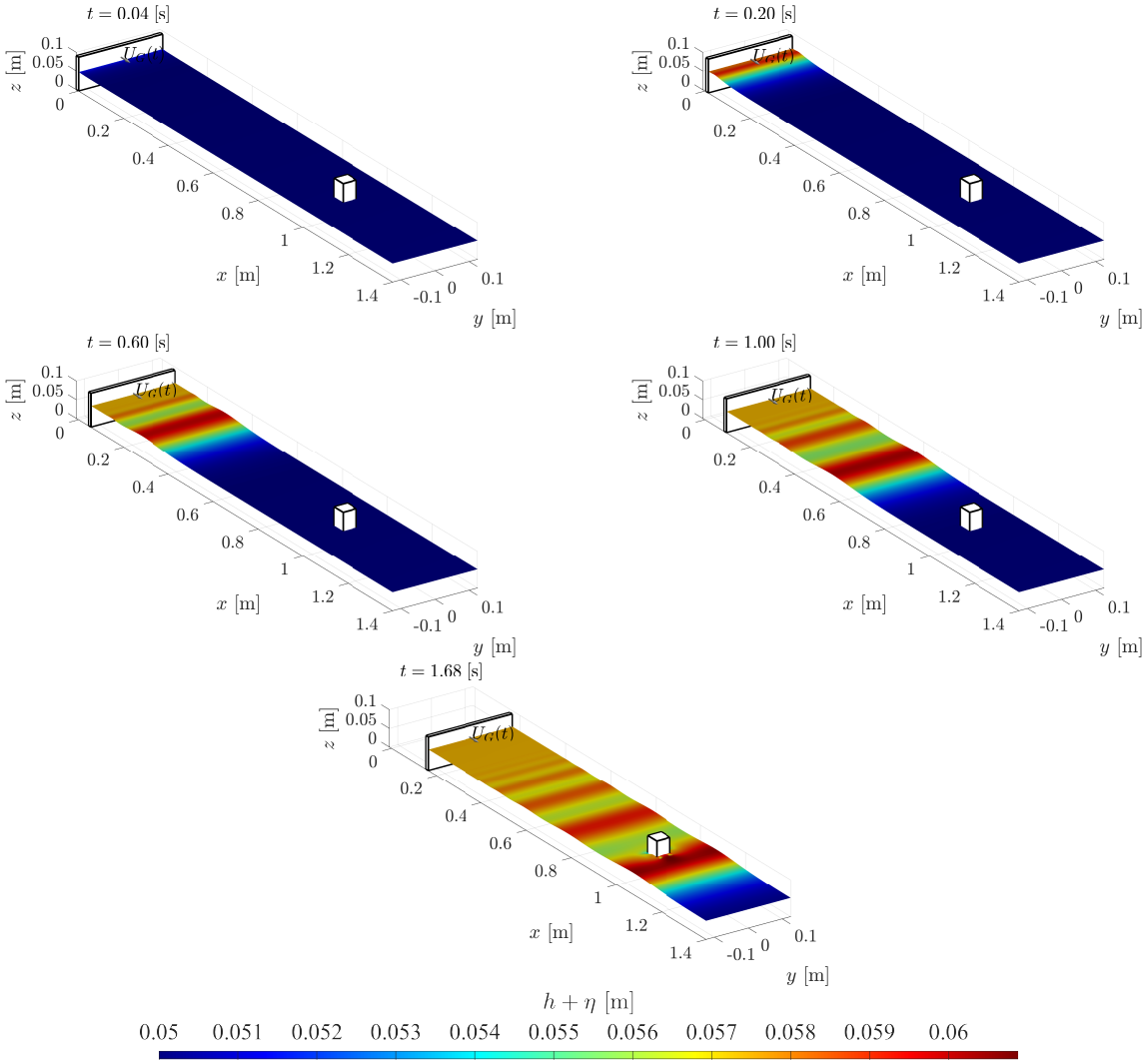

Figure 5.19: Undular bore generation, propagation and interaction with a square vertical cylinder. The wave tank is cropped at $y = \pm 0.12$ m, and $x = 1.4$ m. The different stages of the experiment can be described as: (i) the water level, set at $h = 0.05$ m, is at rest at $t = 0.00$ s, (ii) at $t > 0$ s, the piston wavemaker is put in motion according to equation 5.1 and a deformation of the free-surface takes place, (iii) the undular bore is formed and propagates along the wave tank for times $t < 1.00$ s, (iv) the undular bore interacts with the vertical square cylinder for later times, (v) the undular bore free surface is modified after being perturbed by the cylinder.

field is horizontal, except close to the seabed where a vertical motion is detected. The velocity profile is quite constant along the vertical showing the shallow to intermediate water conditions of the experiment (around 20% of difference between the top and lower part of the profile). As the wiggles are closer to the forcing wavemaker, the velocity profile tends to become straighter and eventually straight for the closest wave, except for the upper part of the profile which shows and sudden increase in the velocity. The wave particle horizontal velocities below the crests and outside of the seabed boundary layer are greater than the wavemaker step velocity but they converge to this former as the crests are closer to the wavemaker. The influence of the seabed boundary layer, which is fully resolved in the simulation in the vicinity of the square cylinder, can be seen at small z as the velocity rapidly drops to 0.

H [m]	a [m]	λ [m]	a/h	h/λ	c_p [m/s]	Fr	H/h	$U_{x,max}$ [m/s]	$(d\eta/dx)_{max}$
0.0102	0.0074	0.255	0.148	0.20	0.769	1.10	0.20	0.151	0.064

Table 5.3: Incident wave characteristics.

The phase celerity of the bore can be computed by looking at the position of the main wave. The results are shown in figure 5.21 where the instantaneous phase celerity is plotted as well as the theoretical shallow water wave celerity defined as $C_p = \sqrt{g(h+H)}$. A least square fit is carried out and is based on the following function, typical of first order systems:

$$C_p = C_{p_0}\left(1 - e^{-\frac{t}{\tau}}\right) \tag{5.2}$$

It leads to a time constant $\tau = 0.22$ s and $C_{p_0} = 0.745$ m/s. This last phase velocity shows a 3.2% error with the theoretical shallow water wave celerity. It can be observed that the bore wave phase celerity is transient during the first instant of the bore generation before it reaches a constant value which is the theoretical wave phase celerity for shallow water. This results allows us to be confident in the mechanism for both wave generation and propagation during the numerical simulation. From these results, we are able to determine the incident wave Froude number, often used to characterize the bore, as: $Fr = c_p/\sqrt{gh} = 1.10$. This value is characteristic of smooth non-breaking undular bore in a rectangular channel as observed in the experiments of Treske (1994).

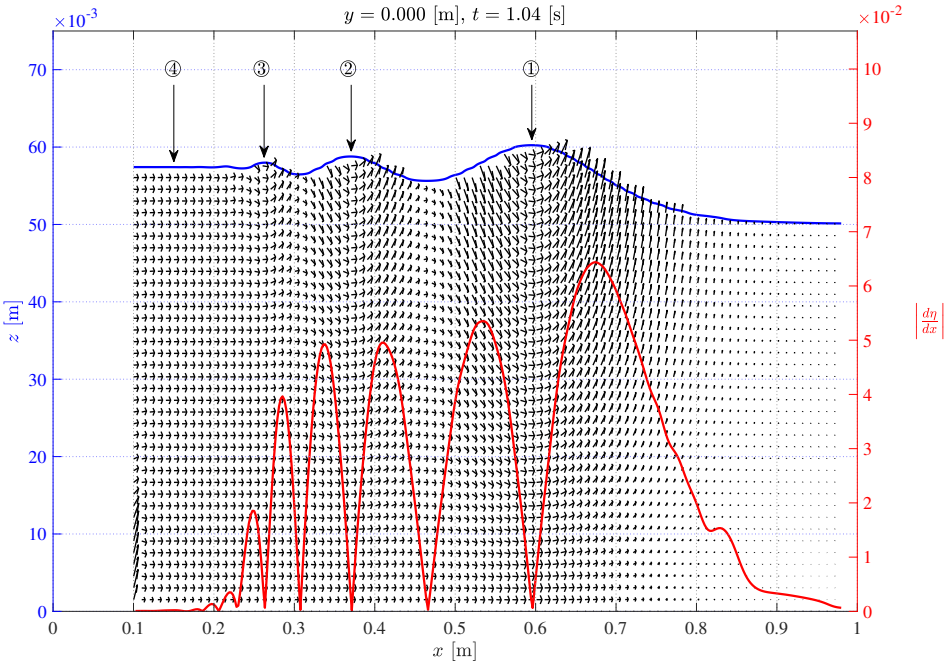

(a)

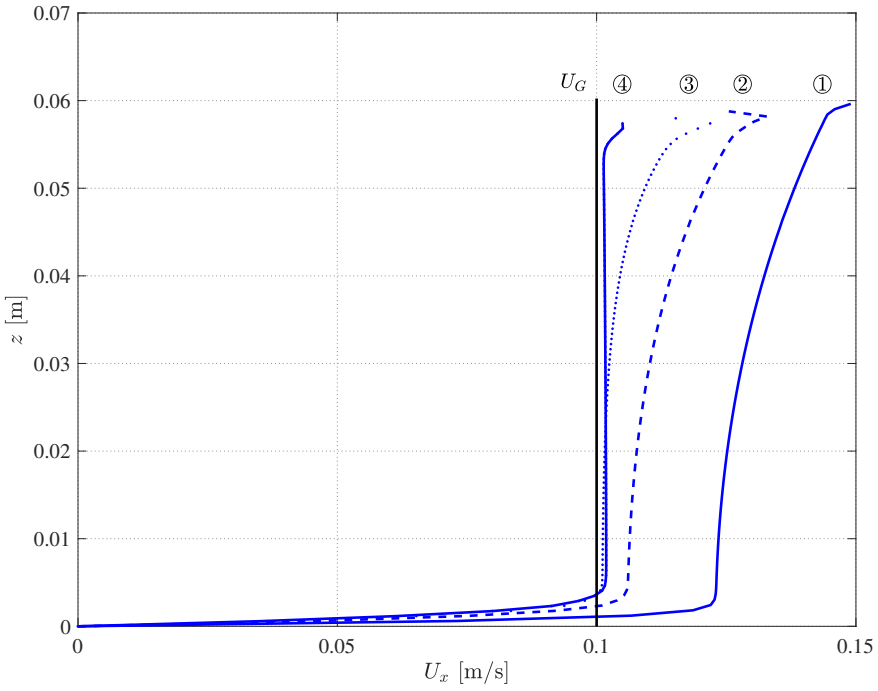

(b)

Figure 5.20: (a) Undular bore profile $\eta(x)$ for $t = 1.04$ s and $y = 0$ m. On the same graph, the velocity field is superimposed (black arrows) as well as the local wave steepness $\partial\eta/\partial x$. The points (1), (2), (3) and (4) are located at the crests of the wiggles and used in the characterization of the vertical profile of the horizontal velocity of figure 5.20b. (b) Horizontal velocity profile $U_x(z)$ at vertical (1), (2), (3) and (4) corresponding to the crests of the undular bore.

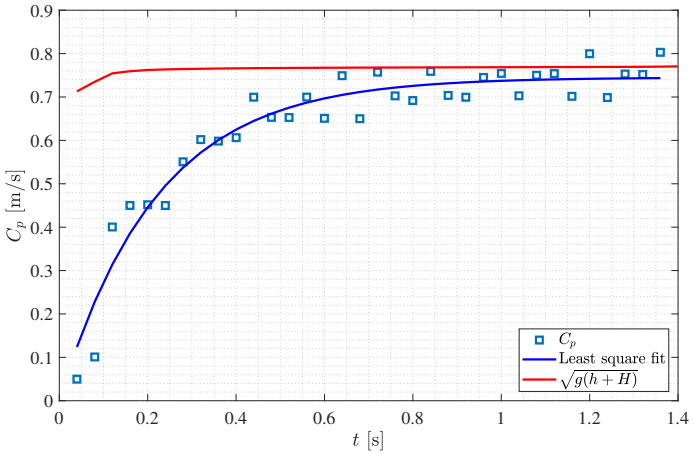

Figure 5.21: Phase celerity $c_p(t)$ of the undular bore (computed from the main wave x-position) as a function of time. The wave shallow water theoretical phase celerity $C_p = \sqrt{g(h+H)}$ is also shown in red.

Both vertical and horizontal velocity at three vertically aligned points ($z = 0.01, 0.025, 0.05$ m) for $x = 0.80$ m and $y = 0.00$ m are presented in figure 6.10 and 5.23 in their dimensionless version. The horizontal velocity can be interpreted as a step of velocity with wiggles at the top, as the change from rest to maximum value is sudden. The wiggle periods follow the ones of the wave height shape, with an increase in the frequency as the bore passes by the probe location. The horizontal velocity amplitude decreases as the measurement point is closer to the seabed, in agreement with figure 5.20b. This characteristic is very close to the wave and current superposition. The vertical wave orbital motion is created by the oscillations of particles from high amplitude to low amplitude as the bore passes by, leading to a final configuration of quasi-1D flow (or current). As the water depth increases, orbital motion becomes flatter with vertical velocities close to 0. Closer to the free-surface, the vertical motion becomes quite important, reaching around one third of the horizontal velocity amplitude.

5.2.3. Vortex generation

When the undular bore reaches the square cylinder, vortices are generated at its four edges and the horseshoe vortex can be observed at the cylinder front. In order to visualize the creation of the vortices, the Q-criterion (Hunt et al., 1988) isosurface (with $Q = 100$ s^{-1}) is shown in figure 5.24, for times between $t = 1.52$ to $t = 3.44$ s. The Q-criterion is defined as:

$$Q = \frac{1}{2}\left(||\boldsymbol{\Omega}||^2 - ||\boldsymbol{S}||^2\right) \tag{5.3}$$

where $||\boldsymbol{\Omega}|| = \left[\mathrm{Tr}\left(\boldsymbol{\Omega}\boldsymbol{\Omega}^{\mathrm{T}}\right)\right]^{\frac{1}{2}}$, $||\boldsymbol{S}|| = \left[\mathrm{Tr}\left(\boldsymbol{S}\boldsymbol{S}^{\mathrm{T}}\right)\right]^{\frac{1}{2}}$. $\boldsymbol{\Omega}$ and $\boldsymbol{S}$ are the skew-symmetric and symmetric component of $\nabla \boldsymbol{U}$ respectively.

Q-criterion is useful as it compares the local vorticity and the shear rate. This figure allows to show that the CFD model is able to both capture the free-surface evolution and the formation

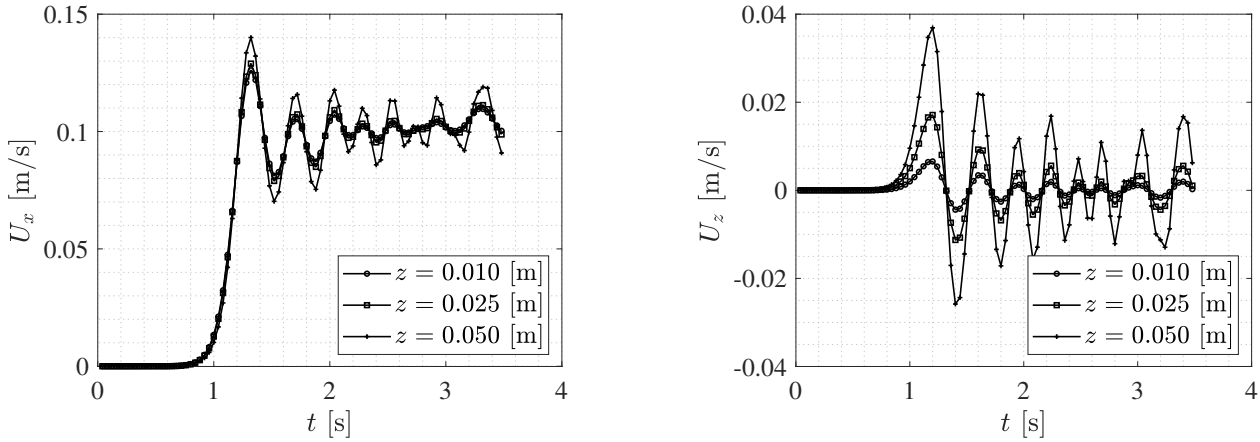

Figure 5.22: Velocities in function of time at three vertically aligned points corresponding to $z = 0.01, 0.025, 0.05$ m, $x = 0.80$ m and $y = 0.00$ m. (a) Horizontal velocity $U_x(t)$. (b) Vertical velocity $U_z(t)$.

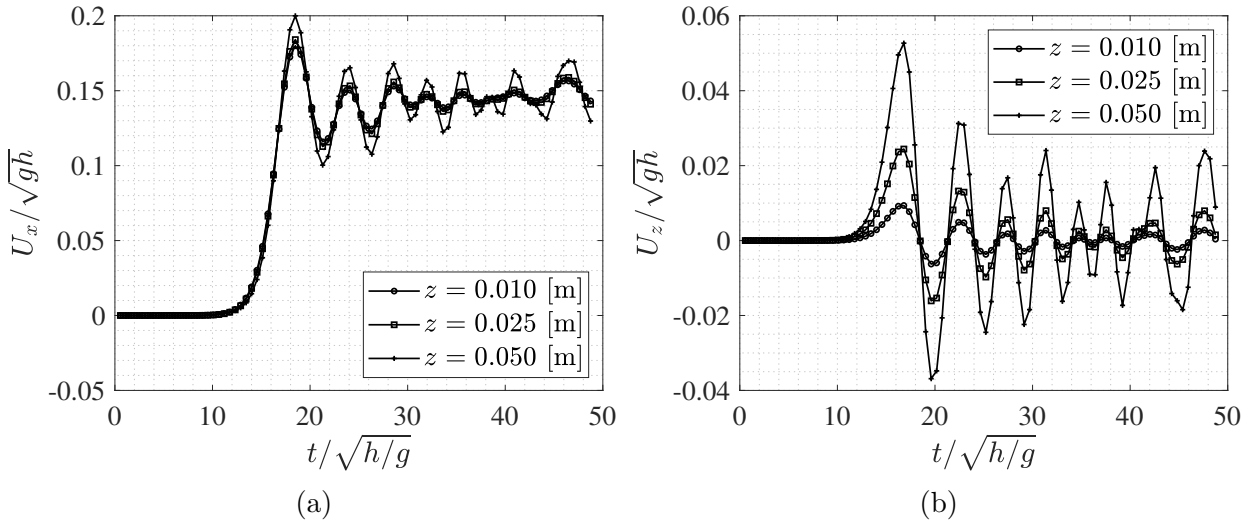

Figure 5.23: Dimensionless velocities in function of time at three vertically aligned points corresponding to $z = 0.01, 0.025, 0.05$ m, $x = 0.80$ m and $y = 0.00$ m. (a) Dimensionless horizontal velocity $U_x(t)$. (b) Dimensionless vertical velocity $U_z(t)$.

of coherent structure for the wave-structure interaction. We are able to witness the formation of the vortices at the edges of the square cylinder, for times $t = 1.52$ s and $t = 1.68$ s as well as the plugholes vortices especially at times 1.68 s and 1.84 s. We can observe the generation of the vortices at the edges as for every wave passing by the cylinder the rotation of water particle initiates at the edges for example at times $t = 1.52$, 2 and 2.92 s. As for the vortices downstream of the cylinder, the Q-isosurface is fairly vertical in the whole water depth while the Q isosurface rapidly deforms for the vortices generated at the side of the cylinder.

With the purpose of visualizing the vortices which are created at the side and downstream of the vertical square cylinder, the instantaneous streamlines are plotted below the free-surface in figure 5.25 for time $t = 1.84$ s. In particular, it allows to visualize the 3D characteristic of the flow: if the streamlines are really close one another close to the seabed, demonstrating the quasi 2D feature of the flow, closer to the interface the flow has an important third component. The vortex tube streamlines show also zones close to the interface where the water particle descend from the interface to the seabed while the particles in lower zones are rising at upper zones.

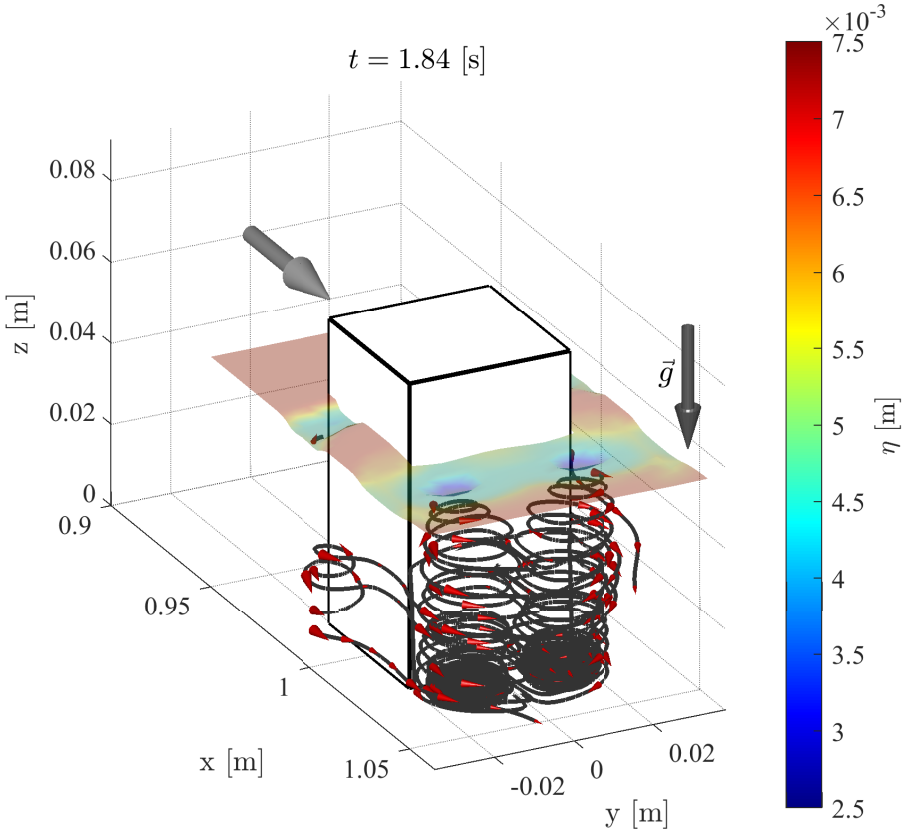

Figure 5.25: Instantaneous streamlines for t = 1.84 s. The wave height is superimposed and the scale is given by the color bar at the right. The black arrow indicates the wave propagation direction.

In order to confirm the extension of the vortices from the free-surface to the seabed, we plot in

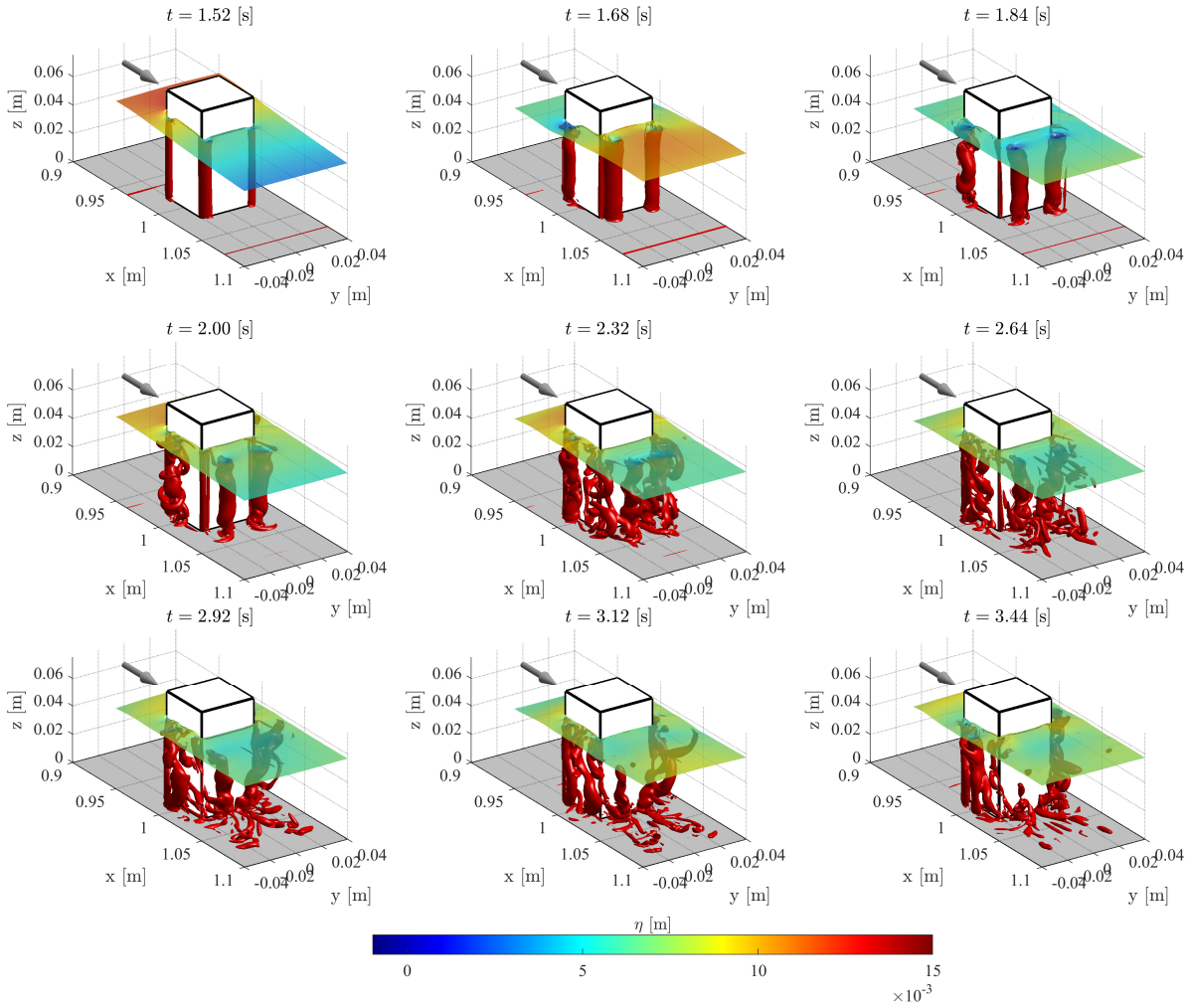

Figure 5.24: Q-criterion (Hunt et al., 1988) isosurface ($Q = 100$ [s^{-1}]) in red and free-surface for times $t = 1.52, 1.68, 1.84, 2.00, 2.32, 2.64, 2.92, 3.12, 3.44$ s. The grey arrow indicates the wave propagation direction.

figure 5.26 and 5.27 the z-component of the vorticity field in the $x-y$ plane close to the square cylinder and for three different vertical levels: at the first grid point from the seabed ($z = 0.195$ mm), at half the mean water level ($z = h/2$) and at the free surface ($z = h + \eta$). The color scale stops at ± 100 s^{-1} but the vorticity value at the first grid point from the square cylinder can reach values as high as 1300 s^{-1}, showing that the vortical structure are generated at the walls. On the same figures the isolines $Q = 100$ s^{-1} are superimposed which allow a clearer identification of the vortical structure. We are able to confirm the formation of vortices through the whole water column even if they tend to disappear or become less strong at zones close to the interface. The vorticity sign differs from the positive y half-plane and the negative one, so that the vortices direction of rotation is opposite, with vortices rotating clockwise in the positive y half-plane and anticlockwise in the negative y half-plane. The concentration of the vertical vorticity differs also, due to the 3D motion of the wave, as it is much more localized at the seabed, where the flow is much closer to a 2D flow, than close to the interface where the flow is fully 3D as the waves pass by. The vorticity at the interface is then not necessarily concentrated at the vortex center, and a look at the velocity field is necessary to determine the vortex position. If the vortices generated at the rear edges downstream of the cylinder remains close to the cylinder during the whole simulation (as seen at the seabed) and constitute a pair of counter-rotating vortices, numerous vortices are generated at the sides of the cylinder and are advected by the flow, before they eventually disappear. Downstream of the cylinder, secondary vortices appear far from it at times superior to 2.64 s which is visible essentially close to the seabed, which corresponds to vortices generated at the rear edges which have escaped the influence zone of the first vortices.

In order to get an idea of the location of the forming vortex centres, the velocity field can be superimposed to the vertical vorticity field in figure 5.28, for $z = h/2$. At the first instants of the interaction between the undular bore and the square cylinder, recirculation zones appear at both the side of the cylinder generated at the front edges, while others take place at the back due to the presence of the rear (trailing) edges. These recirculation spots eventually detach from the cylinder walls and form vortices which are advected by the flow for the ones at the cylinder sides while the ones at the cylinder rear face stay relatively stationary. The side vortices are then advected and finally disappear at the level of the rear edges while the rear vortices are present during the whole interaction with the wave. After the generation of the first vortices, shedding appears at both front edges but the vortices at the side rapidly disappear whereas the ones at the rear edges are advected in the wake of the cylinder, and are not immediately identifiable as they pass by the influence zone of the main rear vortices. We observe the pairing of counter-rotating vortices in the cylinder wake as they appear to interact with each other and evolve together with symmetrical trajectories. The phenomenon is studied in depth in section 5.2.6.

5.2.4. Free surface at cylinder and pressure forces

In this section, the undular bore free-surface deformation due to the vertical square cylinder interaction is presented as well as the pressure forces which apply to the cylinder. The generation

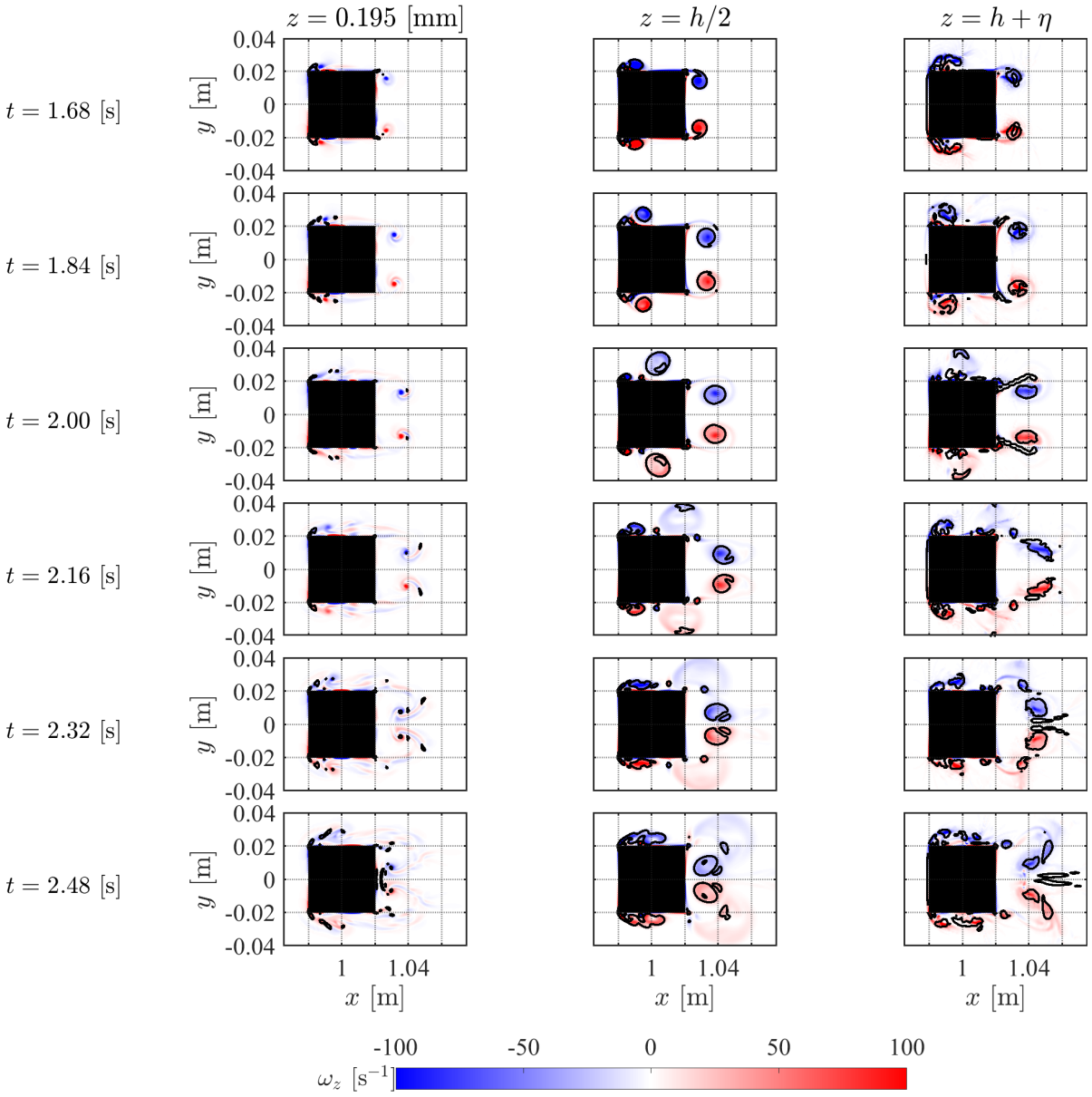

Figure 5.26: Z-component of the vorticity field in the x-y plane close to the square cylinder and for three different z-levels: at the first grid point from the seabed ($z = 0.195$ [mm]), at half the mean water level ($z = h/2$) and at the free surface ($z = h + \eta$). The displayed times ranges from 1.68 s to 2.48 s. Later times are shown in figure 5.27. The undular bore propagates in the increasing x-direction. The black contours represent the isolines $Q = 100$ s^{-1}.

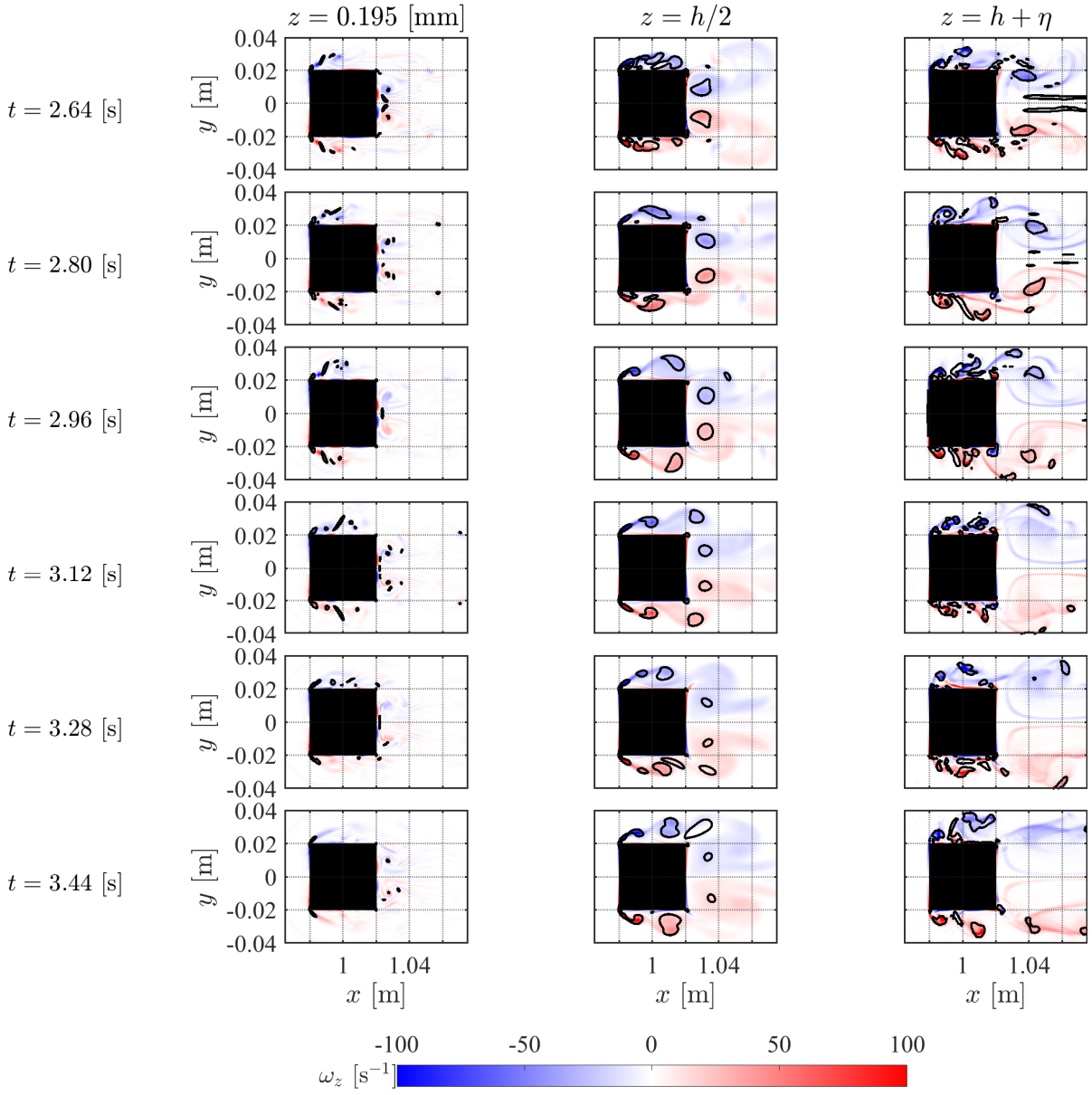

Figure 5.27: Z-component of the vorticity field in the x-y plane close to the square cylinder and for three different z-levels: at the first grid point from the seabed ($z = 0.195$ [mm]), at half the mean water level ($z = h/2$) and at the free surface ($z = h + \eta$). Time ranges from 2.64 s to 3.44 s. The undular bore propagates in the increasing x-direction. The black contours represent the isolines $Q = 100$ s^{-1}.

of plughole deformation is presented and the pressure forces are computed on the cylinder resulting in a net horizontal transient force in the undular bore propagation direction. Results are then compared with available empirical data from previous studies.

The free-surface elevation in the $x - y$ plane is presented in figure 5.29, for times ranging from 1.44 to 3.44 s. We observe the undular bore approaching the square cylinder from the left to the right and the interaction with this last one leads to a deformation of the bore due to diffraction, as the wave crests and trough are no longer aligned with the y-direction. The interaction between the undular bore and the vertical square cylinder starts around $t = 1.50$ s when the blockage effect of the centered vertical cylinder increases the water level at the front face (run-up) of the cylinder to higher levels than the maximum wave height. The main wave generates vortices originating from its four vertical edges and which are traduced by concentric change in water elevation at both sides of the cylinder as well as its back.

These vortices are similar to plughole vortices which are typical of water sink (Ahmed & Lim, 2017). The plugholes disappear quite rapidly for the vortices generated at the front edges (they are present until $t = 1.76$ s), while the ones generated at the rear of the cylinder can be observed almost the whole simulation, only disappearing at $t = 2.80$ s. At the front edges, new plughole vortices can be seen at latter times ($t > 1.92$ s) but with higher water levels (or lower intensity). The free-surface flow exhibits a symmetrical behaviour in general, even if some asymmetries can be viewed especially at time $t = 1.76$ s where the right plughole vortex generated at the front edges is almost nonexistent whereas the one at the opposite side can be easily identified.

The run-up, or maximum water height at the front face, as well as the unbalance between the water levels between the front and rear faces lead to the creation of a force in the x-direction. The maximum run-up is observed at $t = 1.48$ s which also corresponds to the maximum pressure force applying on the square cylinder, whose value is estimated at 0.12 N, as displayed by figure 5.30a. As the bore continues its path, we observe oscillations of the water level at the front and back faces, conducing to positive and negative forces, with however stronger positive forces. The undular bore can be seen as a transient phenomena where the main wave oscillating forcing at the first instant of the interaction with the square cylinder switches to a constant current forcing as shown in the x-velocity recording of figure 5.23.

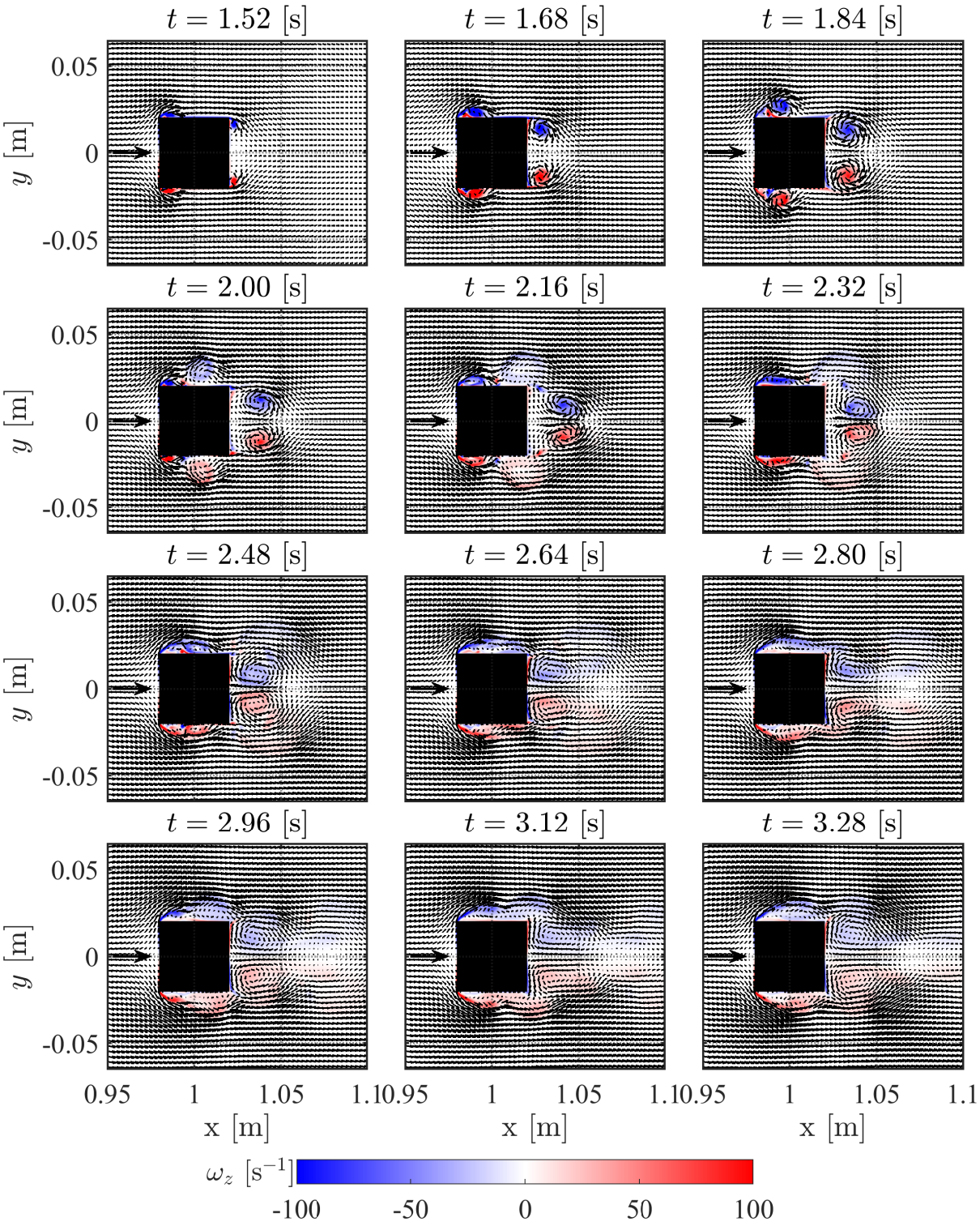

Figure 5.28: Velocity field and vorticity in the $z = h/2$ plane. The black arrow indicates the wave propagation direction.

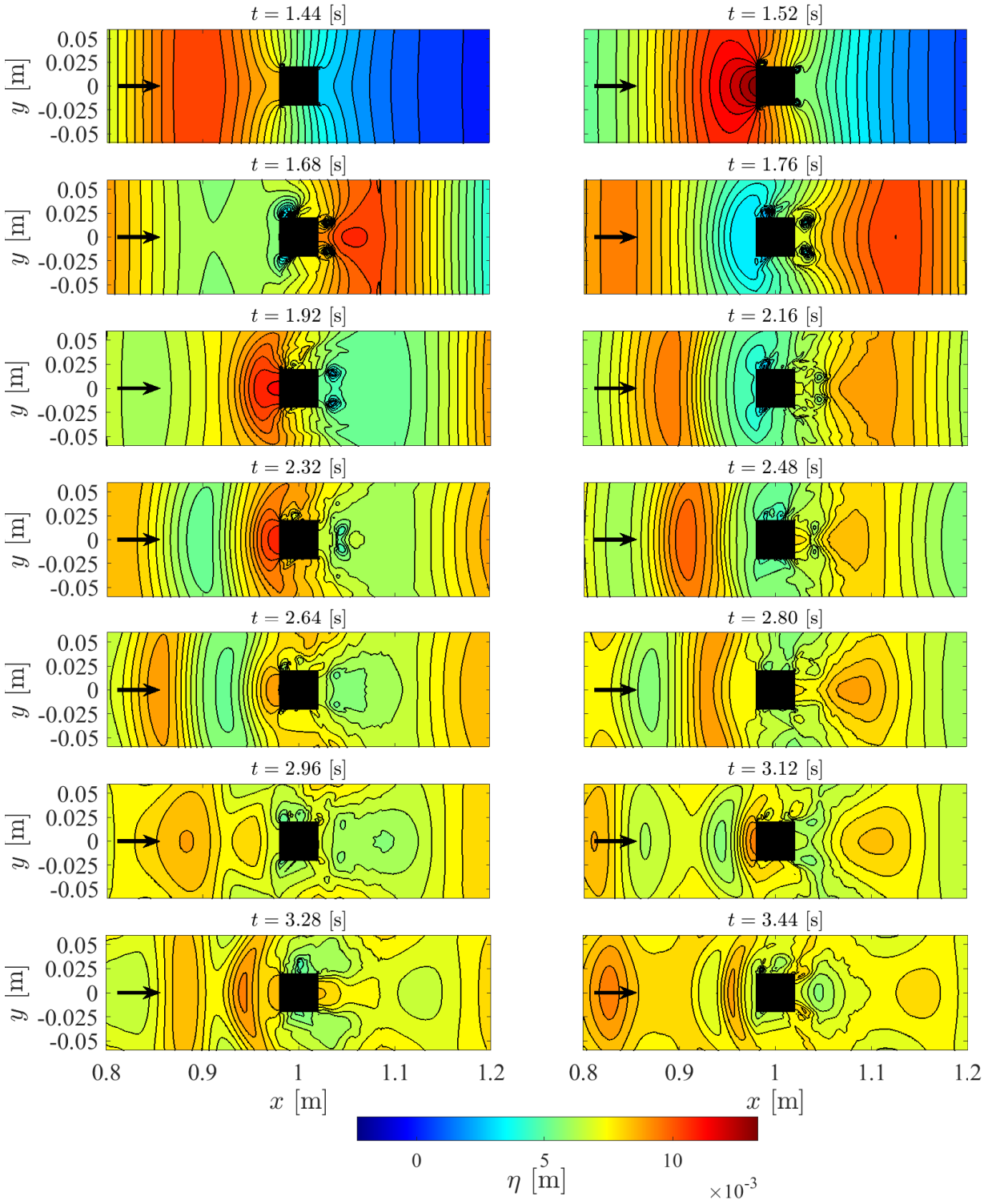

Figure 5.29: Free-surface elevation in the x-y plane close to the square cylinder. The black arrow indicates the wave propagation direction.

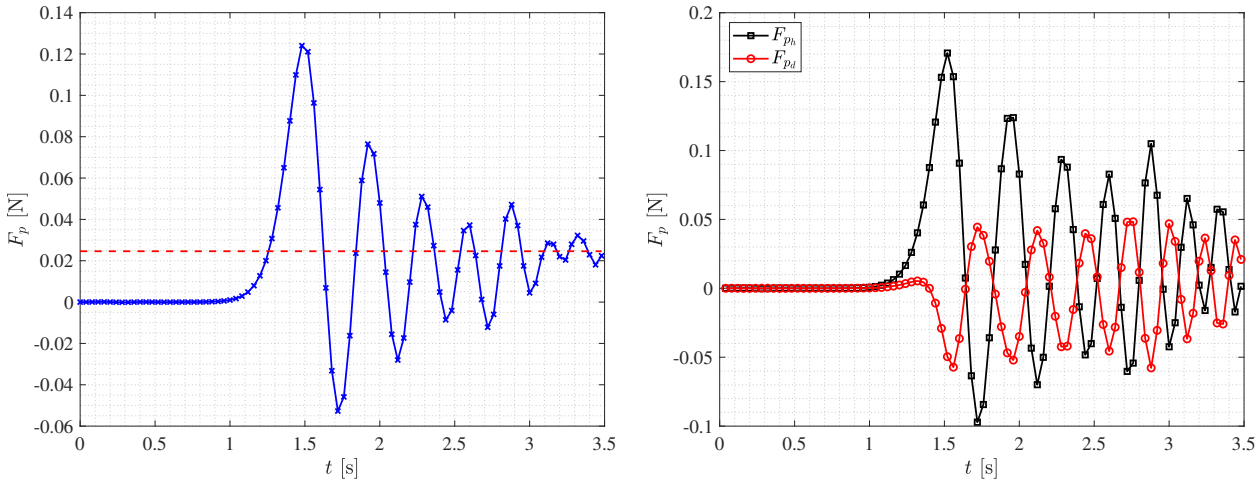

(a) (b)

Figure 5.30: (a) Pressure force on the cylinder in the x-direction as a function of time. The red dashed line represents the empirical force calculations explained in Qi et al. (2014). (b) Decomposition of the pressure force between the hydrostatic component F_p^h and the dynamic one F_p^d.

It is interesting to estimate the drag force applied on the square cylinder in the latter case and we chose the methodology of Qi et al. (2014) who studied the drag force on a surface piercing square cylinder placed in a current channel (for the subcritical case), and takes into account the blockage effect by the vertical structure onto the total force according to the drag coefficient:

$$C_D = C_{D_0}\left(1 + \frac{C_{D_0} D}{2W}\right)^2 \tag{5.4}$$

where W is the wave tank width, D the square cylinder diameter and C_{D_0} is the drag coefficient for an unbounded flow. This last value depends on the ambient turbulence, and drops from $C_{D_0} = 2.1$ to $C_{D_0} = 1.9$ for a 5% turbulence intensity (Tamura & Miyagi, 1999). P. Lin & Li (2003) found a similar drag coefficient for a configuration of wave and current experiment. To estimate the total force from the drag coefficient we use the following standard definition:

$$F_D = \frac{1}{2} C_D \rho U^2 (h + a) D \tag{5.5}$$

where $U = 0.1$ m/s is the permanent bore particle velocity (and in our situation which corresponds to the wavemaker velocity as shown in figure 5.20b) and $h + a$ is the bore height from the seabed. It leads to an estimated value of $F_D = 0.025$ N. We observe that the pressure force converges to this empirical value, so that the drag force switches from a transient wavy excitation to a steady current forcing. This result is consistent with the numerical simulation since the pressure force converges to the empirical results from Qi et al. (2014), showing that the pressure field is correctly estimated.

The maximum peak corresponds to a nearly 400% increase in the drag value compared with the steady state value. The transient forcing of the cylinder is predominant and can reach high values: this observation can be of particular interest for civil engineers when designing high-rise buildings

in coastal areas with high tsunami risks.

In figure 5.30b, the hydrostatic pressure force F_p^h is computed from the water levels records on the front and rear face and substracted from the total pressure force in order to obtain the dynamic pressure force component F_p^d according to $F_p^d = F_p - F_p^h$. This last one is in opposition of phase with the hydrostatic one, partly compensating the efforts on the cylinder and allowing for lower drag forces. The instantaneous frequency of this signal could inform us on the shedding frequency as well, but this particular point will be reviewed in details in section 5.2.5.

5.2.5. Vortex shedding

The vorticity and velocity field are jointly presented with the free-surface elevation in figure 5.31 and 5.32, for the positive y-half-plane only. As the in-plane velocity field is superimposed, it allows for a better visualization of the vortical structures, as they might not fully correspond to the vorticity distribution. The free-surface at the same times is shown in the right column and shows that every time a crest passes through the front (leading) edges, a vortex is generated, so that we are able to say that the vortex generation is triggered by the wave frequency.

The vortex formation and further shedding might be divided in the following stages: a vortex is generated simultaneously in both leading and trailing edges of the square cylinder by the local increase of flow velocity resulting from the elevation difference Δh between front and rear of the cylinder produced by the transit of the main undular bore wave.

Then the vortex influence grows (vorticity in the core increases) and it may be forced by further oscillations of $\Delta h(t)$ resulting from the successive transit of secondary undular bore waves. Finally the vortex detaches from the cylinder similarly as it happens in the von Kármán instability in circular and square cylinders. The wave elevation is in phase opposition compared to the dynamic pressure recorded simultaneously at the leading and trailing edges and displayed in figure 5.33. That means a local wave maxima corresponds to a minimum dynamic pressure and the creation of a vortex. After the two first vortices are detached from the respective edge we can detect two new born vortices on each edge which are associated to the transit of the secondary undular bore waves as it can be clearly observed in figure 5.31 at time $t = 2.12$ s.

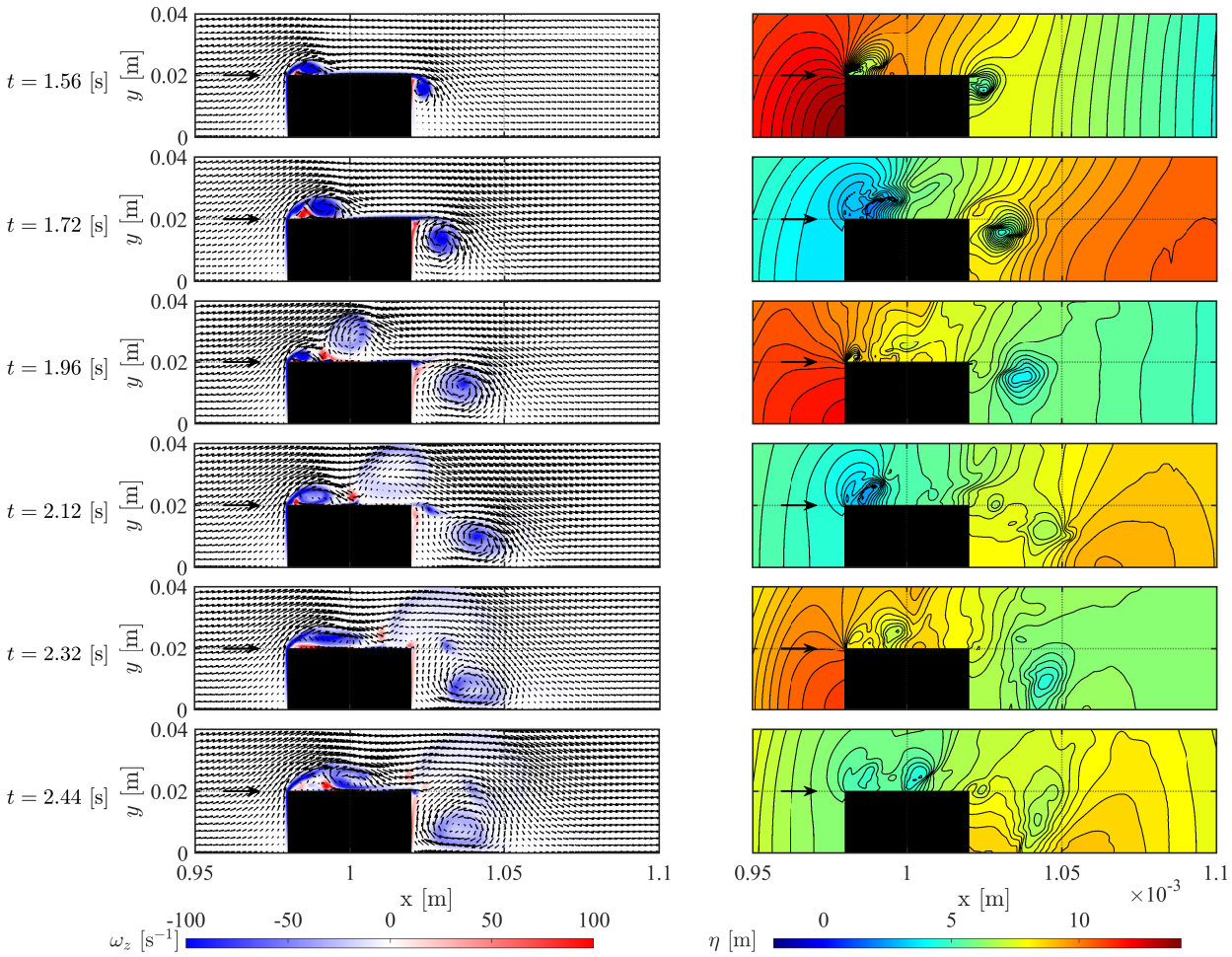

Figure 5.31: Z-component of the vorticity field in the x-y plane at $z = h/2$ close to the square cylinder for times $t = 1.56, 1.72, 1.96, 2.12, 2.32, 2.44$ [s] on the left and wave height η in the x-y plane for the same times on the right. These times corresponds to the local maxima and minima of the dynamic pressure of figure 5.33a. The black arrow indicates the wave propagation direction.

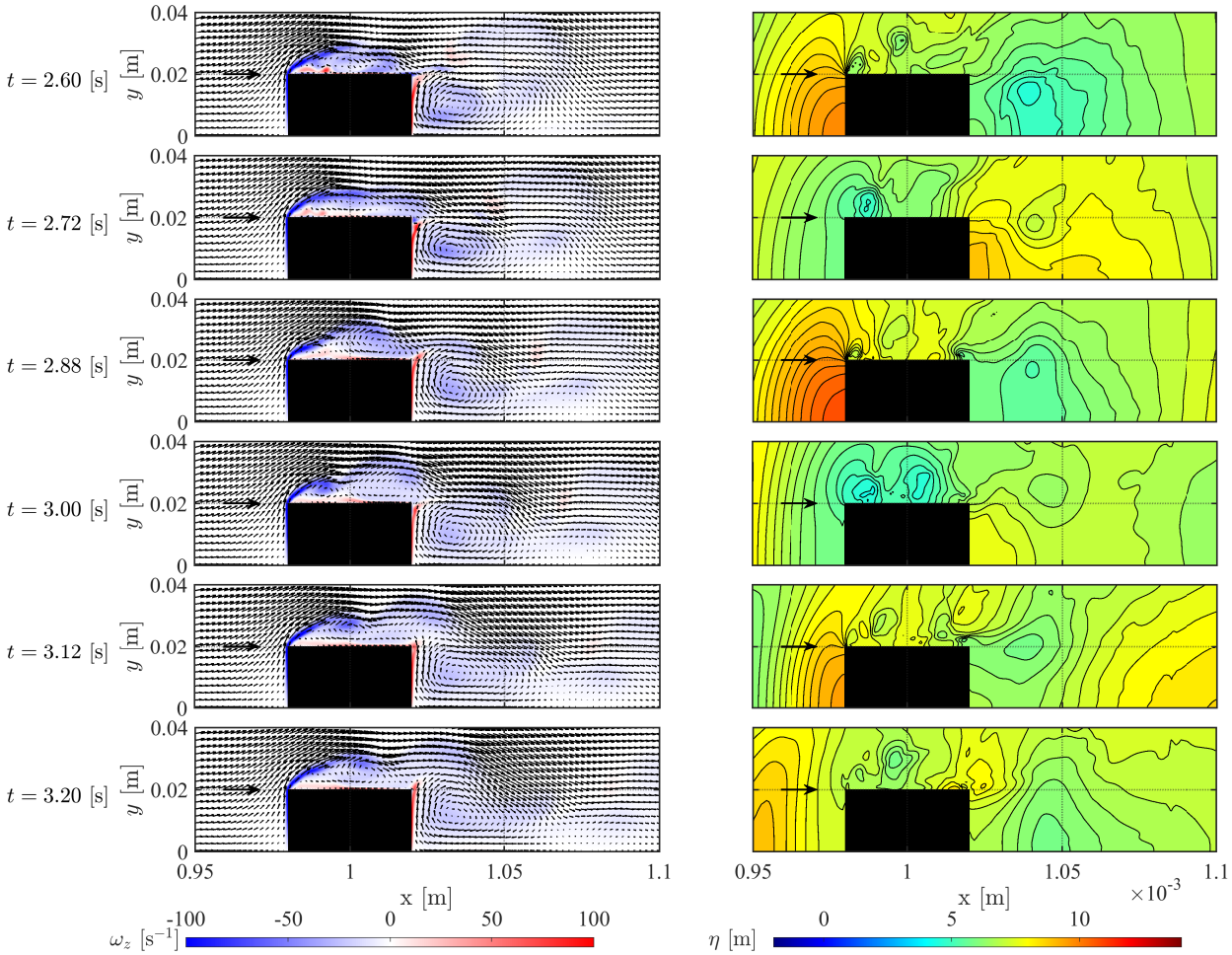

Figure 5.32: Continuation of figure 5.31 for times $t = 2.60, 2.72, 2.88.3.00, 3.12, 3.20$ [s].

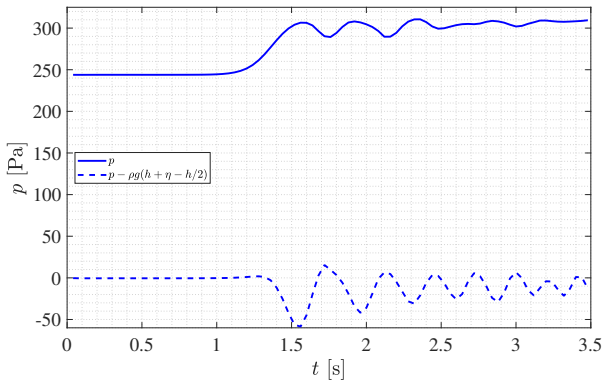

(a) Front edge $(x, y, z) = (0.98, 0.02, h/2)$ m.

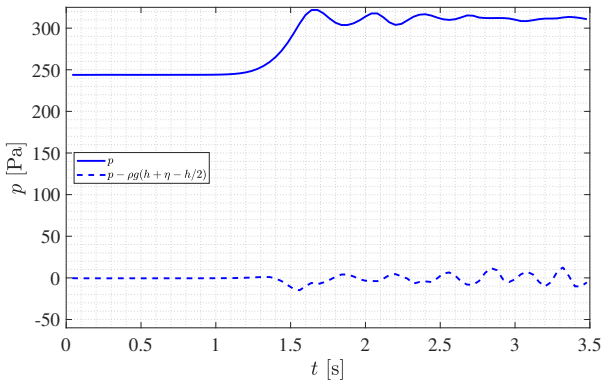

(b) Rear edge $(x, y, z) = (1.02, 0.02, h/2)$ m.

Figure 5.33: Pressure p and dynamic pressure p_d (defined as the pressure minus the hydrostatic pressure: $p_d = p - \rho g(h + \eta - h/2)$) at the front edge $(x, y, z) = (0.98, 0.02, h/2)$ m and the rear edge $(x, y, z) = (1.02, 0.02, h/2)$ m.

To be able to quantify the vortex shedding frequency at the sharp edges of the cylinder, it is decided to look at the pressure at theses edges and for $z = h/2$. The pressure for the edges in the positive y half-plane are presented in figure 5.33, where both the pressure and the dynamic pressure are plotted, so that the contribution due to the vortex formation can be isolated. We can observe that the total pressure is mainly hydrostatic, following the undular wave bore shape, while the dynamic pressure happens to be way lower, with values oscillating around zero. This is true for both edges, even if the oscillations on the rear edge are more irregular. The opposition of phase between the two types of pressures can be observed, and the wave crests passing by the edges correspond to a local minimum in the dynamic pressure record. The instantaneous frequency of each edge recorded pressure signal show an increase with time, as indicated in figure 5.34.

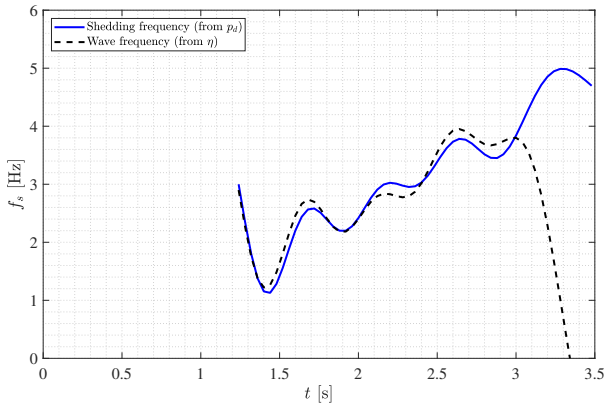

(a) Front edge.

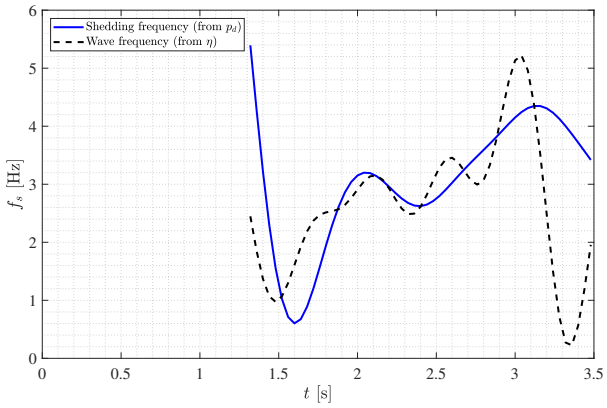

(b) Rear edge.

Figure 5.34: Instantaneous frequency of the dynamic pressure signal (in blue) and the water elevation (in black) for both the front and rear edges.

In order to confirm that the vortex shedding frequency is indeed associated with the wave frequency, the instantaneous frequency of both dynamic pressure and wave height at the front

and rear edges are computed. The Hilbert transform can be used to determine the instantaneous frequency, as

$$f_s(t) = \frac{1}{2\pi}\frac{d\phi}{dt} \tag{5.6}$$

where ϕ is the phase of the Hilbert transform of the time dependent signal. A low pass frequency filter with a cut-off frequency of 2 Hz is applied before plotting the final results. The first observations that can be made from figure 5.34 is that the Hilbert transform method gives important variations at the signal boundaries and this is a common issue known as "end effects" when using this method (N. E. Huang et al., 1998) so that the results before $t \leq 1.50$ s and after $t \geq 3.00$ s are not considered during the analysis of the figure. We observe the similar behavior between the instantaneous wave frequency and the dynamic pressure one, directly linking the process of shedding frequency to the wave frequency, as already observed in P. Lin & Li (2003) in a wave-current study. This analysis confirms that vortex shedding at both the front and rear frequency is triggered by the upcoming wave.

5.2.6. Vortex pairing and subsequent instability

Once these filamentary shaped vortices are shed and drift away from the cylinder, they are submitted to the mechanical forcing of the secondary waves of the undular bore. Their vertical structure is perturbed and may change presenting dynamical fluctuations which should be identified. In order to follow the vortex trajectories and determine their core shape, it is necessary to determine the center of the vortices and the method of Graftieaux et al. (2001) is used to that end. The Γ_1 scalar function is defined as:

$$\Gamma_1(P) = \frac{1}{S}\int_{M\in S} \frac{\left(\overrightarrow{PM} \wedge \overrightarrow{U}(M)\right)\cdot \vec{e_z}}{||\overrightarrow{PM}|| \cdot ||\overrightarrow{U}(M)||}\, dS \tag{5.7}$$

The details of the definitions of points M and P, as well as vectors $\overrightarrow{PM}$ and $\overrightarrow{U(M)}$ are shown in figure 5.35. The Γ_1 function depends on x and y and is equal to 1 when velocity vectors are perpendicular to a line originating from P. By applying the above equation 5.7, we obtain a two dimensional map in multiple horizontal planes of the Γ_1 function and then only points where $\Gamma_1 \geq 0.5$ are selected.

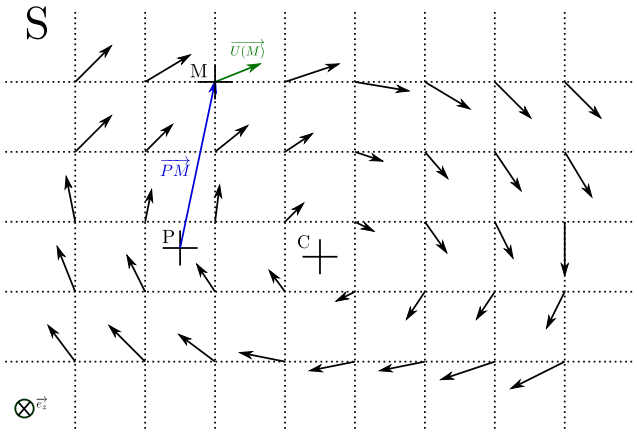

Figure 5.35: The vortex center detection algorithm maps the velocity field S in the $x-y$ plane through the computation of the Γ_1 function. For all points M at which the velocity $\overrightarrow{U(M)}$ is computed, the cross product between $\overrightarrow{PM}$ and $\overrightarrow{U(M)}$ is calculated leading to the two dimensional map $\Gamma_1(P)$ for which the maximum is located.

This strategy allows us to reconstruct the vortex core of these filamentary vortices by determining its center for every horizontal plane. Results are presented in figure 5.36 and 5.37 where the vortex core filaments for both rear vortices are presented with perspective, front and side views. The detection fails in some planes and so some part of the filaments are missing. It however does not impact the interpretation of the results. First, we can observe that the two vortex filaments are symmetric for times until $t = 3.00$ s, where the side view shows a breaking in the symmetry, especially close to the interface. The second observation that can be made concerns the global shape of the filaments, which are perfectly straight and vertical for times until $t = 2.00$ s, except in the closest zones at the seabed and the free-surface. During this phase, the filament motions are unidirectional and flow-wise.

For time $t > 2.00$ s the filaments start to deform as the waves pass over them and create some wavy patterns that evolve in the vertical coordinate along the whole water column. During this phase, the vortex at the seabed returns to a relatively steady position close to the cylinder while the upper part follows the wave motion and slowly drifts away from the cylinder. The last snapshots show a strong deformation of the vortices. If they are still close to the cylinder at the seabed, the vortex location at the free-surface is now further away from the cylinder as they follow the waves which stretch and compress the vortices.

The wavy pattern appears to be similar to the Crow (1970) instability, with, however, an irregularly shaped set of oscillations along the filament. The vortex rings which contribute to the vortex annihilation in Crow (1970)'s work are not observed here and on the contrary it seems that the vortices tend to move away from each other close to the free-surface, while at the seabed they get closer from each other.

Following the previous strategy, the trajectories of the vortices in the plane $z = h/2$ are determined with a function threshold $\Gamma_1 \geq 0.8$. A filter based on position and times at which the detection occurs allow to discard outliers and to assign the detected centers to the vortex trajectories.

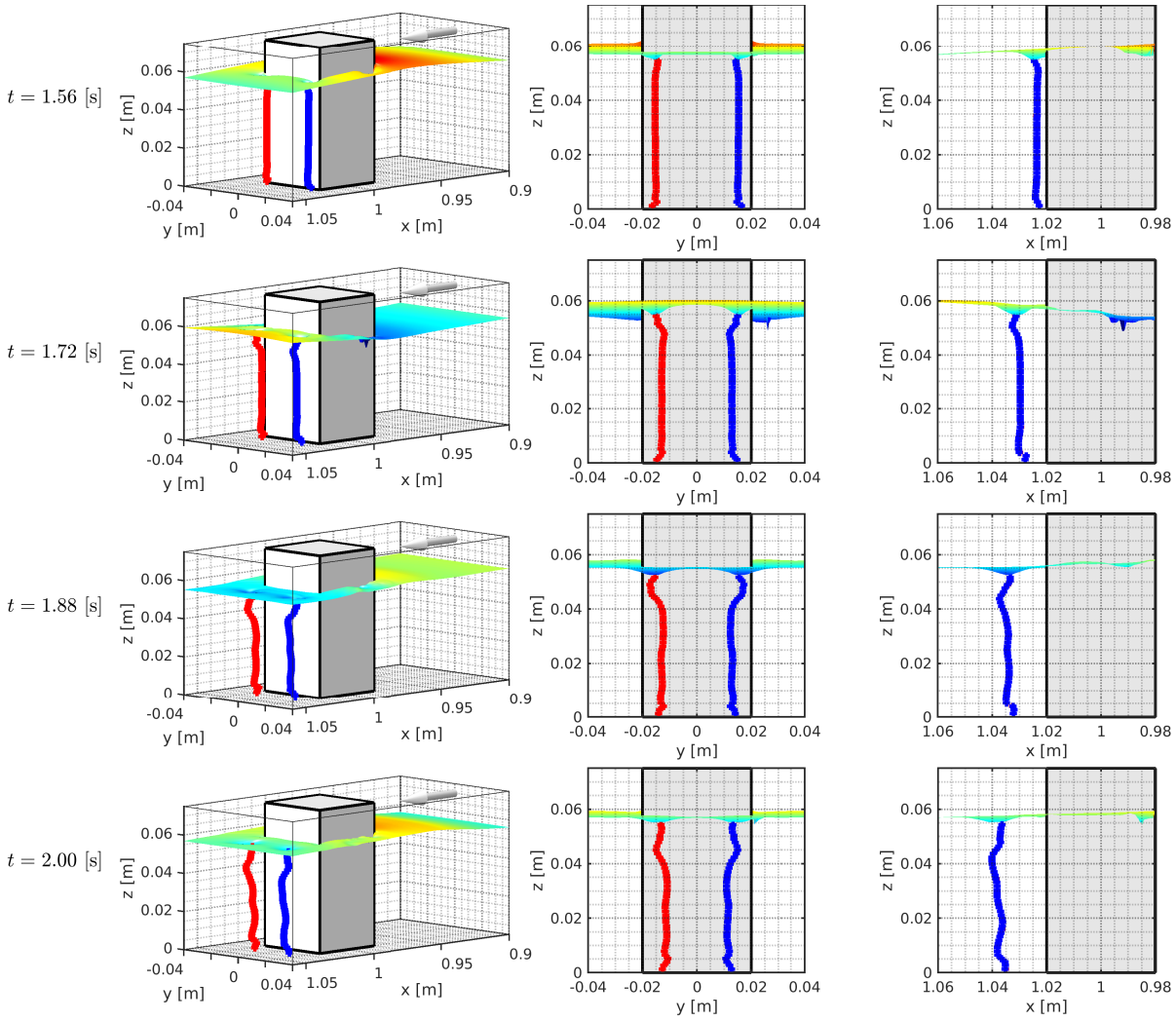

Figure 5.36: Vortex cores at the rear of the cylinder for times $t = 1.56, 1.72, 1.88, 2.00$ s. The three columns display a perspective, front and side view respectively.

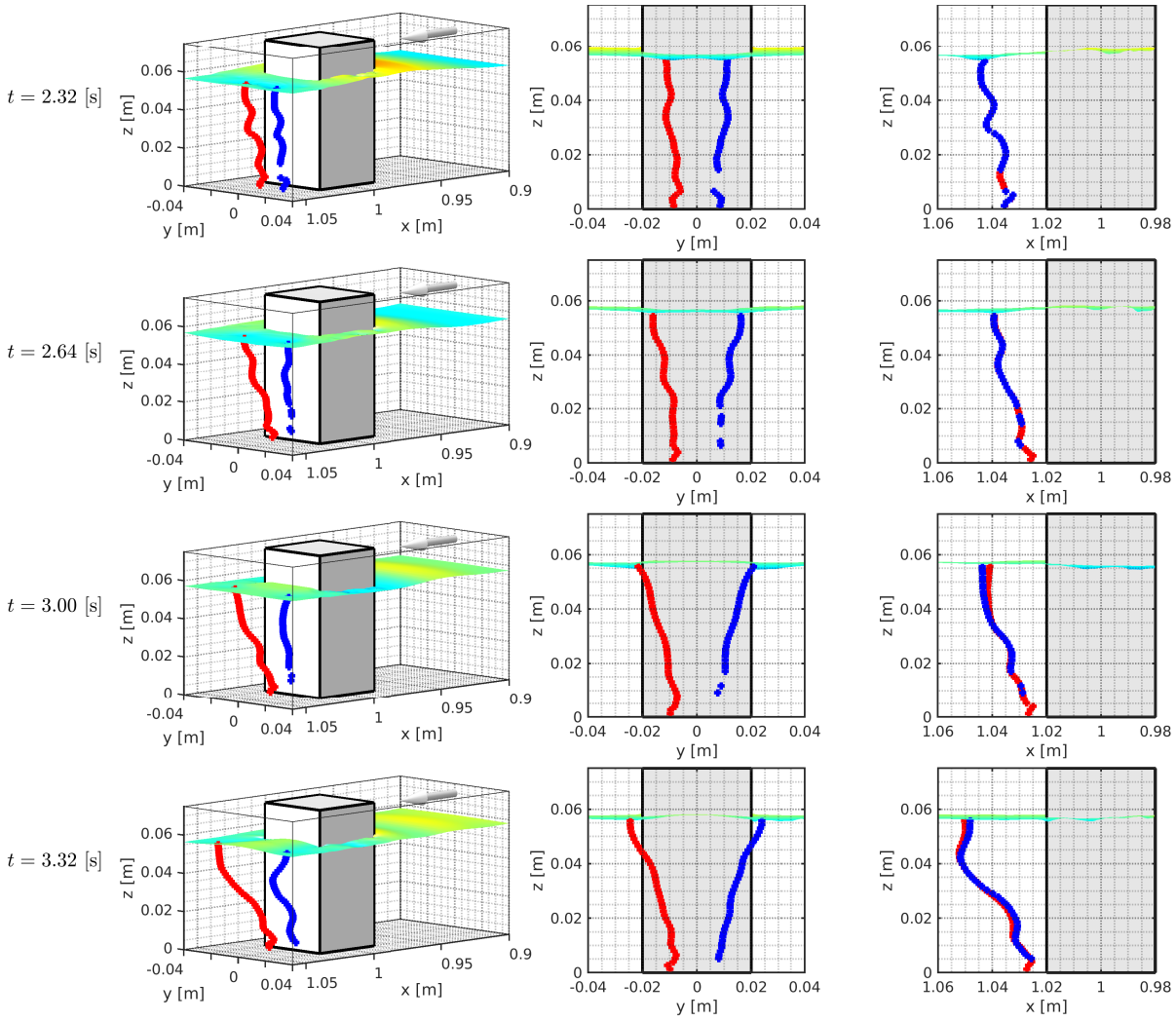

Figure 5.37: Vortex cores at the rear of the cylinder for times $t = 2.32, 2.64, 3.00, 3.32$ s. The three columns display a perspective, front and side view respectively.

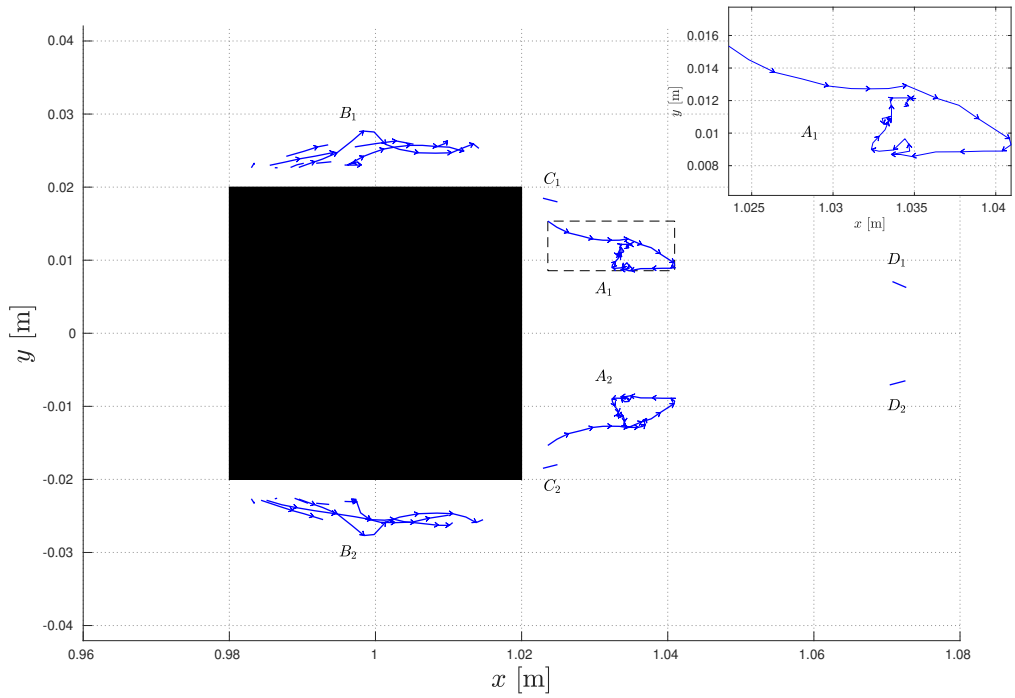

Figure 5.38: Trajectories of vortices in the plane $z = h/2$. The rear vortices are identified by the labels $A_{1,2}$ while the groups of vortices generated at the sides of the cylinder by $B_{1,2}$. At the rear of the cylinder, other vortices are detected, which are noted $C_{1,2}$ and $D_{1,2}$. A zoom over trajectory A_1 is also shown at the top right corner.

The vortex detection very close to the cylinder walls was not possible, thus we display the trajectories from a small spatial offset from the walls, where the vortices are fully formed. The results of this procedure are shown in figure 5.38. We note the vortices at the rear back of the cylinder with the letter $A_{1,2}$ and the one at the side with the letter $B_{1,2}$. If the $B_{1,2}$ vortices are a series of consecutively shed vortices, the $A_{1,2}$ ones are the same during the whole simulation. A focus on the vortex A_1 is also shown. Its trajectory starts at the rear edge and moves away from the cylinder before initiating a buckle motion and comes back toward the cylinder. The vortex trajectory A_2 shows a symmetrical behaviour, with some differences that appear at the end of their trajectories. Secondary vortex $C_{1,2}$ appears at the rear edges of the cylinder but rapidly disappear as approaching to the main vortices $A_{1,2}$. They might reappear in the wake as shown by the detection of vortices $D_{1,2}$. The vortices at the sides, $B_{1,2}$, are numerous and share similar paths. However, if the two first ones can be detected almost for a whole cylinder diameter, the following ones disappear quickly and we are not able to follow them with this technique.

This non-trivial path of the vortices remind us a typical precession motion of the individual axis of vortex rotation. The external forces exerted by the secondary bore waves are probably responsible of an external torque driving this precession mechanism. This symmetric motion will modulate the position of each vortex during the pairing process and notably affect the vortex pair typical properties as we will see in the next figures.

The vortex pairing of the A_1 and A_2 vortices can be characterized by their transversal velocity

profile such as in figure 5.40 for times between $1.68 \leq t \leq 3.44$ s. A focus on times $t = 1.68$ s, $t = 1.84$ s, $t = 2.00$ s and $t = 2.16$ s is carried out in figure 5.41, times for which the vortices are still straight and vertical, and for which the stream-wise velocity $U_x(y)$ profile is plotted for the four different times. A least square method allows to fit two Lamb-Oseen vortices, which are typical of vortex pairing (Leweke & Williamson, 1998), with the difference that an offset $U_0(t)$ is added to take into account the free flow and vortex own motions, according to the following expression:

$$U_x(y) = U_0 + \sum_{i=1}^{2} \frac{\Gamma_i}{2\pi(y - y_i)} \left(1 - \exp\left(-\frac{(y - y_i)^2}{a_i^2}\right)\right) \tag{5.8}$$

with $\Gamma_{1,2}$ is the circulation, $y_{1,2}$ the centers, and $a_{1,2}$ is the core diameter of the fitted vortices. An example of such function is plotted in figure 5.39 where the core diameter as well as vortex centers parameter are shown.

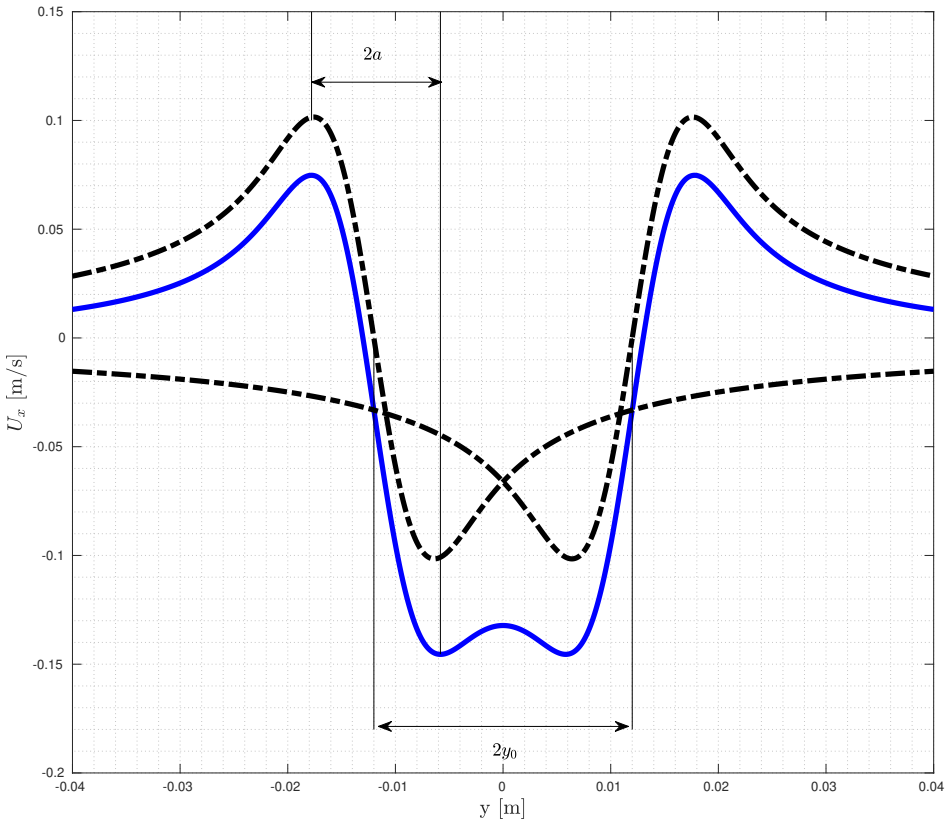

Figure 5.39: Example of a Lamb-Oseen vortex pair velocity profile. The vortices have circulations $\Gamma_1 = 0.005$ m$^2 \cdot$s^{-1} and $\Gamma_2 = -0.005$ m$^2 \cdot$s^{-1}, the same core size $a = a_1 = a_2 = 0.005$ m, their centers are located at $y_1 = y_0 = 0.012$ m and $y_2 = -y_0 = -0.012$ m and U_0 is set to zero. The dashed black lines (–) represents the individual vortices while the blue continuous line (-) the sum of both contributions.

In the case of the numerical simulation of figure 5.40, the individual vortices are shown in dash lines while the total fit is represented with the continuous black lines. The fit is executed with reference to the numerical velocity profile between $-0.02 \leq y \leq 0.02$ m, that is to say the cylinder

projection limits, which are represented in red in figure 5.41. If the velocity profile shows two local velocity minima for times until $t = 2.00$ s, attesting that the vortices are still quite separated, then the profile shows only one global minimum for $t = 2.16$ s, as the vortices are closer.

The velocity profiles reveal that the vortex pair structure evolves rapidly as they are advected by the bore induced flow. Their resemblance to Lamb-Oseen vortices seems to be progressive as the time increases, their overall velocity profile is closer to the theoretical fit, specially in the low velocity center region. But this process takes time. After each vortex is shed from the cylinder edge, the pairing process starts and pushes the vortex pair into the calm rear face region protecting them for an instant from the upcoming secondary bore waves. The pairing process develops thus and produce a Lamb-Oseen vortex pair as it is observed in more detail in figure 5.41. The fit does not vanish far from the cylinder as usually happens with a perfect ideal Lamb-Oseen vortex pair in a fluid at rest. Instead we have to take into account an unsteady offset velocity U_0 produced by the undular bore flow and overlapped to the own downstream motion of the vortex pair due to their cooperative velocity field (Leweke & Williamson, 1998) This particular process allows to identify and associate the parameters of the fit with the underlined physics of the pairing process.

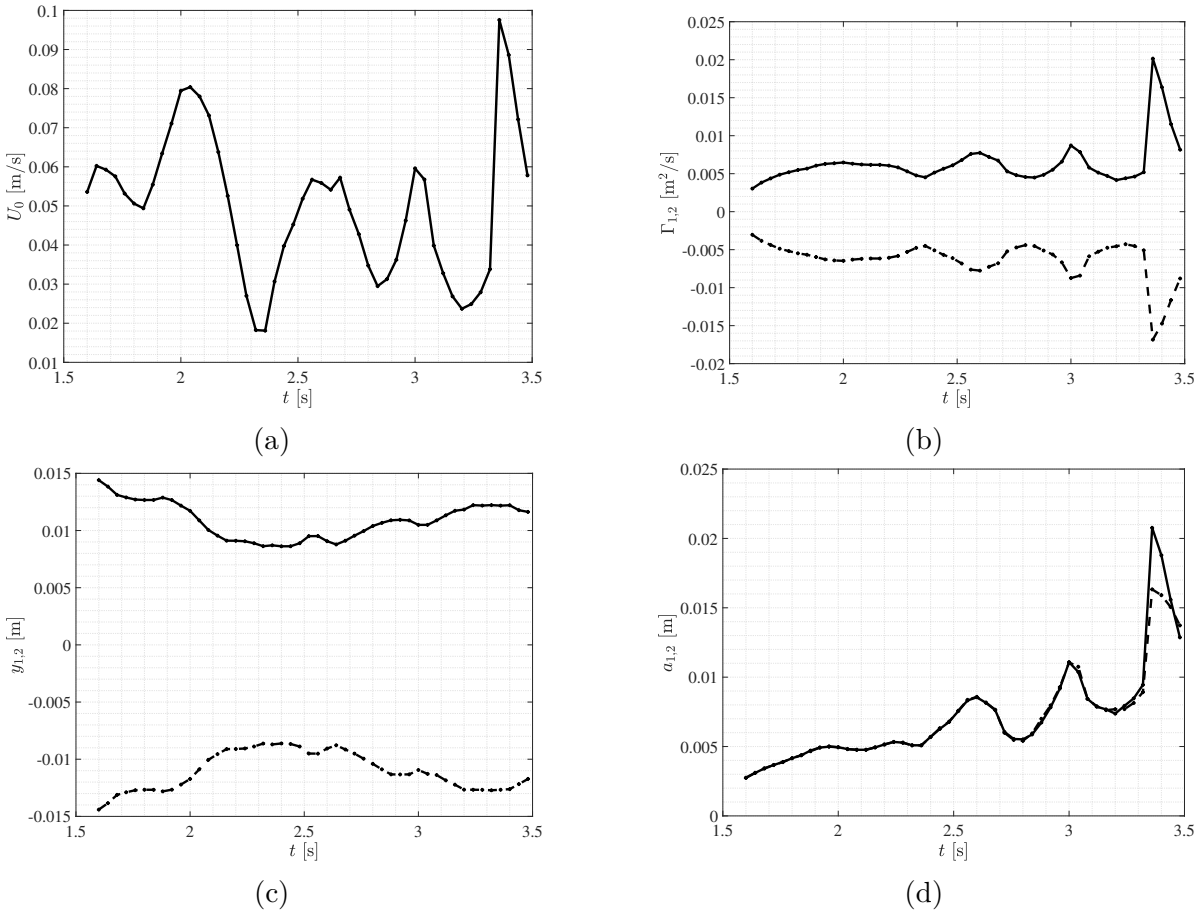

Figure 5.42: Parameters of the fit of figure 5.41. (a) U_0 as a function of time,(b) $\Gamma_{1,2}$ as a function of time, (c) $y_{1,2}$ as a function of time, (d) $a_{1,2}$ as a function of time. Indices $1, 2$ refer to the vortice pair A_1 and A_2 and are respectively shown in the dashed and continuous lines.

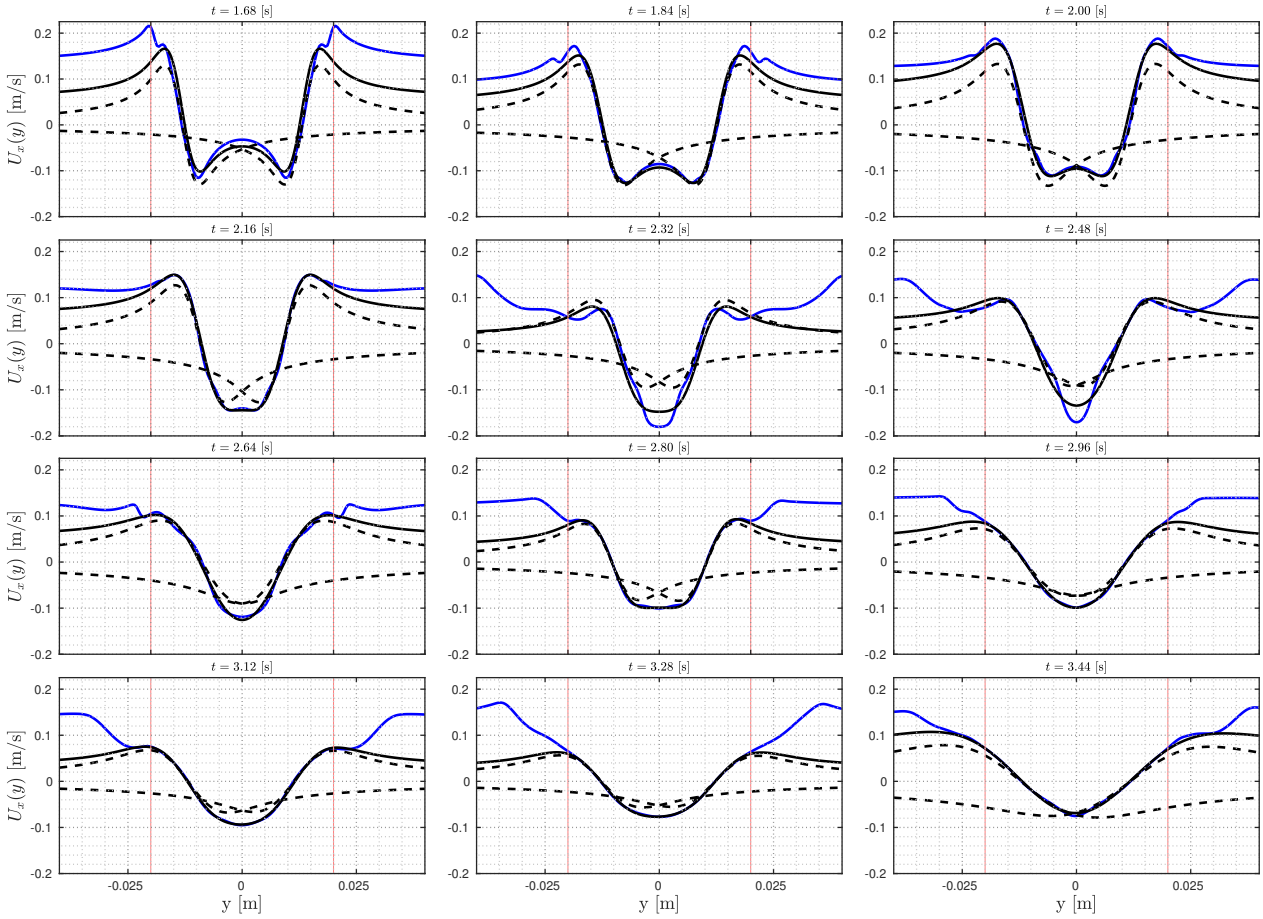

Figure 5.40: Horizontal velocity as a function of y (the transversal direction) for times between $t = 1.68$ and $t = 3.44$ s. The x coordinate follows the evolution of the A_1 vortex center for all times, so that the transversal profile always passes through the vortex center. The blue line (–) represents the numerical results while a least square method allows to fit two Lamb-Oseen vortices (which are axisymmetric two-dimensional vortices with Gaussian vorticity distribution) and an offset according to the following expression: $U_x(y) = U_0 + \sum_{i=1}^{2} \Gamma_i/(2\pi(y - y_i))\left(1 - \exp\left(-(y - y_i)^2/a_i^2\right)\right)$. This last expression is shown in the black continuous line (–) while the individual vortices are plotted in dashed line (- -). The square cylinder boundary projection is shown in red.

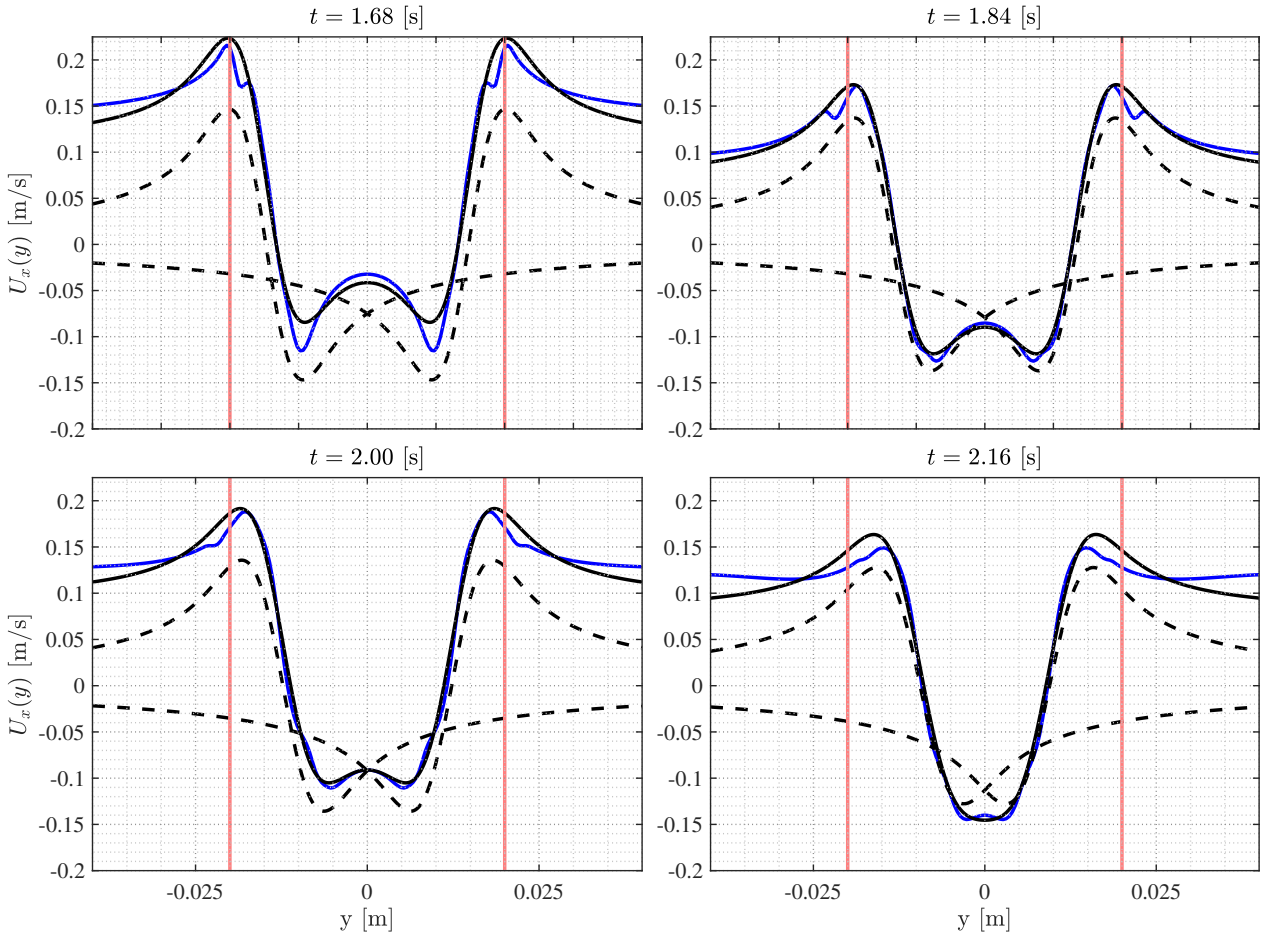

Figure 5.41: Horizontal velocity as a function of y (the transversal direction) for times $t = 1.68$ s, $t = 1.84$ s, $t = 2.00$ s, and $t = 2.16$ s. The x coordinate follows the evolution of the A_1 vortex center for all times, so that the transversal profile always passes through the vortex center. The blue line (–) represents the numerical result while a least square method allows to fit two Lamb-Oseen vortices (which are axisymmetric two-dimensional vortices with Gaussian vorticity distribution) and an offset according to the following expression: $U_x(y) = U_0 + \sum_{i=1}^{2} \Gamma_i/(2\pi(y-y_i))\,(1 - \exp\left(-(y-y_i)^2/a_i^2\right))$. This last expression is shown in the black continuous line (–) while the individual vortices are plotted in dashed line (- -). The square cylinder boundary projection is shown in red.

The fit parameters of figure 5.41 are plotted as a function of time in figure 5.42. They are also reported in table 5.4 for the four times $t = 1.68$, 1.84, 2.00, 2.16 s. The fit allows to show some properties of the vortex pair but also indirect properties of the undular bore. Both rear vortices are anti-symmetrical as long as they are straight and vertical while symmetry is lost for the latest times, which can be observed in the values of the vortex core size $a_{1,2}$ for times $t > 3.2$ s. The circulation $\Gamma_{1,2}$ oscillates at a frequency similar to the one from the undular bore.

The anti-symmetry of the circulation accounts for the opposite sign of the angular rotation of each vortex and shows an abrupt peaked increase which occurs precisely when the vortex core a_i becomes peaked as shown in figure 5.4 (b,d) respectively. The effect is not seen in the vortex pair separation distance, however as this fit process was performed at middle height $h/2$ we did not consider the effects of the vertical evolution of the vortex distance with height observed for later times in figure 5.37. The fit is intended to be representative of the vortex pairing process as long as the vortices are straight and parallel which is no longer valid for $t > 2$. Finally, the offset velocity $U_0(t)$ does not remain constant as it is associated to the undular bore induced flow and the vortex own motion. The frequency of the $U_0(t)$ fluctuations is very close to the secondary bore's waves frequency with, however, a non uniform amplitude.

t [s]	U_0 [m s^{-1}]	Γ_1 [m^2 s^{-1}]	Γ_2 [m^2 s^{-1}]	y_1 [m]	y_2 [m]	a_1 [m]	a_2 [m]
1.68	0.059	4.4×10^{-3}	-4.4×10^{-3}	0.013	-0.015	3.4×10^{-3}	3.4×10^{-3}
1.84	0.049	5.7×10^{-3}	-5.7×10^{-3}	0.013	-0.013	4.4×10^{-3}	4.4×10^{-3}
2.00	0.079	6.5×10^{-3}	-6.5×10^{-3}	0.012	-0.012	4.9×10^{-3}	4.9×10^{-3}
2.16	0.064	6.2×10^{-3}	-6.2×10^{-3}	0.009	-0.009	4.9×10^{-3}	4.9×10^{-3}

Table 5.4: Parameters of the Lamb-Oseen vortex fit analysis.

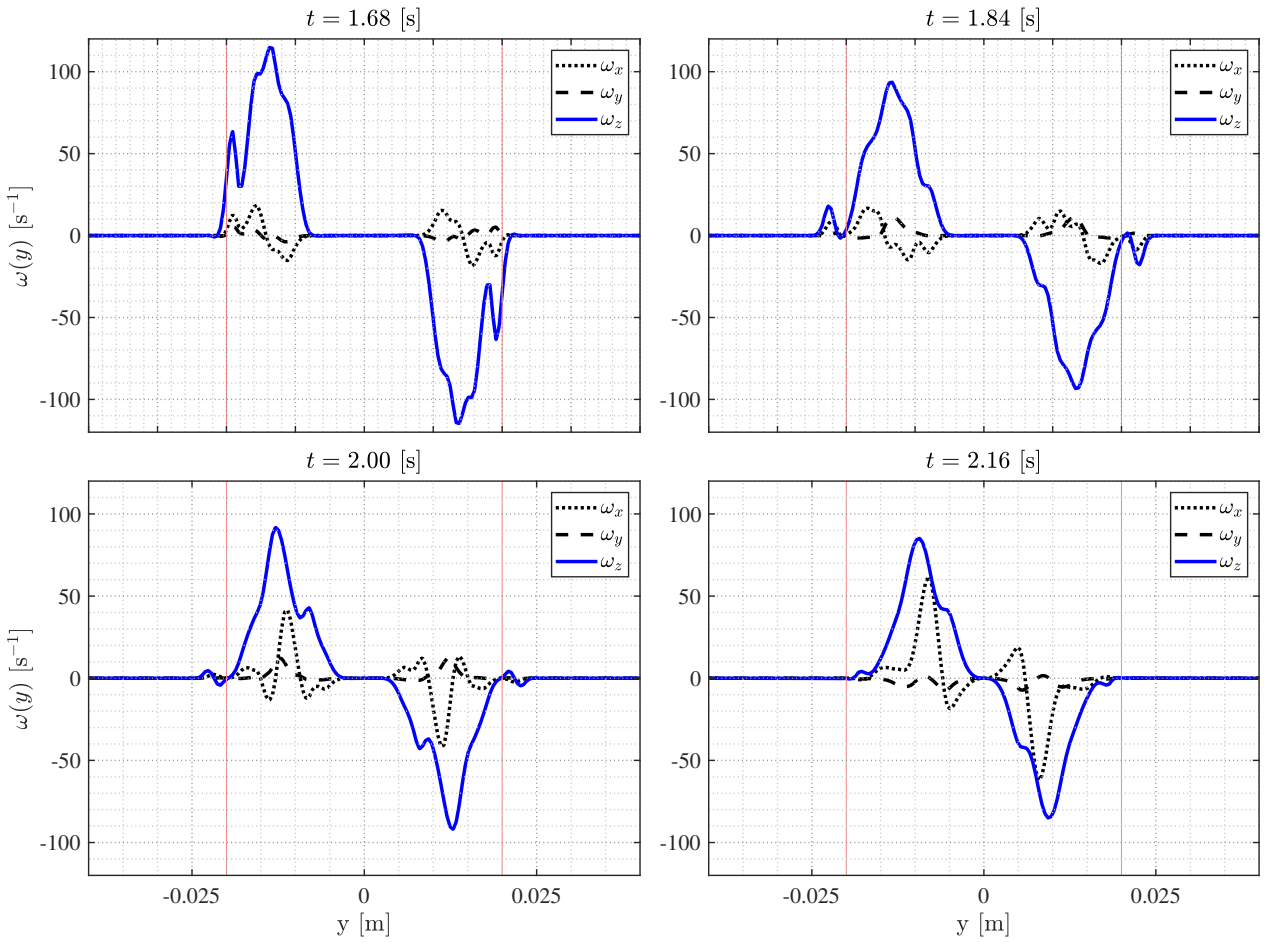

Figure 5.43: Vertical vorticity profile $\omega_z(y)$ for times $t = 1.68$ s, $t = 1.84$ s, $t = 2.00$ s, and $t = 2.16$ s. The x coordinate follows the evolution of the A_1 vortex center for all times, so that the transversal profile always passes through the vortex center.

Another way of detecting the vortices and characterize them is to look for the vorticity profiles, as shown in figure 5.43. In this figure we choose to plot for the same time snapshots shown in figure 5.41. In order to compare the amplitude of the vorticity profiles, the three components are displayed on the same plot (ω_x,ω_y,ω_z). The vertical vorticity component ω_z is for all times the dominant one, which confirms quantitatively that the vortices can be considered in the $x-y$ plane. However, for $t = 2.16$ s, the transversal vorticity components increase in magnitude both in x and y directions and they are no longer negligible.

This result is in agreement with the discussion of the time snapshots of the vortex pairing process in figures 5.36 and 5.37 where at $t = 2.32$ s, the vortices are not fully straight and vertical any more. The red vertical line shows the projection of the square cylinder limits, so that we are able to observe that the vortices occupy the full width of the cylinder. If for the first times, the central zone between the two pairing vortices exhibit a zero vorticity ($\omega_z = 0$ s^{-1}), this zone progressively disappears during the vortex pairing process, so that at time $t = 2.16$ s, both vortices are closer and the vorticity profile becomes what it is expected in a Lamb-Oseen vortex pair, a almost Gaussian vorticity distribution in each vortex core. Notice the gradual spread out of vorticity amplitude of

the vertical component in contrast to the transverse components.

Finally, an attempt is made at quantifying the vertical vorticity which is produced during the undular bore interaction with the square vertical cylinder. We first compute the circulation around the square cylinder for the numerical case with a contour which is rather important in size so that the global circulation does not depend on it. The contour is a rectangle in the positive y half-plane and at three heights: $z = 0.195$ mm, $z = h/2$ and $z = h$. Circulation is defined as:

$$\Gamma = \oint_C \boldsymbol{U} \cdot \boldsymbol{dl} \tag{5.9}$$

The circulation is computed in the $x - y$ plane along the red rectangular contour path C which comprises the square cylinder, for x coordinates $0.95 \leq x \leq 1.20$ m and for y coordinates between $0 \leq y \leq 0.10$ m. We made sure that the closed contour is large enough so that the circulation value does not depend on its shape and size. Close to the seabed ($z = 0.195$ mm), the circulation is small, as the vorticity field close to the seabed is not vertical, and reach a constant value for larger times. For the circulation of plane heights $z = h$ and $z = h/2$, we can observe a sudden increase in the circulation between times $1.25 \leq t \leq 1.64$ s which correspond to the first instant of interaction between the wave and the cylinder, and the generation of the first front and rear vortices, which are vertical as shown in figure 5.36. The circulation then decreases as these two vortices are advected and vorticity enclosed in the contour path is lost. A second increase is observed as the secondary vortices are generated and then they show a weak decrease while they are advected, before a new increase and decrease and so forth. The cycles of vortex shedding and advection corresponds to the increase and decrease of the circulation. The local maxima of the circulation correspond to times where the wave crest leaves the cylinder and the decrease to the passage of the bore troughs. The oscillations are greater for $z = h$ compared to $z = h/2$ since the incident velocity is greater close to the interface and thus leading to stronger vortices and higher circulation. For times $t > 3$ s, the circulation oscillations become small and its frequency higher, and the increase of circulation is nearly linear. Note that the circulation from figure 5.44 is different from the one of figure 5.42b since the second one is computed for the rear vortices only.

If this method is useful to compute the circulation of the whole system, it would be interesting to compute the one associated with the rear vortices. We decide then to carry out a similar calculation but with a different rectangular contour whose limits are $1.02 \leq x \leq 1.06$ m and $0 \leq y \leq 0.02$ m. This contour represents a rectangular of half cylinder diameter width and one diameter long. The choice of this rectangle is motivated by the vorticity which we have seen is mainly contained at the rear between the cylinder boundary projections and its length which correspond to the typical length of the problem. The results of this calculation is presented in figure 5.45 which shows the circulation for the three height $z = 0.195$ mm, $z = h/2$ and $z = h$. The general trend for the circulation close to the seabed is similar to the previous one since we observe low value of vorticity, the vortices not being vertical. The circulation at the other two heights is quite similar, with an increase at the first instants of the interaction, then a small plateau (with no decrease), a second increase reaching the all time maximum before the behavior between the heights starts to differ

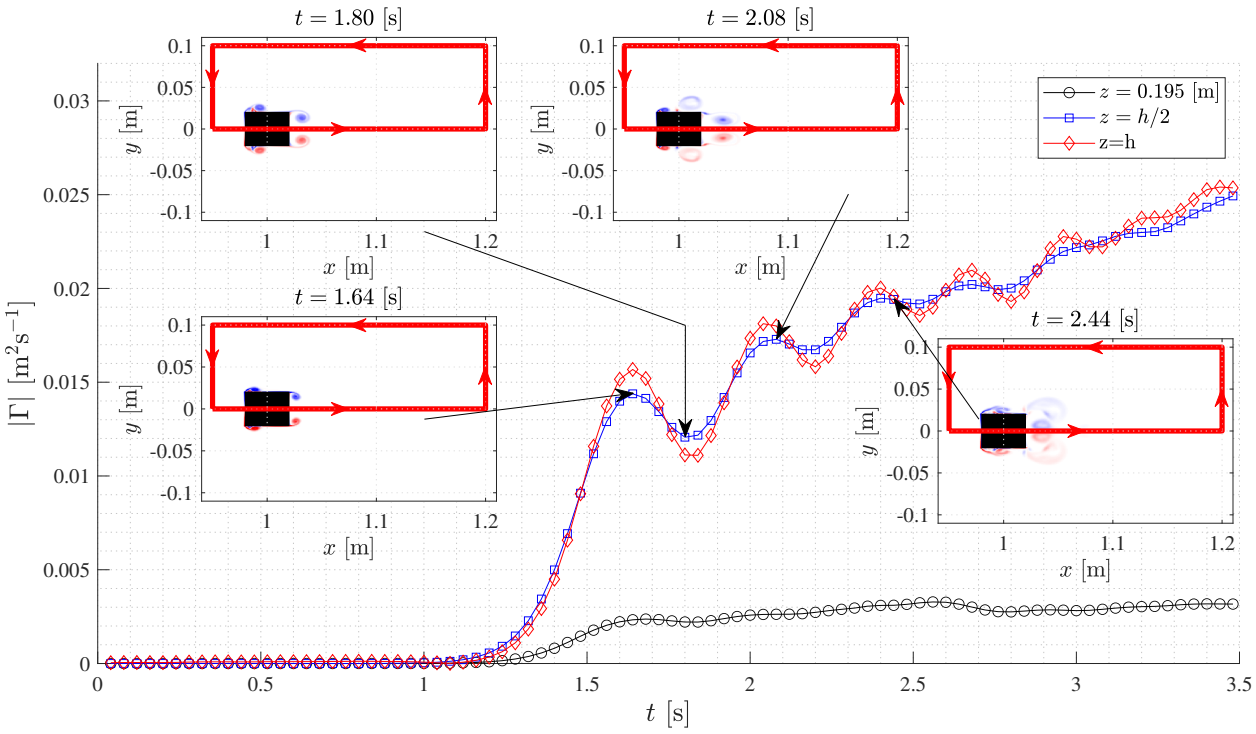

Figure 5.44: Circulation as a function of time. Some of the instantaneous vorticity are also shown for times $t = 1.64, 1.80, 2.08, 2.44$ s and $z = h$, $z = h/2$, $z = 0.195$ mm.

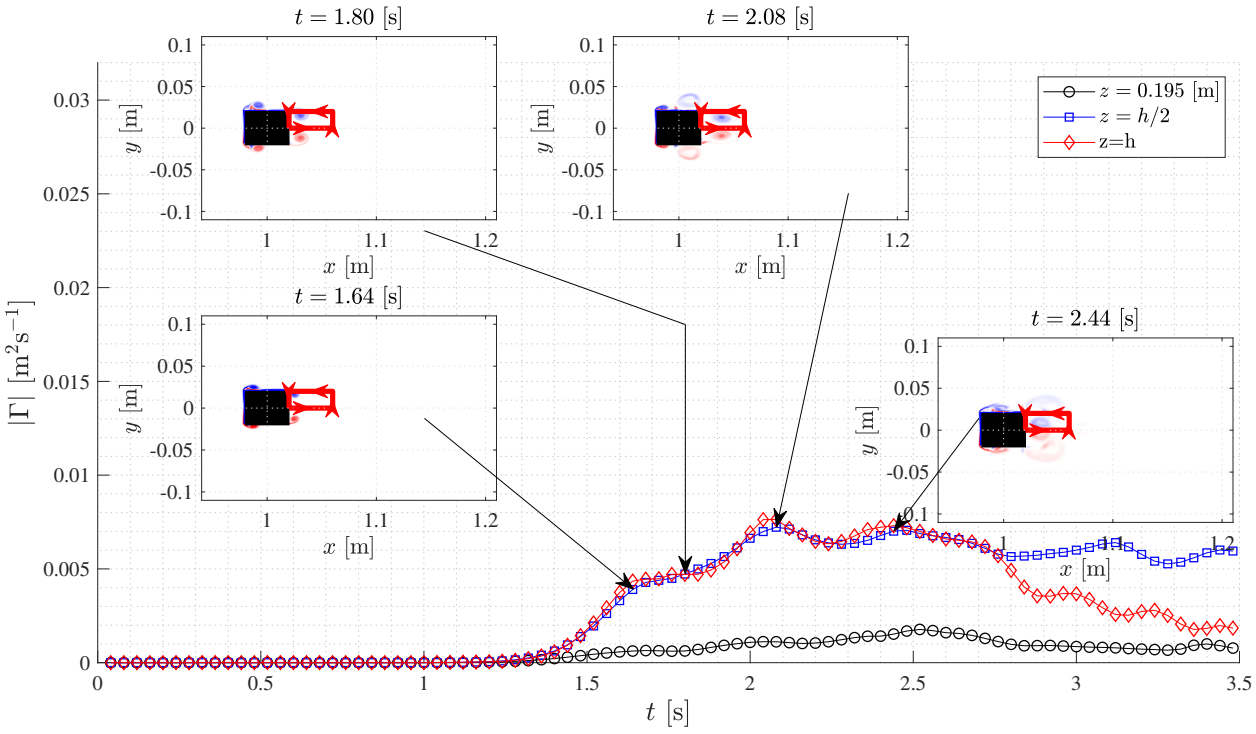

Figure 5.45: Circulation in function of time computed thanks to the red contour at the rear of the cylinder and at $z = h$, $z = h/2$, $z = 0.195$ mm.

greatly. Note that the circulation is slightly higher close to the free surface due to higher incident velocities. The circulation maximum are around half the one found in figure 5.44, which shows that each edge of the cylinder contributes equally to the vorticity creation. If the circulation is rather constant, with a small decay over time for $z = h/2$, the circulation close to the free-surface falls quite quickly after $t = 2.5$ s, showing the transformation, orientation change or disappearance of the vortex in this zone. Comparing with the previous figure, as circulation stops growing after the formation of the rear vortices, we can presume that the vorticity which is created at the rear edges does not feed the rear vortices and these ones are quite stable and independent identities.

5.2.7. Seabed wall shear stress

Even if the study of scour at the cylinder rear face might appear beyond this thesis scope, it is chosen to show some interesting preliminary results from the numerical simulation. The conditions to observe local scour downstream of a vertical solid column (or pile) strongly depend on the action of waves and weak induced currents combined mechanisms. The resulting scour depth below the seabed level downstream the column may be quite intense if von Kármán vortex shedding occurring from the column adds to the effect of currents in comparison with effect exerted only by waves (Kawata & Tsuchiya, 1988). Downstream seabed effects on a single pile can be greatly understood by determining the vortex induced shear at the seabed and the subsequent alternate back and forth forcing due to the upcoming wave motion, like a bore. In what follows we are going to briefly discuss, on the basis of the seabed shear stress tensor, the possible effects on the remotion of typical sediment particles used on recent experiments (Du & Liang, 2019).

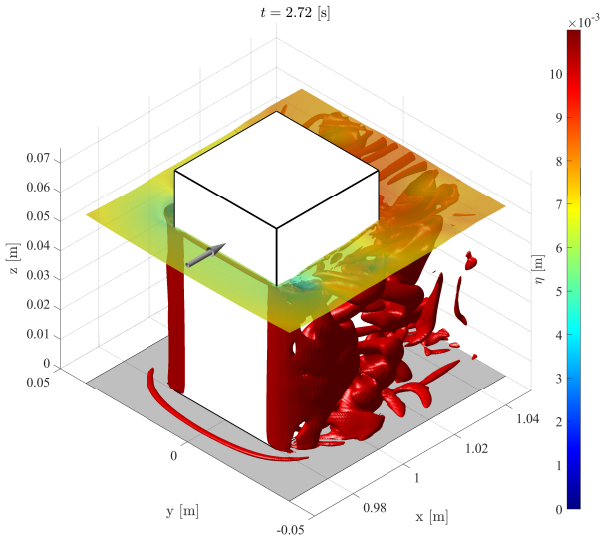

Figure 5.48: Horseshoe vortex at the front face of the square cylinder, visualized with the Q criteria isosurface $Q = 30$ s^{-1} and at $t = 2.72$ s. The grey arrow indicates the wave propagation direction.

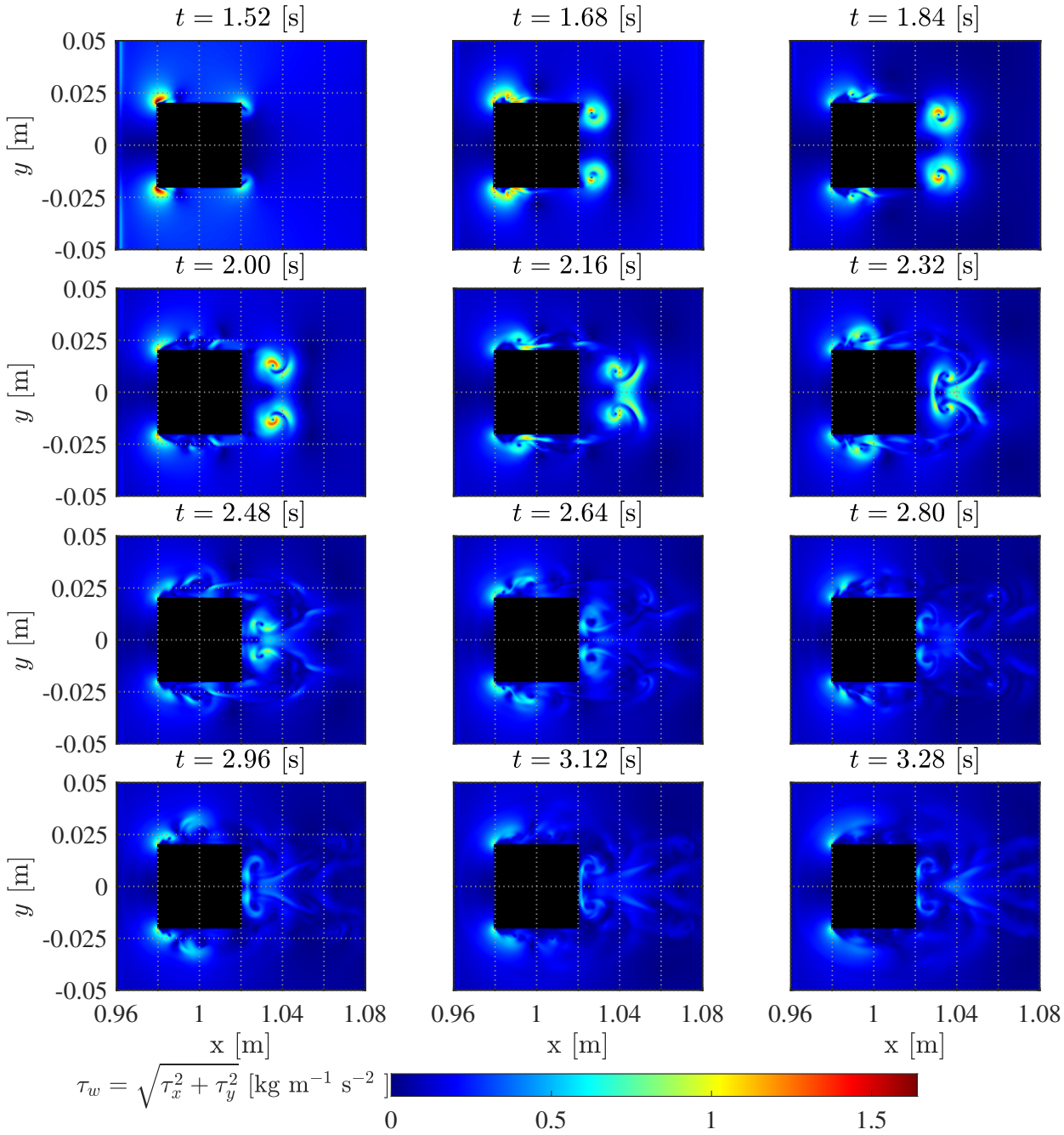

Figure 5.46: Seabed wall shear stress $\tau_w = \sqrt{\tau_x^2 + \tau_y^2}$ in the x-y plane close to the square cylinder.

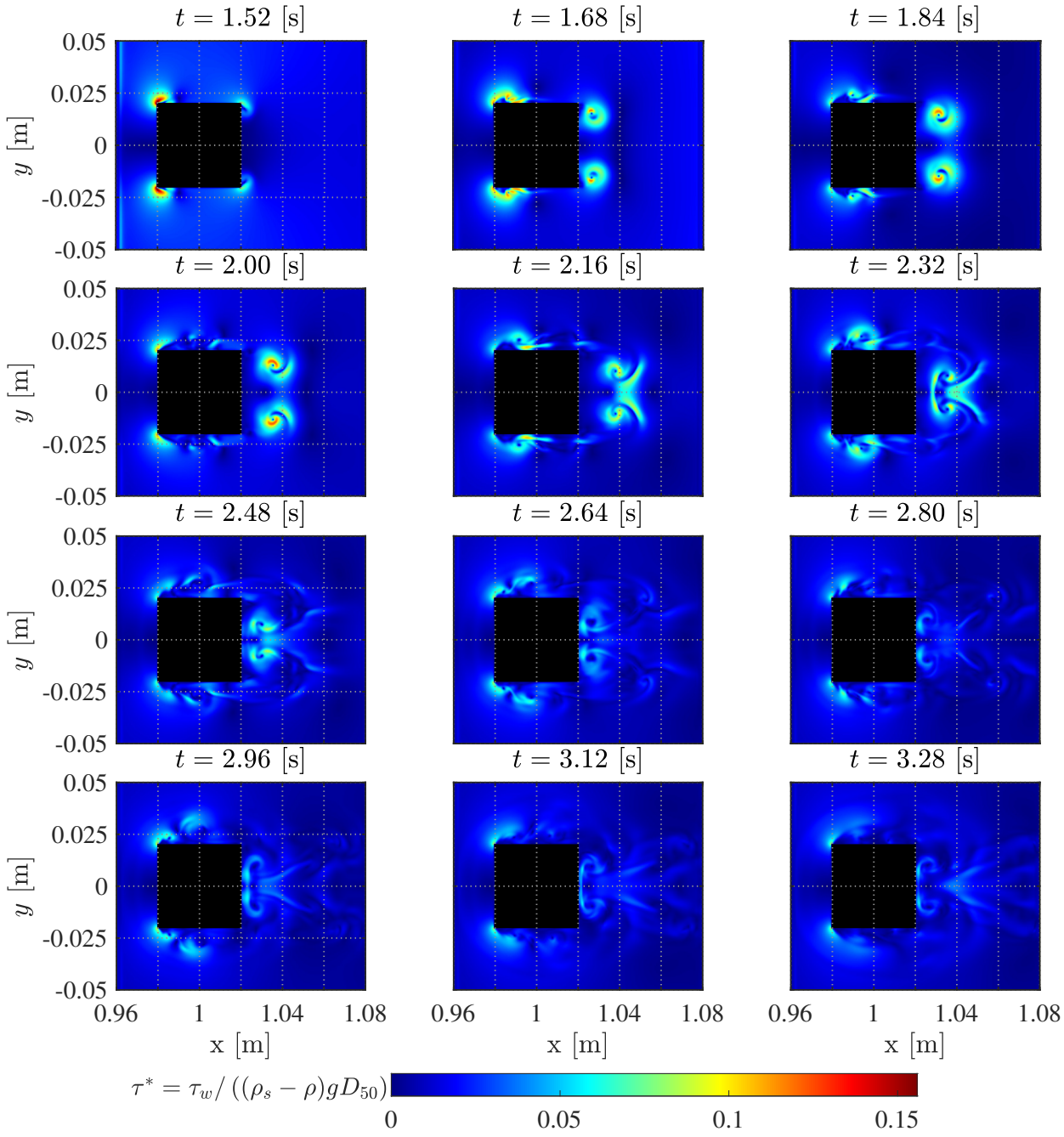

Figure 5.47: Dimensionless seabed wall shear stress $\tau^* = \tau_w / ((\rho_s - \rho) g d_{50})$ in the x-y plane close to the square cylinder.

The seabed shear stress magnitude, defined as $\tau_w = \sqrt{\tau_x^2 + \tau_y^2}$, is shown in figure 5.46 and we observe that local maxima of the shear correspond to the vortex positions close to the seabed, such as at the front edges during the whole simulation, or at the back of the cylinder where the paired vortices are situated. The maximum shear value, which is found at the front edges and for the beginning of the interaction between the undular bore and the cylinder, is $\tau_w = 1.64$ kg m^{-1}s^{-2}. We can also observe a zone of high shear between the two paired vortices in the cylinder center line. Globally, shear diminishes as the bore passes by the cylinder. One of the many applications, which are important in the design of piles, is the possible scour that occurs at the foot of the vertical square cylinder. It corresponds to the removal of sediments from the base of the pile, leaving it unprotected and can lead to the failure of the pile. The motion of sediment is realized from zones of high shear to zones of low shear, if the sediments are not carried away by the flow. We were able to observe the horseshoe vortex upstream of the square cylinder, as shown in figure 5.48. This horizontal vortex is found to greatly contribute to the upstream scour of the piles such as in the works of Kawata & Tsuchiya (1988) and Sumer et al. (1992) where scour around a circular cylinder was studied but also for square pile (Raikar & Dey, 2008). However, the contribution of this vortex to the seabed shear stress is small compared to the one from the vertical vortices that are generated at the edges of the square cylinder.

A first approximation of the particle transport effect at the seabed and associated to the square cylinder can be carried out by considering the Shields (1936) relation. The dimensionless number of Shields (1936), which compares the seabed shear stress exerted on the sediment particle to their weight, is defined as:

$$\tau^* = \frac{\tau_w}{(\rho_s - \rho)\, g d_{50}} \tag{5.10}$$

where τ_w is the seabed shear, ρ_s is the sediment particle density, ρ is the water density, g the acceleration due to gravity and d_{50} is the median grain size. An estimate of the shear effect at the seabed on typical sea sand with properties like $d_{50} = 0.65$ mm, $\rho_s = 2650$ kg m^{-3}, $\rho = 997$ kg m^{-3} and $g = 9.81$ m s^{-2} (Du & Liang, 2019) allows to compute the strength of the shed vortices on sand particles.

The dimensionless Shields' number is to be compared to a critical value, called τ^*_{crit}, from which the flow starts to displace sediment. Shields (1936) gives $\tau^*_{crit} = 0.06$. Regions where $\tau^* \geq \tau^*_{crit}$ corresponds for all times to the front cylinder edge, where the lateral vortices are formed, and also for the rear vortices. In figure 5.46 for times $t \sim 2.32$ s, the criteria is also fulfilled for the V-shape high stress zone between the two rear vortices. The V-shaped pattern is also typical of scouring around circular or square piles, as observed in G.-H. Kim & Park (2017) and Xiang et al. (2020). This analysis allows us to predict sediment displacement at the front edges, as well at the cylinder rear face where the vortices are located.

5.2.8. Conclusion

This work is the first description of the physics of the wave structure interaction between an undular bore and a vertical square cylinder. An undular bore was created thanks to a preliminary study of the piston wavemaker to which a velocity step was applied. Theoretical results which was retrieved from a linear model at low Froude number (Joo et al., 1990) allowed us to validate the CFD simulation of the wave generation. The study was later extended to higher Froude number for which the response to the velocity step is no longer linear, and forces were computed on the wavemaker leading to a quadratic power scaling which can be useful for the design of wavemakers. The piston wavemaker study allowed finally to put forward an active wave absorber based on a feedback proportional controller driving a secondary piston.

The CFD model was then applied to a single 3D test case in which the undular bore interacts with a vertical square cylinder. First, the undular bore was fully characterized by its phase velocity, main wave height, and bore height, as well as Froude number and the velocity profile below the wave was given. Then, the vortex generation at the four edges of the cylinder was detailed, the pressure forces were computed and converged to the empirical results from Qi et al. (2014). Then, a closer look at the vortices allowed us to linked their formation frequency with the one from the undular bore, so that vortex shedding at both the front and rear edges is triggered by the upcoming wave following its instantaneous frequency. A special attention was given to the rear vortices which showed to pair and a Crow instability was observed. The vortex transversal velocity was given and allowed to fit a Lamb-Oseen vortex pair profile for which the vortex strength, core size and center were retrieved. Finally, hints for the scour study were given but should be extended in a dedicated study.

The numerical model can allow us to explore and illustrate most of the phenomena, but it is computationally expensive. Therefore, experimental data could allow for further characterization, in particular, it could be interesting to change the wave characteristics and/or the cylinder diameter in order to observe their influence on the vortex generation and forces applied to the cylinder.

Chapter 6

Experimental results

In this section, the experimental study of the undular bore interaction with a vertical square cylinder is carried out for a set of five undular bores. First, the undular bore generation and propagation is studied, for which the experimental set-up, test cases, wave profiles and particle velocities are given. Then, the focus is directed to the vortex pairs that are generated at the rear of the cylinder. Qualitative observations are made before the vortex strength is computed thanks to a PIV set-up.

6.1. Undular bore propagation

In this section, the different undular bore characteristics, which can be listed as the bore height a, the main wave height H, the phase celerity C_p and the water particle horizontal and vertical velocities (U_x, U_z), are reviewed for the experimental cases. The different cases that are studied in this thesis are reported in table 6.1. The test cases are characterized by the piston wavemaker velocity, for which all cases are preceded by a ramp of 0.1 s. In order to fully determine the parameters which describe the undular bore, a PIV set-up is installed in the wave tank and described in section 6.1.1. This last one allows to measure the wave height, presented in section 6.1.2, as well as the particle velocities below the bore which are reported in section 6.1.3. In the purpose of facilitating the comparison, the numerical case which was previously presented in section 5.2 is also displayed in most of the figures.

Case	Type	U_G [m/s]
E1	Experimental	0.05
E2	Experimental	0.07
E3	Experimental	0.09
E4	Experimental	0.10
E5	Experimental	0.12
N1	Numerical	0.10

Table 6.1: Studied cases in this thesis are composed of 5 experimental undular bores and one numerical one.

6.1.1. Experimental set-up

In the following sections, we first show the different undular bore profiles as a function of time, and we report their characteristics. We then focus on the particle velocities below the bores and comparison are made between the experimental and numerical cases. In order to do so, a PIV experiment is set-up where a vertical laser plane slices the experimental wave tank in half according to figure 6.1a. The undular bore (2) is generated by the piston wavemaker (1) according to a time function which is first composed of a ramp of 0.1 s and then a constant velocity U_G which depends on the study case. The laser (3) generates a plane thanks to a cylindrical lens situated at its end. This laser horizontal plane is deviated by a mirror (4) at a 45° from the horizontal plane, so that the deviation results in a perfectly vertical plane. The CCD camera (5) is placed at the side of the wave tank, at $x = 0.80$ m from the wavemaker initial position, and with a small angle compared to the horizontal plane in order to avoid any blurring due to the wave passage on the side wall. The water is seeded with the Sphericel 110P8 particles, for which an estimation (through image binarization and counting of the particles) of 0.009 particles per pixel per pixel is determined which is in the range of particle density that allows for low bias and RMS errors according to the study of section 4.3.2.3. Images are taken at a 60 Hz frequency and are then automatically post-processed to extract the mask with the radon transform strategy defined in section 4.3.3, as in the example of figure 6.1b shows, and then the PIV post-processing tool of section 4.3.1 is used to compute the velocity field. If 64 x 64 pixels^2 wide window were used for the E1 and E2 cases, these window had to be enlarged to 128 x 128 pixels^2 for the E3 and E4 cases and even 256 x 256 pixels^2 in the E5 case as particle motion is greater in these cases, which cause also blurring and thus measurement at lower windows size was not possible.

6.1.2. Wave profile

6.1.2.1. Wave height

The wave profile is measured thanks to the masking tool of the PIV procedure, and we are able to plot for all cases the wave height as a function of time. The results are shown in figure 6.2. The measurement errors associated with the free-surface detection is considered to be half the interface thickness on the images so that the wave height error is $\epsilon = \pm 0.2$ mm. As expected, we observe undular bores composed of the main wave (or the overshoot wave as seen in section 5.1), whose height H is reported in figure 6.3b, followed by the wiggles of smaller amplitudes which converges toward the bore mean height a which is plotted in figure 6.3a. For graphical purposes, all curves are synchronized so that their maximum wave height happens at the maximum one from the CFD simulation, that is to say at $t = 1.32$ s. It can be observed however, that the number of wiggles is quite limited in the experimental case and for the higher piston velocities. For example, we can count 9 waves including the main wave for the E1 case (smallest piston velocity) while only 2 waves, or three crests are available for the E4 and E5 cases. This is due to the shorter time during which

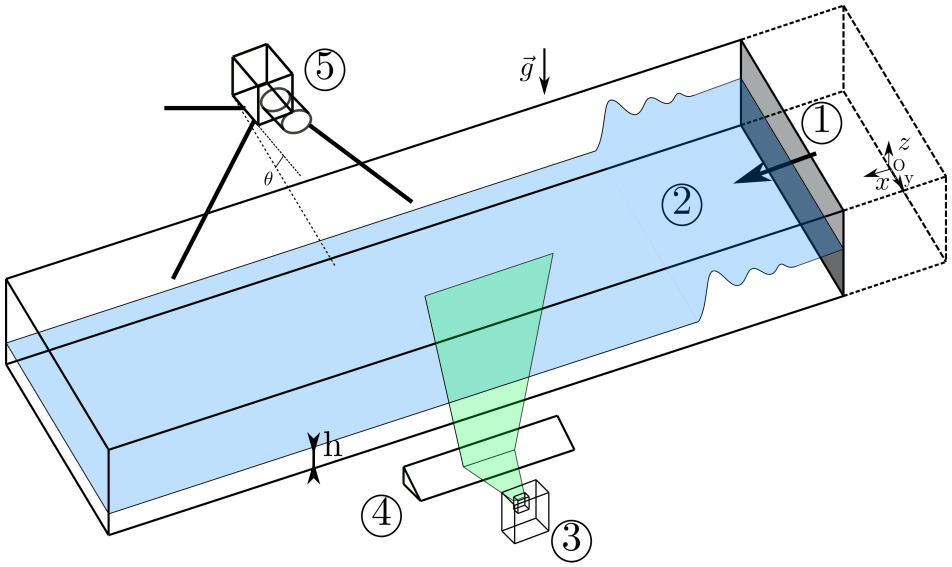

(a)

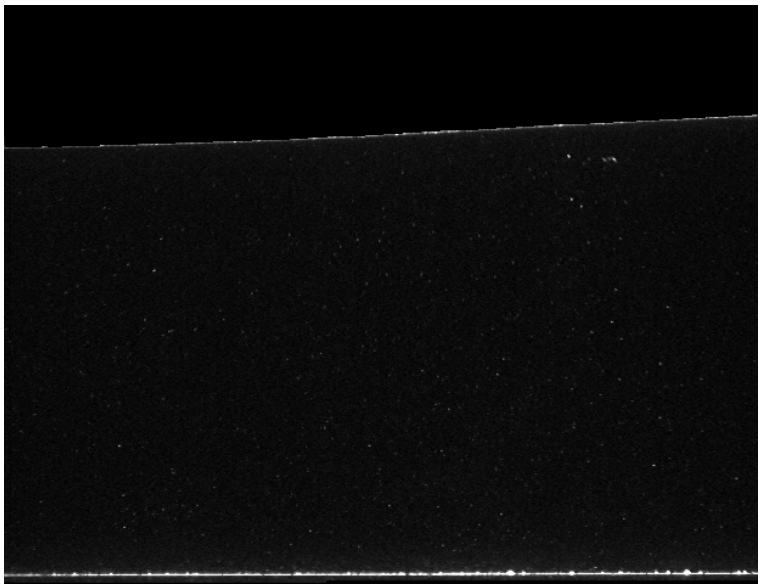

(b)

Figure 6.1: (a) Experimental set-up for the wave profile and velocity field measurements. The piston wavemaker (1) generates an undular bore (2) which propagates along the wave tank. A laser (3) generates a plane which is deviated by a 45° mirror (4) and the images are shot by a CCD camera (5) situated at the side of the wave tank. (b) Example of the PIV images (E5 test case), after masking of the atmosphere part with the radon transform based algorithm.

the piston wavemaker generates the bores, as its stroke is limited to around 17 cm. If the main wave is easily identified, by looking at the maximum of the undular bore height, this is not the case for the bore mean height a which is only easily traceable in the E1 case. This is why we decided to fit an exponential decay function to the wave crests of the bore, according to:

$$f(t) = a_1 + a_2 e^{-t/\tau} \tag{6.1}$$

where a_1 and a_2 are length constants, and τ is the decay time constant. We can observe on figure 6.2 that the fit is quite precise and passes by almost all wave crests and all cases, even if it can be argued that the precision of the fit on the last cases (E3,E4,E5) is much less important due to the reduced number of crests. In particular, in the E4 case, the wave bore height seems to be largely overestimated. We can compute the error basing our analysis on the non-linear fit algorithm (*nlinfit* function of *matlab*) and take the mean of the error in the interval $[1.32; 2.2]$. The error guess however fails for the E3 to E5 cases due to the too low number of wave crests that are generated. The analysis of the different parameters such as the bore height a in the following paragraphs and figure should then be taken with care as the error is not known. We observe however that this method is quite precise in the first experimental case that is to say when the number of wave crests is high enough.

The exponential decay function allows us to compute the mean bore height as this function converges in time toward the bore height. We plot the bore mean height in function of the case (or the piston velocity) in figure 6.3a, as well as the numerical case. A direct comparison between the experimental cases and numerical one is not suitable as the wet-back configuration of the experimental facility gives lower bore. We observe an increase of the mean height with the increase of the piston velocity, and it is important to notice the small discrepancies observed for the E4 case which results from the low number of crests used for the exponential fitting. The bore mean height ranges from 1.5 mm for the E1 case to 7.4 mm for the numerical undular bore N1. It is interesting to observe that this increase follows the linear behavior of the water level at wavemaker studied in section 5.1.1.2, according to $\eta_w \approx h \times Fr$, with a constant difference Δa which can be explained by the water loss at the bottom of the wavemaker in the wet-back set-up of the laboratory and the suction effect that results, leading to a smaller water level at the wall and thus a smaller bore mean height. Finally, we can observe that the numerical value of the bore, also obtained by fitting of the exponential decay corresponds to the value of section 5.1.1.2, showing the good accuracy of the method to determine a.

The undular bore main wave height, which ranges from 3.3 mm for the smallest experimental case to 1.04 cm for the numerical bore, is presented in function of the cases in figure 6.3b. It shows a relative linear increase with the piston velocity, and as for the bore mean height, it follows the tendency of the overshoot wave height at the wavemaker, such as $\eta_o = 1.267 \times h \times Fr$, with a difference ΔH due to the ramp in the experimental velocity function, the suction effect and the fact that the undular bore main wave increases its height during its course. Indeed, we observe an important difference between the maximum wave height of the numerical case N1 and the overshoot

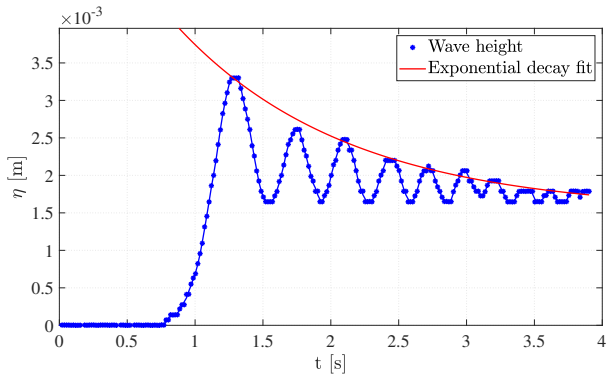

(a) Case E1 - $U_G = 0.05$ [m/s]

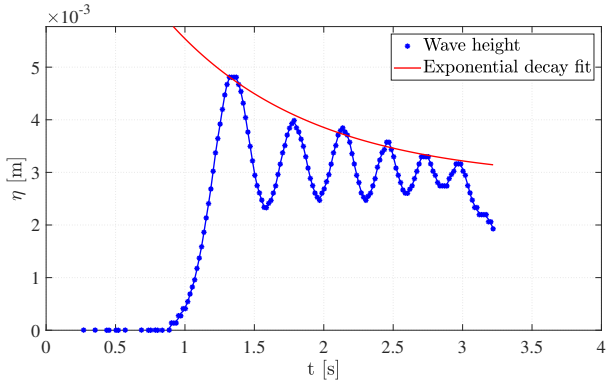

(b) Case E2 - $U_G = 0.07$ [m/s]

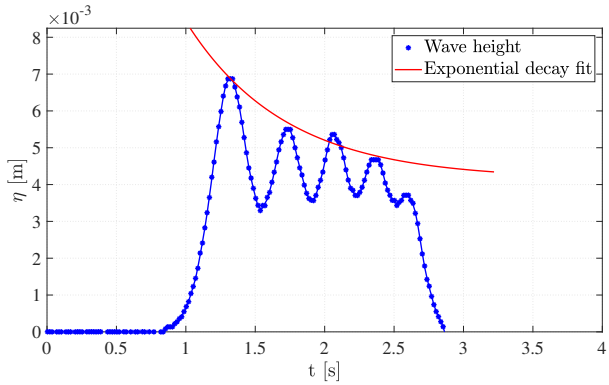

(c) Case E3 - $U_G = 0.09$ [m/s]

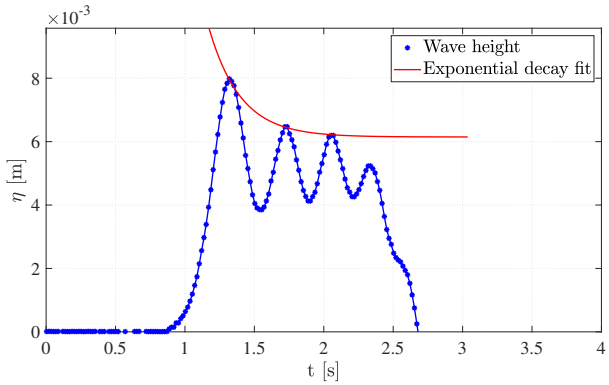

(d) Case E4 - $U_G = 0.10$ [m/s]

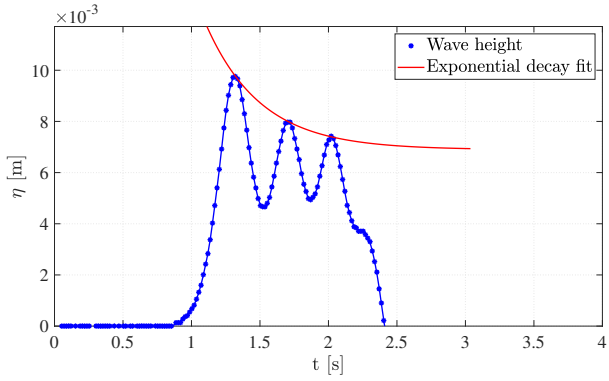

(e) Case E5 - $U_G = 0.12$ [m/s]

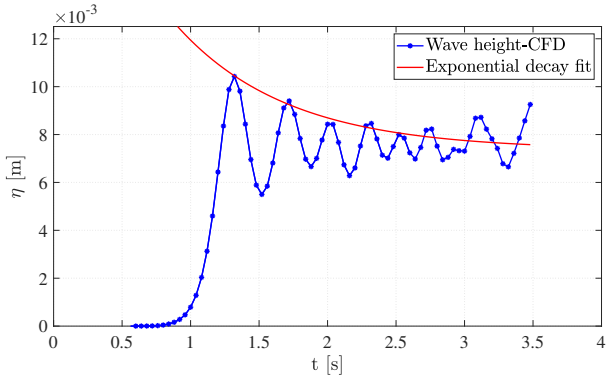

(f) Case N1 - $U_G = 0.10$ [m/s]

Figure 6.2: Undular bore wave profile at $x = 0.80$ m from the wavemaker in function of time for the five experimental cases (E1 to E5), measured with image post-processing and interface detection with the radon-transform, and the CFD case (N1). An exponential decay function $f(t) = a_1 + a_2 e^{-t/\tau}$ fit is computed on the wave crests and results are superimposed and allows to determine the bore mean height a.

value at the wavemaker which is explained by the fact that as the undular bore travels downstream the main wave gains height. In this example, the overshoot/main wave gained 1.4 mm during its 80 cm travel.

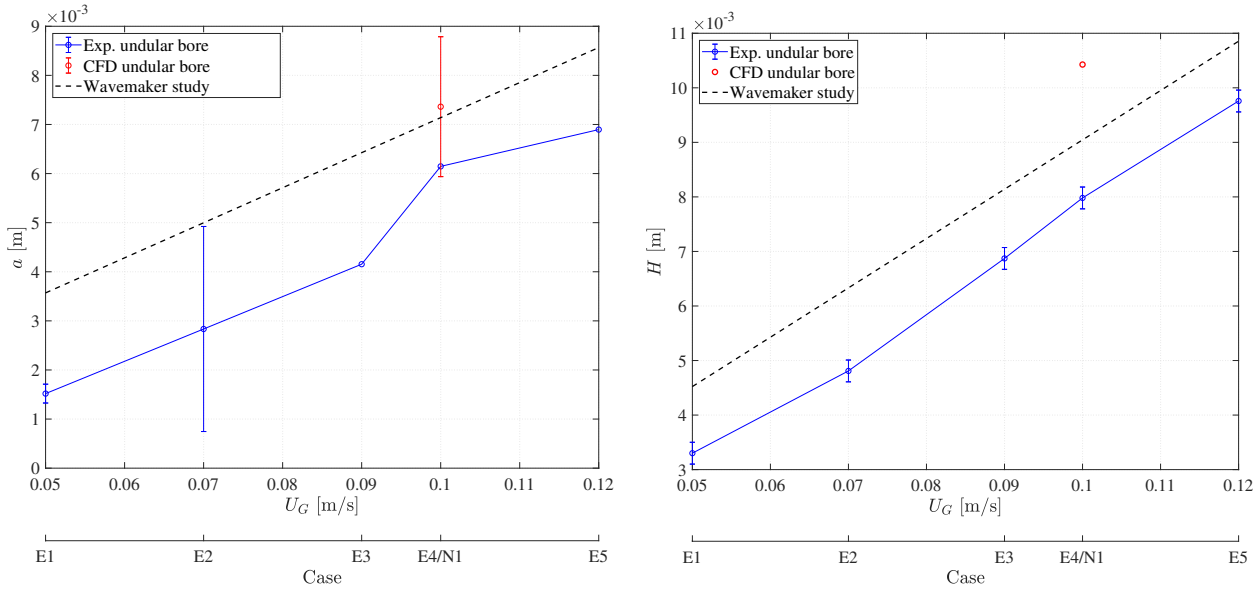

Figure 6.3: (a) Bore height in function of the wavemaker velocity. Error bars are unavailable for case E3, E4 and E5 due to the too low number of wave crests. (b) Main wave height in function of the wavemaker velocity. The wavemaker study refers to the study of section 5.1.1.

We can also plot the decay time constant from equation 6.1 in function of the case, as it is carried out in figure 6.4. The decay time constant informs us on the rapid amplitude decay from the wave main wave to the following crest. We observe that as the main wave is more important, the decay is more important (lower time constant) or otherwise said, as the undular bore Froude number increases, the main wave is much more predominant compared to the secondary waves. Basing our analysis on this figure, we can presume that the time constant for the E4 case is underestimated, due to the low number of wave crests available to apply the fitting procedure.

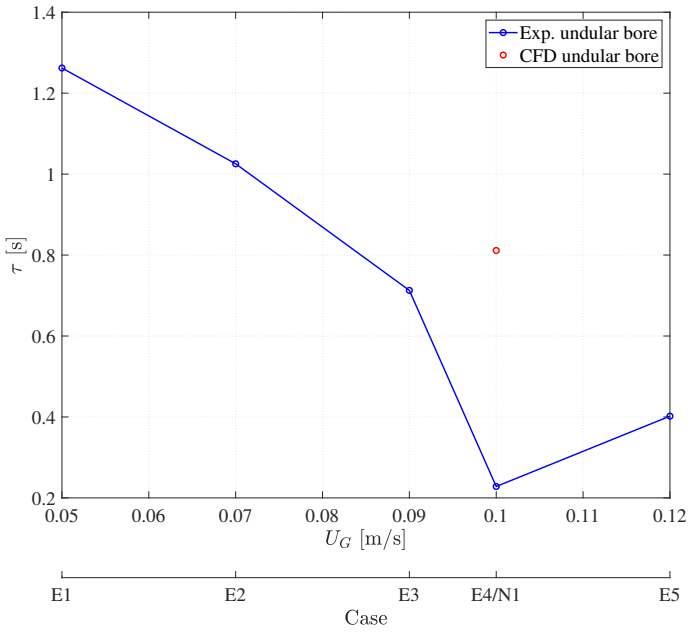

Figure 6.4: Exponential decay time constant τ in function of the wave-maker velocity U_G or the test cases. The time constant τ is retrieved from the exponential decay function $f(t) = a_1 + a_2 e^{-t/\tau}$ fit over the wave crests.

6.1.2.2. Undular bore phase celerity

The phase celerity of the bore can be computed by looking at the position of the main wave. In the case of the experimental phase celerity, it is computed by identifying the times at which the maximum wave height enters the PIV image and the one at which it leaves the image. To do so, a smoothing is applied on the wave height signals and allows to precisely measure these times. We then compute the phase celerity as the mean of the wave celerity during its travel in the image. Results are presented in figure 6.5, where the celerity ranges from 0.711 m/s to 0.772 m/s and the associated Froude number, computed according to $Fr = c_p/\sqrt{gh}$, from 1.01 to 1.10. These values are characteristic of smooth non-breaking undular bore in a rectangular channel as observed in the experiments of Treske (1994). We can compare the phase celerity with its theoretical value given by (Treske, 1994):

$$c_p = \sqrt{g(h + 1.5a + \frac{a^2}{2h})} \tag{6.2}$$

The maximum error between the theory and the computed values from the experiment is 1.4% and correspond to the E4 case, for which the exponential decay fit procedure was not ideal. As the error is small for all cases, we can conclude that the experimental and numerical phase celerity are relatively well calculated. The use of two synchronized capacitive wave gauge placed at a known distance from each other could however be used to improve this measurement.

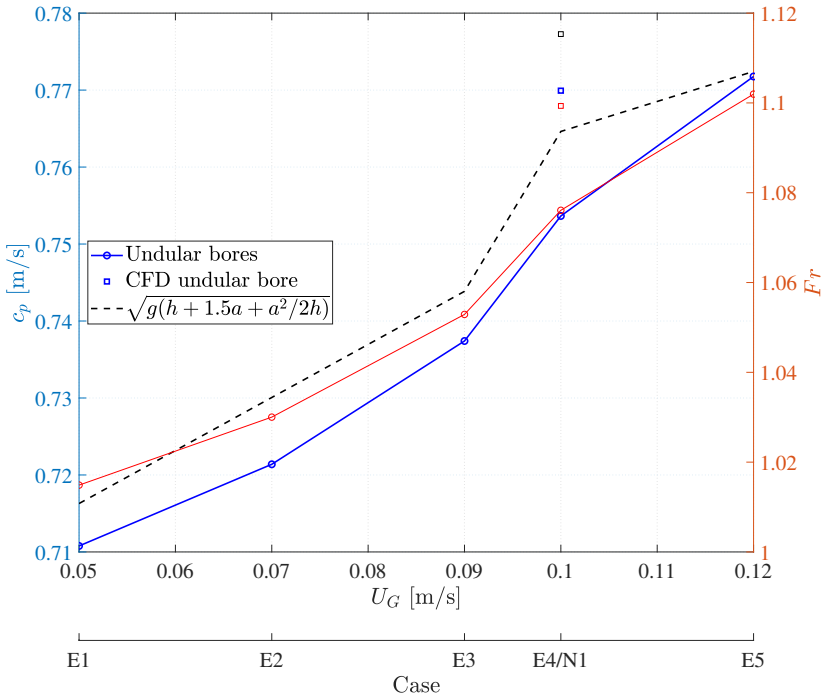

Figure 6.5:

Figure 6.6: Phase celerity (in blue) in function of the test case generation velocity U_G and equivalent as Froude number (in red). The square marks represent the value for the numerical case.

6.1.2.3. Dimensionless analysis

As the conditions between the numerical study and the experiments are slightly different, due to the difference of undular bore generation methods (wet-back system in the experiment versus perfect piston in the CFD simulation), it is decided to work when possible with dimensionless data. For this analysis, the length variables will be converted to dimensionless ones by dividing them by the reference length h (the mean water level), the velocities by $\sqrt{gh}$ (phase velocity), and the time by the constant $\sqrt{h/g}$. We then plot the dimensionless maximum wave height H/h and the mean bore height a/h as a function of the Froude number in figure 6.7. The theoretical mean bore height is also plotted, where the Froude number is related to the dimensionless mean bore height according to (Treske, 1994):

$$Fr = \sqrt{1 + 1.5\frac{a}{h} + \frac{a^2}{2h^2}} \tag{6.3}$$

We observe a linear behavior between both quantities and the Froude number. This is due to the fact that the mean and maximum wave height are much smaller than the mean water level. The value of the mean bore height is however somehow overestimated by the exponential decay technique, as we compare with the theory, even if it gives good trending results. It is also interesting to compare the numerical case to the experimental ones and conclude that the closest experimental case is the E5 case, with similar Froude number and wave height to water depth ratios.

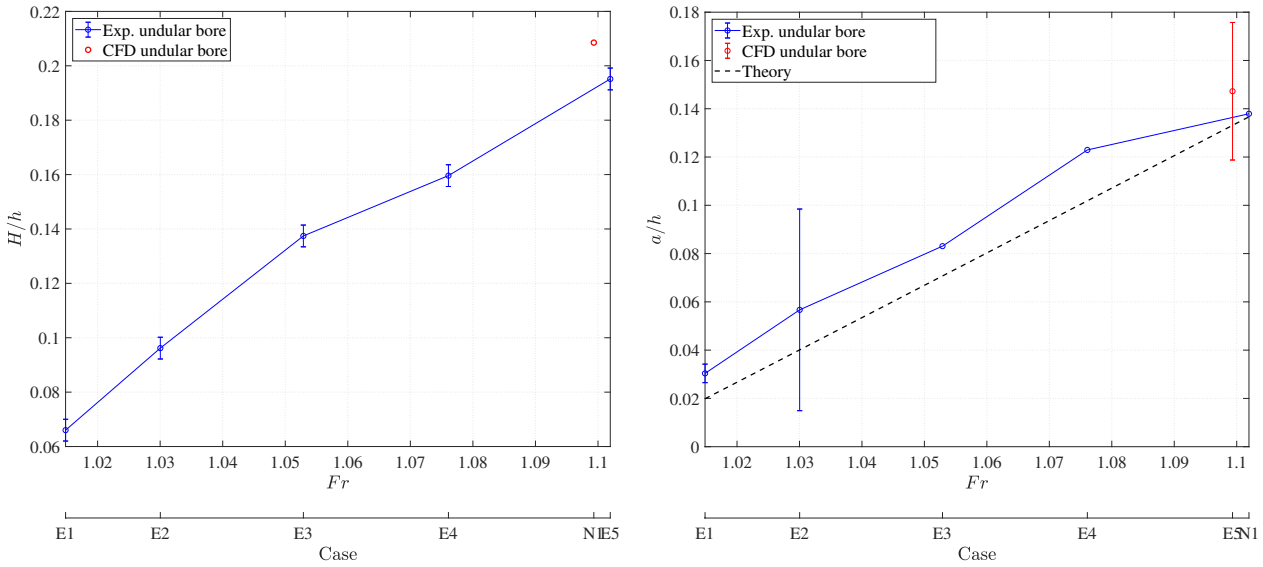

(a) (b)

Figure 6.7: (a) Dimensionless wave height H/h in function of the Froude number $Fr = c_p/\sqrt{gh}$. (b) Dimensionless bore height a/h in function of the Froude number.

6.1.3. Particle velocity below the undular bore

It is important to determine the particle velocities below the undular bore as it is this flow that will interact with the vertical square cylinder. To do so, we will focus on the values at half mean water level $z = h/2$ and a comparison with the numerical ones will be carried out.

The PIV velocity field for the cases E1 and E4 are given in figures 6.8 and 6.9 respectively, where the velocity field is superimposed over the velocity magnitude defined as $||\vec{U}|| = \sqrt{U_x^2 + U_z^2}$. The main difference between the two cases, apart from the velocity magnitude (note the difference of magnitude range in the colored bars between the E1 and E4 cases), is the number of velocity vectors which is reduced for the higher bore due to an increased interrogation window size in the PIV analysis process. If some vectors are missing it can be either due to masking of the atmosphere phase as in figure 6.8c or due to the detection of outlier vectors which have been removed such as in figure 6.9c. This is particularly true close to the free-surface and is explained by the fewer particle present in the interrogation windows since part of it focuses on a huge masked region. It also explains some of the low velocity magnitude in the E1 case and close to the atmosphere which are not physically correct. The image acquisition focuses on a more or less 8 cm wide zone at around $x = 0.80$ m from the wavemaker, and the free-surface variation can be observed as the wave passes by. The seabed boundary layer is not resolved. Times $t = 1.0033, 1.3200, 1.5033, 1.7200, 1.8867, 2.2367$ s are shown and approximately correspond to the crest and troughs of the undular bore. The first observation that can be made from these PIV results is that the flow is much more 2D close to the seabed than the free-surface, as it is expected. This flow characteristics has been emphasized in section 5.2.2 for the numerical test case. We also observe a quite constant velocity magnitude in

space as the velocity is quite constant in the z-vertical and only a reduced part of the wave is filmed in the x-direction.

From these PIV results, we are able to plot the velocity in the x and z directions, respectively written U_x and U_z, at a water depth of $z = h/2$ and in function of time. These plots are available in figure 6.10a and 6.10b. For graphical purposes, all curves are synchronized so that their maximum velocity happens at the maximum one from the CFD simulation, that is to say at $t = 1.32$ s. The x-velocity follows the bore wave heights, with a first increase due to the main wave passage followed by wiggles. As it depends on the bore height, we observe an increase in the velocity from case E1 to E5. Finally, the E5 and N1 cases compare very well for times below $t < 2$ s, which validates the numerical simulation for the wave propagation problem since for two bores of very similar Froude numbers (1.102 and 1.099 for the E5 and N1 cases respectively) and very similar wave height to water depth ratios (0.195 and 0.208 respectively), the maximum velocities are 0.1224 and 0.129 m/s corresponding to a 5.7% difference.

In the case of the vertical velocity U_z, which is plotted in figure 6.10b, we observe oscillatory variations from positive to negative values, and so forth, until the amplitude decreases to a constant value of 0 m/s which correspond to a current flow. The maximum amplitude is, for all cases, approximately ten times lower than the horizontal motion velocity, confirming the quasi-horizontal flow situation. This is however not true close to the free-surface as it has been shown in section 5.2.2 where more details are given since more information is available from the numerical simulation.

6.1.4. Summary and conclusion

A summary of the different experimental and numerical cases is registered in table 6.2. We keep the measured values of the wave height H, the bore height a, and their dimensionless counterpart, the phase celerity, the associated Froude number and the maximum particle velocity at $z = h/2$ for the experimental cases E1 to E5 and the numerical one N1.

Case	H [m]	a [m]	C_p [m/s]	Fr	H/h	a/h	$U_{x,max}$ [m/s]
E1	0.0033	0.0015	0.711	1.015	0.066	0.303	0.044
E2	0.0048	0.0028	0.721	1.030	0.096	0.057	0.064
E3	0.0069	0.0042	0.737	1.053	0.137	0.083	0.090
E4	0.0080	0.0061	0.754	1.076	0.160	0.123	0.101
E5	0.0098	0.0069	0.772	1.102	0.195	0.138	0.122
N1	0.0102	0.0074	0.769	1.099	0.208	0.147	0.129

Table 6.2: Incident wave characteristics summary for the experimental and numerical cases.

In this section, we were able to generate, analyze and categorize a series of experimental undular bores. The undular bore wave profile was measured, leading to the description of the main wave as well as the mean bore height thanks to the fitting of a exponential decay function. The phase

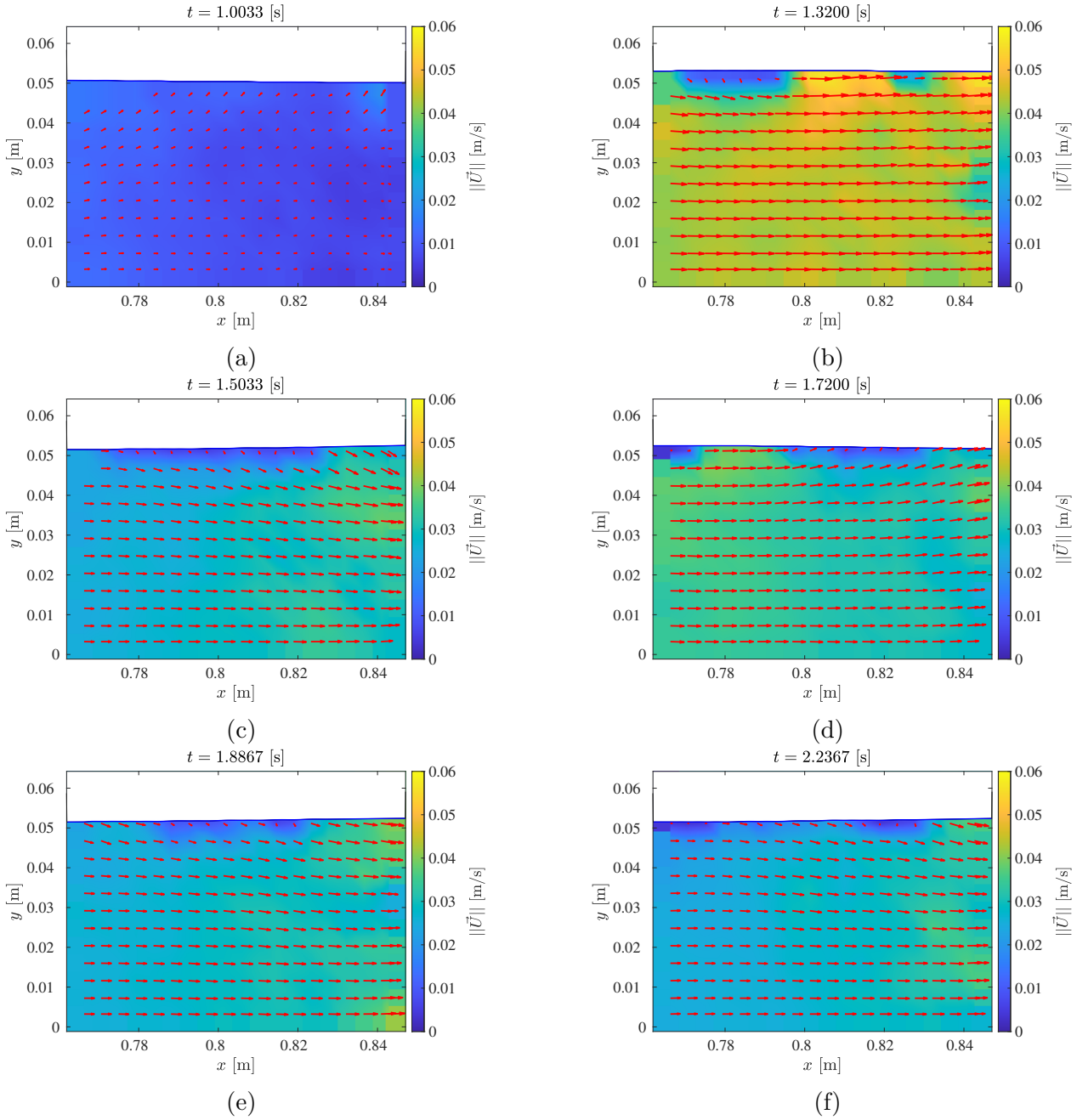

Figure 6.8: PIV velocity field for case E1 - $U_G = 0.05$ m/s at a position $x = 0.080$ m from the wavemaker. Interrogation windows are 64 x 64 pixels^2 wide. The free surface is plotted in blue.

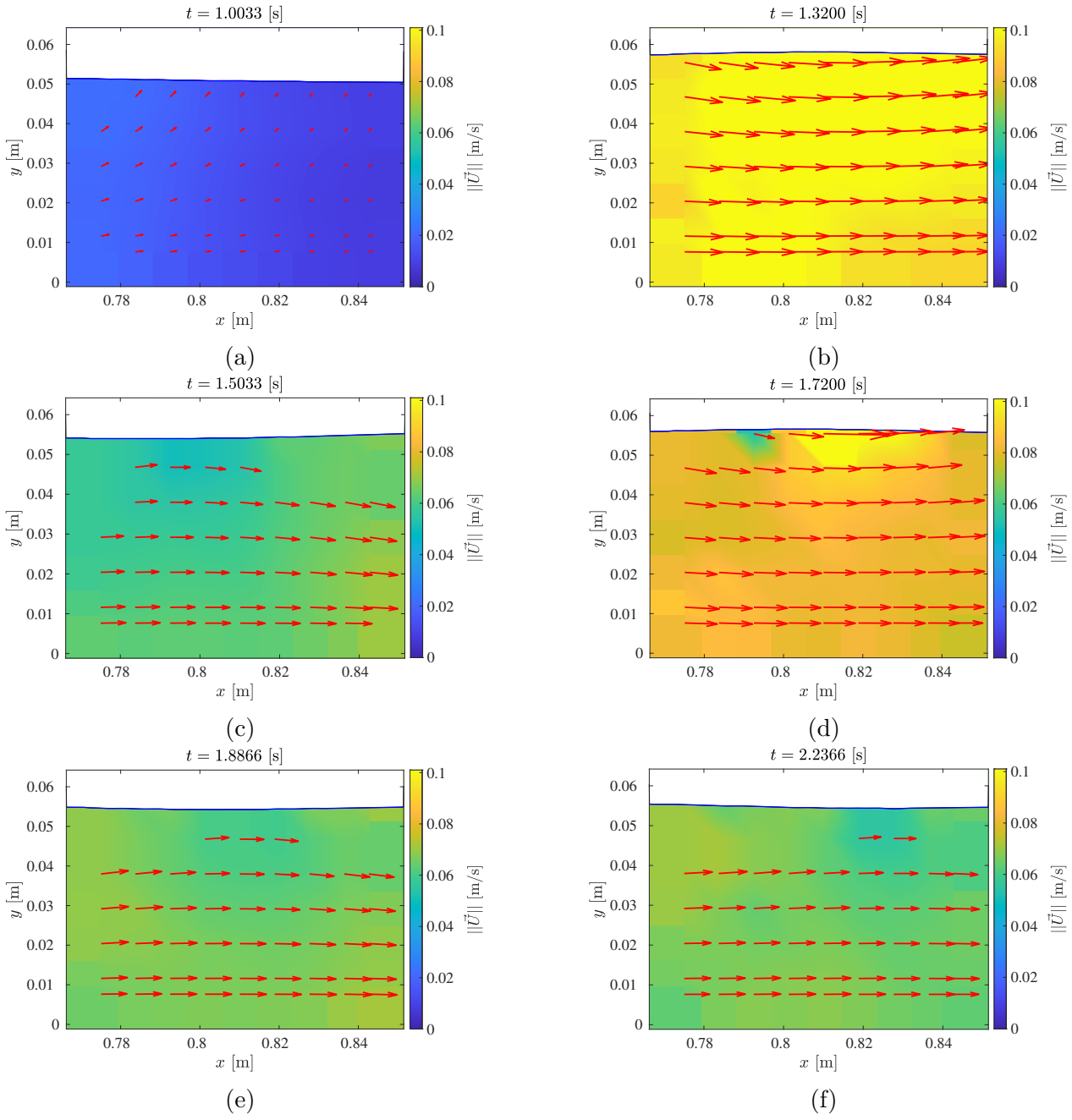

Figure 6.9: PIV velocity field for case E4 - $U_G = 0.10$ m/s at a position $x = 0.080$ m from the wavemaker. Interrogation windows are 128 x 128 pixels^2 wide. The free surface is plotted in blue.

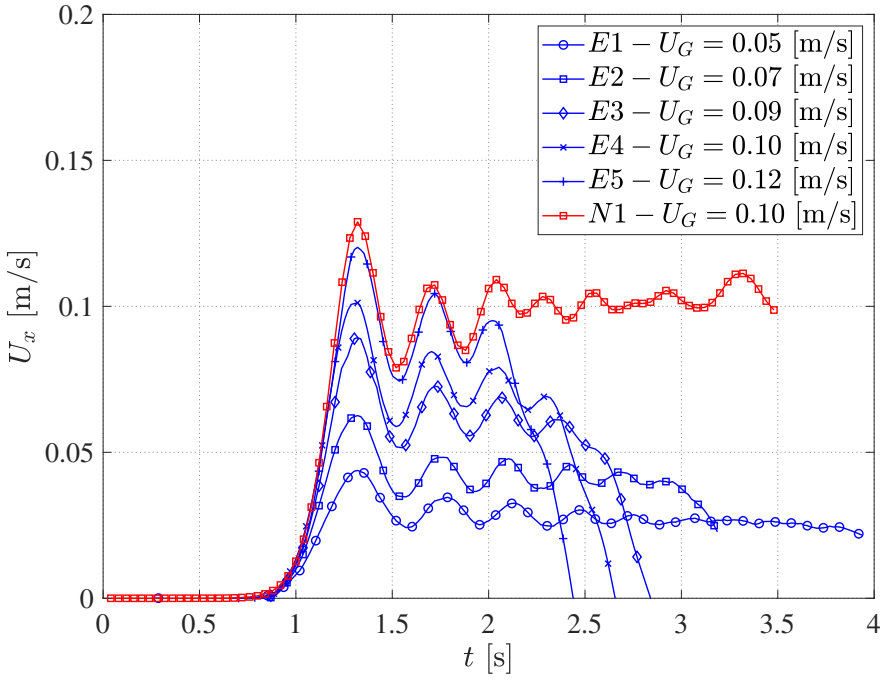

(a)

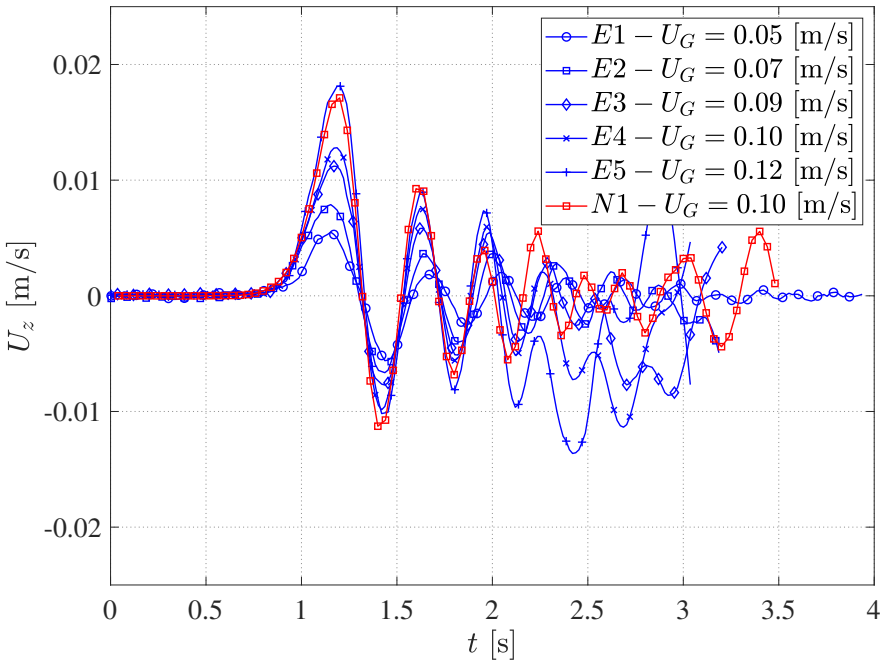

(b)

Figure 6.10: Velocities of cases E1 to E5 measured by PIV and case N1 in function of time at $z = h/2 = 0.025$ m, $x = 0.80$ m and $y = 0.00$ m. (a) Horizontal velocity $U_x(t)$. (b) Vertical velocity $U_z(t)$.

velocity was also measured by image post-processing and we were able to associate a Froude number to every cases, showing notably that cases E5 and N1 (corresponding to the CFD simulation from the previous section) are really similar by their Froude number, wave height to water depth ratio and mean bore height to depth ratio. An extensive flow velocity analysis is also carried out showing that the bore velocities are similar to a velocity step where variations appear at its top and its trend is in all aspect similar to the bore height profile as expected. It is also interesting to observe the convergence of the flow to a 1D flow, thus passing from a wave plus current flow to a simpler current flow. Finally, the numerical wave propagation from the previous section is validated by the data of the experimental data (E5 case).

The results of the following section depends greatly on the Froude number which is measured for all bores. This was achieved thanks to the PIV images, but the method only computes it for the time the bore enters and leaves the image. A better method could be to install two synchronized wave gauge separated by at least 20 or 40 cm which would allow to measure a mean of the phase celerity of the bore. This could also be achieved at the same time as the PIV measurement at the rear back of the cylinder and thus the hypothesis of repeatability which is made in the next section would not be necessary anymore.

6.2. Undular bore interaction with a vertical square cylinder

6.2.1. Experimental set-up

General set-up The interaction of the undular bore with the vertical square structure is experimentally carried out thanks to a PIV set-up which is presented in figure 6.11. It consists first in the generation of an undular bore (2) thanks to the piston wavemaker (1) (such as in the previous section). Then the undular bore propagates along the wave tank and finally interacts with the square cylinder (3) of diameter $D = 4$ cm. An horizontal laser plane is projected at a height $z = h/2 = 0.025$ m and lights the rear part of the cylinder. The water is seeded with the Sphericel particles and images are taken with the CCD camera with the help of a 45° inclined mirror which is placed at the vertical from the cylinder and below the wave tank. The CCD camera takes pictures at a frame rate of 60 Hz, with a resolution of 672×476 pixels x pixels and the field of view is situated at the rear of the cylinder, a zone where vortex pairing is observed as we will discuss in the following sections. An example of such picture can be found in figure 6.12, for which the velocity field retrieved thanks to the PIV tool is also shown. The images, before post-processing are cleaned up by setting to 0 all pixels with a low light (generally lower than 15/255, but in some cases, it gave better results to set to 0 pixels with values as high as 50/255). A mask is applied over the left part of the pictures to cover the cylinder zone and calibration is carried out by measuring the width of the cylinder on the picture. The interrogation window size varied from 32×32 pixels x pixels for the

E1 to E3 cases and 64×64 pixels x pixels for the E4 and E5 cases as particle displacement became too large to allow the PIV tool to resolve the displacement field. A 50 % overlap is used alongside the window deformation algorithm. For example, in the E5 case, 14 rows of vectors were obtained vertically and horizontally giving 196 velocity vector in a field of view representing around 5 cm in the x direction and 4 cm in the y direction. In the case of the smaller interrogation windows, $29 \times 30 = 870$ vectors are obtained. The experiment was carried out only one time by case, due to the long post-processing. After preliminary tests, the generation and wave propagation showed good repeatability so that the study in section 6.1 is considered valid and its output, notably the calculation of the Froude number, will be taken as it is. The wave height was originally to be measured with the capacitive sensor but as repeatability was good, and the main parameter to compare cases is the Froude number which was measured previously by image processing, we decided not to install the capacitive sensor at the side of the cylinder to avoid any unnecessary interaction between the bore and the sensor frame which would impact the flow. The water surface variation at the cylinder edges was not measured for the experimental cases nor the pressure forces, which is left as future tasks and analysis.

Issues during image acquisition and post-processing Some issues appeared during the image acquisition process and the post-processing one which are important to assess. First, the repartition of the particle tended to become heterogeneous, and in particular the particles tended to sink at the bottom of the wave tank after some minutes, so that mixing of the water was necessary before any measurement and a trade-off was taken between water at perfect rest before any action of the wavemaker and a too long wait which implied the sinking of the particles. Second, the field of view is zoomed at the rear part of the cylinder to focus on the vortices that are generated in that zone and to obtain enough resolution of the vortices as the camera resolution is quite low. Finally, blurring of the particles appeared for the cases of higher velocities such as the E5 case, which caused the necessity of larger interrogation windows (and thus lower vector density) and some error in the evaluation of the velocity magnitudes. In particular, some zones gave many outliers resulting in a false evaluation of the rest of vectors due to the smoothing function present in algorithm. It implied then to discard the images with too many outliers and the results presented in this thesis only show the sorted cases.

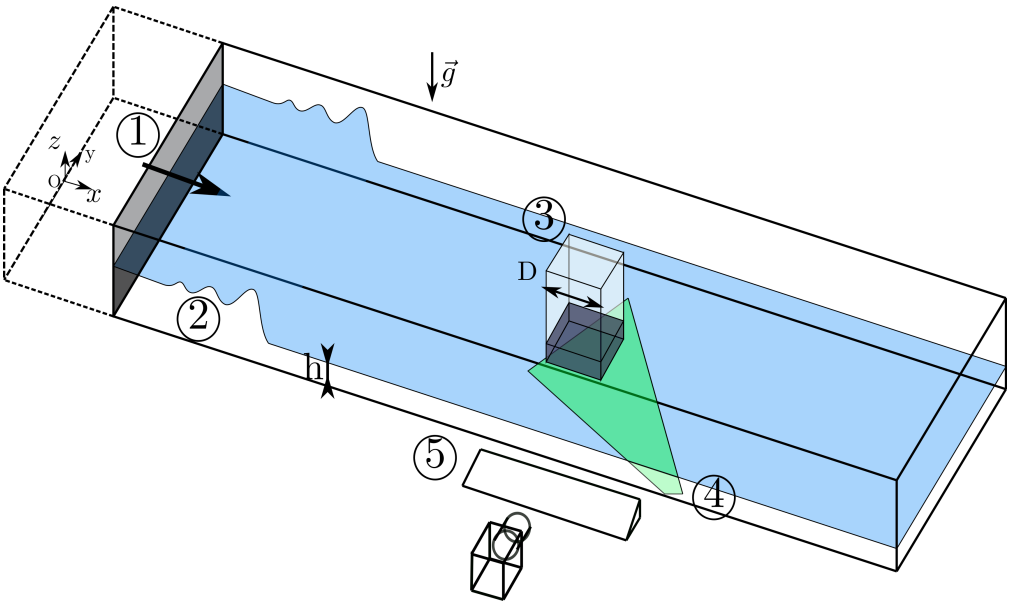

Figure 6.11: PIV set-up for the undular bore structure interaction study. The wavemaker (1) generates an undular bore (2) which interacts with the cylinder (3) of width $D = 4$ cm. A horizontal laser plane (4) at $z = h/2$ is projected at the rear of the cylinder and a camera (5) films the scene through a 45° bended mirror placed below the wave tank.

Ways of improvement for future studies The experimental set-up can be improved by taking a certain amount of measures which are listed now. These measures could not be taken in the present work because of the lack of time (access to the laboratory was restrained during the pandemic). First, the vertical cylinder could be painted in black to avoid reflection which generated some trouble in the post-processing of the images close to the cylinder. A mirror could also be placed vertically and at the opposite vertical tank wall to reflect the light inside the tank so that lighting would be more homogeneous. Indeed, we observed that the PIV post-processing algorithm failed many times in the zone where the light escaped the field of view (opposed to the laser side) due to bad lighting. Finally, another camera, with more resolution (so that the whole cylinder could be viewed), quicker shutter in order to observe less blurring and more frame per seconds to avoid too large displacements would be very useful in gaining precision in the measurements. A numerically controlled focus device would also be appreciated since its set-up "by hand" revealed to be tricky. Despite of all that, the results which are presented in this thesis are coherent, reasonable and precise enough to quantify and well represent the studied phenomena.

6.2.2. Vortex generation

An experimental visualization is carried out in the E4 case by using a high concentration of PIV particles. The resulting images are displayed in figure 6.13 for times $t = 1.6000,\ 1.8333,\ 2.3000\ 2.7500$ s. We can observe the formation of vortices at the edge of the cylinder at time $t = 1.6000$ s before these ones start to move away from the rear wall of the cylinder at time $t = 1.8333$ s. At this time,

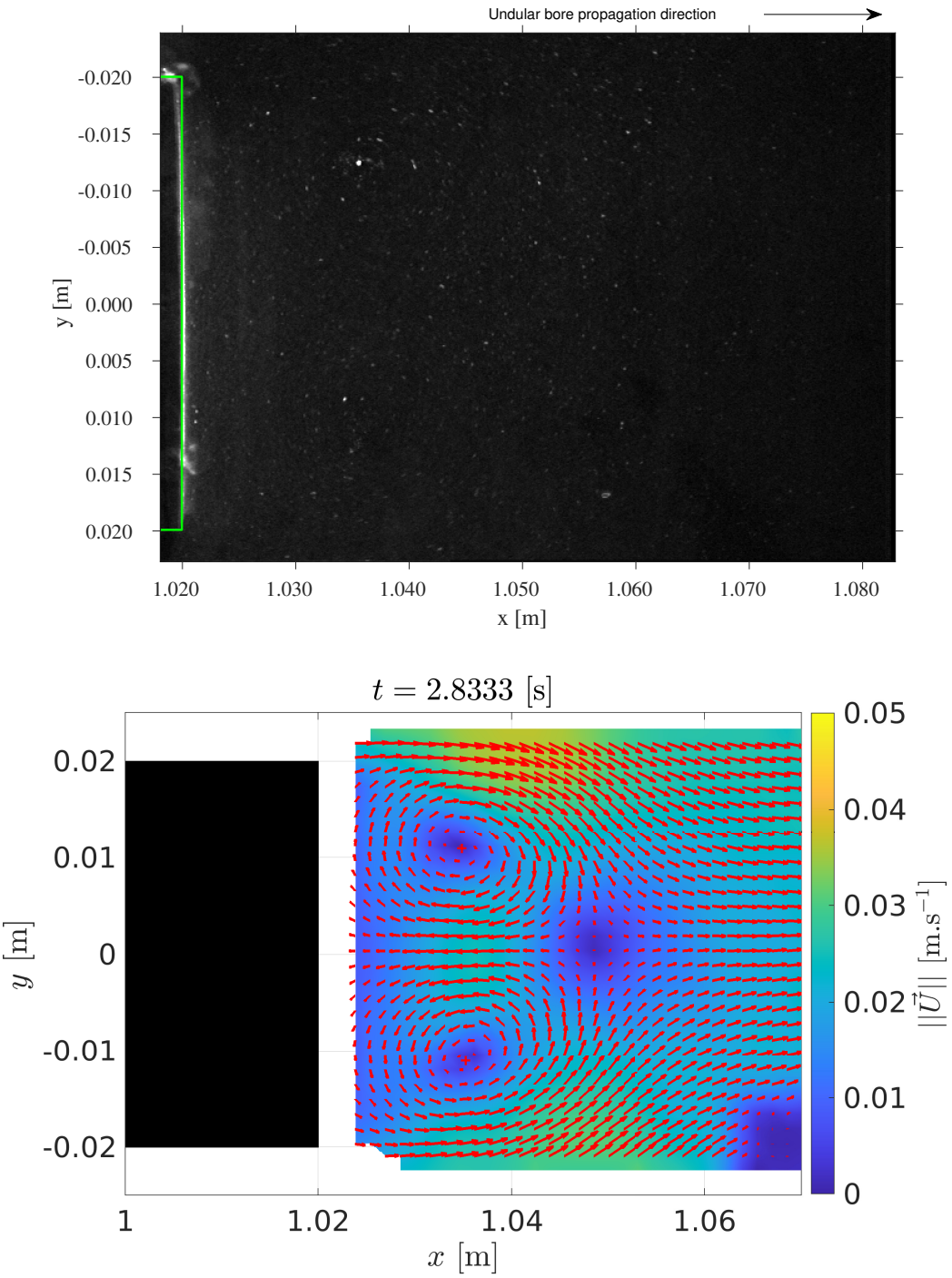

Figure 6.12: (a) Example of an image taken for PIV analysis. It corresponds to the E1 case and time $t = 2.8333$ s. The undular bore propagates from left to right and the cylinder walls are represented in green. (b) Velocity field retrieved from PIV analysis of the previous image at the rear part of the cylinder which is shown in black.

the vortex wrapping can be seen, with particle moving from the far wake towards the cylinder as well as from the side to the center. The vortices then start to get closer at time $t = 2.3000$ s. The vortex size is around half the cylinder diameter so that the vortex pair occupies the whole back of the cylinder. For all these times, there is a perfect symmetry between the vortices which is broken at time $t = 2.7500$ s, where the center line of the vortex pair which is easily identified does no longer coincide with the line $y = 0$ m passing by the cylinder side middle.

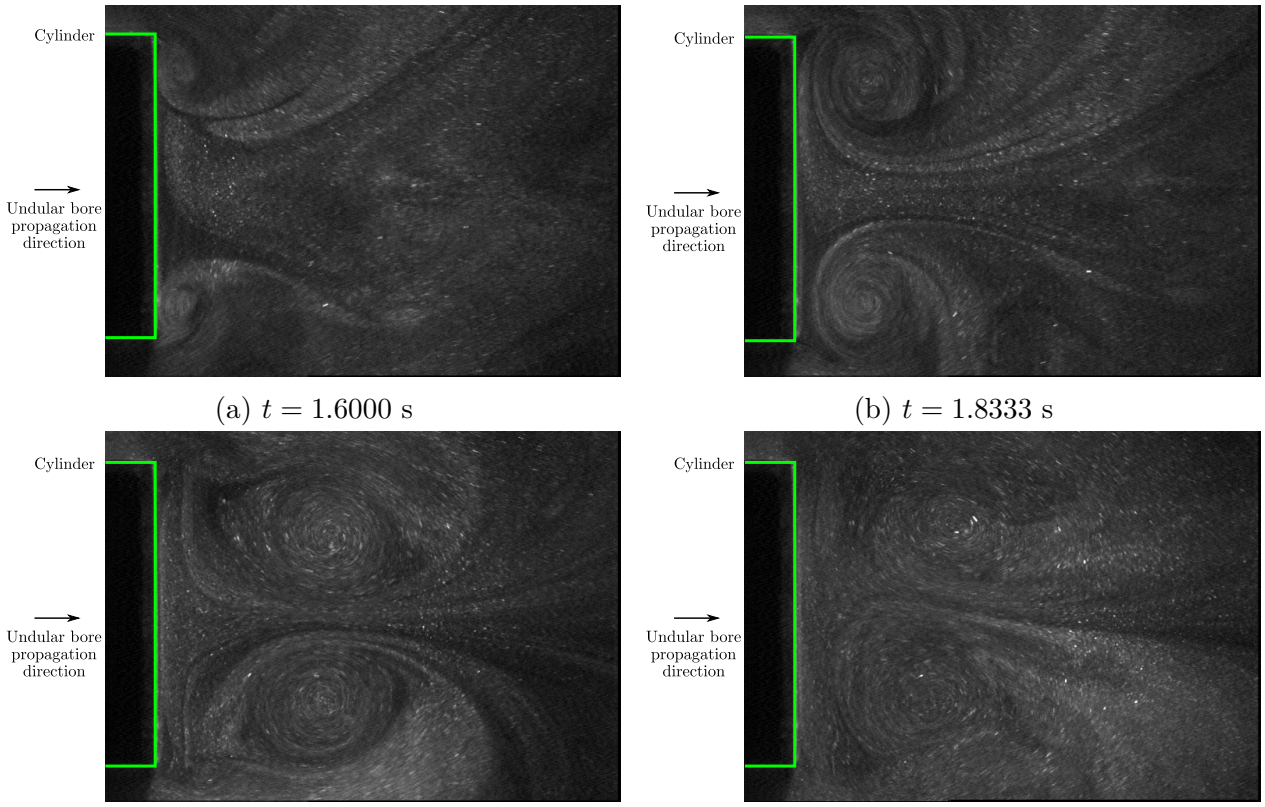

(a) $t = 1.6000$ s (b) $t = 1.8333$ s

(c) $t = 2.3000$ s (d) $t = 2.7500$ s

Figure 6.13: Visualization based on dense PIV particles poured in the tank before the undular bore hits the vertical square cylinder (from left to right) in the E4 case ($U_G = 0.10$ m/s) for times $t = 1.6000$, 1.8333, 2.3000, 2.7500 s. In green, the cylinder walls are represented.

Synchronization between experiment and simulation is made by finding the first picture where particles start to move at the cylinder edge, which corresponds to around $t = 1.25$ s in the numerical simulation N1. The very first images where the rear vortices are close to the cylinder were not possible to analyze so that only further times are shown. The vorticity, defined as $\omega = \nabla \wedge \mathbf{U}$, is computed for the experimental cases E1 and E5 and its vertical component is displayed alongside the velocity vector field in figures 6.14 and 6.15, respectively. Note that the vorticity and the velocity scales are not the same between the cases. These figures show quite clearly the presence of two counter-rotating vortices, one with a positive vorticity in red and the other with negative vorticity in blue. The vortices carry out a back and forth motion, that is to say that they start by getting away from the cylinder before getting closer and find a quite stationary position at the

rear of the cylinder. The vorticity strength is around three times higher in the E5 case, but we suspect that the vorticity field is under evaluated in the E5 case, since we have seen that the vortex motion is quite complicated to measure by PIV in section 4.3.2.2. This point will be further discuss in section 6.2.3. The vector field also shows the vortex pair with a convergence zone in between both vortices where the horizontal velocity component gains amplitude as time passes, whereas we are able to observe a zone of really low velocity at the center line between the vortices and at their back, which demarcates the negative x velocity due to the vortex flow from the positive one due to the bore passage. We also observe that the maximum velocities are found at the exterior of the vortices at the early times while later the maximum ones are located in-between the vortices.

The vortex pairing of the rear vortices can be characterized by their transversal velocity profile. The process to obtain these profiles in the experimental cases E1 to E5 is as follows: first, the centers of both vortices are determined according to the method of section 5.2.6 from the PIV field. In order to give more robustness to this process, outliers are detected by comparing the detected points with local velocity magnitude minimum in the $x-y$ plane. Then a right line is drawn between the vortex centers and velocity vectors are sampled along this line and projected to its perpendicular component. This step is a consequence of the loss of symmetry in some experimental cases such as for time $t = 2.55$ s of the E5 case and shown in figure 6.19. Note that this extra step is not carried out for the numerical case N1 as symmetry is kept almost until the end. After retrieving the velocity along the right line joining the vortex pair centers, a least square method allows to fit two Lamb-Oseen vortices, which are typical of vortex pairing (Leweke & Williamson, 1998), with the difference that an offset $U_0(t)$ is added to take into account the vortex pair own motions, according to the following expression:

$$U_x(y) = U_0 + \sum_{i=1}^{2} \frac{\Gamma_i}{2\pi(y-y_i)} \left(1 - \exp\left(-\frac{(y-y_i)^2}{a_i^2}\right)\right) \tag{6.1}$$

with $\Gamma_{1,2}$ is the circulation, $y_{1,2}$ the centres, and $a_{1,2}$ is the core diameter of the fitted vortices. The fit is executed with reference to the CFD profile between $-0.02 \leq y \leq 0.02$, that is to say the cylinder projection limits, which are represented in red in figure 5.41. The fit is carried out after detecting the vortex center positions through the procedure described in section 5.2.6 so that the y_i are already determined in equation 6.1.

The results of this process are plotted in the following figures: in figure 6.16, the velocity vector field is represented over the velocity magnitude for case E1. On the same figures the vortex centers are plotted with a red cross and the line joining them is in black. A similar plot for case E5 is shown in figure 6.18. The velocity profile along this line is plotted in blue in figures 6.17, 6.19 and 5.41 for cases E1, E5 and N1 respectively. Their corresponding fit is shown in black. The E1 PIV results show a general loss of symmetry in velocity magnitude at the external side of the cylinder, especially for early times. This is explained by different lighting in the PIV images and also the algorithm has more trouble to solve the velocity field at the edges of the images since some particles leaves the image and it does not have neighbor points on one side for the smoothing and outlier detection, sometime leading to false estimate. However, the velocity magnitude ranges from 0 m/s to almost

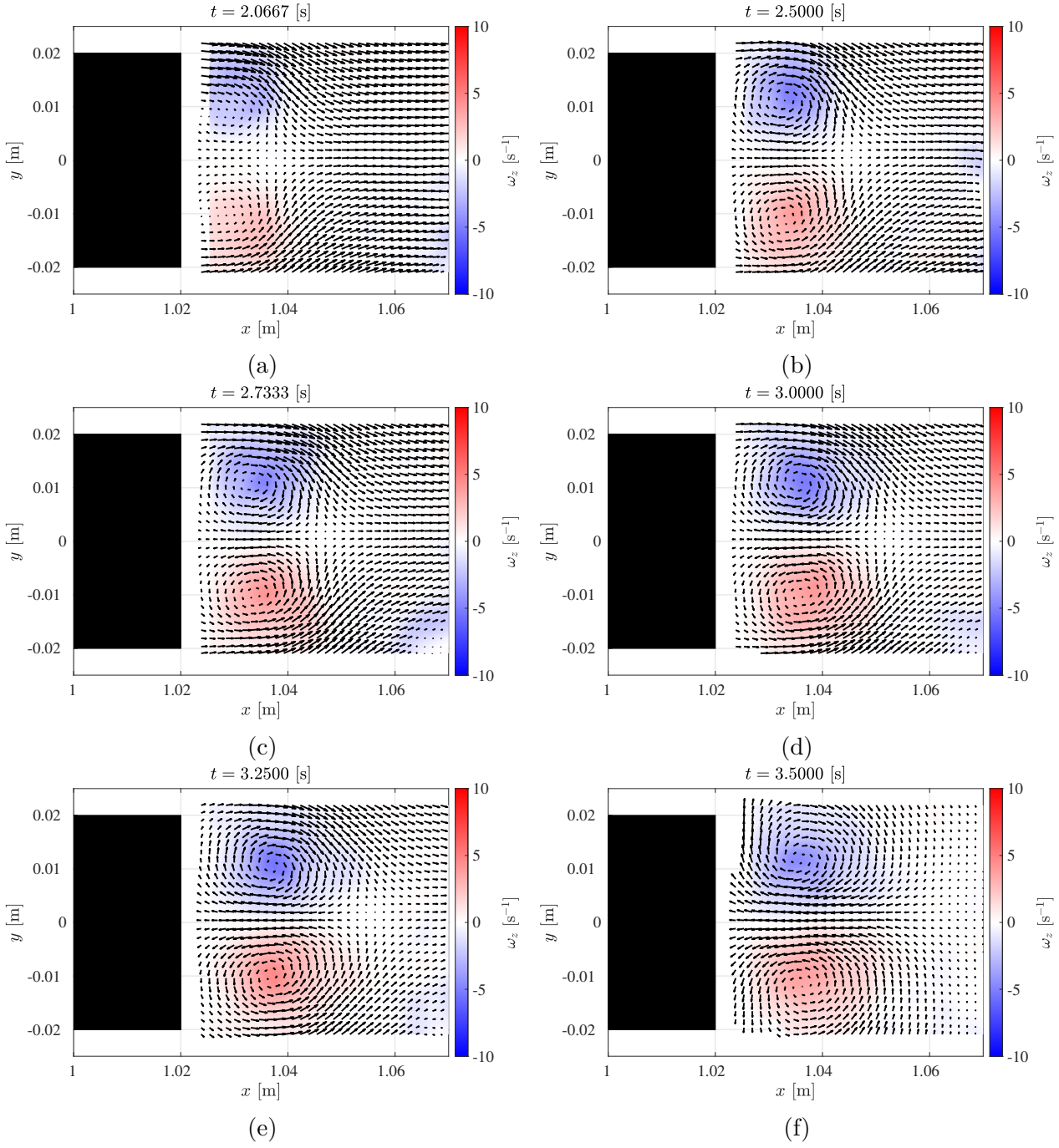

Figure 6.14: Vector field retrieved from PIV and vorticity (calculated as $\omega = \nabla \times \mathbf{U}$) in the E1 test case and for times t = 2.0667, 2.5000, 2.7333, 3.0000, 3.2500, 3.5000 s. Interrogation windows are 32 x 32 pixels^2 wide. The cylinder is represented in black. The undular bore propagates from left to right.

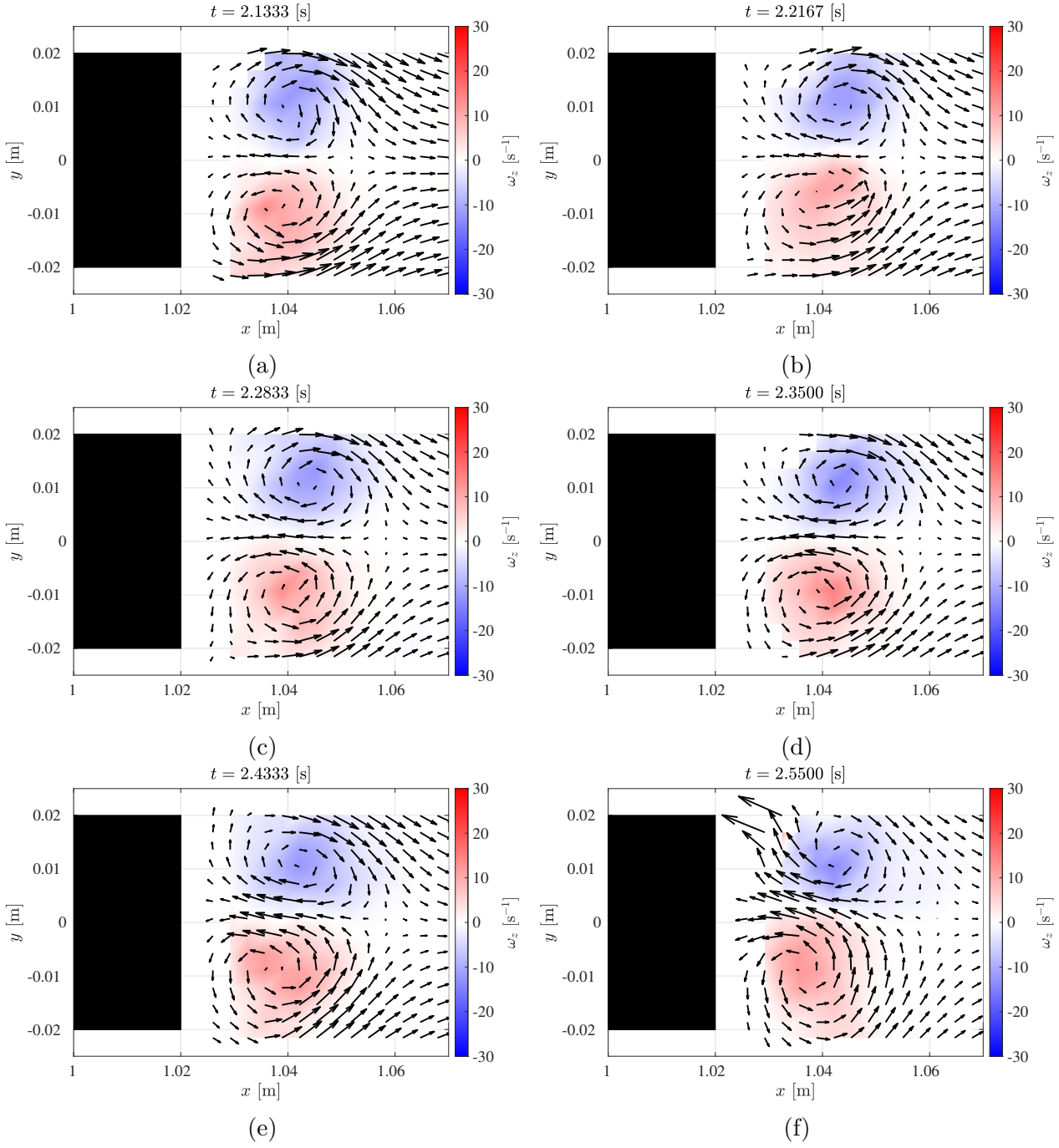

Figure 6.15: Vector field retrieved from PIV and vorticity (calculated as $\omega = \nabla \times \mathbf{U}$) in the E5 test case and for times t = 2.1333, 2.2167, 2.2833, 2.3500, 2.4333, 2.5500 s. Interrogation windows are 64 x 64 pixels^2 wide. The cylinder is represented in black. The undular bore propagates from left to right.

0.05 m/s in the early times which correspond to the order of magnitude of the incident main wave velocity measured by PIV in section 6.1.3. At later times, the end of the experimental bore due to stroke restriction is observed as velocity at $x > 1.06$ m starts to decrease to 0 and even turn to negative ones. The vortex pair is quite parallel with the side of the cylinder during the whole interaction showing great symmetry. Velocity in the inter-vortex zone, as viewed before, is small during the first instants of the interaction and increases progressively.

The velocity profile sampled along the inter-vortex line shows quite a poor symmetry which we explain by the PIV post-processing too low resolution, although the vortex pair is quite far away from each other at the early times which could also explain that an external parameter (cylinder which is not fully perpendicular to the tank wall, or the wave front, edges sharper on one side...) makes the vortex generation different. However, these differences tend to disappear with time as the pairing occurs and at large times the profiles are symmetrical, such as at $t = 3.25$ s. The PIV resolution is enough to allow us to distinguish two velocity minimums at the first displayed time $t = 2.07$ s, corresponding to each vortex as we have seen in the numerical velocity profile of section 5.2.6. For later times, the two velocity minimums disappear to leave a unique minimum velocity which is also observed in the numerical simulations of figure 5.40 and is explained by the core size increase of each vortices, now occupying the whole half-diameter of vertical cylinder. The observations we made about the increase with time of the inter-vortex velocity is also verified. The Lamb-Oseen vortex fit, which is represented in black is relatively well carried out and should give us confidence over the results.

The E5 case is detailed in figures 6.18 and 6.19. Note that the case is only studied between times $t = 2.13$ s and $t = 2.55$ s, which is due to two factors: the first one is the length of the bore which is way shorter than the E1 case due to the limit of the piston stroke, and the second one is the impossibility to resolve the PIV at the fist instant of formation of the vortices as they are still situated close to the cylinder. In the case of the E5 experiment, similar observation can be made about the global symmetry of the vortices which is lost quite quickly after their formation since at time $t = 2.22$ s the vortex are no longer parallel to the cylinder wall. This loss of symmetry only worsen in time so that the vortex in the negative y quadrant is much closer to the cylinder than the other one. As for the velocity magnitude, this one reaches 12 cm/s for example at the exterior of the vortices for time $t = 2.13$ s or at the inter vortex zone for the latest time which is shown: $t = 2.55$ s. This corresponds to the maximum horizontal particle velocity at $z = h/2$ so that the PIV results show great consistency with the bore particle velocity. Finally, as for the first case E1, the inter vortex velocity gains amplitude to eventually reach its maximum at the last times before the bore end reaches this zone. As for the vortex detection process, it seems to be quite precise for a majority of cases even if the lower resolution can affect its results such as for time $t = 2.43$ s where the negative y vortex center seems to be to the left from the real center.

The velocity profiles along the vortex center line, which can be observed in figure 6.19 show good symmetry with reference to the line center $s = 0$ m for all cases (s is the curvilinear abscissa), even if some differences are observed at the external side of the vortices ($|s| > 0.015$ m). The individual vortices are not distinguishable as we have seen in the numerical case, which is either due to too

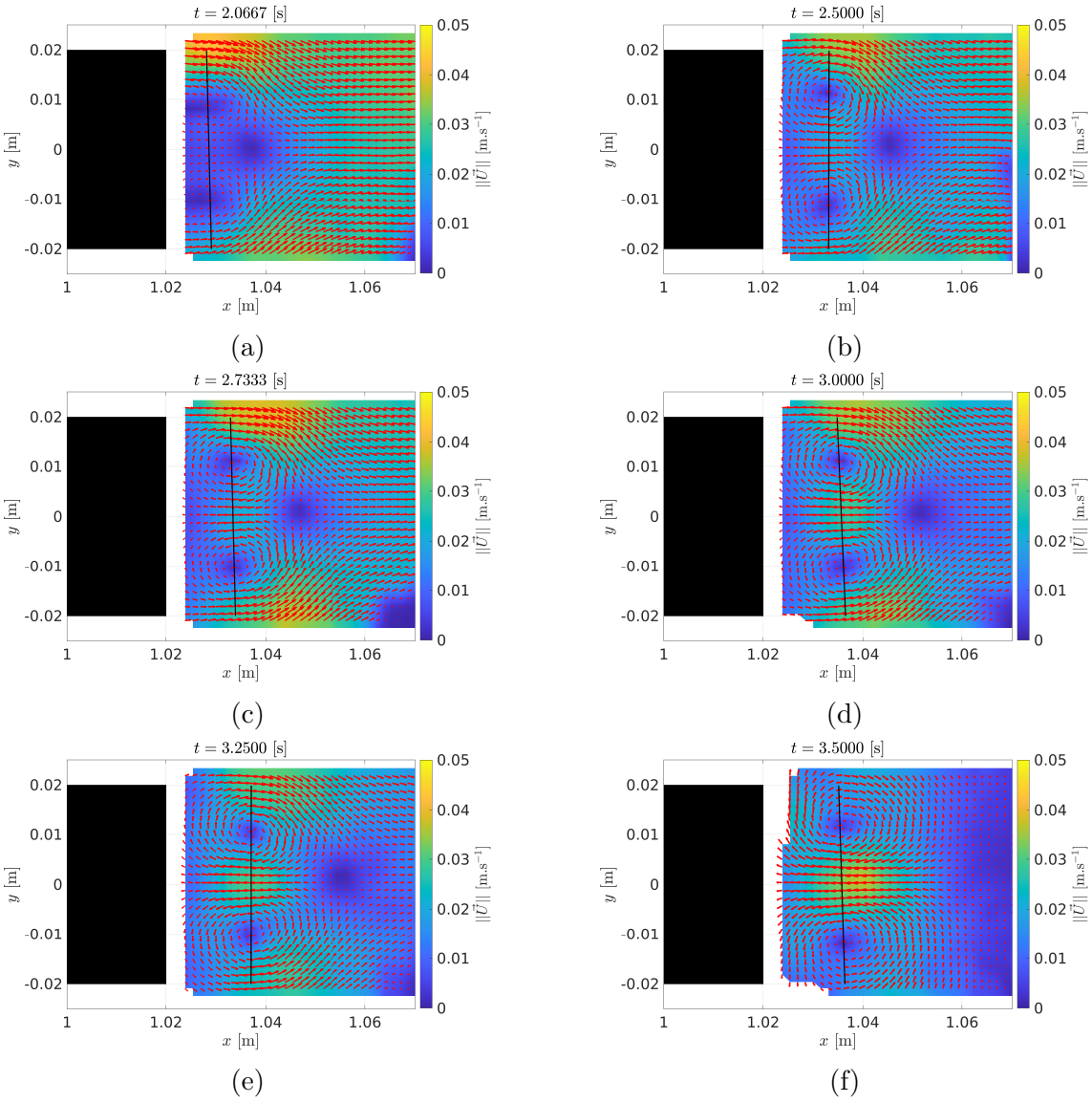

Figure 6.16: Velocity vector field and magnitude (calculated as $||\vec{U}|| = \sqrt{U_x^2 + U_y^2}$) retrieved from PIV in the E1 case for times t = 2.0667, 2.5000, 2.7333, 3.0000, 3.2500, 3.5000 s. Interrogation windows are 32 x 32 pixels^2 wide. The undular bore propagates from left to right. The cylinder is represented in black. Red crosses mark the vortex centers and the black right line joins them. The velocity profiles from figure 6.17 are sampled along this line.

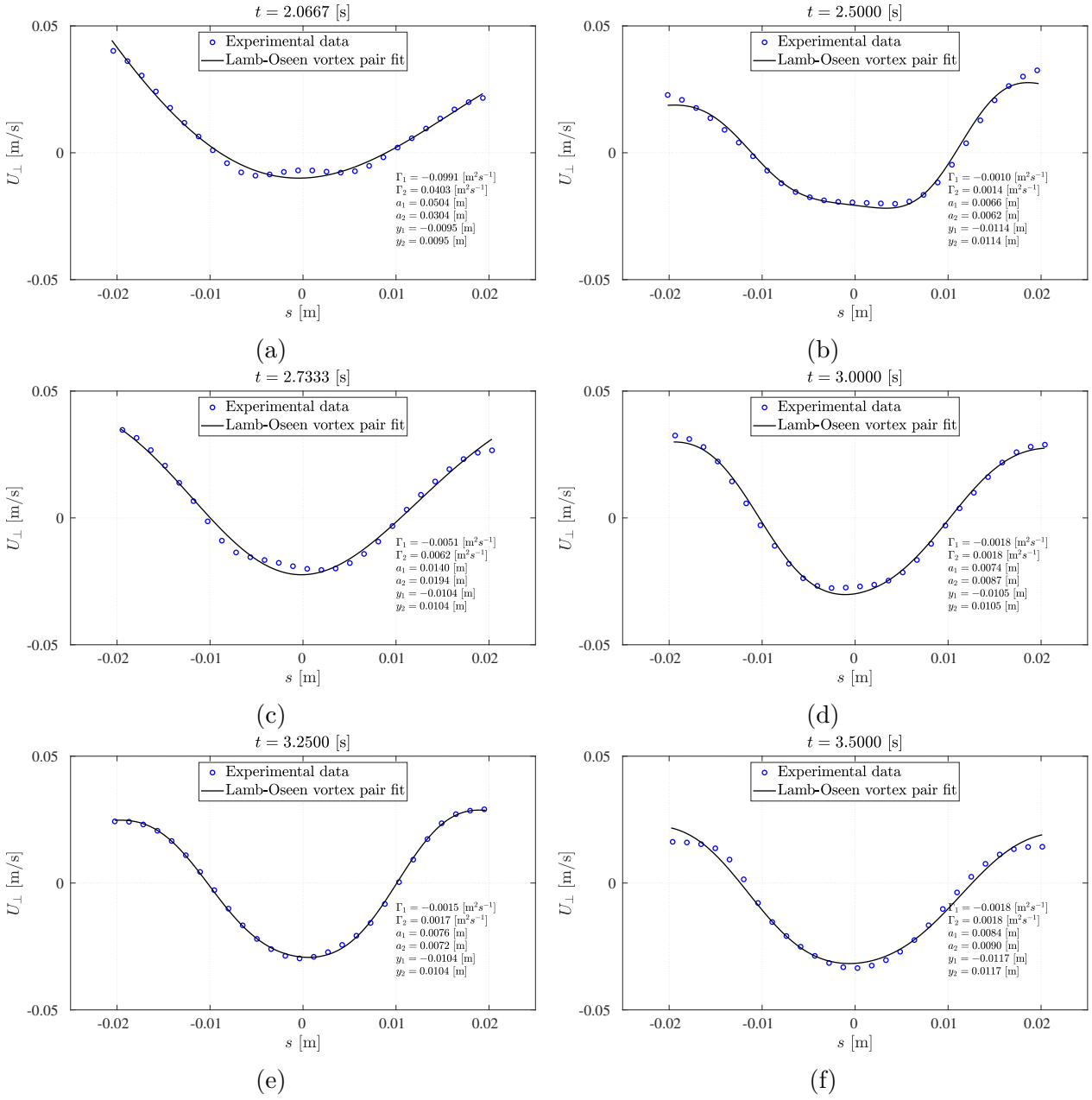

Figure 6.17: Velocity profile along the line joining the vortex centers (see figure 6.16) retrieved from PIV in the E1 case and results of the fit. s is the abscissa along the right line. The blue circles (–) represents the E1 results while a least square method allows to fit two Lamb-Oseen vortices according to the following expression: $U_x(y) = U_0 + \sum_{i=1}^{2} \Gamma_i/(2\pi(y - y_i))\left(1 - \exp\left(-(y - y_i)^2/a_i^2\right)\right)$. This last expression is shown in the black continuous line (–).

low resolution at the inter-vortex zone or more likely the observed times correspond to time where the vortices are close enough so that the two local minimum velocities do not appear. We can also confirm that the inter-vortex velocity decreases its value from around -6 cm/s to -12 cm/s as assessed in the previous paragraph. Finally, the Lamb-Oseen vortex pair fit seems reasonable for the majority of cases even if it can be argued that it does not results as well for the latest one.

6.2.3. Vortex circulation

Contour at rear edges The same method as described in section 5.2.6 for the circulation computation is applied to the experimental cases E1 to E5 and the results are shown in figure 6.20a. Note that due to the PIV output, some vectors were missing so that they were either replaced by using bilinear interpolation or extrapolated with the linear approach if they were at the boundary. If the results show, as expected, an increase of the circulation as the bore height increases, great disparities appeared in the results of the E4 and E5 cases, with many outliers and great variations. After removal of these outlier and smoothing, the converged circulation, which is computed as the mean of the circulation once the maximum is reached and before the bore end is reached, is retrieved and plotted as a dimensionless parameter in function of the Froude number in figure 6.20b. We observe an increase of the circulation with the Froude number, however with a lower slope for the cases E4 and E5 which we understand as an under-evaluation due to bad PIV resolving. Moreover the value obtained for the E5 case is really lower than the one of the numerical case (35 % difference) which would indicates bad calculation either in the numerical computation or the PIV post-processing. These results do not let us conform with the method that is why we decide to compute the circulation using a different one which is presented in the following paragraph.

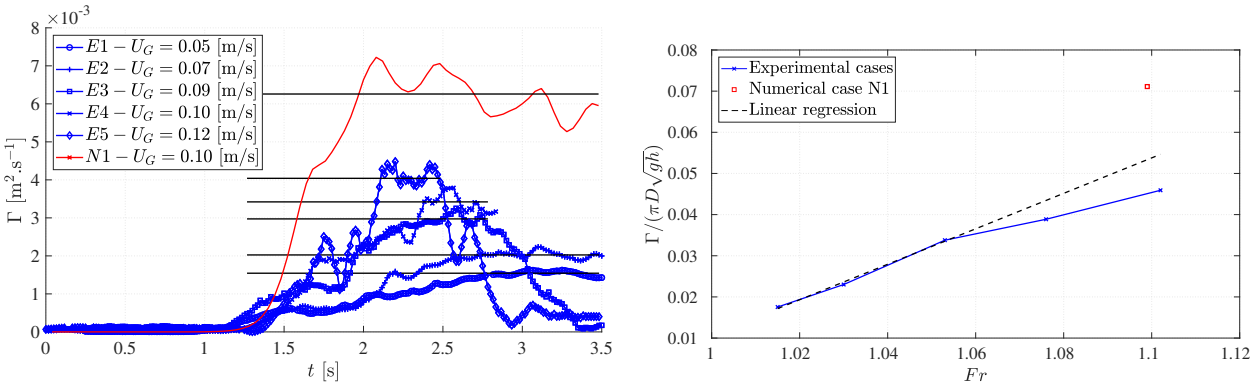

(a) (b)

Figure 6.20: (a) Test cases circulation around the rectangular contour of figure 5.45 in function of time. The black lines indicates the value to which the circulation converges (before an eventual quick fall). (b) Dimensionless converged circulation as a function of the Froude number. A linear regression is carried out based on the E1 to E3 test cases whose results are shown with the dashed line.

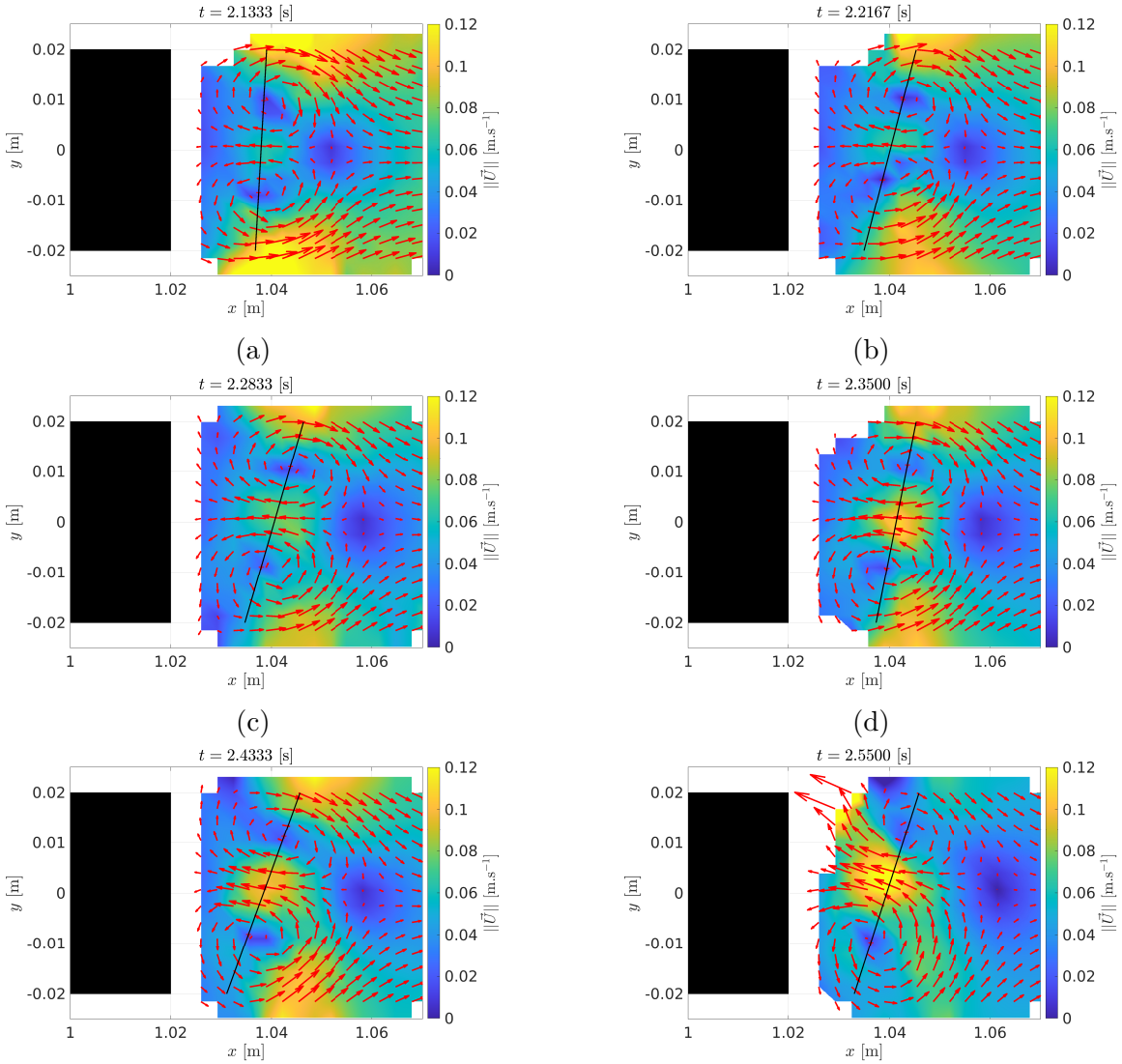

Figure 6.18: Velocity vector field and magnitude (calculated as $||\vec{U}|| = \sqrt{U_x^2 + U_y^2}$) retrieved from PIV in the E5 case for times t = 2.1333, 2.2167, 2.2833, 2.3500, 2.4333, 2.5500 s. Interrogation windows are 64 x 64 pixels^2 wide. The undular bore propagates from left to right. The cylinder is represented in black. Red crosses mark the vortex centers and the black right line joins them. The velocity profiles from figure 6.19 are sampled along this line.

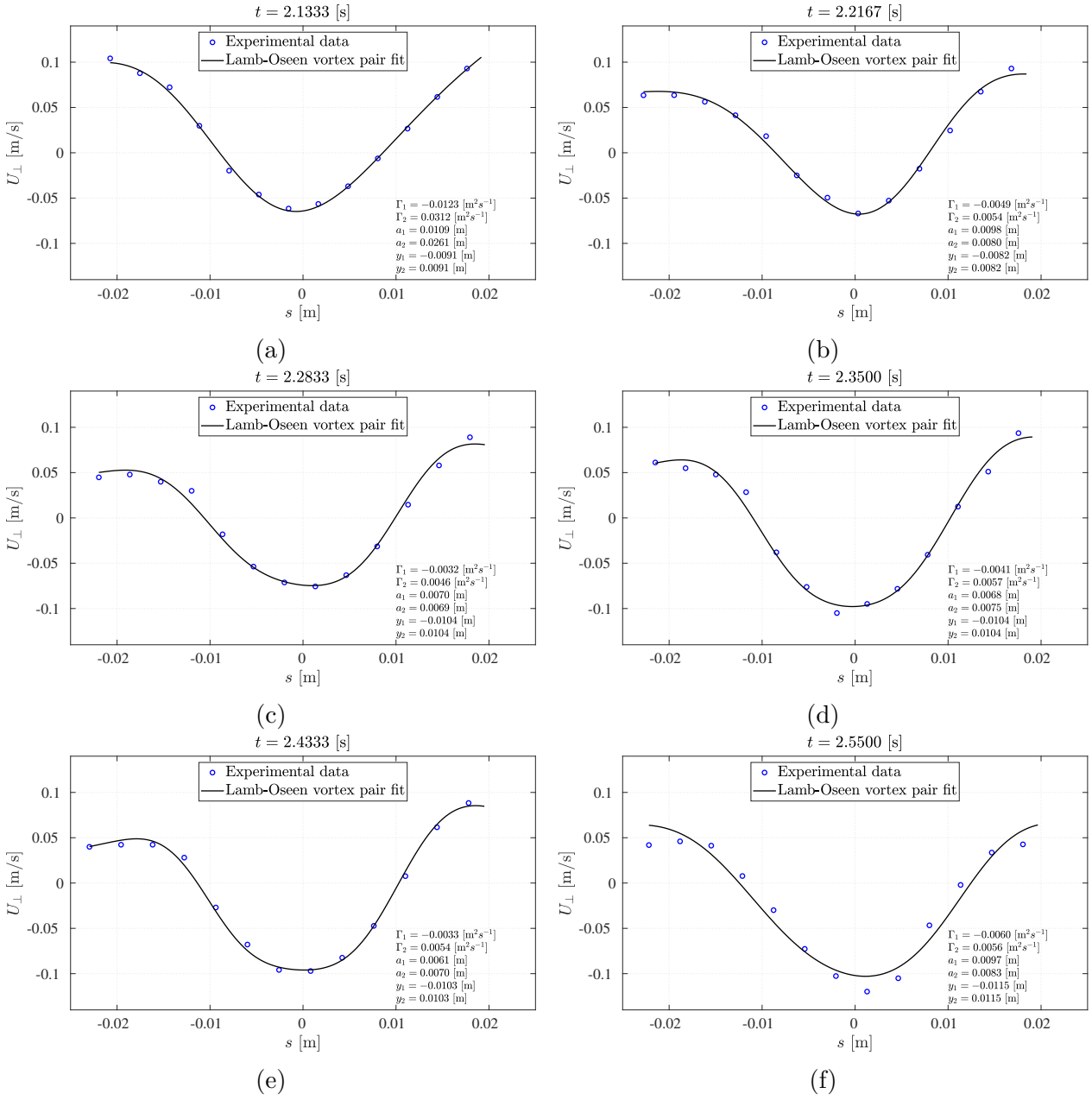

Figure 6.19: Velocity profile along the line joining the vortex centers (see figure 6.18) retrieved from PIV in the E5 case and results of the fit. s is the abscissa along the right line. The blue circles (–) represents the E5 results while a least square method allows to fit two Lamb-Oseen vortices according to the following expression: $U_x(y) = U_0 + \sum_{i=1}^{2} \Gamma_i/(2\pi(y - y_i))\left(1 - \exp\left(-(y - y_i)^2/a_i^2\right)\right)$. This last expression is shown in the black continuous line (–).

Velocity profile method In this part, the circulation is computed as a result of the fit of the Lamb-Oseen vortex pair as described by equation 6.1. The parameters of figure 5.41 are plotted in function of time for the numerical case N1 in figure 5.42. The fitting allows us to show that both rear vortices are fully symmetrical since the circulation and core parameters are equal for both vortices (in absolute value) except for the latest times $t > 3.3$ s where great variations of the circulation is observed and the core size is no longer equal between the two vortices. The core size variations shows a global increase in time with variations that we attribute to vortex stretching: a vortex tube when stretched becomes thinner and inversely, it becomes larger when squeezed and this is a consequence of vorticity conservation.

The circulation behavior is quite interesting: if the numerical case showed that after an original increase, the circulation seems to stall to a constant value with oscillations around a mean value, this mean value is determined and reported in figure 6.21a for the experimental cases. Great variations can be observed depending on the case, especially for the higher bores. A mean computed on the time serie data set and its associated error was extracted and is plotted in figure 6.21b in a dimensionless way so that the circulation is a function of the Froude number of the incident waves. First of all, we can observe that the dimensionless circulation of the E5 case is much closer to the numerical case N1 than for the contour method. The global behavior is an increase which does not appear to be linear. The E2 point seems to be overestimated unless the E3 and E4 cases are underestimated. An improved experiment could however help us in determine what is the correct behavior of the circulation in function of the cases. Nevertheless, a comparison with the contour method is carried out in the following paragraph.

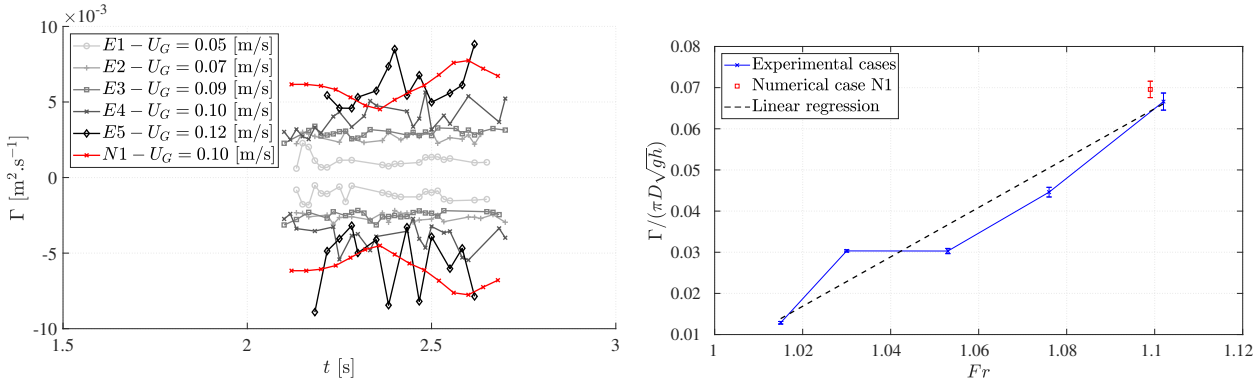

(a) (b)

Figure 6.21: (a) Test cases circulation calculated from the Lamb-Oseen vortex pair fit from equation 6.1 in function of time. (b) Dimensionless mean circulation as a function of the Froude number. A linear regression is carried out whose results are shown with the dashed line.

Comparison between methods A summary of the circulation computed from the contour and velocity profile fit is reported in table 6.3. These data are plotted in a same graph so that they can be compared in figure 6.22. If both methods seem to give similar values for the three first cases, they diverge for the E4 and E5 test cases. However, the numerical case shows both methods

with a really close value (2 % difference) and indicates that the E5 value might be close to these value as computed with the velocity profile fit method. This last method seems to be more suitable for the circulation computations, since no integral is performed and thus if the velocity field is underestimated as it is often the case in PIV experiments with vortex it can give it an advantage. The E5 value also suggests that the CFD simulation is correctly carried out so that it validates the wave-structure interaction. An alternative to the other two methods could be to use the plughole free-surface deformation to compute the strength of the vortices as described in section 2.4.1 and in particular figure 2.10. This would require to precisely measure the free-surface deformation at the rear of the cylinder and could be achieved with the Cobelli et al. (2009) technique of water wave global measurement by Fourier transform profilometry.

Case	Froude number	Contour method circulation [m^2 s^{-1}]	Fit method circulation [m^2 s^{-1}]	Contour method dimensionless circulation	Fit method dimensionless circulation
E1	1.015	0.0015	0.0011	0.0175	0.0129
E2	1.030	0.0020	0.0027	0.0230	0.0303
E3	1.053	0.0030	0.0027	0.0338	0.0303
E4	1.076	0.0034	0.0039	0.0389	0.0446
E5	1.102	0.0040	0.0059	0.0459	0.0666
N1	1.099	0.0063	0.0061	0.0711	0.0696

Table 6.3: Circulation summary from the contour and fit methods.

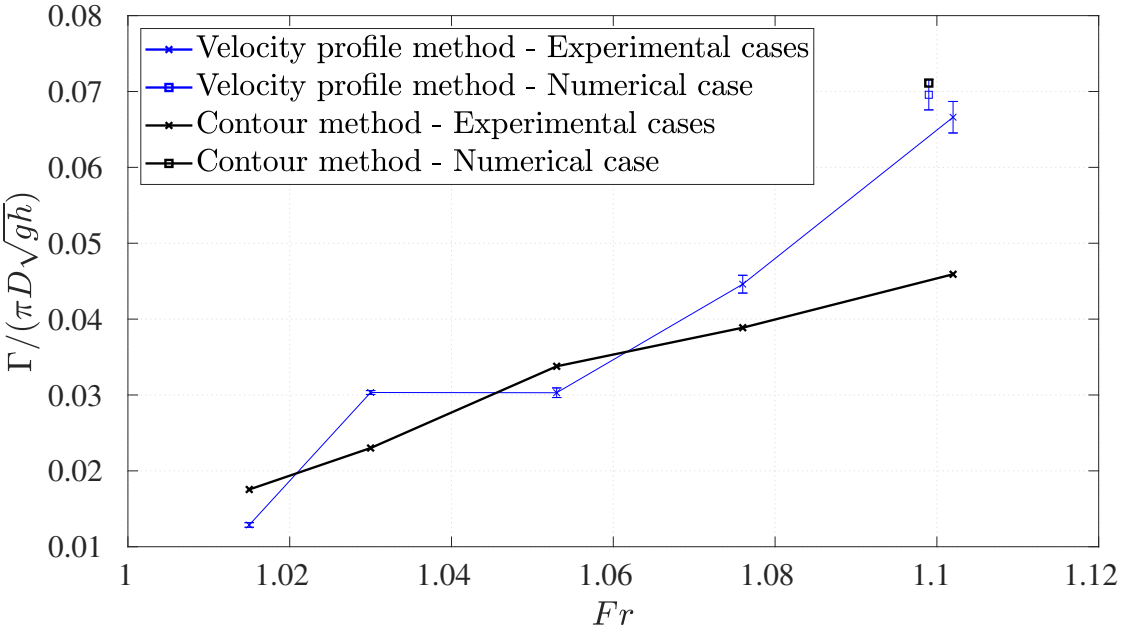

Figure 6.22: Dimensionless mean circulation in function of the Froude number. Comparison between the contour method in black and the velocity profile fit method in blue. The numerical case is represented by the square marks.

Chapter 7

Conclusion

In this thesis, the study of undular bore generation, propagation and interaction with a vertical square cylinder was carried out by means of numerical simulations and experimental trials at laboratory scale. The wave-structure interaction problem was extensively studied, but it is the first time at the author's knowledge the interaction of an undular bore with a vertical square cylinder is described. Undular bores are of particular interest since they have shown to represent quite well tsunami waves, which are a hazard for coastal communities, such as in Chile's coasts.

To study the undular bore generation, propagation and interaction with a square cylinder, various tools were designed and built. A wave tank at small scale was constructed alongside its wave generation system based on a piston wavemaker, and its numerical mirror based on the resolution of Navier-Stokes equations (CFD) was implemented. Both 2D model, used to study the wave generation and propagation, and 3D model used for the interaction with the square cylinder study were implemented in an open-source software, allowing its use in the Universidad de Chile's supercomputer. Then, a capacitive wave gauge was designed according to the scale of the studied problem. Based on a charge amplifier, it allows to get rid of stray capacitances, and shows high sensitiveness. The sensor is also cheap and built from highly available parts so that it can be implemented in any laboratory. The literature review of capacitive sensing and the sensor implementation showed that some more study are necessary to assess the meniscus influence on the measurement when the experiment scale is reduced. Finally, a PIV post-processing tool was implemented, comprising an automatic tool for the free-surface detection which relies on the Radon transform. The PIV was tested on extended sets of synthesis images which allowed us to quantify its sensitivity in function of parameters such as the particle displacement, size, noise,..., shear flows and vortex flows.

Applying a velocity step to a piston wavemaker results in the generation of an undular bore. The piston wavemaker was thus characterized by velocity step numerical experiments based on the 2D Navier-Stokes equations resolution and the solid body motion of the wave-

maker boundary. The water level at the wavemaker showed good agreement with the available theory, and the study was extended to higher Froude number ($Fr > 0.1$). The dimensionless wavemaker water level results allowed the design of an active wave absorption control strategy based on the overshoot of the step response. This was tested on regular and irregular waves and showed to be efficient. This work also allowed to retrieve the proportional constant of widely used piston wave active absorber controller. The forces were computed on the piston wavemaker and a general power input scaling law was determined. We hope this power law can help to the design of future facilities which would comprise piston wavemaker.

Five different bores were generated in the experimental facility at the LEAF-NL laboratory as well as one numerical case solving the full 3D Navier-Stokes equations, which allowed us to characterize the undular bore by measuring the main wave height, the mean bore height, the phase celerity, and their associated Froude number, which ranged from 1.015 to 1.100. The undular bores were also described through the measurement of the particle velocity at a height of half mean water level and the whole velocity profile was given for the numerical case. The generated bores showed that one experimental test case was quite similar to the numerical test case (both in Froude number and wave height to water depth ratio), which allowed us to validate the wave generation and propagation computations of the numerical case.

The final stage of this thesis was the study of the undular bore interaction with the vertical square cylinder, which was carried out by measuring the velocity field in the half mean water level plane and at the rear of the cylinder, while the 3D numerical simulation gave more complete information about the flow around the cylinder. First, a general description was made about vortex shedding at the four cylinder edges notably by looking at the Q criteria and the vorticity field. Then, the pressure force on the cylinder showed strong oscillations around a mean force which corresponds to the one determined in the literature for current-cylinder interaction with a free-surface. It was verified that the instantaneous vortex shedding frequency corresponds to the instantaneous frequency of the undular bore. The vortex pairing phenomena was identified at the rear of the cylinder consisting in the generation of two vortices which evolve together. It is the first time, at the author knowledge, that such quasi-stationary vortex pair are observed in the domain of wave structure interaction. Their motion was described by looking at their core and we could identify the Crow instability. The vortices were characterized by the measurement of their circulation by two distinctive methods, showing that a Lamb-Oseen vortex pair velocity profile fit was a reasonable method for such an end and with the PIV data at our disposition. The dimensionless circulation was determined in function of the Froude number. The comparison between the experimental and numerical case also allowed us to validate the vortex generation numerical computation. However, the reduced resolution (in particular for the higher Froude number cases) is a

limitation to this work and might be resolved by carrying out another set of experiments with a more suited set-up that would allow to perform a more more precise evaluation of the vortex pair velocity field. Finally, the determination of the seabed wall shear stress allowed us to conclude on the eventual scouring that might appear at the cylinder, and might also be important in the design of bridge piles but a dedicated study of the phenomena should be planed to assess the whole complexity of the scouring problem.

In a close future, it would be advisable to keep investigating some of the themes that emerged from this work. The following list, in the author's opinion, are open problems and extensions that might be worth more investigation but is not exhaustive. In the case of the wavemaker step response, the asymmetry between "positive" and "negative" Froude raised concerns about the implications it has on the wave absorption, especially when the error becomes high. Moreover, the space between the wavemaker and the seabed in the wet-back configuration of the experimental facility generates a strong vortex at the rear part of the wavemaker and was observed during our trials. This could strongly influence the forces on the wavemaker, and the effect of suction greatly changes the main wave and bore heights. The evaluation of drag forces on the cylinder needs to be expanded to different Froude numbers since it is an important feature in the assessment of structure resistance to tsunami events. In particular, we showed that the transient force can reach a value as high as four time the steady-state one. More experiments should be carried out at lower and higher Froude numbers so that the evolution of the vortex pair strength can be better evaluated. The stretching and squeezing of the vortex should also be investigated and the circulation changes during the pairing phenomena. Longer numerical simulations or an extension of the laboratory wave tank could also give us a hint on the eventual disappearance of the rear vortices and the mechanisms leading to it. The influence of the cylinder diameter and orientation should also be looked into.

Bibliography

Abid, M., Andreotti, B., Douady, S., & Nore, C. (2002). Oscillating structures in a stretched–compressed vortex. *Journal of Fluid Mechanics*, *450*, 207–233. doi: 10.1017/S0022112001006449

Adrian, R. J. (1984). Scattering particle characteristics and their effect on pulsed laser measurements of fluid flow: speckle velocimetry vs particle image velocimetry. *Applied optics*, *23*(11), 1690–1691.

Adrian, R. J. (1991). Particle-imaging techniques for experimental fluid mechanics. *Annual Review of Fluid Mechanics*, *23*(1), 261-304. Retrieved from https://doi.org/10.1146/annurev.fl.23.010191.001401 doi: 10.1146/annurev.fl.23.010191.001401

Aezinia, F. (2014). *Design of interface circuits for capacitive sensing applications* (Unpublished doctoral dissertation). Applied Sciences: School of Mechatronic Systems Engineering.

Ahmed, R., & Lim, H. (2017). Study of air-core vortical flow structure induced by a plughole vortex. *Journal of Fluid Mechanics*, *823*, 787–818. doi: 10.1017/jfm.2017.329

Airy, G. B. (1841). Tides and waves. In E. Al (Ed.), *Encyclopedia metropolitana (1817–1845).* London.

Aknin, D., & Spinneken, J. (2017). A laboratory investigation concerning the superharmonic free wave suppression in shallow and intermediate water conditions. *Coastal Engineering*, *120*, 112 - 132. Retrieved from http://www.sciencedirect.com/science/article/pii/S0378383916303866 doi: http://dx.doi.org/10.1016/j.coastaleng.2016.11.015

Alam, M. N. (2014). Applications of electromagnetic principles in the design and development of proximity wireless sensors.

Ali, A., & Kalisch, H. (2010). Energy balance for undular bores. *Comptes Rendus - Mecanique*. doi: 10.1016/j.crme.2010.02.003

Altomare, C., Domínguez, J., Crespo, A., González-Cao, J., Suzuki, T., Gómez-Gesteira, M., & Troch, P. (2017). Long-crested wave generation and absorption for sph-based dualsphysics model. *Coastal Engineering*, *127*, 37 - 54. Retrieved from http://www.sciencedirect.com/science/article/pii/S0378383916301831 doi: http://dx.doi.org/10.1016/j.coastaleng.2017.06.004

Anbarsooz, M., Passandideh-Fard, M., & Moghiman, M. (2013). Fully nonlinear viscous wave generation in numerical wave tanks. *Ocean Engineering*, *59*, 73-85.

Andersen, T. L., Clavero, M., Frigaard, P., Losada, M., & Puyol, J. (2016). A new active absorption system and its performance to linear and non-linear waves. *Coastal Engineering*, *114*, 47–60.

Andersen, T. L., Eldrup, M. R., & Frigaard, P. (2017). Estimation of incident and reflected components in highly nonlinear regular waves. *Coastal Engineering*, *119*, 51 - 64. Retrieved from http://www.sciencedirect.com/science/article/pii/S0378383916302137 doi: https://doi.org/10.1016/j.coastaleng.2016.08.013

Arabi, M. G., Sogut, D. V., Khosronejad, A., Yalciner, A. C., & Farhadzadeh, A. (2019). A numerical and experimental study of local hydrodynamics due to interactions between a solitary wave and an impervious structure. *Coastal Engineering*, *147*, 43 - 62. Retrieved from http://www.sciencedirect.com/science/article/pii/S0378383918302333 doi: https://doi.org/10.1016/j.coastaleng.2019.02.004

Babarit, A., & Delhommeau, G. (2015, September). Theoretical and numerical aspects of the open source BEM solver NEMOH. In *11th European Wave and Tidal Energy Conference (EWTEC2015)*. Nantes, France. Retrieved from https://hal.archives-ouvertes.fr/hal-01198800

Baker, C. J. (1979). The laminar horseshoe vortex. *Journal of Fluid Mechanics*, *95*(2), 347–367. doi: 10.1017/S0022112079001506

Baumann, H. (1954). Ein wellentilger für modell-seegangversuche. *Aus Jahrbuch der Schiffbautechnischen Gesellshaft*, *48*(14).

Bearman, P. W., Downie, M. J., Graham, J. M. R., & Obasaju, E. D. (1985). Forces on cylinders in viscous oscillatory flow at low keulegan-carpenter numbers. *Journal of Fluid Mechanics*, *154*, 337–356. doi: 10.1017/S0022112085001562

Bénard, H. (1908). Formation de centres de giration a l'arrière d'un obstacle en movement. *Comptes Rendus Academie des Sciences*, *147*, 839–842.

Benjamin, T. B., Bona, J. L., & Mahony, J. J. (1972). Model equations for long waves in nonlinear dispersive systems. *Philosophical Transactions of the Royal Society of London. Series A, Mathematical and Physical Sciences*, *272*(1220), 47-78. Retrieved from https://royalsocietypublishing.org/doi/abs/10.1098/rsta.1972.0032 doi: 10.1098/rsta.1972.0032

Bera, S. C., Mandal, H., Saha, S., & Dutta, A. (2014). Study of a modified capacitance-type level transducer for any type of liquid. *IEEE Transactions on Instrumentation and Measurement*, *63*(3), 641–649.

Berberović, E., van Hinsberg, N. P., Jakirlić, S., Roisman, I. V., & Tropea, C. (2009). Drop impact onto a liquid layer of finite thickness: Dynamics of the cavity evolution. *Physical Review*, *E79*(036306).

Berkhoff, J. (1972). Computation of combined refraction—diffraction. In *Coastal engineering* (pp. 471–490).

Bernitsas, M. M., Raghavan, K., Ben-Simon, Y., & Garcia, E. M. H. (2008, 09). VIVACE (Vortex Induced Vibration Aquatic Clean Energy): A New Concept in Generation of Clean and Renewable Energy From Fluid Flow. *Journal of Offshore Mechanics and Arctic Engineering*, *130*(4). Retrieved from https://doi.org/10.1115/1.2957913 (041101) doi: 10.1115/1.2957913

Bhinder, M. A., Mingham, C. G., DM, C., MT, R., GA, A., & RV., C. (2009). A joint numerical and experimental study of a surging point absorbing wave energy converter (wraspa). In *28th international conference on offshore mechanics and arctic engineering* (Vol. 4, p. 869-875). doi: 10.1115/OMAE2009-79392

Biesel, F., & Suquet, F. (1951). Les appareils générateurs de houle en laboratoire. *La houille blanche*(2), 147–165.

Bihs, H., Chella, M. A., Kamath, A., & Arntsen, O. A. (2017, 05). Numerical Investigation of Focused Waves and Their Interaction With a Vertical Cylinder Using REEF3D. *Journal of Offshore Mechanics and Arctic Engineering*, *139*(4). Retrieved from https://doi.org/10.1115/1.4036206 (041101) doi: 10.1115/1.4036206

Binnie, A. M., Orkney, J. C., & Relf, E. F. (1955). Experiments on the flow of water from a reservoir through an open horizontal channel ii. the formation of hydraulic jumps. *Proceedings of the Royal Society of London. Series A. Mathematical and Physical Sciences*, *230*(1181), 237-246. Retrieved from https://royalsocietypublishing.org/doi/abs/10.1098/rspa.1955.0126 doi: 10.1098/rspa.1955.0126

Bjørnestad, M., Kalisch, H., Abid, M., Kharif, C., & Brun, M. (2021). Wave breaking in undular bores with shear flows. *Water Waves*, 1–18.

Bjørkavåg, M., & Kalisch, H. (2011). Wave breaking in boussinesq models for undular bores. *Physics Letters A*, *375*(14), 1570-1578. Retrieved from https://www.sciencedirect.com/science/article/pii/S0375960111002714 doi: https://doi.org/10.1016/j.physleta.2011.02.060

Blasius, H. (1907). *Grenzschichten in flüssigkeiten mit kleiner reibung*. Druck von BG Teubner.

Blevins, R. D. (1977). *Flow-induced vibration*.

Blottner, F. (1990). Accurate navier-stokes results for the hypersonic flow over a spherical nosetip. *Journal of spacecraft and Rockets*, *27*(2), 113–122.

Bonneton, P., de Loock, J. V., Parisot, J.-P., Bonneton, N., Sottolichio, A., Detandt, G., ... Pochon, N. (2011). On the occurrence of tidal bores – the garonne river case. *Journal of Coastal Research*, 1462–1466. Retrieved from http://www.jstor.org/stable/26482418

Borrero, J. C., Lynett, P. J., & Kalligeris, N. (2015). Tsunami currents in ports. *Philosophical Transactions of the Royal Society A: Mathematical, Physical and Engineering Sciences*, *373*(2053), 20140372. Retrieved from https://royalsocietypublishing.org/doi/abs/10.1098/rsta.2014.0372 doi: 10.1098/rsta.2014.0372

Boudan, J. (1953). Appareils pour la mesure des niveaux rapidement variables sur modele reduit. *La Houille Blanche*(4), 526–545.

Boussinesq, J. (1872). Théorie des ondes et des remous qui se propagent le long d'un canal rectangulaire horizontal, en communiquant au liquide contenu dans ce canal des vitesses sensiblement pareilles de la surface au fond. *Journal de mathématiques pures et appliquées*, *17*(2), 55-108.

Boussinesq, J. (1877). *Essai sur la théorie des eaux courantes*. Impr. nationale.

Bovis, A. (2009). *Hydrodynamique navale: Théorie et modèles* (Collection Les Cours ed.). Les Presses de l'ENSTA.

Brackbill, J. U., Kothe, D. B., & Zemach, C. (1992). A continuum method for modeling surface tension. *Journal of Computational Physics*, *100*, 335-354.

Bradshaw, P., & Woods, W. A. (1971). *An introduction to turbulence and its measurement* (1st ed.). Pergamon.

Bremm, G. C., Goseberg, N., Schlurmann, T., & Nistor, I. (2015). Long wave flow interaction with a single square structure on a sloping beach. *Journal of Marine Science and Engineering*, *3*(3), 821–844. Retrieved from https://www.mdpi.com/2077-1312/3/3/821 doi: 10.3390/jmse3030821

Brun, M. K., & Kalisch, H. (2018). Convective wave breaking in the kdv equation. *Analysis and Mathematical Physics*, *8*(1), 57–75.

Bruschi, P., Navarrini, D., Barillaro, G., & Gola, A. (2004, Oct 01). A precise capacitance-to-pulse width converter for integrated sensors. *Analog Integrated Circuits and Signal Processing*, *41*(1), 93–97. Retrieved from https://doi.org/10.1023/B:ALOG.0000038288.41566.0f doi: 10.1023/B:ALOG.0000038288.41566.0f

Bruschi, P., Nizza, N., Dei, M., & Barillaro, G. (2007). A low power capacitance to pulse width converter for integrated sensors. In *Circuit theory and design, 2007. ecctd 2007. 18th european conference on* (pp. 108–111).

Buckingham, E. (1914). On physically similar systems; illustrations of the use of dimensional equations. *Physical review*, *4*(4), 345.

Burgers, J. (1940). Application of a Model System to Illustrate Some Points of the Statistical Theory of Free Turbulence. *Proceeding of the Academy of Science Amsterdam*.

Camfield, F. E., & Street, R. L. (1968). The effects of bottom configuration on the deformation, breaking and run-up of solitary waves. In *Coastal engineering* (p. 173-189). Retrieved from https://ascelibrary.org/doi/abs/10.1061/9780872620131.011 doi: 10.1061/9780872620131.011

Casulli, V., & Cheng, R. T. (1992). Semi-implicit finite difference methods for three-dimensional shallow water flow. *International Journal for Numerical Methods in Fluids*, *15*(6), 629-648. Retrieved from https://onlinelibrary.wiley.com/doi/abs/10.1002/fld.1650150602 doi: 10.1002/fld.1650150602

Celik, I. (2003, 01). RANS/LES/DES/DNS: The Future Prospects of Turbulence Modeling. *Journal of Fluids Engineering*, *127*(5), 829-830. Retrieved from https://doi.org/10.1115/1.2033011 doi: 10.1115/1.2033011

Celik, I. B., Ghia, U., Roache, P. J., et al. (2008). Procedure for estimation and reporting of uncertainty due to discretization in {CFD} applications. *Journal of fluids {Engineering-Transactions} of the {ASME}*, *130*(7).

Chakrabarti, S. K. (2005). Chapter 4 - loads and responses. In S. K. CHAKRABARTI (Ed.), *Handbook of offshore engineering* (p. 133 - 196). London: Elsevier. Retrieved from http://www.sciencedirect.com/science/article/pii/B9780080443812500072 doi: https://doi.org/10.1016/B978-008044381-2.50007-2

Chan, I.-C., & Liu, P. L.-F. (2012). On the runup of long waves on a plane beach. *Journal of Geophysical Research: Oceans*, *117*(C8). Retrieved from https://agupubs.onlinelibrary.wiley.com/doi/abs/10.1029/2012JC007994 doi: 10.1029/2012JC007994

Chanson, H. (2010). Undular tidal bores: basic theory and free-surface characteristics. *Journal of Hydraulic Engineering*, *136*(11), 940–944.

Chapman, R., & Monaldo, F. M. (1995). A novel wave height sensor. *Journal of Atmospheric and Oceanic Technology*, *12*(1), 190-196. Retrieved from https://doi.org/10.1175/1520-0426(1995)012<0190:ANWHS>2.0.CO;2 doi: 10.1175/1520-0426(1995)012<0190:ANWHS>2.0.CO;2

Charvet, I., Eames, I., & Rossetto, T. (2013). New tsunami runup relationships based on long wave experiments. *Ocean Modelling*, *69*, 79 - 92. Retrieved from http://www.sciencedirect.com/science/article/pii/S1463500313000942 doi: https://doi.org/10.1016/j.ocemod.2013.05.009

Chella, M. A., Tørum, A., & Myrhaug, D. (2012). An overview of wave impact forces on offshore wind turbine substructures. *Energy Procedia*, *20*, 217–226.

Chen, C.-C., Fang, F.-M., Li, Y.-C., Huang, L.-M., & Chung, C.-Y. (2009). Fluid forces on a square cylinder in oscillating flows with non-zero-mean velocities. *International Journal for Numerical Methods in Fluids*, *60*(1), 79-93. Retrieved from https://onlinelibrary.wiley.com/doi/abs/10.1002/fld.1881 doi: 10.1002/fld.1881

Chen, J., & Katz, J. (2005). Elimination of peak-locking error in piv analysis using the correlation mapping method. *Measurement Science and Technology*, *16*(8), 1605.

Cheng, M., Whyte, D., & Lou, J. (2007). Numerical simulation of flow around a square cylinder in uniform-shear flow. *Journal of Fluids and Structures*, *23*(2), 207 - 226. Retrieved from http://www.sciencedirect.com/science/article/pii/S0889974606001010 doi: https://doi.org/10.1016/j.jfluidstructs.2006.08.011

Chester, W. (1966). A model of the undular bore on a viscous fluid. *Journal of Fluid Mechanics*, *24*(2), 367–377. doi: 10.1017/S0022112066000703

Chetpattananondh, K., Tapoanoi, T., Phukpattaranont, P., & Jindapetch, N. (2014). A self-calibration water level measurement using an interdigital capacitive sensor. *Sensors and Actuators A: Physical*, *209*, 175–182.

Chong, M. S., Perry, A. E., & Cantwell, B. J. (1990). A general classification of three-dimensional flow fields. *Physics of Fluids A: Fluid Dynamics*, *2*(5), 765-777. Retrieved from https://doi.org/10.1063/1.857730 doi: 10.1063/1.857730

Clauss, G. F., Schmittner, C. E., & Stu¨ck, R. (2005, 06). Numerical Wave Tank: Simulation of Extreme Waves for the Investigation of Structural Responses. In (Vol. 24th International Conference on Offshore Mechanics and Arctic Engineering: Volume 3, p. 785-792). Retrieved from https://doi.org/10.1115/OMAE2005-67048 doi: 10.1115/OMAE2005-67048

Cobelli, P. J., Maurel, A., Pagneux, V., & Petitjeans, P. (2009). Global measurement of water waves by fourier transform profilometry. *Experiments in fluids*, *46*(6), 1037–1047.

Cook, G. W. (1951). *A resonant-bridge carrier system for the measurement of minute changes in capacitance* (Tech. Rep.). DAVID TAYLOR MODEL BASIN WASHINGTON DC.

Cortelezzi, L., & Karagozian, A. R. (2001). On the formation of the counter-rotating vortex pair in transverse jets. *Journal of Fluid Mechanics*, *446*, 347–373. doi: 10.1017/S0022112001005894

Courant, R., Friedrichs, K., & Lewy, H. (1928). Über die partiellen differenzengleichungen der mathematischen physik. *Mathematische annalen*, *100*(1), 32–74.

Crow, S. C. (1970). Stability theory for a pair of trailing vortices. *AIAA Journal*, *8*(12), 2172-2179. Retrieved from https://doi.org/10.2514/3.6083 doi: 10.2514/3.6083

Cummins, W. (1962). *The impulse response function and ship motions* (Tech. Rep.). David Taylor Model Basin Washington DC.

Daily, J. W., & Stephan Jr, C., Samuel. (1952). The solitary wave: its celerity, profile, internal velocities and amplitude attenuation in a horizontal smooth channel. *Coastal Engineering Proceedings*, *1*(3), 2–2.

Dargahi, B. (1989). The turbulent flow field around a circular cylinder. *Experiments in Fluids*, *8*(1-2), 1–12.

Da Rios, L. S. (1906). Sul moto d'un liquido indefinito con un filetto vorticoso di forma qualunque. *Rendiconti del Circolo Matematico di Palermo (1884-1940)*, *22*(1), 117–135.

Deardorff, J. W. (1970). A numerical study of three-dimensional turbulent channel flow at large reynolds numbers. *Journal of Fluid Mechanics*, *41*(2), 453–480. doi: 10.1017/S0022112070000691

de Mello, P. C., Carneiro, M. L., Tannuri, E. A., & Nishimoto, K. (2010, 06). USP Active Absorption Wave Basin: From Conception to Commissioning. In (Vols. 29th International Conference on Ocean, Offshore and Arctic Engineering: Volume 4, p. 75-84). Retrieved from https://doi.org/10.1115/OMAE2010-20166 doi: 10.1115/OMAE2010-20166

Demirbilek, Z., & Vincent, C. (2002). *Water wave mechanics, chapter II-1, coastal engineering manual (em 1110-2-1100)* (Tech. Rep.).

De St Venant, B. (1871). Théorie du mouvement non-permanent des eaux avec application aux crues des rivers et a l'introduntion des marées dans leur lit. *Academic de Sci. Comptes Redus*, *73*(99), 148–154.

Devenport, W. J., Rife, M. C., Liapis, S. I., & Follin, G. J. (1996). The structure and development of a wing-tip vortex. *Journal of Fluid Mechanics*, *312*, 67–106.

Devolder, B., Troch, P., & Rauwoens, P. (2018). Performance of a buoyancy-modified k-ω and k-ω SST turbulence model for simulating wave breaking under regular waves using OpenFOAM®. *Coastal Engineering*, *138*, 49–65. doi: 10.1016/j.coastaleng.2018.04.011

Dias, F., & Kharif, C. (1999). Nonlinear gravity and capillary-gravity waves. *Annual Review of Fluid Mechanics*, *31*(1), 301-346. Retrieved from https://doi.org/10.1146/annurev.fluid.31.1.301 doi: 10.1146/annurev.fluid.31.1.301

Dickerson, S. (n.d.). *Surf de chocolate en alaska.* Retrieved from https://www.redbull.com/es-es/red-bull-illume-mejores-fotos-surf ([Online; accessed October 8th, 2020])

Didier, E., Teixeira, P. R., & Neves, M. G. (2016). A 3d numerical wave tank for coastal engineering studies. In *Defect and diffusion forum* (Vol. 372, pp. 1–10).

Dingemans, M. W. (1997). *Water wave propagation over uneven bottoms* (Vol. 13). World Scientific.

Dingemans, M. W., & Otta, A. K. (2001). Nonlinear modulation of water waves. In *Advances in coastal and ocean engineering* (p. 1-75). Retrieved from https://www.worldscientific.com/doi/abs/10.1142/9789812794574_0001 doi: 10.1142/9789812794574_0001

Du, S., & Liang, B. (2019, Aug). Comparisons of local scouring for submerged square and circular cross-section piles in steady currents. *Water*, *11*(9), 1820. Retrieved from http://dx.doi.org/10.3390/w11091820 doi: 10.3390/w11091820

El, G. A., Khodorovskii, V. V., & Tyurina, A. V. (2005). Undular bore transition in bi-directional conservative wave dynamics. *Physica D: Nonlinear Phenomena*, *206*(3), 232–251. Retrieved from http://www.sciencedirect.com/science/article/pii/S0167278905001958 doi: https://doi.org/10.1016/j.physd.2005.05.010

Elsafti, H., Almaghraby, M., Iskander, M., & Goseberg, N. (2019). Hydraulic performance of innovative seashell-shaped artificial armor units for coastal protections (seashellbreakwater). *Coastal Structures 2019*, 577–586.

Estevadeordal, J., & Kleis, S. J. (1999). Double-helical pairing in plane mixing layers. *Physics of Fluids*, *11*(6), 1691-1693. Retrieved from https://doi.org/10.1063/1.870033 doi: 10.1063/1.870033

Falcon, E., Laroche, C., & Fauve, S. (2007). Observation of gravity-capillary wave turbulence. *Physical review letters*, *98*(9), 094503.

Fan, W., Li, H., & Anglart, H. (2019). Numerical investigation of spatial and temporal structure of annular flow with disturbance waves. *International Journal of Multiphase Flow*, *110*, 256 - 272. Retrieved from http://www.sciencedirect.com/science/article/pii/S0301932218302088 doi: https://doi.org/10.1016/j.ijmultiphaseflow.2018.10.003

Favre, H. (1935). Étude théorique et expérimentale des ondes de translation dans les canaux découverts. *Dunod*, *150*.

Foster, A., Rossetto, T., & Allsop, W. (2017). An experimentally validated approach for evaluating tsunami inundation forces on rectangular buildings. *Coastal Engineering*, *128*, 44 - 57. Retrieved from http://www.sciencedirect.com/science/article/pii/S0378383916303544 doi: https://doi.org/10.1016/j.coastaleng.2017.07.006

Frazao, S. S., & Zech, Y. (2002). Undular bores and secondary waves -experiments and hybrid finite-volume modelling. *Journal of Hydraulic Research*, *40*(1), 33-43. Retrieved from https://doi.org/10.1080/00221680209499871 doi: 10.1080/00221680209499871

Frigaard, P., & Andersen, T. L. (2010). *Technical background material for the wave generation software awasys 5* (Tech. Rep.). Department of Civil Engineering, Aalborg University.

Fritz, H. M., Petroff, C. M., Catalán, P. A., Cienfuegos, R., Winckler, P., Kalligeris, N., ... others (2011). Field survey of the 27 february 2010 chile tsunami. *Pure and Applied Geophysics*, *168*(11), 1989–2010.

Gardner, C. S., Greene, J. M., Kruskal, M. D., & Miura, R. M. (1974). Korteweg-devries equation and generalizations. vi. methods for exact solution. *Communications on pure and applied mathematics*, *27*(1), 97–133.

Gavrilyuk, S. L., Liapidevskii, V. Y., & Chesnokov, A. A. (2016). Spilling breakers in shallow water: applications to favre waves and to the shoaling and breaking of solitary waves. *Journal of Fluid Mechanics*, *808*, 441–468. doi: 10.1017/jfm.2016.662

Geist, E., & Yoshioka, S. (1996). Source parameters controlling the generation and propagation of potential local tsunamis along the cascadia margin. *Natural Hazards*, *13*(2), 151–177.

Geist, E. L. (1998). Local tsunamis and earthquake source parameters. In R. Dmowska & B. Saltzman (Eds.), *Tsunamigenic earthquakes and their consequences* (Vol. 39, p. 117 - 209). Elsevier. Retrieved from http://www.sciencedirect.com/science/article/pii/S0065268708602769 doi: https://doi.org/10.1016/S0065-2687(08)60276-9

Goda, Y., & Suzuki, Y. (1976). Estimation of incident and reflected waves in random wave experiments. In *Coastal engineering* (p. 828-845). Retrieved from https://ascelibrary.org/doi/abs/10.1061/9780872620834.048 doi: 10.1061/9780872620834.048

Gonzalez, R. C. (1987). P. wintz digital image processing. *Addision-Wesley Publishing Company*, 275–281.

Gordillo Zavaleta, L. J. (2012). *Non-propagating hydrodynamic solitons in a quasi-one dimensional free surface subject to vertical vibrations* (Unpublished doctoral dissertation).

Goring, D. (1979). *Tsunamis-the propagation of long waves onto a shelf* (Tech. Rep.). W.M. Keck Laboratory of Hydraulics and Water Resources, California Institute of Technology, Pasadena, California, California.

Goseberg, N., Wurpts, A., & Schlurmann, T. (2013). Laboratory-scale generation of tsunami and long waves. *Coastal Engineering*, *79*, 57 - 74. Retrieved from http://www.sciencedirect.com/science/article/pii/S0378383913000823 doi: https://doi.org/10.1016/j.coastaleng.2013.04.006

Graftieaux, L., Michard, M., & Grosjean, N. (2001, aug). Combining PIV, POD and vortex identification algorithms for the study of unsteady turbulent swirling flows. *Measurement Science and Technology*, *12*(9), 1422–1429. Retrieved from https://doi.org/10.1088%2F0957-0233%2F12%2F9%2F307 doi: 10.1088/0957-0233/12/9/307

Grawin, A. (2006). *The sumatra 2004 tsunami reaching the island koh jum off the coast of thailand.* Retrieved from http://www.kohjumonline.com/anders.html ([Online; accessed October 8th, 2020])

Grilli, S. T., Guyenne, P., & Dias, F. (2001). A fully non-linear model for three-dimensional overturning waves over an arbitrary bottom. *International Journal for Numerical Methods in Fluids*, *35*(7), 829-867. Retrieved from https://onlinelibrary.wiley.com/doi/abs/10.1002/1097-0363%2820010415%2935%3A7%3C829%3A%3AAID-FLD115%3E3.0.CO%3B2-2 doi: 10.1002/1097-0363(20010415)35:7<829::AID-FLD115>3.0.CO;2-2

Grue, J. (2011). Two phenomena: Honji instability, and ringing of offshore structures. *Theoretical and Applied Mechanics Letters*, *1*(6), 062001. Retrieved from http://www.sciencedirect.com/science/article/pii/S2095034915300969 doi: https://doi.org/10.1063/2.1106201

Grue, J., Pelinovsky, E. N., Fructus, D., Talipova, T., & Kharif, C. (2008). Formation of undular bores and solitary waves in the strait of malacca caused by the 26 december 2004 indian ocean tsunami. *Journal of Geophysical Research: Oceans*, *113*(C5). Retrieved from https://agupubs.onlinelibrary.wiley.com/doi/abs/10.1029/2007JC004343 doi: https://doi.org/10.1029/2007JC004343

Gui, L., Merzkirch, W., & Fei, R. (2000). A digital mask technique for reducing the bias error of the correlation-based piv interrogation algorithm. *Experiments in fluids*, *29*(1), 30–35.

Guillouzouic, B. (2014). *Collation of wave simulation methods* (Tech. Rep.). Tech. rep.

Guizien, K., & Barthélemy, E. (2002). Accuracy of solitary wave generation by a piston wave maker. *Journal of Hydraulic Research*, *40*(3), 321-331. Retrieved from http://dx.doi.org/10.1080/00221680209499946 doi: 10.1080/00221680209499946

Gyongy, I., Bruce, T., & Bryden, I. (2014). Numerical analysis of force-feedback control in a circular tank. *Applied Ocean Research*, *47*, 329–343.

Haider, M., Mahfouz, M., Islam, S., Eliza, S., Qu, W., & Pritchard, E. (2008). A low-power capacitance measurement circuit with high resolution and high degree of linearity. In *Circuits and systems, 2008. mwscas 2008. 51st midwest symposium on* (pp. 261–264).

Hall, P. (1984). On the stability of the unsteady boundary layer on a cylinder oscillating transversely in a viscous fluid. *Journal of Fluid Mechanics*, *146*, 347–367. doi: 10.1017/S0022112084001907

Hammack, J. L., & Segur, H. (1974). The korteweg-de vries equation and water waves. part 2. comparison with experiments. *Journal of Fluid Mechanics*, *65*(2), 289–314. doi: 10.1017/S002211207400139X

Hart, D. P. (2000). Piv error correction. *Experiments in fluids*, *29*(1), 13–22.

Hasimoto, H. (1972). A soliton on a vortex filament. *Journal of Fluid Mechanics*, *51*(3), 477–485. doi: 10.1017/S0022112072002307

Hatland, S. D., & Kalisch, H. (2019). Wave breaking in undular bores generated by a moving weir. *Physics of Fluids*, *31*(3). Retrieved from http://dx.doi.org/10.1063/1.5085861 doi: 10.1063/1.5085861

Havelock, T. F. (1929). Lix. forced surface-waves on water. *The London, Edinburgh, and Dublin Philosophical Magazine and Journal of Science*, *8*(51), 569-576. doi: 10.1080/14786441008564913

Hernández, R. H., Vial, A., & Barraud, C. (2015). Motion of a free cylinder inside a rotating water-filled drum. *Physics of Fluids*, *27*(8), 083602. Retrieved from https://doi.org/10.1063/1.4928938 doi: 10.1063/1.4928938

Hernández, R. H., & Reyes, T. (2017). Symmetrical collision of multiple vortex rings. *Physics of Fluids*, *29*(10), 103604. Retrieved from https://doi.org/10.1063/1.5004587 doi: 10.1063/1.5004587

Higuera, P., Lara, J. L., & Losada, I. J. (2013). Realistic wave generation and active wave absorption for navier–stokes models. *Coastal Engineering*, *71*, 102 - 118. Retrieved from http://www.sciencedirect.com/science/article/pii/S0378383912001354 doi: http://dx.doi.org/10.1016/j.coastaleng.2012.07.002

Higuera, P., Losada, I. J., & Lara, J. L. (2015). Three-dimensional numerical wave generation with moving boundaries. *Coastal Engineering*, *101*, 35 - 47. Retrieved from http://www.sciencedirect.com/science/article/pii/S0378383915000666 doi: https://doi.org/10.1016/j.coastaleng.2015.04.003

Hirsa, A., & Willmarth, W. W. (1994). Measurements of vortex pair interaction with a clean or contaminated free surface. *Journal of Fluid Mechanics*, *259*, 25–45. doi: 10.1017/S0022112094000029

Hirt, C. W., & Nichols, B. D. (1981). Volume of fluid (vof) method for the dynamics of free boundaries. *Journal of computational physics*, *39*(1), 201–225.

Honji, H. (1981). Streaked flow around an oscillating circular cylinder. *Journal of Fluid Mechanics*, *107*, 509–520. doi: 10.1017/S0022112081001894

Huang, H., Dabiri, D., & Gharib, M. (1997). On errors of digital particle image velocimetry. *Measurement Science and Technology*, *8*(12), 1427.

Huang, H. T., Fiedler, H. E., & Wang, J. J. (1993, Aug 01). Limitation and improvement of piv. *Experiments in Fluids*, *15*(3), 168–174. Retrieved from https://doi.org/10.1007/BF00189883 doi: 10.1007/BF00189883

Huang, N. E., Shen, Z., Long, S. R., Wu, M. C., Shih, H. H., Zheng, Q., ... Liu, H. H. (1998). The empirical mode decomposition and the hilbert spectrum for nonlinear and non-stationary time series analysis. *Proceedings of the Royal Society of London. Series A: mathematical, physical and engineering sciences*, *454*(1971), 903–995.

Hunt, J. C., Wray, A. A., & Moin, P. (1988). Eddies, streams, and convergence zones in turbulent flows.

Huygens, C. (1690). Traité de la lumière.

Ingram, D., Wallace, R., Robinson, A., & Bryden, I. (2014, 4 8). The design and commissioning of the first, circular, combined current and wave test basin. In *Proceedings of oceans 2014 mts/ieee taipei, taiwan.* United States: Institute of Electrical and Electronics Engineers (IEEE).

Ishida, H., & Iwagaki, Y. (1978). Wave forces induced by irregular waves on a vertical circular cylinder. In *Coastal engineering 1978* (p. 2397-2414). Retrieved from https://ascelibrary.org/doi/abs/10.1061/9780872621909.146 doi: 10.1061/9780872621909.146

Israeli, M., & Orszag, S. A. (1981, May). Approximation of radiation boundary conditions. *Journal of Computational Physics*, *41*, 115-135. doi: 10.1016/0021-9991(81)90082-6

Issa, R. I. (1986, January). Solution of the implicitly discretised fluid flow equations by operator-splitting. *Journal of Computational Physics*, *62*, 40-65. doi: 10.1016/0021-9991(86)90099-9

Jagadeesh, P., & Murali, K. (2005). Application of low-re turbulence models for flow simulations past underwater vehicle hull forms. *Journal of Naval Architecture and Marine Engineering*, *2*(1), 41–54.

Jeong, J., & Hussain, F. (1995). On the identification of a vortex. *Journal of Fluid Mechanics*, *285*, 69–94. doi: 10.1017/S0022112095000462

Joo, S. W., Schultz, W. W., & Messiter, A. F. (1990). An analysis of the initial-value wavemaker problem. *Journal of Fluid Mechanics*, *214*, 161–183. doi: 10.1017/S002211209000009X

Kadomtsev, B. B., & Petviashvili, V. I. (1970). On the stability of solitary waves in weakly dispersing media. In *Sov. phys. dokl* (Vol. 15, pp. 539–541).

Kamchatnov, A., Kuo, Y.-H., Lin, T.-C., Horng, T.-L., Gou, S.-C., Clift, R., ... Grimshaw, R. H. (2012). Undular bore theory for the gardner equation. *Physical Review E*, *86*(3), 036605.

Katell, G. (2002). Accuracy of solitary wave generation by a piston wave maker. *Journal of Hydraulic Research*. doi: 10.1080/00221680209499946

Kawata, Y., & Tsuchiya, Y. (1988). Local scour around cylindrical piles due to waves and currents combined. In *Coastal engineering* (p. 1310-1322). Retrieved from https://ascelibrary.org/doi/abs/10.1061/9780872626874.098 doi: 10.1061/9780872626874.098

Keaney, I., Costello, R., & Ringwood, J. V. (2014, 06). *Evanescent Wave Reduction Using a Segmented Wavemaker in a Two Dimensional Wave Tank* (Vol. Volume 8B: Ocean Engineering). Retrieved from https://doi.org/10.1115/OMAE2014-24441 (V08BT06A052) doi: 10.1115/OMAE2014-24441

Keulegan, G. (1966). *The approximate theories of pneumatic wave generators* (Tech. Rep.).

Keulegan, G. H. (1940). Mathematical theory of irrotational translation waves. *J. Res. Natl. Bur. Stand.*, *24*, 47–101.

Keulegan, G. H. (1948). Gradual damping of solitary waves. *Journal of Research of the National Bureau of Standards*, *40*(RP1895). doi: 10.6028/jres.040.041

Keulegan, G. H., & Carpenter, L. H. (1958). Forces on cylinders and plates in an oscillating fluid. *Journal of research of the National Bureau of Standards*, *60*(5), 423–440.

Kim, B. J., & Sung, H. J. (2006). A further assessment of interpolation schemes for window deformation in piv. *Experiments in fluids*, *41*(3), 499–511.

Kim, G.-H., & Park, S. (2017). Development of a numerical simulation tool for efficient and robust prediction of ship resistance. *International Journal of Naval Architecture and Ocean Engineering*.

Kolmogorov, A. N. (1941). The local structure of turbulence in incompressible viscous fluid for very large reynolds numbers. *Cr Acad. Sci. URSS*, *30*, 301–305.

Korteweg, D. J., & de Vries, G. (1895). Xli. on the change of form of long waves advancing in a rectangular canal, and on a new type of long stationary waves. *The London, Edinburgh, and Dublin Philosophical Magazine and Journal of Science*, *39*(240), 422-443. Retrieved from https://doi.org/10.1080/14786449508620739 doi: 10.1080/14786449508620739

Koumoutsakos, P., & Leonard, A. (1995). High-resolution simulations of the flow around an impulsively started cylinder using vortex methods. *Journal of Fluid Mechanics*, *296*, 1–38. doi: 10.1017/S0022112095002059

Kumar, B., Rajita, G., & Mandal, N. (2014). A review on capacitive-type sensor for measurement of height of liquid level. *Measurement and Control*, *47*(7), 219–224.

Kundu, P. K., Cohen, I. M., & Dowling, D. R. (2012). Chapter 5 - vorticity dynamics. In *Fluid mechanics (fifth edition)* (Fifth Edition ed., p. 171 - 196). Boston: Academic Press. Retrieved from http://www.sciencedirect.com/science/article/pii/B9780123821003100058 doi: https://doi.org/10.1016/B978-0-12-382100-3.10005-8

Lamb, H. (1993). *Hydrodynamics*. Cambridge university press.

Larsen, B. E., Fuhrman, D. R., & Roenby, J. (2019). Performance of interfoam on the simulation of progressive waves. *Coastal Engineering Journal*, *61*(3), 380-400. Retrieved from https://doi.org/10.1080/21664250.2019.1609713 doi: 10.1080/21664250.2019.1609713

Larsen, J., & Dancy, H. (1983). Open boundaries in short wave simulations – a new approach. *Coastal Eng*, 285–297.

Laurich, P. (2009). *Awp-24 wave height gauge test results* (Tech. Rep.).

Lecordier, B., & Westerweel, J. (2004). The europiv synthetic image generator (sig). In *Particle image velocimetry: recent improvements* (pp. 145–161). Springer.

Le Méhauté, B. (2013). *An introduction to hydrodynamics and water waves*. Springer Science & Business Media.

Lemoine, R. (1948). Sur les ondes positives de translation dans les canaux et sur le ressaut ondulé de faible amplitude. *La Houille Blanche*, *2*, 183–185.

Leweke, T., & Williamson, C. H. K. (1998). Cooperative elliptic instability of a vortex pair. *Journal of Fluid Mechanics*, *360*, 85–119. doi: 10.1017/S0022112097008331

Li, J., You, Y., Chen, K., & Zhang, X. (2019). Numerical computations of resonant sloshing using the modified isoadvector method and the buoyancy-modified turbulence closure model. *Applied Ocean Research*, *93*, 101829. Retrieved from http://www.sciencedirect.com/science/article/pii/S0141118718309234 doi: https://doi.org/10.1016/j.apor.2019.05.014

Lienhard, J. H. (1966). *Synopsis of lift, drag, and vortex frequency data for rigid circular cylinders.*

Lilly, K. (1966). The representation of small-scale turbulence in numerical simulation experiments.

Lima, V. V., Avilez-Valente, P., Baptista, M. A. V., & Miranda, J. M. (2019). Generation of n-waves in laboratory. *Coastal Engineering*, *148*, 1 - 18. Retrieved from http://www.sciencedirect.com/science/article/pii/S0378383918302060 doi: https://doi.org/10.1016/j.coastaleng.2019.02.012

Lin, C., Kao, M.-J., Wong, W.-Y., Shao, Y.-P., Hu, C.-F., Yuan, J.-M., & Raikar, R. V. (2019). Effect of leading waves on velocity distribution of undular bore traveling over sloping bottom. *European Journal of Mechanics - B/Fluids*, *73*, 75 - 99. Retrieved from http://www.sciencedirect.com/science/article/pii/S0997754617302285 (Breaking Waves) doi: https://doi.org/10.1016/j.euromechflu.2018.05.005

Lin, C., Kao, M.-J., Yuan, J.-M., Raikar, R. V., Wong, W.-Y., Yang, J., & Yang, R.-Y. (2020). Features of the flow velocity and pressure gradient of an undular bore on a horizontal bed. *Physics of Fluids*, *32*(4), 043603. Retrieved from https://doi.org/10.1063/5.0001525 doi: 10.1063/5.0001525

Lin, C.-Y., & Huang, C.-J. (2004). Decomposition of incident and reflected higher harmonic waves using four wave gauges. *Coastal Engineering*, *51*(5), 395 - 406. Retrieved from http://www.sciencedirect.com/science/article/pii/S0378383904000535 doi: https://doi.org/10.1016/j.coastaleng.2004.04.004

Lin, P., & Li, C. W. (2003). Wave–current interaction with a vertical square cylinder. *Ocean Engineering*, *30*(7), 855–876. Retrieved from http://www.sciencedirect.com/science/article/pii/S0029801802000689 doi: https://doi.org/10.1016/S0029-8018(02)00068-9

Lin, P., & Liu, P. L.-F. (1999). Internal wave-maker for navier-stokes equations models. *Journal of Waterway, Port, Coastal, and Ocean Engineering*, *125*(4), 207-215. Retrieved from http://ascelibrary.org/doi/abs/10.1061/%28ASCE%290733-950X%281999%29125%3A4%28207%29 doi: 10.1061/(ASCE)0733-950X(1999)125:4(207)

Liu, P. L. F., Cho, Y.-S., Briggs, M. J., Kanoglu, U., & Synolakis, C. E. (1995). Runup of solitary waves on a circular island. *Journal of Fluid Mechanics*, *302*, 259–285. doi: 10.1017/S0022112095004095

Lloyd, P. M., & Stansby, P. K. (1997). Shallow-water flow around model conical islands of small side slope. I: Surface piercing. *Journal of Hydraulic Engineering*, *123*(12), 1057–1066. doi: 10.1061/(asce)0733-9429(1997)123:12(1057)

Loizou, K., Koutroulis, E., Zalikas, D., & Liontas, G. (2015). A low-cost capacitive sensor for water level monitoring in large-scale storage tanks. In *Industrial technology (icit), 2015 ieee international conference on* (pp. 1416–1421).

Long, S. R., & Huang, N. E. (1976). On the variation and growth of wave-slope spectra in the capillary-gravity range with increasing wind. *Journal of Fluid Mechanics*, *77*(2), 209–228. doi: 10.1017/S0022112076002073

Longoria, R. G., Beaman, J. J., & Miksad, R. W. (1991, 11). An Experimental Investigation of Forces Induced on Cylinders by Random Oscillatory Flow. *Journal of Offshore Mechanics and Arctic Engineering*, *113*(4), 275-285. Retrieved from https://doi.org/10.1115/1.2919931 doi: 10.1115/1.2919931

Longuet-Higgins, M. S., & Cokelet, E. D. (1976). The deformation of steep surface waves on water - i. a numerical method of computation. *Proceedings of the Royal Society of London. A. Mathematical and Physical Sciences*, *350*(1660), 1-26. Retrieved from https://royalsocietypublishing.org/doi/abs/10.1098/rspa.1976.0092 doi: 10.1098/rspa.1976.0092

Lotters, J. C., Olthuis, W., Veltink, P. H., & Bergveld, P. (1999). A sensitive differential capacitance to voltage converter for sensor applications. *IEEE Transactions on Instrumentation and Measurement*, *48*(1), 89–96.

Lourenco, L., & Krothapalli, A. (1995). On the accuracy of velocity and vorticity measurements with piv. *Experiments in fluids*, *18*(6), 421–428.

Lu, X., Dalton, C., & Zhang, J. (1997, 09). Application of Large Eddy Simulation to an Oscillating Flow Past a Circular Cylinder. *Journal of Fluids Engineering*, *119*(3), 519-525. Retrieved from https://doi.org/10.1115/1.2819275 doi: 10.1115/1.2819275

Luo, S., Chew, Y., & Ng, Y. (2003). Hysteresis phenomenon in the galloping oscillation of a square cylinder. *Journal of Fluids and Structures*, *18*(1), 103 - 118. Retrieved from http://www.sciencedirect.com/science/article/pii/S0889974603000847 doi: https://doi.org/10.1016/S0889-9746(03)00084-7

Lu Ting, R. K. a. (1991). *Viscous vortical flows* (1st ed.). Springer Berlin Heidelberg.

Mader, C. L. (2004). *Numerical modeling of water waves*. CRC press.

Madsen, O. S. (1971). *Waves generated by a piston-type wavemaker* (Tech. Rep.). Research Division, US Army Coastal Engineering Research Center.

Madsen, P. A., Fuhrman, D. R., & Schäffer, H. A. (2008). On the solitary wave paradigm for tsunamis. *Journal of Geophysical Research: Oceans*, *113*(C12). Retrieved from https://agupubs.onlinelibrary.wiley.com/doi/abs/10.1029/2008JC004932 doi: 10.1029/2008JC004932

Madsen, P. A., & Schäffer, H. A. (1999). A review of boussinesq-type equations for surface gravity waves. In *Advances in coastal and ocean engineering* (p. 1-94). Retrieved from https://www.worldscientific.com/doi/abs/10.1142/9789812797544_0001 doi: 10.1142/9789812797544_0001

Madsen, P. A., & Svendsen, I. A. (1983). Turbulent bores and hydraulic jumps. *Journal of Fluid Mechanics*, *129*, 1–25. doi: 10.1017/S0022112083000622

Maeda, K., Hosotani, N., Tamura, K., & Ando, H. (2004, April). Wave making properties of circular basin. In *Proceedings of the 2004 international symposium on underwater technology (ieee cat. no.04ex869)* (p. 349-354). doi: 10.1109/UT.2004.1405603

Maguire, A., & Ingram, D. (2009). Hydrodynamics and absorption efficiencies of wavemakers. In *Proceedings of the 8th european wave and tidal energy conference, uppsala, sweden.*

Maguire, A., & Ingram, D. (2010). Wavemaking in a commercial cfd code. In *Proceedings of the third international conference on the application of physical modelling to port and coastal protection.*

Maguire, A. E. (2011). Hydrodynamics, control and numerical modelling of absorbing wavemakers.

Mallock, H. R. A. (1907). On the resistance of air. *Proceedings of the Royal Society of London. Series A, Containing Papers of a Mathematical and Physical Character*, *79*(530), 262-273. Retrieved from https://royalsocietypublishing.org/doi/abs/10.1098/rspa.1907.0038 doi: 10.1098/rspa.1907.0038

Marcus, D. L., & Berger, S. A. (1989). The interaction between a counter-rotating vortex pair in vertical ascent and a free surface. *Physics of Fluids A: Fluid Dynamics*, *1*(12), 1988-2000. Retrieved from https://doi.org/10.1063/1.857471 doi: 10.1063/1.857471

Marshall, J. S. (1992). The effect of axial stretching on the three-dimensional stability of a vortex pair. *Journal of Fluid Mechanics*, *241*, 403–419. doi: 10.1017/S002211209200209X

Martins, K., Bonneton, P., Frappart, F., Detandt, G., Bonneton, N., & Blenkinsopp, C. E. (2017). High frequency field measurements of an undular bore using a 2d lidar scanner. *Remote Sensing*, *9*(5), 462.

Mayer, S., Garapon, A., & Sørensen, L. S. (1998). A fractional step method for unsteady free-surface flow with applications to non-linear wave dynamics. *International Journal for Numerical Methods in Fluids*, *28*(2), 293–315. Retrieved from http://dx.doi.org/10.1002/(SICI)1097-0363(19980815)28:2<293::AID-FLD719>3.0.CO;2-1 doi: 10.1002/(SICI)1097-0363(19980815)28:2<293::AID-FLD719>3.0.CO;2-1

McCowan, J. (1891). Vii. on the solitary wave. *The London, Edinburgh, and Dublin Philosophical Magazine and Journal of Science*, *32*(194), 45–58.

McGovern, D. (2016). Experimental study of the runup of tsunami waves on a smooth sloping beach. In *6th international conference on the application of physical modelling in coastal and port engineering and science.*

McHugh, J. P., & Watt, D. W. (1998). Surface waves impinging on a vertical wall. *Physics of Fluids*, *10*, 324–326.

Menter, F. R., Ferreira, J. C., Esch, T., & Konno, B. (2003). The sst turbulence model with improved wall treatment for heat transfer predictions in gas turbines..

Menter, F. R., Kuntz, M., & Langtry, R. (2003). Ten years of industrial experience with the sst turbulence model. *Turbulence, heat and mass transfer*, *4*(1), 625–632.

Milgram, J. H. (1965). *Compliant water wave absorbers* (Unpublished doctoral dissertation). Massachusetts Institute of Technology.

Millard, N. (1969). The performance of a capacitance-wire wave recorder.

Moiseev, S., & Sagdeev, R. (1963). Collisionless shock waves in a plasma in a weak magnetic field. *Journal of Nuclear Energy. Part C, Plasma Physics, Accelerators, Thermonuclear Research*, *5*(1), 43.

Moon, H. T., & Weidman, P. D. (1988). Local vortex pairing in a free shear layer. *The Physics of Fluids*, *31*(12), 3804-3806. Retrieved from https://aip.scitation.org/doi/abs/10.1063/1.866848 doi: 10.1063/1.866848

Morison, J., Johnson, J., & Schaaf, S. (1950). The Force Exerted by Surface Waves on Piles. *Journal of Petroleum Technology*, *2*(05), 149–154. doi: 10.2118/950149-g

Moukalled, F., Mangani, L., Darwish, M., et al. (2016). *The finite volume method in computational fluid dynamics* (Vol. 113). Springer.

Newman, J. N. (2017). *Marine hydrodynamics*. MIT press.

Nguyen, T. (2016). Capacitive sensing: Water level application.

Nicolau del Roure, F., Socolofsky, S. A., & Chang, K.-A. (2009). Structure and evolution of tidal starting jet vortices at idealized barotropic inlets. *Journal of Geophysical Research: Oceans*, *114*(C5). Retrieved from https://agupubs.onlinelibrary.wiley.com/doi/abs/10.1029/2008JC004997 doi: 10.1029/2008JC004997

Nise, N. S. (2011). Control system engineering, john wiley & sons. *Inc, New York*.

Nishioka, M., & Sato, H. (1978). Mechanism of determination of the shedding frequency of vortices behind a cylinder at low reynolds numbers. *Journal of Fluid Mechanics*, *89*(1), 49–60. doi: 10.1017/S0022112078002451

Nobach, H., & Honkanen, M. (2005). Two-dimensional gaussian regression for sub-pixel displacement estimation in particle image velocimetry or particle position estimation in particle tracking velocimetry. *Experiments in fluids*, *38*(4), 511–515.

Nogueira, J., Lecuona, A., & Rodriguez, P. (1999). Local field correction piv: on the increase of accuracy of digital piv systems. *Experiments in fluids*, *27*(2), 107–116.

Nomura, T., Suzuki, Y., Uemura, M., & Kobayashi, N. (2003). Aerodynamic forces on a square cylinder in oscillating flow with mean velocity. *Journal of Wind Engineering and Industrial Aerodynamics*, *91*(1), 199 - 208. Retrieved from http://www.sciencedirect.com/science/article/pii/S0167610502003458 (Fifth Asia-Pacific Conference on Wind Engineering) doi: https://doi.org/10.1016/S0167-6105(02)00345-8

Nuño, J., Finot, C., Xu, G., Millot, G., Erkintalo, M., & Fatome, J. (2019). Vectorial dispersive shock waves in optical fibers. *Communications Physics*, *2*(1), 1–9.

Okajima, A., Matsumoto, T., & Kimura, S. (1998). Force measurements and flow visualization of circular and square cylinders in oscillatory flow. *JSME International Journal Series B*, *41*(4), 796-805. doi: 10.1299/jsmeb.41.796

Okajima, A., Matsumoto, T., & Kimura, S. (2000). Flow characteristics of a rectangular cylinder with a cross-section of various width/height ratios submerged in oscillatory flow. *JSME International Journal Series B*, *43*(3), 329-338. doi: 10.1299/jsmeb.43.329

Ortega, J. M., Bristol, R. L., & Savas, O. (2003). Experimental study of the instability of unequal-strength counter-rotating vortex pairs. *Journal of Fluid Mechanics*, *474*, 35–84. doi: 10.1017/S0022112002002446

Oseen, C. (1912). Uber die wirbelbewegung in einer reibenden flussigkeit. *Ark. Mat. Astro. Fys.*, *7*.

Otero, A., Fernández, R., Apalkov, A., & Armada, M. (2012). An automatic critical care urine meter. *Sensors*, *12*(10), 13109–13125.

Pal, A., Basu, A., & Choudhury, A. (1973). A simple digital capacitance meter. *IETE Journal of Research*, *19*(12), 659–662.

Patankar, S. (1980). *Numerical heat transfer and fluid flow*. CRC press.

Payas Areny, R. (2004). *Sensores y acondicionadores de señal*.

Penalba, M., Mérigaud, A., Gilloteaux, J.-C., & Ringwood, J. V. (2017). Influence of nonlinear froude–krylov forces on the performance of two wave energy points absorbers. *Journal of Ocean Engineering and Marine Energy*, *3*(3), 209–220.

Peregrine, D. H. (1966). Calculations of the development of an undular bore. *Journal of Fluid Mechanics*, *25*(2), 321–330. doi: 10.1017/S0022112066001678

Peregrine, D. H. (1967). Long waves on a beach. *Journal of fluid mechanics*, *27*(4), 815–827.

Perry, A. E., Chong, M. S., & Lim, T. T. (1982). The vortex-shedding process behind two-dimensional bluff bodies. *Journal of Fluid Mechanics*, *116*, 77–90. doi: 10.1017/S0022112082000378

Petitjeans, Philippe. (2003). Stretching of a vortical structure: filaments of vorticity. *Europhysics News*, *34*(1), 20-23. Retrieved from https://doi.org/10.1051/epn:2003105 doi: 10.1051/epn:2003105

Pétursson, H. Ö., Hákonardóttir, K. M., & Thoroddsen, Á. (2019). Use of openfoam and ramms avalanche to simulate the interaction of avalanches and slush flows with dams. In *International symposium on mitigative measures against snow avalanches and other rapid gravity mass flows*.

P. G. Drazin, N. R. (2006). *The navier-stokes equations: A classification of flows and exact solutions*. Cambridge University Press.

Pierce, J. R. (1943). A Note on the Transmission Line Equation in Terms of Impedance. *Bell System Technical Journal*. doi: 10.1002/j.1538-7305.1943.tb00862.x

Pizer, S. M., Amburn, E. P., Austin, J. D., Cromartie, R., Geselowitz, A., Greer, T., ... Zuiderveld, K. (1987). Adaptive histogram equalization and its variations. *Computer vision, graphics, and image processing*, *39*(3), 355–368.

Pope, S. B. (2004, mar). Ten questions concerning the large-eddy simulation of turbulent flows. *New Journal of Physics*, *6*, 35–35. Retrieved from https://doi.org/10.1088%2F1367-2630%2F6%2F1%2F035 doi: 10.1088/1367-2630/6/1/035

Prandtl, L. (1925). 7. bericht über untersuchungen zur ausgebildeten turbulenz. *ZAMM-Journal of Applied Mathematics and Mechanics/Zeitschrift für Angewandte Mathematik und Mechanik*, *5*(2), 136–139.

Provansal, M., Mathis, C., & Boyer, L. (1987). Benard-von Karman instability: Transient and forced regimes. *Journal of Fluid Mechanics*, *182*(September 1987), 1–22. doi: 10.1017/S0022112087002222

Prunkl, H., Tarnay, K., & Ambrózy, A. (1958). Layer-thickness measurement of enamel-covered wire. *Periodica Polytechnica Electrical Engineering*, *2*(4), 355–369.

Qi, Z., Eames, I., & Johnson, E. (2014). Force acting on a square cylinder fixed in a free-surface channel flow. *Journal of Fluid Mechanics*, *756*, 716–727. doi: 10.1017/jfm.2014.455

Rabinovich, A. B., & Thomson, R. E. (2007). The 26 december 2004 sumatra tsunami: Analysis of tide gauge data from the world ocean part 1. indian ocean and south africa. In K. Satake, E. A. Okal, & J. C. Borrero (Eds.), *Tsunami and its hazards in the indian and pacific oceans* (pp. 261–308). Basel: Birkhäuser Basel.

Radon, J. (2005). 1.1 über die bestimmung von funktionen durch ihre integralwerte längs gewisser mannigfaltigkeiten. *Classic papers in modern diagnostic radiology*, *5*, 21.

Raffel, M., Willert, C. E., Scarano, F., Kähler, C. J., Wereley, S. T., & Kompenhans, J. (2018). *Particle image velocimetry: a practical guide*. Springer.

Raikar, R. V., & Dey, S. (2008). Kinematics of horseshoe vortex development in an evolving scour hole at a square cylinder. *Journal of Hydraulic Research*, *46*(2), 247-264. Retrieved from https://doi.org/10.1080/00221686.2008.9521859 doi: 10.1080/00221686.2008.9521859

Rayleigh, M. A. (1876). Xxxii. on waves. *The London, Edinburgh, and Dublin Philosophical Magazine and Journal of Science*, *1*(4), 257-279. Retrieved from https://doi.org/10.1080/14786447608639037 doi: 10.1080/14786447608639037

Reid, R. O. (1957, Jan.). Correlation of water level variations with wave forces on a vertical pile for nonperiodic waves. *Coastal Engineering Proceedings*, *1*(6), 46. Retrieved from https://icce-ojs-tamu.tdl.org/icce/index.php/icce/article/view/2055 doi: 10.9753/icce.v6.46

Ren, Z., Zhao, X., & Liu, H. (2019). Numerical study of the landslide tsunami in the south china sea using herschel-bulkley rheological theory. *Physics of Fluids*, *31*(5), 056601. Retrieved from https://doi.org/10.1063/1.5087245 doi: 10.1063/1.5087245

Ricca, R. L. (1994). The effect of torsion on the motion of a helical vortex filament. *Journal of Fluid Mechanics*, *273*, 241–259. doi: 10.1017/S0022112094001928

Richardson, L. F. (1911). The approximate arithmetical solution by finite differences of physical problems involving differential equations, with an application to the stresses in a masonry dam. *Philosophical Transactions of the Royal Society of London. Series A, Containing Papers of a Mathematical or Physical Character*, *210*, 307–357.

Richardson, L. F., & Gaunt, J. A. (1927). The deferred approach to the limit. part i. single lattice. part ii. interpenetrating lattices. *Philosophical Transactions of the Royal Society of London. Series A, containing papers of a mathematical or physical character*, *226*, 299–361.

Roache, P. J. (1998). *Verification and validation in computational science and engineering* (Vol. 895). Hermosa Albuquerque, NM.

Rodi, W. (2017). Turbulence modeling and simulation in hydraulics: A historical review. *Journal of Hydraulic Engineering*, *143*(5), 03117001. Retrieved from https://ascelibrary.org/doi/abs/10.1061/%28ASCE%29HY.1943-7900.0001288 doi: 10.1061/(ASCE)HY.1943-7900.0001288

Roenby, J., Bredmose, H., & Jasak, H. (2016). A computational method for sharp interface advection. *Royal Society Open Science*, *3*(11), 160405. Retrieved from https://royalsocietypublishing.org/doi/abs/10.1098/rsos.160405 doi: 10.1098/rsos.160405

Roshko, A. (1954). On the drag and shedding frequency of two-dimensional bluff bodies.

Roshko, A. (1961). Experiments on the flow past a circular cylinder at very high reynolds number. *Journal of Fluid Mechanics*, *10*(3), 345–356. doi: 10.1017/S0022112061000950

Ross, P. (1983). A water-level sensor using a capacitance to frequency converter. *Journal of Physics E: Scientific Instruments*, *16*(9), 827.

Rossetto, T., Allsop, W., Charvet, I., & Robinson, D. I. (2011). Physical modelling of tsunami using a new pneumatic wave generator. *Coastal Engineering*, *58*(6), 517 - 527. Retrieved from http://www.sciencedirect.com/science/article/pii/S0378383911000135 doi: https://doi.org/10.1016/j.coastaleng.2011.01.012

Roth, G., & Katz, J. (2001). Five techniques for increasing the speed and accuracy of piv interrogation. *Measurement Science and Technology*, *12*(3), 238.

Rusche, H. (2002). *Computational fluid dynamics of dispersed two-phase flows at high phase fractions* (Unpublished doctoral dissertation). Imperial College.

Russell, J. S. (1838). Report of the committee on waves. In *Report of the 7th meeting of the british association for the advancement of science, liverpool* (Vol. 417496).

Saffman, P. G. (1993). *Vortex dynamics*. Cambridge University Press. doi: 10.1017/CBO9780511624063

Salter, S. H. (1981). Absorbing wave-makers and wide tanks. *Proceedings of the conference on Directional Wave Spectra Applications*.

Sanchis, A., & Jensen, A. (2011). Dynamic masking of piv images using the radon transform in free surface flows. *Experiments in fluids*, *51*(4), 871–880.

Sander, J., & Hutter, K. (1991). On the development of the theory of the solitary wave. a historical essay. *Acta mechanica*, *86*(1), 111–152.

Sarpkaya, T. (1986). Force on a circular cylinder in viscous oscillatory flow at low keulegan—carpenter numbers. *Journal of Fluid Mechanics*, *165*, 61–71. doi: 10.1017/S0022112086002999

Sarpkaya, T. (2002). Experiments on the stability of sinusoidal flow over a circular cylinder. *Journal of Fluid Mechanics*, *457*, 157–180. doi: 10.1017/S002211200200784X

Sarpkaya, T., et al. (1976). In-line and transverse forces, on cylinders in oscillatory flow at high reynolds numbers. In *Offshore technology conference.*

Scarano, F. (2001). Iterative image deformation methods in piv. *Measurement science and technology*, *13*(1), R1.

Schäffer, H., & Jakobsen, K. (2003). Nonlinear wave generation and active absorption in wave flumes. In *Long waves symposium, thessaloniki, greece.*

Schäffer, H. A., & Klopman, G. (2000). Review of multidirectional active wave absorption methods. *Journal of Waterway, Port, Coastal and Ocean Engineering*. doi: 10.1061/(ASCE)0733-950X(2000)126:2(88)

Scharnowski, S., & Kähler, C. J. (2016a, Jan 20). Estimation and optimization of loss-of-pair uncertainties based on piv correlation functions. *Experiments in Fluids*, *57*(2), 23.

Retrieved from https://doi.org/10.1007/s00348-015-2108-2 doi: 10.1007/s00348-015-2108-2

Scharnowski, S., & Kähler, C. J. (2016b, Jun 27). On the loss-of-correlation due to piv image noise. *Experiments in Fluids*, *57*(7), 119. Retrieved from https://doi.org/10.1007/s00348-016-2203-z doi: 10.1007/s00348-016-2203-z

Schimmels, S., Sriram, V., & Didenkulova, I. (2016). Tsunami generation in a large scale experimental facility. *Coastal Engineering*, *110*, 32 - 41. Retrieved from http://www.sciencedirect.com/science/article/pii/S0378383915002136 doi: https://doi.org/10.1016/j.coastaleng.2015.12.005

Schmitt, P., & Elsaesser, B. (2015). A review of wave makers for 3d numerical simulations. In *Marine 2015 VI international conference on computational methods in marine engineering, rome, italy.*

Schwind, R. (1962). The three-dimensional boundary layer near a strut. *Gas Turbine Lab. Rep.*.

Sciacchitano, A., & Scarano, F. (2014). Piv light reflections elimination via temporal high-pass filter. *Meas. Sci. Technol.*

Shafiei, S., Melville, B. W., & Shamseldin, A. Y. (2016). Experimental investigation of tsunami bore impact force and pressure on a square prism. *Coastal Engineering*, *110*, 1 - 16. Retrieved from http://www.sciencedirect.com/science/article/pii/S0378383915002227 doi: https://doi.org/10.1016/j.coastaleng.2015.12.006

Shavit, U., Lowe, R. J., & Steinbuck, J. V. (2007). Intensity capping: a simple method to improve cross-correlation piv results. *Experiments in Fluids*, *42*(2), 225–240.

Shi, R., Leng, X., & Chanson, H. (2020). On turbulence and turbulent events in a breaking bore. *Mechanics Research Communications*, *104*, 103478. Retrieved from http://www.sciencedirect.com/science/article/pii/S0093641320300070 doi: https://doi.org/10.1016/j.mechrescom.2020.103478

Shields, A. (1936). Application of similarity principles and turbulence research to bed-load movement.

Siffer, T. (2005). Mercator depth gauge recording of 26 december 2004 tsunami. *KNMI (Royal Netherlands Meteorological Institute).*

Skjelbreia, L., & Hendrickson, J. (2011). Fifth order gravity wave theory. *Coastal Engineering Proceedings*, *1*(7), 10. Retrieved from https://icce-ojs-tamu.tdl.org/icce/index.php/icce/article/view/2169 doi: 10.9753/icce.v7.10

Smagorinsky, J. (1963). General circulation experiments with the primitive equations: I. the basic experiment. *Monthly weather review*, *91*(3), 99–164.

Smith, T. B., & Beesmer, K. (1959). *Contrail studies for jet aircraft.* Meteorology Research.

Spinneken, J., & Swan, C. (2009). Second-order wave maker theory using force-feedback control. part i: A new theory for regular wave generation. *Ocean Engineering*, *36*, 539-549.

Spreiter, J. R., & Sacks, A. H. (1951). The rolling up of the trailing vortex sheet and its effect on the downwash behind wings. *Journal of the Aeronautical Sciences*, *18*(1), 21-32. Retrieved from https://doi.org/10.2514/8.1830 doi: 10.2514/8.1830

Stoker, J. J. (1957). Water waves: The mathematical theory with applications.

Stokes, G. (1851). On the effect of the internal friction of fluids on the motion of pendulums trans. *Cambridge Philos. Soc. IX*, 8–106.

Stokes, G. G. (1880). On the theory of oscillatory waves. *Transactions of the Cambridge Philosophical Society.*

Sturm, G. V., & Sorrell, F. Y. (1973, Aug). Optical wave measurement technique and experimental comparison with conventional wave height probes. *Appl. Opt.*, *12*(8), 1928–1933. Retrieved from http://ao.osa.org/abstract.cfm?URI=ao-12-8-1928 doi: 10.1364/AO.12.001928

Sturtevant, B. (1965). Implications of experiments on the weak undular bore. *Physics of Fluids.* doi: 10.1063/1.1761354

Sumer, B. M., Christiansen, N., & Fredsøe, J. (1997). The horseshoe vortex and vortex shedding around a vertical wall-mounted cylinder exposed to waves. *Journal of Fluid Mechanics*, *332*, 41–70. doi: 10.1017/S0022112096003898

Sumer, B. M., Fredsøe, J., & Christiansen, N. (1992). Scour around vertical pile in waves. *Journal of Waterway, Port, Coastal, and Ocean Engineering*, *118*(1), 15-31. Retrieved from https://ascelibrary.org/doi/abs/10.1061/%28ASCE%290733-950X%281992%29118%3A1%2815%29 doi: 10.1061/(ASCE)0733-950X(1992)118:1(15)

Sumer, B. M., et al. (2006). *Hydrodynamics around cylindrical strucures* (Vol. 26). World scientific.

Suthon, P., & Dalton, C. (2012). Observations on the honji instability. *Journal of Fluids and Structures*, *32*, 27 - 36. Retrieved from http://www.sciencedirect.com/science/article/pii/S0889974611001940 (The 7th International Symposium on Fluid-Structure Interactions, Flow-Sound Interactions, and Flow-Induced Vibrations & Noise) doi: https://doi.org/10.1016/j.jfluidstructs.2011.12.008

Svendsen, I. A. (1974). Cnoidal waves over a gently sloping bottom.

Synolakis, C. E. (1987). The runup of solitary waves. *Journal of Fluid Mechanics*, *185*, 523–545. doi: 10.1017/S002211208700329X

Tadepalli, S., & Synolakis, C. E. (1994). The run-up of n-waves on sloping beaches. *Proceedings of the Royal Society of London. Series A: Mathematical and Physical Sciences*, *445*(1923), 99-112. Retrieved from https://royalsocietypublishing.org/doi/abs/10.1098/rspa.1994.0050 doi: 10.1098/rspa.1994.0050

Tamura, T., & Miyagi, T. (1999). The effect of turbulence on aerodynamic forces on a square cylinder with various corner shapes. *Journal of Wind Engineering and Industrial Aerodynamics*, *83*(1), 135 - 145. Retrieved from http://www.sciencedirect.com/science/article/pii/S0167610599000677 doi: https://doi.org/10.1016/S0167-6105(99)00067-7

Taylor, G. I. (1938). Production and dissipation of vorticity in a turbulent fluid. *Proceedings of the Royal Society of London. Series A - Mathematical and Physical Sciences*, *164*(916), 15-23. Retrieved from https://royalsocietypublishing.org/doi/abs/10.1098/rspa.1938.0002 doi: 10.1098/rspa.1938.0002

Tennekes, H., Lumley, J. L., Lumley, J. L., et al. (1972). *A first course in turbulence*. MIT press.

Terzic, E., Terzic, J., Nagarajah, R., & Alamgir, M. (2012). *A neural network approach to fluid quantity measurement in dynamic environments*. Springer Science & Business Media.

Thielicke, W. (2014). *The flapping flight of birds: Analysis and application* (Unpublished doctoral dissertation). University of Groningen.

Timpy, D. L., & Ludwick, J. C. (1985). Bore height measurement with improved wavestaff. *Journal of Waterway, Port, Coastal, and Ocean Engineering*, *111*(3), 495-510. Retrieved from https://ascelibrary.org/doi/abs/10.1061/%28ASCE%290733-950X%281985%29111%3A3%28495%29 doi: 10.1061/(ASCE)0733-950X(1985)111:3(495)

Titov, V. V., & Synolakis, C. E. (1995). Modeling of breaking and nonbreaking long-wave evolution and runup using vtcs-2. *Journal of Waterway, Port, Coastal, and*

Ocean Engineering, *121*(6), 308-316. Retrieved from https://ascelibrary.org/doi/abs/10.1061/%28ASCE%290733-950X%281995%29121%3A6%28308%29 doi: 10.1061/(ASCE)0733-950X(1995)121:6(308)

Treske, A. (1994). Undular bores (favre-waves) in open channels - experimental studies. *Journal of Hydraulic Research*, *32*(3), 355-370. Retrieved from https://doi.org/10.1080/00221689409498738 doi: 10.1080/00221689409498738

Truesdell, C. (1954). *The kinematics of vorticity.* Courier Dover Publications.

Tsuji, Y., Yanuma, T., Murata, I., & Fujiwara, C. (1991). Tsunami ascending in rivers as an undular bore. *Natural Hazards*, *4*(2-3), 257–266.

Tucker, M., & Charnock, H. (1954). A capacitance-wire recorder for small waves. *Coastal Engineering Proceedings*(5), 14–14.

Tyvand, P. A., & Miloh, T. (1995). Free-surface flow due to impulsive motion of a submerged circular cylinder. *Journal of Fluid Mechanics*, *286*, 67–101.

Uddin, J., & Needham, D. (2015). The effects of surface tension on the initial development of a free surface adjacent to an accelerated plate. *Journal of Fluid Mechanics*, *776*, 37–73.

Ursell, F. (1953). The long-wave paradox in the theory of gravity waves. In *Mathematical proceedings of the cambridge philosophical society* (Vol. 49, pp. 685–694).

Ursell, F., Dean, R. G., & Yu, Y. S. (1960). Forced small-amplitude water waves: a comparison of theory and experiment. *Journal of Fluid Mechanics*, *7*(1), 33–52. doi: 10.1017/S0022112060000037

Von Kármán, T. (1911). Über den mechanismus des widerstandes, den ein bewegter körper in einer flüssigkeit erfährt. *Nachrichten von der Gesellschaft der Wissenschaften zu Göttingen, Mathematisch-Physikalische Klasse*, *1911*, 509–517.

Vukcević, V., Roenby, J., Gatin, I., & Jasak, H. (2018). *A sharp free surface finite volume method applied to gravity wave flows.*

Wang, C.-Y. (1968). On high-frequency oscillatory viscous flows. *Journal of Fluid Mechanics*, *32*(1), 55–68. doi: 10.1017/S0022112068000583

Wang, D. (2014). *Fdc1004: Basics of capacitive sensing and applications* (Tech. Rep.).

Wang, D. (2015). Capacitive sensing: Ins and outs of active shielding. *Texas Instruments, Application report SNOA926A–February*.

Weller, H. G., Tabor, G., Jasak, H., & Fureby, C. (1998). A tensorial approach to computational continuum mechanics using object-oriented techniques. *Computers in Physics*, *12*(6), 620-631. doi: 10.1063/1.168744

Westerweel, J. (1993). *Digital particle image velocimetry: theory and application* (Unpublished doctoral dissertation). TU Delft, Delft University of Technology.

Westerweel, J. (1994). Efficient detection of spurious vectors in particle image velocimetry data. *Experiments in Fluids*, *16*(3-4), 236–247.

Westerweel, J., Dabiri, D., & Gharib, M. (1997). The effect of a discrete window offset on the accuracy of cross-correlation analysis of digital piv recordings. *Experiments in fluids*, *23*(1), 20–28.

Westerweel, J., & Scarano, F. (2005). Universal outlier detection for piv data. *Experiments in fluids*, *39*(6), 1096–1100.

White, F. M. (2010). *Fluid mechanics.*

Whitham, G. B. (1974). *Linear and nonlinear waves* (Vol. 42). John Wiley & Sons.

Willert, C. (1996). The fully digital evaluation of photographic piv recordings. *Applied Scientific Research*, *56*(2-3), 79–102.

Willert, C. E., & Gharib, M. (1991, Jan 01). Digital particle image velocimetry. *Experiments in Fluids*, *10*(4), 181–193. Retrieved from https://doi.org/10.1007/BF00190388 doi: 10.1007/BF00190388

Williamson, C. H. K. (1985). Sinusoidal flow relative to circular cylinders. *Journal of Fluid Mechanics*, *155*, 141–174. doi: 10.1017/S0022112085001756

Willmarth, W. W., Tryggvason, G., Hirsa, A., & Yu, D. (1989). Vortex pair generation and interaction with a free surface. *Physics of Fluids A: Fluid Dynamics*, *1*(2), 170–172.

Wilner, L. B. (1960). Variable capacitance liquid level sensors. *Review of Scientific Instruments*, *31*(5), 501-507. Retrieved from https://doi.org/10.1063/1.1931234 doi: 10.1063/1.1931234

Winant, C. D., & Browand, F. K. (1974). Vortex pairing : the mechanism of turbulent mixing-layer growth at moderate reynolds number. *Journal of Fluid Mechanics*, *63*(2), 237–255. doi: 10.1017/S0022112074001121

Wolgamot, H. A., & Fitzgerald, C. J. (2015). Nonlinear hydrodynamic and real fluid effects on wave energy converters. *Proceedings of the Institution of Mechanical Engineers, Part A: Journal of Power and Energy*, *229*(7), 772-794. Retrieved from https://doi.org/10.1177/0957650915570351 doi: 10.1177/0957650915570351

Xiang, Q., Wei, K., Yao, C., Zhang, M., & Li, Y. (2020). Experimental study on local scour around caissons with different shapes under the unidirectional and tidal currents. In *2020 international conference on intelligent transportation, big data smart city (icitbs)* (p. 979-984).

Xie, Z. (2010). *Numerical modelling of breaking waves under the influence of wind*. University of Leeds.

Xing, X., Ji, K., Zou, H., Sun, J., Zhou, S., & Li, Z. (2012). An enhancing normalized radon transform method for ship wake detection in sar imagery. In *Eusar 2012; 9th european conference on synthetic aperture radar* (pp. 559–562).

Yang, S., & Chwang, A. T. (1992). About moving contact lines. *Journal of Engineering Mechanics*, *118*(4), 735-745. doi: 10.1061/(ASCE)0733-9399(1992)118:4(735)

Yang, S.-A., & Chwang, A. T. (1989). *Nonlinear viscous waves produced by an impulsively moving plate* (Tech. Rep.). IOWA INST OF HYDRAULIC RESEARCH IOWA CITY.

Ye, T. (2013). Precision full-wave rectifier, dual supply. *Texas Instruments. Dez*.

Yeh, H. H., Ghazali, A., & Marton, I. (1989). Experimental study of bore run-up. *Journal of Fluid Mechanics*, *206*, 563–578. doi: 10.1017/S0022112089002417

Annexes

Annex A

Gravity waves

In this section, the surface wave propagation problem is described and the different categories the waves can be sorted in are presented. All results are mainly from Bovis' book (Bovis, 2009), unless otherwise specified. The wave tank consists of a parallelepiped rectangle whose bottom face represents the seabed and the top face is the free water level. The origin is taken at top left corner of the forefront lateral face, which implies that the vertical coordinate z of the seabed to be at $z = -h$. The atmosphere is situated above the free surface. In this section, theoretical aspects of linear waves, non linear waves, cnoidal waves, solitary waves, random seas and breaking waves will be reviewed.

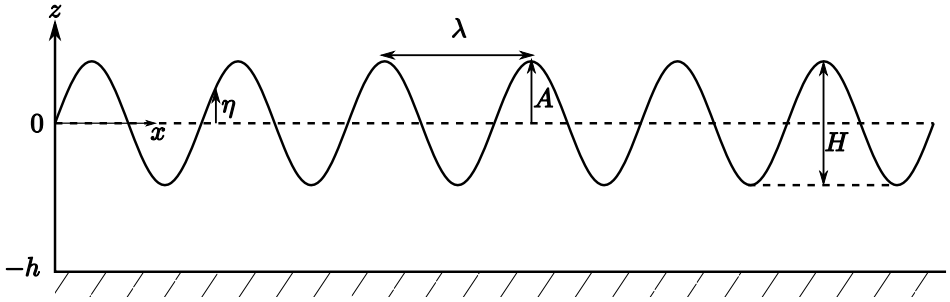

Figure A.1: Scheme of the wave problem

A.1. Wave equations

A scheme of the problem can be found in figure A.1. The following hypothesis are made to describe the fluid motion in the wave generation problem: water is considered as a perfect, incompressible, irrotational fluid which allows the definition of a velocity potential $\phi(x, z, t)$ such as $\mathbf{V}(x, z, t) = \nabla\phi$. The equations describing the fluid motion are the continuity equation (mass conservation) and the Navier-Stokes equations (momentum conservation). The boundary conditions are the following:

– Walls are impermeable. Thus the normal velocity component at seabed is zero and at walls should be equal the wall velocity: $\mathbf{V} \cdot \mathbf{n} = \mathbf{U} \cdot \mathbf{n}$.

– The pressure at free water surface is the atmospheric pressure.

Consequently the continuity equation $\nabla \cdot \mathbf{V} = 0$ becomes:

$$\Delta\phi = 0 \tag{A.1}$$

The equation of momentum conservation, whose form behind the previous hypothesis is now the Euler equation, can be integrated in space and becomes the Bernoulli equations:

$$\frac{\partial\phi}{\partial t} + gz + \frac{p}{\rho} + \frac{1}{2}\left|\nabla\phi\right|^2 = B(t) \tag{A.2}$$

where B is a constant which only depends of t. Equation A.2 allows to compute the pressure when the velocity field is known. The function of the free water surface elevation η is defined as $z = \eta(x,t)$. Breaking waves are not allowed here. At the interface, $p = p_0$ and the Bernouilli constant B is $B(t) = \frac{p_0}{\rho}$, which leads to the free surface dynamic equation :

$$\frac{\partial\phi}{\partial t} + g\eta + \frac{1}{2}\left|\nabla\phi\right|^2 = 0 \quad in \quad z = \eta(x,t) \tag{A.3}$$

Let's now define the function f as:

$$f(x,z,t) = z - \eta(x,t) \tag{A.4}$$

At the interface, f must always be 0 and thus the total derivative also:

$$\frac{Df(x,z,t)}{Dt} = 0 \iff [\frac{\partial}{\partial t} + \mathbf{V}\cdot\nabla]f = 0 \tag{A.5}$$

$$\iff [\frac{\partial}{\partial t} + \mathbf{V}\cdot\nabla](z - \eta(x,t)) = 0 \tag{A.6}$$

$$\iff \frac{\partial\eta}{\partial t} + \frac{\partial\phi}{\partial x}\frac{\partial\eta}{\partial x} = \frac{\partial\phi}{\partial z} \quad \text{at} \quad z = \eta \tag{A.7}$$

This last equation is called the kinematic boundary condition.

A.2. Linear wave theory - Airy waves

The linear wave theory was first proposed by George Biddell Airy (1841). It is valid as long as the wave height is small compared to the wave length ($\eta \ll \lambda$) and also the wave height is small compared to the water depth ($\eta \ll d$). The equation system to solve is then

given by the following equations. Laplace equation gives:

$$\frac{\partial^2 \phi}{\partial x^2} + \frac{\partial^2 \phi}{\partial z^2} = 0 \tag{A.1}$$

At seabed, the vertical velocity should be zero:

$$\frac{\partial \phi}{\partial t} + g\eta = 0 \quad \text{in} \quad z = -h \tag{A.2}$$

After linearization, the equation A.3 becomes:

$$\frac{\partial \phi}{\partial t} + g\eta = 0 \quad \text{at} \quad z = \eta(x,t) \tag{A.3}$$

Airy then proposed to write a monochromatic waves as:

$$\eta(x,t) = A\cos(kx - \omega t) \tag{A.4}$$

The corresponding velocity potential, which satisfies equation A.1, A.2 and A.3 is given by:

$$\boxed{\phi = \frac{g}{\omega} A \frac{\cosh(k(z+h))}{\sinh(kh)} \sin(kx - \omega t)} \tag{A.5}$$

The dispersion equation, which can be calculated from the free surface kinematic boundary condition, is given by:

$$\boxed{\omega^2 = gk\tanh(kh)} \tag{A.6}$$

A.3. Higher order wave theory - Stokes waves

G. G. Stokes (1880) developed a full theory for higher orders of the wave problem. Results, obtained through the use of a perturbation series analysis, also known as the Stokes expansion, lead to non linear wave motion. At these orders, wave particle trajectories are no longer closed. This means there is particle transport with the wave propagation, the so called Stokes drift. We define ϵ such as $\epsilon = kA$, with then $\epsilon << 1$. Stokes expansion is:

$$\eta(x,z,t) = \eta_1(x,z,t) + \epsilon\eta_2(x,z,t) + \epsilon^2\eta_3(x,z,t) + \mathcal{O}(\epsilon^\ni) \tag{A.1}$$

$$\phi(x,z,t) = \phi_1(x,z,t) + \epsilon\phi_2(x,z,t) + \epsilon^2\phi_3(x,z,t) + \mathcal{O}(\epsilon^\ni) \tag{A.2}$$

By solving the equations in section A.1 for each order of magnitude (1, ϵ and ϵ^2), one obtains:

Order 1: The solution is the same as equations A.4 and A.5.

Order 2:

$$\eta_2 = \frac{1}{4}\coth(kh)[3\coth^2(kh) - 1]A^2 k \cos[2(kx - \omega t)] \tag{A.3}$$

$$\phi_2 = \frac{3}{8}\frac{gkA^2}{\omega}\frac{[\coth^2(kh) - 1]^2}{\coth(kh)}\cosh[2k(z + h)]\sin[2(kx - \omega t)] \tag{A.4}$$

Order 3:

$$\begin{aligned}\eta_3 =& -\frac{3}{8}[\coth(kh)^4 - 3\coth(kh)^2 + 3]A^3k^2\cos[kx - \omega t] + \\ & \frac{3}{64}[8\coth(kh)^6 - (\coth(kh)^2 - 1)^2]A^3k^2\cos[3(kx - \omega t)]\end{aligned} \tag{A.5}$$

$$\begin{aligned}\phi_3 =& \frac{1}{64}(\coth(kh)^2 - 1)(\coth(kh)^2 + 3)(9\coth(kh)^2 - 13)\cdot \\ & \frac{\cosh[3k(z + h)]}{\cosh[3kh]}\frac{gk^2A^3}{\omega}\sin[3(kx - \omega t)]\end{aligned} \tag{A.6}$$

The non linear dispersion equation is:

$$\boxed{\omega^2 = gk\tanh(kh)[1 + k^2A^2(\frac{9}{8}(\coth^2(kh) - 1)^2 + \coth^2(kh))]} \tag{A.7}$$

The differences between the orders of Stokes waves are represented in figure A.2a and the importance of the contribution for each order is shown in figure A.2b. Second order waves have higher troughs and higher crests compared to first order Airy waves. Third order waves seems to limit a bit this effect on troughs while increase it on crests.

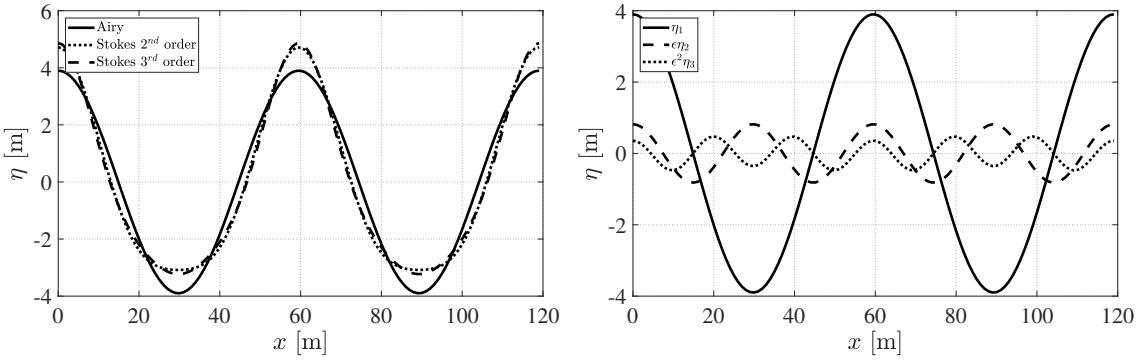

(a) (b)

Figure A.2: (a) Difference between Stokes waves for orders 1, 2 and 3. It corresponds to the following entries: $h = 10$ m, $H = 7.8$ m and $T = 6$ s. (b) Importance of each contribution to the Stokes wave.

The 5th order Stokes theory is presented by Skjelbreia & Hendrickson (2011). A parame-

ter, called here κ is defined (originally called λ in Skjelbreia's paper). They propose a system of equations:

$$\frac{\pi H}{h} = \frac{1}{h/\lambda}\left[\kappa + \kappa^3 B_{33} + \kappa^5 (B_{35} + B_{55})\right] \tag{A.8}$$

$$\frac{h}{\lambda_0} = \left(\frac{h}{\lambda}\right)\tanh(kh)\left[1 + \kappa^2 C_1 + \kappa^4 C_2\right] \tag{A.9}$$

where $\lambda_0 = \frac{gT^2}{2\pi}$. The wave elevation is defined by:

$$\begin{aligned} k\eta = {} & \kappa\, cos(\theta) \\ & + (\kappa^2 B_{22} + \kappa^4 B_{24})\cos(2\theta) \\ & + (\kappa^3 B_{33} + \kappa^5 B_{35})\cos(3\theta) \\ & + \kappa^4 B_{44}\cos(4\theta) \\ & + \kappa^5 B_{55}\cos(5\theta) \end{aligned} \tag{A.10}$$

with $\theta = k(x - ct)$. Knowing h, H and T one can solve equations A.8 and A.9 which give the values of the quotient h/λ and of κ. The coefficients B and C are defined in Skjelbreia's paper and are not shown here but they only depend on h/λ.

A.4. Summary: validity range of waves theories

Ursell (1953) allows to determine the range of validity of the linear small amplitude wave theory applies. The Ursell number is defined as:

$$U_r = \frac{\eta}{\lambda}\left(\frac{\lambda}{h}\right)^3 \tag{A.1}$$

It corresponds to the two first terms of the development in series of the potential ϕ in Stokes derivation. Ursell shows that the common criteria $\frac{\eta}{\lambda} \ll 1$ is incomplete for the validity of the linear theory of surface waves: when the waves are long, $U_r \ll 1$ is also a limitation. A summary of the range of validity of the different wave theories which were previously described can be found in figure A.3. The following parameters are taken into account: the wave period T, the mean sea water level h (called d in the figure A.3) and the wave height H. A summary of the different theories and their hypothesis is shown in figure A.4.

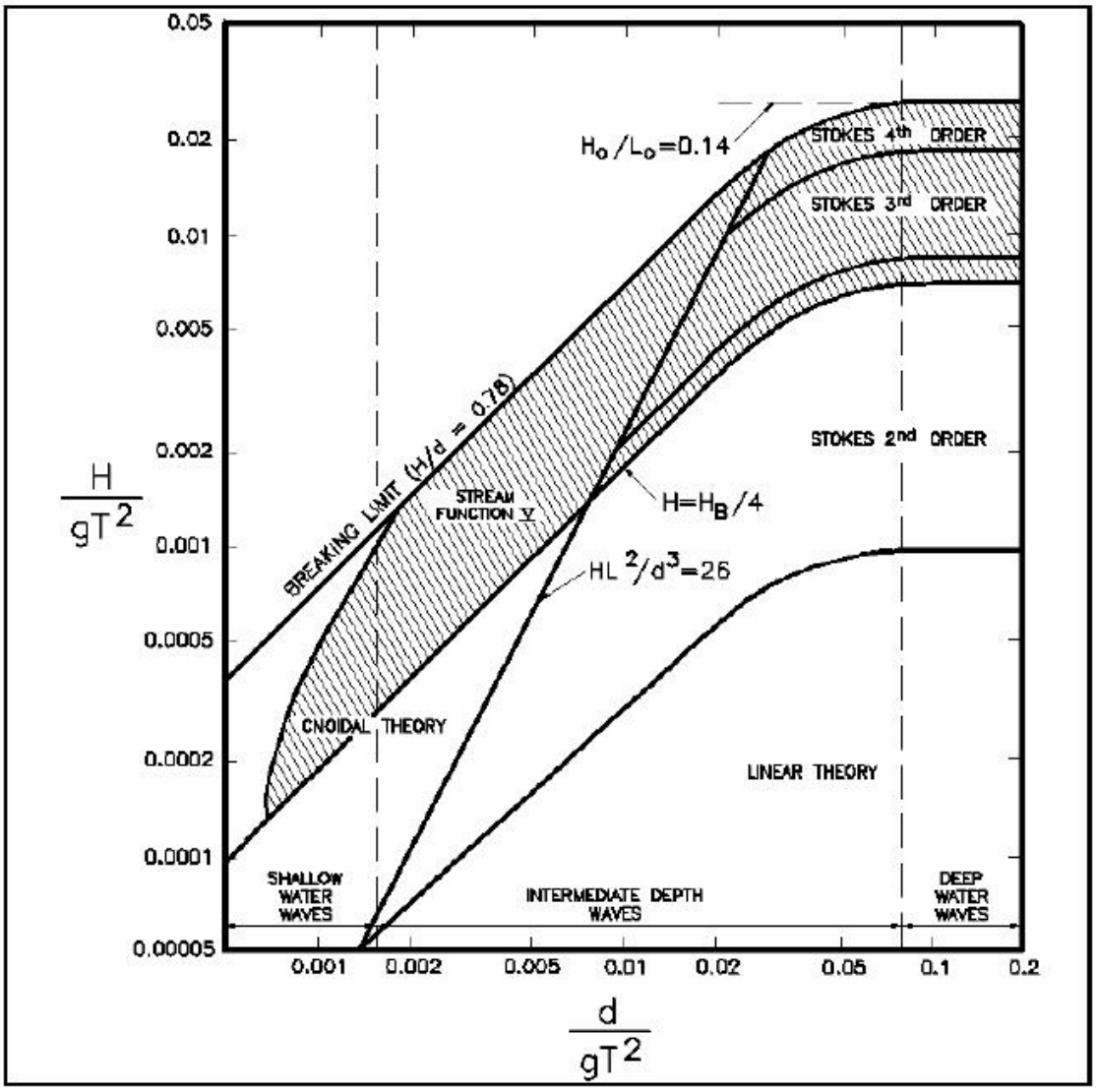

Figure A.3: Validity range of waves theories, according to Le Méhauté (2013) and found in Demirbilek & Vincent (2002).

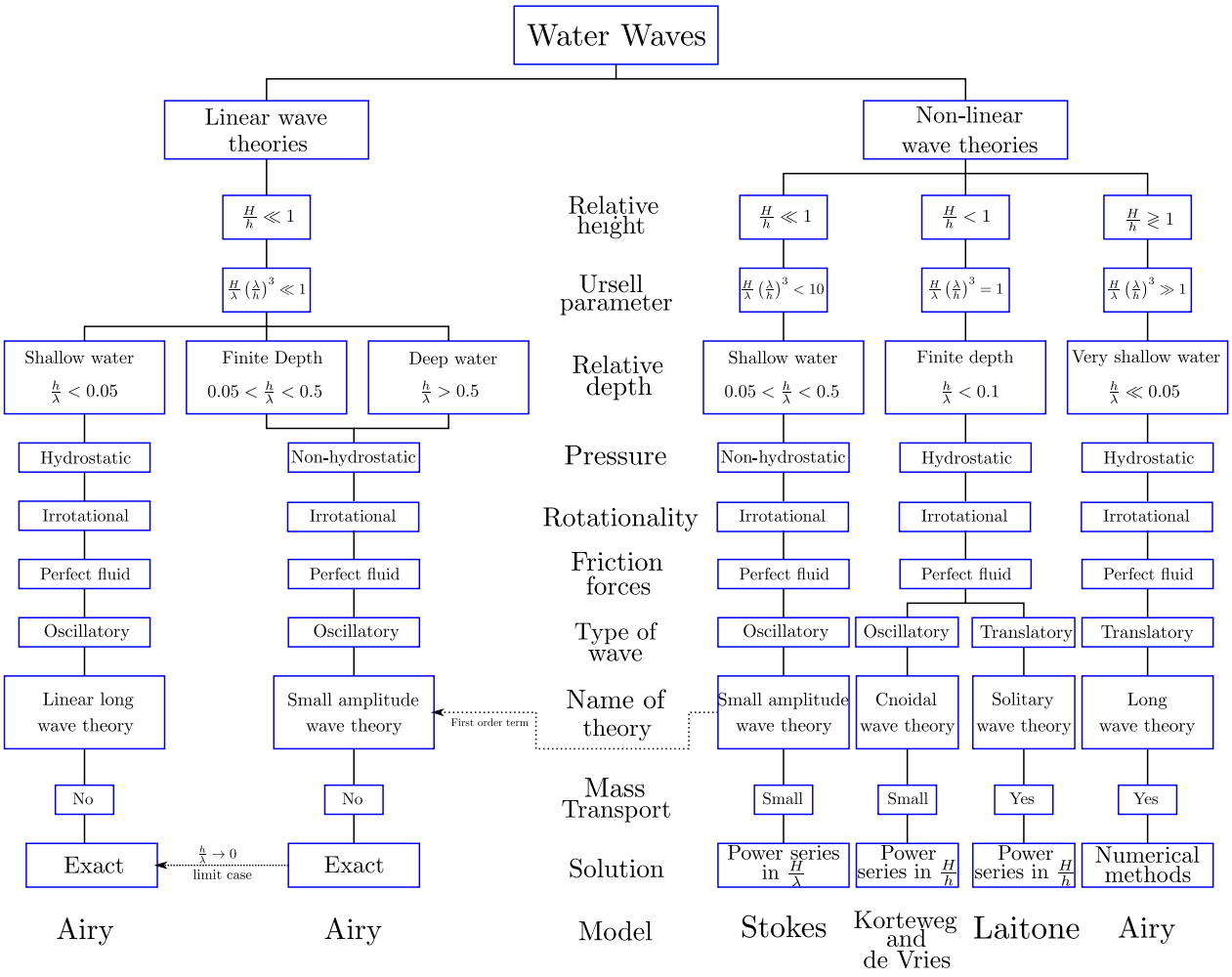

Figure A.4: Hypothesis of the different wave theories after Mader (2004).

A.5. Cnoidal waves

Cnoidal waves are propagative waves solution of the Korteweg-de Vries equation or KdV equation (Korteweg & de Vries, 1895)). Dingemans (1997) gave the complete solutions for periodic waves. The KdV equation is the following:

$$\frac{\partial \eta}{\partial t} + \frac{\partial^3 \phi}{\partial x^3} + 6\phi \frac{\partial \phi}{\partial x} = 0 \tag{A.1}$$

In dimensional form, for $\lambda > 7h$, the KdV equation resulting of the wave propagation problem is the following:

$$\frac{\partial \eta}{\partial t} + \sqrt{gh}\frac{\partial \eta}{\partial x} + \frac{3}{2}\sqrt{\frac{g}{h}}\eta\frac{\partial \eta}{\partial x} + \frac{1}{6}h^2\sqrt{gh}\frac{\partial^3 \eta}{\partial x^3} = 0 \tag{A.2}$$

This equation is dispersive for both frequency and amplitude. A solution is given by:

$$\eta(x,t) = \eta_2 + H\ \mathrm{cn}^2\left(\ \frac{x - c\,t}{\Delta}\ \middle|\ m\ \right) \tag{A.3}$$

where η_2 is the through elevation, H the wave height, m the elliptic parameter, c the phase speed, cn one of the Jacobi elliptic function. The though parameter as well as the width parameter can be expressed as:

$$\eta_2 = \frac{H}{m}\left(1 - m - \frac{E(m)}{K(m)}\right) \quad \text{and} \quad \Delta = \frac{\lambda}{2\,K(m)} = h\sqrt{\frac{4}{3}\frac{m\,h}{H}} \tag{A.4}$$

where K(m) is the complete elliptic integral of the first kind and E(m) the complete elliptic integral of the second kind. The links between wave length λ, phase speed c, wave period T, wave height H, water depth h and elliptic factor m are:

$$\lambda = h\sqrt{\frac{16}{3}\frac{m\,h}{H}}\ K(m), c = \sqrt{gh}\left[1 + \frac{H}{m\,h}\left(1 - \frac{1}{2}\,m - \frac{3}{2}\,\frac{E(m)}{K(m)}\right)\right],\ T = \frac{\lambda}{c} \tag{A.5}$$

When λ, c, T, H and h are known one can find the elliptic parameter m and deduce the wave form. An example can be found in figure A.5a, where it is compared to the Airy and Stokes 3^{rd} order models. The cnoidal wave has higher troughs and crests than the other models. The crests are thiner and the troughs larger implying steeper waves. The influence of the parameter m is shown in figure A.5b.

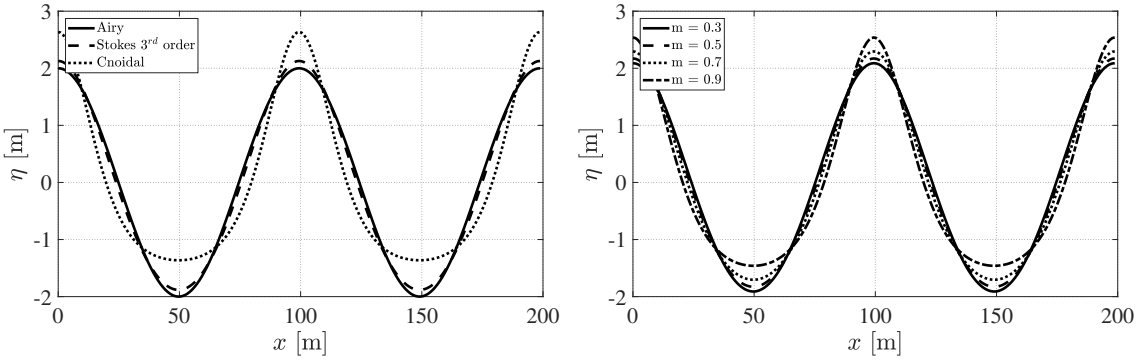

(a) (b)

Figure A.5: (a) Comparison between cnoidal waves and Stokes wave for the following entries: $h = 10$ m, $H = 4$ m and $T = 10$ s. The elliptic parameter m is 0.94. (b) Influence of the elliptic parameter m over the cnoidal wave shape.

A.6. Solitary waves

Solitary waves (tsunami waves) are long period waves which can travel at several hundreds of km/h in deep ocean and reach heights of dozens of meters in shallow water. They represent a tremendous danger for coastal population and can be very destructive for marine infrastructure. Tsunami such as in Aysen in 2007 and the center coast in 2010 (waves of 5 meters in harbour) destroyed many coastal towns and caused many deaths. This is why it is necessary to predict the wave-structure interaction and minimize their impact on offshore and near-shore structures, such as harbour or marine renewable energy infrastructures. They were first studied by Russel in 1838 who made series of experiments in river mouths (Russell, 1838). From its observations he found a relationship for the phase celerity of solitary waves:

$$c = \sqrt{g(h + H)} \tag{A.1}$$

with H the solitary wave height and h the water depth. Russel also denoted some characteristics of such waves (as summarized in Sander & Hutter (1991)):

- The reflection over a vertical wall results in the propagation in the opposite direction of a solitary wave which shape does not change
- The collision of solitary waves does not impact their shape.
- The form of a solitary wave is a trochoid.
- The height of a solitary wave does not change during motion. When it happens it is due to viscosity (the fluid is not perfect).

– The wave breaks if the wave height is larger than water depth.

The first theory was thought by Boussinesq (1872). He demonstrated that one can describe the wave form with the following equation:

$$\eta(x) = Hsech^2\left(\frac{x}{h}\sqrt{\frac{3}{4}\frac{H}{h}}\right) \tag{A.2}$$

G. H. Keulegan (1948) calculated the gradual damping due to friction of such waves. Damping can be really important and should be taken into account, especially when the wave travels great distances. He showed:

$$\eta(x) = h\left[\left(\frac{\eta(x=0)}{h}\right)^{-1/4} + K\frac{x}{h}\right]^{-4} \tag{A.3}$$

with

$$K = \frac{1}{12}\left(1 + \frac{2h}{B}\right)\sqrt{\frac{\nu}{g^{1/2}h^{3/2}}} \tag{A.4}$$

where B is the width of the canal, η_0 is the initial height of wave above undisturbed water and s is the distance that traveled the wave from initial wave height measurement.

Rayleigh (1876) also studied solitary waves founding that wave elevation can be expressed as:

$$\eta(x) = Hsech^2\left(\frac{x}{h}\sqrt{\frac{3}{4}\frac{H}{h+H}}\right) \tag{A.5}$$

McCowan (1891) also made theoretical studies of the phenomenon, showing the complexity of the model that can be reached. For more details on these theories a good summary is made by Daily & Stephan Jr (1952).

A.7. N-Waves

The usual way of modeling tsunami wave is to consider solitary waves (Camfield & Street, 1968; Hammack & Segur, 1974; Synolakis, 1987; Liu et al., 1995). Scientists made observations on real tsunami events showing that the solitary wave representation is not adequate and one should find other alternatives (Tadepalli & Synolakis, 1994; E. Geist & Yoshioka, 1996; Rabinovich & Thomson, 2007; P. A. Madsen et al., 2008; Chan & Liu, 2012), as shown in figure A.6. For example, many reported the rescinding of the shore line before the arriving of the tsunami wave, showing that a depression led wave might be more suitable to model tsunami waves, especially when the seismic event originating the tsunami is close to the shore and thus the wave does not have time to evolve into leading elevation wave or a series of

solitary waves (Tadepalli & Synolakis, 1994). This was also observed for the 2010 tsunami on the Chilean coast as reported by Fritz et al. (2011).

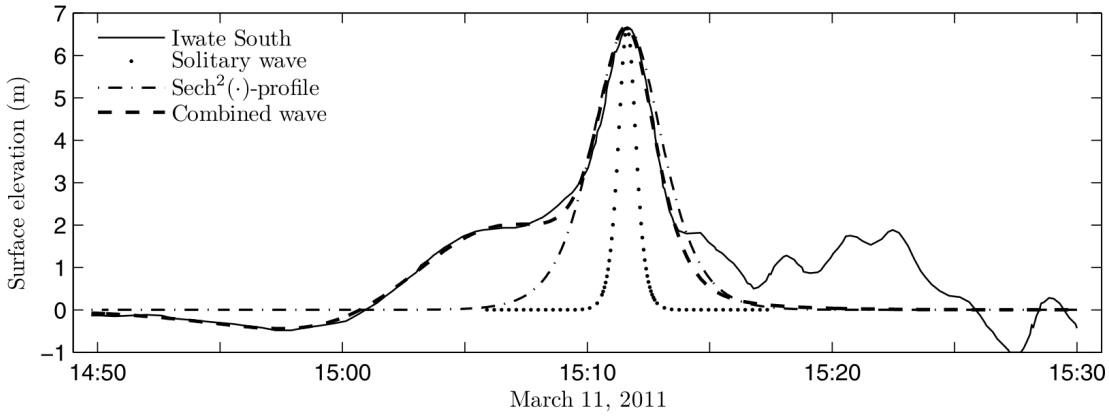

(a)

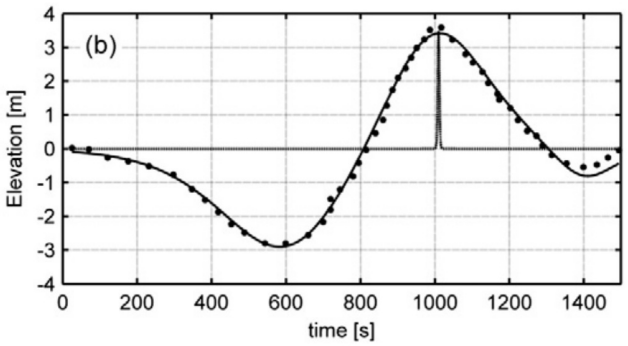

(b)

Figure A.6: (a) Tsunami wave of the 2011 Japan natural disaster according to Chan & Liu (2012). (b) Comparison between on-field data from "Mercator" yacht measurements of the 2004 Indian Ocean tsunami (points, from Siffer (2005)) and a combination between sech^2 functions (continuous line) according to Schimmels et al. (2016).

N-waves were first described in Whitham (1974) for gas dynamics studies. E. L. Geist (1998) studies the relationship between the earthquake source parameters and the N-wave. Two types of N-waves can be considered which are the leading depression N-wave (LDN) and the leading elevation N-wave (LEN). McGovern (2016) recently pointed out the lack of experimental data for N-waves run-up, and also the difficulty of reproducing long waves in laboratory flumes as they still often represent hundreds of meters wave length at scale. In many studies, the experimental generation of long waves is done thanks to the use of a pneumatic wave generator based on volume exchange between the flume and the generator (G. Keulegan, 1966; Rossetto et al., 2011; Charvet et al., 2013; Goseberg et al., 2013; McGovern, 2016), although due to the compression of the air and water phases, disturbances can appear at the free-surface. Schimmels et al. (2016) shows however that the generation of long waves (N waves or solitary waves) are perfectly possible by a piston wavemaker, despite a maximum scale limitation. The full procedure for N-wave generation with a piston wavemaker is given in Lima et al. (2019), following a similar procedure as proposed by Goring (1979)(see also section 2.2). The N-wave profile according to Tadepalli & Synolakis (1994)

is described by:

$$\eta(x,t) = \epsilon(\theta - \kappa\delta) \cdot H \cdot sech^2\theta \tag{A.1}$$

where

- the argument θ is given by $\theta = \kappa(x - ct - x_1)$,
- $\kappa = \sqrt{\frac{3}{4}\frac{H}{h^3}}$ is the generalized wave number according to Peregrine (1967),
- ϵ is a scale factor to define the wave height in function of H,
- $\delta = x_2 - x_1$ is an eccentricity parameter between the inflection point position x_2 at $t = 0$ s and the location of the equivalent solitary wave of height H postion x_1 and at $t = 0$ s (see figure A.7).

One main consequence of considering a depression led N-wave is the run-up much higher than for the solitary wave, showing that considering solitary wave may not be accurate to predict the run-up of tsunami waves (Tadepalli & Synolakis, 1994).

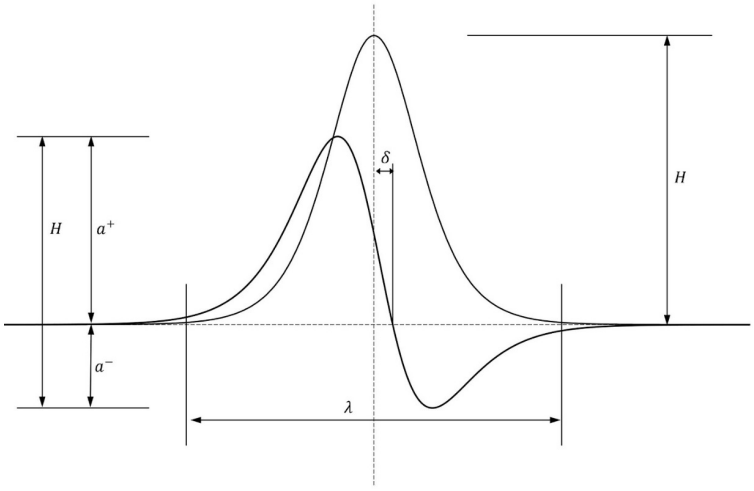

Figure A.7: N-wave profile parameters according to Tadepalli & Synolakis (1994). H is the wave height of the solitary wave model, λ is the wave length, δ is an eccentricity parameter, a^+ and a^- are the positive and negative contribution to the wave height respectively.

A.8. Random sea - Spectrum

As wind is not constant as well as the area it blows on, waves are not monochromatic and unidirectional (see section A.8). Most of the time, wave elevation appears to be chaotic and a random function of time (see figure A.8a). The description of these sea states can be done using statistics. The combination of solutions from the equation A.4, with the introduction

of random phases, frequency and amplitudes, constitutes a solution of the problem described in A.1:

$$\eta(x,t) = \sum_{i=0}^{\infty} A_i \cos(k_i x - \omega_i t) \tag{A.1}$$

A typical representation of these characteristics is the spectrum. One can calculate the Fourier transform F of the signal wave height vs time (called $f(t)$) which is defined as:

$$F(\omega) = \frac{1}{\sqrt{2\pi}} \int_{-\infty}^{+\infty} f(t) e^{-i\omega t}\, dt \tag{A.2}$$

The power spectrum is then computed by the product of the Fourier transform and its conjugate:

$$S(\omega) = |F(\omega)|^2 = F(\omega)F(\omega)^* \tag{A.3}$$

The typical mathematical models to represent these spectra are the following:

– Pierson-Moskowitz (1964): it is the simplest spectrum. It is defined as:

$$S(\omega) = \frac{\alpha g^2}{\omega^5} \exp\left[-\beta \left(\frac{g}{V\omega}\right)^4\right] \tag{A.4}$$

with α and β two parameters which have to be experimentally adjusted, and V is the wind velocity at 19.5 m height from sea water level.

– JONSWAP (1973 - Joint North Sea Wave Project): it was initially used for the representation of the North Sea wave spectrum for the oil and gas industry. It is written as:

$$S(\omega) = \frac{\alpha g^2}{\omega^5} \exp\left[-\frac{5}{4}\left(\frac{\omega_p}{\omega}\right)^4\right] \gamma^r \tag{A.5}$$

with $\alpha = 0.076(\frac{V^2}{Feg})^{0.22}$; $\omega_p = 22(\frac{g^2}{FeV})^{1/3}$; $\gamma = 3.3$; $r = \exp\left[\frac{(\omega-\omega_p)^2}{2\sigma^2\omega_p^2}\right]$ and $\sigma = \begin{cases} 0.07, & \text{if } \omega \leq \omega_p \\ 0.09, & \text{if } \omega > \omega_p \end{cases}$. Fe is the characteristic length (called fetch) where the wave are formed from wind forcing.

– Bretscheider (1978): it was adopted by the NATO has representative of the North Atlantic ocean. It is defined as :

$$S(\omega) = \frac{A\, H_{1/3}^2\, \omega_p^4}{\omega^5} \exp\left[-\frac{B\omega_p^4}{\omega^4}\right] \tag{A.6}$$

with $A = 0.3125$ and $B = 1.25$. ω_p, the modal pulsation is linked to the significant wave

height $H_{1/3}$ by: $\omega_p = 0.4\sqrt{\frac{g}{H_{1/3}}}$. ω_p corresponds to the pulsation giving the maximum peak of the spectrum energy.

JONSWAP spectrum energy is higher than the two others that are quite similar as shown in figure A.8b. The wave power spectra are more complicated than the one presented here in the general case: it can be composed for example of a local sea state (due to local sea conditions) as well as swells that are traveling from further away.

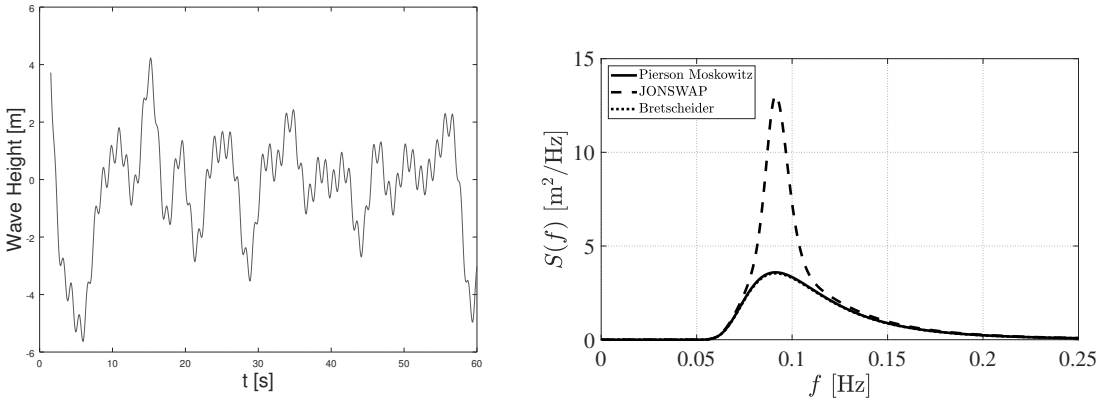

(a) (b)

Figure A.8: (a) Aleatory elevation of waves (artificially created by the author): here wave shapes does not have anything to do with the previous Airy sinusoidal wave. (b) Comparison between power spectrum for cases where all spectra have the same ω_p and bandwidth.

When wind changes of direction and generate new waves, these one will eventually encounter other waves that were already formed, leading to a superposition of waves from different directions. This constitutes the general case at sea. To take into account real sea state characteristics, the directionality (also called spreading) of the waves should be taken into account. In deed, most structures, which do not accept symmetry axis, will respond in different ways depending on the directionality of the hitting wave. It implies that the monochromatic unidirectional model cannot be sufficient. Directionality also explains that most sea states are short crested since wave energy propagates in a certain number of directions. It is generally taken into account by adding a spreading function G to the wave spectrum:

$$S(\omega, \theta) = S(\omega)G(\theta) \tag{A.7}$$

Annex B

Kinematic wave absorption

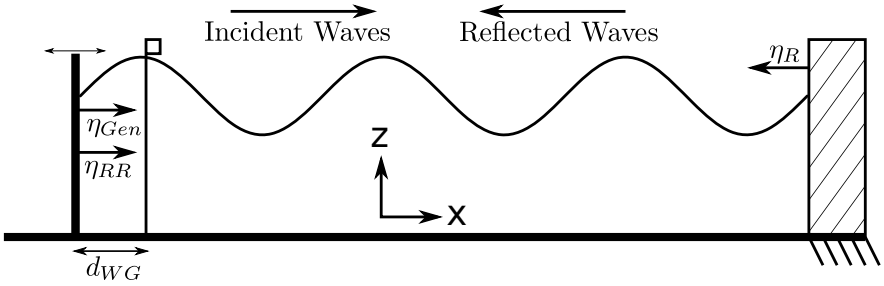

Figure B.1: Scheme of the wave tank on which the calculation of the absorption transfer function is based

We propose to explain the result of Schäffer & Jakobsen (2003) for the kinematic wave absorption strategy which is used in many wave tanks. We choose to keep notations from Schäffer & Jakobsen (2003) and Andersen et al. (2016). A scheme of the problem can be found in figure B.1. First we need to consider the nearfield wave elevation at x and after a time of t which can be expressed as:

$$\eta(x,t) = e_0 \left(C_0 \cos(\omega t - kx) + D(x) \sin(\omega t)\right) \tag{B.1}$$

where

- e_0 is the half wave height ($e_0 = \frac{H}{2}$),
- C_j are the Biésel transfer function coefficients such as $C_j = \frac{4\sinh^2(k_j h)}{2k_j h + \sinh(2k_j h)}$,
- ω is defined as $\omega^2 = k_j g \tanh(k_j h)$,

– $D(x)$ represents the sum of evanescent modes such as

$$D(x) = \sum_{j=1}^{\infty} C_j e^{-k_j x}$$

.

For a wave gauge situated at $x = d_{WG}$ this relation becomes:

$$\begin{aligned}\eta(x = d_{WG}, t) &= e_0 \left[C_0 \left(\cos(\omega t)\cos(k d_{WG}) + \sin(\omega t)\sin(k d_{WG})\right) + D(d_{WG})\sin(\omega t)\right] \\ &= e_0 \left[C_0 \left(\sin\left(\omega t + \frac{\pi}{2}\right)\cos(k d_{WG}) + \sin(\omega t)\sin(k d_{WG})\right) + D(d_{WG})\sin(\omega t)\right] \quad \text{(B.2)}\end{aligned}$$

Let's calculate the Fourier transform of $\sin\left(\omega t + \frac{\pi}{2}\right)$:

$$\begin{aligned}\mathscr{F}\left[\sin\left(\omega t + \frac{\pi}{2}\right)\right] &= \int_{-\infty}^{+\infty} \sin\left(\omega t + \frac{\pi}{2}\right) e^{-i\omega t}\, dt \\ &\qquad \text{by changing variables acoording to} \quad \omega t' = \omega t + \frac{\pi}{2} \\ &= \int_{-\infty}^{+\infty} \sin(\omega t') e^{-i\omega t' + i\frac{\pi}{2}}\, dt \\ &= e^{i\frac{\pi}{2}} \mathscr{F}\left[\sin(\omega t)\right] \quad \text{(B.3)}\end{aligned}$$

Let's call A_{WG} the Fourier transform of η and X_{gen} the Fourier transform of $X(t) = e_0 \sin(\omega t)$. Then the following relation can be found:

$$\begin{aligned}A_{WG} &= \left[C_0 \left(e^{i\frac{\pi}{2}} \cos(k d_{WG}) + \sin(k d_{WG})\right) + D(d_{WG})\right] X_{gen} \\ &= \left[C_0 \left(\left(\cos\left(\frac{\pi}{2}\right) + i \sin\left(\frac{\pi}{2}\right)\right)\cos(k d_{WG}) + \sin(k d_{WG})\right) + D(d_{WG})\right] X_{gen} \\ &= \left[C_0 \left(i\cos(k d_{WG}) + \sin(k d_{WG})\right) + D(d_{WG})\right] X_{gen} \\ &= \left[i C_0 \left(\cos(-k d_{WG}) + i \sin(-k d_{WG})\right) + D(d_{WG})\right] X_{gen} \\ A_{WG} &= \left[i C_0 e^{-ik d_{WG}} + D(d_{WG})\right] X_{gen} \quad \text{(B.4)}\end{aligned}$$

Let's now include the active absorption motion, the reflections and re-reflections (η_R and η_{RR}) at tank ends:

$$\begin{aligned}A_{WG} &= \left[i C_0 e^{-ik d_{WG}} + D(d_{WG})\right] (X_{gen} + X_{abs}) + A_R e^{ik d_{WG}} + A_{RR} e^{-ik d_{WG}} \\ &= \left[i C_0 e^{-ik d_{WG}} + D(d_{WG})\right] (X_{gen} + X_{abs}) + 2A_R \cos(k d_{WG}) \quad \text{(B.5)} \\ &\qquad \text{considering full reflection} \quad A_R = A_{RR}\end{aligned}$$

Let's condider now the far-field incident waves (which are constituted of the waves from the generation paddle and the re-reflected waves):

$$A_I e^{-ikx} = iC_0 e^{-ikx} \left(X_{gen} + X_{abs}\right) + A_R e^{-ikx} \tag{B.6}$$

which allows to isolate the reflection term:

$$A_R = A_I - iC_0 \left(X_{gen} + X_{abs}\right) \tag{B.7}$$

By changing A_R in equation B.5:

$$A_{WG} = \left[iC_0 e^{-ikd_{WG}} + D(d_{WG})\right] \left(X_{gen} + X_{abs}\right) + 2 \left(A_I - iC_0 \left(X_{gen} + X_{abs}\right)\right) \cos(kd_{WG}) \tag{B.8}$$

then,

$$X_{gen} + X_{abs} = \frac{2A_I \cos(kd_{WG}) - A_{WG}}{iC_0 \left[2\cos(kd_{WG}) - e^{-ikd_{WG}}\right] - D(d_{WG})} \tag{B.9}$$

The transfer function H for active absorption is defined as the ratio of the paddle displacement (the output) and the wave height at the wave gauge (the input):

$$H = \frac{X_{gen} + X_{abs}}{2A_I \cos(kd_{WG}) - A_{WG}} = \frac{1}{iC_0 \left[2\cos(kd_{WG}) - e^{-ikd_{WG}}\right] - D(d_{WG})} \tag{B.10}$$

For a wave gauge fixed on the paddle ($d_{WG} = 0$):

$$H = \frac{1}{iC_0 - D(0)} \tag{B.11}$$

This is called the single mode transfer function. In dual-mode use (obtained by eliminating all terms due to wave generation that is to say A_I and X_{gen}), it becomes:

$$X_{abs} = -(A_{WG} - A_{WG,Ref}) H(\omega) \tag{B.12}$$

In the case of long wave and shallow water ($h \ll \lambda$) and no evanescent mode exists, the transfer function becomes:

$$H_{longWave} = \frac{1}{ikh} \tag{B.13}$$

$$= \sqrt{\frac{g}{h}} \frac{1}{i\omega} \tag{B.14}$$

Please note that this transfer function does not take into account the transfer function in-

troduced by mechanical parts of the piston wavemaker.

Annex C

Quality assurance in CFD

In this section, we describe how the numerical simulation results will be verificated through the analysis of the mesh, and the different parameters that compose the solver. Indeed, the quantification of the errors is of most importance in order to verify if a simulation is accurate and represent the physical phenomena. The errors sources, as stated by A. E. Maguire (2011), can be:

- Model error and uncertainty: they can be due to solving the wrong equations, making wrong assumptions, not realistic boundary conditions, etc.
- Discretization error: the continuous equation being solved by the use of discrete numerical approximation results in errors which can be expressed as the difference of the exact solution and a solution obtained on a mesh of defined grid spacing. The greater is the number of points the lower should be the solution. The rate at which the discretization error tends to 0 as the number of grid points increases is determined by the order of the numerical method used.
- Iteration or convergence error: this error appears because, for practical issues (time constraint), the number of iterations leading to a fully converged solution cannot be set to infinity. A balance between time consumption and solution accuracy has to be found.
- Round-off error: as computers have a limit on number of digits ("float", "double" etc which represent the number of bytes available for the number description), round off error appears when this limit is reached.
- User errors: they can appear at any stage of the model and solver implementation. They are expected to decrease with the user experience.
- Code errors: it refers to unintentional programming errors or bugs. Thay can be difficult to track and therefore extensive verification and validation of the code should be done.

Verification studies, in the contrary of validation studies whose objectives are to show how accurate to the physical problem a model is, aim at determining if the model is well implemented according to the code developer concepts and solutions. Or as summarized in Blottner (1990):

- Validation: solving right governing equations,
- Verification: solving governing equations right.

Courant-Friedrichs-Lewy (CFL) condition

This condition is an essential tool for the determination of the minimum time step used in the numerical simulation (see Courant et al. (1928)). It assures stability of the explicit schemes used for time integration. For the 2D case, the CFL condition is described as:

$$C = \frac{u_x \Delta t}{\Delta x} + \frac{u_y \Delta t}{\Delta y} \leq C_{max} \tag{C.1}$$

where

- C is the Courant Number,
- C_{max} is the maximum admissible Courant number which depends on the numerical schemes used. It is usually taken equal to 1 for explicit schemes. Implicit schemes are less sensible to this parameter and thus more important number can be accepted,
- u_x the velocity component in x-direction,
- u_y the velocity component in y-direction,
- Δx and Δx the spacial discretization interval length in respectively x and y direction,
- Δt the time interval length.

One consequence of this criteria is to find a compromise between grid refinement and time-step value: one would find it tempting to decrease the spacial discretization lengths to have more accuracy but this leads to an increase of Courant number. One would decrease the time step but this gives more important simulation time.

The relevant choice of u_x and u_y is, in order to have a conservative approach, to take their maximum values. The particle velocities, according to Airy theory are:

$$u_x = \frac{\partial \phi}{\partial x} = \frac{g}{\omega} Ak \frac{\cosh\left(k(z+h)\right)}{\sinh\left(kh\right)} \cos(kx - \omega t) \tag{C.2}$$

$$u_z = \frac{\partial \phi}{\partial z} = \frac{g}{\omega} Ak \frac{\sinh\left(k(z+h)\right)}{\sinh\left(kh\right)} \sin(kx - \omega t) \tag{C.3}$$

A. E. Maguire (2011) advises to take the phase speed of the wave as the u_x velocity which is greater than the particle velocity. The phase velocity is defined as:

$$C_p = \sqrt{\frac{g}{k} \tanh(kh)} \tag{C.4}$$

It is also possible to chose an adaptive time step, based on the maximum value of the Courant number. This solution has the advantage to be fully automated and solo requires the definition of a maximum allowed Courant number. *OpenFOAM* computes at every time-step the maximum Courant number allowing an easy verification of the criteria.

Uncertainty due to discretization in CFD applications

In this section, a summary of the procedure described by I. B. Celik et al. (2008), from the Fluids Engineering Division of the American Society of Mechanical Engineering, is done. The verification, error detection and control of numerical uncertainty will be done according to this guide during the thesis work. It is advised:

- Code references: it is recommended to use a code fully referenced, that is to say that verification studies have been carried out and should be described and cited.

- Convergence: it must be shown that iterative convergence is achieved with preferably 4 orders of magnitude of decrease of the normalized residuals for every equations that is solved, and thus for every time step.

- Discretization error: the discretization error might be evaluated through the use of Richardson extrapolation error (Richardson, 1911; Richardson & Gaunt, 1927). This is done by using the GCI (Grid Convergence Index) method, which has been used and proved to be reliable in hundreds of CFD simulations. The method is described in the following section.

- GCI (Grid Convergence Index): the CGI method is based on Richardson extrapolation Richardson (1911), but allows for mesh refinement factor r which are not multiple of two. It was proposed in Roache (1998). In this section we explicit the different steps of I. B. Celik et al. (2008) method.

We explain here the different step of the GCI method:

– Step 1: a representative cell size h (average) must be defined for 3D and 2D problems such as:

$$h = \left[\frac{1}{N}\sum_{i=1}^{N}\Delta V_i\right]^{1/3} \tag{C.5}$$

$$h = \left[\frac{1}{N}\sum_{i=1}^{N}\Delta A_i\right]^{1/2} \tag{C.6}$$

where

  – ΔV_i is the volume of the ith cell,
  – ΔA_i is the volume of the ith cell,
  – N is the total number of cells.

– Step 2: three significantly different grid size are chosen. Simulations are run with these grids to determine key variables (representative of the objectives of the simulation or critical for the conclusions). The grid refinement factor, which might be greater than 1.3 (arbitrary value from experience), is defined as:

$$r = \frac{h_{coarse}}{h_{fine}} \tag{C.7}$$

– Step 3: if "1" stands for the finer grid and "3" for the coarser ($h_1 < h_2 < h_3$), and $r_{21} = \frac{h_2}{h_1}$, $r_{32} = \frac{h_3}{h_2}$, the apparent order of the method is defined as:

$$p = \frac{1}{ln\left(r_{21}\right)}\left|ln\left|\frac{\epsilon_{32}}{\epsilon_{21}}\right| + q(p)\right| \tag{C.8}$$

$$q(p) = ln\left(\frac{r_{21}^{p} - s}{r_{32}^{p} - s}\right) \tag{C.9}$$

$$s = 1 \cdot sgn\left(\frac{\epsilon_{32}}{\epsilon_{21}}\right) \tag{C.10}$$

where

  – ϕ_k is the variable solution for the kth grid,
  – $\epsilon_{32} = \phi_3 - \phi_2$,
  – $\epsilon_{21} = \phi_2 - \phi_1$.

$\frac{\epsilon_{32}}{\epsilon_{21}} < 0$ means that convergence is oscillatory and the percentage of occurrence of oscillatory convergence should be reported. If ϵ_{ij} are really close to zero then the procedure does not work. Additional grid refinement might be executed.

– Step 4: calculate the extrapolated values of the variable:

$$\phi_{ext}^{21} = \frac{r_{21}^{p}\phi_1 - \phi_2}{r_{21}^{p} - 1} \tag{C.11}$$

$$\phi_{ext}^{32} = \frac{r_{32}^{p}\phi_2 - \phi_3}{r_{32}^{p} - 1} \tag{C.12}$$

– Step 5: error estimate calculation are to be reported. The approximative relative error is calculated according to:

$$e_a^{21} = \left| \frac{\phi_1 - \phi_2}{\phi_1} \right| \tag{C.13}$$

The extrapolated relative error is:

$$e_{ext}^{21} = \left| \frac{\phi_{ext}^{21} - \phi_1}{\phi_{ext}^{21}} \right| \tag{C.14}$$

The fine grid convergence index is defined as:

$$GCI_{fine}^{21} = \frac{1.25 e_a^{21}}{r_{21}^{p} - 1} \tag{C.15}$$

The value of 1.25 is arbitrary, should be given between 1 and 3 and can be considered as a safety coefficient. For example Roache Roache (1998) recommends the use of 3 if the studies are only performed on two grid sizes, but for studies based on three grid sizes 1.25 should be sufficient (that is to say conservative). Error bars (given by the GCI) might appear on the plots of the presented variables. The value of $p = p_{average}$ should be considered. In future studies, the ASME method will be used to verify our simulations, especially because it gives an estimated error of the computations that are carried out.

Annex D

Experimental methods

D.1. Wavemaker wire connection

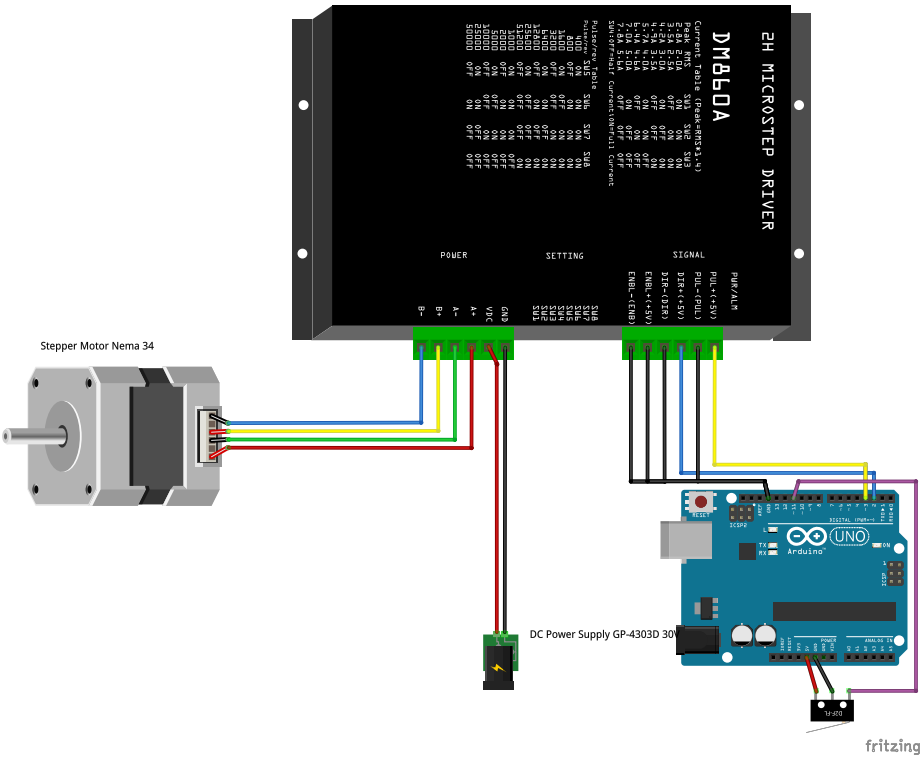

Figure D.1: Wavemaker electronic connection layout (from *Fritzing*) . Connection schematics.

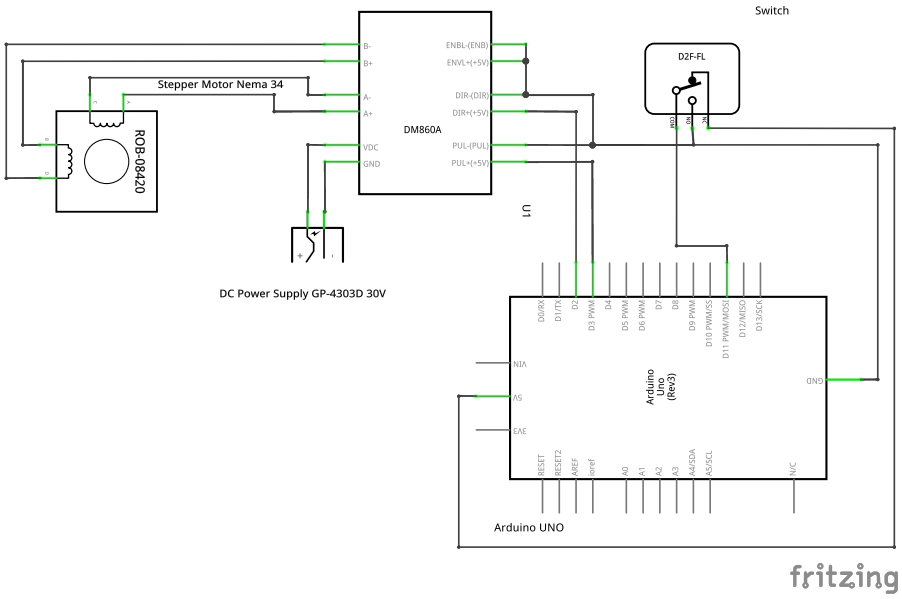

Figure D.2: Wavemaker electronic connection schematics.

D.2. Arduino code

```
/*          ------------------------------------------------------------------------
  stepVelocity.ino
  This function carries out a velocity step preceded by a ramp in order to
  generate the undular bore in the wave tank of the leaf-nl laboratory.
  The stepper motor is driven thanks to the accelStepper library.
  Input velocity signal is stored in an array as a function of time. During
  the run, the stepper velocity is updated in function of the table values.
 CBA - 30 octobre 2020 - charlie.barraud@gmail.com
 - record start position
 - execute ramp and step velocity
 - stop when reaching end
 - wait
 - return slowly to start position
          ------------------------------------------------------------------------          */
#include <AccelStepper.h>
// Define a stepper and the pins it will use
AccelStepper stepper (1,3,2) ;; // Defaults to AccelStepper::FULL4WIRE (4 pins) on 2, 3,
    ↪ 4, 5

#define PI 3.14159265358979323846264338327795
```

```
#define TOTSTEP0 400.00 // number of step/revolution (use for microstepping)
int backward = -1; // set to -1 to go forward, 1 to go backward
float tf = 1.5; // final time of the step
float tr = 0.1; // ramp final time
float UG = float(backward)*0.10; // m/s - Step velocity
float UGSteps = UG*TOTSTEP0/0.008; // stroke in steps/s

const int sensorHandTriggerPin = 11; // pin of the trigger swtich to start step
int valueTrigger = 0;
int i = 0;
const int numElementTimeTablePermanent = 10;
const int numElementTimeTableTransient = 20;
long deltaTPermanent = long((tf-tr)/numElementTimeTablePermanent*1000); //
    ↪ discretization of time in milli seconds
long deltaTTransient = long(tr/numElementTimeTableTransient*1000); // discretization of
    ↪ time in milli seconds
const int totalElements = numElementTimeTablePermanent+
    ↪ numElementTimeTableTransient+2;
long timeTable[totalElements];
float currentSpeed[totalElements]; // useful for plot
long correspondingTime[totalElements]; //useful for plot
float velocityTable[totalElements];
long currentTime;
int time0;
int counter=0;
int currentPosition0;

void setup()
{
  Serial.begin(9600);   //Initiate serie port
  timeTable[0] = 0;
  velocityTable[0] = 0;
  for (int k = 0; k< numElementTimeTableTransient+1; k++) // construct input velocity
    ↪ and time table
  {
     timeTable[k+1] = (k+1)*deltaTTransient;
     velocityTable[k+1] = UGSteps*float(timeTable[k+1])/1000.0/tr; // careful time not in
    ↪ ms
     counter++;
  }
```

```
55   int countInt = counter;
56   for (int k = 0; k< numElementTimeTablePermanent+1; k++)
57   {
58       timeTable[countInt+k] = timeTable[countInt+k-1]+deltaTPermanent;
59       velocityTable[countInt+k] = UGSteps;
60   }
61   for (int k = 0; k< numElementTimeTablePermanent+numElementTimeTableTransient+1;
       ↪ k++)
62   {
63     // print velocity and time table
64     Serial.print(timeTable[k]);
65     Serial.print("\t");
66     Serial.println(velocityTable[k]);
67   }
68   stepper.setMaxSpeed(15000); // max speed of stepper (steps /s)
69   stepper.setAcceleration(150000);// max acceleration of stepper (steps /s/s)
70   stepper.setSpeed(velocityTable[0]);
71   currentPosition0 = stepper.currentPosition(); // record start position
72   currentSpeed[0] = velocityTable[0]; // initiate velocity
73   pinMode(sensorHandTriggerPin , INPUT); //definir pin como entrada
74   Serial.println("Waiting to make some waves ?");
75   valueTrigger = digitalRead(sensorHandTriggerPin);
76   while(valueTrigger != LOW){// check value of switch, if UP start velocity step
77     valueTrigger = digitalRead(sensorHandTriggerPin);
78   }
79   delay(10000); // wait 10 seconds to let you time to start sensors and cameras
80   time0 = millis(); // arduino start time
81 }
82
83 void loop()
84 {
85     stepper.runSpeed(); // run stepper at input velocity
86     currentTime = millis()-time0; // compute real time
87   if (currentTime >= timeTable[i+1]) // update velocity
88   {
89     i++;
90     currentSpeed[i] = velocityTable[i]; // update velocity
91     correspondingTime[i] = currentTime; // record time of velocity update
92     stepper.setSpeed(velocityTable[i]); // set new velocity
93   }
```

```
94  if (currentTime > int(tf*1000)) // print velocity table at the end of the step
95  {
96    Serial.print("idx");
97    Serial.print("\t");
98    Serial.print("Tth");
99    Serial.print("\t");
100   Serial.print("Vth");
101   Serial.print("\t");
102   Serial.print("t");
103   Serial.print("\t");
104   Serial.print("V");
105   Serial.println();
106   for (int k = 0; k<numElementTimeTablePermanent+numElementTimeTableTransient;
      ↪ k++)
107   {
108     Serial.print(k);
109     Serial.print("\t");
110     Serial.print(timeTable[k]);
111     Serial.print("\t");
112     Serial.print(velocityTable[k]);
113     Serial.print("\t");
114     Serial.print(correspondingTime[k]);
115     Serial.print("\t");
116     Serial.print(currentSpeed[k]);
117     Serial.println();
118   }
119   delay(5000);
120   stepper.setSpeed(800);
121   stepper.moveTo(currentPosition0);
122   Serial.print("Start Position");
123   Serial.print("\t");
124   Serial.print("End Position");
125   Serial.print("\t");
126   Serial.print("Total Steps");
127   Serial.println();
128   Serial.print(currentPosition0);
129   Serial.print("\t");
130   Serial.print(stepper.currentPosition());
131   Serial.print("\t");
132   Serial.print(stepper.currentPosition()-currentPosition0);
```

```
133     Serial.println();
134     while (1)
135     {
136       stepper.runSpeedToPosition(); // maintain position at start  position
137     }
138   }
139 }
```

D.3. Capacitive wave gauge

D.3.1. Review of water level sensing

The first technique that can be employed is by using floats, buoyant objects placed at the free surface. When the level changes, the floats follows it. However it does not give a direct measurement of the water level. A system of mechanical components (pulleys, cables and gears) can be used to make the information available for the human eye. Another technique is using hydrostatic devices. A displacer is placed vertically. When the water level increases, the Archimedes' force is stronger and pushes the displacer upward. A force gauge is placed at the top of the displacer and transmit the water displacement. Pressure sensors can also be used and measure the pressure at the bottom of the tank, from which it is possible to deduce the water level in the tank. However, this technique is limited to stationary problem limiting the fluid motion in the tank. This problem is also present for load cells that are placed below the tank which increase when the water level increases and the tank weight also. The most common type of wave gauge are most certainly resistive wave gauge: by measuring the resistance between two wires plunged into the water, one can measure the variation of the water level. Resistive gauges are however very sensitive to the environment (temperature, conductivity) requiring to often calibrate them. Another type of electronic sensors are capacitance wave gauges. A capacitor, whose capacitance value changes with the level of water, is placed in the tank. The sensor generally consists of an immersed insulated wire and the capacitance between the water set to ground and the wire is measured. It provides a continuous level measurement and are generally more stable than resistive gauges. One can also use ultrasonic level transmitters which calculates the travel time of an ultrasonic pulse from the emitter to the water level and back. This technique might need wave guides in order to help containing the pulse. Finally, laser/radar level transmitters are an option. They work as the ultrasonic one but use the speed of light instead of the speed of sound.

D.3.2. Review of capacitive sensing

D.3.2.1. Working principle

Capacitive sensors are widely used to measure humidity, water levels, proximity, or position. A capacitive sensor is made of a capacitance which changes with the variations of its environment, in this case the level of water. General review of capacitance sensing can be found in Aezinia (2014), Terzic et al. (2012) and Nguyen (2016). Kumar et al. (2014) focuses on capacitive sensing for water level applications. Alam (2014) uses capacitive sensor (circular interdigitated topology with charge amplifier) to measure moisture and a urine meter (Otero et al., 2012) are other example of the use of capacitance sensors. Capacitance water level sensors can be found in Ross (1983), S.-A. Yang & Chwang (1989), Bera et al. (2014), and Loizou et al. (2015). In the case of wave height gauge, the pioneers are Boudan (1953) and Tucker & Charnock (1954), with the use of enameled coil wire and they are now widely use (Wilner, 1960; Millard, 1969; Timpy & Ludwick, 1985). The principal provider for laboratory wave tank application is Akamina[1].

A typical capacitor is composed of two plates, the "ground" and the "sensor" (see figure D.3). The capacitance can be expressed as the geometric elements of the sensor and the physical characteristics of the environment:

$$C = \frac{\epsilon_r \epsilon_0 A}{d} \tag{D.1}$$

with:

- A is the area of the plates
- ϵ_r is the dielectric constant of the material between the plates
- ϵ_0 is the permittivity of free space ($8.85 \times 10^{-12} \mathrm{F\,m^{-1}}$)
- d is the distance between the plates

As one these parameter changes, the value of the capacitance also changes.

[1] http://www.akamina.com

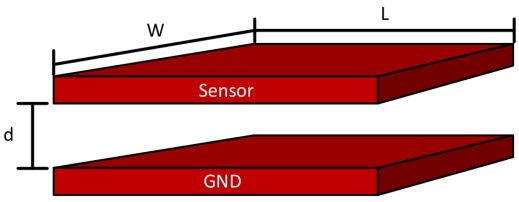

Figure D.3: Parallel plate capacitor (according to D. Wang (2014)). As the central spacing medium changes, the dielectric constant does so and the capacitance changes.

D.3.2.2. Review of capacitance measurement techniques

Direct measurement of a capacitance cannot be done. Signal conditioning is needed to transform the capacitance changes to a voltage, a frequency, a pulse-width, or a current. These techniques can be classified according to the different categories: capacitance to voltage converters (C2V), capacitance to frequency converters (C2F), capacitance to pulse width converter (C2PW), capacitance to digital converter (C2D), or capacitance to current converters (C2C) among others. We present some of these techniques in the following section.

Capacitance to voltage converters (C2V)

RC circuit A RC circuit response is shown in figure D.4. Chetpattananondh et al. (2014) used a RC circuit to measure capacitance with a interdigital sensor (an interdigitated topology rotated of 90 deg). When the capacitance discharges, the theoretical output voltage is:

$$V_O = V_{cc}\, e^{\frac{-t}{RC}} \tag{D.2}$$

When time equals the time constant of the circuit, $t = RC = \tau$:

$$V_O = 0.625 V_{cc} \tag{D.3}$$

The same principle can be used to measure the time constant when the capacitor is charging. A comparator can be set up to measure these time constants.

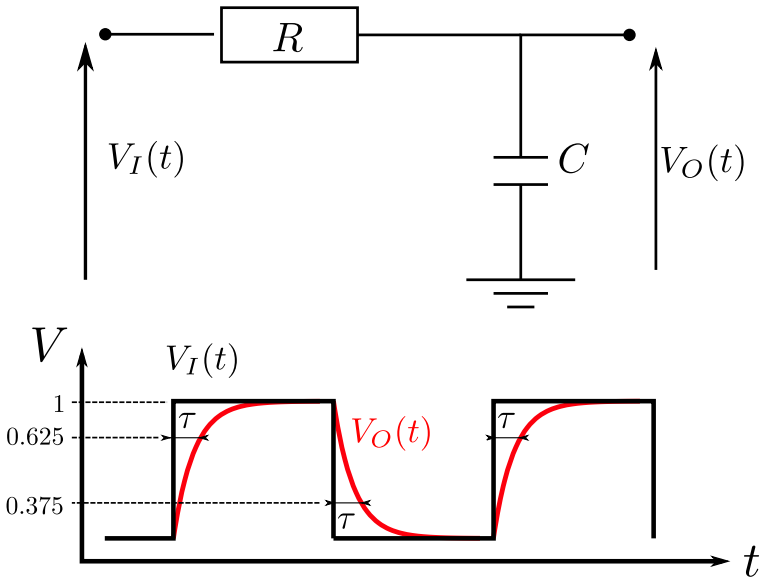

Figure D.4: RC circuit response and principle of measurement of the capacitance.

De Sauty and Schering Bridge A De Sauty bridge is a modified Wheatstone bridge where two elements are capacitors instead of resistors. It measures the value of the sensor capacitance by comparing it with the second one present in the bridge. When balanced, a small change of capacitance conducts to a change of the output voltage. A De Sauty bridge provides a simple and low cost method to measure capacitance but are complex to balance if capacitors are not free from dielectric losses (appearance of a resistance and heat losses). A Schering bridge (or modified Grover bridge) aims at remedying to it. An example can be found in figure D.5 and an application for water level measurement can be reviewed in Bera et al. (2014).

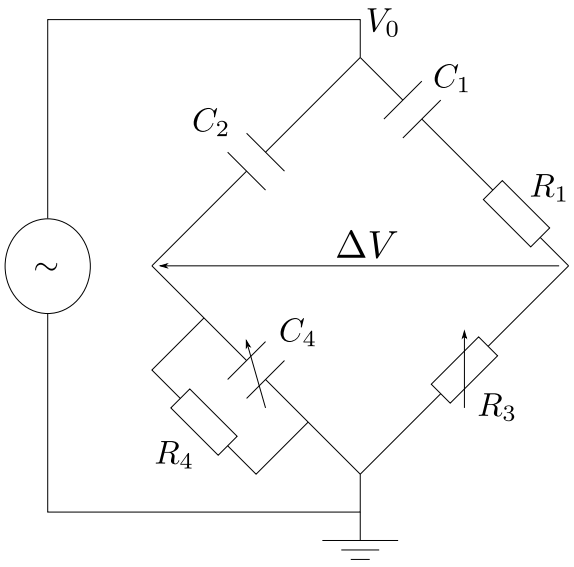

Figure D.5: Modified De Sauty Bridge or Schering bridge for capacitance measurement.

Charge Amplifier An ideal charge amplifier is shown in figure D.6a. Loizou et al. (2015) use a charge amplifier in combination with a full-wave rectifier (transforming AC wave in DC waves) and a low-pass filter. The output is a DC voltage proportional to the capacitance. Otero et al. (2012) also use a charge amplifier (using the figure D.6a circuit) for the use of a capacitive urine meter, in combination of a synchronous demodulator (which acts as double wave rectifier). The role of the charge amplifier is to amplify the charge of a dipole. In deed, for circuit of figure D.6a:

$$\begin{aligned} i_x &= i_f \quad \text{as} \quad i_- = 0 \\ \int_0^t i_x \, dt &= -\int_0^t C_f \frac{dV_O}{dt} \, dt \\ Q &= -C_f V_O \\ V_O &= -\frac{1}{C_f} Q \end{aligned} \tag{D.4}$$

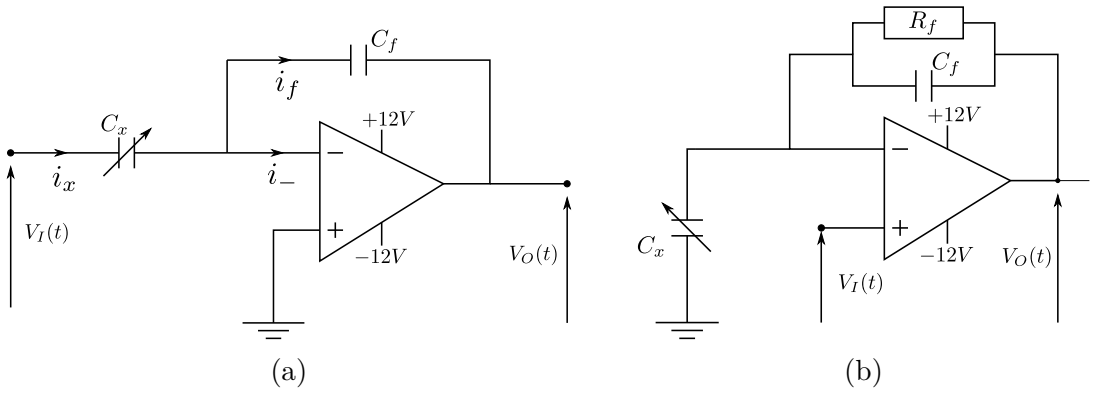

Figure D.6: Alternatives for charge amplifiers. (a) Theoretical charge amplifier. (b) Alternative charge amplifier according to Loizou et al. (2015).

AC to DC - Use of rectifiers and synchronous demodulation By transforming alternating current to direct current, one is able to measure at a higher rate the output signal, and make the post-processing easier as no peak-to-peak voltage has to be computed. If knowing the phase does not matter, one can obtain a DC from the RMS value (defined as $v_{eff} = \left[\frac{1}{T}\int_0^T v^2(t)\,dt\right]^{1/2}$), the peak value or the absolute value (mean value after rectification) Payas Areny (2004). Rectifier allows to do such operations and can be sorted into two categories: half-wave rectifier or full-wave one. The first one only keeps positive tension setting to zero the negative one (see figure D.7a) while a full-wave one gives the absolute value of the input signal. An example of full-wave rectifier is a diode bridge rectifier or Graetz bridge shown in figure D.7c. One can install a capacitor at the output (as shown in figure D.7c in dashed lines) and thus obtain a quasi-perfect constant DC voltage (figure D.7b). Haider et al. (2008), whose work is based on Lotters et al. (1999), uses two charge amplifiers in parallel in combination with a rectifier and an instrumentation amplifier to measure capacitance with low voltage (3 V) for biomedical applications. They achieve a 1 mV DC output for a 1 fF capacitance change. It is however only tested with numerical simulation. Synchronous demodulation is the process used in radio and is widely used in signal conditioning. The purpose of such device is to be able to recover a signal from a high noise environment. It is generally composed of the following steps: a first amplification is carried out before using a mixer which multiplies the received signal with a reference one (the modulation frequency). The following step is to use a band-pass filter to filter the signal at the wanted frequency and finally demodulate the signal using rectifiers as viewed before.

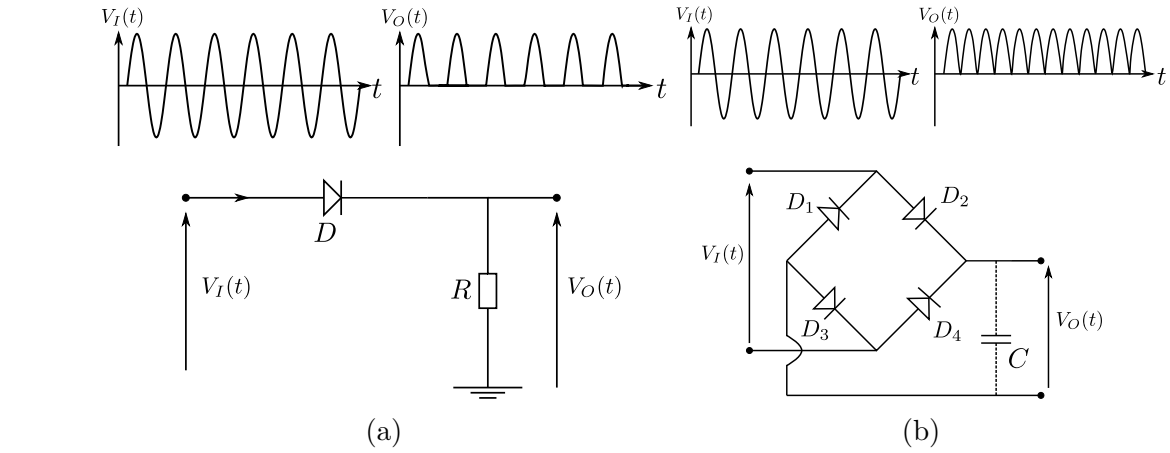

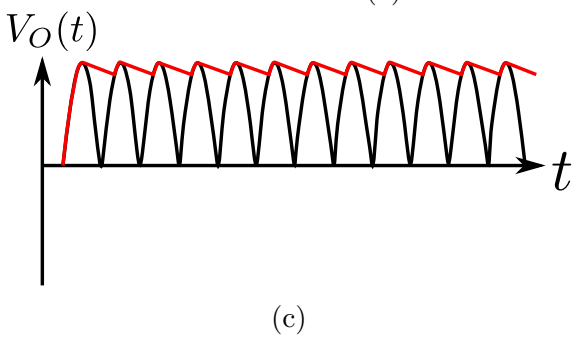

Figure D.7: Examples of wave rectifiers. (a) Half-wave rectifier. (b) Full-wave rectifier (Graetz bridge). (c) Effect of a capacitor at the output of the full-wave rectifier.

Capacitance to frequency converter A C-F converter is based on a reliable voltage to frequency converter Ross (1983). A voltage to frequency converter provides an output pulse train whose frequency is proportional to the input voltage. Its advantages are to be low cost, to operate on a wide range of frequencies, and have an ensured linearity while consuming less power than capacitance to voltage circuit. A way of doing it is to use an oscillator which transforms a DC input into a periodic signal, which often is a sine wave or a square wave. It can be of two types: composed of an amplifier and a feedback circuit or a negative resitance and a resonant cuircuit (not described in this section). One can use a Colpitts oscillator (as shown in figure D.8a) and replace one of the feedback circuit capacitor by the sensor resulting in:

$$f_{out} \propto \frac{1}{\sqrt{L\frac{C_1 C_2}{C_1+C_2}}} \tag{D.5}$$

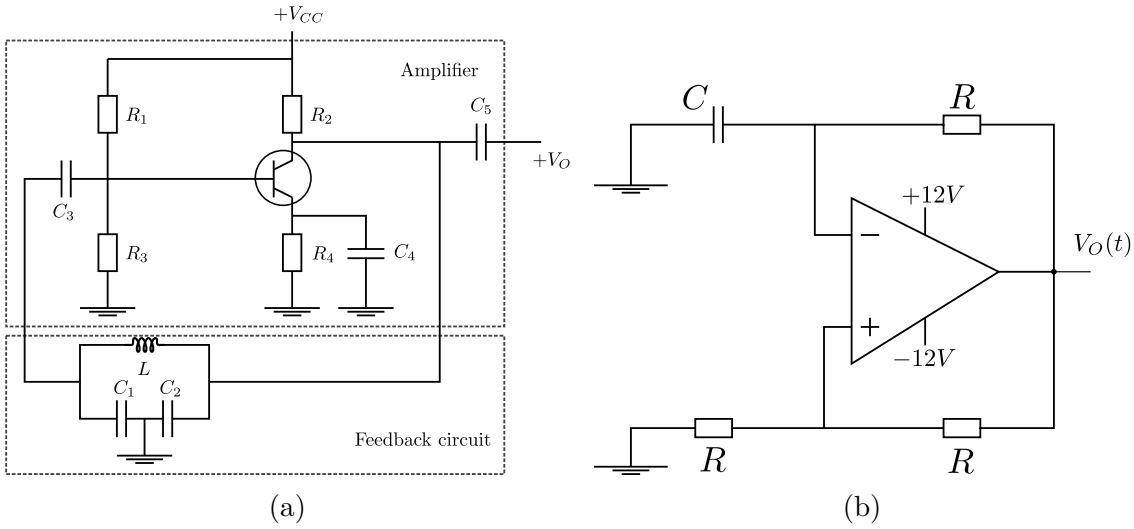

(a) (b)

Figure D.8: Examples of oscillators. (a) Colpitts oscillator. (b) A comparator-based oscillator.

Other example are the Hartley and Clapp oscillator also based on LC circuits or the comparator-based relaxation oscillator based on op-amp. For this last-one, the output is a square wave whose frequency depends on the capacitor value according to:

$$f_{out} = \frac{1}{2\,\ln(3)\,RC} \tag{D.6}$$

A like oscillator devices are multivibrators, based on electronic switches and used in Falcon et al. (2007) for wave gauge applications. Pal et al. (1973) also uses a multivibrator to measure capacitance, converting it to a pulse-rate signal. We do not enter into details for this kind of electronic devices.

Capacitance to pulse width converter (C2PW) and capacitance to digital converter (C2D) This device produces a pulse width signal whose pulse duration is linearly proportional to the capacitance. It greats advantages is that it is not required to add an analog to digital converter which allows the signal to be easily read by a microcontroller. Moreover hardware cost are low. It generally consists of a . An example of such method can be found in Bruschi et al. (2004) for capacitance measurement of the sub-pF range, as well in Bruschi et al. (2007) where the operating wide range of temperature is highlighted.

Capacitance to digital converters directly transforms the capacitance to a digital signal. An example of circuit used for this purpose are sigma-delta converters, whose resolution and accuracy are high. They present however the disadvantage to have long measurement times (Aezinia, 2014).

D.3.2.3. Shielding

According to Payas Areny (2004), an electric shield consists in a conductive surface which surrounds the sensor and is connected to a specific tension. The objective is to keep the capacitance constant whatever happens close to it (for example the presence of a human hand). The shield can either be simple or can be doubled (see figure D.10). The connection to the shield can be multiple. The simple shield is ideal when it is possible to connect one of the sensor terminal to the ground. If not, a double shield is best suited. To reduce noise, it is essential to connect the shield to a potential close to the ones constituting the sensor. This technique is called active shielding. Payas Areny (2004) suggests to connect the shield to the output of the sensor (see figure D.11b), while D. Wang (2015) proposes to connect it directly to the excitation input tension.

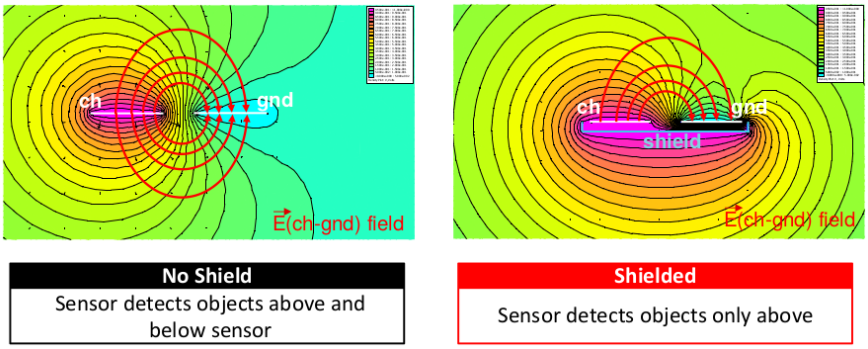

Figure D.9: The installation of a shield allows to give a direction to the sensor, as with a shield, electric lines are only present at one side of the sensor (figure from D. Wang (2015)).

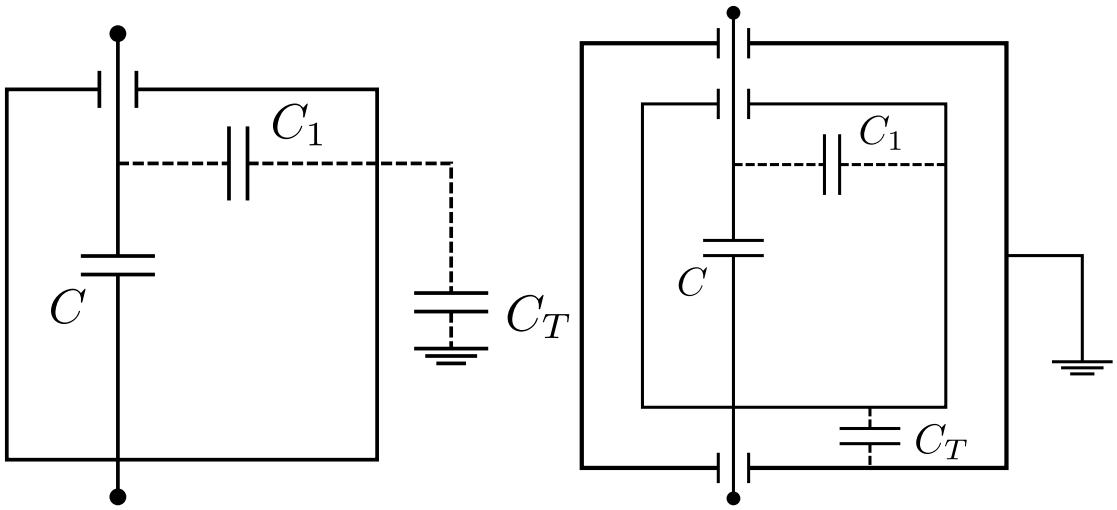

Figure D.10: Shields according to Payas Areny (2004). (a) Simple shield. (b) Double shield.

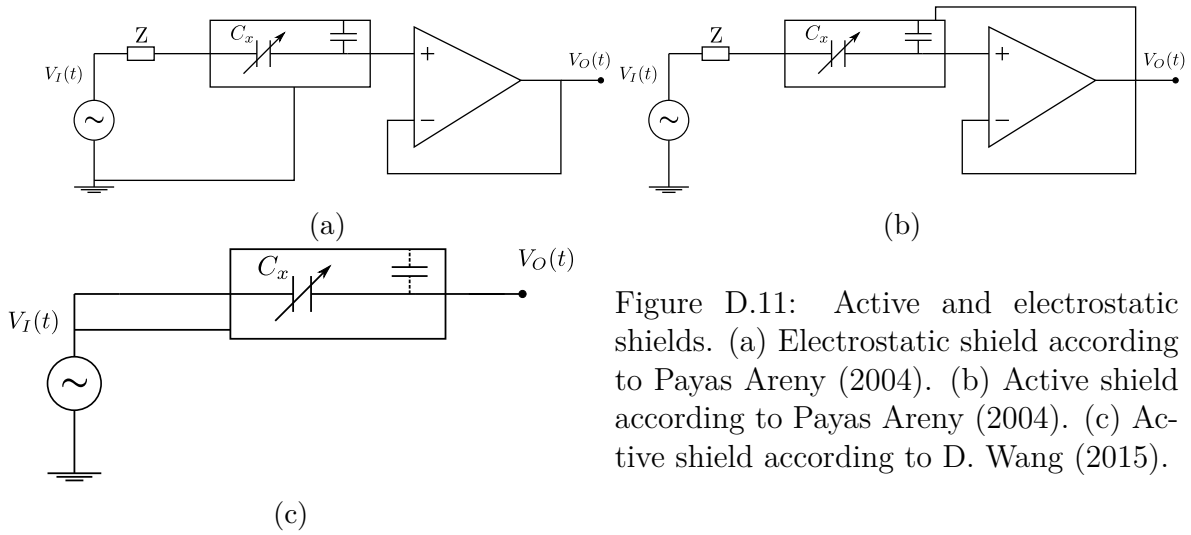

Figure D.11: Active and electrostatic shields. (a) Electrostatic shield according to Payas Areny (2004). (b) Active shield according to Payas Areny (2004). (c) Active shield according to D. Wang (2015).

D.3.3. Impedance of a transmission line

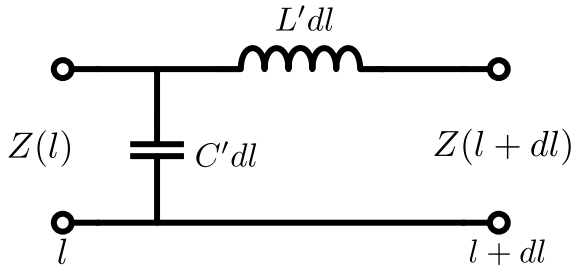

Figure D.12: Transmission line impedance equivalent circuit.

Impedance derivation: The impedance calculation that follows is partly based on the work of Gordillo Zavaleta (2012), and was first described by Pierce (1943) as a follow up of the telegrapher's equation in terms of impedance. By applying the Ampere's law, the inductance per unit of length L' of the system described above can be written as:

$$L' = \frac{1}{2\pi}\mu \ln\left(\frac{r_2}{r_1}\right) \tag{D.7}$$

where μ is the magnetic permeability of the coating. Let's write C' the capacitance per unit of length of the system, such that $C' = 2\pi\epsilon / \ln\left(\frac{r_2}{r_1}\right)$. The sensor can be assimilated to a transmission line and its equivalent circuit is shown in figure D.12. The line is modeled by a infinite number of segments dl in which a capacitor $C'dl$ is connected in parallel with the rest of the line and an inductance $L'dl$ is connected in series. Let's calculate the impedance

of the line at a distance $l + dl$:

$$\begin{aligned} Z(l+dl) &= j\omega L' dl + \frac{1}{j\omega C' dl + \frac{1}{Z(l)}} \\ &= j\omega L' dl + \frac{Z(l)}{j\omega C' dl Z(l) + 1} \end{aligned} \tag{D.8}$$

On the other we can write $Z(l + dl) = Z(l) + dZ$ leading to the following equation:

$$j\omega L' dl + \frac{Z(l)}{j\omega C' dl Z(l) + 1} = Z(l) + dZ \tag{D.9}$$

and finally:

$$\frac{dZ}{dl} = j\omega L' - j\omega C' Z^2 - j\omega C' Z dZ - \omega^2 C' L' Z dl \tag{D.10}$$

By keeping only the first order terms, we obtain the differential equation that governs the impedance of the wire system:

$$\frac{dZ}{dl} = j\omega L' - j\omega C' Z^2 \tag{D.11}$$

whose solution is given in Gordillo Zavaleta (2012):

$$Z(l) = j\sqrt{\frac{L'}{C'}} \tan\left(\omega\sqrt{L'C'}l - \frac{\pi}{2}\right) \tag{D.12}$$

The factor $\omega\sqrt{L'C'}$ is equal to $\omega\mu\epsilon = \omega/c = k$, that is to say the wave number of the light wave propagating in the medium. Let's notice that $\tan(x - \pi/2) = -\cos(x)/sin(x)$ and if $x << 1$, $\tan(x - \pi/2) \approx -1/x$. If $kl \ll 1$, then we can approximate the impedance by:

$$Z(l) \approx \frac{1}{j\omega C' l} \tag{D.13}$$

D.3.4. Electronic components

In the proposed design, many operational amplifiers are used. It is chosen to work with the TL082CP, available in common electronic shops in Chile, as it is very inexpensive and still offers good characteristics such as a wide unit bandwidth (4 MHz), low input noise voltage (16 $nV/\sqrt{Hz}$), high slew-rate (13 $V/\mu s$) and really high input impedance (10^{12} Ω). The diode are Schottky 1N5819 diodes which, even if it is not certain that more ordinary diodes would not give the desired results, offer low voltage drop. Capacitors are ordinary ceramic disks. The sensor, once tested and validated, will be transposed to a PCB plate. The design is created thanks to *Autodesk EAGLE* software which allows to design the PCB from electronic schematics. PCB consists of a two sided layers and the design is presented in

figure D.13. Traces and pads are designed to allow easier soldering of the components. The data acquisition with the sensor in this thesis was however carried out from the protoboard since all electronic workshops at Universidad de Chile stayed closed due to the coronavirus crisis.

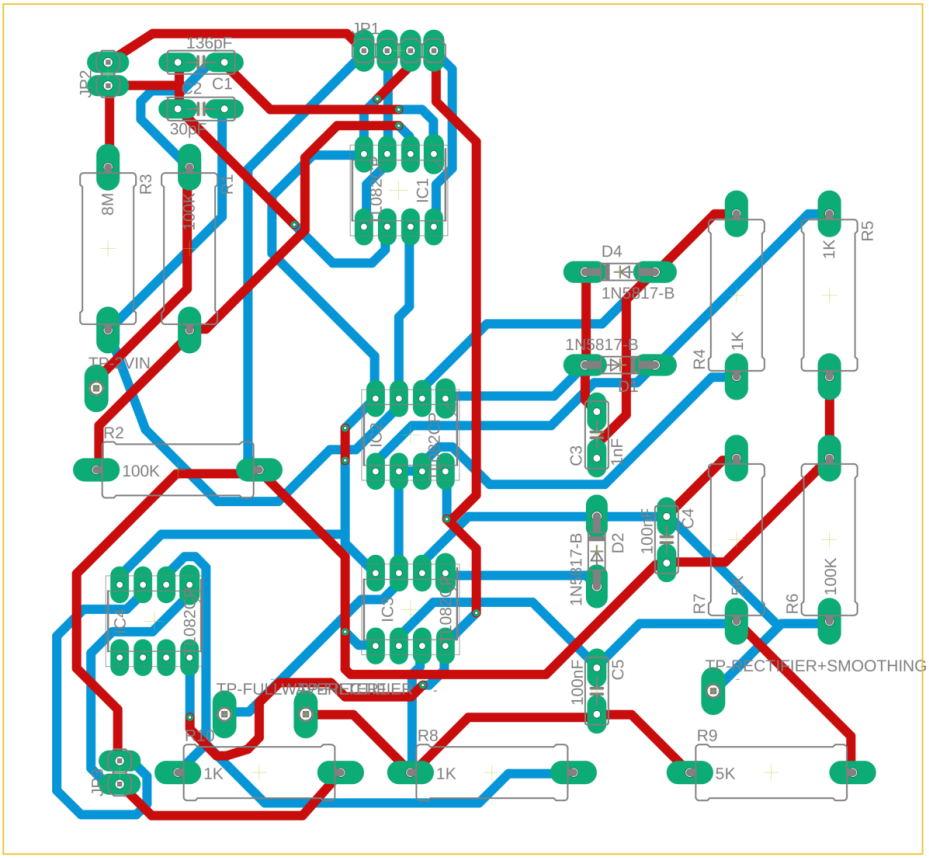

Figure D.13: PCB design from *Autodesk EAGLE*.

D.4. PIV algorithm

The algorithm, as implemented in a *matlab*[2] script, is presented in this section. The image enhancement, algorithm overview, cross-correlation implementation, sub-pixel correction, the elimination of spurious vectors, smoothing and replacement and finally the calculation of field related quantities are detailed below.

D.4.1. Image enhancement

To avoid, or at least reduce the amount of erroneous velocity estimates, a common way is to enhance the images before post-processing takes place by applying filters to the im-

[2] https://www.mathworks.com/products/matlab.html

ages (Raffel et al., 2018; Thielicke, 2014). Typical pre-processing techniques are the Modified Histogram Equalization (MHE) (Roth & Katz, 2001), the min/max technique (Westerweel, 1993), or the Contrast Limited Adaptive Histogram Equalization (CLAHE) (Pizer et al., 1987). Some techniques are presented in the following section, including histogram equalization, intensity capping and high-pass filtering and their effects are shown in figure D.14. Other techniques were also developed as spacial filtering, temporal filtering and binary image conversion (which actually increase measurement uncertainties (Raffel et al., 2018)), but are not described further on because they did not appear to improve the PIV measurements.

Histogram equalization. Histogram equalization goal is to enhance contrasts by adjusting image intensities. To do so, the most common intensities are spread out to the full range of data (from 0 to 255 for 8 bits images) (Thielicke, 2014). Histogram equalization is implemented in the PIV tool at LEAF-NL. An alternative but similar technique is called CLAHE, which applies histogram equalization but over tiles of the images, is widely used in PIV tools and has shown to improve the probability of detecting valid vectors by almost 5% (Thielicke, 2014). CLAHE is not available in *Octave*. An example of histogram equalization can be found in figure D.14b and D.14c, which shows the advantages of the CLAHE technique over the simplest histogram equalization since the reflection at the top does not appear.

Intensity capping. Intensity capping technique, proposed by Shavit et al. (2007), sets the brightest spots of the image to a less important intensity. Bright particles have more weight in the cross-correlation computation than other particles. A threshold of the greyscale intensities is set and all pixels which have a higher value is set to this value. Intensity capping, by only acting on bright spots, does not amplify the background noise and improves the probability of finding valid vectors by around 5 % (Shavit et al., 2007). Intensity capping also has a relatively low computational cost. In this work, we apply the following threshold: $upperLimit = I_{50} + n_{IC} \cdot \sigma_I$ where I_{50} is the median of the image, σ_I the standard deviation of the image and n_{IC} a coefficient usually between 0.5 and 3. An improvement, proposed by Shavit et al. (2007), consists in applying intensity capping locally over tiles of the image instead of doing over the whole image. This function is implemented globally in the PIV tool. An example of intensity capping can be found in figure D.14d.

High-pass filter. According to Raffel et al. (2018), a high-pass filter removes all low-frequency background variations, leaving the particle images unaffected. Thus it can deal with light reflections (Sciacchitano & Scarano, 2014). It is implemented by subtracting a low-pass filtered image to the original image. The filter width should be larger than the diameter of the particles images. An example of histogram equalization can be found in figure D.14e.

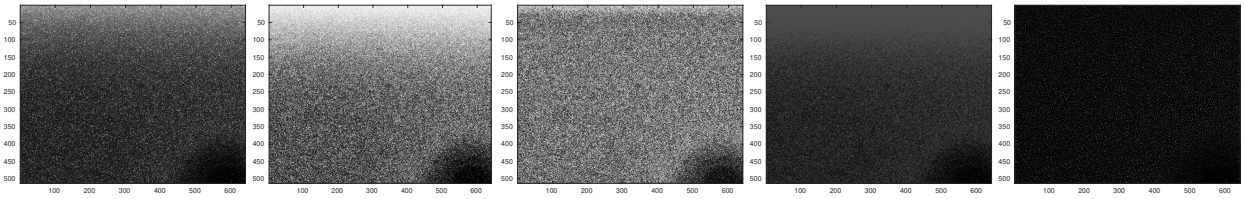

(a) Original image (b) Histogram equalization (c) CLAHE equalization (from *Matlab*). (d) Intensity capping (e) High-pass

Figure D.14: Pre-processing of the images. Original image is from the PIV challenge[a].

[a] see http://www.pivchallenge.org/

D.4.2. Algorithm overview

The first statistical PIV procedure was described in Adrian (1991). Our tool is composed of two algorithm that can be chosen: the integer window shifting (IWS) and the Window Deformation (WD). The first one is less costly while the second one shows more accuracy. For both algorithm, the window slicing process is done considering the size of the windows (always taken as squared) and the overlap between neighboring windows.

Integer window shifting algorithm (IWS) An overview of this algorithm, named integer window shifting (IWS), can be seen in figure D.15a. The different steps are described in the following paragraph:

1. Interrogation windows of image A and image B are the same for the first pass.
2. The cross-correlation is calculated for every windows, and the displacement is determined.
3. A correction is applied to achieve sub-pixel precision.
4. Outlier vectors are detected and eliminated.
5. Missing vectors are replaced through interpolation.
6. Data is smoothed (low-pass filter).
7. At the end of these steps, the displacement $(\Delta x, \Delta y)$ calculated for every windows is used as predictors for the shifting of the windows used in the next iteration. Windows size can be decreased. The shifting is done according to a central scheme; let's consider $(xA_0^{i,j}, yA_0^{i,j})$ the original position of the left down corner of window (i, j) of image A

and $(xB_0^{i,j}, yB_0^{i,j})$ the original position of the left down corner of window (i,j) of image B . Then the new position of the windows will be:

$$\left(xA_1^{i,j}, yA_1^{i,j}\right) = round\left(xA_0^{i,j} - \frac{\Delta x}{2}, yA_0^{i,j} - \frac{\Delta y}{2}\right) \tag{D.1}$$

$$\left(xB_1^{i,j}, yB_1^{i,j}\right) = round\left(xB_0^{i,j} + \frac{\Delta x}{2}, yB_0^{i,j} + \frac{\Delta y}{2}\right) \tag{D.2}$$

8. New iteration starts at point 2.

Window deformation algorithm (WD) An overview of this algorithm, named window deformation (WD), can be seen in figure D.15b. The window deformation technique as presented in H. T. Huang et al. (1993) is used here:

1. A first (or various) pass is done with the IWS algorithm as a first estimation of the displacement field with subpixel precision. This gives the predictor at iteration 0: $(\Delta x_0, \Delta y_0)$.

2. Predictor is extrapolated to every pixels of the images. Bilinear extrapolation is usually used. In *Matlab/Octave*, this operation can lead to unrealistic values at the boundary. More complex algorithm such as "2D spline" can be a convenient solution since values at the boundary are best predicted.

3. Images A and B are deformed according to:

$$A_n(i,j) = A(x_p, y_p) = A\left(i - \frac{\Delta x_n(i,j)}{2}, j - \frac{\Delta y_n(i,j)}{2}\right) \tag{D.3}$$

$$B_n(i,j) = B(x_p, y_p) = B\left(i + \frac{\Delta x_n(i,j)}{2}, j + \frac{\Delta y_n(i,j)}{2}\right) \tag{D.4}$$

   As this process implies taking values at intermediate position (not integer pixels), an interpolation is necesary (re-sampling of the pixels values at intermediate locations (Scarano, 2001)).

4. The cross-correlation is calculated for every windows on the deformed images, and the displacement is determined.

5. A correction is applied to achieve sub-pixel precision.

6. Update predictor with corrector (C_x, C_y) computed on deformed images:

$$(\Delta x_{n+1}, \Delta y_{n+1}) = (\Delta x_n, \Delta y_n) + (C_x, C_y) \tag{D.5}$$

7. Outlier vectors are detected and eliminated.

8. Missing vectors are replaced through interpolation.

9. Data is smoothed (low-pass filter).

10. New iteration starts at point 2 with the updated predictor if convergence is not achieved.

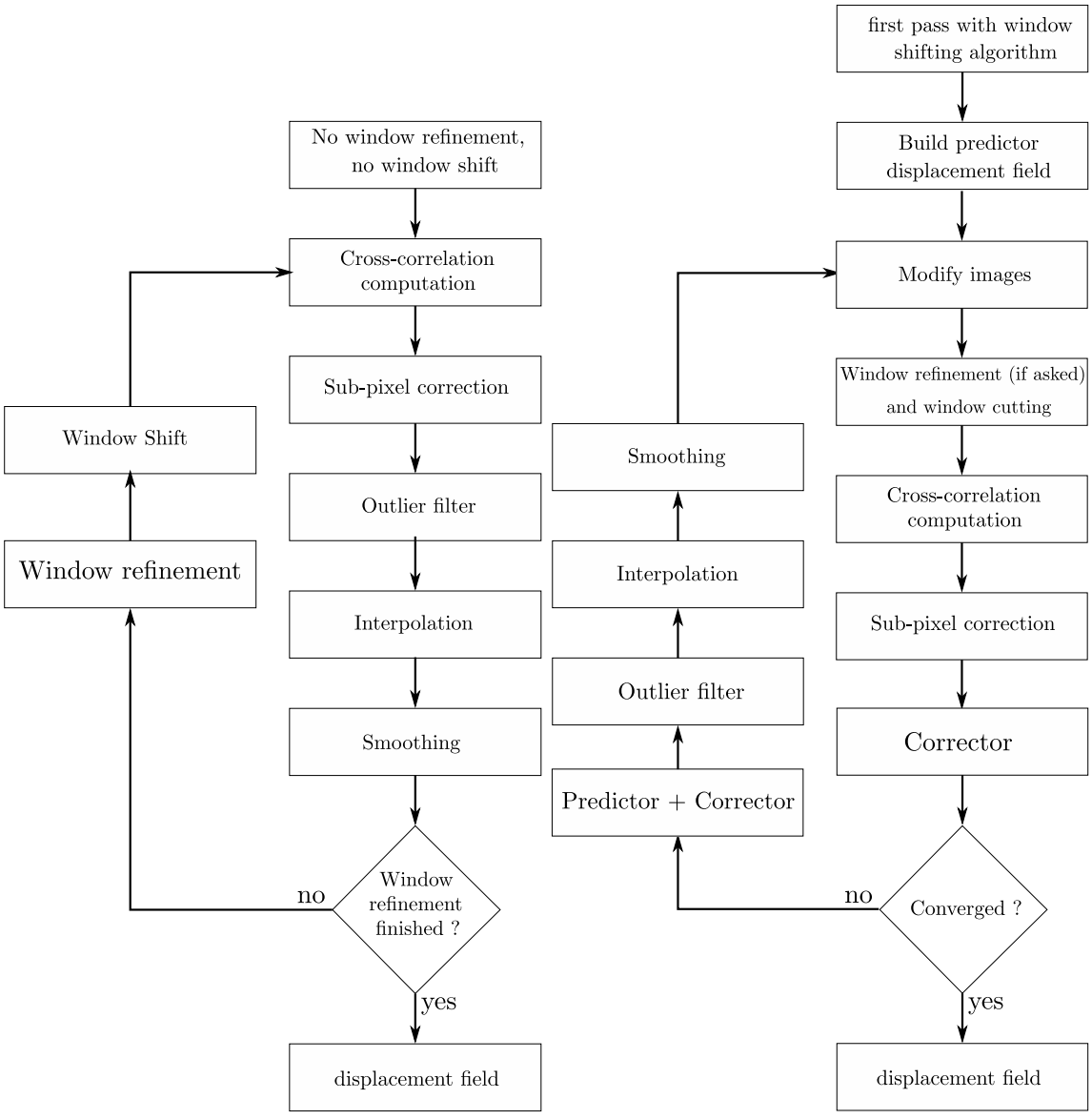

(a) IWS (b) WD

Figure D.15: PIV algorithms used at LEAF-NL lab. (a) Integer window shifting algorithm. (b) Window deformation algorithm.

D.4.3. Cross-correlation

Cross-correlation can either be carried out by Direct Cross-Correlation or using a Fourier transform based technique.

Direct cross-correlation and derived techniques The base, and thus the most important part of any PIV post-processing tool, is the cross-correlation. Squared interrogation windows, generally from 8 to 64 pixels, are compared between image A and B using cross-correlation. The result is the most probable displacement of the particles in the interrogation area (Thielicke, 2014). The 2D discrete cross-correlation function is given by H. Huang et al. (1997):

$$cc(m,n) = \sum_{i=1}^{N}\sum_{j=1}^{N} A(i,j)B(i-m,j-n) \tag{D.6}$$

A high cross-correlation value, close to 1, mean that many particle images match up with their corresponding spatially shifted partners (C. E. Willert & Gharib, 1991). DCC computes the correlation matrix in the spatial domain as shown in figure D.16. The cost of DCC is $\mathscr{O}\left(N^4\right)$ (Raffel et al., 2018), which is relatively important. DCC used as in equation D.6 is sensitive to intensity changes and thus one can use the following normalized cross correlation function (Gonzalez, 1987):

$$cc(m,n) = \frac{\sum\limits_{i=1}^{N}\sum\limits_{j=1}^{N}\left[A(i,j)-\overline{A}\right]\left[B(i-m,j-n)-\overline{B}\right]}{\sqrt{\sum\limits_{i=1}^{N}\sum\limits_{j=1}^{N}\left[A(i,j)-\overline{A}\right]^2\sum\limits_{i=1}^{N}\sum\limits_{j=1}^{N}\left[B(i,j)-\overline{B}\right]^2}} \tag{D.7}$$

H. Huang et al. (1997) used this technique in the PIPM (Particle Image Pattern Matching). Errors are about an order of magnitude smaller than with the cross-correlation function of equation D.6.

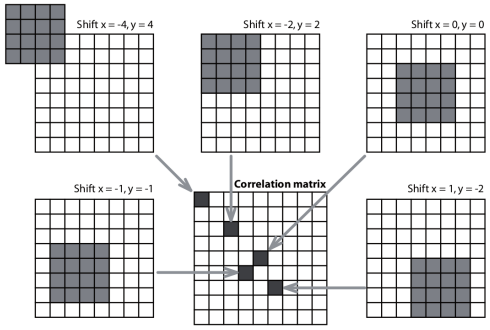

Figure D.16: Calculation of the correlation matrix between a 4×4 pixels interrogation window from image A and a 8×8 pixels interrogation window from image B. The resulting correlation matrix is 9×9 pixels (from Thielicke (2014), adapted from Raffel et al. (2018)).

Fourier transform based cross-correlation Another way of computing the cross-correlation of the image is to use Fourier transform. The following calculation shows the link between cross-correlation and Fourier transform for the 1D case:

$$\begin{aligned}
\mathscr{F}\left[f \star g(\tau)\right] &= \int_{-\infty}^{+\infty} \int_{-\infty}^{+\infty} \overline{f(t)} g(t+\tau) e^{-i\omega\tau} dt d\tau \\
&= \int_{-\infty}^{+\infty} \overline{f(t)} \left[\int_{-\infty}^{+\infty} g(t+\tau) e^{-i\omega\tau} d\tau \right] dt \\
&= \int_{-\infty}^{+\infty} \overline{f(t)} \left[\int_{-\infty}^{+\infty} g(t+\tau) e^{-i\omega(t+\tau)} d\tau \right] e^{i\omega t} dt \\
&= \int_{-\infty}^{+\infty} \overline{f(t)} e^{i\omega t} dt \int_{-\infty}^{+\infty} g(t') e^{-i\omega t'} dt' \\
&= \int_{-\infty}^{+\infty} \overline{f(t)}\ \overline{e^{-i\omega t}} dt \int_{-\infty}^{+\infty} g(t') e^{-i\omega t'} dt' \\
&= \overline{\mathscr{F}\left[f\right]} \cdot \mathscr{F}\left[g\right]
\end{aligned}$$

which leads to:

$$f \star g = \mathscr{F}^{-1}\left[\overline{\mathscr{F}[f]} \cdot \mathscr{F}[g]\right] \tag{D.8}$$

A similar result can be obtained for 2D functions. The cost for Fourier transform based cross-correlation is $\mathscr{O}\left(N^2 \log_2(N)\right)$, which gives it a clear advantage compared to DCC. A further increase in computational efficiency can be achieved when using Fast Fourier Transform (FFT, with N a power of 2) (Raffel et al., 2018). As the FFT technique is periodic, if the displacement is larger than $N/2$, the correlation peak will be folded back into the matrix and will appear on the opposite side (Raffel et al., 2018). Displacement range is then limited to $N/2$. A solution to this problem is to increase the interrogation window size or decrease the time delay between frames. A drawback of FFT based cross-correlation, as interrogation window A and B have to be the same size, is that the error on cross-correlation location

increases when the particle displacement increases as the number of particle leaving window B increases (H. T. Huang et al., 1993). The problem can be overcome by using the shifting technique (Westerweel et al., 1997) or respecting a minimum size for window B as shown in H. T. Huang et al. (1993).

Normalization of the Fourier transform based cross-correlation. We have seen that the normalization of the cross-correlation map can leads to more accurate detection of the displacement peak. In this work, the normalization is carried out according to the following equation:

$$cc = \frac{\mathscr{F}^{-1}\left[\overline{\mathscr{F}[A]} \cdot \mathscr{F}[B]\right]}{\sqrt{\sum_{i=1}^{N}\sum_{j=1}^{N}[A(i,j)]^2 \sum_{i=1}^{N}\sum_{j=1}^{N}[B(i,j)]^2}} \tag{D.9}$$

Elimination of correlation errors Before the detection of the maximum of the cross-correlation coefficient matrix, one can eliminate correlation errors according to the process proposed by Hart (2000). It consists of the direct element-by-element multiplication of the correlation coefficient matrices from adjacent regions. The principle is illustrated in figure D.17a. It is the "correlation of the correlations". According to Hart (2000), this method improves sub-pixel accuracy and eliminates spurious vectors resulting from unmatched particle pairs, out-of-boundary motion, particle overlap, inter-particle correlations and noise (optical and electronic). In our case we multiply the main matrix with the ones situated at the top, bottom, left and right as shown in figure D.17b.

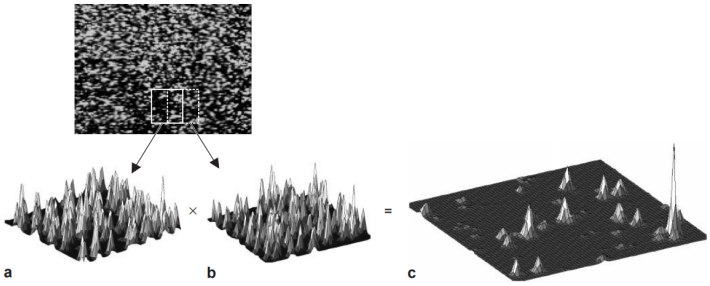

(a) Error elimination according to Hart (2000).

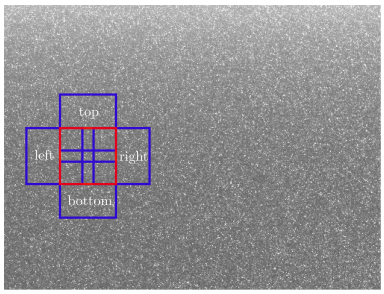

(b) Multiplication of the cross-correlation matrices.

Figure D.17: Elimination of correlation errors by multiplying the correlation coefficient matrices from adjacent regions, from Hart (2000). In this work, we multiply the correlation coefficient matrix of the windows of interest (in red) with the ones of windows at the top, bottom, left and right (in blue) allowing to reduce the correlation error and enabling an easier detection of the peak. In this example, the window overlap is set to 40 %.

D.4.4. Reducing the bias error and random error

Digital mask based bias error reduction. During the development of PIV algorithms, it was well known that velocities calculated from the algorithm were generally lower than the true ones. A weighting function, based on a digital mask, is used to reach a better accuracy of the cross-correlation and thus decrease the bias error. This function can be either based on a housetop-like function (Raffel et al., 2018) or a Gaussian function (Gui et al., 2000). We use a function based on the work of Nogueira et al. (1999) and, if ξ and η denotes the coordinates from the center of the window and N the size of the window, the weighting function is defined as:

$$W(\xi,\eta) = \sqrt{9\left(4\left|\frac{\xi}{N}\right|^2 - 4\left|\frac{\xi}{N}\right| + 1\right)\left(4\left|\frac{\eta}{N}\right|^2 - 4\left|\frac{\eta}{N}\right| + 1\right)} \tag{D.10}$$

An example is found in figure D.18. The use of a weighting window main interest is, as previously written, to reduce the bias error (see 4.3.2.2 for error definitions). This is however true only for small particle displacement (Gui et al., 2000) unless a discrete offset of the interrogation window or window deformation techniques are applied. The random error or RMS error treatment can become tricky: we observed that for the smallest interrogation window (16 and 32 pixels wide) the application of such weighting window causes an increase of the random error. This is also observed by Gui et al. (2000). We chose to apply the weighting window only for window sizes superior to 32 pixels (this last one not being included).

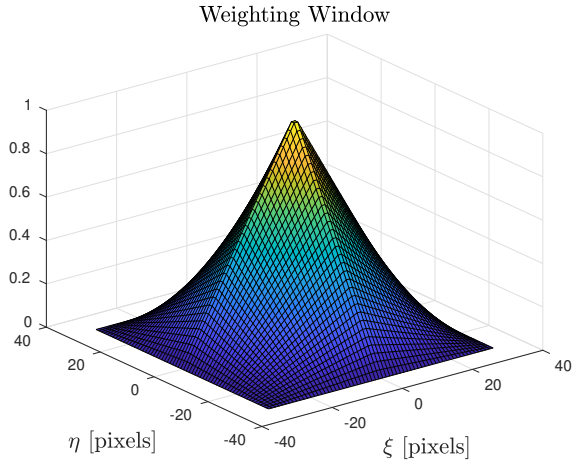

Figure D.18: Weighting window applied to the interrogation windows.

Zero padding of small window sizes. For small window sizes (typically lower or equal to 32 pixels) resolutions problem appear when calculating the cross-correlation of the interrogations images: in deed, as the resolution depends on the total number of points and small

interrogation windows having few points the resulting resolution will be bad. We choose to zero-pad these small windows in order to increase the total number of points and improve the resolution of the cross-correlation map. We increase the window size to twice its size by padding zero in both directions. This is however extremely costly when applying the 2D FFT as the window size increased. Alternatives are proposed in Lourenco & Krothapalli (1995) as the Whittaker's reconstruction. Besides the gain in the random error treatment, it showed to allow the iterative process to converge rapidly.

D.4.5. Sub-pixel correction

The next step is the peak finding, which is quite important. The raw detection, which consists in finding the maximum of the correlation coefficient matrix, gives an integer result. This result can be further refined with sub-pixel precision using a range of methods, usually by fitting a function to the peak such as a centroid, a parabolic or a gaussian (Raffel et al., 2018). It is common to able to represent particle images by a gaussian intensity distribution. Then, $2 \cdot 3$ point fit (2 times 3 point fit) or 9 point fit for Gaussian functions are common methods which have shown accuracy, speed and universality (Thielicke, 2014). In our tool, the $2 \cdot 3$ point fit and the 9 point fit are available. The $2 \cdot 3$ point fit corresponds to the following equations (Nobach & Honkanen, 2005):

$$\Delta x = \frac{ln\left(z_{\chi-1}\right) - ln\left(z_{\chi+1}\right)}{2\left(ln\left(z_{\chi-1}\right) - 2ln\left(z_{\chi}\right) + ln\left(z_{\chi+1}\right)\right)} \tag{D.11}$$

where z_χ is the value of the peak, $z_{\chi-1}$ and $z_{\chi+1}$ are the two neighbors. It is independently applied vertically and horizontally. This method has become the standard in PIV (Nobach & Honkanen, 2005), but has been developed for Gaussian-shaped particle images. The method works best for narrow correlation peaks and for particle images larger than 1.5 pixels (Raffel et al., 2018). Error can appear if the particle images or the peak have an elliptic shape (also known as pixel locking), and can be overcome with the fitting of a two-dimensional Gaussian (Nobach & Honkanen, 2005). The 2D or 9 points fit is given by the following equations:

$$\Delta x = \frac{c_{11}c_{01} - 2c_{10}c_{02}}{4c_{20}c_{02} - c_{11}^2} \tag{D.12}$$

$$\Delta y = \frac{c_{11}c_{10} - 2c_{01}c_{20}}{4c_{20}c_{02} - c_{11}^2} \tag{D.13}$$

with

$$c_{10} = \frac{1}{6} \sum_{i,j=-1}^{1} i \; ln\left(Z_{X+i;Y+j}\right) \tag{D.14}$$

$$c_{01} = \frac{1}{6} \sum_{i,j=-1}^{1} j \; ln\left(Z_{X+i;Y+j}\right) \tag{D.15}$$

$$c_{11} = \frac{1}{4} \sum_{i,j=-1}^{1} ij \; ln\left(Z_{X+i;Y+j}\right) \tag{D.16}$$

$$c_{20} = \frac{1}{6} \sum_{i,j=-1}^{1} \left(3i^2 - 2\right) \; ln\left(Z_{X+i;Y+j}\right) \tag{D.17}$$

$$c_{02} = \frac{1}{6} \sum_{i,j=-1}^{1} \left(3j^2 - 2\right) \; ln\left(Z_{X+i;Y+j}\right) \tag{D.18}$$

$$c_{00} = \frac{1}{9} \sum_{i,j=-1}^{1} \left(5 - 3i^2 - 3j^2\right) \; ln\left(Z_{X+i;Y+j}\right) \tag{D.19}$$

This 2D fitting can perform well for non-deforming window algorithm (DCC, or single pass Fourier transform based correlation) while added value is less pronounced in deforming window implementation (Thielicke, 2014).

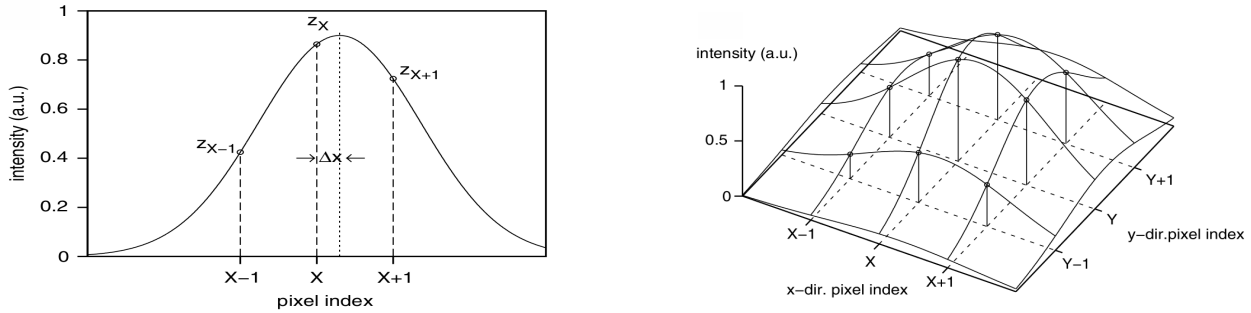

(a) $2 \cdot 3$ point fit (b) 9 point fit

Figure D.19: $2 \cdot 3$ and 9 point fits according to Nobach & Honkanen (2005). x and y axis are evaluated independently in the first case while in the second case the fit is 2D.

D.4.6. Elimination of spurious vectors, smoothing and replacement

Outlier detection Detection of velocities can lead to erroneous vectors as the experiment cannot be perfect: light reflection or particles leaving the laser plane or appearing in it. These vectors deviate in magnitude and direction from their neighbours, and are mainly due to insufficient particle image pairs (Westerweel, 1994). It then necessary to remove

these unphysical vectors and replace them. Thielicke (2014) uses velocity threshold on each component based on the mean and the standard deviation. Other techniques are the global histogram operator, the vector difference test, the dynamic mean value operator, minimum correlation filter, peak height ratio filter or the signal-to-noise filter (Raffel et al., 2018). The median test (Westerweel, 1994) is also a popular filter. In our work, the following "universal" (which does not depend on the experiment) modified median test (Westerweel & Scarano, 2005) is used. First, let's consider the displacement vector U_0 at position (i, j). Let's also consider its 3×3 neighbors whose displacement vectors are $\{U_1, U_2...U_8\}$ and U_m is the median of this set. U_0 is excluded from this set. Residuals are defined as: $r_i = |U_i - U_m|$. The median of the residuals r_m is taken from the set $\{r_1, r_2...r_8\}$. The normalized residual for U_0 is taken as:

$$r_0^* = \frac{|U_0 - U_m|}{r_m + \epsilon} \tag{D.20}$$

where ϵ represent the acceptable fluctuation level due to cross-correlation. A threshold is applied to this criteria: if $r_0^* > threshold$ then the displacement vector at position (i, j) is discarded. The interest of this method is the relatively "universal" method, which leads to values for the threshold and ϵ of 2 and 0.1 respectively (Westerweel & Scarano, 2005). A threshold value more or less important conducts to a more or less restricting filter. According to Raffel et al. (2018), high-quality PIV should not give more than 5% of outlier vectors under challenging experimental situations.

Interpolation After removal of outlier displacement vectors, it is necessary to replace them by interpolated data as they serve as a predictor for the next iteration and also because missing vectors can be problematic when computing other fields based on the derivatives (Thielicke, 2014). Techniques to replace missing data can be $3 \cdot 3$ neighbor mean or a two dimensional interpolation. Spline is a better solution for 2D interpolation but is more costly than linear (Thielicke, 2014). According to Thielicke (2014), a boundary value method is the most accurate (even if he finds that for missing data inferior to 15 %, the error is less than 0.6% pixel). In this work, both 2D linear and spline interpolation are available.

Smoothing It is chosen to smooth data by meaning the values of displacement vectors of the $3 \cdot 3$ neighbors. According to Raffel et al. (2018), median filtering is another effective mean to reduce noise. It has been proven that smoothing allows to get rid of unstabilities that might appear during the iterative process (B. J. Kim & Sung, 2006).

Iterative process The iterative process convergence is evaluated through the computation of residuals. Residuals are defined as follow:

$$r_k = \frac{1}{N^2}\sqrt{\sum_{i=1}^{N}\sum_{j=1}^{N}{\delta_k^{(i,j)}}^2} \tag{D.21}$$

where δ_k are the correctors coordinate in the x and y direction of the displacement field in the window deformation algorithm (see section D.4.2) and i, j represents the velocity vectors indices in the x and y directions. The iterative process is considered to have converged when the residuals in both x and y directions fulfill the following equations:

$$\left|\frac{r_k - r_{k-1}}{r_k}\right| \leq l \tag{D.22}$$

$$\left|\frac{r_k - r_{k-2}}{r_k}\right| \leq l \tag{D.23}$$

$$\left|\frac{r_k - r_{k-5}}{r_k}\right| \leq l \tag{D.24}$$

where $l = 1 \times 10^{-2}$.

D.4.7. Calculation of field related quantities

To recover all terms of Navier-Stokes equations, one should know the pressure, the density and the velocity fields. Obtaining all this quantities are a remaining challenge (Raffel et al., 2018). The PIV results, displacement and velocity fields, allow however to obtain derivative and integral related quantities such as the vorticity field (equation D.25), in plane shear stress (equation D.26), extensional strains (equation D.27), stream function or circulation. The definition of some of these quantities are given below:

$$\omega_z = \frac{\partial v}{\partial x} - \frac{\partial u}{\partial y} \tag{D.25}$$

$$\epsilon_{xy} = \frac{\partial u}{\partial y} + \frac{\partial v}{\partial x} \tag{D.26}$$

$$\eta = \epsilon_{xx} + \epsilon_{yy} = \frac{\partial u}{\partial x} - \frac{\partial v}{\partial y} \tag{D.27}$$

To compute these quantities, one can use different numerical schemes (forward, backward, central difference etc...). Raffel et al. (2018) privileges the least squares difference approach (see equation D.28), since it minimizes the effects of random errors (ϵ_U), even if it tends to

smooth the derivatives.

$$\left(\frac{df}{dx}\right)_i = \frac{2f_{i+2} + fi + 1 - fi - 1 - 2f_{i+2}}{10\Delta X} \tag{D.28}$$

However, this formula is defined for a 1D function while PIV data are 2D. An alternative must be given. Raffel et al. (2018) suggests to use the theorem of Strokes linking vorticity to the circulation according to:

$$\Gamma = \oint \mathbf{U} \cdot d\mathbf{l} = \int (\nabla \times \mathbf{U}) \cdot d\mathbf{S} = \int \omega \cdot d\mathbf{S} \tag{D.29}$$

which gives, by considering the eight points surrounding the point of interest (see figure D.20):

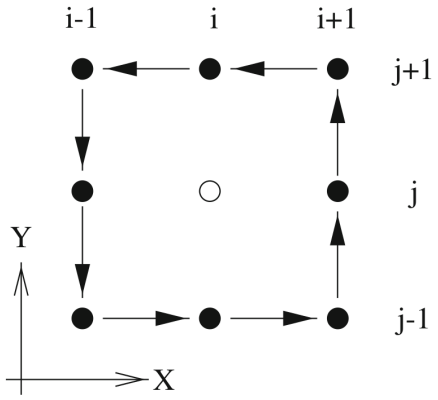

Figure D.20: Contour for the circulation calculation used in the estimation of the vorticity at point (i, j) (from Raffel et al. (2018)).

$$(\omega_z)_{i,j} = \frac{\Gamma_{i,j}}{4\Delta X \Delta Y} \tag{D.30}$$

with

$$\begin{aligned}\Gamma_{i,j} = &\frac{1}{2}\Delta X \left(U_{i-1,j-1} + 2U_{i,j-1} + U_{i+1,j-1}\right) \\ &+ \frac{1}{2}\Delta Y \left(V_{i+1,j-1} + 2V_{i+1,j} + V_{i+1,j+1}\right) \\ &- \frac{1}{2}\Delta X \left(U_{i+1,j+1} + 2U_{i,j+1} + U_{i-1,j+1}\right) \\ &- \frac{1}{2}\Delta Y \left(V_{i-1,j+1} + 2V_{i-1,j} + V_{i-1,j-1}\right)\end{aligned} \tag{D.31}$$

According to Raffel et al. (2018), this estimate performs better than least squares or Richardson methods. The uncertainty in the vorticity estimate is now $\epsilon_\omega \approx 0.61\epsilon_U/\Delta X$ compared with $\epsilon_\omega \approx \epsilon_U/\Delta X$ for the central difference scheme. Similarly, one can obtain the strain and

shear according to:

$$\begin{aligned}(\epsilon_{xy})_{i,j} = &- \frac{U_{i-1,j-1} + 2U_{i,j-1} + U_{i+1,j-1}}{8\Delta Y} \\ &+ \frac{U_{i+1,j+1} + 2U_{i,j+1} + U_{i-1,j+1}}{8\Delta Y} \\ &- \frac{V_{i-1,j+1} + 2V_{i-1,j} + V_{i-1,j-1}}{8\Delta X} \\ &+ \frac{V_{i+1,j-1} + 2V_{i+1,j} + V_{i+1,j+1}}{8\Delta X}\end{aligned} \tag{D.32}$$

$$\begin{aligned}-(\epsilon_{zz})_{i,j} = &\frac{V_{i-1,j-1} + 2V_{i,j-1} + V_{i+1,j-1}}{8\Delta Y} \\ &- \frac{V_{i+1,j+1} + 2V_{i,j+1} + V_{i-1,j+1}}{8\Delta Y} \\ &+ \frac{U_{i+1,j-1} + 2U_{i+1,j} + U_{i+1,j+1}}{8\Delta X} \\ &- \frac{U_{i-1,j+1} + 2U_{i-1,j} + U_{i-1,j-1}}{8\Delta X}\end{aligned} \tag{D.33}$$

Annex E

Publication

Dynamic and kinematic characterization of the impulsive wavemaker system in a numerical wave tank

Charlie BARRAUD and Rodrigo H. HERNÁNDEZ P. *American Institute of Physics Advances*, Volume #10, Issue #11, Issue 2020-11-05
DOI: 10.1063/5.0017376

Dynamic and kinematic characterization of the impulsive wavemaker system in a numerical wave tank

Cite as: AIP Advances **10**, 115306 (2020); https://doi.org/10.1063/5.0017376
Submitted: 22 July 2020 . Accepted: 01 October 2020 . Published Online: 05 November 2020

C. Barraud, and R. H. Hernández

AIP Advances ARTICLE scitation.org/journal/adv

Dynamic and kinematic characterization of the impulsive wavemaker system in a numerical wave tank

Cite as: AIP Advances 10, 115306 (2020); doi: 10.1063/5.0017376
Submitted: 22 July 2020 • Accepted: 1 October 2020 •
Published Online: 5 November 2020

C. Barraud and R. H. Hernández[a)]

AFFILIATIONS

LEAF-NL, Departamento de Ingeniería Mecánica, Universidad de Chile, Casilla 2777, Santiago, Chile

[a)]Author to whom correspondence should be addressed: rohernan@ing.uchile.cl. URL: https://www.leafnl.uchile.cl

ABSTRACT

We study the dynamical response of a piston-type wavemaker in a numerical wave tank. The two-dimensional, fully viscous unsteady Navier–Stokes equations are solved on a two-phase flow configuration using the volume of fluid method to capture the free surface dynamics. The wavemaker is a moving wall driven by an arbitrary signal waveform. The step response of the wavemaker may generate pulse-like waves similar to an undular bore propagating along the tank. Wave elevation at the piston wall has close similarity to the time response of second order systems found in feedback theory. The scaling found for water elevation at the piston wall for different step velocities and mean still water levels is in agreement with that in the available theory at low Froude numbers. The results along the tank for continuous waves agree with those of potential theory. The power input during the step response was determined during the whole wave generation process showing that net piston forces are predominantly hydrostatic. A power scaling for different mean still water levels and step velocities as a function of the Froude number was obtained. An active absorption strategy based upon a feedback controller driving a secondary piston was implemented. Wave absorption was successfully achieved on regular and irregular waves.

I. INTRODUCTION

Wave tanks are centerpieces when it comes to studying hydrodynamics and wave structure interaction in offshore and marine engineering. Experimental or numerical, they can reproduce the offshore environmental conditions (waves, currents, winds for some of them) in order to evaluate the dynamic response to these harsh conditions of vessels, offshore platforms, and marine renewable energy structures such as fixed/floating offshore windmills or wave energy converters. For a long time, these phenomena could only be experimentally studied. The wave tank scaling should be done, according to the similarity principle of dimensional analysis, by matching relevant numbers as the Froude and the Reynolds numbers. This is often complicated especially at small scale as explained in Ref. 1. One approach is to test the model through increasing model scales.[2] The most simple configuration for a wave tank is a 2D tank, which is a long tank where waves are generated on one side and absorbed or broken up on the opposite side.

In order to generate waves at a laboratory scale, one should displace a certain amount of water by means of a wavemaker of choice: piston, hinged paddle, double articulated paddle, plunger, duck. First order wavemaker theory has first been studied in Ref. 3. Wave generation alternatives have been theoretically studied in the 1950s[4] including piston, hinged paddle, or double articulated paddle. In this work, we choose to use a piston wavemaker where the piston stroke along the tank is the physical mechanism to create waves. The resulting waves from a piston wavemaker were investigated in Ref. 4 determining a transfer function or relationship between the piston stroke and the wave height. A validation of the piston wavemaker theory was provided by some experiments.[5] Similarly, Madsen[6] developed a theory of wavemaker generation for pistons providing a detailed expression for wave elevation at any position in a wave tank, and Schäffer[7] developed the second-order wavemaker theory for irregular waves. Goring[8] studied solitary wave generation with a piston wavemaker, basing his solution on the theory of Ref. 9. The impulsive wavemaker was experimentally and numerically

studied in Ref. 10, notably showing wave profiles from the experiment as well as forces on the wavemaker.

Most of the research on wavemaker theory has been conducted on the basis of potential theory avoiding the determination of viscous effects. At the same time, the necessity for local solutions at the piston wavemaker was considered important in order to understand the physics of the first instants in the wave generation. Local solutions near the piston wall are provided by Joo *et al.*[11] using the Laplace equation and expansion series for small Froude numbers and basing their work on Ref. 12. They investigated the contact line motion at initial times of the piston wavemaker for ramp, step, exponential, and harmonic velocities. They later on extended their studies to stratified fluid.[13] A study of the steady motion of a ship bow at high Froude number, which is similar to the piston wavemaker problem, was carried out in Ref. 14. Experimental realization of the velocity step case becomes complicated because imposing a prescribed step-like wavemaker motion involves high piston accelerations and therefore peak power inputs. The practical case is to perform a ramp motion as indicated in Ref. 15.

While experimental wave tanks provide a physical platform to implement such systems, testing may be expensive or not suitable to comply with similarity restrictions, whereas numerical studies once performed exclusively with potential codes (irrotational, incompressible, and nonviscous flows) are now commonly carried out taking into account viscous effects that, nevertheless, require more computational resources.

At present, the use of efficient codes solving viscous Navier–Stokes equations has been reported to be useful in order to model extreme wave conditions where the wave breaking process[16] can be captured and identified as the dominant mechanism (instabilities) involved in extreme loading on marine structures and wave energy converter devices.[17] Numerical wave tanks may recreate realistic waves using moving boundaries (which involves a dynamic mesh) or static boundaries with mathematical implementation (in the domain or at the boundaries). In this work, we use the first option that mimics a viscous piston motion in a physical experiment.[18,19] Most of the numerical wave tank models include the volume of fluid (VOF) to simulate two-phase flows[20] as well as the wave generation and propagation problem.[21–24] Wave tank modeling with active wave absorption was developed in OpenFOAM,[18,25] and recent methods such as Smoothed-Particle Hydrodynamics (SPH) have also been developed to represent two-phase flows.[26,27]

In this work, we present a numerical study of a piston wavemaker at a laboratory scale to investigate the wave generation process and characterize the piston wavemaker dynamics, extending Froude number regimes far beyond the ones that were studied before. We perform fully non-linear and viscous numerical simulations of the wave tank where surface waves are produced by the prescribed motion of a piston wavemaker. The moving boundaries allow reproducing the physics of a real facility. A complete mesh independence study is carried out, and validation is performed with theoretical data. To be able to generate waves of high quality, it is necessary to characterize the wavemaker system. It is chosen here to do so by basing the study on the initial-value problem, theoretically studied in Ref. 11. The numerical simulation allows us to study regimes that do not appear in the theoretical study based on potential flow. We measure the water height at the wavemaker and in the tank for a set of prescribed wavemaker motions, allowing one to characterize the near and far field generated waves and determine the power input needs according to the wavemaker dynamics.

The structure of this article is as follows: the initial-value problem and the required equations are presented in Sec. II, the numerical method, mesh independence tests, and validation are presented in Sec. II C, and finally the resulting characterization of the piston wavemaker and the power input analysis are presented in Sec. III.

II. PROBLEM FORMULATION

The problem is described in the schematics in Fig. 1. We consider a 2D wave tank of length L and height d, equipped with a moving piston wavemaker placed at the left wall, and the opposite wall of the tank is situated on the right. The mean still water level is denoted h and can be varied at will. The origin of the coordinate system is located at the left bottom of the wave tank, and all different measurement stations along the wave tank are referred to this coordinate system. In order to characterize the piston wavemaker and the wave tank behavior, a series of tests will be performed to provide the system response to input velocity signals driving the motion of the piston wavemaker. The overall wave tank response will be obtained from Heaviside $\Theta(t)$ input signals representing a step response test.[28] We consider the system composed by the wavemaker, whose input signal is its velocity U_G and the response is the water level at the piston wavemaker η_w, as shown in Fig. 1. We can define a transfer function associated with the wavemaker system, hereafter called G where the fundamental output/input relationship (transfer function) can be expressed as $G = \eta_w/U_G$, which is crucial when implementing feedback controlled wave-absorbers.[29]

A. Governing equations

The numerical simulation solves the 2D two-phase laminar Navier–Stokes equations with two incompressible fluids (water and air phases). The mass conservation equation is also solved in primitive variables incorporating the VOF model to deal with each fluid phase.[20] These equations can be written in the vector form as

$$\nabla \cdot \mathbf{U} = 0, \tag{1}$$

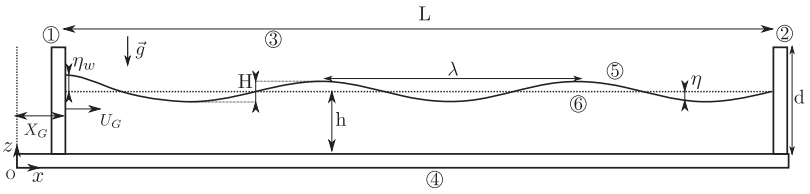

FIG. 1. Schematics of the problem. The numerical domain is composed of (1) the piston wavemaker, (2) the tank end boundary, (3) the atmosphere, and (4) the seabed. The generated waves (5) at the free-water surface are measured with respect to the mean still water level (6) h.

$$\frac{\partial(\rho\mathbf{U})}{\partial t} + \nabla\cdot(\rho\mathbf{U}\,\mathbf{U}) - \nabla\cdot(\mu\nabla\,\mathbf{U}) - \nabla\,\mathbf{U}\cdot\nabla\mu = -\nabla p^{*} - \mathbf{g}\cdot\mathbf{x}\nabla\rho + \sigma\kappa\nabla\alpha, \tag{2}$$

$$\frac{\partial\alpha}{\partial t} + (\nabla\cdot\mathbf{U})\alpha = 0, \tag{3}$$

where $\mathbf{U}$ is the velocity vector, $p*$ is the pseudo-dynamic pressure ($p^{*} = p - \rho\mathbf{g}\cdot\mathbf{x}$), ρ is the density, μ is the dynamic viscosity, g is the gravity acceleration, $\mathbf{x}$ is the position vector, and σ is the fluid surface tension coefficient. The volume fraction α is introduced to deal with the two-phase formulation within the volume of fluid (VOF) framework. κ is defined as follows:

$$\kappa = -\nabla\cdot\frac{\nabla\alpha}{|\nabla\alpha|}. \tag{4}$$

In the two-phase formulation, density and viscosity on each domain cell are computed as a weighted mean of the form[30,31]

$$\rho = \alpha\rho_{water} + (1-\alpha)\rho_{air}, \tag{5}$$

$$\mu = \alpha\mu_{water} + (1-\alpha)\mu_{air}. \tag{6}$$

The relevant dimensionless number in this work is the Froude number $Fr = U_G/\sqrt{gh}$ controlling the wave propagation dynamics. Viscous effects become important during the interaction of the starting wave with the piston wavemaker taking place at the beginning of the wave generation as we will discuss in Sec. III C.

B. Boundary conditions

Boundary conditions employed in this work are summarized in Eq. (7). On the piston wavemaker wall, we impose no-slip condition for all velocity components. The initial still water level h is always established before any wavemaker motion by initializing α. The volume fraction α is bounded and may adopt any value within $0 \le \alpha \le 1$ in any place of the physical domain, and Neumann boundary conditions, set to 0, are applied at all boundaries for the α variable as well. In particular, at the wavemaker, such a condition forces the contact angle of the interface to be perpendicular to the wavemaker wall, which agrees with the experimental results of Refs. 15 and 32 for the case of a continuously accelerated wavemaker. In this work, the piston wavemaker moves according to an input velocity signal displayed in Fig. 3(a). A velocity step U_G drives the piston resulting in linear dependency on time displacement $X_G(t)$. At the piston wavemaker wall, the velocity matches the velocity of the moving boundary in the x-direction only. A no-slip condition is used at the seabed wall and the right end wall. The pressure is set to a reference pressure (in this case 0) at the atmosphere boundary, and 0-Neumann conditions are used at the other locations. A zero-gradient condition is applied at the atmosphere for outflow, and a velocity u_ϕ is assigned for inflow based on the flux in the patch-normal direction. The boundary conditions for the velocity, pressure, and α variables can be summarized as

$$\begin{cases} x = X_G(t) \rightarrow & u_x = U_G(t), & u_z = 0, & \dfrac{\partial p^{*}}{\partial x} = 0, & \dfrac{\partial\alpha}{\partial x} = 0, \\ x = L \rightarrow & u_x = 0, & u_z = 0, & \dfrac{\partial p^{*}}{\partial x} = 0, & \dfrac{\partial\alpha}{\partial x} = 0, \\ z = 0 \rightarrow & u_x = 0, & u_z = 0, & \dfrac{\partial p^{*}}{\partial z} = 0, & \dfrac{\partial\alpha}{\partial z} = 0, \\ z = d \rightarrow & \text{inflow: } u_x = 0, \\ & \text{outflow: } \dfrac{\partial u_x}{\partial z} = 0, & u_z = u_\phi, \\ & & \dfrac{\partial u_z}{\partial z} = 0, & p^{*} + \dfrac{1}{2}|\mathbf{u}|^2 = 0, & \dfrac{\partial\alpha}{\partial z} = 0. \end{cases} \tag{7}$$

C. Numerical method

The governing equations were solved with the open-source software *OpenFOAM* version 5.[33] *OpenFOAM* is an object oriented C++ toolbox for solving continuum mechanics problems with the finite volume method. *OpenFOAM* presents many advantages: as released under the GNU General Public License, it is free and open-source (no licensing fees, unlimited number of jobs, users, and cores). It is also largely used in the scientific community and thus has been validated for many applications. We use *interDyMFoam*, a solver of the Navier–Stokes equations for two incompressible isothermal immiscible phases using the volume of fluid (VOF) method. It increases the capabilities of previous solvers allowing one to handle dynamic mesh motion. *OpenFOAM* solves a single equation of momentum for the two-phase mixture by introducing a volume fraction advection equation of the VOF method used to capture the interface between the phases. Hirt and Nichols[20] presented this method as an efficient and simple way of treating the free surface in numerical simulations, as it stores a minimum amount of information. This method should be carefully used when the surface tension becomes important. Some numerical solvers such as *interDyMFoam* impose some restrictions in order to keep a sharp interface between both fluid phases. An additional term called artificial compression is introduced here,[31]

$$\frac{\partial\alpha}{\partial t} + \nabla\cdot(\alpha\mathbf{U}) + \nabla\cdot(\mathbf{U}_c\alpha(1-\alpha)) = 0, \tag{8}$$

$$U_c = \min(C_\alpha|\mathbf{U}|, \max(|\mathbf{U}|)). \tag{9}$$

C_α is a user defined coefficient whose default value is 1. The additional term is only active close to the interface because of the product $\alpha(1-\alpha)$ and does not impact the solution outside the interface

region. Its role is to compress the interface and maintain α between 0 and 1 if used with discretization techniques. In the post-processing stage, the value of $\alpha = 0.5$ is chosen to detect the free surface, which is carried out thanks to linear interpolation. The *interDyMFoam* solver uses the PIMPLE algorithm, which combines both SIMPLE (Semi-Implicit Method for Pressure Linked Equations)[34] and PISO (Pressure Implicit Split Operator)[35] algorithms and allows for bigger time steps. Simulations were performed on a CPU Xeon E5-2660 v2 cluster running on Simple Linux Utility for Resource Management (Slurm) and based on MPI libraries. The CPU run time for a one second transient simulation and a typical wave was about 2.4 h for a 400 000 element mesh and $\Delta t = 5 \times 10^{-4}$ s time step. The geometry of the wave tank required a fine spatial discretization, particularly in zones such as the water–air interface and zones of high velocity gradients such as the wavemaker walls. Explicit schemes are used so that special care is taken when choosing the time step regarding the mesh size and CFL condition below 1. As a result of the rapid input velocity signals during the wave formation and subsequent progression along the wave tank, the temporal discretization requires time steps smaller than 10^{-3} s; thus, we choose a time step size $\Delta t = 5 \times 10^{-4}$ s for all the simulations.

D. Mesh independence tests

A series of mesh tests are performed to look for mesh independent results. We consider two test cases in order to achieve mesh convergence: (i) the study of the response to an input velocity step characterized by the overshoot and the steady state water height, and the rising, peak, and settling times, as found on the time response of linear dynamical systems, and (ii) the wave propagation of linear waves along the 2D wave tank (wave height, wavelength). In the first case, a set of uniform rectangular cell meshes are generated to look for mesh independence. Most sophisticated meshes, with a uniform zone at the water–air interface, which includes the minimum and the maximum water height during the whole simulation, are also set up. They include refinement at the wavemakers and are denominated "non-uniform." They allow decreasing the computation time as the mesh size is kept in reasonable limits. The mesh, generated thanks to the *blockMesh* program, is built from three characteristic elements: the cell width at the piston wall Δx_w, the cell width in the wave propagation zone (far from the walls) Δx, and the cell height in the wave propagation zone Δz. Δx_w will be determined from the uniform mesh study in (i). From the wavemaker, the longitudinal element size Δx_i is being computed with the following geometric law: $\Delta x_i = \Delta x_w r^{(i-1)} \forall i < n_j$, where r is the geometric growth rate. After n_j cells, the elements reach a constant size Δx in the wave propagation zone. A similar calculation allows us to define the vertical element size from outside the interface zone. Both Δx and Δz are set up considering the number of cells per wavelength and cells per wave height, respectively. These parameters will be set in (ii). Figure 2 shows the mesh in the x–z plane, while one cell size is set up in the y-direction. Mesh type and properties are displayed in Table I. These preliminary tests with different meshes allow an appropriate choice of the mesh size without compromising accuracy and CPU time (cf. Fig. 2). The dynamic mesh is modeled using a mesh expansion/contraction strategy. The mesh uniformly contracts and expands, conserving the global mesh cell volumes as these motions are relatively small compared to the tank length.

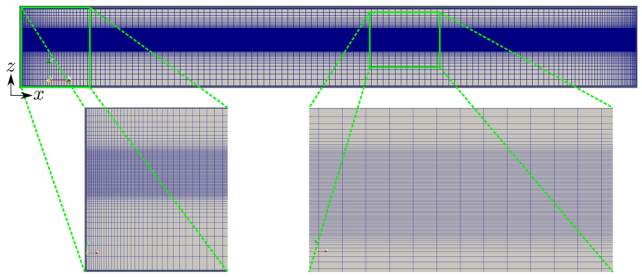

FIG. 2. Non-uniform mesh overview and zoom at the wavemaker and water–air interface. In this case, the wave tank dimensions are 2 m × 0.25 m and water depth is 0.15 m.

1. Step response

In order to fully test the capacity of the code to represent sudden and rapid water surface elevation, we choose to perform a step response of the water tank. The input signal is a velocity step, as

TABLE I. Mesh properties to study the wavemaker response to a velocity step. Δx_w is the cell size in the x-direction at the piston wavemaker, Δx is the cell size in the x-direction in the wave propagation zone, Δz is the cell size in the z-direction at the water–air interface, η_o is the overshoot water height at the piston wavemaker, η_{ss} is its steady state value, and t_r, t_p, t_s are the rising time, the peak time, and the settling time, respectively. The area a is used as an entry for the GCI study.[36]

		Δx_w (m)	Δx (m)	Δz (m)	a (m^2)	Number of cells	η_o (m)	η_{ss} (m)	t_r (s)	t_p (s)	t_s (s)
Uniform	M_U^1	0.0100	0.0100	0.005 0	5×10^{-5}	10 000	0.0356	0.0257	0.0536	0.1253	0.2819
	M_U^2	0.0050	0.0050	0.002 5	1.25×10^{-5}	40 000	0.0342	0.0257	0.0481	0.1116	0.2979
	M_U^3	0.0025	0.0025	0.001 0	2.5×10^{-6}	200 000	0.0340	0.0259	0.0479	0.1298	0.2905
	M_U^4	0.0015	0.0015	0.000 75	1.125×10^{-6}	443 889	0.0340	0.0258	0.0491	0.1237	0.2939
	M_U^5	0.0013	0.0013	0.000 5	6.5×10^{-7}	769 000	0.0341	0.0259	0.0493	0.1246	0.2927
	M_U^6	0.0011	0.0011	0.000 26	2.9×10^{-7}	1 748 916	0.0341	0.0259	0.0494	0.1247	0.2909
Non-uniform	M_{NU}^7	0.0010	0.0363	0.001 0	...	17 115	0.0340	0.0258	0.0491	0.1264	0.2976
	M_{NU}^8	0.0010	0.0181	0.001 0	...	20 055	0.0340	0.0258	0.0492	0.1262	0.2965
	M_{NU}^9	0.0010	0.0091	0.000 57	...	47 025	0.0341	0.0258	0.0488	0.1250	0.2954

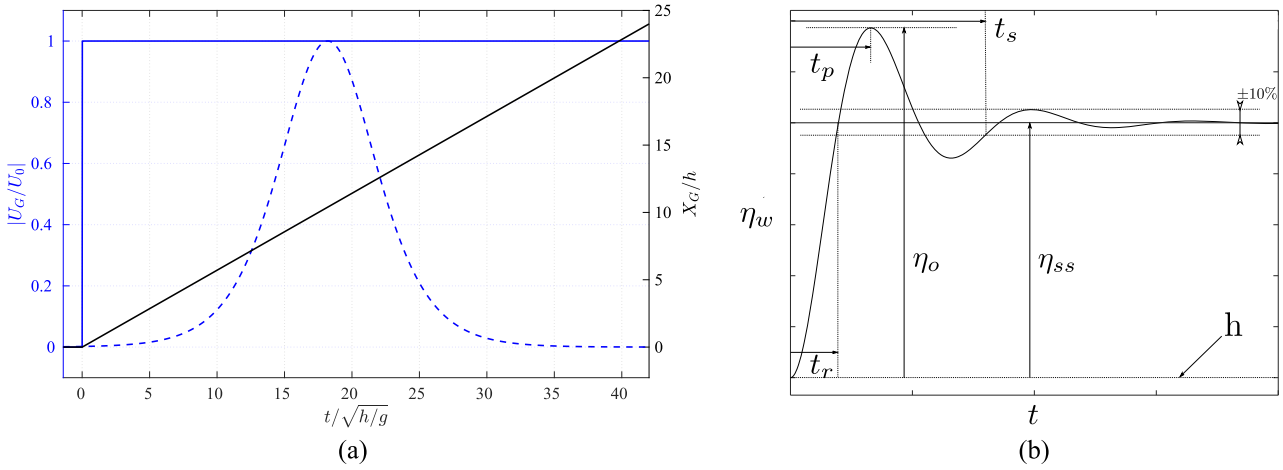

FIG. 3. (a) Normalized input signal for the step response test as a function of non-dimensional time (continuous blue line). The piston velocity $U_G(t)$ is normalized by its maximum value U_0. We also display the piston position X_G normalized by the water depth of the wave tank (continuous black line). The smooth function for the wave train generation in Sec. III D is also shown (by the dashed blue line). (b) Characteristic amplitude and timescales in the step response of a second order system. η_o, η_{ss} are the overshoot and steady state values, respectively, and t_r, t_p, t_s are the rising, peak, and settling times, respectively. The steady state height is $\eta_{ss} > h$ as the piston wavemaker moves constantly at U_G.

shown in Fig. 3(a), and given by

$$U_G(t) = U_0\Theta(t), \tag{10}$$

where $\Theta(t)$ is the Heaviside function. The step value is 0 for negative times and $U_G = U_0$ for positive times, resulting in a linear displacement $X_G(t)$ of the piston wavemaker. In this part of the study, we set the tank length to $L = 4$ m, the tank height to 0.25 m, and the mean still water level to $h = 0.15$ m. Mesh M_U^1 is the coarsest and M_U^6 the finest. M_{NU}^7 to M_{NU}^9 are non-uniform meshes as previously described. They use a cell size at the wall defined later on in the conclusion of the uniform mesh study and geometric growth rate $r = 1.05$ in the x-direction and $r = 1.2$ in the z-direction. For the finest mesh in the z-direction (mesh M_U^6), it is necessary to reduce the time step to keep the Courant number below 1. This is why the time step is set for all meshes to $\Delta t = 10^{-4}$ s. The measured quantity is the water elevation at the wavemaker η_w. The variables of interest are described in Fig. 3(b) and are the following: η_o, η_{ss}, the overshoot and steady state values, respectively, and t_r, t_p, t_s, the rising, peak, and settling times, respectively. Results are reported in Table I and shown in Fig. 4. Figure 4(a) shows the time series of the water elevation at the piston wavemaker, $\eta_w(t)$, for each mesh. The results of the four finest meshes are similar. A Grid Convergence Index (GCI) study[36] is carried out with meshes 4, 5, and 6. The local order of accuracy p ranges from 0.18 to 17.57 with a global average of 4.98. This apparent average order is used to assess the GCI error at every point as suggested in Ref. 36. The error made in the last mesh is really low (the maximum GCI error is 0.3%), which allows us to say that the results do not depend on the mesh. Figure 4(b) shows the error for every point, and a zoom around the overshoot is displayed in the inset where errors increase. The mean error is an order of magnitude lower (0.03%). The errors on the overshoot and the steady state values are very low. Figures 4(c) and 4(d) show the convergence of the different parameters composing the typical response to the step (overshoot and steady state water elevation, rising, peak, and settling times). They show that for these parameters, the limit of convergence is mesh M_U^3. It is chosen, for obvious practical reasons, to work with mesh M_U^3 at the wavemaker, which allows us to decrease computational times while assuring convergence. Non-uniform mesh shows good agreement with the uniform ones for all variables. In the rest of this work, we make sure that the first cell at the piston wavemaker wall is kept below $\Delta x_w = 0.0025$ m in the x-direction and $\Delta z = 0.001$ m in the z-direction in order to keep the results independent of the mesh. The number of cells per wavelength and height in the wave propagation zone is analyzed in the following paragraph.

2. Wave propagation

In order to properly study the wave propagation properties as a function of the mesh type and quality, we use an extended wave tank with $L = 8$ m. The mesh is finer at the water–air interface and is kept uniform in the zone where the wave propagates. At the wavemaker, we set $\Delta x_w = 0.001$ m, and a transition is made with a 1.05 cell to cell ratio. The piston stroke is set to $X_0 = 0.004$ m, the wavemaker frequency to $f = 1.25$ Hz, and the piston wavemaker velocity to $U_G(t) = X_0\omega/2\,\sin(\omega t + \delta)$ with $\delta = -\pi/2$. The corresponding wavelength can be estimated from the dispersion relation $\omega^2 = gk\,\tanh(kh)$, where k is the wave number, and in this case, $\lambda = 0.82$ m. A common discretization is given by 20–25 elements per wave height and 60–70 elements per wavelength in recent works.[37] We conduct our test based on three meshes whose properties are shown in Table II, where M_{NU}^7 is the coarsest mesh and M_{NU}^9 the finest one. The number of cells per wave height ranges from 15 to 60, while the number of cells per wavelength ranges from 60 to 240. The time step is set to $\Delta t = 0.001$ s, and the theoretical CFL number is reported. Even if it shows to have a value below 1, the time step for the finest mesh M_{NU}^9 had to be decreased

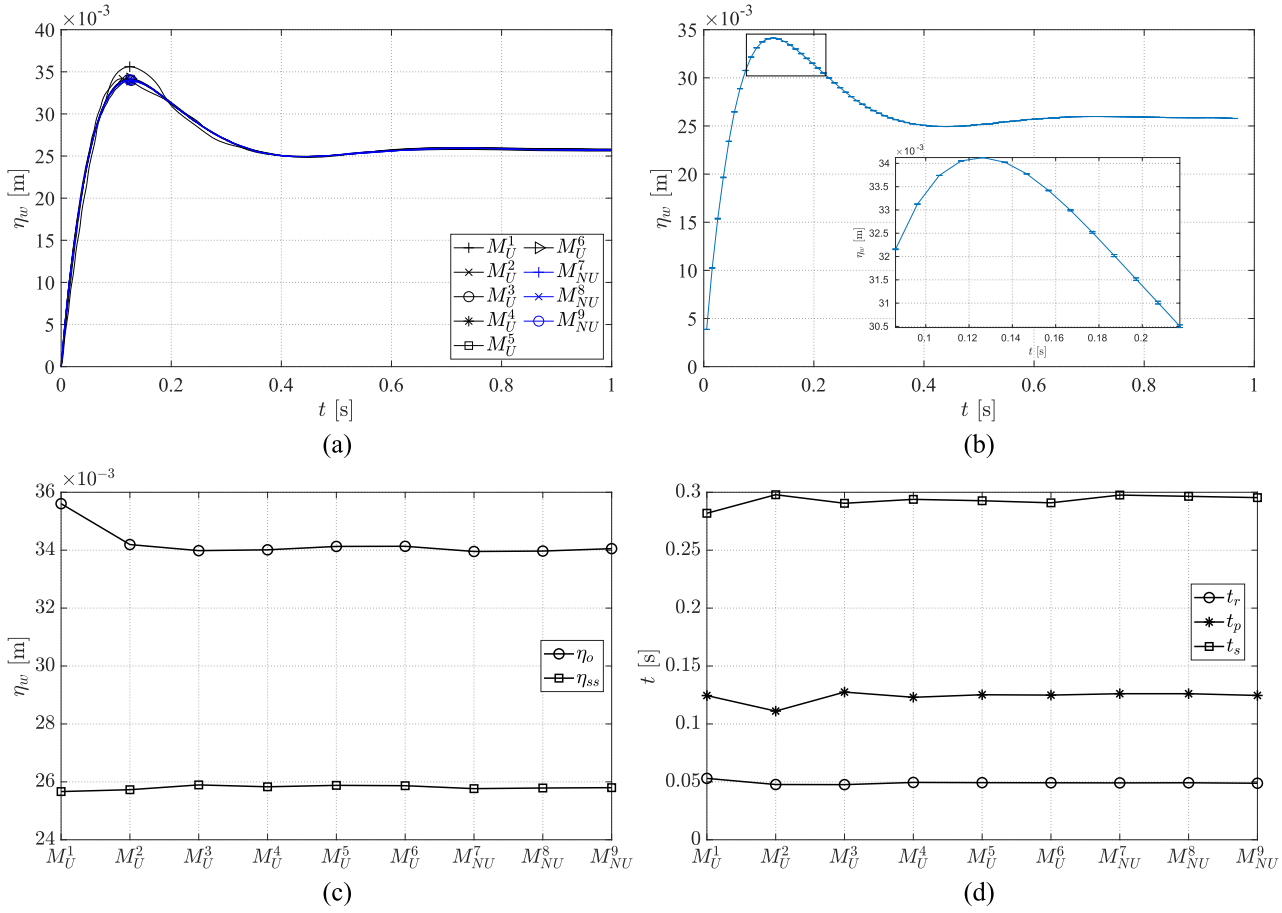

FIG. 4. Step response. (a) Water height at the piston wavemaker for different meshes. Convergence is achieved from mesh M_U^3. (b) Error made due to mesh discretization calculated with the GCI method.[36] A zoom in the overshoot region is also displayed. (c) Overshoot and steady state water height (η_o and η_{ss}, respectively) as a function of the mesh. These variables seem to have converged at mesh M_U^3. (d) Characteristic times (rising time t_r, peak time t_p, and settling time t_s) as a function of the mesh type. Converged values are found from mesh M_U^3.

to $\Delta t = 0.0005$ s to avoid divergence due to the use of explicit schemes. The simulation end time is 10 s, and two probes are set at $x = 2$ m and $x = 4$ m from the origin of the coordinate system (cf. Fig. 1).

TABLE II. Mesh characteristics and their theoretical CFL number for the wave propagation problem.

	M_{NU}^7	M_{NU}^8	M_{NU}^9
Cells/H	15	30	60
Cells/λ	60	120	240
Δx_w (m)	0.001 00	0.001 00	0.001 00
Δx (m)	0.013 60	0.006 80	0.003 40
Δz (m)	0.000 30	0.000 15	0.000 07
Total number of cells	40 734	107 184	303 232
CFL number	0.15	0.29	0.59

Figure 5(a) shows the water level at the wavemaker wall $\eta_w(t)$. No differences between the meshes are observed as expected, since the refinement in the x-direction and in the z-direction is finer than the necessary one studied in (i). Figure 5(b) shows the differences between the meshes that are used at $x = 4$ m. A zoom over the highest value and for three wave periods is shown in Fig. 5(c). The coarse mesh M_{NU}^7 effectively produces minor differences from the other two, specially at the maxima and minima. The results for the probe at $x = 2$ m are compared with the theory in Ref. 6 and shown in Fig. 5(d). The errors of wave crests and troughs with the wavemaker theory are shown in Table III. The results are quite accurate for the three meshes (almost all cases with a rms deviation below 0.1 mm) although the coarse mesh lacks accuracy at the maxima and minima. It is chosen to work with the medium mesh M_{NU}^8 in the rest of this work as it allows accurate wave height data and reduces the computational time compared to the fine mesh. The final mesh characteristics are given in Table IV.

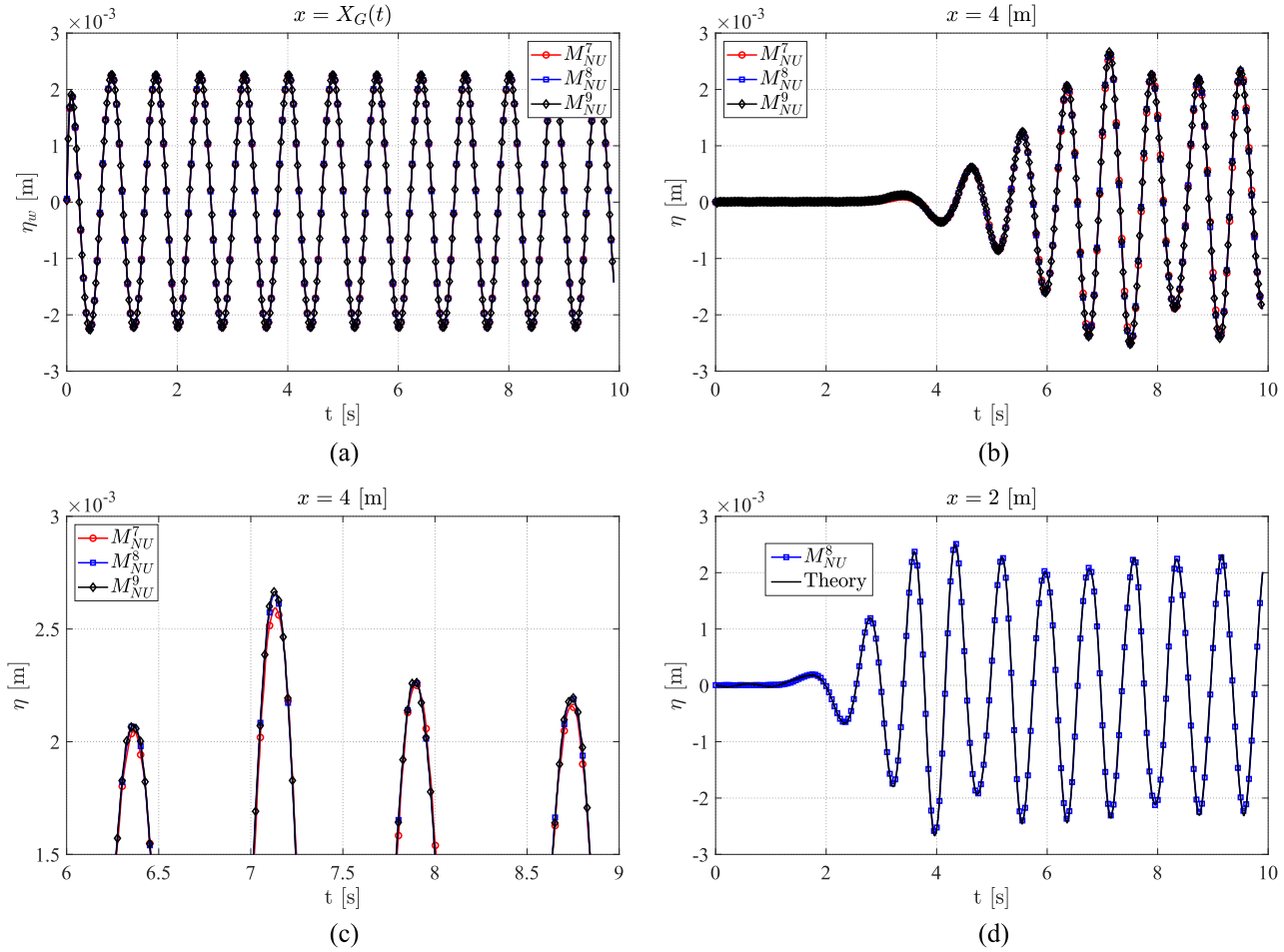

FIG. 5. Continuous wave propagation. (a) Water height at the piston wavemaker η_w as a function of time. (b) Water height at $x = 4$ m as a function of time. (c) Water height at $x = 4$ m as a function of time, with a zoom over times between 6 s and 9 s. (d) Comparison between the medium mesh and the wavemaker theory[6] at $x = 2$ m. The medium mesh well represents the wavemaker theory. It allows us to validate the wave generation process with the medium mesh for small waves.

TABLE III. rms deviation relative to the theory in Ref. 6 over the 10 s simulation for both wave gauges at $x = 2$ m and $x = 4$ m. The rms deviation is calculated according to $\Delta_{RMS} = \sqrt{\sum_{j=1}^{N}\left(\eta_j - \eta_j^{theo}\right)^2}/N$.

	$\Delta_{RMS}(x = 2m)$ (m)	$\Delta_{RMS}(x = 4m)$ (m)
M^7_{NU}	7.2×10^{-5}	1.10×10^{-4}
M^8_{NU}	4.3×10^{-5}	0.80×10^{-4}
M^9_{NU}	4.4×10^{-5}	0.83×10^{-4}

TABLE IV. Characteristics of the final mesh.

Δx_w (m)	Cells/λ	Cells/H	r_x	r_z
0.001	120	30	1.05	1.20

III. RESULTS

One of the objectives in this work is to characterize the piston wavemaker system by applying a series of velocity steps. First, a qualitative approach is taken and observations are made about the wave generation at small times and the generated wave pulse is studied at longer times and far away from the wavemaker. Then, we compare the characteristic variables with the theory developed in Ref. 11 and explore higher Froude number regimes. The forces exerted on the wavemaker and the power involved in the wave generation process are studied, and an active wave absorption strategy is finally designed. The step velocity tests are carried out at four mean still water levels: $h = 0.050$ m, 0.075 m, 0.100 m, 0.150 m, and for velocities ranging from $U_G = 0.005$ m/s to $U_G = 0.4$ m/s. In this problem, the fundamental velocity, length, and timescales are $\sqrt{gh}$, h, and $\sqrt{h/g}$, respectively. The problem can be written as $f(\eta_w, \rho, g, h, t, U_G) = 0$, but according to the Buckingham π theorem,[38] it can be reduced to $f\left(\eta_w^*, t^*, Fr\right) = 0$, where η_w^* and

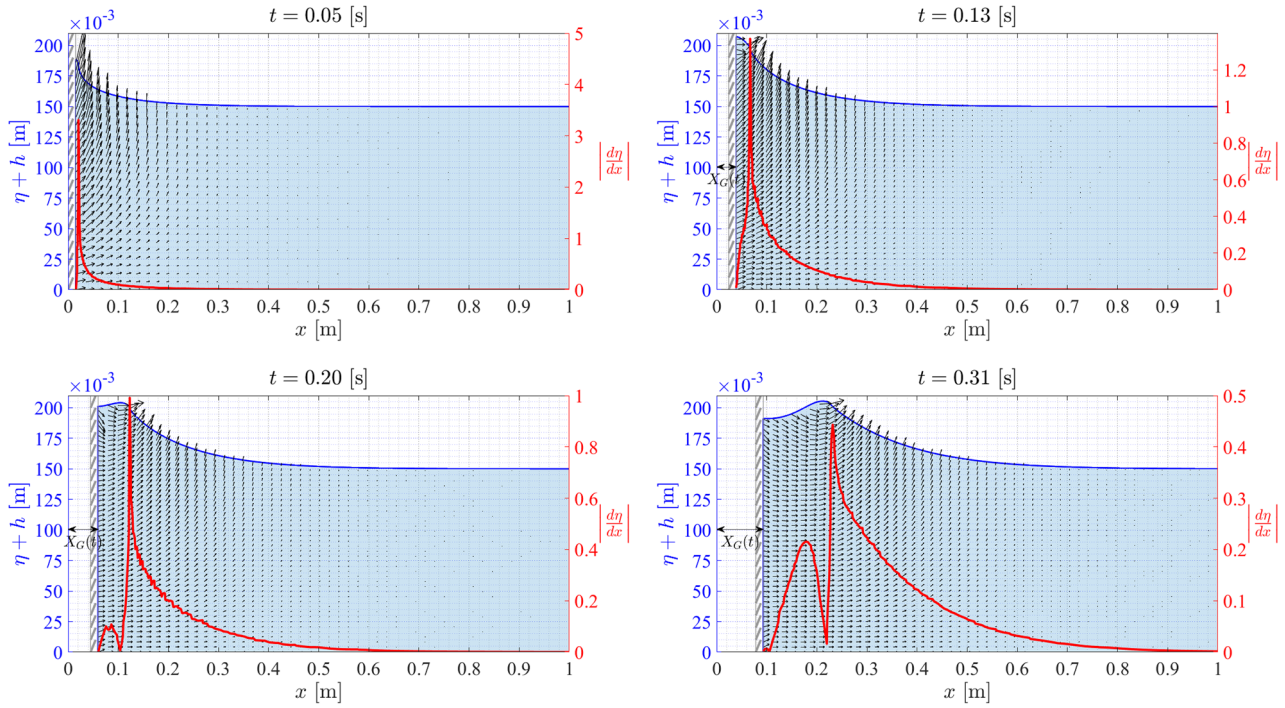

FIG. 6. Time snapshots of the wave pulse generated (from left to right) by a velocity step applied to the wavemaker motion. The wave pulse is called here the overshoot-wave as it is created by the overshoot of the water elevation at the piston wall. The wave profile (wave height as a function of x) is plotted in blue and the wave steepness as a function of x in red. The velocity step is 0.3 m/s, and the mean still water level h is 0.15 m. The shown times are $t = 0.05$ s $\approx t_r$, $t = 0.13$ s $\approx t_p$, $t = 0.20$ s, and $t = 0.31$ s $\approx t_s$.

t^* are the dimensionless water height at the piston wavemaker and time, respectively. In the next sections, as a consequence of this analysis, we will express the results in a dimensionless way using the relevant variables η_w^*, t^*, and Fr.

A. First instants—The overshoot-wave

While applying a velocity step to the wavemaker, one observes the formation of a surface water pulse propagating along the tank as it is shown in Figs. 6 and 7. The wavemaker displaces a given volume of water, and as the fluid is incompressible, this volume is found under the wave profile. The water height at the wavemaker $\eta_w(t)$ first rises along the wall reaching a maximum value, the overshoot. Then, the wave pulse comes off the wall and self-propagates in the positive x-direction, as the phase velocity of the wave becomes higher than the wavemaker velocity $C_p > U_G$. In the time snapshots in Fig. 6, the wave pulse generated by the velocity step is called the overshoot-wave as it is created by the overshoot of the water elevation at the piston wall.

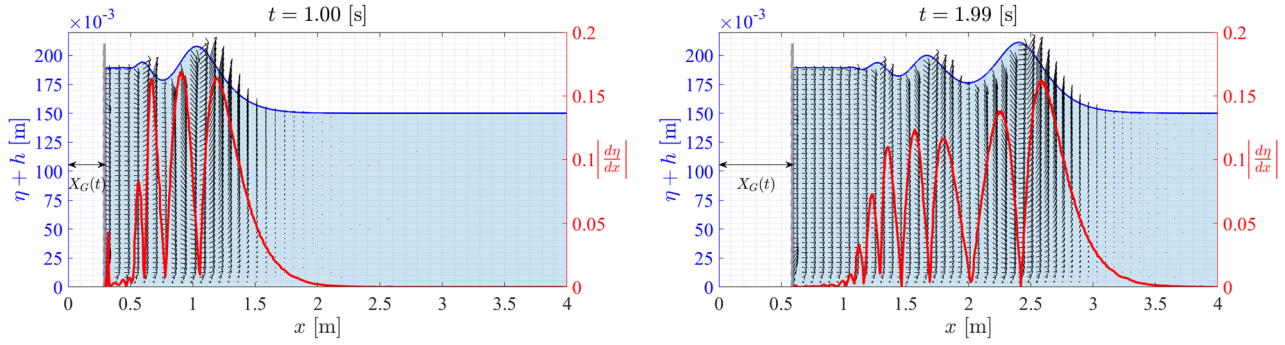

FIG. 7. Snapshots at times $t = 1.00$ s and $t = 1.99$ s of the wave pulse generated (from left to right) by a velocity step applied to the wavemaker motion. The wave profile (wave height as a function of x) is plotted in blue and the wave steepness as a function of x in red. The velocity step is 0.3 m/s, and the mean still water level h is 0.15 m. Note the change in scale in the x abscissa compared to Fig. 6.

After leaving the wavemaker, the water height at the wavemaker remains constant, as indicated in Fig. 9. The wave pulse profile for times $t = 0.05$ s, 0.13 s, 0.20 s, 0.31 s, which correspond to the first instants of the pulse formation, is displayed in Fig. 6. In Fig. 6, the wave steepness, defined as $|d\eta/dx|$, is superimposed. We observe that the wave steepest shape occurs at the very first instants of its formation, i.e., at $t = 0.05$ s, where the maximum steepness is higher than 3. When the pulse starts leaving the piston wavemaker, its steepness decreases to values under 1. Such high steepness is associated with the non-linear properties of the overshoot-wave. Another important parameter useful to evaluate when it comes to apply linear theory is the wave height to mean still water level ratio η/h. It is relatively important (values around 0.5 in this example); therefore, Airy theory of linear waves cannot be applied here. The profile of the generated pulse at longer times is shown in Fig. 7, as well as its steepness as a function of the x-coordinate. We can notice the generation of wiggles after the main pulse propagating downstream as already described. The wiggles are trailing waves whose height decreases in the vicinity of the piston wavemaker, while the front wave height increases as it travels. These wave structures are described in the work of Ref. 11 and are a consequence of wave dispersion. The piston motion creates a wave packet in which each wave travels at different velocities due to dispersion effects. We identify the created wave to be an undular bore, which was experimentally and theoretically studied in Refs. 39 and 40, respectively, while Stoker[41] predicted that an impulsive wavemaker would generate an undular bore as in the present case. Recently, similar bore structures were obtained from a different approach where a moving weir at the bottom of a channel may produce the volumetric water displacements necessary to develop such a wave.[42]

Undular bores are of particular importance as they appear to more likely represent a real tsunami wave instead of a solitary wave.[43] Important values of the wave steepness are observed during the pulse formation, which decrease rapidly as the pulse propagates without evidence of wave breaking. If the bore strength is important, undular bores may display a wave breaking process.[42] In the time snapshots in Figs. 6 and 7, we observe the vector velocity field of the numerical solution of the Navier–Stokes equations. The vector field becomes intense precisely near the steepness peaks as the overshoot-wave propagates along the tank. The higher the wave height, the higher the intensity of the vector field, which is associated with particle velocity.

The starting overshoot-wave displays a phase celerity C_p as a function of time t, which may be compared with two characteristic properties, the shallow water wave speed $C_p = \sqrt{g(h+H)}$ and the piston velocity U_G, as shown in Fig. 8. The overshoot-wave celerity may be estimated from the mean celerity as $C_p = \delta x/\delta t$ between consecutive wave crests or looking for maximum steepness at different time steps during the propagation, as shown in Fig. 6. As the phase celerity of the overshoot-wave is found to be higher than the piston velocity from the first instants of motion, the overshoot-wave travels fast enough to leave the piston wavemaker. As the wave propagates along the tank, its phase celerity increases with time, approaching the shallow water phase speed given by $C_p \to \sqrt{g(h+H)}$. This behavior agrees with that in potential theory and therefore allows us to validate the capabilities of the numerical wave tank for wave propagation.

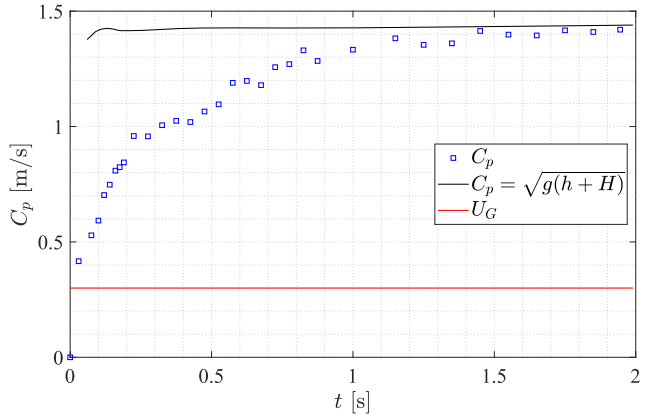

FIG. 8. Instantaneous overshoot-wave phase celerity $C_p(t)$ (in blue) as a function of time for the case $h = 0.15$ m and $U_G = 0.3$ m/s. For times lower than 0.2 s, the maximum of the steepness is used to determine the location of the overshoot-wave. For later times, the maximum of the wave profile is taken as the location of the wave. The wave celerity can be compared to the piston step velocity U_G and to the phase velocity of shallow water waves.

B. Response to a velocity step

A positive velocity step ($U_G > 0$) creates a water pulse, which leaves the wavemaker wall as it propagates along the tank. The step response is recorded as the water height or water elevation at the wavemaker wall $\eta_w(t)$ and is presented in Fig. 9(a).

The water height first increases, reaching a maximum or overshoot η_o at peak time t_p, before approaching a lower steady state value η_{ss}. It is of particular interest to note the similarity of this dynamic response to a step response of the second order system [cf. Figs. 9(a) and 3(b)]. The time response of second order linear systems depends on the type of the input signal. For a step input, the system exhibits a characteristic response defined by the rising time t_r, the maximum overshoot η_o, and the steady state value η_{ss} obtained at a given settling time t_s.[28] In Fig. 9(b), we present the normalized time response using the Froude number as in the theory proposed in Ref. 11. We can observe that after reaching its maximum value, the overshoot, the water height slightly oscillates and decreases to its steady state value $\eta_{ss} = hFr$. The step response for small Froude numbers found in this work is in agreement with that in the theoretical work of Ref. 11. Nevertheless, some differences with the theory are observed in the overshoot behavior for higher Froude numbers. The overshoot starts to increase beyond the theoretical prediction, and the steady state value approaches a slightly higher value than the expected one from theory, $\eta_{ss} = hFr$, as we will discuss in Sec. III B.

The relative deviation from theory[11] is presented in Table V for the four mean still water levels and the velocity range from 0.005 m/s to 0.3 m/s. The relative deviations are defined as $\Delta_o = \left|\eta_o - \eta_o^{ref}\right|/\eta_o^{ref}$ and $\Delta_{ss} = \left|\eta_{ss} - \eta_{ss}^{ref}\right|/\eta_{ss}^{ref}$, where the superscript ref refers to the study of Ref. 11. The arrows indicate how the Froude number changes while varying the step velocity or the mean still water level. It is interesting to note that the relative deviation stays low for the steady state value (< 10.5% for all velocities and mean still water levels). For both overshoot and steady state values, the

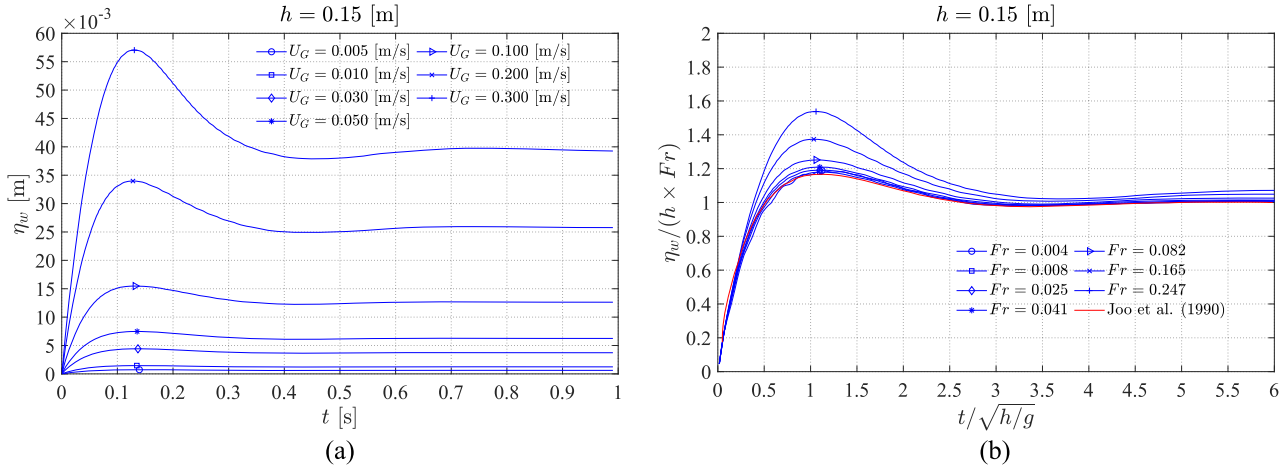

FIG. 9. (a) Water height at the wavemaker as a function of time. (b) Non-dimensional water height as a function of non-dimensional time. A comparison between the CFD simulation and the theoretical study carried out in Ref. 11 is shown.

deviation decreases with the increase in the water level (which actually corresponds, for a given step velocity, to lower Froude numbers). Finally, the deviation for the overshoot value can reach high values (> 40%) for the highest Froude numbers (high velocity, low mean still water level).

The dominant controlling parameter in this work is the Froude number Fr defined as the ratio between inertial ($\rho h^2 U_G^2$) and gravitational ($\rho g h^3$) forces, and thus, $Fr = U_G/\sqrt{gh}$. The similarity of the system response to the typical second order response under a step velocity can be analyzed through the characteristic timescales and maximum overshoot of the response. Timescales as well as the amplitude of the water height response must be plotted as a function of the step velocity U_G. As in many feedback control systems, the time response of a second order system will be completely determined when one knows the maximum overshoot η_o, the steady state amplitude η_{ss}, and the rising, peak, and settling times t_r, t_p, t_s, respectively. If the time response is correctly described by the second order response, we should find a scaling law for the characteristic timescales at different water depths h and step velocities U_G otherwise said the Froude number.

The overshoot η_o as a function of the step velocity U_G is plotted in Fig. 10(a) and the steady state η_{ss} is plotted in Fig. 10(c), both for two mean still water levels h = 0.05 m and h = 0.15 m. The steady state values evolve linearly with the generation step piston velocity as they correspond to the water height of the displaced volume, which increases linearly in time as the step velocity U_G is constant for $t > 0$. However, the overshoot dependence on U_G is not linear as the overshoot-wave originates during a rapid transient process. The curve collapse under the proposed scaling is relatively good in the range of mean still water levels shown as $0.05 \le h \le 0.15$ m. The scaling for the overshoot fails when $Fr > 0.2$ as the overshoot-wave height increases over the linear limit and starts to move faster with higher U_G.

TABLE V. Relative deviation from the model of Ref. 11 at different water depths and step velocities ($0.005 < U_G < 0.3$ m/s). The relative deviation is defined as $\Delta_o = |\eta_o - \eta_o^{ref}|/\eta_o^{ref}$, $\Delta_{ss} = |\eta_{ss} - \eta_{ss}^{ref}|/\eta_{ss}^{ref}$. The superscript *ref* refers to the study of Ref. 11. The arrows indicate how the Froude number varies with the step velocity and the mean still water level.

		h = 0.05 (m)		h = 0.075 (m)		h = 0.10 (m)		h = 0.15 (m)	
	U_G (m/s)	Δ_o (%)	Δ_{ss} (%)	Δ_o (%)	Δ_{ss} (%)	Δ_o (%)	Δ_{ss} (%)	Δ_o (%)	Δ_{ss} (%)
↓ Fr	0.005	5.97	1.86	2.42	0.09	3.64	3.96	1.77	0.61
	0.010	3.33	1.19	2.14	0.16	1.15	0.34	0.98	0.39
	0.030	3.69	1.35	3.26	0.80	2.79	0.85	2.00	0.82
	0.050	5.98	2.40	5.09	1.48	4.54	1.60	3.54	1.26
	0.100	11.96	4.11	10.60	3.42	9.33	2.81	7.20	2.37
	0.200	25.73	7.00	23.02	5.97	20.77	5.35	17.64	4.52
	0.300	43.67	10.48	40.42	8.75	37.72	7.72	31.67	6.39
		← Fr							

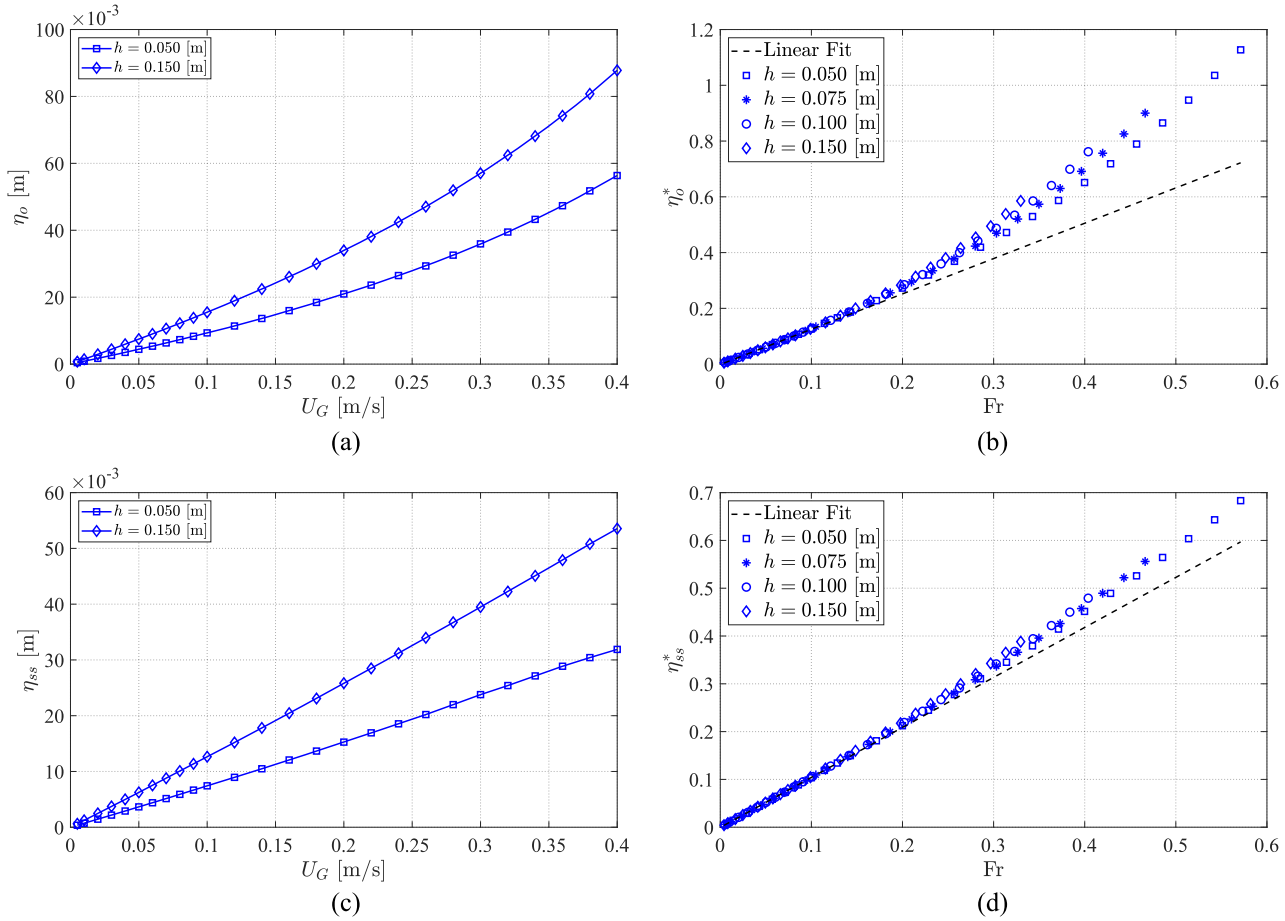

FIG. 10. (a) Overshoot η_o of the water elevation at the piston wall as a function of the piston step velocity U_G. Two still water levels are considered: 0.05 m and 0.15 m. (b) Dimensionless overshoot at the piston wall $\eta_o^* = \eta_o/h$ vs Froude number. A linear fit for low Froude number $Fr < 0.1$ is drawn as a dashed black line for comparison and is given by $\eta_o^* = 1.267 \cdot Fr - 0.0015$ and $R^2 = 0.9994$. (c) Steady state water elevation η_{ss} as a function of the piston step velocity U_G. Two still water levels are considered: 0.05 m and 0.15 m. (d) Dimensionless water height steady state at the piston wall $\eta_{ss}^* = \eta_{ss}/h$ vs Froude number. A linear fit for low Froude number $Fr < 0.1$ is drawn as a dashed black line for comparison and is given by $\eta_{ss}^* = 1.046 \cdot Fr - 0.0005$ and $R^2 = 0.9997$. The different still water levels are represented with symbols.

The evolution of the characteristic timescales of the response to a velocity step is shown in Fig. 11. As it is indicated in Fig. 3, these timescales are associated with a second order dynamical response, where the water height at the piston wall η_w is measured and compared to the steady state height η_{ss}. The rise time t_r and the peak time t_p are associated with the very first instants of the wave motion, when the overshoot-wave is created. Both time constants appear to be independent of the step velocity and provide an interesting scaling independent of the Froude number where the dimensionless timescale is written as

$$t^* = \frac{t}{\sqrt{h/g}}. \tag{11}$$

As shown in Fig. 9, after the main wave leaves the piston zone, the water height on the piston wall scales perfectly with the Froude number as $\eta_w/(hFr) = 1$ because the displaced volume in the steady state regime is entirely determined by the steady state water elevation η_{ss}. The associated settling time t_s is computed within a 10% band and slightly grows with the Froude number. In Fig. 11(b), the time scaling indicated in Eq. (11) produces a very tight collapse of each characteristic time as a function of the Froude number.

The scaling seems to confirm the similarity of the water elevation response with a second order response. As the wave pulse is created by the excess or overshoot of the water elevation at the piston wall, we called it the overshoot-wave. The piston motion produces the displacement of a water volume (per unit depth) given by $V(t) = U_G t h$, which displays an initial transient peak, the overshoot, superimposed into a water slug rising over the mean still water level h. The overshoot-wave has its own dynamics, moving at shallow water speed, running over the water slug, and therefore leaving the displaced volume faster than the linear waves.

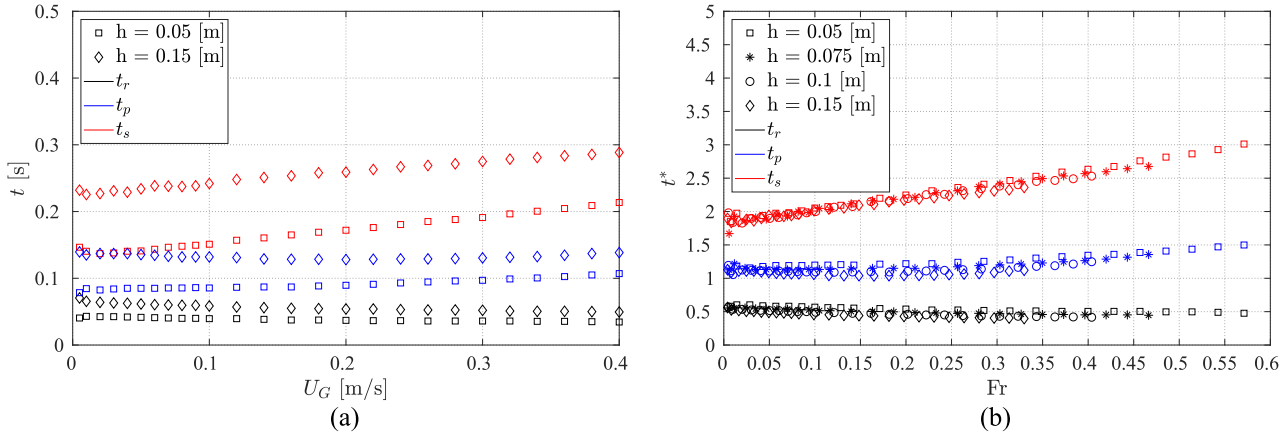

FIG. 11. (a) Characteristic timescales as a function of the wavemaker step velocity U_G. (b) Dimensionless characteristic timescales $t^* = \frac{t}{\sqrt{h/g}}$ as a function of the Froude number.

C. Forces involved in the step response

In this section, we present new findings such as the force decomposition and the maximum power as a function of the Froude number. The objective of this section is to determine the forces originated on the piston wavemaker during the step response. As the problem is 2D, there are only two components of the forces projected on the piston wall in the x-direction and z-direction, which are inertial, pressure, and viscous forces. These forces can be calculated from the pressure and velocity fields at the wavemaker using the stress tensor $\underline{\underline{\varepsilon}}$, the elementary surface area dS (which is in the 2D case an elementary length), and its normal $\mathbf{n}$,

$$\mathbf{F_w} = \int_z \underline{\underline{\varepsilon}} \cdot \mathbf{n}\, dS. \tag{12}$$

The stress tensor is defined as

$$\underline{\underline{\varepsilon}} = -p\begin{bmatrix}1 & 0\\ 0 & 1\end{bmatrix} + 2\mu\begin{bmatrix}\frac{\partial u_x}{\partial x} & \frac{1}{2}\left(\frac{\partial u_z}{\partial x}+\frac{\partial u_x}{\partial z}\right)\\ \frac{1}{2}\left(\frac{\partial u_z}{\partial x}+\frac{\partial u_x}{\partial z}\right) & \frac{\partial u_z}{\partial z}\end{bmatrix}. \tag{13}$$

In Fig. 12, we display the resulting normal and tangential force profiles [$f_x(z)$ and $f_z(z)$, respectively] as a function of the vertical coordinate starting from the bottom of the tank and across both fluid phases. As the mean still water level is $h = 0.15$ m, we note a marked change at the air–water interface $z = 0.15$ m on both types of forces. However, as expected, there is approximately a five orders of magnitude difference between both components. The normal force profile $f_x(z)$ is mainly hydrostatic and insensitive to time, and the viscous or tangential force profile $f_z(z)$ is dependent on time at low U_G values. Wall shear is created during the formation of the overshoot-wave, which indicates the positive increase in the resulting vertical

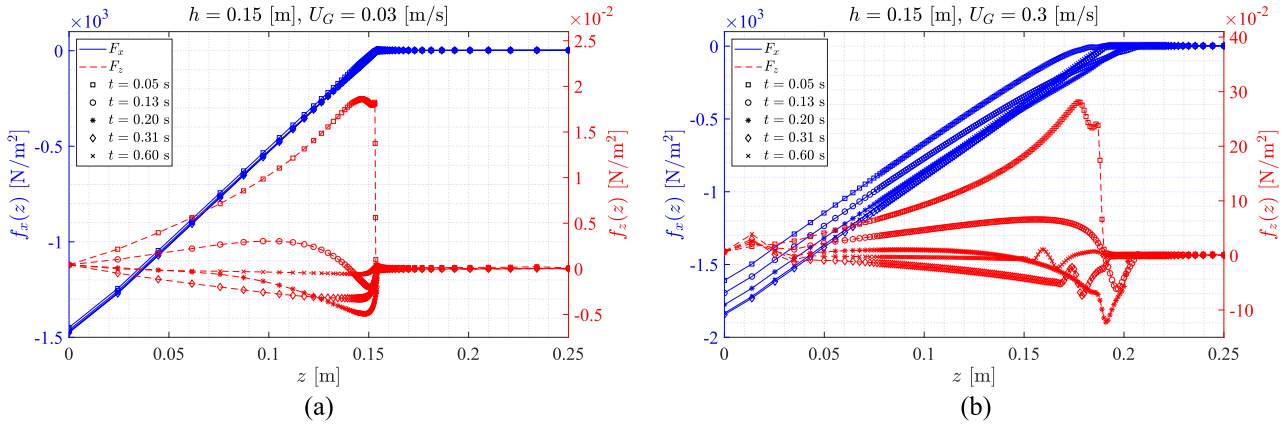

FIG. 12. Normal and tangential force profiles (along the z axis, f_x and f_z, respectively) per unit area at the wavemaker for times 0.05 s, 0.13 s, 0.20 s, 0.31 s, and 0.60 s and $h = 0.15$ m. Notice the difference of power of ten between the two plot vertical axes. (a) $U_G = 0.03$ m/s. (b) $U_G = 0.30$ m/s.

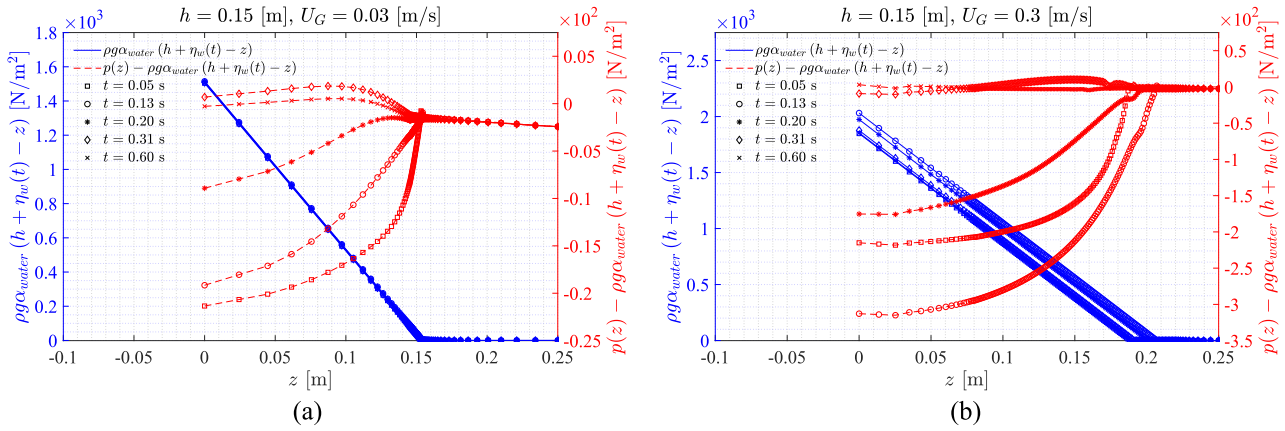

FIG. 13. Pressure forces [hydrostatic $\rho g(h+\eta)$ and $p-\rho g(h+\eta)$] (along the z axis) at the wavemaker for times 0.05 s, 0.13 s, 0.20 s, 0.31 s, and 0.60 s and $h = 0.15$ m. (a) $U_G = 0.03$ m/s. (b) $U_G = 0.30$ m/s.

force $F_z(z)$ in Fig. 14(b). When the overshoot-wave leaves the piston, and the progressing volume pushed by the piston reaches a steady state motion, the shear forces become very small. When the step velocity is increased to $U_G = 0.3$ m/s, the normal force profile $f_x(z)$ displays notorious changes in time but finally evolves into an almost hydrostatic vertical profile, as shown in Fig. 13(b).

In order to verify the effects of the initial fluid motion on the pressure field during the step response, we recorded the pressure profiles at both step velocities $U_G = 0.03$ m/s and $U_G = 0.3$ m/s. The sudden increase in water elevation at the piston wall is more important at higher U_G, which is explained by the higher volume displaced during the initial times. Shear forces change in sign during the formation of the overshoot-wave, as shown in Fig. 12 at both step velocity values. The first water elevation motion produces a positive shear on the piston wall and therefore a positive shear force, which start to decrease, becoming negative as the overshoot-wave leaves the piston wall and the force points downward before vanishing in the steady state regime. The pressure profile is dominated by hydrostatics, as shown in Fig. 12. However, when we subtract hydrostatic pressure due to the initial wave elevation along the z axis, i.e., we plot $p(z) - \rho g(h+\eta)$, we observe traces of the creation of the overshoot-wave on the remanent pressure. As time progresses and the overshoot-wave leaves the piston wavemaker, this remanent dynamic pressure contribution approaches very low values with respect to hydrostatics.

In order to compute the power delivery involved in the process, we must get a good estimate of the resulting forces on the piston. In Fig. 14, we present the normal and tangential forces on the piston wall as a function of time, uncovering the initial transient associated with the overshoot-wave formation and during the steady state regime. The normal and tangential force profiles are obtained integrating the force profiles in Fig. 12 along the piston

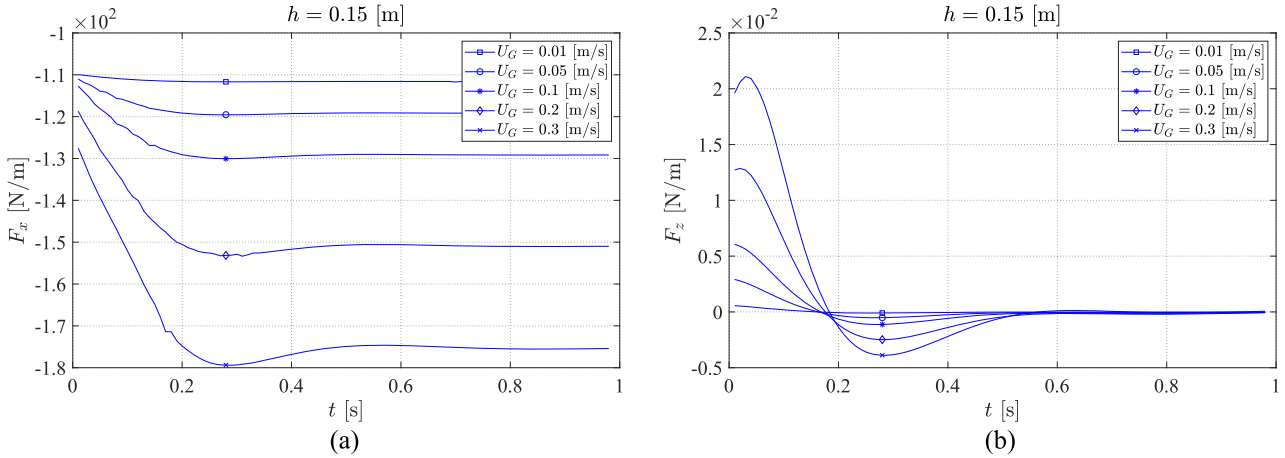

FIG. 14. Resulting net forces per unit length as a function of time. (a) Normal net force $F_x(t)$ and (b) tangential net force $F_z(t)$. The mean still water level is $h = 0.15$ m, and the step velocity range is 0.01 m/s $\leq U_G \leq 0.3$ m/s.

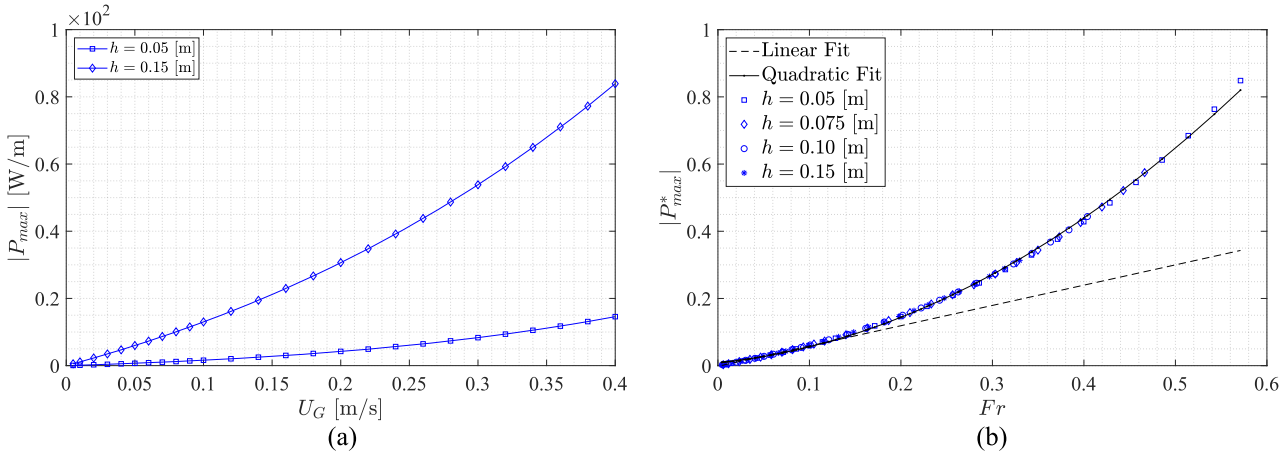

FIG. 15. Power delivery during wave generation. (a) Maximum power per unit length P_{max} vs step velocity U_G at $h = 0.05$ m and $h = 0.15$ m. (b) Dimensionless maximum power per unit length P^*_{max} as a function of the Froude number Fr at different mean still water levels. A quadratic fit is carried out and gives $P^* = 2.0079Fr^2 + 0.2740Fr + 0.0087$ (with the correlation coefficient $R^2 = 0.999\,06$).

wall during each time step, providing an accurate estimation of the net forces shown in Fig. 14. The resulting normal forces $F_x(t)$ are negative as they oppose the piston motion. If we plot the absolute values, we find a time evolution very similar to that of water elevation $\eta_w(t)$ in Fig. 9. The first rising part is associated with the force excess resulting from the creation of the overshoot-wave followed by a steady state force associated with the progressive motion of the mass of the water slug moving at constant velocity U_G. On the other side, the tangential averaged forces $F_z(t)$ shown in Fig. 14 display a change in sense (sign), indicating how the fluid is moving on a boundary layer created on the piston wall. At first, the fluid moves upward, then stops, and then moves downward reaching a local (downward) maximum precisely when the overshoot-wave leaves the piston. The critical time when the resultant shear force is zero $t \sim 0.2$ s does not correspond to the peak time as water is still rising at the bottom of the wavemaker, as shown in Fig. 6. X-force characteristic times (rise and peak times) are much larger than those for the kinematic observations. The minimum shear force time corresponds to the maximum force in the x-direction, showing the correlation between both phenomena. We can imagine that a feedback controlled piston wavemaker might also be designed by measuring the vertical force instead of the one in the direction of the piston motion. If the overshoot-wave is going away leading to a fluid flow downward at the interface, the global motion is more complicated, with a flow still going upward at the base of the piston.

During the design of a piston wavemaker, it is important to evaluate the power input during the step response associated with the wave generation process, as it can be particularly useful in determining the scaling. For example, the *Flowave* facility power demand can creep close to 300 kW when it creates a sea state moving the 168 paddles.[44] Dimensioning the necessary power supply is then of crucial importance. This section is devoted to the evaluation of the energy input required to create a wave pulse resulting from a piston velocity step. The power involved in the step motion of the piston wavemaker is calculated according to the following equation:

$$P(t) = \mathbf{F}_w \cdot \mathbf{U}_w. \tag{14}$$

In this case, the piston wall velocity is $\mathbf{U}_w = U_G\hat{x}$, which is the Heaviside step function. Maximum power delivery as a function of the step velocity is shown in Fig. 15(a). The maximum power corresponds to the maximum water elevation at the piston wall. An expected power increase is found when the step velocity increases, but more impressive is the radical change in the power delivery when the mean still water level is increased. If we look for a scaling of the power delivery, we may use a characteristic force per unit length and velocity to perform the normalization. The normalized maximum instantaneous power can be written as

$$P^* = \frac{P}{\rho g h \sqrt{gh}} = \frac{P}{\rho g^{3/2} h^{5/2}},$$

where P is the power per unit length. The involved force is the hydrostatic pressure force, and the velocity is the corresponding shallow wave celerity $\sqrt{gh}$. In Fig. 15(b), the normalized maximum power P^* vs Froude number collapse for different mean still water levels confirms that the scaling has been properly defined and it follows accurately a quadratic fit (obtained by least square fitting). This law can be used as an entry design tool to define the maximum power that is necessary to generate waves.

D. Active wave absorption

An active wall driven by a feedback controller may be useful not only to cancel wave reflections but also to attenuate wave impacts associated with extreme waves on a vertical wall and reduce their consequences.[45] We have here implemented an active wave absorption strategy using our results from the response of the wavemaker to velocity steps discussed in Sec. III B. First, consider a wave created at the wavemaker, propagating from left to right, whose shape is a leading trough, as shown in Fig. 16. To absorb this wave at the right active wall, a wave crest of nearly opposite phase has to be superimposed, which is generated by the motion of a wave-absorber, a

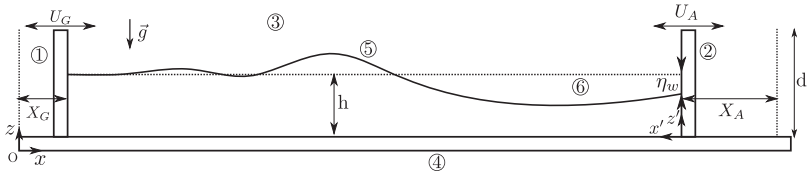

FIG. 16. Schematics of the wave absorption problem. The numerical domain is composed of (1) the piston wavemaker, (2) the piston wave-absorber on which the water level η_w is measured, (3) the atmosphere, and (4) the seabed. The generated waves (5) at the free-water surface are referenced to the mean still water level (6) h. A second frame of reference, on the wave-absorber, is indicated as (x', z').

wavemaker situated at the right side of the tank, according to the following strategy.

Consider a wave-absorber consisting of an active flat wall with a sensor that measures the water level at the wall η_w. On the frame of reference (x', z') associated with this wave-absorber, the positive motion is from right to left (note that x'-direction is the opposite of x). The wall water level η_w can be compared to a reference value $\eta_{ref} = 0$ in order to attenuate reflections. The error $\varepsilon = \eta_{ref} - \eta_w$ is permanently computed and fed into a proportional controller of gain K, which provides the absorption velocity $U_A = K\varepsilon$. The corresponding block diagram of the feedback control strategy using a proportional controller is shown in Fig. 17(a). The efficiency of the control strategy relies on the choice of K where we propose to use the kinematic results of the step response rather than typical methods.[28] In Sec. III B, we have shown that the wall water level at the wavemaker reaches an overshoot value after a short time (as seen in Fig. 9) corresponding to the standard peak time of the system (see Fig. 11). The overshoot η_0, the maximum water level at the wavemaker during the step, was related to the piston velocity U_G by a linear relationship at the lower part ($Fr < 0.2$) of Fig. 10(b). If we want to absorb a wave of given amplitude at the wave-absorber wall, then we are more efficient if the change in amplitude, $\eta_w \to \eta_0(U_G)$, takes into account the corresponding step velocity U_G.

The slope of the linear scaling in Fig. 10(b) (the lower part of the plot) will determine the proportional controller gain K. The absorption velocity is then computed as $U_A = K\varepsilon = -K\eta_w$, where $K = 1/1.267\sqrt{g/h}$ represents the inverse of the linear fit slope in Fig. 10(b).

The dimensionless controller gain $K^* = K\sqrt{h/g}$ is reproduced in Fig. 17(b) at different water levels, for a better understanding of the gain selection.

In order to determine the efficiency and limits of the feedback strategy, an irregular wave train, an undular bore, and regular wave cases were tested. The first example of the implementation of such an absorption strategy for irregular waves is shown in Fig. 18. A wave train is generated by the wavemaker on the left with the help of a smooth velocity pulse function defined as

$$U_G(t) = -\frac{S}{\tau}\mathrm{sech}^2\left(\frac{t - t_0}{\tau}\right), \tag{15}$$

with $S = 0.077$ m, $t_0 = 1.30$ s, and $\tau = 0.342$ s. This function can be visualized in Fig. 3(a). The wave train is moving in the direction of the wave-absorber at the right end part of the wave tank and is formed of a leading trough followed by wiggles (see time $t = 3.5$ s). The waves are then absorbed according to the feedback control strategy with an update of the absorption velocity at every time step, where the error at the wave-absorber wavemaker is plotted in

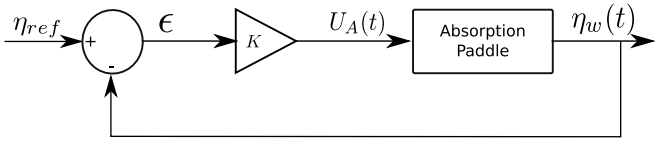

(a)

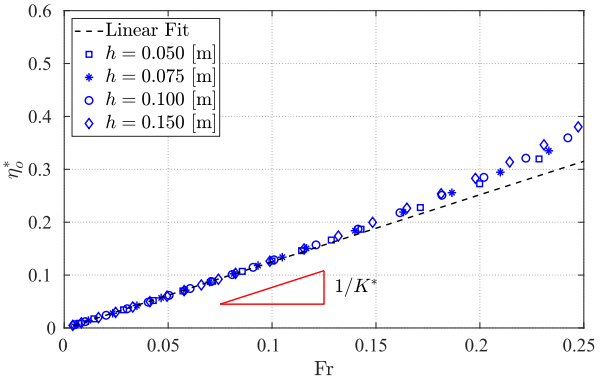

(b)

FIG. 17. (a) Absorption block system. A proportional controller compares the value of the water level at the wave-absorber wavemaker η_w with a reference value η_{ref}. It multiplies then the error with a constant coefficient K, which gives the absorption velocity U_A. Error ε and absorption velocity as a function of time. (b) Dimensionless overshoot-wave height at the paddle as a function of the Froude number, zoomed-in view of Fig. 10(b). The dimensionless proportional coefficient K^* is represented on the curve as the inverse of the slope (in red). $K^* = 1/1.267$ so that $K = 1/1.267\sqrt{g/h}$.

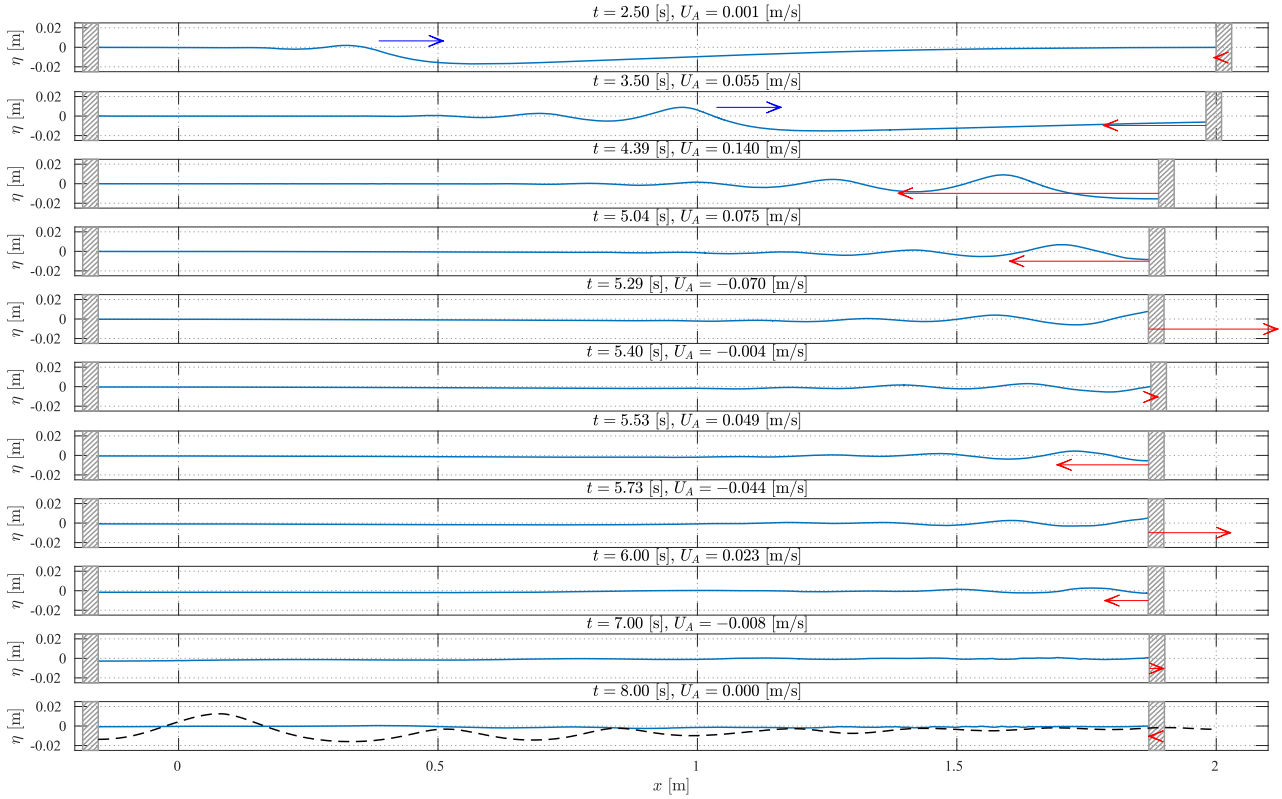

FIG. 18. Wave profile η as a function of the x-coordinate and for times from 2.50 s to 8.00 s. For times t = 2.20 s and 3.50 s, a blue arrow indicates the direction of the incident wave train. The active feedback absorber velocity and direction [in the frame of reference (x', z')] are shown with red arrows. For the last time (t = 8 s), the wave state for the case without absorption is superimposed in the dashed black line.

Fig. 19(a). The error alternates between positive and negative values causing the absorption velocity U_A, which is also shown in the same graph, to behave similarly. The error decreases to zero while the wave-absorber performs the canceling action. The maximum error corresponds to 21% of the mean water level, that is to say, at the limit of the non-linear portion of the plot in Fig. 10(b). It results in an almost fully absorbed wave state at times t = 7 s and 8 s, where the water surface is calm at every location of the wave tank. Note that a reflected wave will take a time greater than $t > 8$ s to arrive into the wave-absorber after reflection at the left wavemaker. That means the error $\varepsilon(t)$ falls to zero rapidly. In Fig. 18, in the last snapshot at t = 8 s, the black dashed curve is obtained with the controller off, and thus, the wave-absorber is at rest, allowing one to qualitatively compare the efficiency of the absorption strategy. It is possible to compute the energy of the wave tank in order to evaluate (and propose) the absorption efficiency of our method. The kinetic energy and potential energy per unit width (in J/m) for the water phase are defined as

$$E_c = \frac{1}{2}\rho \int_{X_G}^{X_A} \int_0^{h+\eta} \left(u_x^2 + u_z^2\right) dxdz,$$
$$E_p = \rho g \int_{X_G}^{X_A} \int_0^{h+\eta} z dxdz, \tag{16}$$

where u_x and u_z are the horizontal and vertical fluid velocities, respectively. The initial energy (at t = 0 s) is equal to the potential energy of the still water level, that is to say, $E_0 = \rho g L h^2/2$. As the tank length is not constant in time since both generating and absorbing wavemakers move at positions $X_G(t)$ and $X_A(t)$, a reference energy, which corresponds to the potential energy of the tank for a still water level retrieved by volume conservation considering these new positions, is defined as

$$E_{ref}(t) = \frac{1}{2}\rho g \left(\frac{L^2 h^2}{X_A(t) - X_G(t)} \right). \tag{17}$$

Results of the energy computations are shown in Fig. 19(b), and they are shown with the initial energy state E_0 as a basis. We observe the decrease in the energy in the system during the generation process (t < 2 s), then a plateau corresponding to the wave propagation stage (2 s ≤ t ≤ 3 s), and finally an increase in the energy (until t = 8 s), which is due to the wave absorption of the incident waves and its convergence until a final energy value. We can compare these results with the case without absorption where we observe a nearly constant value of the total energy once the generating wavemaker stops. It is interesting to note the permanent trade between kinetic and potential energies as the waves reflect on the still wavemakers. The slight decrease in total energy is due to wave attenuation during

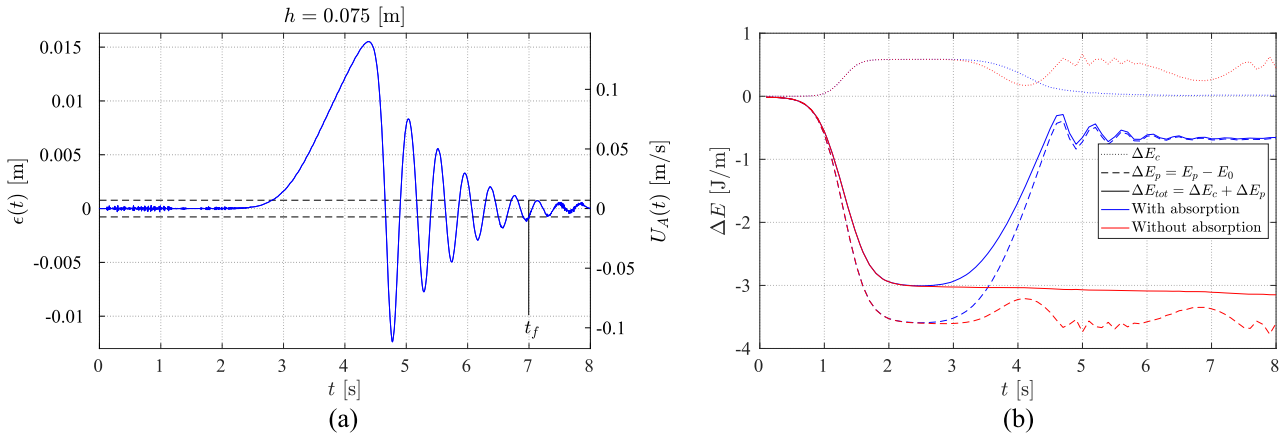

FIG. 19. Case of the absorption of an irregular wave train generated by Eq. (15) for a still water level $h = 0.075$ m. (a) Proportional controller error ε as a function of time. The corresponding velocity of the wave-absorber [in the frame of reference (x', z')] is indicated in the second y axis on the right. The 5% error band is indicated by the black dashed curve, and the corresponding final time $t_f = 7.00$ s is indicated. (b) Energy as a function of time. Kinetic, potential, and total energies are shown with reference to the initial energy in the tank E_0.

propagation and reflection against the still walls. An estimation of the reflection coefficient can be made by computing the energy ratio between incident and reflected waves (adapted from Ref. 46),

$$C_R = \sqrt{\frac{E_R}{E_I}} = \sqrt{\frac{|E_p(t_f) + E_c(t_f) - E_{ref}(t_f)|}{\max(|E_p(t) + E_c(t) - E_{ref}(t)|)}}, \qquad (18)$$

where E_I and E_R are the incident and reflected wave energies and t_f is the time when the error reaches and stays inside 5% of the error band such that $|\varepsilon(t \geq t_f)| \leq \max(|\varepsilon(t)|) \times 5/100$ is verified. The time t_f as well as the 5% error band is indicated in Fig. 19(a). We make sure that at this time, no re-reflection on the absorbing wavemaker has occurred. Perfect wave absorption would lead to $E_{tot} = E_{ref}(t_f)$, but as some reflection happens, this energy level is not reached. It is important to take into account the reference energy as the length of the wave tank is not constant, thus impacting the general level of potential energy. The computation of the reflection coefficient with this method leads to $C_R = 16\%$. Another analysis is carried out thanks to the separation of incident and reflected wave fields by means of the Fourier transform of two wave gauge data recordings at different tank locations.[46] It leads to the value of $C_R = 15\%$, which is similar to the previous one and shows the attenuation in the wave absorption process.

The waterfall plot in Fig. 20(a) helps to visualize the motion of the wavemakers as illustrated by the extension of the wave tank at the left during the wave generation and the oscillations of the wave-absorber wavemaker as the incident waves make contact with the wall sensor. Finally, the efficiency of the process can be observed as

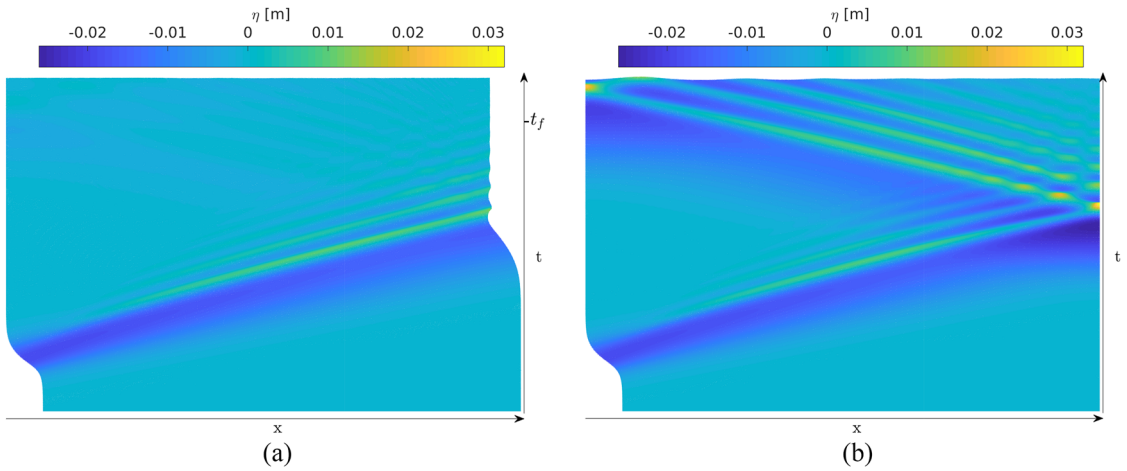

FIG. 20. Waterfall plot of the wave train propagating in the wave tank for a still water level of $h = 0.075$ m. The generating wavemaker follows the velocity defined by Eq. (15). (a) With active absorption. (b) Without active absorption.

the reflected waves are small compared to the initial waves. A comparison with the case without absorption is also plotted in Fig. 20(b) and shows that the wave height at the (still, controller off) wave-absorber wavemaker fully fluctuates between low ($\eta_w < -0.025$ m) and high ($\eta_w > 0.03$ m) values. When the controller is turned on, those fluctuations disappear and $\eta_w \to 0$ as a result of the absorption mechanism.

The second test case consists in an undular bore, which is generated with a velocity square function defined as

$$U_G(t) = U_0(\Theta(t) - \Theta(t - t_0)), \tag{19}$$

where $U_0 = 0.2$ m/s, $t_0 = 2.5$ s, and Θ is the Heaviside function, for a 4 m long wave tank and a still water level of $h = 0.075$ m. The undular bore, shown in Fig. 21, is generated on the left, propagates toward the wave-absorber wavemaker on the right, and is absorbed according to the proportional strategy. In this case, the error is almost always negative at the wave-absorber wall, with variations due to the incoming bore wiggles, as shown in Fig. 22(a). The starting error is important due to the high amplitude incoming undular bore, but rapidly the controller action decreases it and makes the stationary error converge to zero. In Fig. 22(b), the energy analysis is shown and a similar behavior is observed as in the previous case, with an increase in the total energy during the wave generation and a constant level during the propagation stage ($0\,\text{s} \le t \le 2.5$ s for the first one and $2.5\,\text{s} \le t \le 4$ s for the second one).

The total energy then decreases as long as the wave-absorber actuates and converges to the final energy, which corresponds to the final still position of both wavemakers. An estimation of the reflection coefficient can be made with the energy analysis and conducts to $C_R = 10\%$. The analysis of the reflection coefficient in Ref. 46 leads to $C_R = 16\%$. The difference can be explained by the method in Ref. 46, which is not well suited for high amplitude non-linear waves as can be the undular bore. This analysis shows that the strategy is interesting and can effectively absorb non-regular waves, even steep waves.

Finally, tests are carried out on harmonic cases, consisting of the absorption of regular waves generated as for the wave propagation mesh study in Sec. II D 2. The excitation functions and general setups are reported in Table VI. The reflection coefficient is calculated according to Ref. 46 and leads to a value lower than 10% for both cases, showing the efficiency of the proposed strategy in order to absorb waves. A summary of all test cases is reported in Table VI, and the reflection coefficients are given.

When we considered the steady state value of the step response, η_{ss}, it was shown that the water level at the wavemaker reached a constant value after a short time, t_s, at which $\eta_w/h = Fr$, as shown in Fig. 9(b). The absorption velocity and constant coefficient K may be

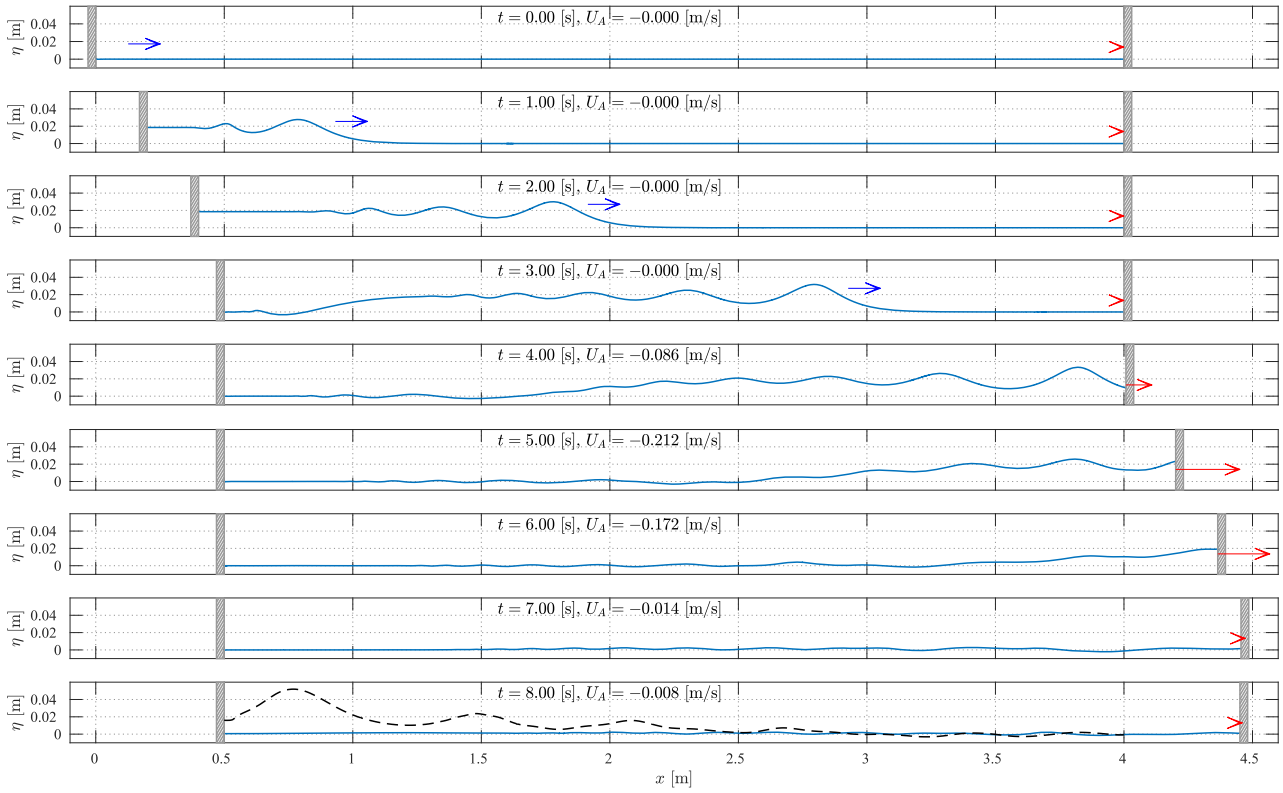

FIG. 21. Wave profile η as a function of the x-coordinate and for times from 0 s to 8.00 s for the undular bore absorption. For times $t = 0$ s and 3 s, a blue arrow indicates the direction of the incident wave train. The active feedback absorber velocity and direction [in the frame of reference (x', z')] are shown with red arrows. For the last time ($t = 8$ s), the wave state for the case without absorption is superimposed in the dashed black line.

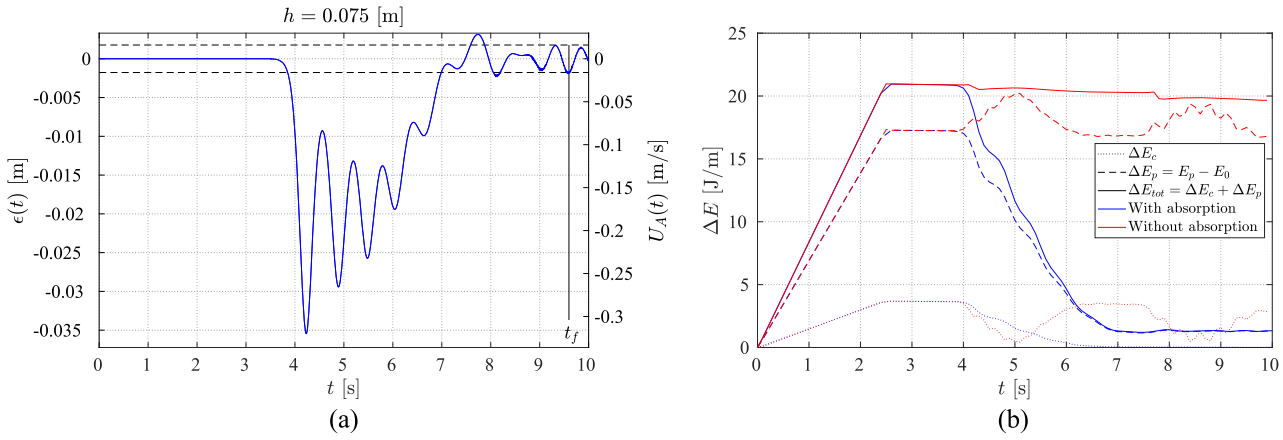

FIG. 22. Case of the absorption of an undular bore generated by Eq. (19) for a still water level $h = 0.075$ m. (a) Proportional controller error ε as a function of time. The corresponding velocity of the wave-absorber [in the frame of reference (x', z')] is indicated in the second y axis on the right. The 5% error band is indicated by the black dashed curve, and the corresponding final time $t_f = 9.49$ s is indicated. (b) Energy as a function of time. Kinetic, potential, and total energies are shown with reference to the initial energy in the tank E_0.

TABLE VI. Test cases for the absorption controller and reflection coefficients.

Wave type	Piston velocity function $U_G(t)$	Parameters	Reflection coefficient C_R	
			Method in Ref. 46 (%)	Energy method (%)
Irregular wave train	$-\frac{S}{\tau}\mathrm{sech}^2\left(\frac{t-t_0}{\tau}\right)$	$h = 0.075$ m, $S = 0.077$ m, $\tau = 0.342$ s, $t_0 = 1.30$ s, $L = 2$ m	15	16
Undular bore	$U_0(\Theta(t) - \Theta(t - t_0))$	$h = 0.075$ m, $U_0 = 0.2$ m/s, $t_0 = 2.5$ s, $L = 4$ m	16	10
Harmonic	$X_0\pi f \sin(2\pi ft + \delta)$	$h = 0.15$ m, $X_0 = 0.004$ m, $f = 1.25$ Hz, $\delta = -\pi/2$, $L = 8$ m	5	...
Harmonic	$X_0\pi f \sin(2\pi ft + \delta)$	$h = 0.05$ m, $X_0 = 0.04$ m, $f = 0.5$ Hz, $\delta = -\pi/2$, $L = 8$ m	9	...

alternatively defined according to $U_A = K\varepsilon(t)$ with $K = \sqrt{g/h}$. This coefficient was already given in Ref. 47 and was deduced from a mathematical study of the problem. The choice of the first strategy based on the overshoot ($K = 1/1.267\sqrt{g/h}$) rather than this last one is justified by the peak time t_p associated with the overshoot, which is shorter than the settling time t_s associated with the steady state, as shown in Fig. 11, or better said, the wavemaker moving at constant speed generates a transient wave that is used to cancel the incident wave.

The active wall driven by a feedback controller has proven to be useful not only to cancel wave reflections but also to attenuate high amplitude irregular wave impacts as in the undular bore example. In the future work, we will push further the absorption strategy to effectively reduce the consequences of extreme high amplitude waves using controllers for non-linear waves.

IV. CONCLUSION

In this work, we performed numerical simulations of a two-dimensional wave tank in order to study the piston-type wavemaker initial-value problem and wave generation using the free and open-source code *OpenFOAM*. The numerical model reproduced the motion of a solid body piston-type wavemaker by moving a solid boundary driven by an external arbitrary signal waveform. We considered a fully viscous model solving the unsteady Navier–Stokes equations on the basis of a two-phase flow strategy and the volume of fluid method to capture the free surface dynamics. Velocity step signals (Heaviside functions) were applied to the piston-type wavemaker, generating a pulse-like wave that propagated along the tank followed by smaller waves or wiggles, which was identified as an undular bore. Recording of the wave elevation time series at the moving wall and in different tank locations was compared with theoretical data, providing a very good agreement and proving the capabilities of the *OpenFOAM* solver *interDyMFoam* to simulate two-phase flows with wave propagation involving both free surfaces and moving boundaries. Wave elevation at the piston wall was found to have close similarity to the time response of the second order system found in feedback theory. In particular, the overshoot and rise, peak, and settling timescales were very close to those in the theory. The scaling found for water elevation at the piston wall at different step

velocities and mean still water levels was in close agreement with that in the theory for low Froude numbers.[11] At higher Froude numbers, the scaling differs considerably from that in the theory, being unable to take into account the main wave dynamics. The resulting main wave pulse is generated and detaches from the piston wall at the same time as the overshoot takes place in the wall elevation signal; thus, we call this wave the overshoot-wave. Results along the tank downstream agree with those of potential theory. The overshoot-wave propagates faster than piston velocity increasing its velocity and reaching asymptotically the shallow water celerity downstream the tank. As we solved fully viscous equations, we were able to quantitatively determine the power input during the step response associated with the wave generation process using the entire stress tensor at the piston wall. Net piston forces were obtained integrating pressure and shear stresses on the piston wall. A power scaling was found for different mean still water levels and step velocities as a function of the Froude number.

Finally, in this work, we proposed a feedback proportional controller driving a secondary piston for wave absorption, where the controller gain was determined from the wavemaker step response. The feedback controlled piston method proved to be very efficient on both regular and irregular wave absorption. This novel approach provided the basis from which more complex active wave generation/absorption strategies can be further implemented on numerical and experimental wave tanks to improve efficiency under the influence of different parameters such as the water depth, the wave steepness, and negative velocity steps.

AUTHORS' CONTRIBUTIONS

C.B. and R.H.H. contributed equally to this work.

ACKNOWLEDGMENTS

C.B. wants to thank LEAF-NL for the use of the computing cluster and experimental facilities. This work was funded by National Agency for Research and Development (ANID)/ Scholarship Program / Doctorado Nacional/2016–21160553. This research was partially supported by the supercomputing infrastructure of the NLHPC (ECM-02). The authors are also grateful to the Marine Energy Research & Innovation Center (MERIC) and the Mechanical Engineering Department (DIMEC) at Universidad de Chile.

DATA AVAILABILITY

The data that support the findings of this study are available from the corresponding author upon reasonable request.

REFERENCES

[1] G. Payne, "Guidance for the experimental tank testing of wave energy converters," Supergen Marine technical report, 2008.
[2] B. Holmes, "Tank testing of wave energy conversion systems: Marine renewable energy guides," EMEC technical report, 2009.
[3] T. H. Havelock, London, Edinburgh Dublin Philos. Mag. J. Sci. **8**, 569 (1929).
[4] F. Biésel and F. Suquet, Houille Blanche **6**, 147 (1951).
[5] F. Ursell, R. G. Dean, and Y. S. Yu, J. Fluid Mech. **7**, 33 (1960).
[6] O. S. Madsen, Coastal Eng. Proc. **1**, 36 (1970).
[7] H. A. Schäffer, Ocean Eng. **23**, 47 (1996).
[8] D. G. Goring, "Tsunamis–the propagation of long waves onto a shelf," Technical Report 38, 1978.
[9] J. Boussinesq, J. Math. Pures Appl. **17**, 55 (1872).
[10] W. M. Lin, J. J. Newman, and D. K. Yue, in *Proceedings of 15th Symposium on Naval Hydrodynamics* (Washington National Academy Press, 1984), pp. 33–49.
[11] S. W. Joo, W. W. Schultz, and A. F. Messiter, J. Fluid Mech. **214**, 161 (1990).
[12] A. J. Roberts, Q. J. Mech. Appl. Math. **40**, 129 (1987).
[13] S. W. Joo and M. S. Park, J. Mech. Sci. Technol. **20**, 882 (2006).
[14] M. A. Grosenbaugh and R. W. Yeung, J. Fluid Mech. **209**, 57 (1989).
[15] J. Uddin and D. J. Needham, J. Fluid Mech. **776**, 37 (2015).
[16] C. Song and A. I. Sirviente, Phys. Fluids **16**, 2649 (2004).
[17] H. A. Wolgamot and C. J. Fitzgerald, Proc. Inst. Mech. Eng., Part A **229**, 772 (2015).
[18] P. Higuera, I. J. Losada, and J. L. Lara, Coastal Eng. **101**, 35 (2015).
[19] A. Khait and L. Shemer, Phys. Fluids **30**, 057103 (2018).
[20] C. W. Hirt and B. D. Nichols, J. Comput. Phys. **39**, 201 (1981).
[21] G. Clauss and C. E. Schmittner *et al.*, in *ASME 2005 24th International Conference on Offshore Mechanics and Arctic Engineering* (American Society of Mechanical Engineers Digital Collection, 2005), pp. 785–792.
[22] A. Maguire and D. Ingram, in *Eighth European Wave and Tidal Energy Conference* (EWTEC, Uppsala, Sweden, 2009), pp. 7–10.
[23] A. Maguire and D. Ingram, in *Proceedings on the Third International Conference of the Application of Physical Modelling to Port and Coastal Protection* (COASTLAB, 2010), p. 1.
[24] M. A. Bhinder, C. G. Mingham, D. M. Causon, M. T. Rahmati, G. A. Aggidis, and R. V. Chaplin, "A joint numerical and experimental study of a surging point absorbing wave energy converter (WRASPA)," in Ocean Engineering; Ocean Renewable Energy; Ocean Space Utilisation, Parts A and B (2009), Vol. 4, pp. 869–875.
[25] P. Higuera, J. L. Lara, and I. J. Losada, Coastal Eng. **71**, 102 (2013).
[26] C. Altomare, J. M. Domínguez, A. J. C. Crespo, J. González-Cao, T. Suzuki, M. Gómez-Gesteira, and P. Troch, Coastal Eng. **127**, 37 (2017).
[27] D. Liang, W. Jian, S. Shao, R. Chen, and K. Yang, J. Fluids Struct. **69**, 72 (2017).
[28] N. S. Nise, *Control System Engineering* (John Wiley & Sons, New York, 2011).
[29] A. E. Maguire, http://hdl.handle.net/1842/5780, 2011.
[30] E. Berberović, N. P. Van Hinsberg, S. Jakirlić, I. V. Roisman, and C. Tropea, Phys. Rev. E: Stat., Nonlinear, Soft Matter Phys. **79**, 036306 (2009).
[31] H. Rusche, "Computational fluid dynamics of dispersed two-phase flows at high phase fractions," Ph.D. thesis, University of London, 2002.
[32] S. A. Yang and A. T. Chwang, J. Eng. Mech. **118**, 735 (1992).
[33] H. G. Weller, G. Tabor, H. Jasak, and C. Fureby, Comput. Phys. **12**, 620 (1998).
[34] S. Patankar, *Numerical Heat Transfer and Fluid Flow* (CRC Press, 1980).
[35] R. I. Issa, J. Comput. Phys. **62**, 40 (1986).
[36] I. B. Celik, U. Ghia, P. J. Roache, and C. J. Freitas, J. Fluids Eng. **130**, 078001 (2008).
[37] E. Didier, P. R. F. Teixeira, and M. G. Neves, Defect Diffus. Forum **372**, 1 (2017).
[38] E. Buckingham, Phys. Rev. **4**, 345 (1914).
[39] H. Favre, *Étude théorique et expérimentale des ondes de translation dans les canaux découverts* (Dunod, 1935), Vol. 150.
[40] D. H. Peregrine, J. Fluid Mech. **25**, 321 (1966).
[41] J. J. Stoker, *Water Waves: The Mathematical Theory with Applications* (Wiley-Interscience, 1957), p. 328.
[42] S. D. Hatland and H. Kalish, Phys. Fluids **31**, 033601 (2019).
[43] P. A. Madsen, D. R. Fuhrman, and H. A. Schäffer, J. Geophys. Res.: Oceans **113**, C12012 (2008).
[44] D. Ingram, R. Wallace, A. Robinson, and I. Bryden, in *Proceedings of Oceans 2014 MTS/IEEE* (Institute of Electrical and Electronics Engineers, IEEE, Taipei, Taiwan, USA, 2014).
[45] J. P. McHugh and D. W. Watt, Phys. Fluids **10**, 324 (1998).
[46] Y. Goda and Y. Suzuki, "Estimation of incident and reflected waves in random wave experiments," Coastal Eng. **1**(15), 47 (1976).
[47] H. A. Schäffer and K. Jakobsen, "Non-linear wave generation and active absorption in wave flumes," in Long Waves Symposium, Thessaloniki, Greece, 2003.